

ELECTRONIC SPECTROSCOPY, PHOTOCHEMISTRY, AND REACTIVITY OF
ISOPRENE-DERIVED CRIEGEE INTERMEDIATES

Michael F. Vansco

A DISSERTATION

in

Chemistry

Presented to the Faculties of the University of Pennsylvania

in

Partial Fulfillment of the Requirements for the

Degree of Doctor of Philosophy

2020

Supervisor of Dissertation

Dr. Marsha I. Lester, Edmund J. Khan Distinguished Professor

Graduate Group Chairperson

Dr. Daniel J. Mindiola, Brush Family Professor of Chemistry

Dissertation Committee

Dr. Jessica M. Anna, Assistant Professor of Chemistry

Dr. Joseph Subotnik, Edmund J. and Louise W. Kahn Endowed Term Professor of Chemistry

Dr. Feng Gai, Edmund J. and Louise W. Kahn Endowed Term Professor of Chemistry

ELECTRONIC SPECTROSCOPY, PHOTOCHEMISTRY, AND REACTIVITY OF ISOPRENE-
DERIVED CRIEGEE INTERMEDIATES

COPYRIGHT

2020

Michael F. Vansco

DEDICATION

To my friends and family.

ACKNOWLEDGMENTS

The first year of graduate school was extremely challenging for me, and at times, I did not think I was cut out for this journey. It is imperative that I first acknowledge my PhD advisor, Marsha Lester, for taking a chance on a kid coming out of the University of Rhode Island, seeing the potential in me, supporting me, and pushing me to become the best that I can be. I have grown tremendously as a scientist and as a professional from her mentorship. Joining Marsha's group was the professional best decision I could have made and will be forever grateful to her.

Next, I'd like to acknowledge our collaborators at Sandia National Laboratory (Dr. Craig Taatjes, Dr. David Osborn, and Dr. Kendrew Au), Argonne National Laboratory (Dr. Stephen Klippenstein), and NASA Jet Propulsion Laboratory (Dr. Carl Percival, Dr. Fred Winiberg, and Dr. Kristen Zuraski). It has been an honor and pleasure to work with you all on complex problems related to chemical physics and atmospheric chemistry.

I'd like to give a special acknowledgement to Dr. Rebecca Caravan for mentoring me on several projects associated with this dissertation. She has been incredibly supportive of me throughout my PhD and I have learned so much from her. I am extremely excited to continue my journey in science with her at Argonne National Laboratory.

I'd also like to acknowledge my committee members Dr. Jessica Anna, Dr. Joseph Subotnik, and Dr. Feng Gai for their thoughtful guidance throughout my PhD. In addition, I'd like to thank Dr. Patrick Walsh and Dr. Nisalak Trongsiwat for synthesizing the precursors for the isoprene-derived Criegee intermediates. Without you, none of this work could be possible.

To my past and present lab mates in the Lester group: I am extremely proud and thankful to have worked alongside and learned from each one of you. To Hongwei Li: thank you for mentoring me my first summer in the group, answering my endless questions, teaching me the wonderful velocity map imaging technique, and preparing me to be successful in the group. To Dr. Amy Green: thank you for teaching me the tricks of the time-of-flight experiment, for taking me

to get burgers and milk shakes after a hard day in the lab, and for all of the advice you have given me. To Dr. Yi Fang: it was a pleasure learning from you in the lab, bouncing ideas off you in the office, and bonding with you over basketball. To Dr. Barbara Marchetti: some of my fondest memories in lab are working with you; it was always a pleasure. Thank you for teaching me so much about electronic spectroscopy, photochemistry, and velocity map imaging. Also, thank you and Tolga for always being so generous to me. To Shubranshu Pandit: thank you for always being so willing to discuss interesting topics and ideas with me. You are extremely knowledgeable, generous, and kind, and I am grateful to have learned from you. To Anne Reinholdt: it has been a pleasure being your office mate this past year. Thank you for all the great science and life discussions. I always look forward to catching up with you about what is going on in our lives and look forward to continuing our friendship for years to come. To Trisha Bhagde, Guanghan Wang, Vincent Esposito, Tianlin Liu, Ziao Liu, Meijun Zou, Olivia Werba, and Trent McHenry, thank you for the fun times in lab, for getting lunch with me, and being wonderful lab mates. I am excited to hear about your future successes and hope we cross paths again. Finally, I'd like to give a special acknowledgement to Dr. Tori Barber, who has been a wonderful and supportive friend to me since the beginning of graduate school. She introduced me to so many places in Philadelphia and I have come to love this city almost as much as she does. The door to her home has always been open for dinners, barbecues, fun games, or just for a good hang. She is an extraordinary human being and I am so excited to watch her career in science blossom.

Finally, thank you to my partner, Sara Beenders, whose support through my failures and successes of graduate school has been unwavering. Thank you for always making sure I was taking care of myself while recognizing how important my work is to me. I am so excited to see where life takes us.

ABSTRACT

ELECTRONIC SPECTROSCOPY, PHOTOCHEMISTRY, AND REACTIVITY OF ISOPRENE-DERIVED CRIEGEE INTERMEDIATES

Michael F. Vansco

Marsha I. Lester

Ozonolysis is an important sink of alkenes in Earth's troposphere, leading to the formation of highly reactive carbonyl oxide ($R_1R_2C=O^+O^-$) species known as Criegee intermediates. Ozonolysis of isoprene, the most abundant non-methane volatile organic compound emitted into the atmosphere, can generate three distinct Criegee intermediates: formaldehyde oxide (CH_2OO), methyl vinyl ketone oxide (MVK-oxide), and methacrolein oxide (MACR-oxide). Due to the abundance of isoprene in the atmosphere, the unimolecular and bimolecular reactions of Criegee intermediates may significantly impact the composition of the troposphere. The laboratory synthesis and direct detection of MVK-oxide and MACR-oxide is achieved through reaction of photolytically generated, resonance-stabilized iodoalkene radicals with oxygen. MVK-oxide and MACR-oxide are characterized on their first $\pi^* \leftarrow \pi$ transition using a ground-state depletion method under jet-cooled conditions. These Criegee intermediates exhibit broad ultraviolet-visible (UV-vis) spectra with strong absorption (ca. $10^{17} \text{ cm}^2 \text{ molec}^{-1}$). Electronic excitation of Criegee intermediates results in nonadiabatic coupling to repulsive potentials and prompt release of O 1D products. Velocity map imaging is used to determine the angular and velocity distributions of the O-atom products following UV-vis excitation of the isoprene-derived Criegee intermediates. UV-vis transient absorption spectroscopy permits study of the bimolecular reactions of MVK-oxide with SO_2 , formic

acid, and water vapor under thermal conditions. Complimentary experiments using multiplexed photoionization mass spectrometry (MPIMS) identify products resulting from reaction of MVK-oxide with SO₂ and formic acid. The reaction of MVK-oxide with deuterated formic acid reveals multiple reaction channels including adduct formation and formic acid catalyzed isomerization yielding a vinyl hydroperoxide. Through a combination of experiment, theory, and global modeling, *syn* conformers of MVK-oxide are shown to survive high-humidity tropospheric environments and play a role in sulfuric acid formation and formic acid removal. In contrast, *anti*-MVK-oxide and *syn*-MACR-oxide conformers are predicted to be removed rapidly from the atmosphere via electrocyclic ring closure to form a cyclic dioxole, which subsequently decays to oxygenated hydrocarbon radical products. These radicals react rapidly with oxygen and their stable carbonyl products are detected using MPIMS.

TABLE OF CONTENTS

ACKNOWLEDGMENTS	IV
LIST OF TABLES	XIII
CHAPTER 1 INTRODUCTION.....	1
1. Isoprene Derived Criegee Intermediates	5
2. Photoionization, Electronic spectroscopy, and kinetic measurements of Criegee intermediates	6
3. Unimolecular decay and bimolecular reactions of Criegee intermediates	12
4. Summary of Thesis	37
References	43
CHAPTER 2 PROMPT RELEASE OF O ¹D PRODUCTS UPON UV EXCITATION OF CH₂OO CRIEGEE INTERMEDIATES.....	48
I. Introduction	49
II. Experimental Methods.....	55
III. Results	56
IV. Discussion.....	61
V. Conclusions	68
Acknowledgments	69
References	69
CHAPTER 3 ELECTRONIC SPECTROSCOPY OF METHYL VINYL KETONE OXIDE: A FOUR-CARBON UNSATURATED CRIEGEE INTERMEDIATE FROM ISOPRENE OZONOLYSIS.....	71
I. Introduction	72
II. Theoretical Methods and Results.....	76
III. Experimental Methods.....	87

IV. Results	90
V. Discussion	103
A. Comparison of experimental and theoretical MVK-oxide UV-vis spectra.....	103
B. Electronic transitions of other possible isomers	105
VI. Conclusions	109
Acknowledgements	111
References	111
CHAPTER 4 SYNTHESIS, ELECTRONIC SPECTROSCOPY, AND PHOTOCHEMISTRY OF METHACROLEIN OXIDE: A FOUR-CARBON UNSATURATED CRIEGEE INTERMEDIATE FROM ISOPRENE OZONOLYSIS	114
1. Introduction	115
2. Results	123
2.1 Laboratory synthesis of MACR-oxide	123
2.2. Electronic transitions of MACR-oxide: Theoretical predictions and experimental findings	127
2.3. Photodissociation dynamics of MACR-oxide	141
3. Discussion	148
3.1 Weak oscillatory structure at long wavelengths.....	148
3.2 Comparison of MACR-oxide and MVK-oxide	150
3.3 Electronic transitions of other possible isomers.....	151
4. Conclusions	155
Acknowledgements	157
References	158
CHAPTER 5 FIRST DIRECT KINETIC MEASUREMENTS AND THEORETICAL PREDICTIONS OF AN ISOPRENE-DERIVED CRIEGEE INTERMEDIATE....	161
Introduction/background	162
Results/discussion	167
Spectroscopy and unimolecular decay	167
Bimolecular Kinetics.....	176
Atmospheric modelling.....	193
Conclusions	194
Methods and Materials	197
Acknowledgements	198

References	199
------------------	-----

**CHAPTER 6 EXPERIMENTAL EVIDENCE OF DIOXOLE UNIMOLECULAR
DECAY PATHWAY FOR ISOPRENE-DERIVED CRIEGEE INTERMEDIATES
..... 202**

I. Introduction	203
-----------------------	-----

II. Background	208
----------------------	-----

III. Methods	217
--------------------	-----

IV. Results	220
-------------------	-----

A. MVK-oxide	220
--------------------	-----

B. MACR-oxide	229
---------------------	-----

V. Discussion	237
---------------------	-----

A. Product Yields	237
-------------------------	-----

B. Scavenger experiments	239
--------------------------------	-----

C. Atmospheric implications	243
-----------------------------------	-----

VI. Conclusions	246
-----------------------	-----

Acknowledgements	247
------------------------	-----

References	248
------------------	-----

**CHAPTER 7 FORMIC ACID CATALYZED ISOMERIZATION AND ADDUCT
FORMATION OF AN ISOPRENE-DERIVED CRIEGEE INTERMEDIATE:
EXPERIMENT AND THEORY..... 252**

I. Introduction	253
-----------------------	-----

II. Experimental	260
------------------------	-----

III. Results	261
--------------------	-----

IV. Discussion	277
----------------------	-----

A. H/D Exchange	279
-----------------------	-----

B. Product Branching	280
----------------------------	-----

C. Comparison of MVK-oxide and CH ₂ OO reactions with formic acid	282
--	-----

V. Conclusion	283
---------------------	-----

Acknowledgements	284
------------------------	-----

References	285
------------------	-----

**APPENDIX I PROMPT RELEASE OF O¹D PRODUCTS UPON UV
EXCITATION OF CH₂OO CRIGEE INTERMEDIATES SUPPLEMENTARY
MATERIAL 288**

References 296

**APPENDIX II ELECTRONIC SPECTROSCOPY OF METHYL VINYL KETONE
OXIDE: A FOUR-CARBON UNSATURATED CRIGEE INTERMEDIATE FROM
ISOPRENE OZONOLYSIS SUPPLEMENTARY MATERIAL 297**

**APPENDIX III SYNTHESIS, ELECTRONIC SPECTROSCOPY AND
PHOTOCHEMISTRY OF METHACROLEIN OXIDE: A FOUR-CARBON
UNSATURATED CRIGEE INTERMEDIATE FROM ISOPRENE OZONOLYSIS
SUPPORTING INFORMATION..... 311**

Section S1. Synthesis of (*E*)-1,3-diiodo-2-methylprop-1-ene 312
S1.1. Overview of (*E*)-1,3-diiodo-2-methylprop-1-ene precursor synthesis..... 312
S1.2. Diethyl methylmalonate¹ 312
S1.3. Diethyl 2-(diiodomethyl)-2-methylmalonate²..... 314
S1.4. (*E*)-3-Iodo-2-methylprop-2-enoic acid² 315
S1.5. (*E*)-3-Iodo-2-methylprop-2-en-1-ol² 315
S1.6. (*E*)-3-Iodo-2-methylallyl methanesulfonate³ 316
S1.7. (*E*)-1,3-Diiodo-2-methylprop-1-ene³ 316

Section S2. Ground state energies and vertical excitation energies of MACR-oxide 328

Section S3. Spectroscopic Methods 341

Section S4. Details of Lorentzian fitting to MACR-oxide electronic spectrum..... 348

**Section S5. Details of theoretical absorption profile calculations and dissociation energies
..... 349**

S5.1. Theoretical absorption profiles 349
S5.2. Dissociation energies 356

**Section S6. Excitation of MACR-oxide on its second $\pi^* \leftarrow \pi$ transition and VMI
background subtraction 356**

References 372

**APPENDIX IV FIRST DIRECT KINETIC MEASUREMENTS AND
THEORETICAL PREDICTIONS OF AN ISOPRENE-DERIVED CRIGEE
INTERMEDIATE SUPPORTING INFORMATION..... 374**

1. Methods 376
1.1 Sandia transient absorption experiment 376
1.2 Sandia MPIMS 377
1.3 IAMS transient absorption experiment..... 378

1.4 Global atmospheric modelling.....	379
1.5 Computational kinetics and mechanistic investigations.....	384
2. Computational MVK-oxide isomerization kinetics	384
3. MVK-oxide kinetics and reaction mechanisms.....	390
3.1 MVK-oxide formation and unimolecular decay	390
3.2 MVK-oxide + SO ₂	390
3.3 MVK-oxide + formic acid	412
3.4 MVK-oxide + water monomer	426
4. Global chemical modelling evaluation of particulate formation from MVK-oxide + SO₂	438
5. <i>Ab initio</i> optimized geometries and frequencies	443
5.1 MVK-oxide.....	443
5.2 MVK-oxide + H ₂ O.....	446
5.3 MVK-oxide + SO ₂	476
5.4 MVK-oxide + formic acid.....	503
APPENDIX V EXPERIMENTAL EVIDENCE OF DIOXOLE UNIMOLECULAR DECAY PATHWAY FOR ISOPRENE-DERIVED CRIEGEE INTERMEDIATES SUPPORTING INFORMATION.....	507
Section S1. Product branching analysis	508
Section S2. Theoretical calculations.....	515
Section S3. MESMER input file	516
Vinoxy radical + O ₂ MESMER input.....	520
2-methyl-vinoxy + O ₂ MESMER input	537
References	554
APPENDIX VI FORMIC ACID CATALYZED ISOMERIZATION AND ADDUCT FORMATION OF AN ISOPRENE-DERIVED CRIEGEE INTERMEDIATE: EXPERIMENT AND THEORY.....	555
Section S1. MVK-oxide + H₂-formic acid.....	556
Section S2: Theoretical reaction pathways.....	556
Overview	556
Stationary Point Energies.....	559
Temperature and Pressure Dependent Kinetics.....	591
Section S3: H/D Exchange	600
Section S4. Stationary point geometries	613
References.....	651

LIST OF TABLES

CHAPTER 1 INTRODUCTION.....	1
Table 1.....	11
Table 2.....	18
Table 3.....	21
Table 4.....	26
Table 5.....	29
Table 6.....	32
CHAPTER 2 PROMPT RELEASE OF O¹D PRODUCTS UPON UV EXCITATION OF CRIEGEE INTERMEDIATES.....	48
CHAPTER 3 ELECTRONIC SPECTROSCOPY OF METHYL VINYL KETONE OXIDE: A FOUR-CARBON UNSATURATED CRIEGEE INTERMEDIATE FROM ISOPRENE OZONOLYSIS.....	71
Table 1.....	77
CHAPTER 4 SYNTHESIS, ELECTRONIC SPECTROSCOPY, AND PHOTOCHEMISTRY OF METHACROLEIN OXIDE: A FOUR-CARBON UNSATURATED CRIEGEE INTERMEDIATE FROM ISOPRENE OZONOLYSIS	114
Table 1.....	128
Table 2.....	129
CHAPTER 5 FIRST DIRECT KINETIC MEASUREMENTS AND THEORETICAL PREDICTIONS OF AN ISOPRENE-DERIVED CRIEGEE INTERMEDIATE....	161
CHAPTER 6 EXPERIMENTAL EVIDENCE OF DIOXOLE UNIMOLECULAR DECAY PATHWAY FOR ISOPRENE-DERIVED CRIEGEE INTERMEDIATES	202
CHAPTER 7 FORMIC ACID CATALYZED ISOMERIZATION AND ADDUCT FORMATION OF AN ISOPRENE-DERIVED CRIEGEE INTERMEDIATE: EXPERIMENT AND THEORY.....	252

APPENDIX I PROMPT RELEASE OF O¹D PRODUCTS UPON UV EXCITATION OF CH₂OO CRIGEE INTERMEDIATES SUPPLEMENTARY MATERIAL	288
--	------------

APPENDIX II ELECTRONIC SPECTROSCOPY OF METHYL VINYL KETONE OXIDE: A FOUR-CARBON UNSATURATED CRIGEE INTERMEDIATE FROM ISOPRENE OZONOLYSIS SUPPLEMENTARY MATERIAL	297
--	------------

Table S1	305
Table S2	306
Table S3	307
Table S4	308
Table S5	310

APPENDIX III SYNTHESIS, ELECTRONIC SPECTROSCOPY AND PHOTOCHEMISTRY OF METHACROLEIN OXIDE: A FOUR-CARBON UNSATURATED CRIGEE INTERMEDIATE FROM ISOPRENE OZONOLYSIS SUPPORTING INFORMATION.....	311
---	------------

Table S1	326
Table S2	331
Table S3	333
Table S4	334
Table S5	342
Table S6	352
Table S7	357
Table S8	358
Table S9	362
Table S10	367
Table S11	369
Table S12	371

APPENDIX IV FIRST DIRECT KINETIC MEASUREMENTS AND THEORETICAL PREDICTIONS OF AN ISOPRENE-DERIVED CRIEGEE INTERMEDIATE SUPPORTING INFORMATION..... 374

Table S1 381

Table S2 386

Table S3 388

Table S4 389

Table S5 401

Table S6 414

Table S7 420

Table S8 429

Table S9 432

Table S10 433

APPENDIX V EXPERIMENTAL EVIDENCE OF DIOXOLE UNIMOLECULAR DECAY PATHWAY FOR ISOPRENE-DERIVED CRIEGEE INTERMEDIATES SUPPORTING INFORMATION..... 507

Table S1 517

Table S2 519

APPENDIX VI FORMIC ACID CATALYZED ISOMERIZATION AND ADDUCT FORMATION OF AN ISOPRENE-DERIVED CRIEGEE INTERMEDIATE: EXPERIMENT AND THEORY SUPPORTING INFORMATION..... 555

Table S1 561

Table S2 565

Table S3 581

Table S4 582

Table S5 583

Table S6 589

Table S7 611

LIST OF ILLUSTRATIONS

CHAPTER 1 INTRODUCTION.....	1
Scheme 1	2
Scheme 2	4
Scheme 3	7
Scheme 4	14
Scheme 5	15
Scheme 6	17
Scheme 7	23
Scheme 8	27
Scheme 9	30
Figure 1	36
CHAPTER 2 PROMPT RELEASE OF O¹D PRODUCTS UPON UV EXCITATION OF CH₂OO CRIEGEE INTERMEDIATES.....	48
Figure 1	54
Figure 2	58
Figure 3	64
CHAPTER 3 ELECTRONIC SPECTROSCOPY OF METHYL VINYL KETONE OXIDE: A FOUR-CARBON UNSATURATED CRIEGEE INTERMEDIATE FROM ISOPRENE OZONOLYSIS.....	71
Scheme 1	73
Figure 1	80
Figure 2	83
Figure 3	86
Figure 4	92
Figure 5	95

Figure 6	98
Figure 7	101
Scheme 2	106
Scheme 3	108
CHAPTER 4 SYNTHESIS, ELECTRONIC SPECTROSCOPY, AND PHOTOCHEMISTRY OF METHACROLEIN OXIDE: A FOUR-CARBON UNSATURATED CRIGEEE INTERMEDIATE FROM ISOPRENE OZONOLYSIS	114
Scheme 1	116
Figure 1	120
Scheme 2	124
Scheme 3	126
Figure 2	131
Figure 3	134
Figure 4	137
Figure 5	140
Figure 6	143
Figure 7	146
Scheme 4	153
Scheme 5	154
CHAPTER 5 FIRST DIRECT KINETIC MEASUREMENTS AND THEORETICAL PREDICTIONS OF AN ISOPRENE-DERIVED CRIGEEE INTERMEDIATE....	161
Scheme 1	163
Figure 1	169
Scheme 2	171
Scheme 3	172
Figure 2	175

Figure 3	179
Figure 4	181
Scheme 4	182
Figure 5	185
Figure 6	187
Scheme 5	188
Figure 7	191
Figure 8	196
CHAPTER 6 EXPERIMENTAL EVIDENCE OF DIOXOLE UNIMOLECULAR DECAY PATHWAY FOR ISOPRENE-DERIVED CRIEGEE INTERMEDIATES	202
Scheme 1	204
Scheme 2	206
Scheme 3	209
Scheme 4	211
Scheme 5	213
Scheme 6	214
Scheme 7	216
Scheme 8	218
Scheme 9	219
Figure 1	223
Figure 2	226
Figure 3	228
Figure 4	231
Figure 5	233
Figure 6	236
Figure 7	241

CHAPTER 7 FORMIC ACID CATALYZED ISOMERIZATION AND ADDUCT FORMATION OF AN ISOPRENE-DERIVED CRIEGEE INTERMEDIATE: EXPERIMENT AND THEORY PAPER	252
Scheme 1	255
Scheme 2	258
Scheme 3	259
Scheme 4	262
Scheme 5	263
Figure 1	265
Figure 2	268
Figure 3	270
Figure 4	273
Scheme 6	276
 APPENDIX I PROMPT RELEASE OF O¹D PRODUCTS UPON UV EXCITATION OF CH₂OO CRIEGEE INTERMEDIATES SUPPLEMENTARY MATERIAL	 288
Figure S1	290
Figure S2.....	292
Figure S3.....	294
Table S1	295
 APPENDIX II ELECTRONIC SPECTROSCOPY OF METHYL VINYL KETONE OXIDE: A FOUR-CARBON UNSATURATED CRIEGEE INTERMEDIATE FROM ISOPRENE OZONOLYSIS SUPPLEMENTARY MATERIAL	 297
Scheme S1	298
Figure S1	300
Figure S2.....	302
Figure S3.....	304

**APPENDIX III SYNTHESIS, ELECTRONIC SPECTROSCOPY AND
PHOTOCHEMISTRY OF METHACROLEIN OXIDE: A FOUR-CARBON
UNSATURATED CRIEGEE INTERMEDIATE FROM ISOPRENE OZONOLYSIS
SUPPORTING INFORMATION ELECTRONIC 311**

Figure S1	319
Figure S2.....	321
Figure S3.....	323
Figure S4.....	325
Figure S5.....	330
Figure S6.....	340
Figure S7.....	344
Figure S8.....	347
Figure S9.....	351
Figure S10.....	355
Figure S11.....	361
Figure S12.....	364
Figure S13.....	366

**APPENDIX IV FIRST DIRECT KINETIC MEASUREMENTS AND
THEORETICAL PREDICTIONS OF AN ISOPRENE-DERIVED CRIEGEE
INTERMEDIATE SUPPORTING INFORMATION..... 374**

Figure S1	392
Figure S2.....	394
Figure S3.....	397
Figure S4.....	400
Figure S5.....	406
Figure S6.....	408
Figure S7.....	410
Figure S8.....	417

Figure S9.....	422
Figure S10.....	425
Figure S11.....	435
Figure S12.....	440

**APPENDIX V EXPERIMENTAL EVIDENCE OF DIOXOLE UNIMOLECULAR
DECAY PATHWAY FOR ISOPRENE-DERIVED CRIEGEE INTERMEDIATES
SUPPORTING INFORMATION..... 507**

Figure S1.....	510
Figure S2.....	512
Figure S3.....	514

**APPENDIX VI FORMIC ACID CATALYZED ISOMERIZATION AND ADDUCT
FORMATION OF AN ISOPRENE-DERIVED CRIEGEE INTERMEDIATE:
EXPERIMENT AND THEORY SUPPORTING INFORMATION..... 555**

Figure S1.....	558
Figure S2.....	567
Figure S3.....	571
Figure S4.....	573
Figure S5.....	576
Figure S6.....	578
Figure S7.....	580
Figure S8.....	585
Figure S9.....	588
Figure S10.....	594
Figure S11.....	596
Figure S12.....	602
Figure S13.....	604
Figure S14.....	606

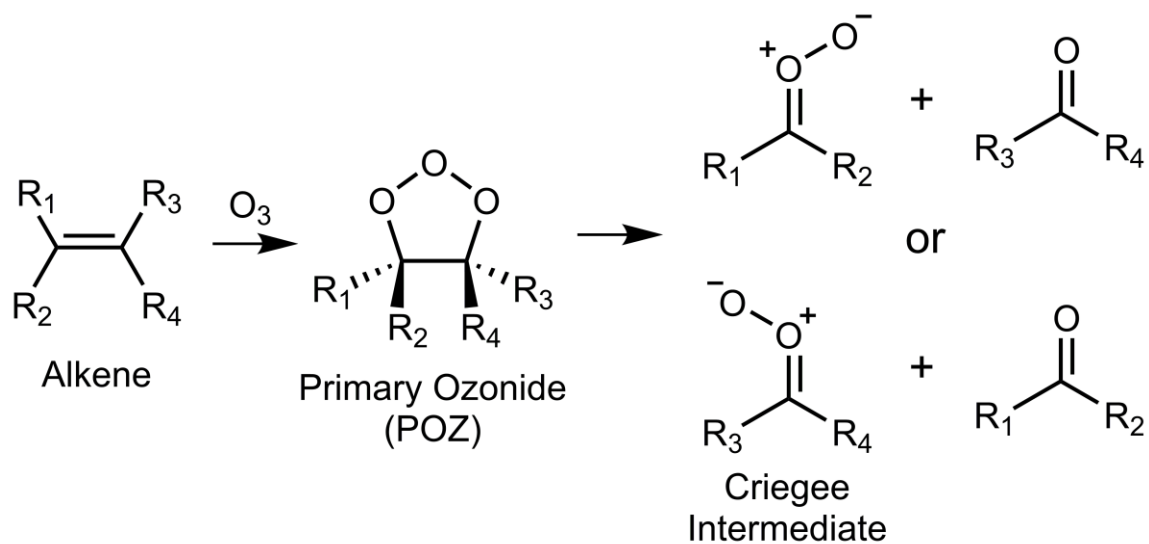
Figure S15	608
Scheme S1	610

CHAPTER 1

Introduction

Alkenes are the most abundant non-methane volatile organic compounds (VOCs) emitted into the Earth's atmosphere, having both biogenic and anthropogenic sources.^{1,2} Ozonolysis is a significant removal pathway for alkenes and generates reactive carbonyl oxide species ($R_1R_2C=O^+O^-$) called Criegee intermediates that significantly impact the composition of the atmosphere.³ Ozonolysis proceeds through the cycloaddition of ozone across the C=C double bond of an alkene to form a primary ozonide (POZ) as illustrated in Scheme 1. This process is highly exothermic (ca. 50 kcal mol⁻¹)⁴ and results in decomposition of the POZ, generating a Criegee intermediate and a carbonyl coproduct. The nascent Criegee intermediates are formed with a broad distribution of internal energies.³ The fraction of the Criegee intermediates that are formed with a high degree of internal excitation will undergo prompt unimolecular decomposition to hydroxyl (OH) radicals,^{5,6} the most important oxidant in the atmosphere,^{7,8} and other products.

The remaining Criegee intermediates will be thermalized through collisions to form so-called stabilized Criegee intermediates. Stabilized Criegee intermediates can have a variety of fates that depend on their substituents (R^1 and R^2) as well as their conformational form (Section 3).^{9,10} They can undergo thermal unimolecular decay to form OH radicals and other products, further impacting the oxidative capacity of the atmosphere.^{5,6,11-14} Field measurements have shown that alkene ozonolysis is responsible for ca. $\frac{1}{3}$ of the OH radicals formed in the daytime,^{15,16} and essentially all of the OH radicals formed at night.¹⁷ If thermal unimolecular decay is slow, the stabilized Criegee intermediates can act as atmospheric oxidants themselves by reacting with

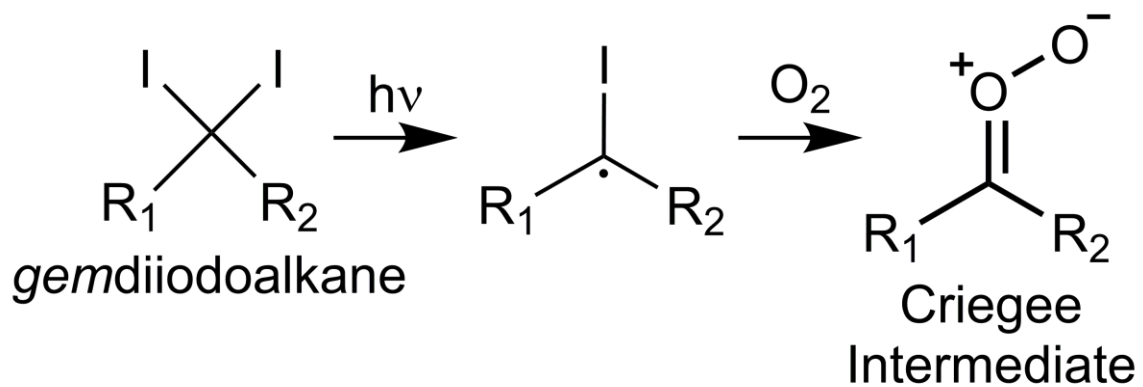


Scheme 1. Illustration of the alkene ozonolysis reaction, in which ozone adds across the double bond of an alkene in an exothermic reaction to form a primary ozonide (POZ) that subsequently decays to carbonyl oxide (Criegee intermediate) and carbonyl co-products.

water vapor¹⁸⁻³¹ or other trace atmospheric species such as SO₂^{19, 31-42} and organic acids.^{31, 43-50} These reactions generate a variety of highly oxygenated molecules including functionalized hydroperoxides and SO₃ that are implicated in the formation of secondary organic aerosols (SOA), which impact air quality and climate.^{10, 34, 42, 51-53}

Alkene ozonolysis gives rise to a diverse pool of Criegee intermediates, each with nuanced decomposition pathways that results in a rich body of chemistry. An overwhelming amount of unimolecular and bimolecular reaction rates, including temperature and pressure dependences, must be well determined to accurately assess the impact Criegee intermediates have on the atmosphere. Laboratory experiments aim to establish benchmarks for the reactivity of Criegee intermediates such that theory-based structure-activity relationships for their reaction rates can be accurately determined and implemented in global models.⁹ However, accurate kinetic measurements of Criegee intermediates formed from alkene ozonolysis is extremely difficult owing to low steady state concentrations ($\leq 10^4 \text{ cm}^{-3}$)^{9, 10, 54-56} from slow formation via ozonolysis and rapid loss from unimolecular and bimolecular processes.³

Although the Criegee mechanism for alkene ozonolysis was originally proposed by Rudolph Criegee in 1949,⁵⁷ Criegee intermediates eluded detection until 2012 when Welz. *et al.*³³ developed an alternate synthetic method that enabled direct measurements of Criegee intermediates. This method involves the photolysis of *gem*-diiodoalkane precursors to form monoiodoalkene radicals, which rapidly react with O₂ to form the Criegee intermediate as shown in Scheme 2. This approach has enabled generation of a variety of Criegee intermediates in sufficient concentration for spectroscopic and kinetic measurements by a variety of methods including photoionization mass spectrometry,^{19, 29, 33, 38, 44, 45, 49, 58-67} electronic



Scheme 2. Alternate synthetic method for Criegee intermediate generation via photolysis of *gem*-diiidoalkane precursors in the presence of O₂.

spectroscopy,^{21, 22, 25, 29, 31, 39, 41, 44, 46, 48, 56, 60-63, 65, 66, 68-92} infrared spectroscopy,^{26, 93-108} Fourier transform microwave (FTMW) spectroscopy,^{30, 50, 109-116} and others.^{117, 118}

1. Isoprene Derived Criegee Intermediates

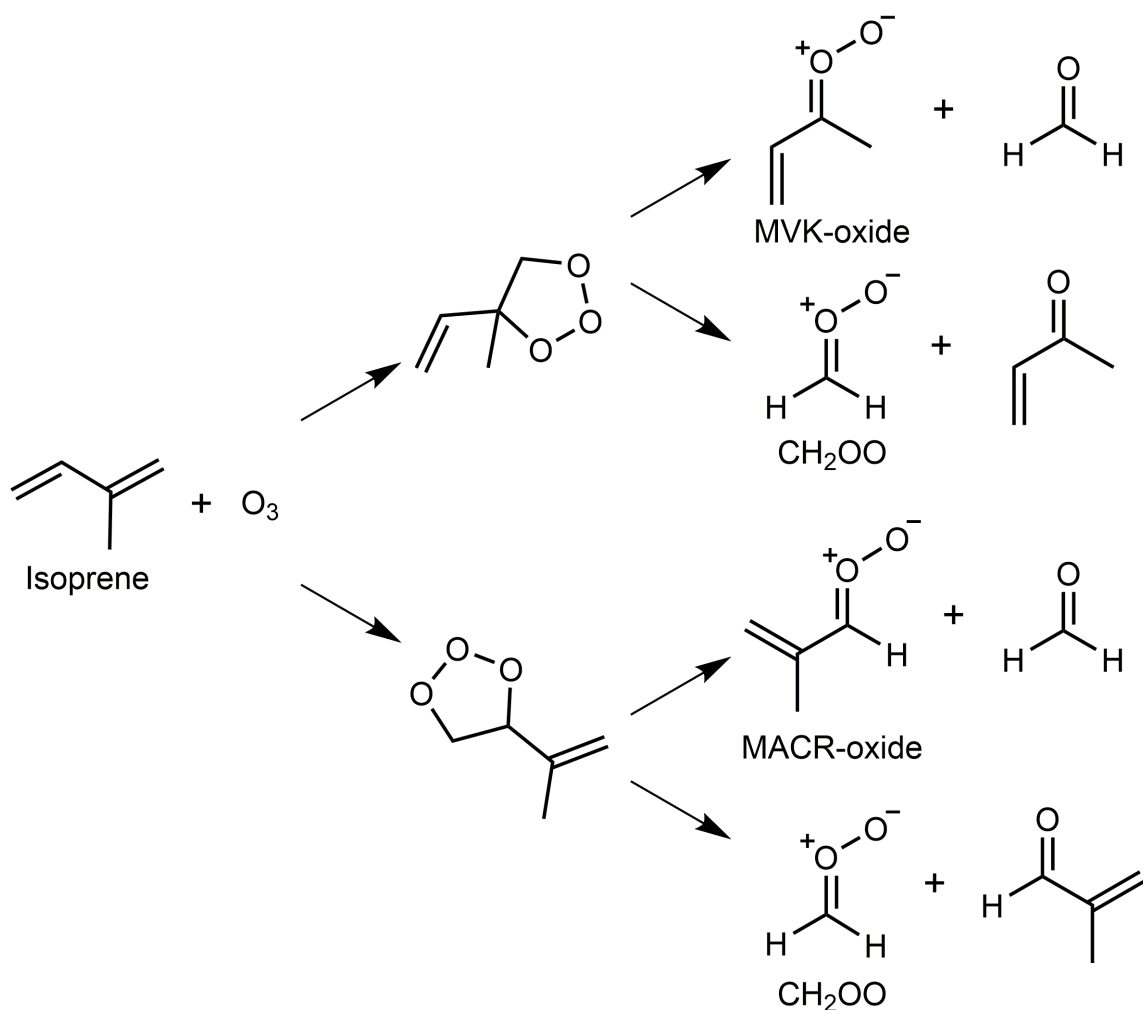
Up to 90% of non-methane VOCs are emitted into the atmosphere from biogenic sources.¹¹⁹ Of these biogenic VOCs, ~85% are comprised of isoprene ($\text{CH}_2=\text{C}(\text{CH}_3)\text{CH}=\text{CH}_2$), monoterpenes (2 isoprene units), or sesquiterpenes (3 isoprene units).¹²⁰ Isoprene makes up an overwhelming ~82% of total terpene emissions, with ca. 600 Tg of isoprene emitted into the troposphere annually.¹²⁰ Ozonolysis of these more complex biogenic alkenes yields highly functionalized Criegee intermediates (e.g. R = CH_3 , $\text{CH}=\text{CH}_2$, $\text{CH}=\text{O}$, etc.) that are predicted to have novel unimolecular reaction pathways,^{67, 104, 121-124} and in some cases, considerably different bimolecular reactivity than the simplest Criegee intermediate (CH_2OO).^{9, 67, 104, 121, 122, 124-127} Thus, while the information learned about the reactivity of simple Criegee intermediates is critical when assessing their overall impact on the atmosphere, it cannot be readily extended to the reactivity of these more complex systems.

The analogous geminal diiodo precursors necessary for the laboratory synthesis of these more complex Criegee intermediates are not stable molecules. In 2018, Barber *et al.*¹⁰⁴ demonstrated that photolysis of a diiodo alkene precursor generates a resonance stabilized monoiodoalkene radicals that can subsequently react with O_2 to generate methyl vinyl ketone oxide (MVK-oxide), a four-carbon unsaturated isoprene-derived Criegee intermediate. This method was extended to generate methacrolein oxide (MACR-oxide),⁶⁶ the other four-carbon unsaturated Criegee intermediate generated from isoprene ozonolysis, which will be discussed in Chapter 4.

The mechanism for formation of MVK-oxide, MACR-oxide, CH₂OO, and the corresponding carbonyl co-products generated in isoprene ozonolysis is shown in Scheme 3.^{121, 122, 126} Functionalized Criegee intermediates have additional complications in that they can have multiple conformational forms. For asymmetrically substituted Criegee intermediates such as the methyl and ethyl substituted Criegee intermediates (CH₃CHOO and CH₃CH₂CHOO, respectively), two conformational forms (*syn* and *anti*) are available, which differ in the orientation of the carbonyl oxide terminal oxygen with respect to the substituents. The carbonyl oxide group (C=O⁺O⁻) has substantial C=O double bond character, leading to a high barrier for interconversion between *syn* and *anti* conformational forms (30-40 kcal mol⁻¹).^{125, 128} Therefore, *syn* and *anti* conformers of the same Criegee intermediate generally behave as chemically distinct species, and can exhibit significantly different spectroscopic properties.

The four-carbon isoprene derived Criegee intermediates have additional conformational forms that refer to the orientation of the C=C and C=O bonds with respect to each other (*cis* and *trans*). Interconversion between *cis* and *trans* conformational forms is rapid under thermal conditions even though there is extended conjugation between the vinyl and carbonyl oxide groups of MVK-oxide and MACR-oxide.^{31, 104} The synthesis of suitable precursors to generate MVK-oxide and MACR-oxide is not straightforward compared to those for simple Criegee intermediates. However, they provide the ability to conduct direct spectroscopic^{65, 66, 104, 129} and kinetic³¹ measurements on these atmospherically important reaction intermediates.

2. Photoionization, Electronic spectroscopy, and kinetic measurements of Criegee intermediates



Scheme 3. Criegee intermediates and corresponding carbonyl products generated in isoprene ozonolysis. Ozonolysis can occur on either C=C double bond of isoprene to generate two distinct primary ozonides. The primary ozonides decay to form CH_2OO , MVK-oxide, and MACR-oxide Criegee intermediates.

The first direct observation of the simplest Criegee intermediate, CH₂OO, from photolysis of a *gem*-diiodoalkane precursor in the presence of O₂ was accomplished in a slow flow reactor using Multiplexed Photoionization Mass Spectrometry (MPIMS)¹³⁰ interfaced with the tunable vacuum ultraviolet (VUV) radiation of the Advanced Light Source (Lawrence Berkeley National Laboratory).³³ MPIMS provides three-dimensional data: molecular mass, reaction time, and photoionization energy. Tunable VUV radiation is utilized for near threshold ionization of Criegee intermediates without inducing fragmentation such that its parent mass channel can be monitored by time of flight mass spectrometry (TOF-MS). This results in the ability to monitor the kinetics and product branching of Criegee intermediate reactions. CH₂OO was unambiguously identified by matching its experimentally determined photoionization efficiency (PIE) curve with high level theoretical predictions.³³ In addition, the reaction kinetics of CH₂OO with SO₂ and NO₂ were accurately determined, as well as upper limits for its reaction with H₂O and NO.³³ The rate coefficient for the reaction between CH₂OO and SO₂ was found to be 10,000 times faster than inferred from ozonolysis studies, and generates SO₃, a critical sulfuric acid precursor in the troposphere that results in sulfate aerosol production.^{34, 42, 52, 53} This finding demonstrates that the ability to directly monitor the reaction kinetics of Criegee intermediates is critical when assessing their impact on the atmosphere.

Direct detection of Criegee intermediates by photoionization mass spectrometry has been extended to alkyl-substituted Criegee intermediates,^{19, 31, 33, 44, 48, 51, 59-63, 65, 66} and more recently isoprene-derived Criegee intermediates with vinyl substituents (Chapters 3 and 4).^{65, 66} The unimolecular and bimolecular reactions of the isoprene derived Criegee intermediates will be discussed in Chapters 5-7 of this work.^{31, 67, 131}

Lester and coworkers adapted the alternate synthetic method developed by Welz *et al.*³³ to generate Criegee intermediates in a capillary reactor tubed coupled to a pulsed

supersonic expansion to investigate their electronic spectroscopy in photoionization mass spectrometry experiments.^{61-63, 65, 66} Later, Lester and coworkers developed diiodoalkene precursors to generate the four-carbon isoprene-derived Criegee intermediates in laboratory experiments.^{66, 104} They found that Criegee intermediates have a very strong $\pi^* \leftarrow \pi$ transition with an oscillator strength (f) on the order of ~ 0.1 that is associated with the four π electrons of the zwitterionic carbonyl oxide ($\text{C}=\text{O}^+\text{O}^-$) group.^{61-63, 65, 66} The parent mass of the Criegee intermediate is monitored by photoionization using VUV (10.5 eV, 118 nm) probe laser radiation. UV-Vis radiation from a pump laser (ca. 280-450 nm) introduced prior in time to the probe laser induces large ground state depletions of the Criegee intermediate and corresponding VUV photoionization signal of the parent mass channel, providing mass and isomer specific detection of the Criegee intermediate. Large ground state depletions ($> 50\%$) are indicative of large absorption cross sections and rapid photodissociation of the Criegee intermediate in the excited state. The $1^1\pi\pi^*$ state that is accessed upon UV excitation of the Criegee intermediate couples via conical intersections to multiple repulsive potentials that produce $\text{O } ^1\text{D}$ fragments with corresponding singlet carbonyl co-products in the lowest spin-allowed channel.^{65, 66, 68-71, 132} The magnitude of the ground state depletion and area of the laser beams were used to estimate large absorption cross sections for the UV-Vis transition of Criegee intermediates (ca. $10^{-17} \text{ cm}^2 \text{ molec}^{-1}$).^{61, 62}

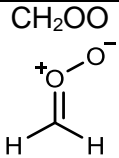
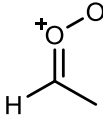
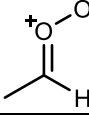
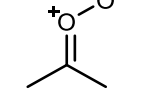
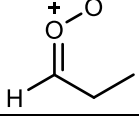
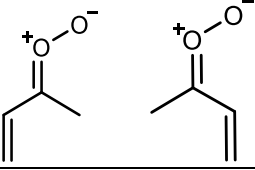
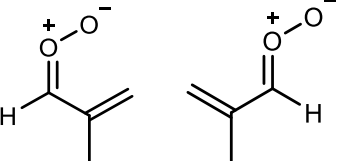
The electronic spectroscopy of several Criegee intermediates with varying substituents have now been investigated.^{31, 41, 61-63, 65, 66, 73, 74, 76} In general, the UV spectra of Criegee intermediates are relatively broad and unstructured, although some Criegee intermediates exhibit some structure in the long wavelength tail region that is attributed to vibrational resonances associated with the $1^1\pi\pi^*$ state.^{66, 71, 74} In addition, significant

shifts in the UV spectra are observed that correlate with the substituents and conformational form of the Criegee intermediate as summarized in Table 1.

Spectral shifts in the UV spectra of Criegee intermediates generally originates from vertical displacements in the Franck-Condon excitation energies due to differences in the relative stability of the ground and $1^1\pi\pi^*$ excited states. For example, the peak position the UV spectrum of *syn*-CH₃CHOO (ca. 320 nm), where the terminal O-atom is oriented toward the methyl group (Table 1), is shifted to shorter wavelength (higher energy) than that for CH₂OO (ca. 335 nm) and *anti*-CH₃CHOO (360 nm), where the terminal O-atom is oriented toward a hydrogen atom. This shift is attributed to a combination of the relative ground stability of *syn*-CH₃CHOO compared to *anti*-CH₃CHOO (3.6 kcal mol⁻¹) and destabilization of the $1^1\pi\pi^*$ state arising from π^* character extending from the carbonyl oxide onto the methyl hydrogen atoms.⁶² The UV spectra of the two four-carbon Criegee intermediates from isoprene ozonolysis, MVK-oxide and MACR-oxide are shifted to longer wavelengths than alkyl-substituted Criegee intermediates, as discussed in Chapters 3 and 4.^{65, 66} These Criegee intermediates have extended conjugation across the vinyl and carbonyl oxide groups. This delocalization helps stabilize the $1^1\pi\pi^*$ state compared to that of CH₂OO and alkyl substituted Criegee intermediates and results in a spectral shift of their maximum UV absorption to significantly longer wavelength (388 nm and 380 nm, respectively).^{65, 66}

The long wavelength tail region of the UV-Vis spectra of Criegee intermediates overlaps with the UV-Vis sunlight radiation that penetrates the upper atmosphere and reaches the troposphere.⁷ This results in daytime photolysis of Criegee intermediates and generates O-atoms and a carbonyl co-fragment. The O-atoms are primarily produced electronically excited (O ¹D) and will subsequently react with water vapor in the troposphere to produce two OH radicals.⁷ The photochemical loss rate due to solar

Table 1. Peak position (nm) of the UV-Vis spectra of various Criegee intermediates.

Criegee Intermediate	Peak Position (nm)	References
CH_2OO 	335 340 355	Beames <i>et al.</i> ⁶¹ Ting <i>et al.</i> ⁷⁴ Sheps ⁷²
<i>syn</i> - CH_3CHOO 	320 323 328	Beames <i>et al.</i> ⁶² Sheps <i>et al.</i> ⁷³ Smith <i>et al.</i> ⁷⁶
<i>anti</i> - CH_3CHOO 	360	Sheps <i>et al.</i> ⁷³
$(\text{CH}_3)_2\text{COO}$ 	323 330	Liu <i>et al.</i> ⁶³ Huang <i>et al.</i> ⁴¹
<i>syn</i> - $\text{CH}_3\text{CH}_2\text{CHOO}$ 	322	Liu <i>et al.</i> ⁶³
<i>syn/anti</i> -MVK-oxide 	388 ^a 370 ^b	Vansco <i>et al.</i> ⁶⁵ Caravan <i>et al.</i> ³¹
<i>syn/anti</i> -MACR-oxide 	380	Vansco <i>et al.</i> ⁶⁶

- a. UV spectrum contains contribution from *syn* and *anti*-MVK-oxide conformers
b. *syn*-MVK-oxide is assigned as the primary spectral carrier

irradiation (k_p) is estimated by combining the UV absorption cross section of Criegee intermediates ($\sigma(\lambda)$) and the solar actinic flux ($F(\lambda)$) assuming a 0° zenith angle at the Earth's surface and a photodissociation quantum yield ($\varphi(\lambda)$) of one according to equation (1):

$$k_p = \int_{\lambda_1}^{\lambda_2} \varphi(\lambda) \sigma(\lambda) F(\lambda) d\lambda \quad (1)$$

The photolysis lifetime of Criegee intermediates is generally on the order of a few seconds, which is slow compared to typical unimolecular and bimolecular reaction rates for Criegee intermediates.^{6, 9, 10, 14, 41} Nevertheless, the strong UV-Vis absorption of Criegee intermediates (ca. 10^{-17} cm² molec⁻¹) provides a sensitive probe for transient absorption experiments that are designed to measure reaction kinetics.^{21, 22, 25, 29, 31, 39, 41, 44, 46, 48, 56, 60, 73, 77, 78, 81-83} Section 3 of this introduction will overview the chemistry of Criegee intermediates, including those generated from isoprene ozonolysis, and highlight areas where additional investigations are required to fully characterize their impact on the atmosphere.

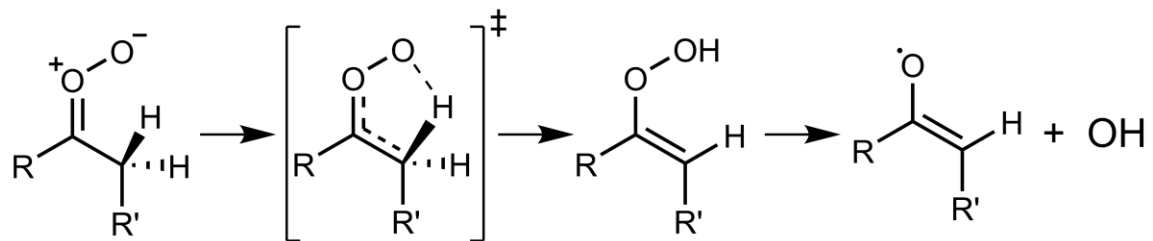
3. Unimolecular decay and bimolecular reactions of Criegee intermediates

The development of alternate synthetic methods to generate Criegee intermediates in the laboratory led to a significant increase in experimental and theoretical investigations of their unimolecular and bimolecular reactivity. These discoveries in combination with global and regional modeling reveal the impact Criegee intermediates have in the atmosphere. Mechanisms for the various unimolecular decomposition pathways of Criegee intermediates and their most atmospherically relevant bimolecular reactions are discussed below. In addition, effective rates for the unimolecular and

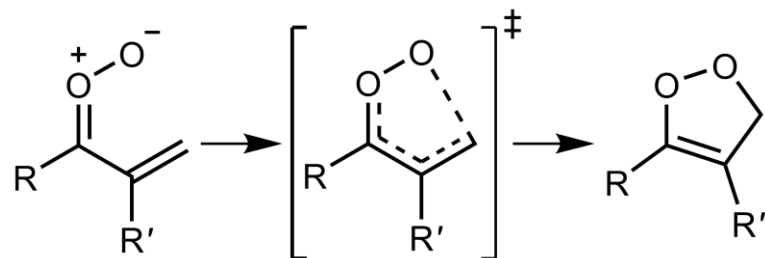
bimolecular reactions of Criegee intermediates under atmospheric conditions are estimated from literature data for several Criegee intermediates.

The unimolecular decomposition of Criegee intermediates is a significant non-photolytic source of OH radicals in the atmosphere.¹⁷ Criegee intermediates containing an alkyl H-atom on the α -carbon with respect to the terminal oxygen (e.g. *syn*-CH₃CHOO) generate OH radicals through a 1,4 H-atom transfer mechanism (Scheme 4). The alkyl H-atom transfers to the terminal oxygen of the carbonyl oxide via a 5-membered ring transition state (TS) and generates a vinyl hydroperoxide (VHP). The H-atom transfer is sufficiently exothermic to facilitate rapid homolysis of the O-O bond to yield OH and vinyloxy radical products.^{5, 94-96, 98-100, 102-105, 107, 108, 133} The resultant thermal unimolecular decay rate has been shown to be significantly enhanced by quantum mechanical tunneling.^{100, 102-105} The reaction of vinyloxy radicals with O₂ have been shown to generate OH radical products and/or highly oxygenated molecules that may be precursors to secondary organic aerosols.¹³⁴⁻¹³⁸

For Criegee intermediates that do not have an alkyl substituent adjacent to the terminal O-atom, unimolecular decay proceeds via different mechanisms. Criegee intermediates with a vinyl substituent adjacent to the carbonyl oxide group, such as *syn*-MVK-oxide and *anti*-MACR-oxide, are predicted to undergo rapid 1,5 electrocyclic ring closure via a low TS barrier (ca. 12 kcal mol⁻¹) to form a dioxole intermediate as shown in Scheme 5.^{9, 104, 121, 122, 124} This unimolecular decay mechanism is predicted to be the dominant atmospheric sink for *syn*-MVK-oxide and *anti*-MACR-oxide. The products from this pathway and their subsequent (or secondary) chemistry in the atmosphere are discussed in Chapter 6.



Scheme 4. Unimolecular decay of alkyl-substituted Criegee intermediates via a 1,4 H-atom transfer mechanism to OH and vinyloxy radical products.

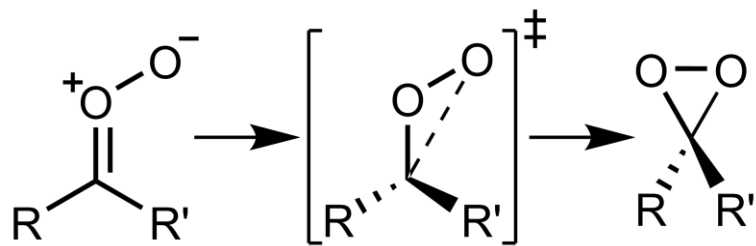


Scheme 5. Unimolecular decay of vinyl substituted Criegee intermediates via a 1-5 electrocyclic ring closure to dioxole.

Criegee intermediates with a H-atom adjacent to the terminal O-atom (e.g. CH_2OO and *anti*- CH_3CHOO) undergo unimolecular decomposition through a 1,3 electrocyclic ring-closure mechanism to yield a dioxirane intermediate as shown in Scheme 6.^{82, 113, 139} Dioxirane formation proceeds over a high transition state barrier (ca. 20 kcal mol⁻¹), resulting in a relatively slow thermal unimolecular decay rate.^{9, 14, 121, 122, 139} Dioxirane can undergo further isomerization to form a carboxylic acid that subsequently decays in an exothermic reaction to OH radicals and other products.^{82, 139-141}

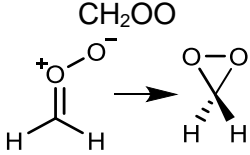
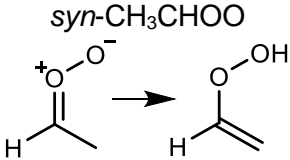
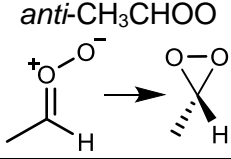
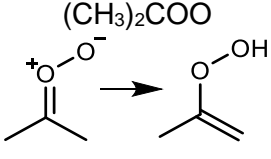
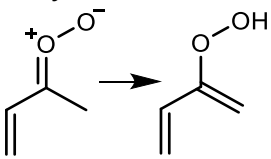
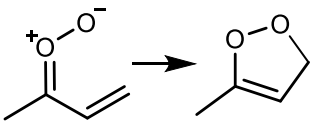
Precise thermal unimolecular decay rate measurements are rare^{80, 118, 142} due to difficulties in accounting for other first-order losses (e.g. wall losses) in slow flow reactor experiments.^{19, 39, 60, 72, 77, 80, 143} Oftentimes, the most accurate unimolecular decay rates for Criegee intermediates are obtained from theoretical calculations. From a theoretical perspective, characterization of Criegee intermediate reactivity is inherently difficult due to their mixed biradical and zwitterionic character in the ground state.¹⁴⁴ These multireference effects must be properly treated in order to obtain accurate results.^{26, 31, 104, 128, 145-148} Even high levels of theory have problems with obtaining accurate energetics for kinetic predictions,²⁷ as discussed by Vereecken.⁹ A combination of experimentally determined and theoretically predicted unimolecular decay rates (298 K; 1 atm) of Criegee intermediates with various substituents and conformational forms are presented in Table 2.

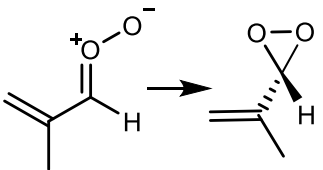
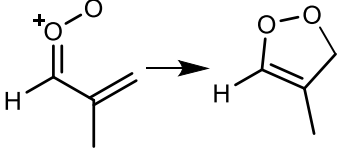
Bimolecular reactions with trace atmospheric species are expected to be the dominant sink for Criegee intermediates that undergo relatively slow unimolecular decomposition.¹⁰ Criegee intermediates have been shown to undergo substantive reaction with a variety of trace atmospheric species including water vapor (monomer and dimer),^{18, 20-22, 24, 27, 29, 30, 91, 150-152} SO_2 ,^{32, 34, 37, 39-41, 117, 153, 154} carboxylic acids,^{43, 44, 46-50, 116, 150} NO_x ,^{64, 155} alcohols,^{81, 88, 92, 150, 156} and aldehydes,^{58, 150} among others.^{84, 85, 89, 106, 157}



Scheme 6. Unimolecular decay of Criegee intermediates via a 1,3 electrocyclic ring-closure to dioxirane.

Table 2. Unimolecular decay mechanisms and rates (298 K; 1 atm) of several Criegee intermediates. The chosen data includes direct experimental measurements and post-CCSD(T) theoretical calculations.

Criegee Intermediate	Unimolecular Decay rate / s ⁻¹	Method
CH_2OO 	0.25 0.3 0.3 <11.6 0.3	T: RRKM ^a T: CVTST ^b T: SCTST ^c E: UV Absorption ^d T: CTST ^e
$\text{syn-CH}_3\text{CHOO}$ 	166 328 122 136 182 ± 66	T: RRKM ^f T: CVTST ^b T: RRKM; E: K(E) ^g T: CTST ^e E: High-repetition-rate LIF ^l
$\text{anti-CH}_3\text{CHOO}$ 	55.4 53	T: CVTST ^b T: CTST ^e
$(\text{CH}_3)_2\text{COO}$ 	369 276 305 ± 70 361 ± 49 400 478	T: RRKM ^f T: RRKM; E: K(E) ^h E: UV Absorption ⁱ E: UV Absorption ^j T: SCTST ^j T: CTST ^e
syn-MVK-oxide 	33 50	T: RRKM ^k T: CTST ^e
anti-MVK-oxide 	2140 7700	T: RRKM ^k T: CTST ^e

<p><i>anti</i>-MACR-oxide</p> 	2500	T: CTST ^e
<p><i>syn</i>-MACR-oxide</p> 	10	T: CTST ^e

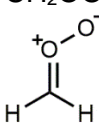
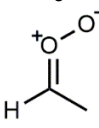
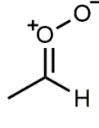
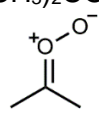
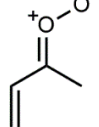
- a. Berndt *et al.*, 2015, ref. 23, (CHEAT1 modified, 297 K).
- b. Long *et al.*, 2016, ref. 24, (W3X-L//CCSD(T)-F12; 298 K).
- c. Nguyen *et al.*, 2016, ref. 149, (HEAT-345(Q), 298 K).
- d. Chhantyal-Pun *et al.*, 2015, ref. 39, (293 K).
- e. Vereecken *et al.*, 2017, ref. 9, (CCSD(T)/aVTZ//M06-2X, with barrier corrections, 298 K).
- f. Fang *et al.* 2016, ref. 98, (CCSD(T)-F12/CBS//B3LYP, 298 K).
- g. Fang *et al.* 2016, ref. 100, (CCSD(T)-F12/CBS//B2PLYPD3, 298 K).
- h. Fang *et al.* 2017, ref. 102, (CCSD(T)-F12/CBS//B2PLYPD3, 298 K).
- i. Chhantyal-Pun *et al.*, 2017, ref. 60, (293 K).
- j. Smith *et al.*, 2016, ref. 80, (QCISD(T)/CBS//B3LYP, 298 K).
- k. Barber *et al.*, 2018, ref. 104, (CCSD(T)-F12/CBS//B2PLYPD3, 298 K).
- l. Zhou *et al.*, 2019, ref. 118, (298 K).

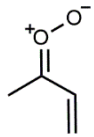
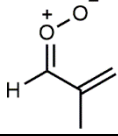
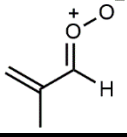
Even though many of these atmospheric species undergo rapid reaction with Criegee intermediates, only reactants with appreciable concentrations in the atmosphere and sufficient rate coefficients for reaction will be significant loss processes for Criegee intermediates. For this discussion, the reaction of Criegee intermediates with water vapor (monomer and dimer), SO₂, and organic acids are considered.

A potential major sink for Criegee intermediates is reaction with water vapor due to its high concentration in the troposphere. Rate constants for the reaction between water vapor (monomer and dimer) and several Criegee intermediates are tabulated in Table 3. The reaction between Criegee intermediates and water monomer proceeds via the formation of a pre-reactive complex with a hydrogen bonding interaction between the terminal O-atom of the Criegee intermediate and a H-atom of the water molecule. The reaction proceeds over a positive transition state barrier relative to reactants via a 1,2-insertion mechanism. The H-atom involved in the hydrogen bonding interaction transfers to the terminal O-atom of the Criegee intermediate while the residual OH group of the water molecule bonds to the central carbon of the Criegee intermediate (Scheme 7, top). A highly oxygenated hydroxyl alkyl hydroperoxide adduct is formed, which has implications in the formation of secondary organic aerosols.^{48, 92, 158, 159}

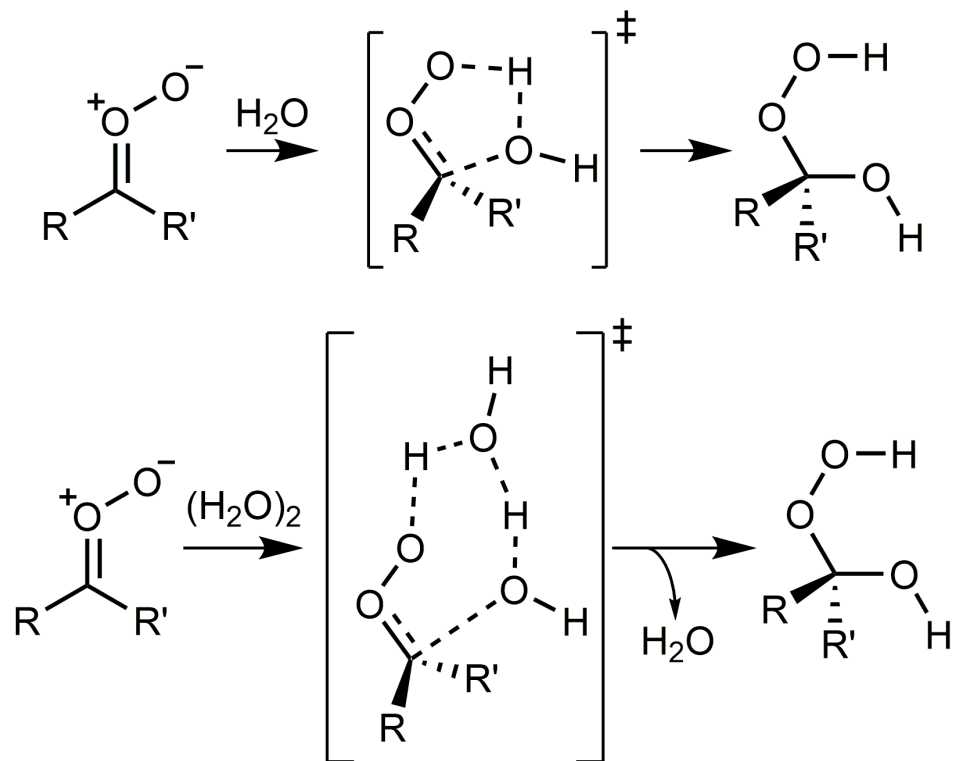
While the reaction between Criegee intermediates and water monomer proceeds over a positive transition state barrier relative to reactants, theoretical studies show that their reaction with water dimer dramatically reduces the barrier.^{9, 21, 25-27, 29, 38, 91, 151} In some cases, the transition state barrier becomes submerged relative to reactants, which significantly enhances the reaction rate. A schematic illustrating the reaction between Criegee intermediates and water dimer is shown in the bottom of Scheme 7. Two water molecules form a bridge across the carbonyl oxide group of the Criegee intermediate through two hydrogen bonding interactions resulting in a less strained transition state

Table 3. Rate constants from direct experimental measurements and *ab initio* theory for the bimolecular reactions of Criegee intermediates with water vapor (monomer and dimer).

Criegee Intermediate	H ₂ O k / cm ³ s ⁻¹	(H ₂ O) ₂ k / cm ³ s ⁻¹	Method
CH_2OO 	$< 4 \times 10^{-15}$ $< 1.5 \times 10^{-15}$ $(2.4 \pm 1.6) \times 10^{-16}$ 3.7×10^{-16} 3.0×10^{-16} 2.4×10^{-16}	$(6.5 \pm 0.8) \times 10^{-12}$ $(6.6 \pm 0.7) \times 10^{-12}$ $(7.4 \pm 0.6) \times 10^{-12}$ $(4.0 \pm 1.2) \times 10^{-12}$ 5.4×10^{-12} 1.7×10^{-10}	E: MPIMS ^a E: UV Absorption ^b E: UV Absorption ^c E: UV Absorption ^d E: UV Absorption ^e T: SCTST ^f T: VTST ^g T: CVTST ^h
$\text{syn-CH}_3\text{CHOO}$ 	$< 4 \times 10^{-15}$ $< 2 \times 10^{-16}$ 2.0×10^{-19} 2.9×10^{-18} 5.7×10^{-20}	2.6×10^{-14} 4.8×10^{-13}	E: MPIMS ⁱ E: UV Absorption ^j T: SCTST ^f T: VTST ^g T: CVTST ^h
$\text{anti-CH}_3\text{CHOO}$ 	$(1.0 \pm 0.4) \times 10^{-14}$ $(2.4 \pm 0.4) \times 10^{-14}$ $(1.3 \pm 0.3) \times 10^{-14}$ 3.4×10^{-14} 1.4×10^{-13} 6.3×10^{-15}	$(4.4 \pm 0.3) \times 10^{-11}$ 1.6×10^{-11} 5.9×10^{-10}	E: MPIMS ⁱ E: UV Absorption ^j E: UV Absorption ^k T: SCTST ^f T: VTST ^g T: CVTST ^h
$(\text{CH}_3)_2\text{COO}$ 	$< 1.5 \times 10^{-16}$ 2.4×10^{-17}	$< 1.3 \times 10^{-13}$ 3.7×10^{-13}	E: UV Absorption ^l T: VTST ^g
syn-MVK-oxide 	$< 4.0 \times 10^{-17}$ 8.1×10^{-20} 1.1×10^{-19}	$< 3.0 \times 10^{-14}$ 3.1×10^{-16}	E: UV Absorption ^m T: CTST ^{g,n} T: AITSTME ^m

<i>anti</i> -MVK-oxide 	1.8×10^{-20}	4.8×10^{-15}	T: CTST ^{g,n}
<i>syn</i> -MACR-oxide 	1.5×10^{-19}	5.6×10^{-16}	T: CTST ^{g,n}
<i>anti</i> -MACR-oxide 	1.9×10^{-16}	3.6×10^{-13}	T: CTST ^{g,n}

- a. Welz *et al.*, 2012, ref. 33, (298 K).
- b. Chao *et al.*, 2015, ref. 22, (298 K).
- c. Sheps *et al.*, 2017, ref. 29, (293 K).
- d. Smith *et al.*, 2015, ref. 91, (298 K).
- e. Lewis *et al.*, 2015 ref. 21, (294 K).
- f. Lin *et al.*, 2016, ref. 26, (QCISD(T)/CBS//B3LYP, 298 K).
- g. Anglada and Sole, 2016, ref. 27, (CCSD(T)//B3LYP, 298 K).
- h. Long *et al.*, 2016, ref. 24, (W3X-L//CCSD(T)-F12, 298 K).
- i. Taatjes *et al.*, 2013, ref. 19, (298 K).
- j. Sheps *et al.*, 2014, ref. 73, (293 K).
- k. Lin *et al.*, 2016, ref. 25, (298 K).
- l. Huang *et al.*, 2015, ref. 41, (298 K).
- m. Caravan *et al.*, 2020, ref. 31, (298 K, CCSD(T)-F12/cc-pVTZ-F12, 298 K).
- n. Vereecken, 2017, ref. 9, reevaluation of the rate constant obtained by Anglada and Sole including corrections to account for the level of theory used.



Scheme 7. Illustration of the reaction of Criegee intermediates with water monomer (Top) and (Bottom) water dimer.

geometry.^{9, 26, 27, 151} This extended interaction results in a lower transition state barrier. In addition, the extended network facilitates a double H-atom transfer that occurs simultaneously with OH addition to the central carbon of the carbonyl oxide group. The same functionalized hydroperoxide adduct is formed, along with regeneration of a water molecule. Thus, the presence of a second water molecule effectively catalyzes the 1,2-insertion reaction mechanism.

There is strong experimental evidence that two water molecules play an important role in the reaction between Criegee intermediates and water vapor. Transient absorption experiments revealed a quadratic dependence on water vapor concentration in the reaction of CH₂OO with water.^{21, 22} The dramatically reduced barrier for reaction between CH₂OO and with water dimer results in an orders of magnitude larger rate constant compared to the reaction with a single water molecule. Consequently, the reaction between CH₂OO and water vapor dominates its atmospheric removal.

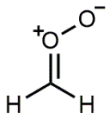
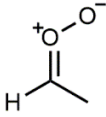
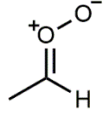
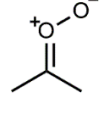
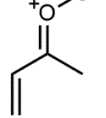
While the reaction between water vapor and Criegee intermediates with a H-atom *syn* to the carbonyl oxide group (e.g. CH₂OO, *anti*-CH₃CHOO) is relatively fast (ca. 10⁻¹⁴-10⁻¹⁵ cm³ s⁻¹), the corresponding reaction for Criegee intermediates with an alkyl group *syn* to the carbonyl oxide group (e.g. *syn*-CH₃CHOO and (CH₃)₂COO) are 10-100 times slower due to steric hindrance from the alkyl substituent. The rate constants are further reduced for reaction of *syn*-MVK-oxide with water vapor due to a disruption of the extended conjugation of *syn*-MVK-oxide at the transition state. The reaction of *anti*-MACR-oxide with water vapor presents an interesting scenario because its carbonyl oxide group is oriented toward an H-atom (similar to CH₂OO and *anti*-CH₃CHOO), yet it has extended conjugation with the vinyl substituent. While its reaction with water vapor has not been measured experimentally, recent theoretical predictions indicate that *anti*-MACR-oxide will react significantly faster with water vapor than the *syn* conformational

form of MACR-oxide.^{9, 27} Nevertheless, the energetic penalty associated with disrupting the extended conjugation of *anti*-MACR-oxide is predicted to slow its reaction with water vapor compared to CH₂OO and *anti*-CH₃CHOO. This clearly demonstrates that the substituents and conformational form of Criegee intermediates can dramatically affect their bimolecular reactivity.

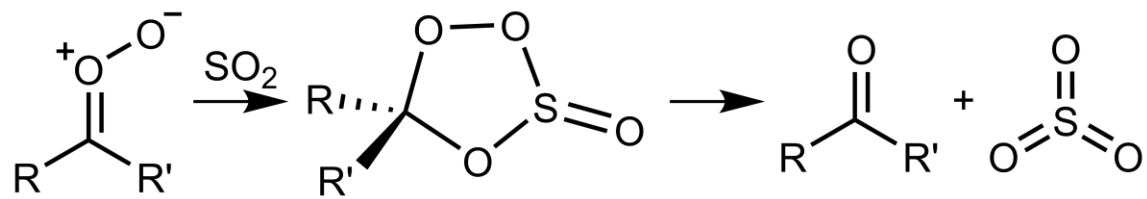
While other species such as SO₂ and organic acids are less abundant in the atmosphere than water vapor, they react rapidly with Criegee intermediates to form low-volatility products, which are implicated in the formation of secondary organic aerosols.^{48, 92, 158, 159} The reaction between Criegee intermediates with SO₂ leads to the formation of SO₃, which reacts with water vapor to form sulfuric acid (H₂SO₄).^{36, 53, 153} Formation of H₂SO₄ is known to enhance nucleation rates through the formation of secondary organic aerosols that generate clouds.^{42, 52, 160} Experimental and theoretical studies show the rate of reaction of Criegee intermediates with SO₂ is rapid (ca. 10⁻¹¹ cm³s⁻¹) as shown in Table 4.^{19, 31, 33, 38, 39, 41, 60, 72, 73, 117, 153, 161-164} Atmospheric modeling suggests that the tropospheric processing of SO₂ to SO₃ by Criegee intermediates is comparable to its removal by OH in areas where Criegee intermediates concentrations are largest.¹⁰ Further, the reaction of Criegee intermediates with SO₂ can account for as much as 50% of sulfuric acid production at ground level, significantly impacting particle nucleation rate.³⁴ Thus, the reaction of Criegee intermediates with SO₂ has important implications in air quality, climate, and human health.

The reaction of Criegee intermediates with SO₂ proceeds via the formation of a dipole-dipole pre-reactive complex. This long range interaction facilitates cycloaddition of the C=O⁺-O⁻ group of the Criegee intermediate across one of the S=O bonds of SO₂ via a submerged transition state barrier to form a 5-membered secondary ozonide (SOZ) as shown in Scheme 8. The SOZ can be collisionally stabilized in a deep potential energy

Table 4. Rate constants from direct experimental measurements and *ab initio* theory for the bimolecular reactions of Criegee intermediates with SO₂.

Criegee Intermediate	SO ₂ k / cm ³ s ⁻¹	Method
CH ₂ OO 	$(3.9 \pm 0.7) \times 10^{-11}$ $(3.80 \pm 0.04) \times 10^{-11}$ $(4.1 \pm 0.3) \times 10^{-11}$	E: MPIMS ^a E: UV Absorption ^b E: UV Absorption ^c
<i>syn</i> -CH ₃ CHOO 	$(2.4 \pm 0.3) \times 10^{-11}$ $(2.9 \pm 0.3) \times 10^{-11}$	E: MPIMS ^d E: UV Absorption ^e
<i>anti</i> -CH ₃ CHOO 	$(6.7 \pm 1.0) \times 10^{-11}$ $(22.0 \pm 2.0) \times 10^{-11}$	E: MPIMS ^d E: UV Absorption ^e
(CH ₃) ₂ COO 	$(7.5 \pm 0.5) \times 10^{-11}$ $(13.2 \pm 1.3) \times 10^{-11}$	E: UV Absorption ^f E: UV Absorption ^g
<i>syn</i> -MVK-oxide 	$(4.2 \pm 0.6) \times 10^{-11}$ 3.9×10^{-11}	E: UV Absorption ^h T: CCSD(T)-F12/cc-pVTZ-F12, AITSTME

- Welz *et al.*, 2012, ref. 33, (298 K).
- Chhantyal-Pun *et al.*, 2015, ref. 39, (293 K).
- Sheps, 2013, ref. 72, (295 K).
- Taatjes *et al.*, 2013, ref. 19, (298 K).
- Sheps *et al.*, 2014, ref. 73, (293 K).
- Chhantyal-Pun *et al.*, 2017, ref. 60, (298 K).
- Huang *et al.*, 2015, ref. 41, (298 K).
- Caravan *et al.*, 2020, ref. 31, (298 K).



Scheme 8. Illustration of the reaction of Criegee intermediates with SO₂.

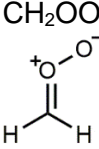
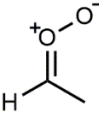
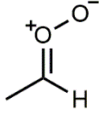
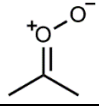
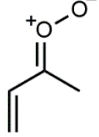
well (ca. $-30 \text{ kcal mol}^{-1}$ relative to reactants) or undergo cycloreversion via a strongly submerged barrier to form carbonyl and SO_3 products. Master equation simulations predict a prompt carbonyl + SO_3 yield of $>95\%$ for the reaction of Criegee intermediates with SO_2 .^{31, 162}

Unlike for the reaction of Criegee intermediates with water vapor, the rate constants for the reaction of Criegee intermediates with SO_2 are relatively unchanged with respect to substituents and conformational form. This is because Criegee intermediate reactions with SO_2 proceed through strongly submerged barriers relative to reactants. While the energy of the transition state barrier is affected due to alkyl substitution and the extended conjugation present in the isoprene-derived Criegee intermediates, there is minimal perturbation in the overall bimolecular rate coefficients. Criegee intermediates have also been shown to react extremely fast with organic acids, as shown in Table 5. Strong hydrogen bonding interactions between Criegee intermediates and organic acids facilitate the formation of a pre-reactive complex over long distances (ca. 6 \AA).^{31, 47} This, in combination with a strongly submerged transition state barrier, results in rate constants for reaction that approach the collision limit (ca. $10^{-10} \text{ cm}^3 \text{ s}^{-1}$). The reaction proceeds via a concerted 1,4-insertion mechanism, in which a H-atom from the acid transfers to the terminal O-atom of the Criegee intermediate with simultaneous bond formation between the carbonyl O-atom of the acid and the central carbon of the Criegee intermediate (Scheme 9). The reaction generates a more highly oxygenated and functionalized adduct that is implicated in the formation of secondary organic aerosols.^{48,}

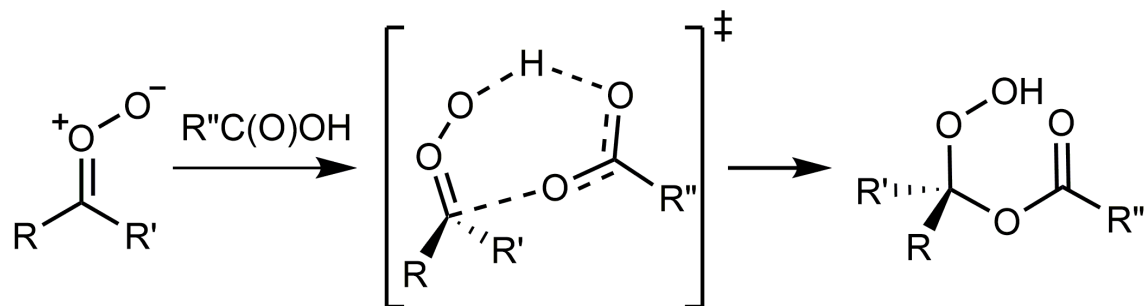
92, 158, 159

Similar to the reaction of Criegee intermediates with SO_2 , changes in substituents and conformational form does not significantly impact the rate coefficient for reaction with organic acids. The kinetic bottleneck for the reaction of Criegee intermediates with

Table 5. Rate constants from direct experimental measurements and theoretical predictions for the bimolecular reactions of Criegee intermediates with formic acid and acetic acid.

Criegee Intermediate	HC(O)OH k / cm ³ s ⁻¹	CH ₃ (O)OH k / cm ³ s ⁻¹	Method
CH_2OO 	$(1.1 \pm 0.1) \times 10^{-10}$ $(1.14 \pm 0.06) \times 10^{-10}$	$(1.3 \pm 0.1) \times 10^{-10}$ $(1.47 \pm 0.09) \times 10^{-10}$	E: MPIMS/UV absorption ^a UV absorption ^b
$\text{syn-CH}_3\text{CHOO}$ 	$(2.5 \pm 0.3) \times 10^{-10}$	$(1.7 \pm 0.1) \times 10^{-10}$	E: MPIMS ^a
$\text{anti-CH}_3\text{CHOO}$ 	$(5 \pm 3) \times 10^{-10}$	$(2.5 \pm 0.6) \times 10^{-10}$	E: MPIMS ^a
$(\text{CH}_3)_2\text{COO}$ 	$(3.1 \pm 0.2) \times 10^{-10}$	$(3.1 \pm 0.2) \times 10^{-10}$	E: UV Absorption ^b
syn-MVK-oxide 	$(3.0 \pm 0.1) \times 10^{-10}$ 4.9×10^{-10}	N/A	E: UV Absorption ^c T: CCSD(T)-F12/cc-pVTZ-F12, AITSTME

- a. Welz *et al.*, 2014, ref. 44, (293 K).
b. Chhantyal-Pun *et al.*, 2018, ref. 48, (293 K).
c. Caravan *et al.*, 2020, ref. 31, (298 K).



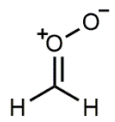
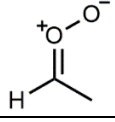
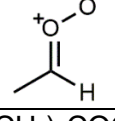
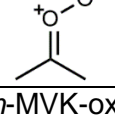
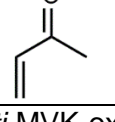
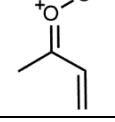
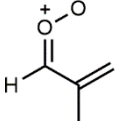
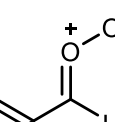
Scheme 9. Illustration of the reaction of Criegee intermediates with organic acids.

organic acids occurs during the long-range attraction between reactants rather than the chemical transformation that has highly submerged barriers.^{31, 47} The long-range interaction between Criegee intermediates and organic acids is highly effective due to strong charge separation, high dipole moments, and hydrogen bonding.^{31, 47} Although reaction of Criegee intermediates with organic acids is extremely fast, it is not a dominant atmospheric sink for Criegee intermediates due to relatively low organic acid concentrations (ca. 2 ppb).^{165, 166, 167-169} However, global modeling indicates that Criegee intermediates significantly contribute to the removal of formic acid, particularly in areas where Criegee intermediates are most abundant.¹⁰ In areas such as the Amazon, reaction with Criegee intermediates exceeds 60% of the total organic acid loss, significantly reducing their atmospheric lifetime.

As discussed above, the unimolecular and bimolecular reaction rates of Criegee intermediates can change drastically depending on their substituents and conformational form. One can evaluate the primary atmospheric removal pathway for a specific stabilized Criegee intermediate by comparing its unimolecular decay rate to effective rates for bimolecular reaction with atmospheric species. The latter can be estimated by using the known bimolecular rate constant and a typical atmospheric concentration of the reactant. Global atmospheric models are necessary to quantitatively ascertain the reactive sinks for Criegee intermediates due to spatial changes in the concentration of reactants, and the temperature and pressure dependence of the rate constants. Nevertheless, this analysis demonstrates trends in the reactivity of Criegee intermediates with respect to specific substituents and conformational form.

The effective rates for the unimolecular decay and bimolecular reactions of Criegee intermediates is shown in Table 6. For the reaction of Criegee intermediates with water

Table 6. Effective pseudo-first order rates of reaction of Criegee intermediates with water vapor (monomer and dimer, 60% RH),¹⁷⁰ unimolecular decay, SO₂ (15 ppb),¹⁷¹ and organic acids (2.3 ppb formic acid, 2 ppb acetic acid)^{165, 166,167-169} at 298 K.

Criegee Intermediate	Water Vapor ^a (s ⁻¹)	Unimolecular Decay ^b (s ⁻¹)	SO ₂ ^c (s ⁻¹)	Organic Acids ^d (s ⁻¹)
CH ₂ OO 	3112	2.5	15	14
<i>syn</i> -CH ₃ CHOO 	125	188	10	23
<i>anti</i> -CH ₃ CHOO 	28810	54	53	41
(CH ₃) ₂ COO 	193	342	38	33
<i>syn</i> -MVK-oxide 	0.2	33	16	32
<i>anti</i> -MVK-oxide 	3	2140	16	32
<i>syn</i> -MACR-oxide 	0.3	2500	16	32
<i>anti</i> -MACR-oxide 	264	10	16	32

- a. Average of the experimentally determined rate constants (CH_2OO , *syn*- CH_3CHOO , *anti*- CH_3CHOO , $(\text{CH}_3)_2\text{COO}$), or the best available theoretically determined rate constants (MVK-oxide and MACR-oxide) listed in Table 3. The rates reported for *syn/anti* MVK-oxide and MACR-oxide represent a Boltzmann weighted distribution of the *cis/trans* conformational forms at 298 K. Accounts for water monomer and dimer (60% RH).¹⁷⁰
- b. Average of the thermal unimolecular decay rates of Criegee intermediates listed in Table 2.
- c. Average of the experimentally determined rate constants listed in Table 4 multiplied by the average United States concentration of SO_2 in 2018, 15 ppb.¹⁷¹ Rate constants for the isoprene-derived Criegee intermediates that have not been directly experimentally measured or theoretically determined are assumed to be similar to *syn*-MVK-oxide
- d. Average of the experimentally determined rate constants listed in Table 5 multiplied by the average formic acid or acetic acid concentrations measured in many locations around the world.^{165, 166 167-169} Rate constants for the isoprene-derived Criegee intermediates that have not been directly experimentally measured or theoretically determined are assumed to be similar to *syn*-MVK-oxide.

vapor (monomer and dimer), the effective rates were calculated using a relative humidity (RH) of 60% and corresponding equilibrium constant determined for H₂O and (H₂O)₂.¹⁷⁰ For the reaction of Criegee intermediates with SO₂ and organic acids, the effective rates were calculated using the average concentration of SO₂ in the United States in 2018 (15 ppb),¹⁷¹ and the average concentration of formic and acetic acids measured in many locations around the world,^{165, 166 167-169} respectively. The unimolecular and bimolecular rate constants for specific isoprene-derived Criegee intermediates have not been measured experimentally (*syn/anti*-MVK-oxide, and *syn/anti*-MACR-oxide). For these Criegee intermediates, the best available theoretically determined rate constant for unimolecular decay and reaction with water vapor (monomer and dimer) are used.^{9, 27, 31} In addition, the rate constants for their reaction with SO₂ and organic acids are assumed to be similar to that experimentally determined for *syn*-MVK-oxide (and other Criegee intermediates).

Trends in the reactivity of Criegee intermediates with respect to substitution and conformational form are illustrated in Figure 1 by showing the calculated effective rates in pie graphs. Figure 1 shows that the reactivity of Criegee intermediates change dramatically depending on their substituents and conformational form. For example, reaction with water vapor dominates the atmospheric removal of Criegee intermediates with a H-atom adjacent to the terminal O-atom (CH₂OO, *anti*-CH₃CHOO, *anti*-MACR-oxide). While reaction of *anti*-MACR-oxide with water vapor is the dominant removal pathway, it is slower than that for CH₂OO and *anti*-CH₃CHOO, as discussed above.

Unimolecular decay is the dominant removal process for *anti*-MVK-oxide and *syn*-MACR-oxide due to the low barrier (ca. 12 kcal mol⁻¹) for dioxole formation. While unimolecular decay is a primary removal pathway for *syn*-CH₃CHOO, (CH₃)COO, and *syn*-MVK-oxide, bimolecular reactions can compete for their removal. Even though the

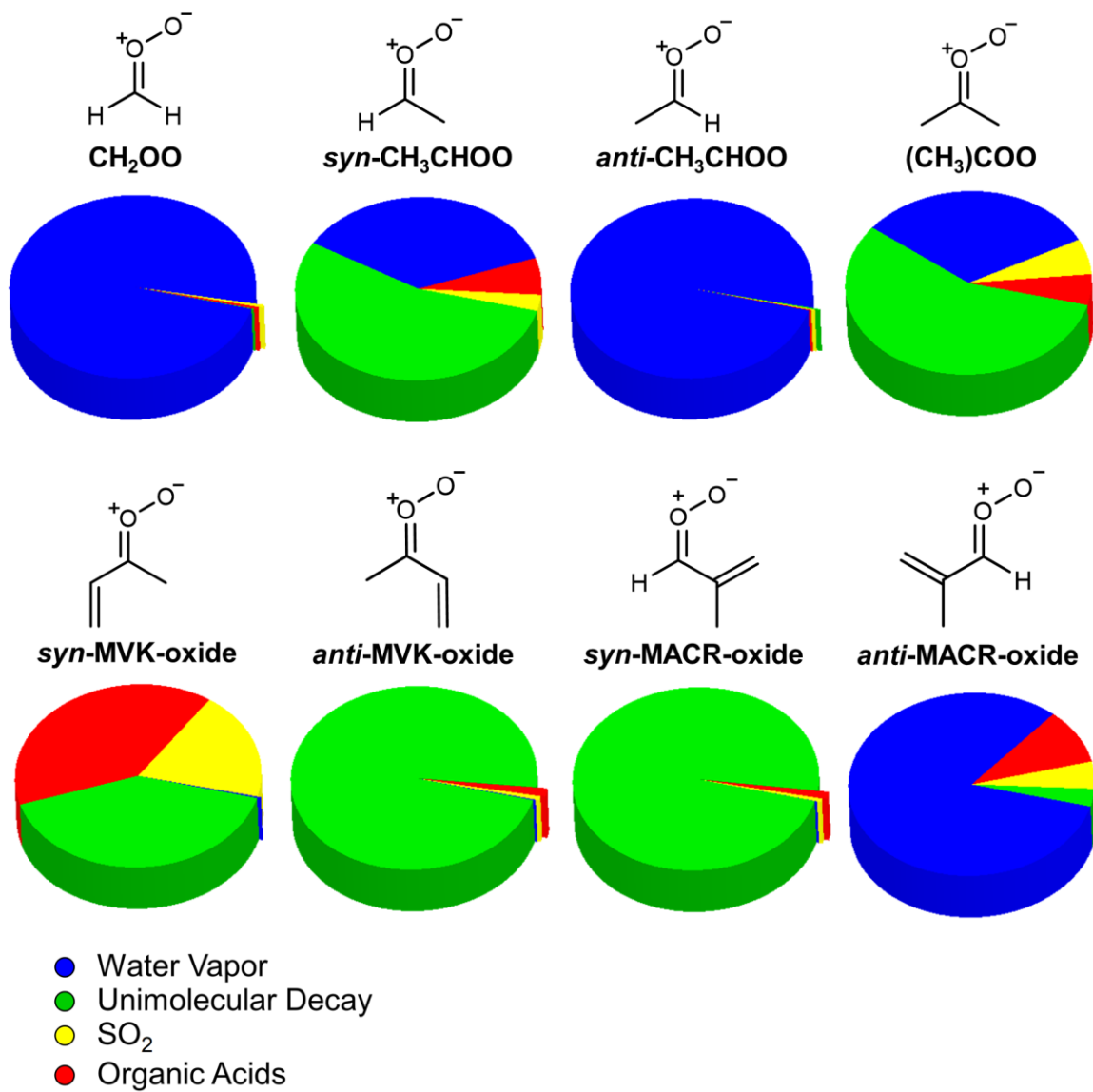


Figure 1. Pie charts illustrating the dominant unimolecular and bimolecular reaction pathways for prototypical and isoprene-derived Criegee intermediates under typical atmospheric conditions. Effective rates for the processes are listed in Table 6.

rate constants for reaction of *syn*-CH₃CHOO and (CH₂)₂COO with water vapor is order of magnitudes lower than that for CH₂OO and *anti*-CH₃CHOO, reaction with water vapor still contributes to their removal due its abundance in the atmosphere. In contrast, the reaction of *syn*-MVK-oxide with water vapor is negligible, owing to steric hindrance as well as disruption of its extended conjugation during reaction. This results in a high transition state barrier for reaction and a corresponding small rate constant for reaction. In addition, the rate for unimolecular decay of *syn*-MVK-oxide is relatively slow (33 s⁻¹) resulting in a relatively long atmospheric lifetime, which allows for reaction with organic acids and SO₂.

It is clear from Figure 1 that there are pronounced substituent and conformer effects on the reactivity of Criegee intermediates. Direct kinetic measurements of isoprene-derived Criegee intermediates as well as rates of reaction for Criegee intermediates derived from other atmospherically abundant alkenes are still needed. These measurements will enable better constraints on atmospheric modeling to evaluate their impact.

4. Summary of Thesis

This work focuses on the electronic spectroscopy, photochemistry, and reactivity of isoprene-derived Criegee intermediates (CH₂OO, MVK-oxide, and MACR-oxide). Criegee intermediates are generated in this work via the alternate synthetic methods described in Sections 2 and 3.^{33, 66, 104} The electronic spectroscopy and photochemistry of these Criegee intermediates are investigated under jet-cooled conditions and discussed in Chapters 2-4.^{65, 66, 71} Jet cooling prepares the Criegee intermediate in well-defined quantum states in a collision free environment for fundamental studies of their UV-vis absorption and photodissociation dynamics. Using the wealth of information

gained from these fundamental studies, the reactivity of the four-carbon Criegee intermediates from isoprene ozonolysis are then investigated under thermal conditions (298 K, 10 Torr) and discussed in Chapters 5-7.^{31, 67, 131}

The electronic spectra of the isoprene derived Criegee intermediates are measured using a UV pump-VUV probe depletion technique (Chapters 3 and 4).^{65, 66} The VUV probe (118 nm, 10.5 eV) is used for photoionization of the Criegee intermediate, which is detected by time-of-flight mass spectrometry (TOF-MS). UV-vis excitation of a $\pi^* \leftarrow \pi$ transition associated with the carbonyl oxide group of the Criegee intermediate induces a depletion of the ground-state population and is detected after a short time delay ($\Delta t \sim 50$ ns) as a reduced VUV photoionization signal. The electronic spectrum associated with the transition is obtained by scanning the UV-vis pump laser, while monitoring the induced depletion of the VUV photoionization signal. Comparison of the UV-vis spectrum to high-level *ab initio* calculations along with the mass specificity of the experiment provides positive identification of Criegee intermediates as the spectral carriers.

The photochemistry associated with the $\pi^* \leftarrow \pi$ transition of Criegee intermediates is investigated in complimentary experiments using velocity map imaging (VMI). Resonant excitation of Criegee intermediates on a $\pi^* \leftarrow \pi$ transition accesses an excited electronic state potential that couples to repulsive states via conical intersection(s), which lead to O¹D and singlet carbonyl products. Analysis of the angular distribution and total kinetic energy release of O¹D products provides insight into the photodissociation dynamics of the Criegee intermediates.

In Chapter 2, VMI is used to characterize the angular and velocity distributions of O¹D photofragments arising from UV excitation of the simplest Criegee intermediate CH₂OO in the long wavelength tail region (364 to 417 nm) of its electronic spectrum. The O¹D images exhibit anisotropic angular distributions indicative of rapid dissociation to

H₂CO X¹A₁ + O ¹D products, which occurs faster than the rotational period (ps) of CH₂OO. The weak oscillatory structure reported previously in the long wavelength region of the UV absorption spectrum is attributed to short-lived resonances associated with the excited 1¹ππ* state of CH₂OO, which decay by nonadiabatic coupling to repulsive singlet states. The total kinetic energy distributions show that nearly half of the available energy, on average, is partitioned to product translation. The balance results in significant internal excitation of the H₂CO co-fragments. The product anisotropy and energy partitioning are unchanged across the UV spectrum and consistent with previously reported experimental and theoretical findings of the CH₂OO π* ← π transition dipole moment and dissociation energy to H₂CO X¹A₁ + O ¹D products.

In Chapter 3, the electronic spectroscopy and photochemistry of MVK-oxide is investigated and compared to CH₂OO and alkyl-substituted Criegee intermediates. The UV-vis spectrum associated with the first π* ← π transition of MVK-oxide is investigated via the UV-visible induced depletion of the *m/z* 86 mass channel. The electronic spectrum is broad and unstructured with its peak at 388 nm. The MVK-oxide spectrum is shifted to a significantly longer wavelength than CH₂OO and alkyl-substituted Criegee intermediates studied previously due to extended conjugation across the vinyl and carbonyl oxide groups. Similar to CH₂OO and alkyl-substituted Criegee intermediates, electronic excitation results in rapid dissociation at λ ≤ 430 nm to methyl vinyl ketone and O ¹D products, the latter detected by 2 + 1 resonance enhanced multiphoton ionization using velocity map imaging. Complementary electronic structure calculations (CASPT2(12,10)/AVDZ) predict two π* ← π transitions with significant oscillator strength for each of the four conformers of MVK-oxide with vertical excitation energies (and corresponding wavelengths) in the 3.1-3.6 eV (350-400 nm) and 4.5-5.5 eV (220-280 nm) regions. The computed electronic absorption profile of MVK-oxide, based on a

Wigner distribution of ground state configurations and summed over the four conformers, is predicted to peak at 397 nm. UV-visible spectroscopy on the first $\pi^* \leftarrow \pi$ transition is shown by a combination of experiment and theory to provide a sensitive means for detection of the MVK-oxide Criegee intermediate that will enable further studies of its photochemistry and unimolecular and bimolecular reaction dynamics (Chapter 5-7).

Chapter 4 presents the first laboratory synthesis of MACR-oxide via the reaction of photolytically generated, resonance-stabilized iodoalkene radicals with oxygen and detection by electronic spectroscopy. MACR-oxide is characterized on its first $\pi^* \leftarrow \pi$ electronic transition using the ground-state depletion method. MACR-oxide exhibits a broad UV-visible spectrum peaked at 380 nm with weak oscillatory structure at long wavelengths, similar to that observed in the UV-vis spectrum of CH_2OO , ascribed to vibrational resonances. Complementary theory predicts two strong $\pi^* \leftarrow \pi$ transitions arising from extended conjugation across MACR-oxide with overlapping contributions from its multiple conformers. Electronic promotion on the first $\pi^* \leftarrow \pi$ transition to the $1^1\pi\pi^*$ state agrees well with experiment, and results in nonadiabatic coupling and prompt release of $\text{O } ^1\text{D}$ products observed as anisotropic velocity-map images. This UV-visible spectrum of MVK-oxide also enables study of its unimolecular and bimolecular reactions under thermal conditions of relevance to the atmosphere.

Chapter 5 presents the first direct kinetic measurements of MVK-oxide reactions with key atmospheric species using absorption spectroscopy. Direct UV-Vis absorption spectra from two independent flow cell experiments overlap with the spectrum obtained under jet-cooled conditions (Chapter 3). Differences in the spectra suggest different conformer distributions under jet-cooled and thermal conditions. Comparison of the experimental lifetime under thermal conditions with theory indicates that only the *syn*-conformers are observed, as the *anti*-conformers are predicted to decay much more

rapidly via an alternate unimolecular decay pathway. MVK-oxide is shown by experiment and theory to react rapidly with SO₂ and formic acid, similar to prototypical Criegee intermediates. In contrast, MVK-oxide is shown to undergo slow removal in the presence of water. Complimentary MPIMS experiments identify SO₃ and organic hydroperoxide formation from the reaction of MVK-oxide with SO₂ and formic acid, respectively. The tropospheric implications of these reactions are evaluated using a global chemistry and transport model.

The experimental lifetime of MVK-oxide in the direct UV-vis absorption experiments indicates *anti*-conformers undergo rapid unimolecular decomposition and do not contribute to the electronic spectrum at early times in the experiment (ca. ms). Chapter 6 provides evidence for the rapid unimolecular decay of *anti*-MVK-oxide and *syn*-MACR-oxide Criegee intermediates via detection of stable products. The extended conjugation between the vinyl and carbonyl oxide groups of these Criegee intermediates facilitates rapid electrocyclic ring closures that form five-membered cyclic peroxides, known as dioxoles. The dioxoles are predicted to undergo further unimolecular decay to oxygenated hydrocarbon radical products that include acetyl, vinoxy, formyl, and 2-methylvinoxy radicals. In the presence of O₂, these radicals rapidly react to form peroxy radicals (ROO), which quickly decay via carbon-centered radical intermediates (QOOH) to stable carbonyl products that are identified in this work. The carbonyl products were detected under thermal conditions (298 K, 10 Torr) using MPIMS. These products are predicted to be formed with OH or HO₂ radical co-products. Unimolecular decay of these Criegee intermediates via dioxole is predicted to be their dominant sink in the atmosphere.

In Chapter 7, the reaction of MVK-oxide with formic acid under thermal conditions (298 K, 10 Torr) is investigated in detail. Products from the catalyzed isomerization and

adduct formation pathways for the reaction between formic acid and MVK-oxide are identified. Specific conformational forms of MVK-oxide (*syn*) undergo intramolecular 1,4 H-atom transfer to form an isomeric vinyl hydroperoxide intermediate, 2-hydroperoxybuta-1,3-diene (HPBD), which subsequently decomposes to hydroxyl and vinyloxy radical products. In this work, HPBD is generated by the formic acid catalyzed isomerization of MVK-oxide and detected using MPIMS. The acid catalyzed isomerization of MVK-oxide proceeds by a double hydrogen-bonded interaction followed by a concerted H-atom transfer via submerged barriers to produce HPBD and regenerate formic acid. The analogous isomerization pathway catalyzed with deuterated formic acid (D₂-formic acid) enables migration of a D atom to yield partially deuterated HPBD (DPBD), which is identified by its distinct mass (*m/z* 87) compared to MVK-oxide (*m/z* 86). In addition, bimolecular reaction of MVK-oxide with D₂-formic acid forms a functionalized hydroperoxide adduct, which is the dominant product channel, and is compared to a previous bimolecular reaction study with normal formic acid (Chapter 5). Complementary high-level *ab initio* calculations are performed to investigate the reaction pathways and kinetics.

References

1. J. O. Nriagu, in *Advances in environmental science and technology*, edited by J. O. Nriagu (John Wiley & Sons, Inc, New York, 1992), Vol. 24. 2.
2. A. H. Goldstein and I. E. Galbally, *Environ. Sci. Technol.* **41**, 1514-1521 (2007).
3. D. Johnson and G. Marston, *Chem. Soc. Rev.* **37**, 699-716 (2008).
4. C. A. Taatjes, D. E. Shallcross and C. J. Percival, *Phys. Chem. Chem. Phys.* **16**, 1704-1718 (2014).
5. G. T. Drozd, T. Kurtén, N. M. Donahue and M. I. Lester, *J. Phys. Chem. A* **121**, 6036-6045 (2017).
6. M. I. Lester and S. J. Klippenstein, *Acc. Chem. Res.* **51**, 978-985 (2018).
7. B. J. Finlayson-Pitts and J. N. Pitts, *Chemistry of the Upper and Lower Atmosphere*. (Academic Press, San Diego, 2000).
8. R. P. Wayne, *Chemistry of atmospheres: An introduction to the chemistry of the atmospheres of earth, the planets, and their satellites*, 3rd ed. (Oxford University Press, Oxford, 2000).
9. L. Vereecken, A. Novelli and D. Taraborrelli, *Phys. Chem. Chem. Phys.* **19**, 31599-31612 (2017).
10. M. A. H. Khan, C. J. Percival, R. L. Caravan, C. A. Taatjes and D. E. Shallcross, *Environ. Sci.: Process. Impacts* **20**, 437-453 (2018).
11. J. H. Kroll, S. R. Sahay, J. G. Anderson, K. L. Demerjian and N. M. Donahue, *J. Phys. Chem. A* **105**, 4446-4457 (2001).
12. N. M. Donahue, G. T. Drozd, S. A. Epstein, A. A. Presto and J. H. Kroll, *Phys. Chem. Chem. Phys.* **13**, 10848-10857 (2011).
13. J. P. Hakala and N. M. Donahue, *J. Phys. Chem. A* **120**, 2173-2178 (2016).
14. T. A. Stephenson and M. I. Lester, *Int. Rev. Phys. Chem.* **39**, 1-33 (2020).
15. K. M. Emmerson, N. Carslaw, D. C. Carslaw, J. D. Lee, G. McFiggans, W. J. Bloss, T. Gravesstock, D. E. Heard, J. Hopkins, T. Ingham, M. J. Pilling, S. C. Smith, M. Jacob and P. S. Monks, *Atmos. Chem. Phys.* **7**, 167-181 (2007).
16. Y. F. Elshorbany, R. Kurtenbach, P. Wiesen, E. Lissi, M. Rubio, G. Villena, E. Gramsch, A. R. Rickard, M. J. Pilling and J. Kleffmann, *Atmos. Chem. Phys.* **9**, 2257-2273 (2009).
17. K. M. Emmerson and N. Carslaw, *Atmos. Environ.* **43**, 3220-3226 (2009).
18. A. S. Hasson, M. Y. Chung, K. T. Kuwata, A. D. Converse, D. Krohn and S. E. Paulson, *J. Phys. Chem. A* **107**, 6176-6182 (2003).
19. C. A. Taatjes, O. Welz, A. J. Eskola, J. D. Savee, A. M. Scheer, D. E. Shallcross, B. Rotavera, E. P. F. Lee, J. M. Dyke, D. K. W. Mok, D. L. Osborn and C. J. Percival, *Science* **340**, 177-180 (2013).
20. M. Nakajima and Y. Endo, *J. Chem. Phys.* **140**, 134302 (2014).
21. T. R. Lewis, M. A. Blitz, D. E. Heard and P. W. Seakins, *Phys. Chem. Chem. Phys.* **17** (7), 4859-4863 (2015).
22. W. Chao, J.-T. Hsieh, C.-H. Chang and J. J.-M. Lin, *Science* **347**, 751-754 (2015).
23. T. Berndt, R. Kaethner, J. Voigtlander, F. Stratmann, M. Pfeifle, P. Reichle, M. Sipila, M. Kulmala and M. Olzmann, *Phys. Chem. Chem. Phys.* **17**, 19862-19873 (2015).
24. B. Long, J. L. Bao and D. G. Truhlar, *J. Am. Chem. Soc.* **138**, 14409-14422 (2016).
25. L.-C. Lin, W. Chao, C.-H. Chang, K. Takahashi and J. J.-M. Lin, *Phys. Chem. Chem. Phys.* **18**, 28189-28197 (2016).
26. L.-C. Lin, H.-T. Chang, C.-H. Chang, W. Chao, M. C. Smith, C.-H. Chang, J. Jr-Min Lin and K. Takahashi, *Phys. Chem. Chem. Phys.* **18**, 4557-4568 (2016).
27. J. M. Anglada and A. Solé, *Phys. Chem. Chem. Phys.* **18**, 17698-17712 (2016).
28. J. Jr-Min Lin and W. Chao, *Chem. Soc. Rev.* **46**, 7483-7497 (2017).
29. L. Sheps, B. Rotavera, A. J. Eskola, D. L. Osborn, C. A. Taatjes, K. Au, D. E. Shallcross, M. A. H. Khan and C. J. Percival, *Phys. Chem. Chem. Phys.* **19**, 21970-21979 (2017).
30. C. Cabezas and Y. Endo, *J. Chem. Phys.* **148**, 014308 (2018).
31. R. L. Caravan, M. F. Vansco, K. Au, M. A. H. Khan, Y.-L. Li, F. A. F. Winiberg, K. Zuraski, Y.-H. Lin, W. Chao, N. Trongsiriwat, P. J. Walsh, D. L. Osborn, C. J. Percival, J. J.-M. Lin, D. E. Shallcross, L. Sheps, S. J. Klippenstein, C. A. Taatjes and M. I. Lester, *Proc. Natl. Acad. Sci.* **117**, 9733-9740 (2020).
32. L. Vereecken, H. Harder and A. Novelli, *Phys. Chem. Chem. Phys.* **14**, 14682-14695 (2012).
33. O. Welz, J. D. Savee, D. L. Osborn, S. S. Vasu, C. J. Percival, D. E. Shallcross and C. A. Taatjes, *Science* **335**, 204-207 (2012).
34. M. Boy, D. Mogensen, S. Smolander, L. Zhou, T. Nieminen, P. Paasonen, C. Plass-Dülmer, M. J. Sipilä, T. Petaja, R. Mauldin III, H. Berresheim and M. Kulmala, *Atmos. Chem. Phys.* **13**, 1680-7316 (2013).
35. C. J. Percival, O. Welz, A. J. Eskola, J. D. Savee, D. L. Osborn, D. O. Topping, D. Lowe, S. R. Utembe, A. Bacak, G. M. c Figgans, M. C. Cooke, P. Xiao, A. T. Archibald, M. E. Jenkin, R. G. Derwent, I. Riipinen, D. W. K. Mok, E. P. F. Lee, J. M. Dyke, C. A. Taatjes and D. E. Shallcross, *Faraday Discuss.* **165**, 45-73 (2013).
36. T. Berndt, J. Voigtlander, F. Stratmann, H. Junninen, R. L. Mauldin III, M. Sipila, M. Kulmala and H. Herrmann, *Phys. Chem. Chem. Phys.* **16**, 19130-19136 (2014).
37. T. Berndt, T. Jokinen, M. Sipilä, R. L. Mauldin III, H. Herrmann, F. Stratmann, H. Junninen and M. Kulmala, *Atmos. Environ.* **89**, 603-612 (2014).
38. D. Stone, M. Blitz, L. Daubney, N. U. M. Howes and P. Seakins, *Phys. Chem. Chem. Phys.* **16**, 1139-1149 (2014).
39. R. Chhantyal-Pun, A. Davey, D. E. Shallcross, C. J. Percival and A. J. Orr-Ewing, *Phys. Chem. Chem. Phys.* **17**, 3617-3626 (2015).

40. M. J. Newland, A. R. Rickard, M. S. Alam, L. Vereecken, A. Munoz, M. Rodenas and W. J. Bloss, *Phys. Chem. Chem. Phys.* **17**, 4076-4088 (2015).
41. H.-L. Huang, W. Chao and J. J.-M. Lin, *Proc. Natl. Acad. Sci.* **112**, 10857-10862 (2015).
42. R. L. Mauldin III, T. Berndt, M. Sipilä, P. Paasonen, T. Petäjä, S. Kim, T. Kurtén, F. Stratmann, V. M. Kerminen and M. Kulmala, *Nature* **488**, 193 (2012).
43. M. Kumar, D. H. Busch, B. Subramaniam and W. H. Thompson, *Phys. Chem. Chem. Phys.* **16**, 22968-22973 (2014).
44. O. Welz, A. J. Eskola, L. Sheps, B. Rotavera, J. D. Savee, A. M. Scheer, D. L. Osborn, D. Lowe, A. Murray Booth, P. Xiao, M. A. H. Khan, C. J. Percival, D. E. Shallcross and C. A. Taatjes, *Angew. Chem. Int. Ed.* **53**, 4547-4550 (2014).
45. F. Liu, Y. Fang, M. Kumar, W. H. Thompson and M. I. Lester, *Phys. Chem. Chem. Phys.* **17**, 20490-20494 (2015).
46. R. Chhantyal-Pun, M. R. McGillen, J. M. Beames, M. A. H. Khan, C. J. Percival, D. E. Shallcross and A. J. Orr-Ewing, *Angew. Chem. Int. Ed.* **56**, 9044-9047 (2017).
47. L. Vereecken, *Phys. Chem. Chem. Phys.* **19**, 28630-28640 (2017).
48. R. Chhantyal-Pun, B. Rotavera, M. R. McGillen, M. A. H. Khan, A. J. Eskola, R. L. Caravan, L. Blacker, D. P. Tew, D. L. Osborn, C. J. Percival, C. A. Taatjes, D. E. Shallcross and A. J. Orr-Ewing, *ACS Earth and Space Chem.* **2**, 833-842 (2018).
49. C. A. Taatjes, M. A. H. Khan, A. J. Eskola, C. J. Percival, D. L. Osborn, T. J. Wallington and D. E. Shallcross, *Environ. Sci.: Process. Impacts* **53**, 1245-1251 (2019).
50. C. Cabezas and Y. Endo, *Phys. Chem. Chem. Phys.* **22**, 446-454 (2020).
51. C. A. Taatjes, *Annu. Rev. Phys. Chem.* **68**, 183-207 (2017).
52. R. A. Cox and S. A. Penkett, *J. Chem. Soc., Faraday Trans. 1* **68**, 1735-1753 (1972).
53. R. A. Cox and S. A. Penkett, *Nature* **230** (5292), 321-322 (1971).
54. A. Novelli, K. Hens, C. Tatum Ernest, M. Martinez, A. C. Nölscher, V. Sinha, P. Paasonen, T. Petäjä, M. Sipilä, T. Elste, C. Plass-Dülmer, G. J. Phillips, D. Kubistin, J. Williams, L. Vereecken, J. Lelieveld and H. Harder, *Atmos. Chem. Phys.* **17**, 7807-7826 (2017).
55. M. A. H. Khan, W. C. Morris, M. Galloway, Beth M. A. Shallcross, C. J. Percival and D. E. Shallcross, *Int. J. Chem. Kinet.* **49**, 611-621 (2017).
56. R. Chhantyal-Pun, M. A. H. Khan, R. Martin, N. Zachhuber, Z. J. Buras, C. J. Percival, D. E. Shallcross and A. J. Orr-Ewing, *ACS Earth and Space Chemistry* **3**, 2363-2371 (2019).
57. R. Criegee and G. Wenner, *Justus Liebigs Annalen der Chemie* **564**, 9-15 (1949).
58. C. A. Taatjes, O. Welz, A. J. Eskola, J. D. Savee, D. L. Osborn, E. P. F. Lee, J. M. Dyke, D. W. K. Mok, D. E. Shallcross and C. J. Percival, *Phys. Chem. Chem. Phys.* **14**, 10391-10400 (2012).
59. C. A. Taatjes, F. Liu, B. Rotavera, M. Kumar, R. Caravan, D. L. Osborn, W. H. Thompson and M. I. Lester, *J. Phys. Chem. A* **121**, 16-23 (2017).
60. R. Chhantyal-Pun, O. Welz, J. D. Savee, A. J. Eskola, E. P. F. Lee, L. Blacker, H. R. Hill, M. Ashcroft, M. A. H. Khan, G. C. Lloyd-Jones, L. Evans, B. Rotavera, H. Huang, D. L. Osborn, D. K. W. Mok, J. M. Dyke, D. E. Shallcross, C. J. Percival, A. J. Orr-Ewing and C. A. Taatjes, *J. Phys. Chem. A* **121**, 4-15 (2017).
61. J. M. Beames, F. Liu, L. Lu and M. I. Lester, *J. Am. Chem. Soc.* **134**, 20045-20048 (2012).
62. J. M. Beames, F. Liu, L. Lu and M. I. Lester, *J. Chem. Phys.* **138**, 244307 (2013).
63. F. Liu, J. M. Beames, A. M. Green and M. I. Lester, *J. Phys. Chem. A* **118**, 2298-2306 (2014).
64. R. L. Caravan, M. A. H. Khan, B. Rotavera, E. Papajak, I. O. Antonov, M.-W. Chen, K. Au, W. Chao, D. L. Osborn, J. J.-M. Lin, C. J. Percival, D. E. Shallcross and C. A. Taatjes, *Faraday Discuss.* **200**, 313-330 (2017).
65. M. F. Vansco, B. Marchetti and M. I. Lester, *J. Chem. Phys.* **149**, 244309 (2018).
66. M. F. Vansco, B. Marchetti, N. Trongsirawat, G. Wang, T. Bhagde, P. J. Walsh, S. J. Klippenstein and M. I. Lester, *J. Am. Chem. Soc.* **141**, 15058-15069 (2019).
67. M. F. Vansco, R. L. Caravan, K. Zuraski, F. A. F. Winiberg, K. Au, N. Trongsirawat, P. J. Walsh, D. L. Osborn, C. J. Percival, M. A. H. Khan, D. E. Shallcross, C. A. Taatjes and M. I. Lester, *J. Phys. Chem. A* **124**, 3542-3554 (2020).
68. J. H. Lehman, H. Li, J. M. Beames and M. I. Lester, *J. Chem. Phys.* **139**, 141103 (2013).
69. H. Li, Y. Fang, N. M. Kidwell, J. M. Beames and M. I. Lester, *J. Phys. Chem. A* **119**, 8328-8337 (2015).
70. H. Li, Y. Fang, J. M. Beames and M. I. Lester, *J. Chem. Phys.* **142**, 214312 (2015).
71. M. F. Vansco, H. Li and M. I. Lester, *J. Chem. Phys.* **147**, 013907 (2017).
72. L. Sheps, *J. Phys. Chem. Lett.* **4**, 4201-4205 (2013).
73. L. Sheps, A. M. Scully and K. Au, *Phys. Chem. Chem. Phys.* **16**, 26701-26706 (2014).
74. W.-L. Ting, Y.-H. Chen, W. Chao, M. C. Smith and J. J.-M. Lin, *Phys. Chem. Chem. Phys.* **16**, 10438-10443 (2014).
75. W.-L. Ting, C.-H. Chang, Y.-F. Lee, H. Matsui, Y.-P. Lee and J. J.-M. Lin, *J. Chem. Phys.* **141**, 104308 (2014).
76. M. C. Smith, W.-L. Ting, C.-H. Chang, K. Takahashi, K. A. Boering and J. J.-M. Lin, *J. Chem. Phys.* **141**, 074302 (2014).
77. Z. J. Buras, R. M. I. Elsamra and W. H. Green, *J. Phys. Chem. Lett.* **5**, 2224-2228 (2014).
78. Z. J. Buras, R. M. I. Elsamra, A. Jalan, J. E. Middaugh and W. H. Green, *J. Phys. Chem. A* **118**, 1997-2006 (2014).
79. Y.-P. Chang, C.-H. Chang, K. Takahashi and J. J.-M. Lin, *Chem. Phys. Lett.* **653**, 155-160 (2016).
80. M. C. Smith, W. Chao, K. Takahashi, K. A. Boering and J. J.-M. Lin, *J. Phys. Chem. A* **120**, 4789-4798 (2016).
81. S. V. Tadayon, E. S. Foreman and C. Murray, *J. Phys. Chem. A* **122**, 258-268 (2018).

82. D. Stone, K. Au, S. Sime, D. J. Medeiros, M. Blitz, P. W. Seakins, Z. Decker and L. Sheps, *Phys. Chem. Chem. Phys.* **20**, 24940-24954 (2018).
83. R. Chhantyal-Pun, R. J. Shannon, D. P. Tew, R. L. Caravan, M. Duchi, C. Wong, A. Ingham, C. Feldman, M. R. McGillen, M. A. H. Khan, I. O. Antonov, B. Rotavera, K. Ramasesha, D. L. Osborn, C. A. Taatjes, C. J. Percival, D. E. Shallcross and A. J. Orr-Ewing, *Phys. Chem. Chem. Phys.* (2019).
84. Y. Q. Liu, C. T. Yin, M. C. Smith, S. Y. Liu, M. D. Chen, X. H. Zhao, C. L. Xiao, D. X. Dai, J. J. M. Lin, K. Takahashi, W. Dong and X. Yang, *Phys. Chem. Chem. Phys.* **20**, 29669-29676 (2018).
85. Y. H. Lin, K. Takahashi and J. J. M. Lin, *J. Phys. Chem. Lett.* **9**, 184-188 (2018).
86. W. Chao, C. Yin, K. Takahashi and J. J. M. Lin, *Phys. Chem. Chem. Phys.* **21**, 22589-22597 (2019).
87. W. Chao, C. T. Yin, K. Takahashi and J. J. M. Lin, *J. Phys. Chem. A* **123**, 8336-8348 (2019).
88. W. Chao, Y.-H. Lin, C. T. Yin, W. H. Lin, K. Takahashi and J. J. M. Lin, *Phys. Chem. Chem. Phys.* **21**, 13633-13640 (2019).
89. Y. L. Li, Y. H. Lin, C. T. Yin, K. Takahashi, C. Y. Chiang, Y. P. Chang and J. J. M. Lin, *J. Phys. Chem. A* **123**, 4096-4103 (2019).
90. W. Chao, J. J. M. Lin, K. Takahashi, A. Tomas, L. Yu, Y. Kajii, S. Batut, C. Schoemaeker and C. Fittschen, *Angew. Chem. Int. Ed.* **58**, 5013-5017 (2019).
91. M. C. Smith, C.-H. Chang, W. Chao, L.-C. Lin, K. Takahashi, K. A. Boering and J. J.-M. Lin, *J. Phys. Chem. Lett.* **6**, 2708-2713 (2015).
92. M. R. McGillen, B. F. E. Curchod, R. Chhantyal-Pun, J. M. Beames, N. Watson, M. A. H. Khan, L. McMahon, D. E. Shallcross and A. J. Orr-Ewing, *ACS Earth and Space Chem.* **1**, 664-672 (2017).
93. Y.-T. Su, H.-Y. Lin, R. Putikam, H. Matsui, M. C. Lin and Y.-P. Lee, *Nat. Chem.* **6**, 477-483 (2014).
94. F. Liu, J. M. Beames, A. S. Petit, A. B. McCoy and M. I. Lester, *Science* **345** (6204), 1596-1598 (2014).
95. F. Liu, J. M. Beames and M. I. Lester, *J. Chem. Phys.* **141**, 234312 (2014).
96. Y. Fang, F. Liu, S. J. Klippenstein and M. I. Lester, *J. Chem. Phys.* **145**, 044312 (2016).
97. H.-Y. Lin, Y.-H. Huang, X. Wang, J. M. Bowman, Y. Nishimura, H. A. Witek and Y.-P. Lee, *Nat. Commun.* **6**, 7012 (2015).
98. Y. Fang, F. Liu, V. P. Barber, S. J. Klippenstein, A. B. McCoy and M. I. Lester, *J. Chem. Phys.* **144**, 061102 (2016).
99. N. M. Kidwell, H. Li, X. Wang, J. M. Bowman and M. I. Lester, *Nat. Chem.* **8**, 509-514 (2016).
100. Y. Fang, F. Liu, V. P. Barber, S. J. Klippenstein, A. B. McCoy and M. I. Lester, *J. Chem. Phys.* **145**, 234308 (2016).
101. H. Li, N. M. Kidwell, X. Wang, J. M. Bowman and M. I. Lester, *J. Chem. Phys.* **145**, 104307 (2016).
102. Y. Fang, V. P. Barber, S. J. Klippenstein, A. B. McCoy and M. I. Lester, *J. Chem. Phys.* **146**, 134307 (2017).
103. A. M. Green, V. P. Barber, Y. Fang, S. J. Klippenstein and M. I. Lester, *Proc. Natl. Acad. Sci.* **114**, 12372-12377 (2017).
104. V. P. Barber, S. Pandit, A. M. Green, N. Trongsiwat, P. J. Walsh, S. J. Klippenstein and M. I. Lester, *J. Am. Chem. Soc.* **140**, 10866-10880 (2018).
105. V. P. Barber, S. Pandit, V. J. Esposito, A. B. McCoy and M. I. Lester, *J. Phys. Chem. A* **123**, 2559-2569 (2019).
106. Y. P. Chang, H. H. Chang and J. J. M. Lin, *Phys. Chem. Chem. Phys.* **20**, 97-102 (2018).
107. V. P. Barber, A. S. Hansen, Y. Georgievskii, S. J. Klippenstein and M. I. Lester, *J. Chem. Phys.* **152**, 094301 (2020).
108. A. S. Hansen, Z. Liu, S. Chen, M. G. Schumer, P. J. Walsh and M. I. Lester, *J. Phys. Chem. A* **124**, 4929-4938 (2020).
109. M. Nakajima and Y. Endo, *J. Chem. Phys.* **139**, 101103-101103 (2013).
110. M. C. McCarthy, L. Cheng, K. N. Crabtree, O. Martinez, T. L. Nguyen, C. C. Womack and J. F. Stanton, *J. Phys. Chem. Lett.* **4**, 4133-4139 (2013).
111. M. Nakajima and Y. Endo, *J. Chem. Phys.* **140**, 011101 (2014).
112. A. M. Daly, B. J. Drouin and S. Yu, *Journal of Molecular Spectroscopy* **297**, 16-20 (2014).
113. M. Nakajima, Q. Yue and Y. Endo, *J. Mol. Spectrosc.* **310**, 109-112 (2015).
114. C. Cabezas, J.-C. Guillemin and Y. Endo, *J. Chem. Phys.* **145**, 224314 (2016).
115. C. Cabezas, J.-C. Guillemin and Y. Endo, *J. Chem. Phys.* **146**, 174304 (2017).
116. C. Cabezas and Y. Endo, *Phys. Chem. Chem. Phys.* **21**, 18029-18408 (2019).
117. Y. Liu, F. Liu, S. Liu, D. Dai, W. Dong and X. Yang, *Phys. Chem. Chem. Phys.* **19**, 20786-20794 (2017).
118. X. Zhou, Y. Liu, W. Dong and X. Yang, *J. Phys. Chem. Lett.* **10**, 4817-4821 (2019).
119. A. Guenther, C. N. Hewitt, D. Erickson, R. Fall, C. Geron, T. Graedel, P. Harley, L. Klinger, M. Lerdau, W. A. McKay, T. Pierce, B. Scholes, R. Steinbrecher, R. Tallamraju, J. Taylor and P. Zimmerman, *J. Geophys. Res. Atmos.* **100**, 8892 (1995).
120. K. Sindelarova, C. Granier, I. Bouarar, A. Guenther, S. Tilmes, T. Stavrou, J. F. Müller, U. Kuhn, P. Stefani and W. Knorr, *Atmos. Chem. Phys.* **14**, 9317-9341 (2014).
121. K. T. Kuwata, L. C. Valin and A. D. Converse, *J. Phys. Chem. A* **109**, 10725 (2005).
122. K. T. Kuwata and L. C. Valin, *Chem. Phys. Lett.* **451**, 186-191 (2008).
123. A. Bagchi, Y. Yu, J.-H. Huang, C.-C. Tsai, W.-P. Hu and C. C. Wang, *Phys. Chem. Chem. Phys.* **22**, 6528-6537 (2020).
124. B. Long, J. L. Bao and D. G. Truhlar, *Nat. Comm.* **10**, 2003 (2019).
125. K. T. Kuwata, M. R. Hermes, M. J. Carlson and C. K. Zogg, *J. Phys. Chem. A* **114**, 9192-9204 (2010).
126. T. B. Nguyen, G. S. Tyndall, J. D. Crouse, A. P. Teng, K. H. Bates, R. H. Schwantes, M. M. Coggon, L. Zhang, P. Feiner, D. O. Miller, K. M. Skog, J. C. Rivera-Rios, M. Dorris, K. F. Olson, A. Koss, R. J. Wild, S. S. Brown, A. H.

- Goldstein, J. A. de Gouw, W. H. Brune, F. N. Keutsch, J. H. Seinfeld and P. O. Wennberg, *Phys. Chem. Chem. Phys.* **18**, 10241-10254 (2016).
127. J. Qiu, S. Ishizuka, K. Tonokura, A. Colussi and S. Enami, *J. Phys. Chem. A* **122**, 7910-7917 (2018).
128. J. M. Anglada, J. M. Bofill, S. Olivella and A. Solé, *J. Am. Chem. Soc.* **118**, 4636-4647 (1996).
129. Y. Endo, H. A. Witek, C.-A. Chung and Y.-P. Lee, *J. Phys. Chem. A* **124**, 6203-6206 (2020).
130. D. L. Osborn, P. Zou, H. Johnsen, C. C. Hayden, C. A. Taatjes, V. D. Knyazev, S. W. North, D. S. Peterka, M. Ahmed and S. R. Leone, *Rev. Sci. Instrum.* **79**, 104103 (2008).
131. M. F. Vansco, R. L. Caravan, S. Pandit, K. Zuraski, F. A. F. Winiberg, K. Au, T. Bhagde, N. Trongsiriwat, P. J. Walsh, D. L. Osborn, C. J. Percival, S. J. Klippenstein, C. A. Taatjes and M. I. Lester, *In Preparation* (2020).
132. K. Samanta, J. M. Beames, M. I. Lester and J. E. Subotnik, *J. Chem. Phys.* **141**, 134303 (2014).
133. V. P. Barber, V. J. Esposito, T. Trabelsi, A. S. Hansen, T. A. McHenry, J. S. Francisco and M. I. Lester, *Chem. Phys. Lett.* **751**, 137478 (2020).
134. M. M. Davis, J. D. Weidman, A. S. Abbott, G. E. Douberly, J. M. Turney and H. F. Schaefer III, *J. Chem. Phys.* **151**, 124302 (2019).
135. J. D. Weidman, R. T. Allen, K. B. Moore III and H. F. Schaefer III, *J. Chem. Phys.* **148**, 184308 (2018).
136. K. T. Kuwata, A. S. Hasson, R. V. Dickinson, E. B. Peterson and L. C. Valin, *J. Phys. Chem. A* **109**, 2514-2524 (2005).
137. F. Bianchi, T. Kurtén, M. Riva, C. Mohr, M. P. Rissanen, P. Roldin, T. Berndt, J. D. Crouse, P. O. Wennberg, T. F. Mentel, J. Wildt, H. Junninen, T. Jokinen, M. Kulmala, D. R. Worsnop, J. A. Thornton, N. Donahue, H. G. Kjaergaard and M. Ehn, *Chem. Rev.* **119**, 3472-3509 (2019).
138. T. F. Mentel, M. Springer, M. Ehn, E. Kleist, I. Pullinen, T. Kurtén, M. Rissanen, A. Wahner and J. Wildt, *Atmos. Chem. Phys.* **15**, 6745-6765 (2015).
139. T. L. Nguyen, H. Lee, D. A. Matthews, M. C. McCarthy and J. F. Stanton, *J. Phys. Chem. A* **119**, 5524-5533 (2015).
140. M. S. Alam, M. Camredon, A. R. Rickard, T. Carr, K. P. Wyche, K. E. Hornsby, P. S. Monks and W. J. Bloss, *Phys. Chem. Chem. Phys.* **13**, 11002-11015 (2011).
141. J. H. Kroll, N. M. Donahue, V. J. Cee, K. L. Demerjian and J. G. Anderson, *J. Am. Chem. Soc.* **124**, 8518-8519 (2002).
142. Y. L. Li, M. T. Kuo and J. J. M. Lin, *RSC Advances* **10**, 8518-8524 (2020).
143. J. D. Fenske, A. S. Hasson, A. W. Ho and S. E. Paulson, *J. Phys. Chem. A* **104**, 9921-9932 (2000).
144. L. Vereecken, D. R. Glowacki and M. J. Pilling, *Chem. Rev.* **115**, 4063-4114 (2015).
145. B. Z. Chen, J. M. Anglada, M. B. Huang and F. Kong, *J. Phys. Chem. A* **106**, 1877-1884 (2002).
146. P. Aplincourt, E. Henon, F. Bohr and M. F. Ruiz-Lopez, *Chem. Phys.* **285**, 221-231 (2002).
147. D.-C. Fang and X.-Y. Fu, *J. Phys. Chem. A* **106**, 2988-2993 (2002).
148. J. Kalinowski, M. Räsänen, P. Heinonen, I. Kilpeläinen and R. B. Gerber, *Angew. Chem. Int. Ed.* **53**, 265-268 (2014).
149. T. L. Nguyen, L. McCaslin, M. C. McCarthy and J. F. Stanton, *J. Chem. Phys.* **145**, 131102 (2016).
150. H. J. Tobias and P. J. Ziemann, *J. Phys. Chem. A* **105**, 6129-6135 (2001).
151. A. B. Ryzhkov and P. A. Ariya, *Phys. Chem. Chem. Phys.* **6**, 5042-5050 (2004).
152. C. Yin and K. Takahashi, *Phys. Chem. Chem. Phys.* **20**, 20217-20227 (2018).
153. T. Berndt, T. Jokinen, R. L. Mauldin III, T. Petäjä, H. Herrmann, H. Junninen, P. Paasonen, D. R. Worsnop and M. Sipila, *J. Phys. Chem. Lett.* **3**, 2892-2896 (2012).
154. M. J. Newland, A. R. Rickard, L. Vereecken, A. Muñoz, M. Ródenas and W. J. Bloss, *Atmos. Phys. Chem* **15**, 9521-9536 (2015).
155. B. Ouyang, M. W. McLeod, R. L. Jones and W. J. Bloss, *Phys. Chem. Chem. Phys.* **15**, 17070-17075 (2013).
156. N. A. I. Watson, J. A. Black, T. M. Stonelake, P. J. Knowles and J. M. Beames, *J. Phys. Chem. A* **123**, 218-229 (2019).
157. L. Vereecken, A. R. Rickard, M. J. Newland and W. J. Bloss, *Phys. Chem. Chem. Phys.* **17**, 23847-23858 (2015).
158. Y. Zhao, L. M. Wingen, V. Perraud, J. Greaves and B. J. Finlayson-Pitts, *Phys. Chem. Chem. Phys.* **17**, 12500-12514 (2015).
159. A. Sadezky, R. Winterhalter, B. Kanawati, A. Römpf, B. Spengler, A. Mellouki, G. Le Bras, P. Chaimbault and G. K. Moortgat, *Atmos. Chem. Phys.* **8**, 2667-2699 (2008).
160. M. Kulmala, L. Pirjola and J. M. Mäkelä, *Nature* **404**, 66-69 (2000).
161. T. Kurtén, J. R. Lane, S. Jørgensen and H. G. Kjaergaard, *J. Phys. Chem. A* **115**, 8669-8681 (2011).
162. K. T. Kuwata, E. J. Guinn, M. R. Hermes, J. A. Fernandez, J. M. Mathison and K. Huang, *J. Phys. Chem. A* **119**, 10316-10335 (2015).
163. T. Berndt, H. Herrmann and T. Kurtén, *J. Am. Chem. Soc.* **139**, 13387-13392 (2017).
164. J. Ahrens, P. T. M. Carlsson, N. Hertl, M. Olzmann, M. Pfeifle, J. L. Wolf and T. Zeuch, *Angew. Chem. Int. Ed.* **53**, 715-719 (2014).
165. A. Chebbi and P. Carlier, *Atmos. Environ.* **30**, 4233-4249 (1996).
166. F. Paulot, D. Wunch, J. D. Crouse, G. C. Toon, D. B. Millet, P. F. DeCarlo, C. Vigouroux, N. M. Deutscher, G. Gonzalez Abad, J. Notholt, T. Warneke, J. W. Hannigan, C. Warnecke, J. A. De Gouw, E. J. Dunlea, M. De Maziere, D. W. T. Griffith, P. Bernath, J. L. Jiminez and P. O. Wennberg, *Atmos. Chem. Phys.* **11**, 1989-2013 (2011).
167. T. J. Bannan, A. Bacak, J. B. A. Muller, A. M. Booth, B. Jones, M. Le Breton, K. E. Leather, M. Ghalaieny, P. Xiao, D. E. Shallcross and C. J. Percival, *Atmos. Environ.* **83**, 301-310 (2014).

168. T. J. Bannan, A. M. Booth, M. Le Breton, A. Bacak, J. B. A. Muller, K. E. Leather, M. A. H. Khan, J. D. Lee, R. E. Dunmore, J. R. Hopkins, Z. L. Fleming, L. Sheps, C. A. Taatjes, D. E. Shallcross and C. J. Percival, *J. Geophys. Res. Atmos.* **122**, 12488-12498 (2017).
169. D. B. Millet, M. Baasandorj, D. K. Farmer, J. A. Thornton, K. Baumann, P. Brophy, S. Chaliyakunnel, J. A. De Gouw, M. Graus, L. Hu, A. Koss, B. H. Lee, F. D. Lopez-Hilfiker, J. A. Neuman, F. Paulot, J. Peischl, I. B. Pollack, T. B. Ryerson, C. Warnecke, B. J. Williams and J. Xu, *Atmos. Chem. Phys.* **15**, 6283-6304 (2015).
170. J. M. Anglada, G. J. Hoffman, L. V. Slipchenko, M. T. C. Martins-Costa, M. F. Ruiz-López and J. S. Francisco, *J. Phys. Chem. A* **117**, 10381-10396 (2013).
171. United States Environmental Protection Agency, Sulfur Dioxide Trends (2019) <https://www.epa.gov/air-trends/sulfur-dioxide-trends>

CHAPTER 2
PROMPT RELEASE OF O ¹D PRODUCTS UPON
UV EXCITATION OF CH₂OO CRIEGEE INTERMEDIATES

This research has been reproduced from *The Journal of Chemical Physics*, **147**, 013907 (2017) with the permission of AIP publishing. The research was performed with graduate student Hongwei Li and Marsha I. Lester (*Department of Chemistry, University of Pennsylvania*).

I. Introduction

The simplest carbonyl oxide CH_2OO is a key intermediate in the ozonolysis of ethene and other terminal alkenes, including isoprene and β -pinene.^{1,2} Ozonolysis is also a significant atmospheric loss process for alkenes. While collisional stabilization of the simplest Criegee intermediate formed in the exothermic reaction of ethene with ozone has been predicted or indirectly inferred for some time,^{3,4} the direct detection of CH_2OO remained elusive until an alternate synthetic route for efficient production of CH_2OO was developed.⁵ Following this breakthrough, the CH_2OO Criegee intermediate has been investigated extensively in spectroscopic, kinetic, dynamical, and theoretical studies summarized in recent review articles.⁶⁻⁸ Nevertheless, the direct detection of stabilized CH_2OO produced in ethene ozonolysis continues to be a challenge, as evident from a recent Fourier transform microwave (FTMW) study.⁹ Thus far, CH_2OO has been detected by VUV photoionization,⁵ UV,¹⁰⁻¹² IR,¹³ and FTMW,^{9,14} and among these methods direct UV absorption has been utilized most often for laboratory kinetic studies.¹⁵⁻²¹ UV absorption is sensitive and easy to implement, and therefore a comprehensive understanding of the resultant photophysical decay pathways is of special interest.

In 2012, Beames et al. reported a very strong $\pi^* \leftarrow \pi$ ($\text{B}^1\text{A}' - \text{X}^1\text{A}'$) transition for the simplest Criegee intermediate CH_2OO peaked at 335 nm with large cross section (on the order of 10^{-17} cm^2) spanning from ca. 280 to 380 nm.¹⁰ The absorption cross section measurements were made by UV depletion of the photoionization signal at $m/z=46$ (CH_2OO^+) obtained with 118 nm (10.5 eV) radiation. Very large UV-induced depletions – approaching 100% near the peak with unfocussed UV laser radiation – suggested that CH_2OO promoted to the excited $\text{B}^1\text{A}'$ state undergoes rapid dynamics.¹⁰ In these

studies, CH₂OO was prepared via the alternative synthetic route of photolytically generated CH₂I radicals with O₂, and cooled in a supersonic expansion to ~10 K.²² The UV depletion data were recorded at discrete wavelengths generated with many dyes and dye mixtures to cover the broad spectral region, and fit to a simple Gaussian form. UV-induced depletions of at least 2-3% were required for reliable measurements.

Later, Sheps¹¹ and Ting et al.¹² carried out standard Beer's law UV absorption measurements of CH₂OO prepared by reaction of CH₂I + O₂ in a flow cell at room temperature. These groups obtained similar UV spectra for CH₂OO in the region of peak absorption, refined the absorption cross section [$1.2(2) \times 10^{-17}$ cm² at 340 nm],¹² and found a weak tail extending to longer wavelengths with broad oscillatory structure. The broad oscillatory structure associated with the long wavelength region permits more distinctive spectroscopic identification of CH₂OO than the unstructured region near the peak of the UV spectrum. The dynamical processes that occur following CH₂OO absorption in the long wavelength tail region has been a matter of debate. Sheps¹¹ suggested that "The weakly resolved, regularly spaced peak progression, most likely corresponds to excitation of long-lived vibrational states." He further indicated that "these bound states must relax by fluorescence or by intersystem crossing to lower-lying electronic states." By contrast, Ting et al.¹² argued that "the measurement of photoproduct anisotropy indicates that the photodissociation (308-360 nm) is faster than rotation which is in the picosecond timescale." Most recently, Foreman et al.²³ reported high-resolution absorption spectra of CH₂OO in the long wavelength region beyond 360 nm, varied the temperature, and concluded that the broad oscillatory features on the long wavelength tail lacked rotational structure and were not due to hot bands. They

speculated that the “rapid excited state dynamics evidenced by broad bandwidths must be attributed to non-dissociative population transfer.”

The comment by Ting et al.¹² on photodissociation refers to velocity map imaging (VMI) studies by Lehman et al.²⁴ of O ¹D products observed following UV excitation of CH₂OO on the B¹A' – X¹A' transition at 308, 330, and 360 nm, which revealed anisotropic images indicative of rapid (ps) dissociation to the lowest spin-allowed H₂CO X¹A₁ + O ¹D product channel. The present work extends the O ¹D VMI studies to the long wavelength tail region of the CH₂OO absorption spectrum from 364 to 417 nm. Previously, VMI studies were also conducted for O ³P products associated with the higher energy, spin-allowed H₂CO a³A'' + O ³P product channel following UV excitation of CH₂OO on the B¹A' – X¹A' transition at 330 and 350 nm.²⁵ Again, anisotropic angular distributions were observed, indicating that dissociation to O ³P occurs more rapidly than the rotational period of CH₂OO (ps).

The VMI images revealed broad and unstructured total kinetic energy release (TKER) distributions indicative of a high degree of internal (vibrational and/or rotational) excitation of the H₂CO X¹A₁ or a³A'' co-fragments.^{24, 25} The termination of the kinetic energy distribution for the H₂CO a³A'' + O ³P channel was used to establish an energetic threshold for this channel of ca. 76 kcal mol⁻¹.²⁵ This work also showed that the O ³P yield is quite small for $\lambda \geq 360$ nm and is energetically closed at 378 nm. This threshold, along with the well-known singlet-triplet energy spacings in formaldehyde and oxygen atoms,^{26, 27} yielded an upper limit for the dissociation energy of CH₂OO X¹A₁ to H₂CO X¹A₁ + O ¹D products of 49.0 ± 0.3 kcal mol⁻¹. This compares favorably with recent theoretical predictions, including zero-point corrections, of 47.0 kcal mol⁻¹ from Dawes et al.²⁸ using explicitly correlated MRCI-F12 and 49.2 kcal mol⁻¹ from Lehman et al.²⁴ using

MRCI//CASSCF(12,11)/aug-cc-pVTZ level electronic structure calculations. Prior work by Nguyen et al.²⁹ estimated 51.2 kcal mol⁻¹, Anglada et al.³⁰ computed 32.4 kcal mol⁻¹, and the earliest report by Cremer et al.³¹ predicted a dissociation energy of 47.0 kcal mol⁻¹.

While there have been several high level calculations of the excited electronic states of CH₂OO,^{28, 32-34} Dawes et al.²⁸ carried out the most accurate calculation to date using explicitly correlated MRCI-F12 electronic structure theory and large active spaces. The computed potentials for CH₂OO in its ground and excited electronic singlet states along the O-O dissociation coordinate are reproduced in Figure 1. Their calculated UV absorption spectrum (using a 1D model and potential) is similar to experiment in terms of central peak position and overall shape, and also displays evidence of weak oscillatory structure in the long wavelength tail. The calculations indicate a significant well in the B¹A' state ($D_e \sim 5980$ cm⁻¹ relative to the H₂CO a³A'' + O ³P limit), which is sufficiently deep to suggest that bound states or recurrences of the wave packet may be the origin of the weak oscillations observed in experimental spectra at long wavelengths.^{11, 12, 23}

The present study focuses on the photodissociation dynamics of jet-cooled CH₂OO at longer wavelengths (364 to 417 nm) than explored previously utilizing velocity map imaging of the O ¹D products. The 2+1 resonance-enhanced multiphoton ionization (REMPI) scheme provides sensitive detection of the O ¹D products, and velocity map imaging enables determination of the angular and velocity distributions of the O ¹D products. The UV pump and REMPI probe scheme is shown in Figure 1. Velocity map images of the O ¹D products are obtained upon excitation in the long wavelength tail of the CH₂OO UV absorption spectrum. The VMI results demonstrate that CH₂OO undergoes rapid UV-induced dissociation to H₂CO X¹A₁ + O ¹D products on a timescale

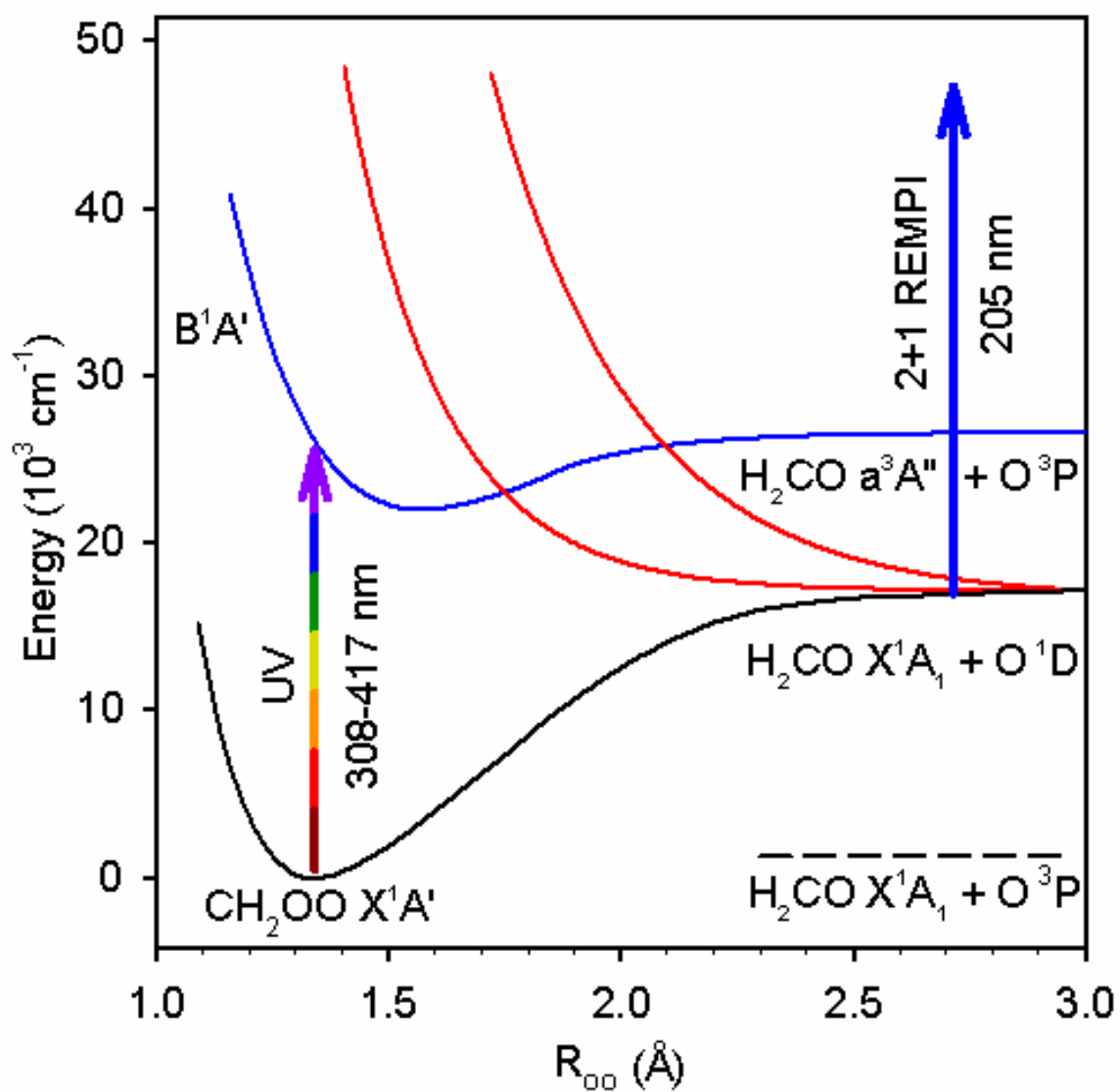


Figure 1. Diabatic potential energy surfaces for CH₂OO in its ground and excited electronic singlet states along the O-O dissociation coordinate adapted from Dawes et al. (Figure 1 of Ref. 28; adapted with permission from R. Dawes, B. Jiang and H. Guo, J. Am. Chem. Soc. **137**, 50-53 (2015). Copyright (2015) American Chemical Society.) UV excitation from 308 to 417 nm promotes CH₂OO from its ground X¹A' state to the excited B¹A' state (blue), and leads to prompt dissociation along repulsive surfaces (red) to H₂CO X¹A₁ + O ¹D products. In this study, the O ¹D products are detected by 2+1 REMPI at 205 nm and characterized using velocity map imaging. Previous experiments probed the O ³P products from the higher-energy, spin-allowed H₂CO a³A'' + O ³P channel. The spin-forbidden H₂CO X¹A₁ + O ³P asymptotic limit (dashed) is also shown, but not observed.

faster than the rotational period of CH₂OO (ps) at these excitation energies and also indicate that the weak oscillatory structure in the long wavelength tail of the CH₂OO absorption spectrum arises from short-lived resonances.

II. Experimental Methods

The vapor of diiodomethane (CH₂I₂, Sigma Aldrich >98%) is entrained in a 10% O₂/Ar carrier gas (15 psig) and pulsed from a solenoid valve (Parker-Hannifin General Valve) through an affixed quartz capillary tube (~1 mm inner diameter; 40 mm length) into a vacuum chamber. The 248 nm output of a KrF excimer laser (Coherent, Compex 102) is focused along the length of the capillary tube by a cylindrical lens to photolyze the CH₂I₂ precursor. Molecular oxygen reacts with the photolytically generated CH₂I radicals to generate the simplest Criegee intermediate, CH₂OO. The CH₂OO and other products are collisionally stabilized in the capillary tube and cooled as the gas mixture undergoes supersonic expansion.^{10, 24, 25}

After traveling ~4 cm downstream into the laser interaction region, the products are crossed by UV pump radiation (300-420 nm), which is generated by frequency doubling the output of a Nd:YAG (Continuum Surelite) pumped dye laser (Continuum ND6000) utilizing many dyes (LDS 698, LDS 765, LDS 798, and LDS821). After a 50 ns time delay, a counter-propagating UV probe laser at 205.47 nm ionizes the O ¹D products by 2+1 REMPI.³⁵ The probe laser radiation is generated by frequency tripling the output of another Nd:YAG (Radiant Dyes Innolas or Continuum 9010, 532 nm) pumped dye laser (Radiant Dyes Innolas or NarrowscanK, Rh 610/640 mix). A lens (50 cm focal length) is used to focus the probe laser in the interaction region, where it is spatially overlapped with the unfocused pump radiation. The pump laser polarization is

set parallel to the plane of the detector. The frequencies of the lasers are calibrated with a wavemeter (Coherent Wavemaster).

The calibration and function of the velocity map imaging (VMI) apparatus are described in detail in previous publications.^{24, 36} In brief, the $O^+ 2D$ ions generated by 2+1 REMPI are accelerated on axis with the supersonic expansion by ion optics. The ions subsequently propagate through a field free time-of-flight (TOF) region, and are separated according to mass. The velocity focused ions are detected by a dual MCP/phosphor screen coupled with a CCD camera that is electronically gated for O^+ mass ($m/z = 16$) detection. In collecting data, the probe dye laser is repeatedly scanned over the O-atom Doppler profile ($\pm 0.3 \text{ cm}^{-1}$). The camera captures a 2D spatial image of the O^+ ions. Angular and velocity distributions are obtained by analysis of the reconstructed 3D image from the pBASEX program.³⁷

Background O^+ ions are produced in the experiment from IO, which is formed as a byproduct in the generation of CH_2OO .^{11, 12, 38-40} Photolysis of IO by the probe laser (205 nm) yields $I^*(^2P_{1/2})$ and background $O 1D$.⁴⁰ The $O 1D$ is also ionized by the probe laser via the 2+1 REMPI process described above.³⁵ By operating the UV pump and probe lasers at 5 Hz and 10 Hz, respectively, the O^+ ions originating from IO can be subtracted on a shot-by-shot basis. In addition, the IO photodissociation process has been well established and is used to calibrate the VMI setup (see Figure S1).⁴⁰ The ion optic voltages are optimized and give an energy resolution ($\Delta E/E$) of $\sim 10\%$.

III. Results

Previously, velocity map imaging (VMI) was utilized to characterize the velocity and angular distributions of $O 1D$ products resulting from UV excitation of CH_2OO on the $B^1A' - X^1A'$ transition at 308, 330, and 360 nm, which yields $H_2CO X^1A_1 + O 1D$

products.²⁴ In the present study, VMI is again utilized to examine the UV photodissociation dynamics of CH₂OO to H₂CO X¹A₁ + O ¹D products, but at longer wavelengths than reported previously. Images of the O ¹D products were obtained following UV excitation at seven distinct wavelengths in the 364-417 nm region,⁴¹ where prior UV absorption studies indicated a weak tail with oscillatory structure extending over this spectral region.^{11, 12, 23} The O ¹D VMI images were collected at or near the previously reported peaks of the oscillatory structure.²³ Scans of the UV radiation within each dye or dye mixture range were carried out to confirm the presence of the weak oscillatory structure under the present experimental conditions with O ¹D detection. The UV O ¹D action spectrum of jet-cooled CH₂OO obtained by scanning the UV radiation from 370-390 nm (LDS 765 dye) with O ¹D detection is shown in Figure S2. The peak positions and shape of the broad oscillatory structure in the UV O ¹D action spectrum are similar to those reported previously in direct absorption measurements.^{11, 12, 23} Other segments of the UV O ¹D action spectrum in the 390 to 420 nm range (not shown) exhibit analogous broad oscillatory structure as that reported previously.

The two-dimensional ion images of the O ¹D products obtained upon longer wavelength excitation of CH₂OO in this study show very similar anisotropic angular distributions aligned along the pump laser polarization direction as those reported previously at 308, 330, and 360 nm.¹ Representative images of O ¹D products obtained upon 389 and 417 nm excitation of CH₂OO are shown in Figure 2; images recorded at other wavelengths are shown in Figure S3. The observation of clearly anisotropic images demonstrates that electronically excited CH₂OO dissociates more rapidly than the rotational period of CH₂OO (ps) throughout the spectrum (308-417 nm), including excitation of CH₂OO in the long wavelength tail region of the absorption spectrum that

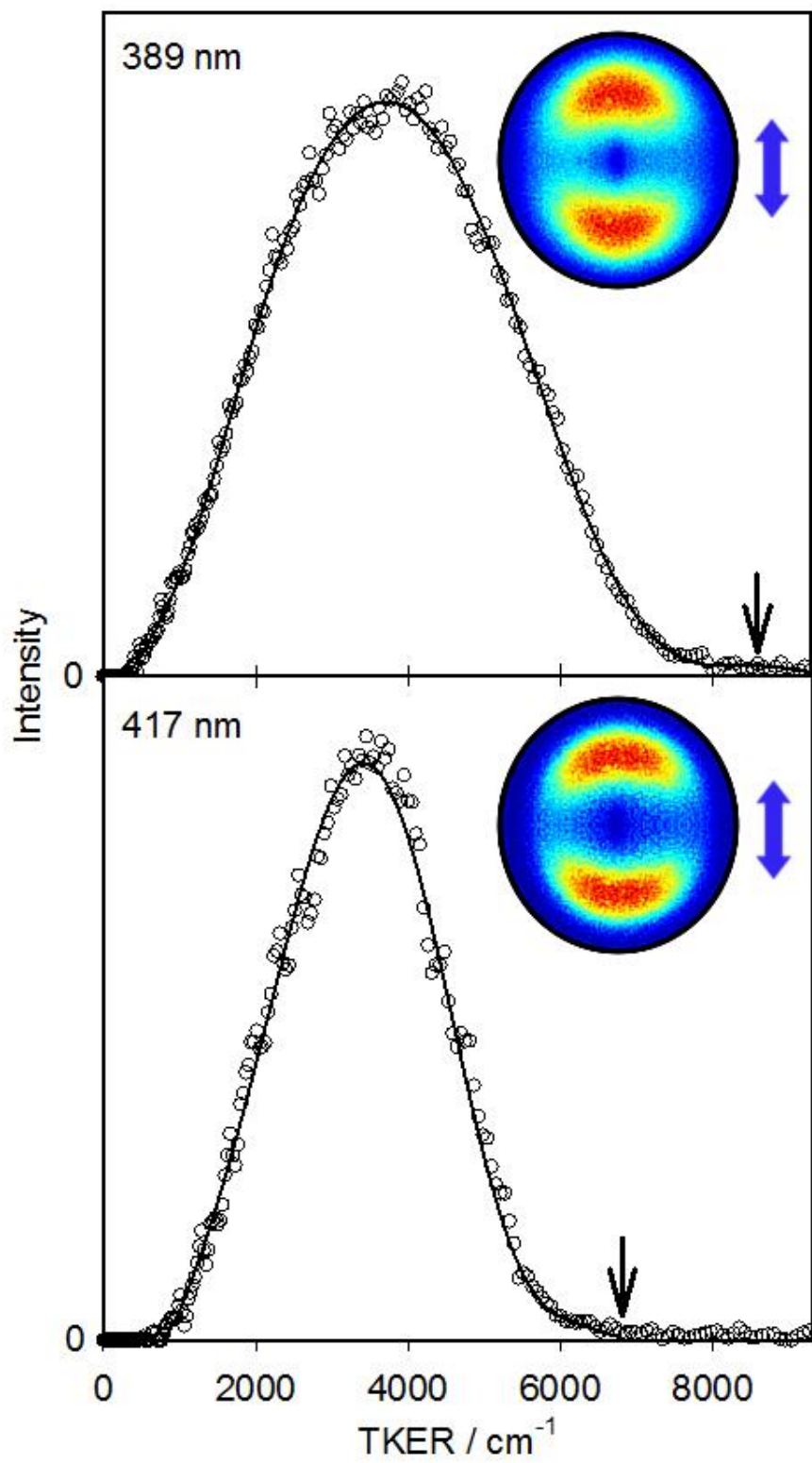


Figure 2. Velocity map images (symmetrized) of O ¹D products following UV excitation of CH₂OO X¹A' at 389 nm (top) and 417 nm (bottom) with vertical polarization (blue arrow) in the plane of the detector. In each case, the reconstructed image yields the total kinetic energy release (TKER) distribution with polynomial fit leading to H₂CO X¹A₁ + O ¹D products. The energy available (E_{avl}) to the recoiling products is indicated by an arrow (black).

exhibits oscillatory structure. A rotational period on the order of a ps (upper limit) is deduced from the experimental rotational constants for CH₂OO X¹A'.¹⁴

At each CH₂OO excitation energy, the velocity distribution of the O ¹D products is obtained from the radial distribution of the ion image after integrating over the angular coordinate. The total kinetic energy release (TKER) distribution is then derived using conservation of linear momentum. Excitation of CH₂OO at 389 and 417 nm yields the TKER distributions shown in Figure 2; those obtained at other wavelengths are shown in Figure S3. In all cases, the TKER distributions are quite broad and unstructured. An eight parameter polynomial fit of each TKER distribution is depicted in Figures 2 and S3. The fits are utilized to extract the most probable total kinetic energy release (peak), the average total kinetic energy release $\langle \text{TKER} \rangle$, the breadth (FWHM) of the TKER distribution, and the highest total kinetic energy where the TKER distribution terminates ($E_{T,\text{max}}$), which are reported in Table S1. Specifically, 389 nm excitation of CH₂OO yields a product TKER distribution peaked at 3720 cm⁻¹ with average $\langle \text{TKER} \rangle$ of 3800 cm⁻¹, breadth (FWHM) of 3990 cm⁻¹, and span ($E_{T,\text{max}}$) of ca. 7900 cm⁻¹. At the long wavelength extreme of 417 nm, excitation of CH₂OO results in a TKER distribution peaked at 3400 cm⁻¹ with the same average value of 3400 cm⁻¹, FWHM of 2670 cm⁻¹, and $E_{T,\text{max}}$ of ca. 6800 cm⁻¹. Trends in the TKER distributions obtained at different CH₂OO excitation wavelengths are discussed below.

The angular distributions, $I(\theta)$, of the velocity map images can be more quantitatively described by an anisotropy (β) parameter.⁴² In the lab frame, $I(\theta)$ can be represented as $I(\theta) \propto 1 + \beta P_2(\cos \theta)$, where P_2 is a second-order Legendre polynomial and θ is the angle between the recoil direction and the polarization of the UV photolysis

laser. The β parameters associated with the angular distributions of the O 1D products following excitation of CH₂OO at nine distinct wavelengths are shown in Figure S3. The β values are nearly unchanged with kinetic energy release across the central FWHM of the TKER distributions. The average β values, derived from the TKER distributions at each wavelength, are ca. 0.8-1.0 as listed in Table S1 and together have a weighted average of 0.93(4). β values can range from -2 to 1, with zero indicating an isotropic distribution as would occur if dissociation is slower than the rotational period of CH₂OO. The β values can be related to the angle χ between the transition dipole moment and the recoil velocity vector in the molecular frame by $\beta = 2\langle P_2(\vec{\mu} \cdot \vec{v}) \rangle = 2\langle P_2(\cos \chi) \rangle$.⁴² On average, the resultant angle χ is ca. 37(1)° (see Table S1), which is in good accord with prior experimental determinations of χ in the central region of the CH₂OO UV absorption profile at 308, 330, and 360 nm.²⁴ This indicates that the orientation of the transition dipole moment is essentially unchanged relative to the O-O bond axis across the CH₂OO spectrum from 308 to 417 nm.

IV. Discussion

Using conservation of energy, the energy available E_{avl} to the H₂CO X¹A₁ + O ¹D products can be expressed as

$$E_{\text{avl}} = h\nu - D = \text{TKER} + E_{\text{int}}(\text{H}_2\text{CO})$$

where $h\nu$ is the photon energy and D is the energy required for dissociation of CH₂OO X¹A' to H₂CO X¹A₁ + O ¹D products. The internal energy of CH₂OO X¹A' is assumed to be negligible due to cooling in the supersonic expansion ($T_{\text{rot}} \sim 10$ K).²² E_{avl} is distributed to products as kinetic energy, represented by the TKER distribution, and/or internal (vibrational and/or rotational) energy of the H₂CO X¹A₁ co-products. Previously, the

dissociation energy from CH₂OO X¹A' to H₂CO X¹A₁ + O ¹D products was established as $D \leq 49.0 \pm 0.3 \text{ kcal mol}^{-1}$.²⁵

The energy available E_{avl} for translational and/or internal energy of the H₂CO X¹A₁ + O ¹D products decreases from ca. 15000 to 7000 cm⁻¹ across the range of CH₂OO excitation wavelengths from 308 to 417 nm. Associated with this decrease in E_{avl} , the most probable (peak) and average values of the TKER distributions shift to lower energy and the breadths of the TKER distributions become narrower. Specifically, the peak and average values of the TKER distributions decrease from ca. 6400 to 3400 cm⁻¹. The peak and average values are nearly the same as a result of the relatively symmetric shapes of the TKER distributions. The breadths of the TKER distributions also narrow from ca. 6800 to 2700 cm⁻¹. These changes in the TKER distributions are evident in Figure 3, where the polynomial fits of the TKER distributions are replotted relative to the photon energy as $h\nu - \text{TKER}$. The parameters derived from the fits to the TKER distributions are compiled in Table S1.

The peak or average value of the TKER distribution accounts for about 43±3% of the available energy, on average, throughout the 308 to 417 nm excitation range. Similarly, the breadth of the TKER distribution corresponds to 43±3% of the available energy on average. Thus, the proportion of energy released to translation of the H₂CO X¹A₁ + O ¹D products is nearly unchanged as the UV excitation of CH₂OO is changed.

For UV excitation of CH₂OO from 308 to 417 nm, the highest kinetic energies of the resultant TKER distributions ($E_{\text{T,max}}$) are consistent with E_{avl} based on the previously established dissociation energy to H₂CO X¹A₁ + O ¹D products (solid vertical line in Figure 3). The corresponding span of the TKER distribution decreases from ca. 14000 to 6500 cm⁻¹ as the CH₂OO excitation wavelength is increased from 308 to 417 nm. The

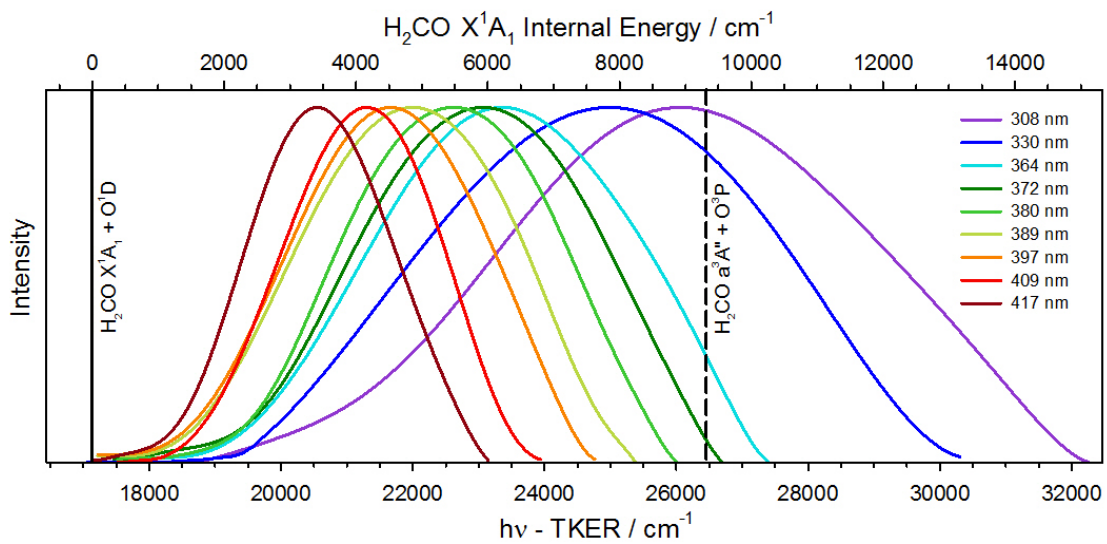


Figure 3. Polynomial fits to total kinetic energy release (TKER) distributions obtained for the $\text{H}_2\text{CO X}^1\text{A}_1 + \text{O } ^1\text{D}$ product channel following UV excitation of the simplest Criegee intermediate CH_2OO at distinct wavelengths from 308 to 417 nm and plotted relative to the photon energy ($h\nu$) as $h\nu - \text{TKER}$. An upper limit of $49.0 \pm 0.3 \text{ kcal mol}^{-1}$ established previously for dissociation of $\text{CH}_2\text{OO X}^1\text{A}'$ to $\text{H}_2\text{CO X}^1\text{A}_1 + \text{O } ^1\text{D}$ products is indicated (vertical line);²⁵ the upper axis indicates the corresponding internal (vibrational and/or rotational) excitation of the $\text{H}_2\text{CO X}^1\text{A}_1$ product. Also shown is the higher energy $\text{H}_2\text{CO a}^3\text{A}'' + \text{O } ^3\text{P}$ product asymptote (dashed vertical line).

available energy exceeds the span of the TKER distribution ($E_{T,max}$) by as much as ca. 1400 cm^{-1} at 308 nm, showing that the $\text{H}_2\text{CO X}^1\text{A}_1$ co-product is released with at least this amount of internal excitation. At longer UV excitation wavelengths, the span decreases and approaches E_{avl} , indicating less internal excitation of the $\text{H}_2\text{CO X}^1\text{A}_1$ co-product. On average, the internal energy of the H_2CO co-product decreases from 7600 cm^{-1} to 3400 cm^{-1} upon excitation of CH_2OO from 308 to 417 nm. At 417 nm excitation, the most probable H_2CO internal energy corresponds to approximately two quanta of C-O stretch ($2\nu_2$) excitation.

Previously, Li et al.²⁵ developed a theoretical model to predict the partitioning of available energy in the UV photodissociation of CH_2OO to $\text{H}_2\text{CO X}^1\text{A}_1 + \text{O }^1\text{D}$ products. Because the dissociation is prompt, the available energy may be released into formaldehyde vibrational modes in a non-statistical manner that reflects the structural changes between $\text{CH}_2\text{OO X}^1\text{A}'$ and the $\text{H}_2\text{CO X}^1\text{A}_1$ product (neglecting nonadiabatic effects in the dissociation dynamics). The most significant structural changes arise from the C-O bond character, which is mixed single (biradical) and double (zwitterionic) bond character for the CH_2OO Criegee intermediate and double bond character for the formaldehyde product.^{14, 43} This results in shortening of the C-O bond, tightening of the H-C-H angle, and slight lengthening of the C-H bonds. The frequencies of analogous vibrational modes also change from $\text{CH}_2\text{OO X}^1\text{A}'$ to $\text{H}_2\text{CO X}^1\text{A}_1$, notably the CO stretch, CH_2 wag, and symmetric and antisymmetric CH stretches.⁴⁴ Thus, the geometric and vibrational changes predict C-O stretch and possibly excitation of other vibrational modes (e.g. CH_2 wag) of $\text{H}_2\text{CO X}^1\text{A}_1$. Li et al.²⁵ also carried out a harmonic normal mode analysis,²² which showed that at least one quantum of ν_2 excitation, predominantly C-O stretch, is required to distort $\text{H}_2\text{CO X}^1\text{A}_1$ from its minimum energy

configuration to the geometry of the formaldehyde moiety within the Criegee intermediate structure. Vibrational excitation of the H₂CO X¹A₁ products, e.g. CO stretch and/or CH₂ wag modes, is consistent with the lack of observable structure in the TKER distributions at the highest energies (lowest H₂CO internal energies) at the present experimental resolution ($\Delta E/E \sim 10\%$). In addition, anharmonic coupling to other modes and nonadiabatic effects may alter the vibrational energy distribution of the H₂CO X¹A₁ products.

Anisotropic angular distributions of the O ¹D products are observed following UV excitation of CH₂OO from 308 to 417 nm, which includes the long wavelength tail region investigated in this study. This demonstrates that dissociation is prompt and occurs on a picosecond or faster timescale. The broad oscillatory features in the long wavelength region can therefore be attributed to short-lived resonances associated with the excited B¹A' state of CH₂OO, which undergoes rapid nonadiabatic coupling to repulsive singlet states that yield H₂CO X¹A₁ + O ¹D products. The timescale for dissociation is faster than the rotational period of CH₂OO (ps) and far more rapid than radiative decay.

The average anisotropy parameter β extracted from the angular distributions of the O ¹D products, based on the central FWHM of the TKER distributions, is nearly unchanged across the UV spectrum of CH₂OO (Table S1). The weighted average value for β is 0.93(4) and corresponds to an average angle χ of 37(1)° between the transition dipole moment (TDM) and recoil velocity vector in the molecular frame, which is in good accord with a prior theoretical predictions that place the TDM at 30° relative to the O-O bond.^{24, 45} The uniform orientation of the electronic transition moment across the UV absorption spectrum provides support for accessing a single excited electronic state,

namely the B¹A' state, which couples to repulsive singlet states that result in dissociation.

As evident from theoretical calculations,^{28, 32} UV excitation of CH₂OO will result in dissociation via multiple coupled potential energy surfaces with several regions of strong non-adiabatic coupling (see Figure 1). These regions of strong nonadiabatic coupling could potentially alter the angular distribution of the O ¹D products and/or the internal energy distribution of the H₂CO X¹A₁ products, yet such effects are not observed: The anisotropy parameter is unchanged with UV excitation wavelength. In addition, the breadth of the TKER distribution (or equivalently the internal energy of the H₂CO co-product) uniformly narrows with increasing wavelength (decreasing E_{avl}). The regions of strong nonadiabatic coupling may also affect the product branching ratio between the spin-allowed lower energy H₂CO X¹A₁ + O ¹D and higher energy H₂CO a³A' + O ³P channels at CH₂OO excitation wavelengths ($\lambda \leq 378$ nm) where both product channels are energetically open.²⁵ The present study focuses on the long wavelength tail region of the CH₂OO B-X absorption spectrum, where H₂CO X¹A₁ + O ¹D is the predominant or only energetically accessible, spin-allowed product channel.

Previously, the solar photolysis rate coefficient (*J*-value) for CH₂OO was estimated to be ≤ 1 s⁻¹ based on the UV absorption spectrum, solar flux at a zenith angle of 0°, and assumed photodissociation quantum yield of unity.^{46, 47} The latter assumption is supported by the VMI images, which show that CH₂OO promptly dissociates upon B-X excitation, including in the long wavelength tail region that overlaps most significantly with the solar actinic flux. The solar photolysis rate of CH₂OO is much slower than its bimolecular reaction with water dimer under atmospheric conditions.^{19, 21} Nevertheless,

O ¹D generated following solar photolysis of CH₂OO will react with atmospheric water vapor and provide a secondary source of OH radicals.

V. Conclusions

The present VMI studies reveal anisotropic angular distributions of the O ¹D products following UV excitation of CH₂OO in the long wavelength tail region of the B-X absorption spectrum. The anisotropic distributions demonstrate that dissociation is rapid compared to the rotational period of CH₂OO and occurs on a picosecond or faster timescale. Thus, the broad oscillatory structure observed in the long wavelength region of the UV absorption spectrum is attributed to short-lived resonances associated with the excited B¹A' state of CH₂OO, which decay by nonadiabatic coupling to repulsive singlet states to yield H₂CO X¹A₁ + O ¹D products.

The long wavelength excitation of CH₂OO leads to similar partitioning of available energy to product translation, on average 43±3%, as found in the central region of the UV absorption spectrum. In addition, long wavelength excitation of CH₂OO yields product translational energy distributions that are consistent with the previously reported dissociation energy for CH₂OO X¹A' to H₂CO X¹A₁ + O ¹D products of $\leq 49.0 \pm 0.3$ kcal mol⁻¹. Finally, the orientation of the transition dipole moment is consistent at 37(1)° with respect to the O-O bond dissociation axis for excitation of CH₂OO across the broad spectral region from 308 to 417 nm. Thus, the strong UV absorption spectrum over the entire wavelength range arises from electronic excitation of CH₂OO from its ground X¹A' state to a single excited electronic state, namely the B¹A' state, which couples to repulsive singlet states that result in rapid O-O bond breakage and dissociation.

Supplementary Material

See supplementary material for further details about experimental resolution, UV O ¹D action spectrum of CH₂OO, as well as velocity map images, anisotropy parameters, and total kinetic energy release distributions following excitation of CH₂OO at distinct wavelengths from 308 to 417 nm.

Acknowledgments

This research was supported by the U.S. Department of Energy-Basic Energy Sciences (DE-FG02-87ER13792). The authors thank Yi Fang (University of Pennsylvania), Fang Liu (Columbia), and Julia Lehman (Leeds) for helpful comments.

References

1. B. J. Finlayson-Pitts and J. N. Pitts, *Chemistry of the Upper and Lower Atmosphere*. (Academic Press, San Diego, 2000).
2. D. Johnson and G. Marston, *Chem. Soc. Rev.* **37**, 699 (2008).
3. M. S. Alam, M. Camredon, A. R. Rickard, T. Carr, K. P. Wyche, K. E. Hornsby, P. S. Monks and W. J. Bloss, *Phys. Chem. Chem. Phys.* **13**, 11002 (2011).
4. T. L. Nguyen, M. C. McCarthy and J. F. Stanton, *J. Phys. Chem. A* **119**, 7197 (2015).
5. O. Welz, J. D. Savee, D. L. Osborn, S. S. Vasu, C. J. Percival, D. E. Shallcross and C. A. Taatjes, *Science* **335**, 204 (2012).
6. C. A. Taatjes, D. E. Shallcross and C. J. Percival, *Phys. Chem. Chem. Phys.* **16**, 1704 (2014).
7. Y. P. Lee, *J. Chem. Phys.* **143**, 020901 (2015).
8. D. L. Osborn and C. A. Taatjes, *Int. Rev. Phys. Chem.* **34**, 309 (2015).
9. C. C. Womack, M.-A. Martin-Drumel, G. G. Brown, R. W. Field and M. C. McCarthy, *Sci. Adv.* **1**, e1400105 (2015).
10. J. M. Beames, F. Liu, L. Lu and M. I. Lester, *J. Am. Chem. Soc.* **134**, 20045 (2012).
11. L. Sheps, *J. Phys. Chem. Lett.* **4**, 4201 (2013).
12. W.-L. Ting, Y.-H. Chen, W. Chao, M. C. Smith and J. J.-M. Lin, *Phys. Chem. Chem. Phys.* **16**, 10438 (2014).
13. Y.-T. Su, Y.-H. Huang, H. A. Witek and Y.-P. Lee, *Science* **340**, 174 (2013).
14. M. Nakajima and Y. Endo, *J. Chem. Phys.* **139**, 101103 (2013).
15. O. Welz, A. J. Eskola, L. Sheps, B. Rotavera, J. D. Savee, A. M. Scheer, D. L. Osborn, D. Lowe, A. M. Booth, P. Xiao, M. A. H. Khan, C. J. Percival, D. E. Shallcross and C. A. Taatjes, *Angew. Chem. Int. Ed.* **53**, 4547 (2014).
16. Z. J. Buras, R. M. I. Elsamra and W. H. Green, *J. Phys. Chem. Lett.* **5**, 2224 (2014).
17. Z. J. Buras, R. M. I. Elsamra, A. Jalan, J. E. Middaugh and W. H. Green, *J. Phys. Chem. A* **118**, 1997 (2014).
18. R. Chhantyal-Pun, A. Davey, D. E. Shallcross, C. J. Percival and A. J. Orr-Ewing, *Phys. Chem. Chem. Phys.* **17**, 3617 (2015).
19. W. Chao, J.-T. Hsieh, C.-H. Chang and J. J.-M. Lin, *Science* **347**, 751 (2015).
20. E. S. Foreman, K. M. Kapnas and C. Murray, *Angew. Chem. Int. Ed.* **55**, 10419 (2016).
21. T. R. Lewis, M. A. Blitz, D. E. Heard and P. W. Seakins, *Phys. Chem. Chem. Phys.* **17**, 4859 (2015).
22. F. Liu, J. M. Beames, A. S. Petit, A. B. McCoy and M. I. Lester, *Science* **345**, 1596 (2014).
23. E. S. Foreman, K. M. Kapnas, Y. Jou, J. Kalinowski, D. Feng, R. B. Gerber and C. Murray, *Phys. Chem. Chem. Phys.* **17**, 32539 (2015).
24. J. H. Lehman, H. Li, J. M. Beames and M. I. Lester, *J. Chem. Phys.* **139**, 141103 (2013).
25. H. Li, Y. Fang, J. M. Beames and M. I. Lester, *J. Chem. Phys.* **142**, 214312 (2015).
26. C. E. Moore, in *CRC Series in Evaluated Data in Atomic Physics*, edited by J. W. Gallagher (CRC Press, Boca Raton, FL, 1993), pp. 339.

27. G. Herzberg, *Molecular Spectra and Molecular Structure: III. Electronic Spectra and Electronic Structure of Polyatomic Molecules*. (D. Van Nostrand Company, Inc., New York, NY, 1966).
28. R. Dawes, B. Jiang and H. Guo, *J. Am. Chem. Soc.* **137**, 50 (2015).
29. M. T. Nguyen, T. L. Nguyen, V. T. Ngan and H. M. T. Nguyen, *Chem. Phys. Lett.* **448**, 183 (2007).
30. J. M. Anglada, J. M. Bofill, S. Olivella and A. Solé, *J. Am. Chem. Soc.* **118**, 4636 (1996).
31. D. Cremer, J. Gauss, E. Kraka, J. F. Stanton and R. J. Bartlett, *Chem. Phys. Lett.* **209**, 547 (1993).
32. K. Samanta, J. M. Beames, M. I. Lester and J. E. Subotnik, *J. Chem. Phys.* **141**, 134303 (2014).
33. Q. Meng and H.-D. Meyer, *J. Chem. Phys.* **141**, 124309 (2014).
34. J. Kalinowski, E. S. Foreman, K. M. Kapnas, C. Murray, M. Rasanen and R. B. Gerber, *Phys. Chem. Chem. Phys.* **18**, 10941 (2016).
35. S. T. Pratt, P. M. Dehmer and J. L. Dehmer, *Physical Review A* **43**, 4702 (1991).
36. J. H. Lehman, H. Li and M. I. Lester, *Chem. Phys. Lett.* **590**, 16 (2013).
37. G. A. Garcia, L. Nahon and I. Powis, *Rev. Sci. Instrum.* **75**, 4989 (2004).
38. W.-L. Ting, C.-H. Chang, Y.-F. Lee, H. Matsui, Y.-P. Lee and J. J.-M. Lin, *J. Chem. Phys.* **141**, 104308 (2014).
39. A. J. Eskola, D. Wojcik-Pastuszka, E. Ratajczak and R. S. Timonen, *Phys. Chem. Chem. Phys.* **8**, 1416 (2006).
40. K. S. Dooley, J. N. Geidosch and S. W. North, *Chem. Phys. Lett.* **457**, 303 (2008).
41. Specifically at 363.69, 372.10, 380.40, 388.86, 397.08, 408.69, and 417.29 nm.
42. B. Whitaker, *Imaging in Molecular Dynamics Technology and Applications*. (Cambridge University Press, 2003).
43. D. J. Clouthier and D. A. Ramsay, *Annu. Rev. Phys. Chem.* **34**, 31 (1983).
44. E. P. F. Lee, D. K. W. Mok, D. E. Shallcross, C. J. Percival, D. L. Osborn, C. A. Taatjes and J. M. Dyke, *Chemistry – A European Journal* **18**, 12411 (2012).
45. W. R. Wadt and W. A. Goddard, *J. Am. Chem. Soc.* **97**, 3004 (1975).
46. J. M. Beames, F. Liu, L. Lu and M. I. Lester, *J. Chem. Phys.* **138**, 244307 (2013).
47. M. C. Smith, W.-L. Ting, C.-H. Chang, K. Takahashi, K. A. Boering and J. J.-M. Lin, *J. Chem. Phys.* **141**, 074302 (2014).

CHAPTER 3

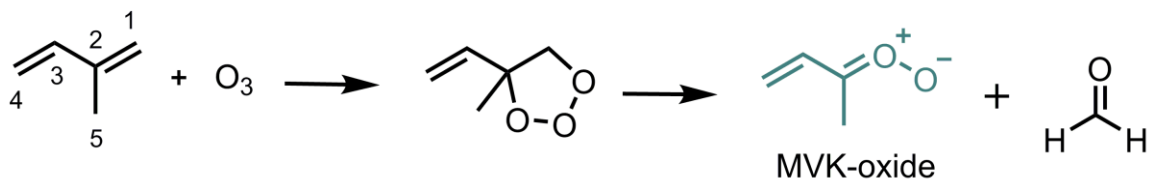
ELECTRONIC SPECTROSCOPY OF METHYL VINYL KETONE OXIDE: A FOUR-CARBON UNSATURATED CRIEGEE INTERMEDIATE FROM ISOPRENE OZONOLYSIS

This research has been reproduced from *The Journal of Chemical Physics*, **149**, 244309 (2018) with the permission of AIP publishing. This research was performed with postdoctoral researcher Barbara Marchetti and Marsha I. Lester (*Department of Chemistry, University of Pennsylvania*).

I. Introduction

Alkenes are important unsaturated hydrocarbon species that are introduced into the atmosphere from both anthropogenic and biogenic sources. Among these, isoprene (2-methyl-1,3-butadiene, $\text{CH}_2=\text{C}(\text{CH}_3)-\text{CH}=\text{CH}_2$) with global emissions on the order of 500 Tg/yr,¹ primarily from foliar sources, is the most abundant nonmethane volatile organic compound in the Earth's troposphere. Isoprene and other alkenes are removed from the atmosphere through their reactions with the hydroxyl radical (OH), ozone (O_3), and the nitrate radical (NO_3 , nighttime only).²⁻⁴ Here, we focus on alkene ozonolysis, which proceeds by ozone addition across the olefinic double bond to yield a primary ozonide (POZ).⁵ The POZ rapidly decomposes to form energized carbonyl (e.g. aldehydes or ketones) and carbonyl oxide species, the latter known as the Criegee intermediate. The resultant Criegee intermediate can undergo unimolecular decay to OH radicals and other products,⁶⁻⁹ and/or bimolecular reaction with atmospheric species, including water vapor and SO_2 ,¹⁰⁻¹⁶ that may lead to aerosol formation and impact on climate.¹⁷

Ozonolysis of isoprene can occur at two distinct double bond locations. Due to the asymmetry of each double bond site, ozonolysis at the $\text{C}_{(1)}=\text{C}_{(2)}$ bond results in a POZ that generates methyl vinyl ketone oxide ($((\text{CH}_2=\text{CH})(\text{CH}_3)\text{COO}$, MVK-oxide) with formaldehyde, as shown in Scheme 1, or formaldehyde oxide (CH_2OO) with methylvinylketone ($((\text{CH}_2=\text{CH})(\text{CH}_3)\text{CO}$, MVK).¹⁸⁻²¹ Ozonolysis at the $\text{C}_{(3)}=\text{C}_{(4)}$ bond yields a different POZ and forms methacrolein oxide ($((\text{CH}_2=\text{C}(\text{CH}_3))\text{CHOO}$, MACR-oxide) with formaldehyde or CH_2OO with methacrolein ($((\text{CH}_2=\text{C}(\text{CH}_3))\text{CHO}$, MACR). Very little is known about the four-carbon unsaturated MVK-oxide and MACR-oxide



Scheme 1. Ozonolysis of isoprene proceeds via a primary ozonide to methyl vinyl ketone oxide (MVK-oxide) and formaldehyde products.

species, which are estimated to account for 23% and 19%, respectively, of the Criegee intermediates formed in isoprene ozonolysis.^{21, 22}

A new synthetic route was introduced in 2012 that enabled direct experimental investigation of CH₂OO and simple alkyl-substituted Criegee intermediates.^{23, 24} In this method, a *gem*-diiodo alkane precursor is photolyzed to produce a monoiodo alkyl radical, which subsequently reacts with O₂ to produce the Criegee intermediate. Unfortunately, analogous *gem*-diiodo precursors cannot be readily synthesized to produce the four-carbon unsaturated Criegee intermediates. Recently, this laboratory demonstrated that photolysis of 1,3-diiodobut-2-ene generates a resonance-stabilized monoiodoalkene radical that reacts with O₂ to produce MVK-oxide.²⁵ Thus far, MVK-oxide has been characterized by infrared action spectroscopy with detection of OH products arising from unimolecular decay.²⁵ Here, we report the UV-visible (vis) absorption spectrum of MVK-oxide and present initial results on its photochemistry.

The characteristic UV absorption of Criegee intermediates is of great importance as a sensitive detection technique for laboratory studies of their bimolecular reactions with atmospheric species. For example, UV absorption of CH₂OO was utilized to reveal its substantive rate of removal and quadratic dependence on water vapor concentration.^{12, 15} The very strong UV transitions of prototypical Criegee intermediates with oscillator strength on the order of $f \sim 0.1$ involve a $\pi^* \leftarrow \pi$ transition associated with the four π electrons of the carbonyl oxide (C=O⁺O⁻) group with zwitterionic character.²⁶⁻³⁰ The UV spectra are peaked at 335 nm for CH₂OO,^{27, 31, 32} ca. 320 nm for *syn*-CH₃CHOO,^{28, 33, 34} (CH₃)₂COO and CH₃CH₂CHOO,^{29, 35} and ca. 360 nm for the less stable *anti*-conformer of CH₃CHOO.³³ In general, the UV spectra of the Criegee intermediates are relatively broad and unstructured due to rapid dissociation in the

excited electronic state, although CH₂OO exhibits some structure in the long wavelength tail region attributed to vibrational resonances.^{36, 37} The excited electronic state accessed upon UV excitation of the Criegee intermediates couples via conical intersections to multiple repulsive potentials that produce O ¹D fragments and associated singlet carbonyl co-products in the lowest spin-allowed channel.^{30, 36, 38}

Here, we provide a detailed experimental and theoretical examination of the UV-vis spectrum of MVK-oxide, which should enable sensitive spectroscopic detection of MVK-oxide for laboratory studies of its photochemistry, and unimolecular and bimolecular reactions. MVK-oxide is distinctly different than previously studied Criegee intermediates because the associated vinyl group couples to the carbonyl oxide group to extend the π -conjugation that then involves six π electrons. MVK-oxide is predicted to have four conformational forms with stabilities that differ by only 3 kcal mol⁻¹, yet significant barriers separate the conformers and restrict interconversion between them.^{19, 25} The four conformers of MVK-oxide are labeled as *syn* or *anti*, depending on the orientation of the methyl group with respect to the terminal O atom, and *cis* or *trans*, designating the relative orientation of the C=C and C=O double bonds. The four conformers of MVK-oxide are expected to be populated, and have similar and potentially overlapping UV-vis spectra.

The UV spectra of simple Criegee intermediates have been recorded using a variety of techniques including direct absorption,^{32, 33, 39} UV action spectroscopy with O-atom detection,^{40, 41} and UV-induced depletion of the associated VUV photoionization signal.²⁷⁻²⁹ Here, we demonstrate 10.5 eV photoionization of MVK-oxide and detection on the parent m/z=86 mass channel. Next, we obtain a UV-vis spectrum of MVK-oxide through UV-vis induced depletion of the photoionization signal and compare with a high-level calculation of the absorption spectra for the four MVK-oxide conformers and other

relevant isomeric species. Finally, we examine the UV-vis induced dissociation dynamics of the MVK-oxide conformers to MVK X $^1A'$ + O 1D products, again comparing with theoretical calculations of their relative stabilities, electronic transitions, and asymptotic energies.

II. Theoretical Methods and Results

In a previous study,²⁵ ground state optimizations were carried out for the four conformers of MVK-oxide using the B2PLYP-D3/VTZ method and basis⁴²⁻⁴⁴ as implemented in Gaussian 09.⁴⁵ The zero-point corrected energies of the four conformers were evaluated using the ANL0-B2F method (a slightly modified version of the ANL0-F12 approach).⁴⁶ The relative energies and optimized structures are given in Table S1 and Figure S1. In addition, vertical and adiabatic ionization energies of the four conformers were calculated at the CCSD(T)-F12/CBS(TZ-F12,QZ-F12)//B2PLYP-D3/VTZ level of theory and are listed in Table 1.

In this work, electronic excitation energies and oscillator strengths are calculated using the Complete Active Space with Second Order Perturbation Theory (CASPT2)⁴⁷⁻⁴⁹ coupled with Dunning's augmented correlation consistent basis set of double- ζ (AVDZ)⁵⁰ for the lowest six singlet electronic transitions. The calculations are carried out using MOLPRO v2010.1.⁵¹ The CASPT2 calculations are based on a seven-singlet state-averaged Complete Active Space-Self Consistent Field (SA7-CASSCF) reference wave function and involve an active space of 12 electrons in 10 orbitals. The occupied orbitals consist of three delocalized π orbitals, a $2p$ lone pair orbital localized on the oxygen atoms, and two σ orbitals arising from overlap of the in-plane oxygen orbitals. The unoccupied orbitals are two π^* orbitals that are delocalized across the whole

Table 1. Vertical excitation energies (VEE, eV), corresponding wavelengths (λ , nm), and oscillator strengths (f) computed at the CASPT2(12,10)/AVDZ level of theory for electronic transitions of the four conformers of MVK-oxide to the $1^1\pi\pi^*$ and $2^1\pi\pi^*$ states. Vertical and adiabatic ionization energies (VIE and AIE, eV) evaluated at the CCSD(T)-F12/CBS(TZ-F12,QZ-F12)//B2PLYP-D3/cc-pVTZ level of theory from Ref. 25.

Conformer	VEE/eV (λ /nm)	f	VIE (AIE)/eV
<i>anti-cis</i>	3.31 (375)	0.070	8.80 (8.65)
	4.68 (265)	0.043	
<i>anti-trans</i>	3.16 (392)	0.211	8.65 (8.54)
	5.55 (223)	0.345	
<i>syn-cis</i>	3.25 (381)	0.111	8.66 (8.55)
	4.52 (274)	0.091	
<i>syn-trans</i>	3.54 (350)	0.147	8.96 (8.61)
	4.52 (274)	0.109	

molecule, and the σ^* and 3s Rydberg orbitals of the O atom. The first and second π^* orbitals are molecular orbitals nominally associated with the carbonyl oxide and vinyl groups, respectively. Selected orbitals of the four conformers of MVK-oxide are shown in Figure 1, while the full set of orbitals utilized in the active space for the CASSCF/CASPT2 calculations are depicted in Figure S2. The first and second π^* orbitals are involved in the two optically bright $\pi^* \leftarrow \pi$ transitions that are the focus of the present theoretical study.

CASPT2(12,10)/AVDZ vertical excitation energies and oscillator strengths (f) are evaluated for the lowest six singlet electronic transitions of the four conformers of MVK-oxide (Table S2). The oscillator strengths (f_{ij}) for the spin allowed transitions are calculated using the CASSCF transition dipole moments (μ_{ij})⁵²

$$f_{ij} = \frac{2}{3} E_{ij} \sum_{a=x,y,z} |\mu_{ij}|_a^2$$

associated with electronic transitions from initial (i) to final (j) states with CASPT2 energies E_{ij} . The lowest excited electronic state ($1^1 n\pi^*$) with $n\pi^*$ character has negligible oscillator strength and is optically dark.

The next electronic state ($1^1 \pi\pi^*$) of $\pi\pi^*$ character is predicted to have significant oscillator strength in MVK-oxide, ranging from 0.07 for *anti-cis* to 0.21 for *anti-trans* (Tables 1 and S2), as found for the prototypical Criegee intermediates studied previously.^{26-28, 53} The vertical excitation energies (Table 1, Figure 2) for transitions to the $1^1 \pi\pi^*$ states of the four conformers of MVK-oxide are computed at ca. 3.2 to 3.5 eV, corresponding to 390 to 350 nm. As a result, the first strong $\pi^* \leftarrow \pi$ transitions for the MVK-oxide conformers are expected to lie to considerably lower energy / longer wavelength than the observed transitions for CH₂OO and alkyl-substituted Criegee

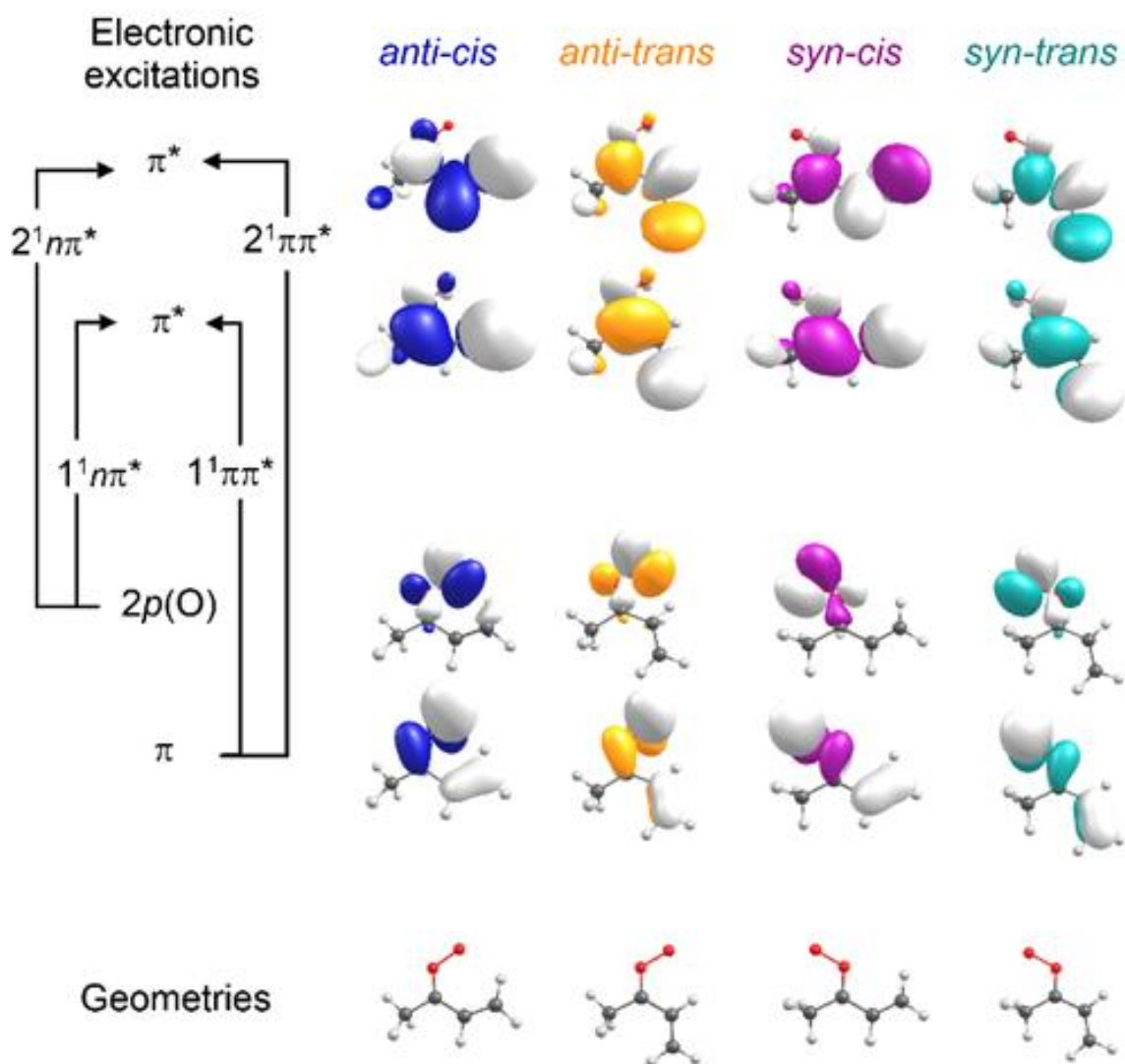


Figure 1. Selected orbitals utilized in the active space for CASSCF/CASPT2 calculations of vertical excitation energies for electronic transitions of the four conformers of MVK-oxide. The arrows illustrate orbital promotions involved in forming the designated excited singlet states of MVK-oxide.

intermediates. A similar spectral shift to longer wavelength was recently predicted for a model vinyl-substituted Criegee intermediate.⁵³

A higher electronic $\pi^* \leftarrow \pi$ transition is predicted to have even larger oscillator strength for one conformer, specifically 0.35 for the *anti-trans* conformer. Vertical excitation on the second $\pi^* \leftarrow \pi$ transitions of the four conformers of MVK-oxide are predicted to occur at ca. 4.5 to 5.5 eV, corresponding to ca. 223 to 274 nm (Table 1, Figure 2). Experimental studies to $2^1\pi\pi^*$ states will be presented in a future publication. Additional excited electronic states of $n3s$, $n\pi^*$, and $\pi3s$ character are predicted toward higher energy (Table S2), but in general have much weaker oscillator strength.

UV-vis absorption profiles for the two strong $\pi^* \leftarrow \pi$ transitions of the four conformers of MVK-oxide are then simulated using an approach similar to that implemented in Newton-X.⁵⁴⁻⁵⁸ For each conformer, an ensemble of 300 (N) initial geometries is sampled using a Wigner distribution based on the ground state normal mode harmonic frequencies (calculated with B3LYP functional⁵⁹ and 6-311+G(d,p) basis set⁶⁰ using Gaussian09⁴⁵). The vertical excitation energies and oscillator strengths for the two $\pi^* \leftarrow \pi$ transitions are evaluated for each of the N initial geometries using CASPT2(10,8)/AVDZ. A Lorentzian line shape function with a broadening factor of 0.25 eV is assumed for each transition. The simulated absorption spectra for the four conformers of MVK-oxide are obtained by summing the intensities of the broadened transitions in the ensemble.

The resultant absorption spectra computed for the four conformers of MVK-oxide are shown in Figure 2, along with a cumulative absorption profile for MVK-oxide obtained by summing the spectra of the four conformers assuming equal population (reduced in scale by a factor of 1.5 in Figure 2). Figure S3 illustrates the ensemble of vertical

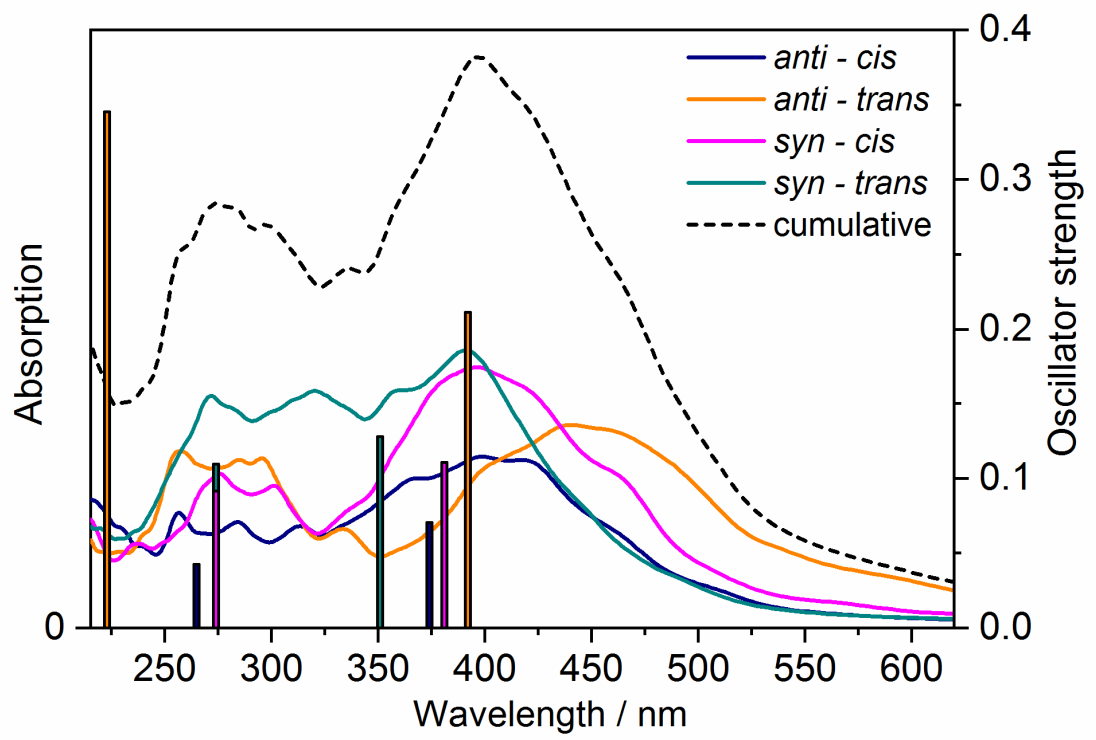


Figure 2. Computed vertical electronic transitions and oscillator strengths to the $1^1\pi\pi^*$ and $2^1\pi\pi^*$ states of the four conformers of MVK-oxide (vertical bars) at the CASPT2(12,10)/AVDZ level of theory. Electronic absorption spectra (solid curves) based on a harmonic-oscillator Wigner distribution of ground state configurations are shown for *anti-cis* (blue), *anti-trans* (orange), *syn-cis* (purple) and *syn-trans* (cyan) conformers of MVK-oxide. The cumulative MVK-oxide electronic spectrum (dashed black curve) is the sum of the four conformer spectra, assuming equal ground state populations, but reduced in scale by a factor of 1.5.

transitions originating from the 300 N initial configurations that contribute to the absorption bands associated with the $1^1\pi\pi^*$ and $2^1\pi\pi^*$ states of the *syn-trans* conformer. The ensemble of individual transitions shows that the breadth of the two absorption bands for each conformer originates primarily from the Franck-Condon profiles associated with the N initial ground state configurations sampled. The simulated spectra are predicted to have maxima at 391 nm (*syn-trans*), 396 nm (*syn-cis*), 399 nm (*anti-cis*), and 440 nm (*anti-trans*). The cumulative spectrum for MVK-oxide is predicted to peak at 397 nm. Transitions to the $2^1\pi\pi^*$ states of the four MVK-oxide conformers are predicted to occur in the 225-325 nm region with the sum peaked at ca. 274 nm. The two absorption bands of each conformer exhibit some overlap, and appear to merge together for the *syn-trans* conformer.

Potential energy curves (unrelaxed) along the O-O dissociation coordinate are also evaluated using the CASPT2(12,10)/AVDZ level of theory by elongating the O-O bond while keeping other degrees of freedom fixed at the ground state optimized geometry for the *syn-trans* conformer of MVK-oxide. The resultant diabatic singlet potential curves (unrelaxed) are shown in Figure 3. Vertical excitation of the *syn-trans* conformer to the $1^1\pi\pi^*$ state at 3.54 eV (351 nm) is predicted to access a repulsive region of the excited state potential, which leads to a conical intersection with a repulsive potential (estimated at ca. 2.78 eV; 446 nm) and results in dissociation to *trans*-MVK X $^1A'$ + O 1D products. (Note that more extensive calculations, which are beyond the scope of the present work, are required to map the conical intersection region accurately.) A similar dissociation pathway has previously been mapped out for CH₂OO following electronic excitation to an analogous $1^1\pi\pi^*$ state.^{30, 36, 38} The vertical transition and simulated absorption spectrum for *syn-trans*-MVK-oxide are also shown (Figure 3).

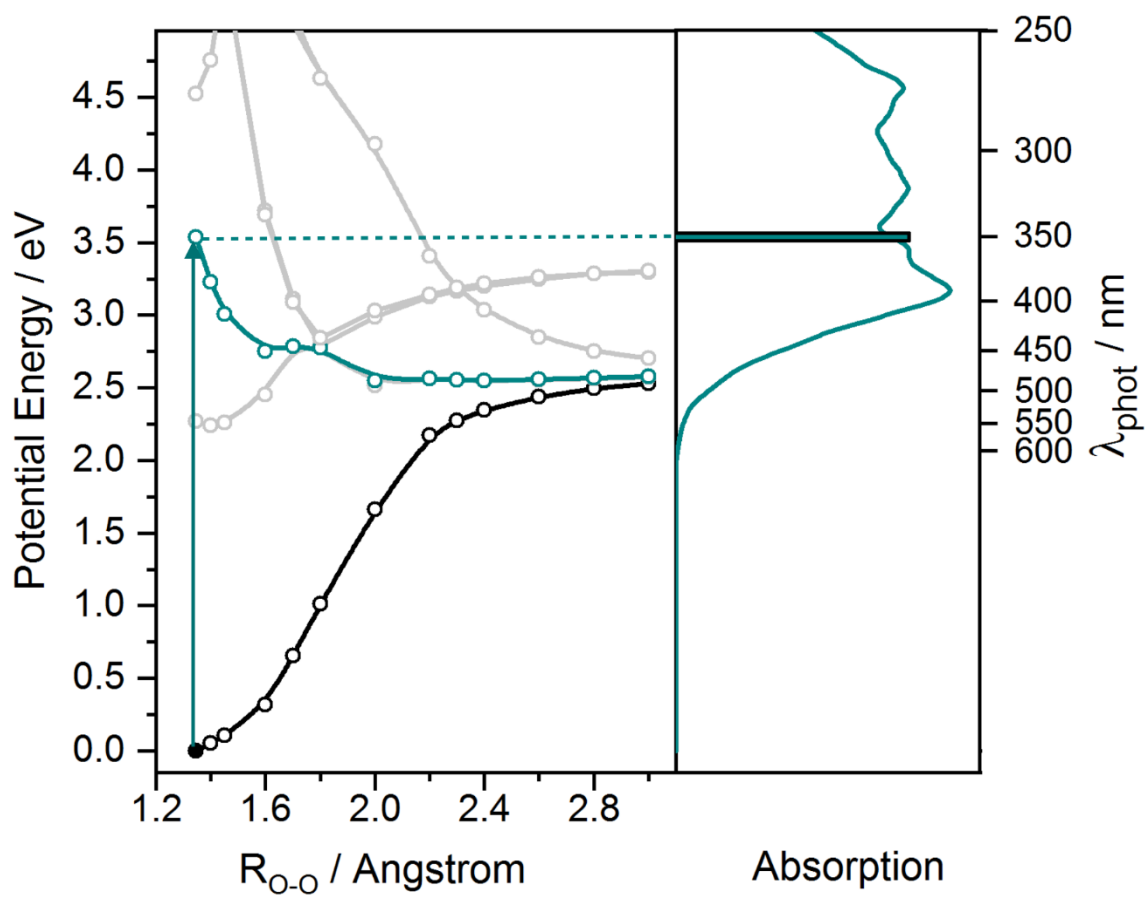


Figure 3. (Left panel) Potential energy curves (unrelaxed) computed along the O-O bond dissociation coordinate for the lowest seven singlet states of the *syn-trans* conformer of MVK-oxide. The lower potentials curves (including black, cyan curves) lead to *trans*-MVK X $^1A'$ + O 1D products, while the higher potential curves dissociate to *trans*-MVK a $^3A''$ + O 3P products. Calculations are performed at CASPT2(12,10)/AVDZ level of theory. Vertical transition (arrow) from the ground S_0 electronic state (black curve) to the $1^1\pi\pi^*$ state (cyan curve) is predicted at 3.54 eV (351 nm). (Right panel) Computed vertical electronic transition (bar) and associated absorption spectrum (curve) for $\pi^* \leftarrow \pi$ transitions based on a harmonic-oscillator Wigner distribution for the S_0 state.

The zero-point corrected energy required for spin-allowed dissociation of the *syn-trans* conformer of MVK-oxide to *trans*-MVK X $^1A'$ + O 1D is computed to be 2.25 eV (18180 cm^{-1} , 550 nm) based on a relaxed optimization at large O-O separation. The dissociation energy predicted for MVK-oxide to its lowest spin-allowed asymptote is similar to that determined previously for $\text{CH}_2\text{OO X } ^1A'$ to $\text{H}_2\text{CO X } ^1A_1 + \text{O } ^1D$ products.^{40, 41, 61} Zero-point corrected dissociation energies for other MVK-oxide conformers (Table S3) are evaluated by taking into account their relative ground state stabilities (Table S1) and the small energy splitting (84 cm^{-1} ; B2PLYP-D3/VTZ) predicted between the *cis* and *trans* conformers of the MVK product.

Previously, the vertical and adiabatic ionization energies for several possible isomers of MVK-oxide were also calculated at the CCSD(T)-F12/CBS(TZ-F12, QZ-F12)//B2PLYP-D3/VTZ level of theory (Table S1, Ref. 25). In this work, the vertical electronic transitions and oscillator strengths for these possible isomers of MVK-oxide are also evaluated at the CASPT2(12,10)/AVDZ level of theory and are given in Table S4. Potential isomers of MVK-oxide that may be generated and their detection by photoionization and/or UV-vis spectroscopy are considered in the discussion section.

III. Experimental Methods

A new synthetic route is used to generate MVK-oxide starting from a (*Z/E*)-1,3-diodobut-2-ene precursor as described previously.²⁵ As shown in Scheme S1, photolysis of 1,3-diodobut-2-ene at 248 nm results in preferential dissociation of the weaker allylic $-\text{C}_{(1)}\text{I}$ bond due to resonance stabilization of the resultant allylic monoiodoalkene radical product Int(1). Although the radical center is initially formed at the $-\text{C}_{(1)}$ carbon, delocalization will lead to the preferred radical site on the $\text{C}_{(3)}$ carbon. Subsequent addition of O_2 is barrierless at the $\text{C}_{(3)}$ carbon site of Int(1), transiently

forming an energized iodoalkene peroxy radical Int(2) that can readily rotate about the C-C and C-O bonds, prior to dissociation to produce MVK-oxide. The O₂ reaction step is similar to that leading to other Criegee intermediates from their corresponding geminal diiodo precursors.

The generation of Criegee intermediates in a pulsed supersonic expansion in this laboratory has been described previously.²⁷⁻²⁹ In the present study, the diiodoalkene precursor is heated (60 °C) in a pulsed solenoid valve (Parker-Hannifin General Valve) with a Peltier thermoelectric heating module (Laird Technologies, PC4). The temperature is monitored with a thermocouple (Cole-Parmer, Type K digital thermometer). The precursor is seeded in a 20% O₂/Ar carrier gas (12 psig) and pulsed through a nozzle (1 mm orifice) into a quartz capillary tube reactor (1 mm ID; ca. 25 mm length). The precursor is photolyzed along the length of the capillary tube using the cylindrically focused 248 nm output (25 mJ pulse⁻¹) of a KrF excimer laser (Coherent, Compex 102, 10 Hz), which induces C-I bond dissociation. Subsequent reaction of the resonance-stabilized monoiodoalkene radical with O₂ produces the MVK-oxide intermediate. MVK-oxide is collisionally stabilized in the capillary tube and cooled in the ensuing supersonic expansion to a rotational temperature of ca. 10 K.

For photoionization measurements, the gas mixture travels ~4 cm downstream into a collision free region. Here, it is crossed by focused VUV radiation (118 nm) that is generated by frequency tripling the third harmonic output (~35 mJ/pulse) of a Nd:YAG laser (Continuum Powerlite 9010) in a phase matched Xe:Ar gas mixture. Single photon excitation with 118 nm (10.5 eV) radiation results in ionization. The m/z=86 mass channel is monitored using a Wiley McLaren linear TOF mass spectrometer (R.M. Jordan).

UV-vis radiation is generated using a broadly tunable BBO-OPO source (EKSPLA 342NT, pulse width of 3-5 ns, $< 5 \text{ cm}^{-1}$ linewidth). The signal output is utilized in the 410-500 nm region and sum frequency generation (SFG) of the frequency-doubled signal output + 1064 nm Nd:YAG fundamental is utilized in the 305-409 nm region. The wavelength (vacuum) of the BBO-OPO output is calibrated using a high resolution wavemeter (Coherent WaveMaster). The UV-vis OPO power is carefully adjusted and measured with a power meter (Gentec TPM3/300).

UV-vis depletion measurements of MVK-oxide are performed by introducing UV-vis radiation ~ 50 ns prior to VUV photoionization, as described previously.²⁷⁻²⁹ The counterpropagating UV-vis radiation is focused (30 cm focal length) and spatially overlapped with the VUV radiation in the ionization region of the TOF. The VUV laser is operated at 10 Hz, while the BBO-OPO is run at 5 Hz to obtain the UV-vis induced fractional depletion $[(\text{UV-vis off} - \text{UV-vis on}) / (\text{UV-vis off})]$ or percentage depletion (when multiplied by 100%) of the photoionization signal on alternating shots.

In addition, velocity-map images (VMI) of the O ^1D products are obtained following UV-vis excitation of MVK-oxide, as described previously for other Criegee intermediates.^{37, 40, 41, 61} Again, UV-vis excitation is generated from the BBO-OPO source (~ 2 mJ/pulse) and focused (70 cm focal length) in the interaction region. The O ^1D dissociation products are ionized via 2+1 resonance enhanced multiphoton ionization (REMPI) at 205.47 nm,⁶² which is generated by frequency tripling of the output of a Nd:YAG (Continuum Powerlite 8010) pumped dye laser (Continuum, ND6000, Rh 610) and scanned over the O-atom Doppler profile ($\pm 0.4 \text{ cm}^{-1}$). The counterpropagating UV probe laser is focused (40 cm focal length) into the interaction region, where it is spatially overlapped with the UV-vis pump OPO at a time delay of 50 ns. The UV-vis

pump and UV probe polarizations are aligned and both oriented parallel to the MCP detection plane. The ions are velocity focused onto the spatially sensitive MCP detector, which is gated for the O⁺ mass channel (m/z=16). The central region of detector is protected using a beam block, which prevents ions with low translational energy (<150 cm⁻¹) from striking the MCP plate.^{40, 41} The pancaked image is then analyzed using the pBASEX inversion method to extract the angular and velocity distributions of the O ¹D products.⁶³ An active background subtraction scheme is implemented by running the UV-vis OPO at 5 Hz, while the REMPI laser is operated at 10 Hz. The subtracted background originates from 205 nm excitation of the IO by-product⁶⁴ and the 2¹ $\pi\pi^*$ transition of MVK-oxide, both of which yield O ¹D products.

IV. Results

The MVK-oxide Criegee intermediate was initially detected by photoionization using 10.5 eV (118 nm) VUV radiation on the m/z=86 mass channel of the TOF mass spectrometer as shown in Figure 4. The VUV photoionization signal at m/z=86 is observed upon excimer photolysis of the diiodo alkene precursor in the reactor tube with O₂ in the carrier gas mixture. The 10.5 eV photoionization energy exceeds the computed ionization energy of 8.5-9.0 eV (Table 1) for the four MVK-oxide conformers; other isomers that may be generated in the source and ionized at 10.5 eV will also be considered in the discussion. Here, we assume that the four MVK-oxide conformers are generated with similar yield, have similar ionization efficiencies at 10.5 eV, and contribute equally to the photoionization signal at m/z=86. Further studies will be needed to determine the MVK-oxide conformer distribution, for example, by conformer specific unimolecular²⁵ and/or bimolecular³³ reaction rates. Recently, MVK-oxide was characterized utilizing IR action spectroscopy, in which characteristic IR transitions of

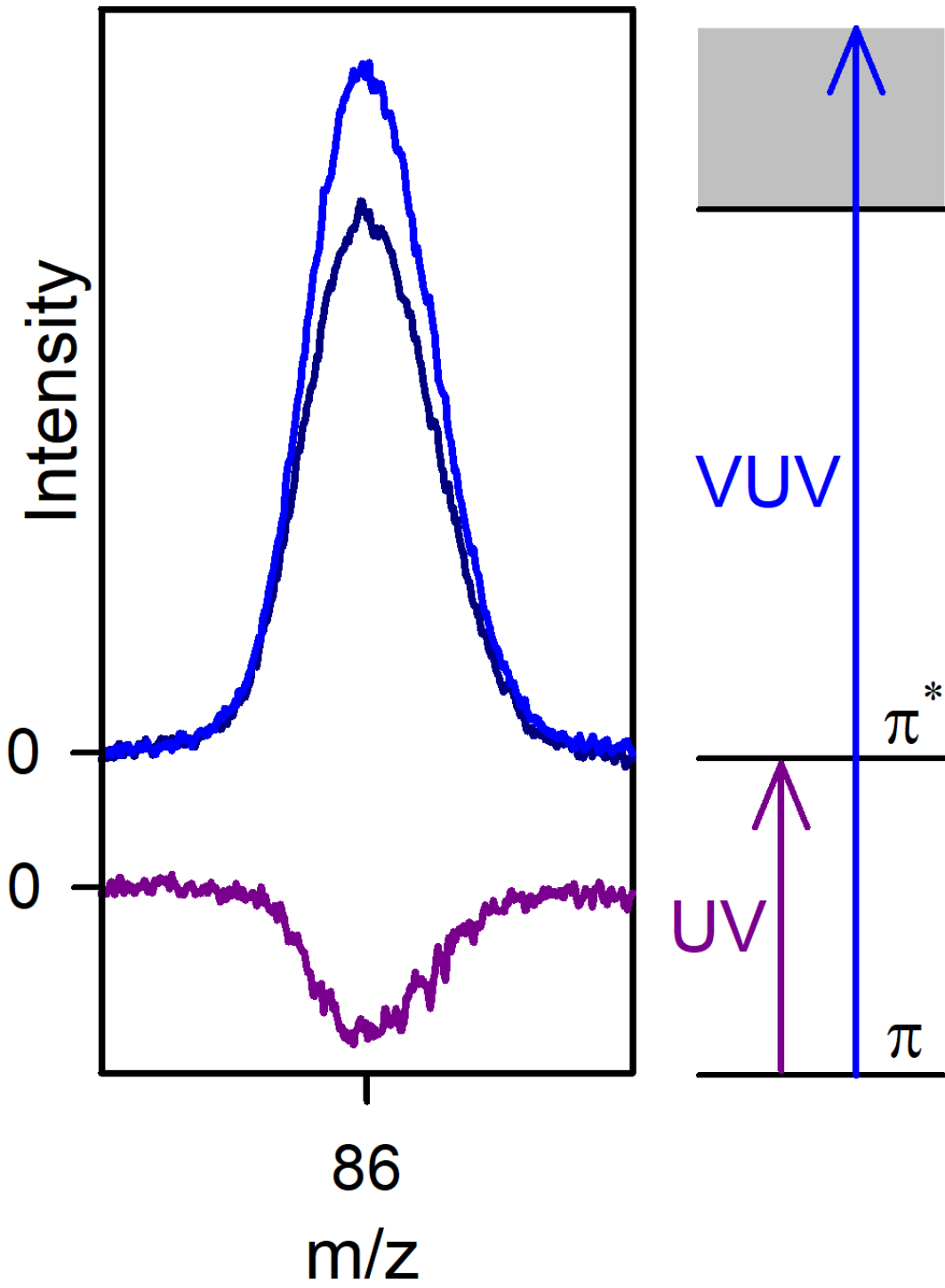


Figure 4. Mass spectra ($m/z=86$) arising from photoionization of MVK-oxide with VUV radiation at 118 nm (10.5 eV). The top trace (blue) shows the photoionization signal. The middle trace (dark blue) show the significant reduction (ca. 20%) in the photoionization signal upon focused UV excitation at 390 nm (0.7 mJ/pulse) on the first $\pi^* \leftarrow \pi$ transition, which results in ground state depletion. The lower trace (purple) shows the depletion signal (UV on – UV off). Also shown is a schematic energy level diagram indicating the π and π^* states, and ionization limit (shaded) for the MVK-oxide Criegee intermediate.

MVK-oxide were identified at ca. 6000 cm^{-1} and detected through the resultant appearance of OH products.²⁵ The present study focuses on characterizing MVK-oxide through the very strong $\pi^* \leftarrow \pi$ electronic transitions (Figure 2, Table 1) predicted for its four conformers in the UV-vis region.

Here, we demonstrate that UV-vis excitation resonant with the first $\pi^* \leftarrow \pi$ electronic transition depletes the ground-state population of one or more of the four MVK-oxide conformers. The ground state depletion is readily detected after a short time delay ($\Delta t \sim 50$ ns) using VUV photoionization as a reduced signal at $m/z=86$. Figure 4 shows a representative example, in which UV excitation at 390 nm (0.7 mJ/pulse) induces a ca. 20% decrease in the VUV photoionization signal at $m/z=86$. The signal $[(\text{UV off} - \text{UV on}) / \text{UV off}] \times 100\%$ yields a ca. 20% depletion. The depletion increases with UV power, as shown in Figure 5, reaching a maximum depletion of ca. 25% at 400 nm. A minimum depletion of 2-3% can be reliably measured at the current signal levels. The magnitude of the depletion can be expressed as $(N_0 - N)/N_0$ with ground state abundances N_0 before and N after UV irradiation. The corresponding absorbance, $-\ln(N/N_0)$, scales linearly with OPO power up to ca. 0.8 mJ/pulse. The linear dependence indicates a one-photon absorption process. The magnitude of the depletion is unchanged beyond 25% at higher power. This suggests that more than one MVK-oxide conformer, isomer, or possibly a dissociative ionization fragment may contribute to the $m/z=86$ photoionization signal. Such additional species do not appear to strongly absorb and/or rapidly dissociate upon UV-vis excitation. Nevertheless, the large magnitude of the depletion and associated absorbance are indicative of a strong electronic transition for MVK-oxide, as observed previously for other carbonyl oxide species.²⁷⁻²⁹ UV-vis

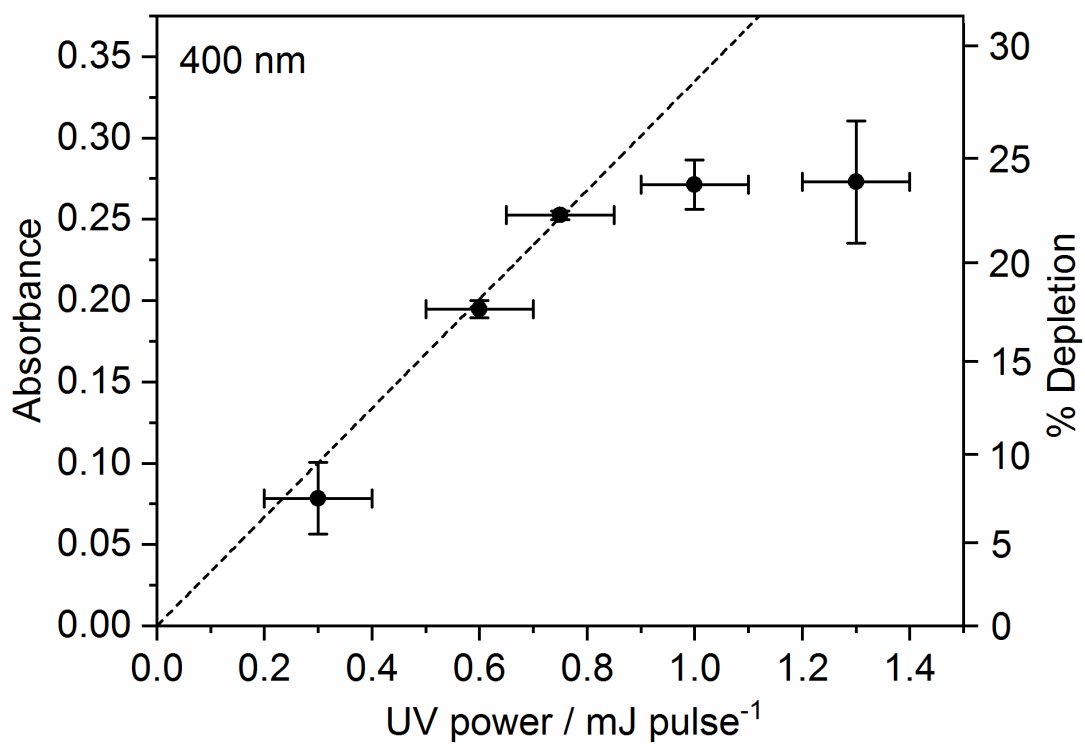


Figure 5. Percentage depletion of the $m/z = 86$ (MVK-oxide⁺) ion signal $(N_0 - N)/N_0$ * 100% with ground state abundances N_0 before and N after irradiation as a function of the OPO power at 400 nm. The error bars represent the standard deviation ($\pm 1\sigma$) derived from repeated measurements. The corresponding absorbance, $-\ln(N/N_0)$, changes linearly (dashed line) at excitation energies up to 0.8 mJ/pulse indicating a one-photon process. No further depletion is observed at higher OPO powers. This suggests that more than one MVK-oxide conformer, isomer, or dissociative ionization fragment may contribute to the photoionization signal at $m/z = 86$, but does not strongly absorb and/or dissociate upon UV-vis excitation.

excitation also results in a small increase in the $m/z=70$ mass, likely due to photoionization of MVK.

The UV-vis radiation from the BBO-OPO is scanned across the UV-vis region from 305 to 480 nm to obtain the electronic spectrum of MVK-oxide by means of the UV-vis induced depletion of the associated VUV photoionization signal. The resultant UV-vis spectrum shown in Figure 6 is recorded in 1 nm steps and normalized to OPO power, which is maintained at less than 1 mJ/pulse throughout the entire spectral region (specifically, 0.5-0.7 mJ/pulse in the central 360-420 nm region). The data points are averages of repeated measurements with $\pm 1\sigma$ uncertainty indicated by the shaded region; the smooth line is a polynomial fit through the data. The broad and unstructured experimental MVK-oxide spectrum exhibits an asymmetric shape with its peak at 388 nm. The experimental spectrum decreases to half maximum at 345 nm on the shorter wavelength side and falls off sharply to half maximum at 412 nm on the longer wavelength side. The spectrum drops to a minimal observable level at ca. 450 nm and terminates by ca. 475 nm. The unusual shape of the experimental spectrum originates in part from overlapping absorption spectra of the four conformers of MVK-oxide as predicted theoretically (Figure 2). The peak of the experimental spectrum agrees well with the predicted peak at 397 nm of the cumulative absorption spectrum involving the first optically bright $\pi^* \leftarrow \pi$ ($1^1\pi\pi^*$) transition computed theoretically. The experimental spectrum does not terminate at 305 nm and actually increases again to shorter wavelength (not shown), which is likely due to excitation to the $2^1\pi\pi^*$ state and will be presented in a future publication. However, the experimental spectrum falls off far more sharply on the long wavelength side than predicted theoretically in the cumulative absorption spectrum. We consider possible reasons for the discrepancy between

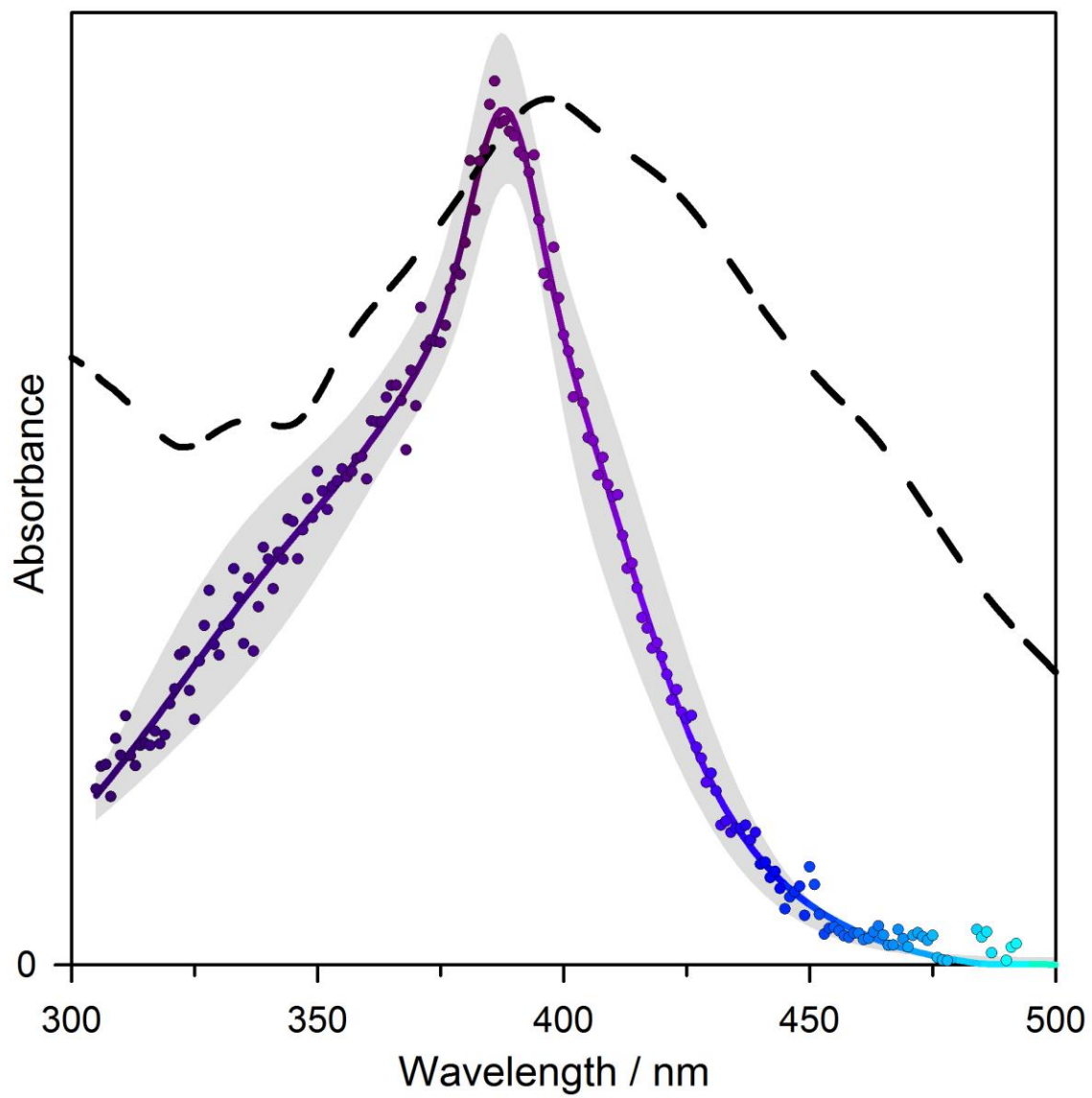


Figure 6. Experimental UV-vis spectrum of MVK-oxide from 305 to 480 nm derived from depletion of the photoionization signal on the $m/z=86$ mass channel. The corresponding absorbance (points) is plotted after normalizing for OPO power. The solid line represents a polynomial fit through the experimental data, while the shaded area indicates the $\pm 1\sigma$ uncertainty. The overall MVK-oxide electronic absorption spectrum (dashed line) computed for the four conformers is shown for comparison.

experiment and theory in the long wavelength falloff region in the discussion section (Sec. V).

We can roughly estimate the absorption cross section $\sigma(\lambda)$ of MVK-oxide at 388 nm by dividing the absorbance by the photon flux Φ (mJ/cm²) of the focused UV beam in the interaction region. At an UV power of 0.7 mJ/pulse and an approximate area of ~ 0.05 cm², corresponding to a photon flux of 14 mJ/cm², we estimate a peak absorption cross section on the order of 10^{-17} cm² molec⁻¹. This estimate is in good accord with absorption cross sections obtained previously for prototypical Criegee intermediates at their peak wavelengths.^{27-29, 34, 35} However, this rough estimate does not take into account that the four conformers of MVK-oxide may make different contributions (based on conformer population, photoionization efficiency at 10.5 eV, and/or absorption cross section at 390 nm) to the UV-induced depletion at 390 nm. In addition, other species (see discussion) may contribute to the photoionization signal at $m/z = 86$, but not result in a UV-induced depletion at 390 nm, thereby reducing the apparent absorbance of MVK-oxide. Finally, the estimated cross section does not take into account the spatial profile of the UV-vis OPO beam.

Additional pump-probe experiments are carried out using UV-vis excitation of MVK-oxide and 2+1 REMPI detection of O ¹D products. The O⁺ ions are detected using velocity map imaging, which reveals the velocity and angular distribution of the fragments. O ¹D VMI images are obtained at discrete wavelengths from 234 to 420 nm, although here we focus exclusively on the images obtained at 390 and 420 nm that are shown in Figure 7; VMI results at other wavelengths will be presented in a future publication. The O ¹D signal drops off rapidly at longer excitation wavelengths with only a very weak signal at ca. 430 nm (insufficient for an image) and no detectable signal

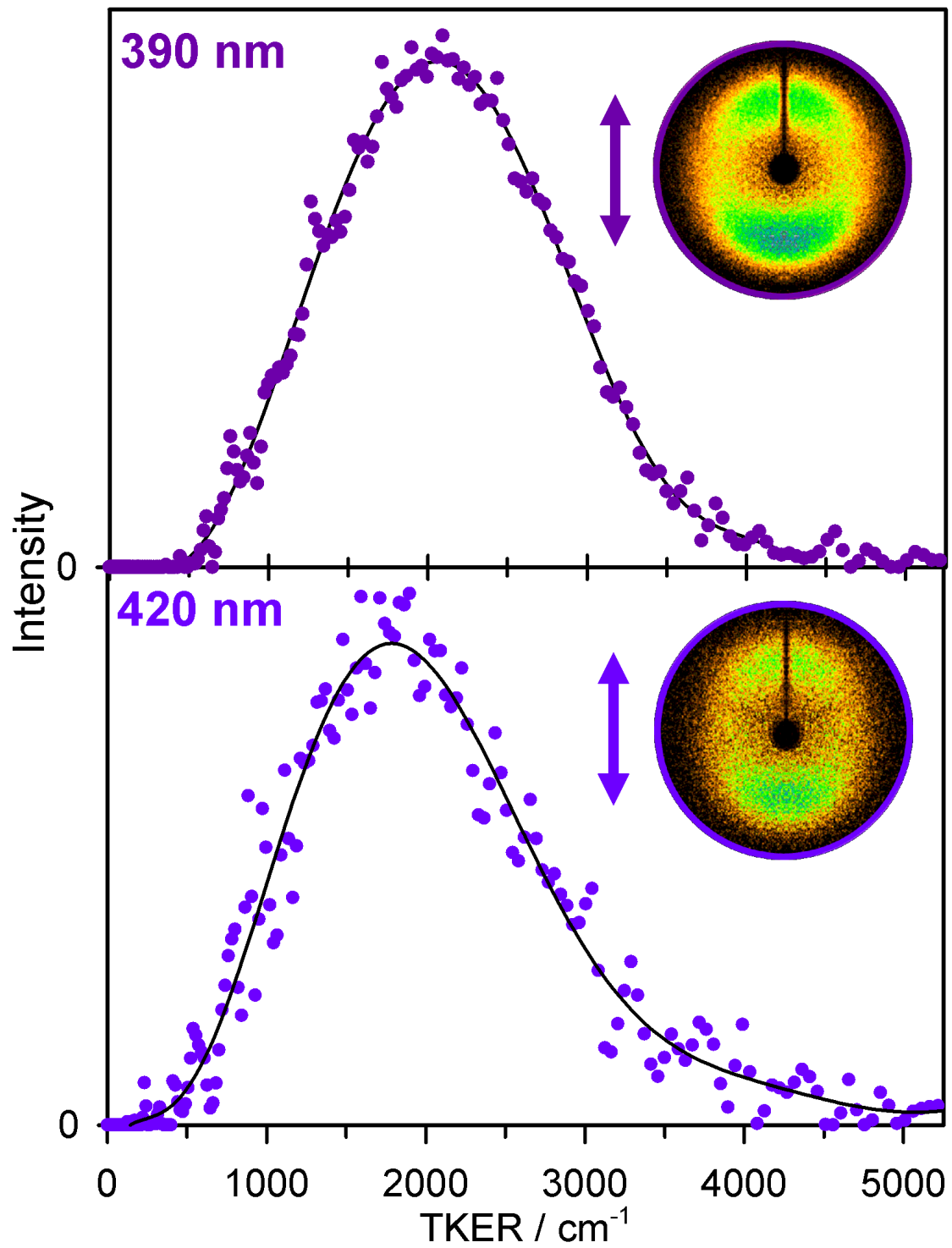


Figure 7. Total kinetic energy release (TKER) distributions (points) and polynomial fits (line) for the O(¹D) + MVK products obtained by velocity map imaging following UV-vis excitation of MVK-oxide at 390 nm (upper panel) and 420 nm (lower panel). Corresponding raw images of the O(¹D) photoproducts are shown as insets. The blue double-sided arrows represent the polarization of the UV-vis OPO (parallel to the detector plane).

beyond 440 nm. The lack of observable O ¹D products beyond 440 nm (less than 2.8 eV) is consistent with long wavelength falloff of the depletion spectrum. Dissociation of MVK-oxide to MVK X ¹A' + O ¹D products is theoretically predicted to be accessible at much lower energies (2.25 eV product asymptote for *syn-trans* conformer), corresponding to wavelengths beyond 550 nm (see Table S3).

As evident in Figure 7, the VMI images at 390 and 420 nm show distinctive angular distributions indicative of rapid dissociation to O ¹D products on a timescale faster than the MVK-oxide rotational period (ca. 100 ps). The implication is that electronic excitation of MVK-oxide at $\lambda \leq 420$ nm accesses repulsive regions of the $1^1\pi\pi^*$ potential energy curve (Figure 3), which results in prompt dissociation to MVK X ¹A' + O ¹D products. The resultant total kinetic energy release (TKER) distributions are broad and structureless. Remarkably, the TKER distributions have similar average translational energies of ca. 2100 cm⁻¹, breadths of ca. 1750 cm⁻¹, and extend out to ca. 4000 cm⁻¹. The similar TKER distributions are notable given that far more energy (1830 cm⁻¹) is available to products upon 390 nm vs. 420 nm excitation of MVK-oxide. The similar kinetic energy release suggests the possibility of a barrier along the dissociation pathway to products with the kinetic energy release reflecting the barrier height.⁶⁵ In this case, the barrier would be associated with the conical intersection (estimated at ca. 2.78 eV) leading to products as discussed in the next section. A comprehensive analysis of the VMI images yields parameters for the angular anisotropy and total kinetic energy release given in Table S5, which will be detailed in a future publication. The theoretically predicted dissociation energy (zero-point corrected) for the *syn-trans* conformer of MVK-oxide to *trans*-MVK X ¹A' + O ¹D products is 2.25 eV (Table S3), from which we estimate

a much greater energy available (E_{avl}) to products of 7460 and 5360 cm^{-1} (Table S5) at 390 and 420 nm, respectively, than observed experimentally.

V. Discussion

A. Comparison of experimental and theoretical MVK-oxide UV-vis spectra

The experimental UV-vis spectrum for MVK-oxide, recorded by depletion of the photoionization signal at $m/z=86$, peaks at 388 nm and compares favorably with the peak of the computed cumulative absorption spectrum for MVK-oxide on the first $\pi^* \leftarrow \pi$ transition at 397 nm. The theoretical prediction assumes equal population of the four conformers of MVK-oxide, each of which has its own broad, but distinctive absorption spectrum. Both experiment and theory demonstrate that the MVK-oxide spectrum peaks at significantly longer wavelength than previously characterized Criegee intermediates (CH_2OO at 335 nm;^{27, 31, 32} *syn*- CH_3CHOO ,^{28, 33, 34} $(\text{CH}_3)_2\text{COO}$ and $\text{CH}_3\text{CH}_2\text{CHOO}$ at ca. 320 nm;^{29, 35} and *anti*- CH_3CHOO at ca. 360 nm).³³ The first $\pi^* \leftarrow \pi$ transition of MVK-oxide is shifted to longer wavelength as a result of extended conjugation spanning across the carbonyl oxide and vinyl groups.⁵³

The experimental and computed spectra for MVK-oxide (Figure 6) differ in the long wavelength region beyond the peak of the cumulative theoretical spectrum predicted using CASPT2 (Figure 2). From the theoretical perspective, it is possible that the Wigner distribution of initial MVK-oxide geometries oversample distorted (higher energy) ground state configurations that would require lower excitation energies to reach the excited $1^1\pi\pi^*$ state. (There may also be limitations in the CASPT2 calculations at these geometries.) This could extend the theoretically predicted absorption spectrum to longer wavelengths. Another possible explanation might be that some MVK-oxide conformers (e.g. *anti-trans* with predicted maximum at 440 nm) are significantly less

populated than other conformers under our experimental conditions. Further experiments examining conformer-specific unimolecular and/or bimolecular reaction will be required to determine the conformer distribution. However, we note that a recent IR experimental study provides evidence that both *syn* and *anti* conformers of MVK-oxide are generated from the diiodoalkene precursor and observed under similar conditions.²⁵

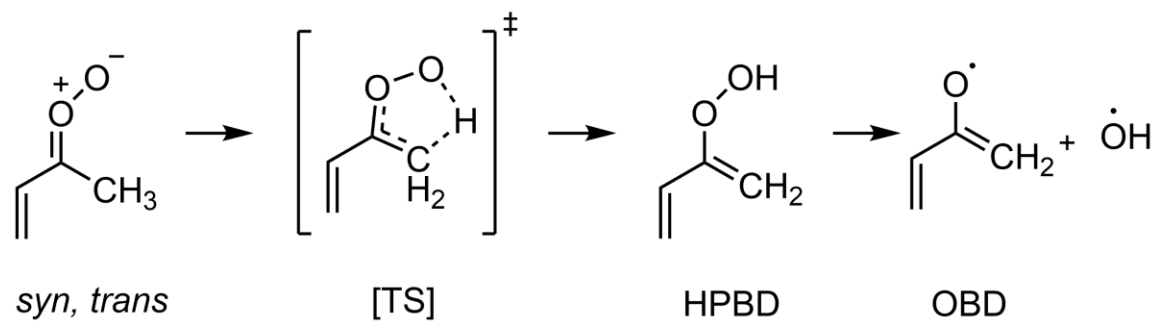
The UV-vis spectrum of MVK-oxide obtained by the depletion method will be equivalent to a standard absorption measurement if MVK-oxide promoted to the $1^1\pi\pi^*$ excited state undergoes prompt dynamics that preclude ionization and detection at $m/z=86$. Rapid dissociation (≤ 100 ps) to MVK + O 1D is demonstrated in the present study by detection of an anisotropic distribution of O 1D products in VMI images at $\lambda \leq 420$ nm. Theoretical calculations also indicate that UV-vis excitation of MVK-oxide at $\lambda \leq 420$ nm accesses a repulsive region of the $1^1\pi\pi^*$ potential (Figure 3). This leads to a conical intersection with strong coupling to repulsive singlet potential(s) and results in dissociation to MVK X $^1A'$ + O 1D products. Electronic excitation of MVK-oxide at energies above the conical intersection region is expected to result in prompt O-O bond dissociation. The energy release associated with the effective barrier to products (ca. 4000 cm^{-1}) is expected to flow primarily into kinetic energy,⁶⁵ and is qualitatively consistent with the range of TKER observed experimentally. At lower energies, an effective barrier associated with the conical intersection would preclude dissociation except possibly through O-atom tunnelling on a much slower timescale.⁶⁶

Theoretical calculations predict that the long wavelength region of the MVK-oxide absorption spectrum extends beyond the conical intersection region (ca. 450 nm) and the MVK X $^1A'$ + O 1D product asymptote (ca. 550 nm, Table S3), corresponding to energies below the conical intersection region (ca. 2.78 eV) and product asymptote (2.25

eV for the *syn-trans* conformer, Table S3). In this long wavelength region, electronically excited MVK-oxide may not dissociate and could decay by a different mechanism. Alternative decay pathways such as internal conversion or fluorescence to the ground electronic state are expected to be fast compared to the 50 ns delay prior to VUV photoionization. In particular, internal conversion would result in vibrationally excited MVK-oxide that can rapidly undergo various unimolecular decay processes and lead to fragmentation (see Sec. B and Ref. 25). As a result, repopulation of the ground electronic state of MVK-oxide and subsequent photoionization that could reduce and/or eliminate the depletion in the photoionization signal at long wavelengths ($\lambda \geq 450$ nm) seems to be an unlikely scenario.³¹ Nevertheless, the present depletion measurements will be compared with future direct absorption measurements, and together will provide a further test of the calculated absorption spectrum.

B. Electronic transitions of other possible isomers

In a recent study, this laboratory demonstrated that vibrational activation of *syn*-MVK-oxide with two quanta of CH stretch induces unimolecular decay to OH products,²⁵ as found for other *syn*-methyl substituted Criegee intermediates.^{7-9, 67-69} Infrared spectral features and associated unimolecular decay rates were obtained with detection of the OH products. Unimolecular decay of *syn*-MVK-oxide proceeds via a 1,4 H-atom transfer mechanism through a transition state (TS) to 2-hydroperoxybuta-1,3-diene ((CH₂=CH)(CH₂)COOH, HPBD) with subsequent O-O bond fission to OH + oxybutadiene ((CH₂=CH)(CH₂)CO, OBD) radicals as depicted in Scheme 2. Master equation modeling showed that unimolecular decay of *syn*-MVK-oxide is also expected occur under atmospheric conditions with a rate of ca. 33 s⁻¹ (298 K, 1 atm). Here, we consider whether the HPBD intermediate, e.g. formed in the capillary reactor tube, could

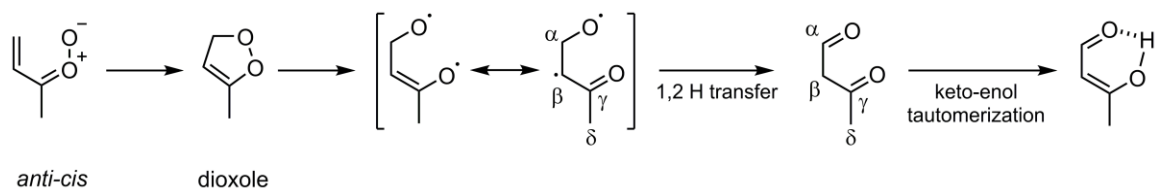


Scheme 2. 1,4 H-atom transfer pathway for unimolecular decay of *syn*-MVK-oxide Criegee intermediate via HPBD to OH radical.

contribute to the UV-vis spectrum attributed to MVK-oxide (Figure 6). While HPBD could be ionized at 10.5 eV (Table S1, Ref. 25), the present CASPT2(12,10)/AVDZ calculations indicate that neither *trans*- nor *cis*-HPBD are expected to absorb in the 300-500 nm region (Table S4); HPBD's electronic transitions are predicted to lie further to the UV (below 220 nm). An alternative unimolecular reaction pathway of HPBD was identified theoretically to lead to 1-hydroxybut-3-en-2-one ($\text{CH}_2\text{CHC}(\text{O})\text{CH}_2\text{OH}$, HB).²⁵ HB may be formed via a roaming induced isomerization at long range involving addition of OH to the CH_2 group of OBD. Again, the HB roaming product may be ionized at 10.5 eV,²⁵ but HB is only predicted to absorb strongly below 205 nm (Table S4).

For *anti*-MVK-oxide, a recent theoretical examination of unimolecular decay pathways indicated that isomerization to 5-methyl-3H-1,2-dioxole (cyc- $\text{CH}_2\text{OOC}(\text{CH}_3)\text{CH}$, dioxole) is the most likely initial step to products. *anti*-MVK-oxide is predicted to undergo an electrocyclic ring-closing reaction via a low barrier to form the 5-membered ring of dioxole as shown in Scheme 3. Master equation modeling suggests a relatively fast thermal unimolecular reaction rate to dioxole of 2140 s^{-1} (298 K, 1 atm)²⁵ and potentially a high yield (36-42%).¹⁹ Again, if dioxole is formed and stabilized, e.g. in the reactor tube, it could be ionized at 10.5 eV, but its first strong electronic transition is predicted at 211 nm. Initially formed dioxole would likely be internally excited and could decay by O-O bond fission to form a diradical, which can rearrange to a number of dicarbonyl and enol compounds.¹⁹ Representative examples of product compounds, e.g. 3-oxobutanal ($\text{CH}(\text{O})\text{CH}_2\text{C}(\text{O})\text{CH}_3$, β -dicarbonyl) and 3-hydroxybut-2-enal ($\text{CH}(\text{O})\text{CHCH}(\text{OH})\text{CH}_3$, enol), could again be ionized at 10.5 eV, but are only predicted to have strong electronic transitions below 300 nm (Table S4).

While there are many possible isomers of MVK-oxide that may be ionized at 10.5 eV (Table S1, Ref. 25), we have not identified a plausible isomer that is also predicted to



Scheme 3. Mechanism from *anti*-MVK-oxide unimolecular decay via dioxole intermediate and other unimolecular rearrangements

have strong electronic transitions in the 300-500 nm region. On the other hand, the present CASPT2(12,10)/AVDZ calculations for each of the four conformers of MVK-oxide indicate a strong $\pi^* \leftarrow \pi$ transition with vertical excitation in the 350-400 nm region and simulated absorption spectra spanning from 325 to 600 nm. The experimental spectrum peaks at 388 nm, which is in very good accord with the cumulative calculated absorption profile with its maximum 397 nm.

VI. Conclusions

The four-carbon unsaturated Criegee intermediate MVK-oxide, produced in nature by isoprene ozonolysis, has been generated in the laboratory by an alternative synthetic route involving a resonantly stabilized iodoalkene radical. The UV-vis spectrum of MVK-oxide on its first $\pi^* \leftarrow \pi$ electronic transition has been recorded by the UV-vis induced depletion of the VUV (10.5 eV) photoionization signal at $m/z=86$. The strong UV-vis induced depletion (up to 25%) of one or more of the four MVK-oxide conformers peaks at 388 nm in a one-photon absorption process. The broad and unstructured experimental spectrum recorded with a continuously tunable BBO-OPO spans from at least 300 to 430 nm. Additional velocity map imaging experiments demonstrate that electronic excitation of MVK-oxide in this spectral region results in rapid dissociation (≤ 100 ps) to O 1D products.

Complementary theoretical calculations predict vertical transition energies and large oscillator strengths for transitions of MVK-oxide to the $1^1\pi\pi^*$ and $2^1\pi\pi^*$ states in the 3.1-3.6 eV (350-400 nm) and 4.5-5.5 eV (220-280 nm) regions, respectively. These two optically bright transitions are nominally associated with the carbonyl oxide and vinyl groups, but the calculations demonstrate that the π and π^* orbitals of MVK-oxide are delocalized across the entire molecule. The UV-vis absorption profiles of the MVK-oxide

conformers are computed using a Wigner distribution of initial configurations. The resultant cumulative absorption spectrum for the first $\pi^* \leftarrow \pi$ transition, based on equal population of the four conformers, is computed to peak at 397 nm and extend to long wavelengths beyond the MVK X $^1A'$ + O 1D product asymptote at ca. 550 nm (ca. 2.25 eV for *syn-trans* conformer).

Electronic excitation of MVK-oxide to the $1^1\pi\pi^*$ state accesses a repulsive region of the excited state potential energy surface, leading to a conical intersection (estimated at ca. 2.78 eV; 446 nm for *syn-trans* conformer) with a repulsive potential that results dissociation. At excitation energies above the conical intersection region, the resultant dissociation is expected to be prompt to MVK X $^1A'$ + O 1D products. At lower energies, the conical intersection may act as an effective barrier to dissociation. As a result, comparison of the present depletion measurements with future direct absorption measurements are planned to further evaluate the predicted theoretical spectrum. Finally, electronic transitions of several possible isomers of MVK-oxide are predicted to absorb at much shorter wavelength than the first strong $\pi^* \leftarrow \pi$ transition identified for the four-carbon unsaturated MVK-oxide Criegee intermediate in this study.

The strong $\pi^* \leftarrow \pi$ electronic transition of MVK-oxide is distinctive from previously studied Criegee intermediates due to extended conjugation across the carbonyl oxide and vinyl groups. Identification of the UV-vis spectrum of MVK-oxide is expected to enable future studies of its photochemistry, unimolecular decay processes, and bimolecular reactions with key atmospheric species. In turn, these ongoing and future studies may help unravel the contributions of the four conformers of MVK-oxide to the UV-vis spectrum presented here.

Supplementary Material

See Supplementary Material for the precursor synthesis method, additional figures and tables providing details on the electronic structure calculations of MVK-oxide and several possible isomers, and parameters extracted from experimental velocity map imaging experiments.

Acknowledgements

This research was supported by the U.S. Department of Energy-Basic Energy Sciences under grant DE-FG02-87ER13792 (MIL). Partial equipment support was provided through the National Science Foundation under grant CHE-1664572 (MIL). BM acknowledges a postdoctoral fellowship from the European Union's Horizon 2020 research and innovation programme under the Marie Skłodowska-Curie Grant Agreement PhARRAO - 746593. The authors thank T. N. V. Karsili (University of Louisiana) for help on the theoretical spectral simulations. The authors thank N. Trongsirawat and P. J. Walsh (University of Pennsylvania) for synthesizing the (*Z/E*)-1,3-diodobut-2-ene precursor and Amy M. Green (University of Pennsylvania) for carrying out preliminary experimental measurements. Finally, the authors thank Stephen J. Klippenstein (Argonne) for performing high-level computations including the ionization energies of MVK-oxide conformers and its possible isomers.

References

1. K. Sindelarova, C. Granier, I. Bouarar, A. Guenther, S. Tilmes, T. Stavrakou, J. F. Müller, U. Kuhn, P. Stefani and W. Knorr, *Atmos. Chem. Phys.* **14**, 9317-9341 (2014).
2. R. Atkinson and J. Arey, *Acc. Chem. Res.* **31**, 574-583 (1998).
3. R. Atkinson and J. Arey, *Chem. Rev.* **103**, 4605-4638 (2003).
4. R. Atkinson and J. Arey, *Atmos. Environ.* **37**, 197-219 (2003).
5. D. Johnson and G. Marston, *Chem. Soc. Rev.* **37**, 699-716 (2008).
6. G. T. Drozd, T. Kurten, N. M. Donahue and M. I. Lester, *J. Phys. Chem. A.* **121**, 6036-6045 (2017).
7. Y. Fang, V. P. Barber, S. J. Klippenstein, A. B. McCoy and M. I. Lester, *J. Chem. Phys.* **146**, 134307 (2017).
8. Y. Fang, F. Liu, V. P. Barber, S. J. Klippenstein, A. B. McCoy and M. I. Lester, *J. Chem. Phys.* **145**, 234308 (2016).
9. Y. Fang, F. Liu, V. P. Barber, S. J. Klippenstein, A. B. McCoy and M. I. Lester, *J. Chem. Phys.* **144**, 061102 (2016).

10. R. L. Mauldin III, T. Berndt, M. Sipilä, P. Paasonen, T. Petäjä, S. Kim, T. Kurtén, F. Stratmann, V. M. Kerminen and M. Kulmala, *Nature* **488**, 193-196 (2012).
11. J. P. Hakala and N. M. Donahue, *J. Phys. Chem. A* **120**, 2173-2178 (2016).
12. W. Chao, J.-T. Hsieh, C.-H. Chang and J. J.-M. Lin, *Science* **347**, 751-754 (2015).
13. H.-L. Huang, W. Chao and J. J.-M. Lin, *Proc. Natl. Acad. Sci.* **112**, 10857-10862 (2015).
14. L.-C. Lin, H.-T. Chang, C.-H. Chang, W. Chao, M. C. Smith, C.-H. Chang, J. J.-M. Lin and K. Takahashi, *Phys. Chem. Chem. Phys.* **18**, 4557-4568 (2016).
15. T. R. Lewis, M. A. Blitz, D. E. Heard and P. W. Seakins, *Phys. Chem. Chem. Phys.* **17**, 4859-4863 (2015).
16. J. H. Kroll and J. H. Seinfeld, *Atmos. Environ.* **42**, 3593-3624 (2008).
17. T. F. Mentel, M. Springer, M. Ehn, E. Kleist, I. Pullinen, T. Kurtén, M. Rissanen, A. Wahner and J. Wildt, *Atmos. Chem. Phys.* **15**, 6745-6765 (2015).
18. R. Gutbrod, E. Kraka, R. N. Schindler and D. Cremer, *J. Am. Chem. Soc.* **119**, 7330-7342 (1997).
19. K. T. Kuwata, L. C. Valin and A. D. Converse, *J. Phys. Chem. A* **109**, 10710-10725 (2005).
20. K. T. Kuwata and L. C. Valin, *Chem. Phys. Lett.* **451**, 186-191 (2008).
21. T. B. Nguyen, G. S. Tyndall, J. D. Crouse, A. P. Teng, K. H. Bates, R. H. Schwantes, M. M. Coggon, L. Zhang, P. Feiner, D. O. Miller, K. M. Skog, J. C. Rivera-Rios, M. Dorris, K. F. Olson, A. Koss, R. J. Wild, S. S. Brown, A. H. Goldstein, J. A. de Gouw, W. H. Brune, F. N. Keutsch, J. H. Seinfeld and P. O. Wennberg, *Phys. Chem. Chem. Phys.* **18**, 10241-10254 (2016).
22. S. M. Aschmann and R. Atkinson, *Environ. Sci. Technol.* **28**, 1539-1542 (1994).
23. C. A. Taatjes, O. Welz, A. J. Eskola, J. D. Savee, A. M. Scheer, D. E. Shallcross, B. Rotavera, E. P. F. Lee, J. M. Dyke, D. K. W. Mok, D. L. Osborn and C. J. Percival, *Science* **340**, 177-180 (2013).
24. O. Welz, J. D. Savee, D. L. Osborn, S. S. Vasu, C. J. Percival, D. E. Shallcross and C. A. Taatjes, *Science* **335**, 204-207 (2012).
25. V. P. Barber, S. Pandit, A. M. Green, N. Trongsirawat, P. J. Walsh, S. R. Klippenstein and M. I. Lester, *J. Am. Chem. Soc.* **140**, 10866-10880 (2018).
26. P. Aplincourt, E. Henon and F. Bohr, *Chem. Phys.* **285**, 221-231 (2002).
27. J. M. Beames, F. Liu, L. Lu and M. I. Lester, *J. Am. Chem. Soc.* **134**, 20045-20048 (2012).
28. J. M. Beames, F. Liu, L. Lu and M. I. Lester, *J. Chem. Phys.* **138**, 244307 (2013).
29. F. Liu, J. M. Beames, A. M. Green and M. I. Lester, *J. Phys. Chem. A* **118**, 2298-2306 (2014).
30. K. Samanta, J. M. Beames, M. I. Lester and J. E. Subotnik, *J. Chem. Phys.* **141**, 134303 (2014).
31. L. Sheps, *J. Phys. Chem. Lett.* **4**, 4201-4205 (2013).
32. W.-L. Ting, Y.-H. Chen, W. Chao, M. C. Smith and J. J.-M. Lin, *Phys. Chem. Chem. Phys.* **16**, 10438-10443 (2014).
33. L. Sheps, A. M. Scully and K. Au, *Phys. Chem. Chem. Phys.* **16**, 26701-26706 (2014).
34. M. C. Smith, W. L. Ting, C. H. Chang, K. Takahashi, K. A. Boering and J. J. Lin, *J. Chem. Phys.* **141**, 074302 (2014).
35. Y.-P. Chang, C.-H. Chang, K. Takahashi and J. J.-M. Lin, *Chem. Phys. Lett.* **653**, 155-160 (2016).
36. R. Dawes, B. Jiang and H. Guo, *J. Am. Chem. Soc.* **137**, 50-53 (2015).
37. M. F. Vansco, H. Li and M. I. Lester, *J. Chem. Phys.* **147**, 013907 (2017).
38. Q. Meng and H. D. Meyer, *J. Chem. Phys.* **141**, 124309 (2014).
39. R. Chhantyal-Pun, A. Davey, D. E. Shallcross, C. J. Percival and A. J. Orr-Ewing, *Phys. Chem. Chem. Phys.* **17**, 3617-3626 (2015).
40. H. Li, Y. Fang, J. M. Beames and M. I. Lester, *J. Chem. Phys.* **142**, 214312 (2015).
41. H. Li, Y. Fang, N. M. Kidwell, J. M. Beames and M. I. Lester, *J. Phys. Chem. A* **119**, 8328-8337 (2015).
42. L. Goerigk and S. Grimme, *J. Chem. Theory Comput.* **7**, 291-309 (2011).
43. S. Grimme, S. Ehrlich and L. Goerigk, *J. Comput. Chem.* **32**, 1456-1465 (2011).
44. R. A. Kendall, T. H. Dunning and R. J. Harrison, *J. Chem. Phys.* **96**, 6796-6806 (1992).
45. M. J. Frisch, G. W. Trucks, H. B. Schlegel, G. E. Scuseria, M. A. Robb, J. R. Cheeseman, G. Scalmani, V. Barone, B. Mennucci, G. A. Petersson, H. Nakatsuji, M. Caricato, X. Li, H. P. Hratchian, A. F. Izmaylov, J. Bloino, G. Zheng, J. L. Sonnenberg, M. Hada, M. Ehara, K. Toyota, R. Fukuda, J. Hasegawa, M. Ishida, T. Nakajima, Y. Honda, O. Kitao, H. Nakai, T. Vreven, J. A. Montgomery Jr., J. E. Peralta, F. Ogliaro, M. Bearpark, J. J. Heyd, E. Brothers, K. N. Kudin, V. N. Staroverov, R. Kobayashi, J. Normand, K. Raghavachari, A. Rendell, J. C. Burant, S. S. Iyengar, J. Tomasi, M. Cossi, N. Rega, J. M. Millam, M. Klene, J. E. Knox, J. B. Cross, V. Bakken, C. Adamo, J. Jaramillo, R. Gomperts, R. E. Stratmann, O. Yazyev, A. J. Austin, R. Cammi, C. Pomelli, J. W. Ochterski, R. L. Martin, K. Morokuma, V. G. Zakrzewski, G. A. Voth, P. Salvador, J. J. Dannenberg, S. Dapprich, A. D. Daniels, Ö. Farkas, J. B. Foresman, J. V. Ortiz, J. Cioslowski and D. J. Fox, *Gaussian 09* (Gaussian, Inc., Wallingford CT, 2009).
46. S. J. Klippenstein, L. B. Harding and B. Ruscic, *J. Phys. Chem. A* **121**, 6580-6602 (2017).
47. B. O. Roos, P. Linse, P. E. M. Siegbahn and M. R. A. Blomberg, *Chem. Phys.* **66**, 197-207 (1982).
48. K. Andersson, P. A. Malmqvist, B. O. Roos, A. J. Sadlej and K. Wolinski, *J. Phys. Chem.* **94**, 5483-5488 (1990).
49. K. Andersson, P. Å. Malmqvist and B. O. Roos, *J. Chem. Phys.* **96**, 1218-1226 (1992).
50. T. H. Dunning, *J. Chem. Phys.* **90**, 1007-1023 (1989).
51. H.-J. Werner, P. J. Knowles, G. Knizia, F. R. Manby, M. Schütz, P. Celani, W. Györfy, D. Kats, T. Korona, R. Lindh, A. Mitrushenkov, G. Rauhut, K. R. Shamasundar, T. B. Adler, R. D. Amos, A. Bernhardsson, A. Berning, D. L. Cooper, M. J. O. Deegan, A. J. Dobbyn, F. Eckert, E. Goll, C. Hampel, A. Hesselmann, G. Hetzer, T. Hrenar, G. Jansen, C. Köppl, Y. Liu, A. W. Lloyd, R. A. Mata, A. J. May, S. J. McNicholas, W. Meyer, M. E. Mura, A. Nicklaß, D. P. O'Neill, P. Palmieri, D. Peng, K. Pflüger, R. Pitzer, M. Reiher, T. Shiozaki, H. Stoll, A. J. Stone, R. Tarroni, T. Thorsteinsson, M. Wang and M. Welborn, *MOLPRO, a Package of ab initio Programs*; 2015. www.molpro.net
52. B. Marchetti, T. N. V. Karsili, M. Ciprian, C. S. Hansen and M. N. R. Ashfold, *J. Chem. Phys.* **147**, 013923 (2017).
53. C. Yin and K. Takahashi, *Phys. Chem. Chem. Phys.* **20**, 16247-16255 (2018).

54. M. Barbatti, G. Granucci, M. Persico, M. Ruckebauer, M. Vazdar, M. Eckert-Maksić and H. Lischka, *J. Photochem. Photobiol. A* **190**, 228-240 (2007).
55. M. Barbatti, A. J. A. Aquino and H. Lischka, *Phys. Chem. Chem. Phys.* **12**, 4959-4967 (2010).
56. M. Barbatti, M. Ruckebauer, F. Plasser, J. Pittner, G. Granucci, M. Persico and H. Lischka, *Wiley Interdiscip. Rev. Comput. Mol. Sci.* **4**, 26-33 (2014).
57. T. N. V. Karsili, B. Marchetti and M. N. R. Ashfold, *Dalton Trans.* **45**, 18921-18930 (2016).
58. T. N. V. Karsili, M. Thodika, L. Nguyen and S. Matsika, *Chem. Phys.* **515**, 434-440 (2018).
59. A. D. Becke, *J. Chem. Phys.* **98**, 5648-5652 (1993).
60. R. Krishnan, J. S. Binkley, R. Seeger and J. A. Pople, *J. Chem. Phys.* **72**, 650-654 (1980).
61. J. H. Lehman, H. Li, J. M. Beames and M. I. Lester, *J. Chem. Phys.* **139**, 141103 (2013).
62. S. T. Pratt, P. M. Dehmer and J. L. Dehmer, *Phys. Rev. A* **43**, 4702-4711 (1991).
63. G. A. Garcia, L. Nahon and I. Powis, *Rev. Sci. Instrum.* **75**, 4989-4996 (2004).
64. K. S. Dooley, J. N. Geidosch and S. W. North, *Chem. Phys. Lett.* **457**, 303-306 (2008).
65. D. H. Mordaunt, D. L. Osborn and D. M. Neumark, *J. Chem. Phys.* **108**, 2448-2457 (1998).
66. D. J. Hadden, G. M. Roberts, T. N. Karsili, M. N. Ashfold and V. G. Stavros, *Phys. Chem. Chem. Phys.* **14**, 13415-13428 (2012).
67. F. Liu, J. M. Beames, A. S. Petit, A. B. McCoy and M. I. Lester, *Science* **345**, 1596-1598 (2014).
68. Y. Fang, F. Liu, S. J. Klippenstein and M. I. Lester, *J. Chem. Phys.* **145**, 044312 (2016).
69. F. Liu, J. M. Beames and M. I. Lester, *J. Chem. Phys.* **141**, 234312 (2014).

CHAPTER 4

SYNTHESIS, ELECTRONIC SPECTROSCOPY, AND PHOTOCHEMISTRY OF METHACROLEIN OXIDE: A FOUR-CARBON UNSATURATED CRIEGEE INTERMEDIATE FROM ISOPRENE OZONOLYSIS

This research has been previously published in *The Journal of the American Chemical Society*, **141**, 15058 (2018) and reproduced with permission from the American Chemical Society.

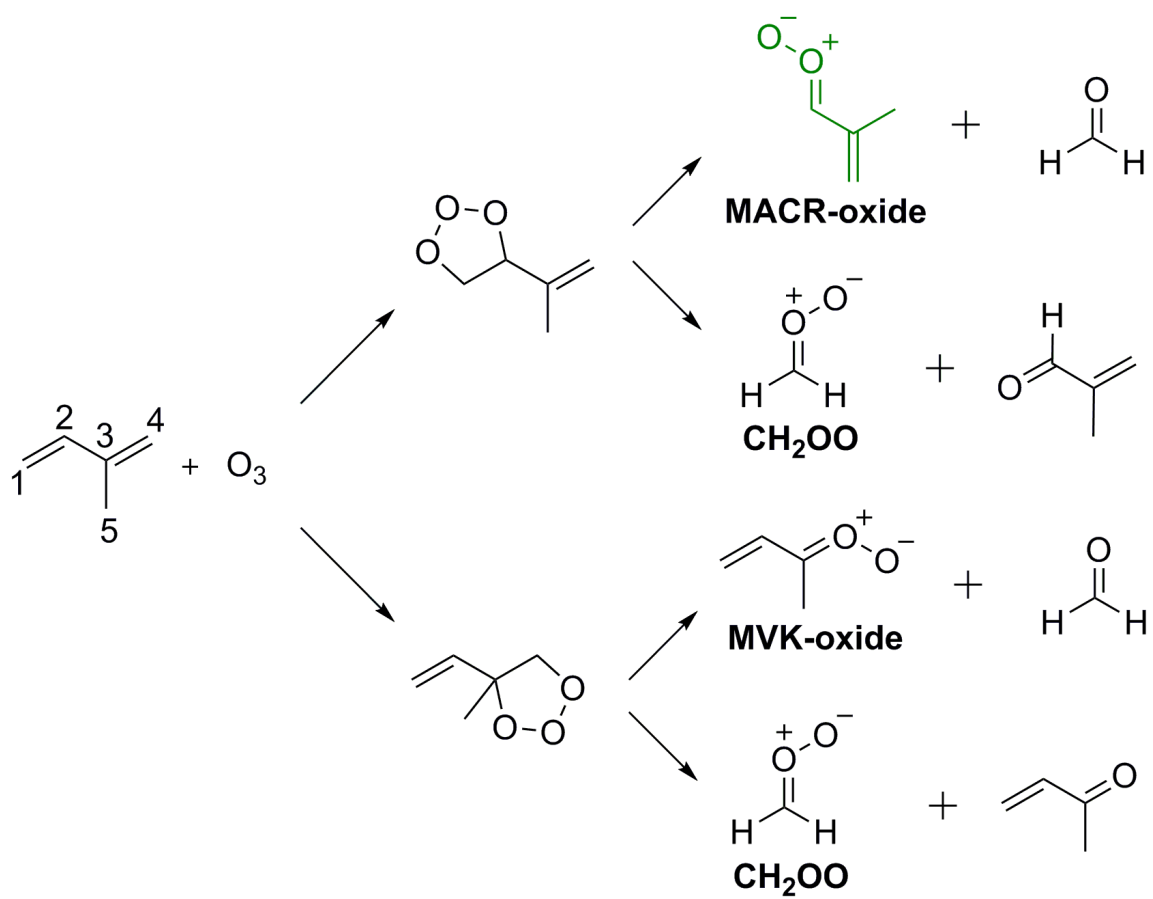
Experimental research was performed with graduate students Trisha Bhagde, and Guanghan Wang, and postdoctoral researcher Barbara Marchetti and Marsha I. Lester (*Department of Chemistry, University of Pennsylvania*). Synthetic work was performed by graduate student Nisalak Trongsiwat and Patrick J. Walsh (*Department of Chemistry, University of Pennsylvania*). Theoretical research was performed by postdoctoral researcher Barbara Marchetti (*Department of Chemistry, University of Pennsylvania*) and in collaboration with Stephen J. Klippenstein (*Chemical Sciences and Engineering Division, Argonne National Laboratory*).

1. Introduction

Isoprene (2-methyl-1,3-butadiene) is the most abundant nonmethane volatile organic compound in the Earth's troposphere with emissions approaching 600 Tg per year.¹ The primary source of isoprene is foliar emission (> 90%), while its removal is controlled by oxidation reactions initiated by hydroxyl radicals (OH), ozone (O₃), and nitrate radicals (NO₃).²⁻⁴ Ozonolysis accounts for ca. 10% of atmospheric isoprene loss and occurs with a relatively slow rate coefficient of $1.19 \times 10^{-17} \text{ cm}^3 \text{ molecule}^{-1} \text{ s}^{-1}$.⁵⁻⁶ Critical reaction intermediates arising from isoprene ozonolysis are the focus of the present study.

Ozonolysis of isoprene proceeds by cycloaddition of ozone across one of the two C=C bonds to form two distinct primary ozonides (POZ) as depicted in Scheme 1. The two POZ promptly decompose via highly exothermic reactions to form carbonyl and zwitterionic carbonyl oxide products, the latter known as Criegee intermediates. Ozonolysis at the C₍₁₎=C₍₂₎ bond results in a POZ that generates methyl vinyl ketone oxide ((CH₂=CH)(CH₃)COO, MVK-oxide) with formaldehyde (CH₂O) or formaldehyde oxide (CH₂OO) with methyl vinyl ketone ((CH₂=CH)(CH₃)CO, MVK). Ozonolysis at the C₍₃₎=C₍₄₎ bond results in a POZ that generates methacrolein oxide ((CH₂=C(CH₃))CHOO, MACR-oxide) with formaldehyde or CH₂OO with methacrolein ((CH₂=C(CH₃))CHO, MACR).^{5, 7-9} The overall branching of Criegee intermediates from isoprene ozonolysis is estimated to be 58% CH₂OO, 23% MVK-oxide, and 19% MACR-oxide.^{5, 10}

Given the importance of isoprene ozonolysis, it is remarkable that very little is known about the two four-carbon unsaturated Criegee intermediates MVK-oxide and MACR-oxide.¹¹ In contrast, there has been extensive spectroscopic characterization of CH₂OO and its bimolecular reactions with key atmospheric species.¹²⁻¹⁶ This paper



Scheme 1. Criegee intermediates and carbonyl co-products formed in ozonolysis of isoprene.

presents the first laboratory synthesis and direct observation of MACR-oxide by UV-vis spectroscopy. The experimental results are complemented by theoretical predictions of the strong $\pi^* \leftarrow \pi$ electronic transitions of MACR-oxide and resultant dissociation pathways. This study builds on recent reports from this laboratory of IR action and UV-vis depletion spectra of MVK-oxide.¹⁷⁻¹⁸ MACR-oxide cannot be detected by an analogous IR action spectroscopy technique because OH radicals are not a significant reaction product. Various unimolecular decay processes and bimolecular reactions of MVK-oxide and MACR-oxide with atmospheric species (e.g. water vapor, SO₂, NO_x, and organic acids) are expected to yield a wide range of products,^{14-15, 19-20} including aerosols that effect climate.²¹

The four-carbon unsaturated MVK-oxide and MACR-oxide intermediates are predicted to be distinctly different than previously investigated saturated carbonyl oxides including CH₂OO and alkyl-substituted Criegee intermediates.²²⁻²⁴ In contrast to the four π electron system of saturated carbonyl oxides, both MVK-oxide and MACR-oxide have extended π -conjugation involving six π electrons across the vinyl (CH₂=C) and carbonyl oxide (C=O⁺O⁻) functional groups.²⁵⁻²⁶ The extended π conjugation is expected to fundamentally change the electronic properties of unsaturated Criegee intermediates,⁸⁻⁹ and potentially their unimolecular and bimolecular chemistry in the atmosphere. MVK-oxide and MACR-oxide are isomers, both having vinyl and methyl substituents, but differ in the position of the methyl group. MVK-oxide and MACR-oxide are each predicted to have four distinct conformers with similar ground state energies (within ca. 3.2 kcal mol⁻¹), yet have significant barriers to rotation that restrict interconversion between the conformers.^{8-9, 17} In MACR-oxide, the four conformers differ in the relative orientation of the terminal O atom with respect to the methine H atom (*syn* vs. *anti*) and in the relative

orientation of the C=C and C=O bonds (*cis* vs. *trans*), as depicted in Figure 1. In isoprene ozonolysis, the distribution of *syn/anti* conformers of MACR-oxide are predicted to be asymmetric with 80% *anti* and 20% *syn*.

The rates and mechanisms for unimolecular decay of the four-carbon unsaturated carbonyl oxide intermediates are predicted to differ significantly for MACR-oxide and MVK-oxide, and are further expected to be highly dependent on the conformational form.^{8-9, 17, 27-28} Prior theoretical studies indicate that unimolecular decay of various MVK-oxide and MACR-oxide conformers will proceed by distinctly different pathways under thermal conditions (298 K, high pressure limit). For MVK-oxide, *syn* conformers decay slowly (33 s^{-1}) via 1,4 H-atom transfer to yield OH radical products,^{8, 17, 27-28} while *anti* conformers are predicted to undergo rapid unimolecular decay (ca. 2000 s^{-1}) via an electrocyclic ring closure mechanism, forming a 5-membered cyclic peroxide known as dioxole.^{8, 17, 28} The 1,4 H-atom transfer pathway is not available for MACR-oxide. For MACR-oxide, *anti* conformers are expected to decay rather slowly (10 s^{-1}) by ring closure of the carbonyl oxide group to form a cyclic dioxirane.^{9, 28} In contrast, the *syn-cis* conformer of MACR-oxide is predicted to undergo rapid unimolecular decay (2500 s^{-1}) to form dioxole.^{9, 28}

For MVK-oxide and MACR-oxide conformers that undergo slow unimolecular decay, bimolecular reactions with water vapor or other trace species may play a role in their atmospheric chemistry.²⁷⁻³⁰ The effective bimolecular rate coefficient (298 K, 100% RH) for *anti*-MACR-oxide with water monomer and dimer is predicted to be $k_{\text{eff}} = 8.7 \times 10^{-15} \text{ cm}^3 \text{ molecule}^{-1} \text{ s}^{-1}$.³⁰ By contrast, the bimolecular reaction of *syn*-MVK-oxide with water vapor is predicted to be negligibly slow ($k_{\text{eff}} = 2.0 \times 10^{-18} \text{ cm}^3 \text{ molecule}^{-1} \text{ s}^{-1}$).³⁰ The

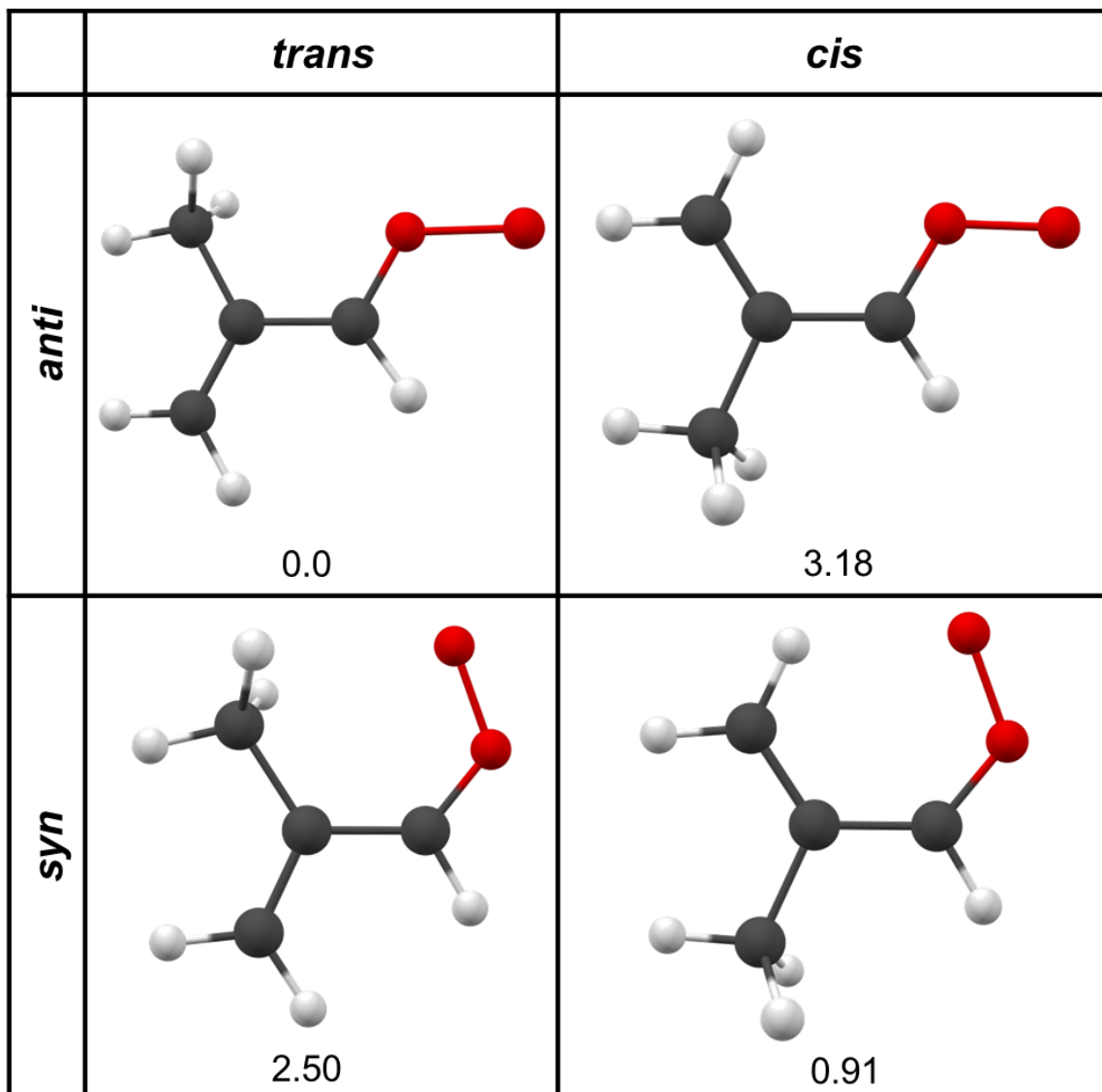


Figure 1. B2PLYP-D3/VTZ optimized geometries of the four conformers of MACR-oxide. The relative stabilities (kcal mol^{-1}) are computed from zero-point energy corrected CCSD(T)-F12/CBS(TZ-F12,QZ-F12)//B2PLYP-D3/cc-pVTZ energies.

rates and mechanisms for many atmospheric reactions of the four-carbon unsaturated Criegee intermediates are ripe for further study.

Recently, our team introduced a new synthetic approach to generate MVK-oxide directly. This involved UV photolysis of a 1,3-diiodobut-2-ene precursor to create a resonance-stabilized mono-iodoalkene radical that reacts with O₂ to produce MVK-oxide.¹⁷⁻¹⁸ Here, we demonstrate an analogous reaction scheme to generate MACR-oxide, starting from a 1,3-diiodo-2-methylprop-1-ene precursor, which demonstrates the generality of this strategy to prepare unsaturated Criegee intermediates. In both cases, we take advantage of resonance stabilization of the mono-iodoalkene radical in order to generate the four-carbon unsaturated Criegee intermediates from isoprene ozonolysis.

Thus far, MVK-oxide has been characterized experimentally using IR action spectroscopy,¹⁷ UV-vis spectroscopy on its first strong $\pi^* \leftarrow \pi$ electronic transition, and VUV photoionization.¹⁸ The IR action spectrum was obtained by excitation of MVK-oxide with two quanta of CH stretch and detection of the resultant OH products. The UV-vis excitation spectrum was recorded via depletion of the associated VUV photoionization signal ($m/z=86$) as well as detection of the resulting O ¹D products. Extensive theoretical calculations have also been carried out for the four conformers of MVK-oxide to predict their IR spectra, electronic transitions, and ionization energies, as well as various unimolecular and photochemical decay processes. These fundamental experimental and theoretical studies lay the groundwork for future investigations of unimolecular and bimolecular reactions of MVK-oxide under atmospheric temperature/pressure conditions.

Prototypical Criegee intermediates examined previously have large oscillator strengths ($f \sim 0.1$) involving $\pi^* \leftarrow \pi$ transitions associated with the four π electrons of the

carbonyl oxide ($\text{C}=\text{O}^+\text{O}^-$) group.^{22-24, 31-32} The UV spectra are peaked at 335 nm for CH_2OO ,^{22, 33-34} ca. 320 nm for *syn*- CH_3CHOO ,^{23, 35-36} $(\text{CH}_3)_2\text{COO}$ and $\text{CH}_3\text{CH}_2\text{CHOO}$,^{24, 37} and ca. 360 nm for *anti*- CH_3CHOO .³⁵ By contrast, the electronic spectrum associated with the first $\pi^*\leftarrow\pi$ transition of MVK-oxide (six π electrons), arising from overlapping spectra of four conformers, is shifted to longer wavelength and peaks at 388 nm.¹⁸ In general, the UV-vis spectra are relatively broad and unstructured, although CH_2OO exhibits some oscillatory structure in the long wavelength tail region^{33-34, 38-39} ascribed to vibrational resonances.³⁹⁻⁴⁰ Theoretical calculations indicate that the $^1\pi\pi^*$ excited electronic state accessed upon UV-vis excitation of the Criegee intermediates couples via conical intersection to repulsive potential(s), which lead to $\text{O } ^1\text{D}$ and singlet carbonyl products.^{32, 40-41}

Several groups are pursuing other promising approaches for direct detection of Criegee intermediates formed in ozonolysis reactions. These include infrared detection of Criegee intermediates from β -pinene,⁴² Fourier transform microwave spectroscopy of CH_2OO from ethylene,⁴³ spin traps and proton-transfer reaction mass spectrometry detection of Criegee intermediates from α -pinene,⁴⁴ and chemical ionization mass spectrometry of CH_2OO and cyclohexene-derived Criegee intermediates.⁴⁵

In this paper, we present the first direct observation of the MACR-oxide Criegee intermediate. We introduce a new synthetic method to produce MACR-oxide and we demonstrate 10.5 eV photoionization detection of MACR-oxide on the parent $m/z=86$ mass channel. We provide the first experimental study of the electronic spectrum of MACR-oxide by means of UV-vis induced depletion of the photoionization signal and generation of $\text{O } ^1\text{D}$ products, and complementary high-level calculation of the absorption spectra for the four conformers of MACR-oxide. The electronic spectrum of MACR-

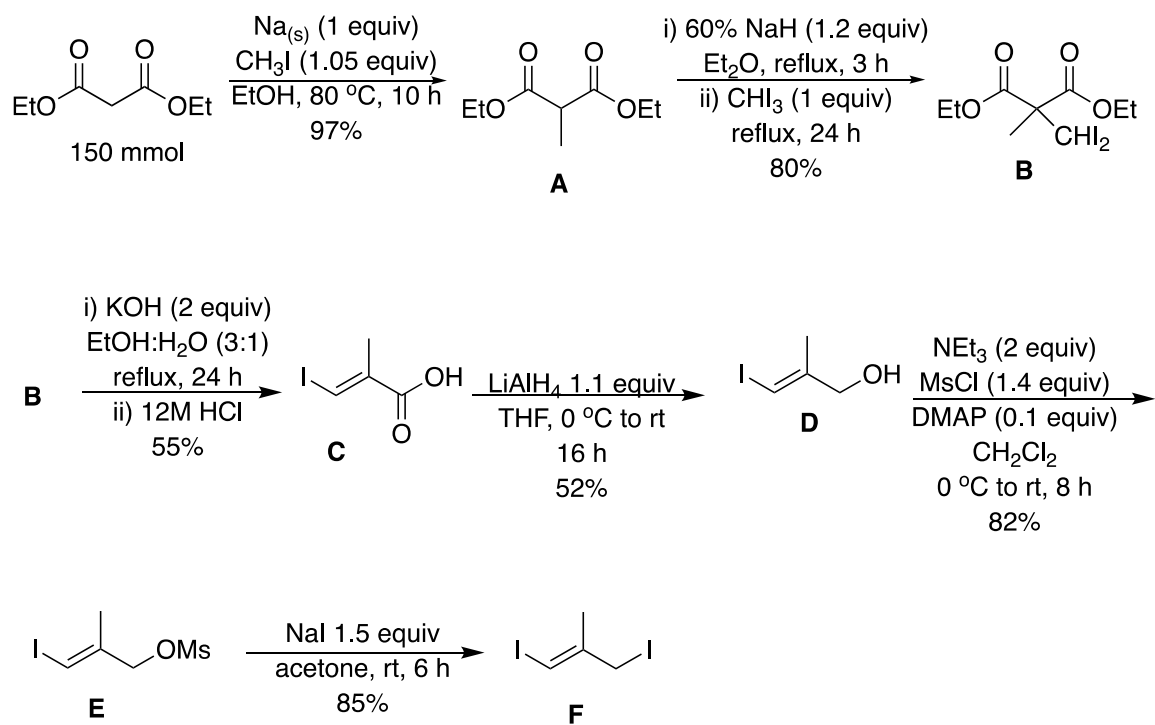
oxide is compared and contrasted with that for MVK-oxide,¹⁸ since both systems have extended conjugation across the vinyl and carbonyl oxide groups. In addition, we examine the UV-vis induced dissociation dynamics of MACR-oxide to MACR X ¹A' + O ¹D products and associated theoretical predictions. We anticipate that UV-vis excitation, when coupled with transient absorption or cavity ringdown spectrometers,^{16, 46-47} will enable spectroscopic detection of MACR-oxide in future laboratory studies of its unimolecular decay dynamics and bimolecular reactions with atmospheric species.

2. Results

2.1 Laboratory synthesis of MACR-oxide

A novel synthetic route is used to generate the methacrolein oxide (MACR-oxide) Criegee intermediate starting from the (*E*)-1,3-diiodo-2-methylprop-1-ene precursor. In devising a synthetic route to the precursor, several attributes were important. Allylic iodides are very reactive and light-sensitive species,⁴⁸ and their synthesis and handling must be performed with significant care. We viewed the synthesis, purification, storage, and use of an allylic diiodide containing the 3,3-diiodoprop-1-ene motif (CH₂=CHCHI₂) as fraught with potential problems. Thus, we chose a less reactive 1,3-diiodo-2-prop-1-ene motif, bearing allylic and sp²-hybridized C-I bonds. Given the sensitivity of the final diiodide, a stable intermediate near the end of the synthesis that would be easily stored was considered essential.

A reaction scheme showing each step of the precursor synthesis is shown in Scheme 2. The optimized synthesis commenced with 150 mmol diethyl malonate, which was deprotonated with in situ generated sodium ethoxide (NaOEt) and methylated with methyl iodide (MeI) to afford the methylated product **A** in 97% isolated yield.⁴⁹ Diethyl methylmalonate (**A**) was deprotonated with sodium hydride (NaH) and alkylated with

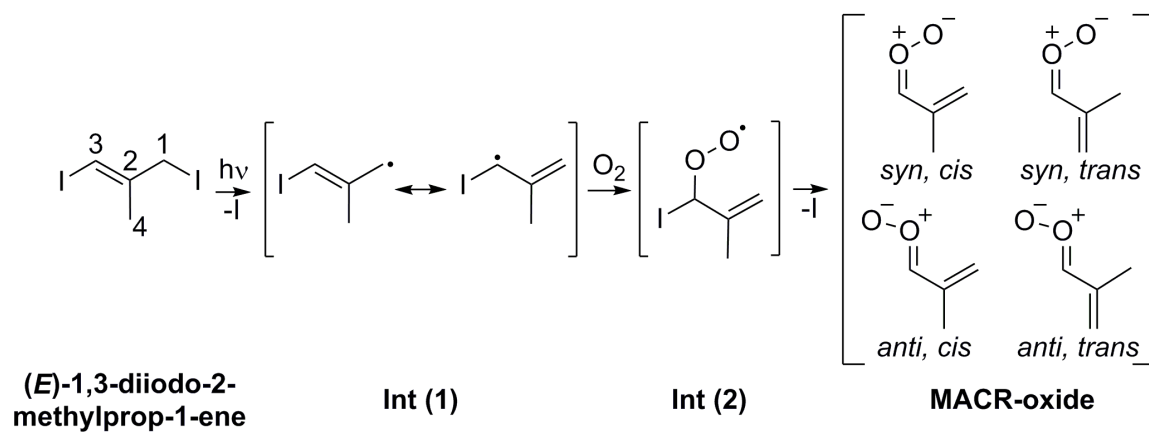


Scheme 2. Synthetic route to generate (*E*)-1,3-diiodo-2-methylprop-1-ene (**F**).

CHI₃ to generate diiodide **B** in 80% after workup.⁵⁰ Intermediate **B**, used without purification, was subjected to a tandem hydrolysis/elimination mediated by KOH in refluxing ethanol/water (EtOH/H₂O 3:1). The carboxylic acid **C** was isolated after acidic workup and column chromatography in 55% yield as a single double bond isomer. The solid acid **C** proved to be an excellent intermediate to store material.

Reduction of the acid **C** was performed with lithium aluminum hydride at room temperature to afford alcohol **D** in 52% yield after purification. Alcohol **D** was treated with methanesulfonyl chloride, triethylamine, and catalytic DMAP (4-*N,N*-dimethylaminopyridine) to generate mesylate **E** in 82% yield.⁵¹ The reactive mesylate was directly subject to NaI in acetone to perform the final substitution. The reaction was conducted in a dark fume hood with the reaction vial covered by aluminum foil to exclude light. The desired precursor (*E*)-1,3-diiodo-2-methylprop-1-ene (**F**) was obtained in 85% yield after purification by column chromatography. The precursor **F** could be stored in the dark in a refrigerator for 2–3 weeks. The Supporting Information (SI) provides full details on the multistep synthesis of the precursor (Sec. S1), along with its analytical characterization (Figures S1-S3) and related theoretical calculations (Figure S4, Table S1).

A novel synthetic route is then used to generate the methacrolein oxide (MACR-oxide) Criegee intermediate starting from the (*E*)-1,3-diiodo-2-methylprop-1-ene precursor. The 1,3-diiodo-2-methylprop-1-ene precursor absorbs strongly at 248 nm (Figure S2) and is expected to preferentially dissociate the weaker allylic C₍₁₎-I bond to form a resonance stabilized mono-iodo allylic radical intermediate, Int (1), as shown in Scheme 3. Resonance delocalization will lead to radical character on the C₍₃₎ carbon. Subsequent reaction with O₂ at C₍₃₎ will transiently form an iodoalkene peroxy radical, Int (2), prior to dissociation of I and formation of MACR-oxide. (Alternatively, if O₂ adds



Scheme 3. Synthetic route to generate MACR-oxide.

at the C₍₁₎ carbon site of Int (1), then dioxole would likely be formed, as shown in Scheme S2 of Ref. ¹⁷, instead of MACR-oxide.) The internally excited Int (2) should permit internal rotation about its single C-C and C-O bonds, and thus we assume that all four conformers of MACR-oxide are formed. An analogous reaction scheme was recently utilized to generate MVK-oxide.¹⁷⁻¹⁸

The minimum energy structures and zero-point energy (ZPE) corrected energies computed for the four conformers of MACR-oxide are given in Figure 1 and Table 1, and are in good agreement with a previous theoretical prediction.⁹ See SI Sec. S2 for related theoretical calculations (Figure S5, Tables S2-S4). The four conformers have similar energies, differing by less than 3.2 kcal mol⁻¹, with the *anti-trans* conformer predicted to be most stable. The computed barriers for interconversion between *syn* and *anti* conformers are quite high (ca. 20 kcal mol⁻¹), while those between *cis* and *trans* conformers are relatively low (ca. 9 kcal mol⁻¹).⁹

2.2. Electronic transitions of MACR-oxide: Theoretical predictions and experimental findings

The present study focuses on characterizing MACR-oxide through the strong $\pi^* \leftarrow \pi$ electronic transitions anticipated for the four conformers based on CASSCF/CASPT2 calculations (detailed in SI Sec. S2). The theoretical calculations indicate that two distinct excited singlet states of $\pi\pi^*$ character will have high oscillator strength ($f \sim 0.1$, Table 2) and are therefore expected to be 'optically bright'. Vertical transitions to the $1^1\pi\pi^*$ state of the four conformers of MACR-oxide are predicted between 342 and 380 nm (3.62 to 3.26 eV), while the second singlet $\pi^* \leftarrow \pi$ transitions are predicted between 228 and 304 nm (5.43 to 4.07 eV). The predominant orbitals contributing to the $\pi^* \leftarrow \pi$ transitions are shown in Figure 2. The orbitals show that

Table 1. Ground state stability (minima) and vertical (VIE) and adiabatic (AIE) ionization energies computed at the CCSD(T)-F12/CBS(TZ-F12,QZ-F12)//B2PLYP-D3/cc-pVTZ level of theory^a for the four conformers of MACR-oxide.

MACR-oxide Conformer	Minima ^a / kcal mol ⁻¹	VIE ^{c,d} / eV	AIE ^{b,d} / eV
<i>anti-cis</i>	3.18	8.90	8.77
<i>anti-trans</i>	0.00	8.85	8.73
<i>syn-cis</i>	0.91	9.17	9.01
<i>syn-trans</i>	2.50	8.90	8.78

^aMinima derived from other theoretical methods and previous work are given in Table S3.

^bIncluding ZPE correction.

^cWithout ZPE correction.

^dIncludes an approximate higher level excitation and core-valence correction of 0.07 eV obtained from CCSDT(Q)/cc-pVDZ and CCSD(T)/CBS(cc-pcVTZ,cc-pcVQZ) calculations for CH₂CHCHO.

Table 2. Vertical excitation energies (VEE/eV) corresponding wavelengths (λ /nm), and oscillator strengths (f) computed at CASPT2(12,10)/AVDZ level of theory for $\pi^* \leftarrow \pi$ electronic transitions with high oscillator strengths for the four conformers of MACR-oxide.^a

MACR-oxide Conformer	VEE / eV (λ / nm)	f
<i>anti-cis</i>	3.26 (380)	0.093
	4.07 (304)	0.083
<i>anti-trans</i>	3.31 (374)	0.116
	4.31 (288)	0.082
<i>syn-cis</i>	3.62 (342)	0.057
	4.36 (285)	0.062
<i>syn-trans</i>	3.29 (377)	0.094
	5.43 (228)	0.110

^aCompilation of vertical excitation energies and oscillator strengths computed for the lowest six singlet electronic transitions of each conformer are given in Table S5.

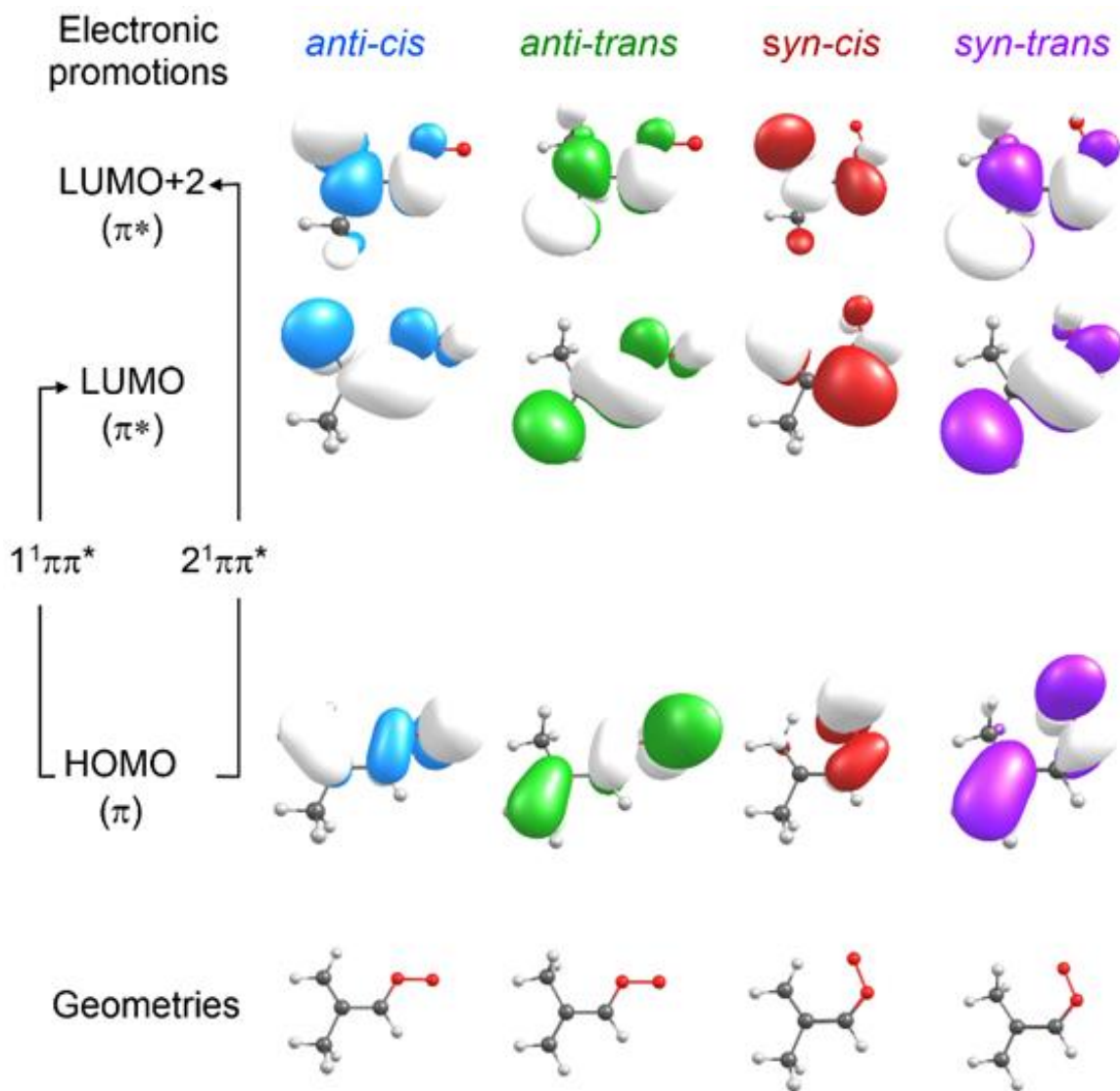


Figure 2. Selected orbitals within the active space of the CASSCF/CASPT2 calculations used to compute the lowest six singlet vertical transitions for the four conformers of MACR-oxide. (All orbitals are shown in Figure S6.) The orbitals displayed are of π and π^* nature and are involved in the electronic transitions associated with the highest oscillator strength (Table 2). The arrows illustrate orbital promotions involved in forming the designated excited singlet states of MACR-oxide.

excitation to the $1^1\pi\pi^*$ state is mainly associated with electronic promotion from the HOMO (π) orbital to the LUMO (π^*) orbital, the latter of which shows increased antibonding character around the carbonyl oxide moiety. In contrast, $2^1\pi\pi^*$ excitation to the LUMO+2 (π^*) orbital is associated with additional antibonding character in the vinyl substituent.

Experimentally, the diiodo alkene precursor is entrained in a 20% O₂/Ar gas mixture, pulsed into a quartz capillary reactor tube, and photolyzed at 248 nm with an excimer laser (see SI Sec. S3). MACR-oxide is collisionally stabilized and cooled in a supersonic expansion as it passes into a collision free region for spectroscopic studies. MACR-oxide is initially detected by photoionization using 10.5 eV (118 nm) VUV radiation, generated by frequency tripling the 3rd harmonic output of a Nd:YAG laser, on the $m/z=86$ parent mass channel of a time-of-flight mass spectrometer (Figure S7). The 10.5 eV photoionization energy exceeds the ionization thresholds computed for the four MACR-oxide conformers (8.7-9.0 eV, Table 1). Other isomers that could potentially be generated in the source and ionized at 10.5 eV are discussed later.

Resonant excitation on the first $\pi^*\leftarrow\pi$ transition of MACR-oxide is observed as a UV-vis induced depletion of the ground state population of one or more of the conformers. The resultant ground state depletion is detected after a short time delay ($\Delta t \sim 50$ ns) as a reduced VUV photoionization signal at $m/z=86$. Figure 3 shows a representative ground state depletion in which resonant UV excitation induces a significant decrease in the VUV photoionization signal at $m/z=86$.

The magnitude of the depletion, expressed as $(N_0 - N)/N_0$ with ground state abundances N_0 before and N after UV excitation, increases with UV power to a maximum depletion of ca. 35% (Figure S8). A minimum depletion of 2-3% can be

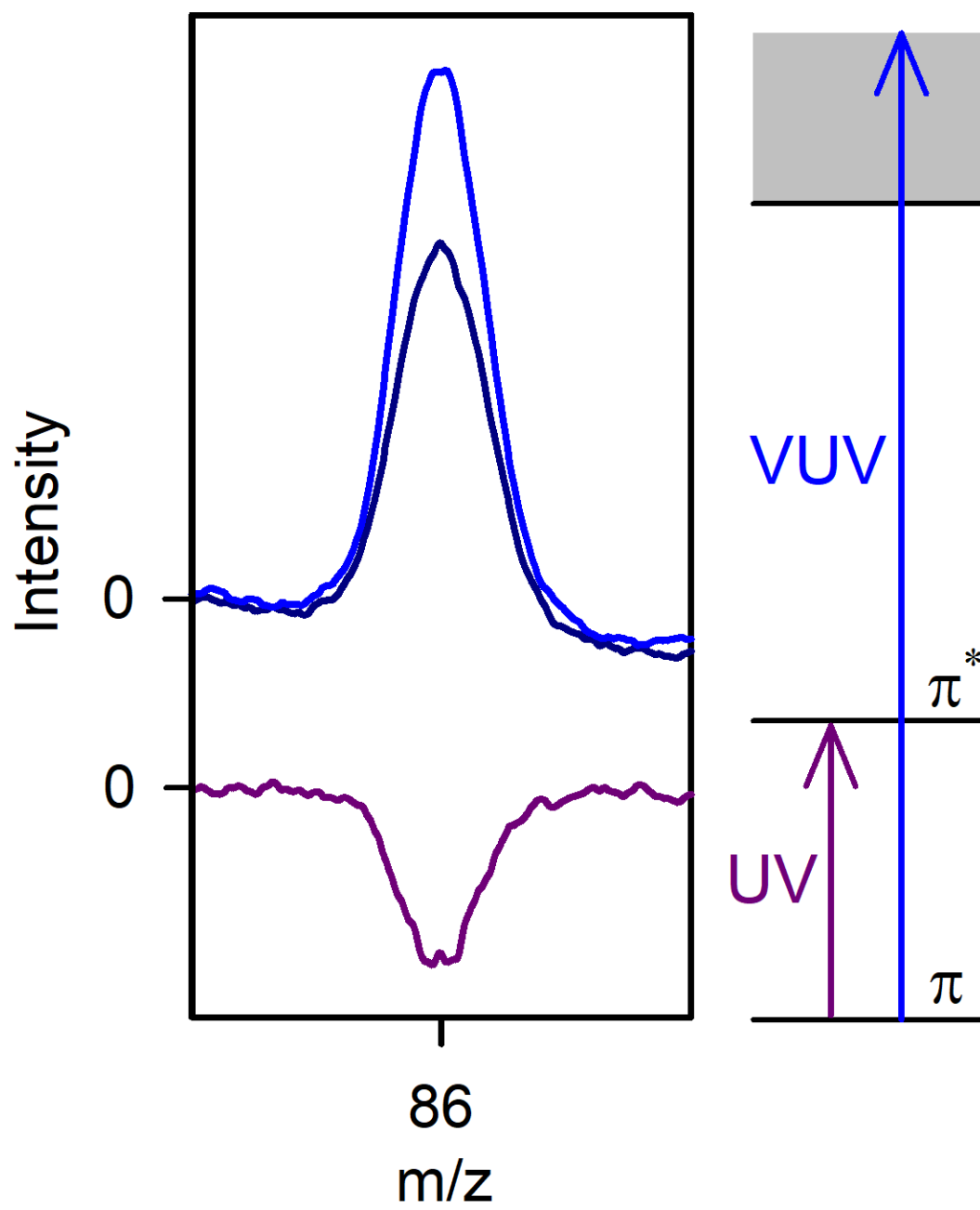


Figure 3. Mass spectra ($m/z=86$) arising from photoionization of MACR-oxide using 118 nm (10.5 eV) VUV radiation. The top trace (blue) shows the photoionization signal. The middle trace (dark blue) shows a significant reduction in the photoionization signal that occurs upon resonant UV excitation, which results in ground state depletion. The lower trace (violet) shows the depletion signal (UV on – UV off). The right panel shows a schematic energy level diagram illustrating the $\pi^* \leftarrow \pi$ electronic transition and ionization limit (shaded) for the MACR-oxide Criegee intermediate.

reliably measured. The corresponding absorbance, $-\ln(N/N_0)$, scales linearly with UV power up to ca. 3.6 mJ/pulse, demonstrating a one-photon process. The significant ground state depletion indicates a strong electronic transition, as observed previously for other Criegee intermediates.^{18, 22-24}

A qualitative estimate of the absorption cross section $\sigma(\lambda)$ of MACR-oxide is evaluated by dividing the absorbance by the photon flux Φ (mJ/cm²) of the focused UV-vis beam in the interaction region. At an UV power of 2.5 mJ/pulse and an approximate area of ~ 0.05 cm², corresponding to a photon flux of 50 mJ/cm², we estimate the absorption cross section for MACR-oxide at 380 nm to be $\sim 3 \times 10^{-18}$ cm² molecule⁻¹ and a corresponding atmospheric lifetime of 10 s. This estimate does not consider that the four MACR-oxide conformers may have different ground state populations, photoionization efficiencies at 10.5 eV, and/or absorption cross sections. The estimated σ will be a lower limit if other possible isomers contribute to the photoionization signal at 10.5 eV.

The electronic spectrum associated with excitation to the $1^1\pi\pi^*$ state of MACR-oxide is obtained by scanning a broadly tunable BBO optical parametric oscillator (OPO, see SI Sec. S3) across the UV-vis region from 315 to 500 nm, while monitoring the induced depletion of the VUV photoionization signal at $m/z=86$. The resultant UV-vis spectrum, recorded with 1 and 0.5 nm step sizes in the 315-380 and 380-500 nm regions, respectively, is shown in Figure 4.

The spectrum is normalized to laser power, which is maintained near 2.5 mJ/pulse to ensure linear scaling with power. The data points are averages of repeated measurements with $\pm 1\sigma$ uncertainty indicated by the shaded region. A smoothed version of the spectrum is superimposed on the plot to guide the eye. The resultant

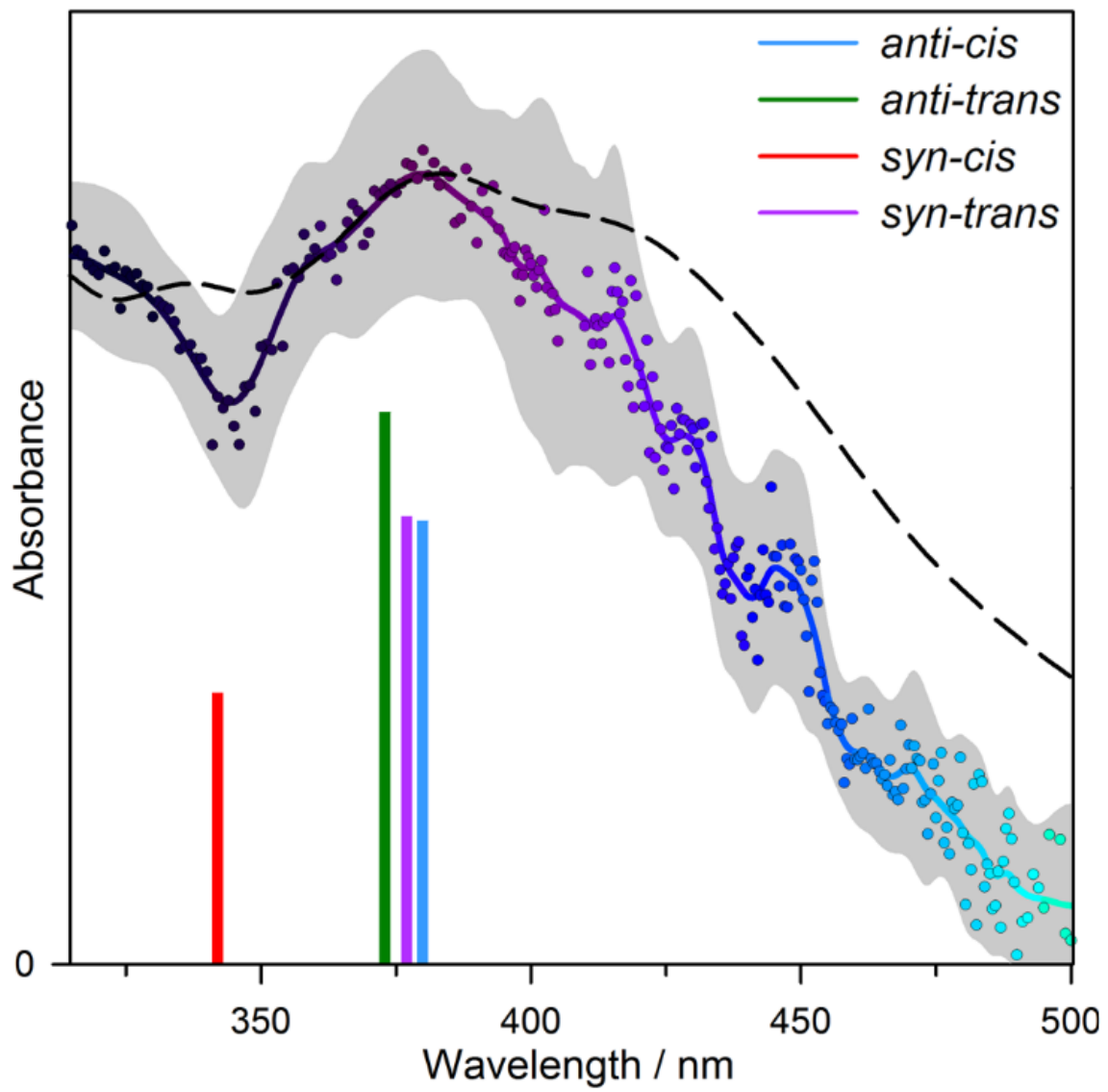


Figure 4. Experimental UV-vis spectrum of MACR-oxide from 315 to 500 nm derived from depletion of the photoionization signal on the $m/z=86$ mass channel. The corresponding absorbance (points) is normalized to the UV-vis laser power. The solid line represents a smoothed curve (11 point smooth) through the experimental data and the shaded area illustrates the experimental uncertainty derived from repeated measurements. For comparison, CASPT2(12,10)/AVDZ vertical excitation energies and associated oscillator strengths (bars) are shown for promotion of MACR-oxide to the excited $1^1\pi\pi^*$ state for the *anti-cis* (blue), *anti-trans* (green), *syn-cis* (red) and *syn-trans* (violet) conformers. Also shown is the overall MACR-oxide electronic spectrum (dashed line) predicted for the four conformers.

experimental spectrum for MACR-oxide is broad, spanning across the entire 315 to 500 nm spectral region, and peaks at 380 nm. The peak of the experimental spectrum is in excellent accord with the computed vertical transitions (Table 2) to the $1^1\pi\pi^*$ state of the four MVK-oxide conformers as shown in Figure 4. On the shorter wavelength side, the experimental spectrum initially falls off, exhibiting a dip at 343 nm to ca. 70% of its maximum absorbance, and then increases again, the latter likely due to the onset of excitation to the higher energy $2^1\pi\pi^*$ state that will be explored in future work. On the longer wavelength side, the spectrum falls off to half maximum at ca. 436 nm and drops to a minimum observable level at ca. 490 nm. Weak oscillatory structure is evident in the longer wavelength side of the spectrum with local maxima at 416.4, 430.9, and 448.1 nm, as determined from fits of the local structure with Lorentzian profiles (see SI Sec. S4, Table S6, Figure S9), and will be discussed later. Only CH₂OO, the simplest Criegee intermediate, has shown analogous oscillatory structure on the long wavelength side of its broad UV absorption band.^{33-34, 38-39}

For comparison, the purely electronic excitation spectrum originating from the ground state of each conformer of MACR-oxide was theoretically computed using an approach similar to that implemented in Newton-X.⁵²⁻⁵⁶ For each conformer, vertical transitions were computed for an ensemble of 300 initial ground state geometries sampled using a Wigner distribution based on normal mode harmonic frequencies. The transitions were broadened (0.25 eV Lorentzian lineshape) and summed to generate the absorption spectra shown in Figure 5 (see SI Sec. S5, Figure S10). The computed spectra for the four conformers are overlapping with largest contributions to the first $\pi^*\leftarrow\pi$ transition in the 370-440 nm region for *anti-trans*, *anti-cis*, and *syn-trans* conformers and in the 355-380 nm region for the *syn-cis* conformer. Contributions from

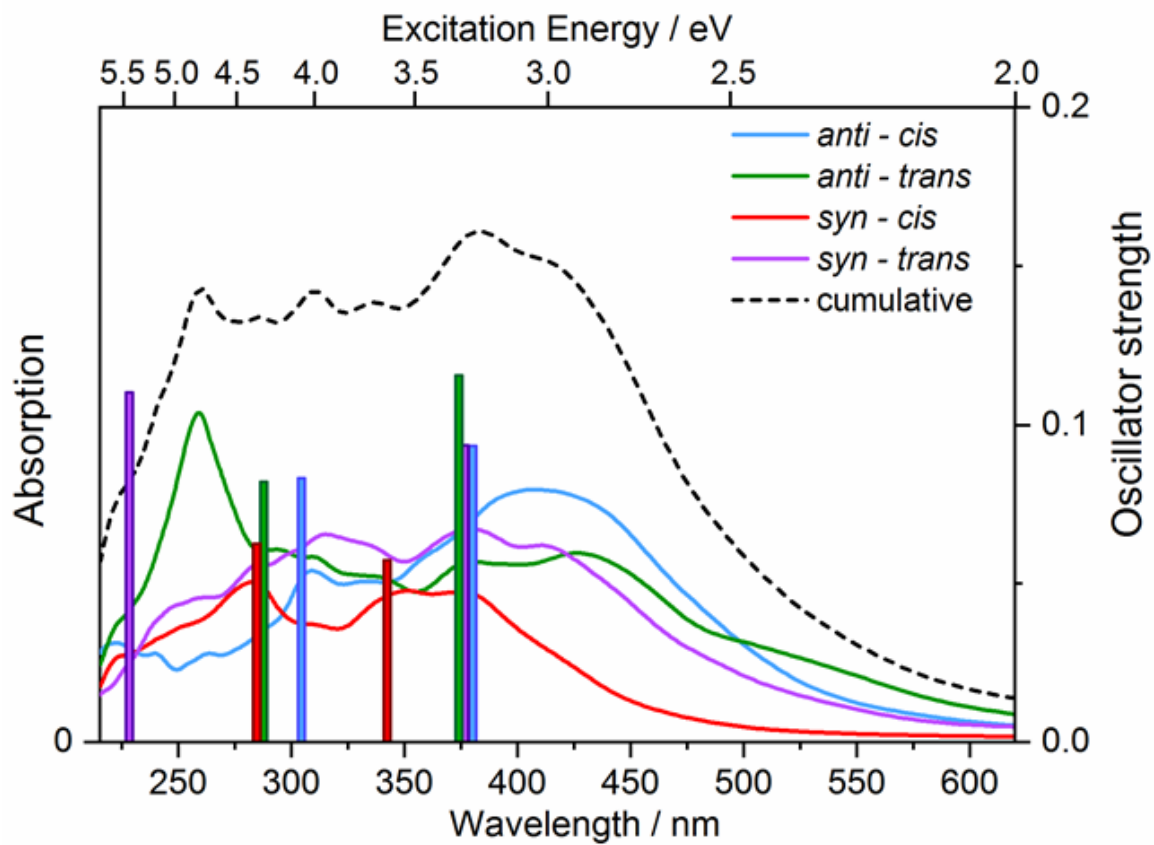


Figure 5. CASPT2(12,10)/AVDZ vertical excitation energies (vertical bars) to the $1^1\pi\pi^*$ and $2^1\pi\pi^*$ states and associated oscillator strengths for *anti-cis* (blue), *anti-trans* (green), *syn-cis* (red) and *syn-trans* (violet) conformers of MACR-oxide. The calculated electronic absorption spectra (solid curves) are derived for a harmonic-oscillator Wigner distribution of ground state configurations for each of the four conformers of MACR-oxide. The cumulative MACR-oxide electronic spectrum (dashed black curve) is the sum of the four individual spectra, assuming equal ground state populations, but reduced in scale by a factor of 1.5.

the second $\pi^* \leftarrow \pi$ transition for each conformer are predicted at shorter wavelength and are again overlapping, and merge to some extent with those from the first transition. The cumulative absorption spectrum for MACR-oxide (rescaled by a factor of 1.5 in Figure 5) is obtained by summing the absorption spectra for each conformer and assuming equal population of the conformers. The resultant cumulative spectrum for MACR-oxide peaks at 383 nm and falls off on the longer wavelength side to half maximum at 475 nm. On the shorter wavelength side, the cumulative spectrum drops by ca. 15% at 345 nm and continues with similar absorbance in a relatively flat region arising from overlapping contributions of the two $\pi^* \leftarrow \pi$ transitions down to ca. 275 nm before falling off to half maximum at ca. 230 nm. The theoretically predicted spectrum for the $\pi^* \leftarrow \pi$ transitions of the four conformers of MACR-oxide agrees well with the 380 nm peak and broad span of the experimental spectrum. We discuss the origin of the oscillatory structure below.

2.3. Photodissociation dynamics of MACR-oxide

UV-vis excitation of MACR-oxide results in prompt dissociation and yields O 1D products that are readily detected by 2+1 resonance-enhanced multiphoton ionization (REMPI), as found previously for other Criegee intermediates.^{18, 39, 57-59} Here, we examine the UV-vis induced dissociation dynamics of MACR-oxide conformers to MACR X $^1A'$ + O 1D products from experimental and theoretical perspectives. Starting with theory, we map out potential energy curves (unrelaxed) along the lowest, spin-allowed O-O dissociation coordinate for the most stable *anti-trans* conformer of MACR-oxide. The resultant diabatic potential curves (unrelaxed) are shown in Figure 6.

Vertical excitation of the *anti-trans* conformer from the ground S_0 electronic state to the $1^1\pi\pi^*$ excited state (3.31 eV) is predicted to access a repulsive region of the

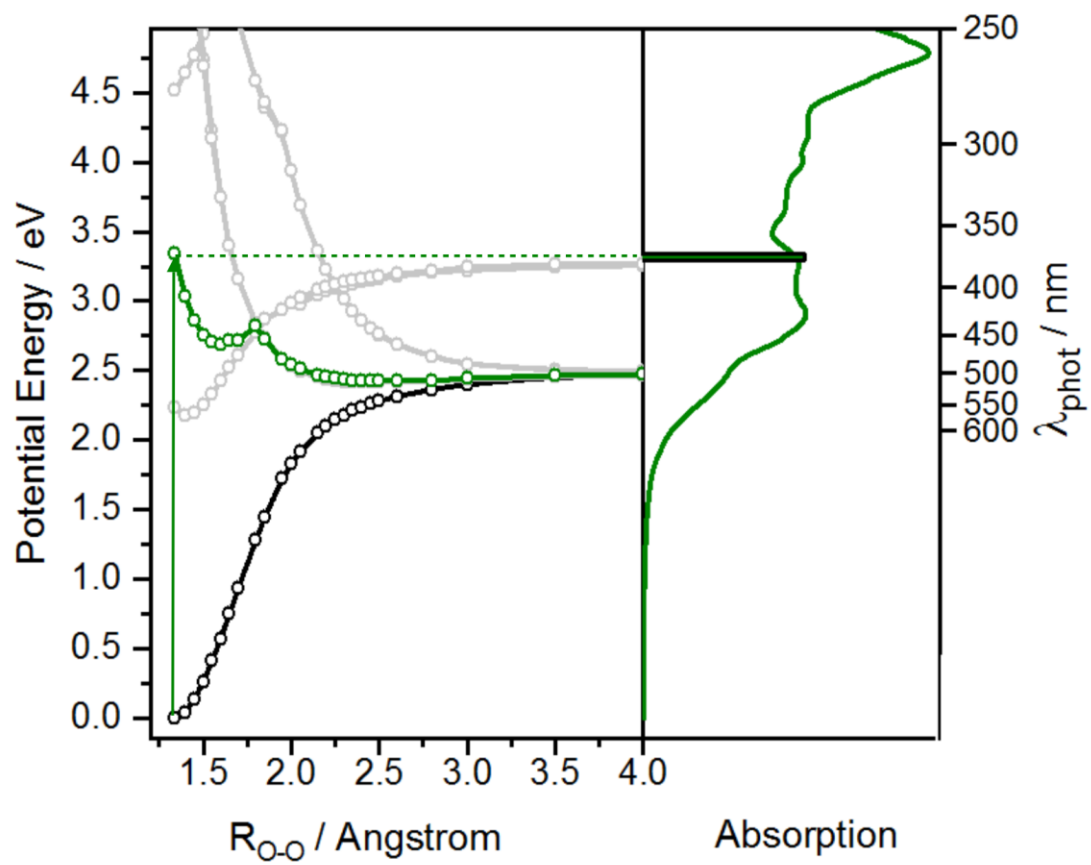


Figure 6. CASPT2(12,10)/AVDZ potential energy curves (unrelaxed) calculated along the O-O bond stretching coordinate for the lowest seven singlet states of the most stable conformer of MACR-oxide (*anti-trans*). Vertical excitation from the ground S_0 electronic state (black) to the $1^1\pi\pi^*$ state (green) is predicted at 3.31 eV (374 nm). The $1^1\pi\pi^*$ state is crossed by $(n/\pi)\sigma^*$ dissociative states (gray) at extended O-O bond distances. Predissociation of the $1^1\pi\pi^*$ state via $(n/\pi)\sigma^*$ states leads to the lowest spin-allowed dissociation asymptote of *trans*-MACR X $^1A'$ + O 1D products at 2.46 eV. The higher asymptotic channel results in *trans*-MACR a $^3A''$ + O 3P products at 3.26 eV. (Right panel) Computed vertical electronic transition (bar) and associated absorption spectrum (curve) for the $\pi^* \leftarrow \pi$ transitions based on a harmonic-oscillator Wigner distribution of initial configurations in the S_0 state.

excited state potential. The vertical electronic transition and broad simulated absorption spectrum for *anti-trans*-MACR-oxide are also shown in Figure 6. The $1^1\pi\pi^*$ excited state couples via conical intersection (estimated at 2.83 eV) with a repulsive potential(s) at extended O-O bond distances and leads to the lowest spin-allowed dissociation asymptote of *trans*-MACR X $^1A'$ + O 1D . The zero-point corrected energy required for spin-allowed dissociation of the *anti-trans* conformer of MACR-oxide to *trans*-MACR X $^1A'$ + O 1D is computed to be 2.08 eV utilizing a relaxed optimization at large O-O separation (see SI Sec. S5 and Tables S7-S8). ZPE dissociation energies for other MACR-oxide conformers (Table S8) are evaluated by taking into account their relative ground state stabilities (Table 1) and the computed energy splitting between the *cis* and *trans* conformers of the MACR product.

Experimentally, velocity map imaging (VMI) experiments are carried out with UV-vis excitation of MACR-oxide and detection of O 1D fragments arising from the lowest spin-allowed product channel. Details regarding VMI experimental conditions are discussed in the SI (Sec. S3). The velocity and angular distributions of the O 1D products reveal information on the energy partitioning to products and the timescale for dissociation, respectively. VMI images of the O 1D products are recorded (after background subtraction) at discrete excitation wavelengths from 385 to 471 nm, specifically near the peak of the UV-vis spectrum (385 nm, Figure 7), the peaks of the weak oscillatory structure (416, 431, and 448 nm), and close to the extreme of the long wavelength tail region (471 nm, Figure 7). The O 1D signal drops off rapidly at longer excitation wavelengths with only a very weak signal at ca. 500 nm (insufficient for an image), which is consistent with the depletion spectrum (Figure 4). The theoretical calculations confirm that dissociation of MACR-oxide to MACR X $^1A'$ + O 1D products

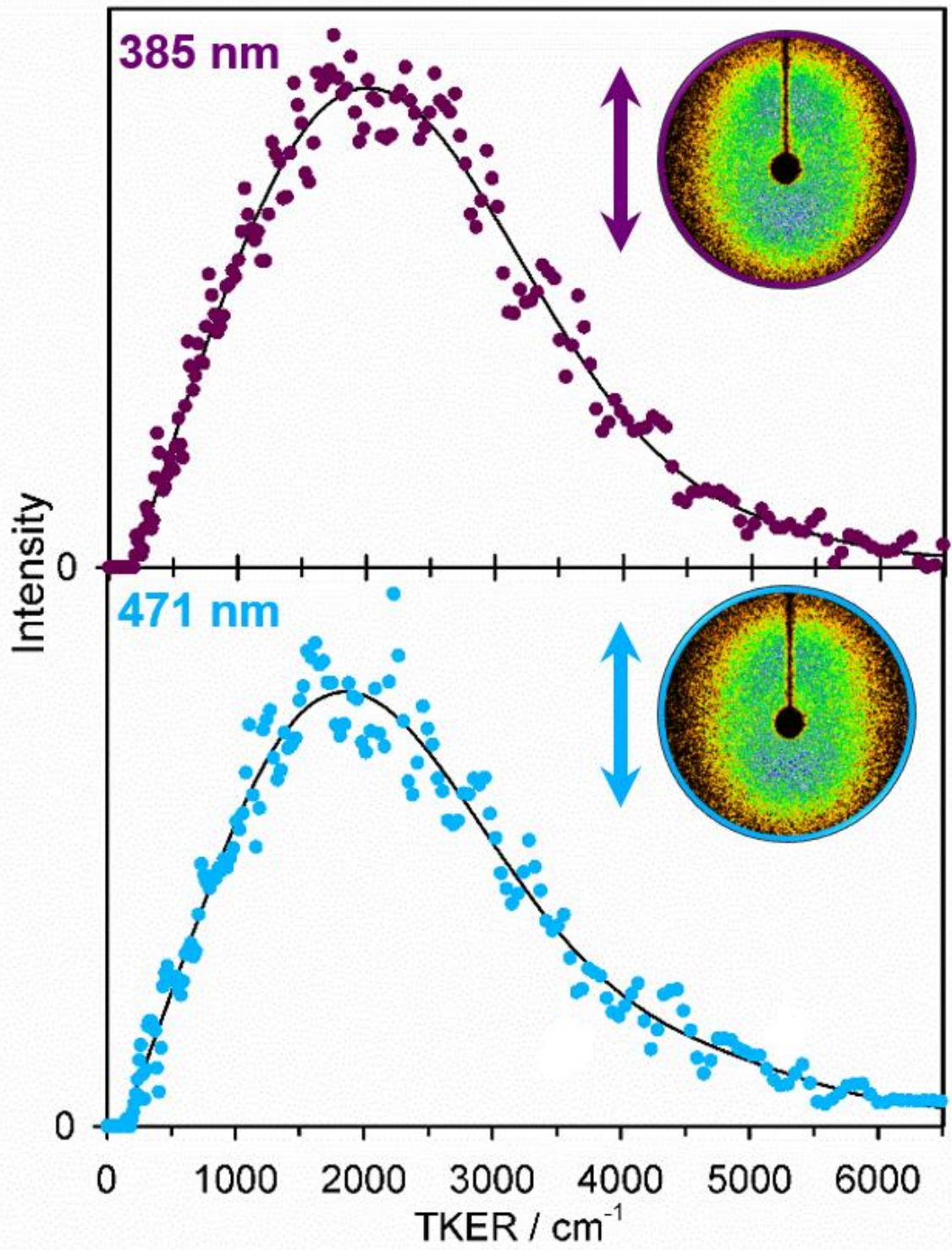


Figure 7. Total kinetic energy release (TKER) distributions (with black curve through data points from polynomial fit) to the MACR + O ¹D products resulting from UV-vis excitation of MACR-oxide at 385 nm (violet, top panel) and 471 nm (blue, lower panel). The TKER distributions are deduced from analysis of the O ¹D velocity map images (insets). The double-sided vertical arrows represent the polarization of the UV-vis OPO (parallel to the detector plane)

should be energetically accessible throughout the observed spectral region (Table S8, dissociation energies of 1.97-2.18 eV, corresponding to 629-568 nm, depending on the conformer).

The O ¹D VMI images at 385 and 471 nm (Figure 7) exhibit anisotropic angular distributions indicative of rapid dissociation compared to the rotational period of MACR-oxide (ca. 100 ps). This demonstrates that electronic excitation of MACR-oxide to the ¹ $1\pi\pi^*$ state at $\lambda \leq 500$ nm accesses regions of strong coupling to repulsive potential(s) (Figure 6) that result in rapid dissociation to MACR X ¹A' + O ¹D products. Similarly, the anisotropic VMI images of O ¹D products recorded at the local maxima of the weak oscillatory structure (416, 431, and 448 nm) show that the excited state accessed is short-lived.

The rapid dissociation (≤ 100 ps) of MACR-oxide upon electronic excitation to the ¹ $1\pi\pi^*$ state precludes its subsequent detection by photoionization on the parent $m/z=86$ mass channel after a 50 ns experimental time delay. As a result, the UV-vis spectrum of MACR-oxide on the first $\pi^* \leftarrow \pi$ transition obtained by the depletion method will be equivalent to a standard absorption method. Although not the main focus of the present study, prompt dissociation to O ¹D products is also seen for MACR-oxide promoted to the ² $1\pi\pi^*$ state at 205 nm (SI Sec. S6, Figure S11).

Excitation of MACR-oxide in the 385 to 471 nm range gives rise to MACR X ¹A' + O ¹D products with broad and unstructured total kinetic energy release (TKER) distributions having remarkably similar average translational energies (ca. 2700 cm^{-1}) and breadths (FWHM ~ 3000 cm^{-1}) as shown in Figure 7 (Table S9). The similarity of the TKER distributions is notable given that the range of excitation wavelengths results in a nearly 5000 cm^{-1} change in energy available to products (e.g. decrease from ca.

10,200 to 5500 cm^{-1} for *anti-trans* conformer). This suggests the possibility of a barrier, e.g. associated with the conical intersection (roughly estimated at 2.83 eV for the *anti-trans* conformer), along the reaction path to products. The energy associated with the barrier is expected to flow preferentially into translational energy, while excess energy above the barrier would be statistically distributed and principally result in vibrational excitation of MACR.⁶⁰ The dissociation energy predicted for *anti-trans* MACR-oxide to *trans*-MACR X $^1\text{A}' + \text{O } ^1\text{D}$ products is 2.08 eV (Table S8), which suggests that a barrier energy of 0.75 eV (6000 cm^{-1}) would flow into translation. This is in good accord with the range of kinetic energies observed in the experimental TKER distributions. Finally, we note that excitation at energies in the vicinity of the barrier associated with the conical intersection, yet above the MACR X $^1\text{A}' + \text{O } ^1\text{D}$ asymptote, may access quasi-bound vibrational levels in the excited $1^1\pi\pi^*$ state of MACR-oxide. This, in turn, could give rise to the weak oscillatory structure observed in the electronic spectrum at long wavelengths, although higher-level calculations of the conical intersection region(s) will be needed to test this hypothesis.

3. Discussion

3.1 Weak oscillatory structure at long wavelengths

Here, we examine the origin of the weak oscillatory structure observed in the long wavelength tail region of the experimental spectrum of MACR-oxide (Figure 4). The oscillatory structure is superimposed on a broad profile spanning from 371 to 500 nm, which is simulated as a Lorentzian profile with peak at 374.8 nm and accounts for ca. 90% of the total signal. The local structure associated with the weak oscillations, together accounting for about 10% of the total signal, is fit using three Lorentzian profiles with local maxima at 416.4, 430.9, and 448.1 nm (SI Sec. S4). The local maxima are

separated by ca. 810 and 890 cm^{-1} , respectively. The simulation of the weak oscillations yields relatively large and variable breadths (FWHM) of 1810, 310, and 560 cm^{-1} , respectively.

The weak oscillatory structure observed for MACR-oxide is reminiscent of the more extensive progression seen previously in the long wavelength tail region of the electronic spectrum of the simplest Criegee intermediate CH_2OO .^{33-34, 38-39} In CH_2OO , the progression was attributed to short-lived resonances originating from congested vibrational structure involving several modes (e.g. O-O stretch and COO bend)³⁸ in the excited B $^1\text{A}'$ electronic state.³⁹⁻⁴⁰ The emergence of oscillatory structure in the long wavelength region of the MACR-oxide spectrum is surprising, because the theoretical calculations indicate that multiple conformers will have overlapping electronic spectra in this region. (The current theoretical approach yields purely electronic transitions and cannot predict vibrational structure.)

The average spacing of the oscillatory structure evident in the MACR-oxide electronic spectrum (ca. 850 cm^{-1}) is larger than that observed in the long wavelength tail region of CH_2OO , where an average spacing of ca. 610 cm^{-1} was dominant in an extended progression. For comparison, the vibrational frequency of the O-O stretch (harmonic) is predicted to be ca. 900 cm^{-1} for CH_2OO in the excited $1^1\pi\pi^*$ state,³⁸ which is in accord with typical O-O stretches in the excited states of peroxide molecules.⁶¹⁻⁶⁵ The oscillatory structure in the MACR-oxide spectrum likely has contributions from several vibrational modes including the O-O stretch (dissociation coordinate) and/or multiple conformers. This could explain the greater breadth and variability of the oscillatory features in the MACR-oxide spectrum compared to the average breadth (ca. 300 cm^{-1}) and deviation seen in the CH_2OO UV spectrum.^{33-34, 38-39}

Finally, VMI images recorded at the local maxima in the MACR-oxide spectrum reveal rapid dissociation to $\text{MACR X } ^1\text{A}' + \text{O } ^1\text{D}$ products, as has been found previously for CH_2OO .³⁹ Thus, by analogy to CH_2OO , the broad oscillatory structure in the long wavelength region of the MACR-oxide spectrum is ascribed to short-lived vibrational resonances associated with the excited $1^1\pi\pi^*$ electronic state, which decay by nonadiabatic coupling to repulsive singlet states.

3.2 Comparison of MACR-oxide and MVK-oxide

Experimentally, the peak of the UV-vis spectrum of MACR-oxide (380 nm) is similar to that reported recently for MVK-oxide (388 nm), the other four-carbon, unsaturated Criegee intermediate from isoprene ozonolysis. However, the MACR-oxide spectrum falls off more slowly to longer wavelength than MVK-oxide (Figure S12). In addition, the MACR-oxide spectrum exhibits weak oscillatory structure in the long wavelength tail region, which was not observed for MVK-oxide. Theory predicts that both MACR-oxide and MVK-oxide have strong electronic transitions to the $1^1\pi\pi^*$ state originating from four conformers with broad overlapping contributions to their cumulative spectra. The largest oscillator strength for MACR-oxide, which is associated with vertical electronic excitation of the most stable *anti-trans* conformer (Table 2), is predicted to be about a factor of two weaker than that for the strongest transition for MVK-oxide (*anti-trans* conformer). Similarly, the peak experimental absorption cross section estimated for MACR-oxide is somewhat less than that estimated for MVK-oxide. This is evident by the higher UV-vis OPO power required to reach the maximum depletion for MACR-oxide (ca. 3.5 mJ/pulse) than that needed for MVK-oxide (ca. 1 mJ/pulse).

Additional direct theoretical comparisons can be made between MACR-oxide and MVK-oxide because they are isomers. This permits direct comparison of the ground state stabilities (using the same method/basis with ZPE correction) of MACR-oxide and MVK-oxide for the four conformers of each isomer, along with the stabilities of the MACR and MVK isomer products. Specifically, this comparison shows that the most stable (*anti-trans*) conformer of MACR-oxide is 5.95 kcal mol⁻¹ less stable in absolute energy than the most stable conformer of MVK-oxide (*syn-trans*).

In addition, the dissociation energies computed for the MACR-oxide conformers can be directly compared with those for MVK-oxide (Figure S13). This shows that less energy is required for dissociation of the *anti-trans*, *syn-trans*, and *anti-cis* conformers of MACR-oxide to the MACR + O ¹D product channel than the energy required for all four conformers of MVK-oxide to the analogous MVK + O ¹D product channels. Only the *syn-cis* conformer of MACR-oxide requires a similar energy for dissociation as MVK-oxide.

3.3 Electronic transitions of other possible isomers

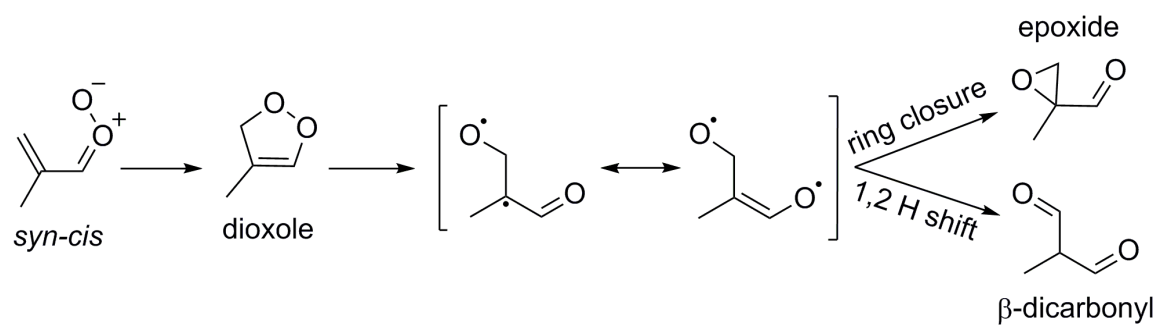
For MACR-oxide, a maximum UV-vis induced depletion of 35% is observed when detected by 10.5 eV photoionization on the m/z=86 mass channel. This suggests that more than one isomer (or possibly a dissociative ionization fragment) may contribute to the photoionization signal at m/z=86. Such additional species do not appear to strongly absorb UV-vis radiation. To test this hypothesis, we calculate vertical excitation energies and oscillator strengths (Tables S10-S11) of plausible isomers (e.g. dioxole, dioxirane, methacrylic acid, β-dicarbonyl, epoxide), which may result from unimolecular decay of MACR-oxide as elaborated below.^{9, 66-67} Atmospheric chemistry of isoprene

also generates isoprene-derived peroxy radicals [HO-C₅H₈(Iso)-O₂] that have an overlapping absorption band in the near UV from 300 to 400 nm.⁶⁸

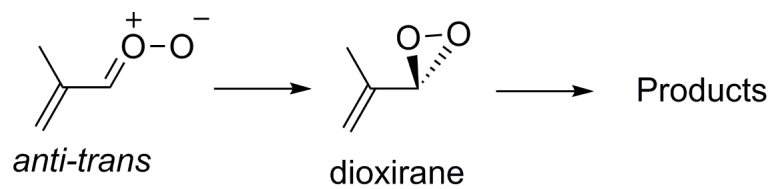
The lowest energy pathways for unimolecular decay of MACR-oxide are predicted to be distinctly different for the four conformers. For the *syn-cis* conformer, unimolecular decay is expected to start with very rapid 1,5 electrocyclic ring closure (2500 s⁻¹)²⁸ to form the 5-membered ring of dioxole (4-methyl-3H-1,2-dioxole, Scheme 4)⁹ that can lead to several products as outlined below.^{9, 17, 28}

For *anti*-conformers of MACR-oxide, the lowest energy pathway is predicted to be rather slow decay (10 s⁻¹) via 1,3 ring closure of the carbonyl oxide group to form a three-membered cyclic dioxirane ([3-(prop-1-en-2-yl) dioxirane], Scheme 5),⁹ and subsequent products. A small portion of the *anti*-conformers are predicted to form hot methacrylic acid (2-methyl-2-propenoic acid, not shown).⁵ By contrast, the 1,4 H-atom transfer mechanism available to *syn*-conformers of MVK-oxide and methyl (or alkyl) substituted Criegee intermediates is not feasible for MACR-oxide because it lacks an α -H in a methyl (or alkyl) group adjacent to the terminal O atom.

If dioxole and/or dioxirane products are formed and stabilized, e.g. in the reactor tube, they could be ionized at 10.5 eV (Table S12). However, neither are predicted to have strong electronic transition in the 350 to 500 nm region observed for MACR-oxide. The first strong electronic transitions of dioxole and dioxirane are predicted to have vertical excitation energies below 250 nm (Table S10). As shown in Scheme 4, initially formed dioxole will be internally excited and could decay by O-O bond fission to form a diradical, which could then rearrange by a 1,2 H-atom shift to form a β -dicarbonyl (2-methyl-3-oxopropanal) and/or by ring closure to epoxide (1,2-epoxy-2-methyl-3-propanal) products, and/or undergo fission to various bimolecular products.⁹ While such



Scheme 4. Mechanism for *syn-cis*-MACR-oxide unimolecular decay to dioxole intermediate and subsequent products.



Scheme 5. Mechanism for *anti-trans*-MACR-oxide unimolecular decay to dioxirane intermediate and subsequent products.

β -dicarbonyl and epoxide products could be ionized at 10.5 eV (Table S12), their first strong electronic transitions are predicted below 200 nm (Table S10). Similarly, methacrylic acid, if formed, will be ionized at 10.5 eV,⁶⁹ but the onset of its UV spectrum occurs below 230 nm⁷⁰ and its strong electronic transitions are predicted below 200 nm (Table S10). Finally, dioxiranes with allylic functionality can undergo ring opening to a dioxy biradical, which can further rearrange or decompose.^{5, 9, 66-67}

4. Conclusions

MACR-oxide, a four-carbon unsaturated Criegee intermediate generated in isoprene ozonolysis, is synthesized in the laboratory setting for the first time by photolysis of an (*E*)-1,3-diiodo-2-methylprop-1-ene precursor and reaction of the resultant resonance stabilized mono-iodo allylic radical with O₂. The electronic spectrum of jet-cooled MACR-oxide is recorded by a depletion method, in which UV-vis excitation induces depletion of the ground state population of one or more of its four conformers and results in an associated decrease in the VUV (10.5 eV) photoionization signal on the *m/z*=86 parent mass channel. The resultant UV-vis spectrum peaks at 380 nm, spans across the 315-500 nm region, and exhibits weak oscillatory structure in the long wavelength region. The spectrum increases again below 343 nm, likely due to the onset of the second $\pi^* \leftarrow \pi$ transition. Additional velocity map imaging experiments demonstrate that electronic excitation of MACR-oxide throughout the entire spectral region results in rapid dissociation (≤ 100 ps) to O ¹D products that are detected by 2+1 REMPI. The rapid dissociation of MACR-oxide in the excited $1^1\pi\pi^*$ state assures that the electronic spectrum obtained by the depletion method is equivalent to a direct absorption method. The weak oscillatory structure of the MACR-oxide spectrum, which

is analogous to an extended progression observed previously for CH_2OO ,^{33-34, 39} is likely due to short lived vibrational resonances in the excited $1^1\pi\pi^*$ state.

Complementary theoretical calculations examined the ground state stabilities of the four MACR-oxide conformers (within $3.2 \text{ kcal mol}^{-1}$), along with their vertical transitions energies and oscillator strengths. Strong vertical transitions are predicted to the $1^1\pi\pi^*$ state in the 3.26-3.62 eV (342-380 nm) region and to the $2^1\pi\pi^*$ state in the 4.07-5.43 eV (228-304 nm) region. These transitions are nominally associated with the carbonyl oxide and vinyl groups, respectively. UV-vis absorption profiles for the MACR-oxide conformers are also computed using a Wigner distribution of initial configurations. The resultant cumulative absorption spectrum for the first $\pi^*\leftarrow\pi$ transition, assuming equal contributions of the four conformers, is computed to peak at 383 nm and agrees well with the experimental spectrum.

MACR-oxide and its isomer MVK-oxide, the other four-carbon unsaturated Criegee intermediate formed in isoprene ozonolysis, exhibit similar strong absorption spectra, peaked at 380 nm and 388 nm, respectively, arising from the first $\pi^*\leftarrow\pi$ transitions of their four conformers. The MACR-oxide spectrum extends to longer wavelength than MVK-oxide, and also displays weak oscillatory structure not seen for MVK-oxide. The electronic spectra of MACR-oxide and MVK-oxide, both with extended conjugation across the carbonyl oxide and vinyl groups, are shifted to longer wavelength than previously investigated Criegee intermediates, e.g. CH_2OO , CH_3CHOO , and $(\text{CH}_3)_2\text{COO}$. Direct theoretical comparison of four-carbon isomers shows that the lowest energy conformer (*anti-trans*) of MACR-oxide is less stable (by ca. $6.0 \text{ kcal mol}^{-1}$) than the lowest energy conformer (*syn-trans*) of MVK-oxide. In addition, less energy is required for dissociation of the lowest energy conformer of MACR-oxide to $\text{MACR X } ^1\text{A}'$

+ O ¹D (48.0 kcal mol⁻¹) than that for MVK-oxide to MVK X ¹A' + O ¹D (52.0 kcal mol⁻¹). Finally, MACR-oxide and MVK-oxide are predicted to have very different unimolecular decay pathways and bimolecular reactivity with water vapor and potentially other atmospheric species.²⁸⁻³⁰

The first identification of the four-carbon unsaturated MACR-oxide Criegee intermediate presented in this work is based on laboratory synthesis, VUV photoionization, UV-vis spectroscopy, and photo-induced dissociation to MACR X ¹A' + O ¹D products. These advances are expected to enable future studies of its conformer-dependent unimolecular decay processes and bimolecular reactions with key atmospheric species.

Supporting Information

Additional material on the synthesis of the (*E*)-1,3-diiodo-2-methylprop-1-ene precursor, details of electronic structure calculations, spectroscopic methods and analysis, including Figures S1-S13 and Tables S1-S12.

Acknowledgements

This research was supported by the U.S. Department of Energy - Basic Energy Sciences under grant DE-FG02-87ER13792 (MIL). Partial support was provided through the National Science Foundation under grants CHE-1664572 (MIL) and CHE-1464744 (P JW). BM acknowledges a postdoctoral fellowship from the European Union's Horizon 2020 research and innovation programme under the Marie Skłodowska-Curie Grant Agreement PhARRAO - 746593. The authors thank T. N. V. Karsili (University of Louisiana) for help on the theoretical spectral simulations and Amy Green (University of Pennsylvania) for carrying out preliminary measurements. NT thanks the Thai government for financial support. This material is based in part on research at Argonne

National Laboratory supported by the U.S. Department of Energy, Office of Science, Office of Basic Energy Sciences, Division of Chemical Sciences, Geosciences, and Biosciences under Contract No. DE-AC02-06CH11357.

References

1. Sindelarova, K.; Granier, C.; Bouarar, I.; Guenther, A.; Tilmes, S.; Stavrou, T.; Müller, J. F.; Kuhn, U.; Stefani, P.; Knorr, W., Global Data Set of Biogenic VOC Emissions calculated by the MEGAN Model Over the Last 30 years. *Atmos. Chem. Phys.* **2014**, *14*, 9317-9341.
2. Atkinson, R.; Arey, J., Atmospheric Chemistry of Biogenic Organic Compounds. *Acc. Chem. Res.* **1998**, *31*, 574-583.
3. Atkinson, R.; Arey, J., Atmospheric Degradation of Volatile Organic Compounds. *Chem. Rev.* **2003**, *103*, 4605-4638.
4. Atkinson, R.; Arey, J., Gas-phase Tropospheric Chemistry of Biogenic Volatile Organic Compounds: a Review. *Atmos. Environ.* **2003**, *37*, 197-219.
5. Nguyen, T. B.; Tyndall, G. S.; Crouse, J. D.; Teng, A. P.; Bates, K. H.; Schwantes, R. H.; Coggon, M. M.; Zhang, L.; Feiner, P.; Miller, D. O.; Skog, K. M.; Rivera-Rios, J. C.; Dorris, M.; Olson, K. F.; Koss, A.; Wild, R. J.; Brown, S. S.; Goldstein, A. H.; de Gouw, J. A.; Brune, W. H.; Keutsch, F. N.; Seinfeld, J. H.; Wennberg, P. O., Atmospheric Fates of Criegee Intermediates in the Ozonolysis of Isoprene. *Phys. Chem. Chem. Phys.* **2016**, *18*, 10241-10254.
6. Klawatsch-Carrasco, N.; Doussin, J. F.; Carlier, P., Absolute rate constants for the gas-phase ozonolysis of isoprene and methylbutenol. *Int. J. Chem. Kinet.* **2004**, *36*, 152-156.
7. Gutbrod, R.; Kraka, E.; Schindler, R. N.; Cremer, D., Kinetic and Theoretical Investigation of the Gas-Phase Ozonolysis of Isoprene: Carbonyl Oxides as an Important Source for OH Radicals in the Atmosphere. *J. Am. Chem. Soc.* **1997**, *119*, 7330-7342.
8. Kuwata, K. T.; Valin, L. C.; Converse, A. D., Quantum Chemical and Master Equation Studies of the Methyl Vinyl Carbonyl Oxides Formed in Isoprene Ozonolysis. *J. Phys. Chem. A* **2005**, *109*, 10710-10725.
9. Kuwata, K. T.; Valin, L. C., Quantum Chemical and RRKM/Master Equation Studies of Isoprene Ozonolysis: Methacrolein and Methacrolein Oxide. *Chem. Phys. Lett.* **2008**, *451*, 186-191.
10. Aschmann, S. M.; Atkinson, R., Formation Yields of Methyl Vinyl Ketone and Methacrolein from the Gas-Phase Reaction of O₃ with Isoprene. *Environ. Sci. Technol.* **1994**, *28*, 1539-1542.
11. Johnson, D.; Marston, G., The Gas-Phase Ozonolysis of Unsaturated Volatile Organic Compounds in the Troposphere. *Chem. Soc. Rev.* **2008**, *37*, 699-716.
12. Welz, O.; Saeve, J. D.; Osborn, D. L.; Vasu, S. S.; Percival, C. J.; Shallcross, D. E.; Taatjes, C. A., Direct Kinetic Measurements of Criegee Intermediate (CH₂OO) Formed by Reaction of CH₂I with O₂. *Science* **2012**, *335*, 204-207.
13. Buras, Z. J.; Elsamra, R. M. I.; Jalan, A.; Middaugh, J. E.; Green, W. H., Direct Kinetic Measurements of Reactions between the Simplest Criegee Intermediate CH₂OO and Alkenes. *J. Phys. Chem. A* **2014**, *118*, 1997-2006.
14. Lewis, T. R.; Blitz, M. A.; Heard, D. E.; Seakins, P. W., Direct Evidence for a Substantive Reaction between the Criegee Intermediate, CH₂OO, and the Water Vapour Dimer. *Phys. Chem. Chem. Phys.* **2015**, *17*, 4859-4863.
15. Chao, W.; Hsieh, J.-T.; Chang, C.-H.; Lin, J. J.-M., Direct Kinetic Measurement of the Reaction of the Simplest Criegee Intermediate with Water Vapor. *Science* **2015**, *347*, 751-754.
16. Chhantyal-Pun, R.; Davey, A.; Shallcross, D. E.; Percival, C. J.; Orr-Ewing, A. J., A kinetic study of the CH₂OO Criegee intermediate self-reaction, reaction with SO₂ and unimolecular reaction using cavity ring-down spectroscopy. *Phys. Chem. Chem. Phys.* **2015**, *17*, 3617-3626.
17. Barber, V. P.; Pandit, S.; Green, A. M.; Trongsrirawat, N.; Walsh, P. J.; Klippenstein, S. R.; Lester, M. I., Four carbon Criegee intermediate from isoprene ozonolysis: Methyl vinyl ketone oxide synthesis, infrared spectrum, and OH production. *J. Am. Chem. Soc.* **2018**, *140*, 10866-10880.
18. Vansco, M. F.; Marchetti, B.; Lester, M. I., Electronic spectroscopy of methyl vinyl ketone oxide: A four-carbon unsaturated Criegee intermediate from isoprene ozonolysis. *J. Chem. Phys.* **2018**, *149*, 244309.
19. Mauldin III, R. L.; Berndt, T.; Sipilä, M.; Paasonen, P.; Petäjä, T.; Kim, S.; Kurtén, T.; Stratmann, F.; Kerminen, V. M.; Kulmala, M., A New Atmospherically Relevant Oxidant of Sulphur Dioxide. *Nature* **2012**, *488*, 193-196.
20. Huang, H.-L.; Chao, W.; Lin, J. J.-M., Kinetics of a Criegee Intermediate that would Survive High Humidity and may Oxidize Atmospheric SO₂. *Proc. Natl. Acad. Sci. U. S. A.* **2015**, *112*, 10857-10862.
21. Mentel, T. F.; Springer, M.; Ehn, M.; Kleist, E.; Pullinen, I.; Kurtén, T.; Rissanen, M.; Wahner, A.; Wildt, J., Formation of Highly Oxidized Multifunctional Compounds: Autoxidation of Peroxy Radicals formed in the Ozonolysis of Alkenes – Deduced from Structure–Product Relationships. *Atmos. Chem. Phys.* **2015**, *15*, 6745-6765.
22. Beames, J. M.; Liu, F.; Lu, L.; Lester, M. I., Ultraviolet Spectrum and Photochemistry of the Simplest Criegee Intermediate CH₂OO. *J. Am. Chem. Soc.* **2012**, *134*, 20045-20048.
23. Beames, J. M.; Liu, F.; Lu, L.; Lester, M. I., UV Spectroscopic Characterization of an Alkyl Substituted Criegee Intermediate CH₃CHOO. *J. Chem. Phys.* **2013**, *138*, 244307.
24. Liu, F.; Beames, J. M.; Green, A. M.; Lester, M. I., UV Spectroscopic Characterization of Dimethyl- and Ethyl-Substituted Carbonyl Oxides. *J. Phys. Chem. A* **2014**, *118*, 2298-2306.
25. Yin, C.; Takahashi, K., How does Substitution Affect the Unimolecular Reaction Rates of Criegee Intermediates? *Phys. Chem. Chem. Phys.* **2017**, *19*, 12075-12084.

26. Yin, C.; Takahashi, K., Effect of unsaturated substituents in the reaction of Criegee intermediates with water vapor. *Phys. Chem. Chem. Phys.* **2018**, *20*, 20217-20227.
27. Kuwata, K. T.; Hermes, M. R.; Carlson, M. J.; Zogg, C. K., Computational Studies of the Isomerization and Hydration Reactions of Acetaldehyde Oxide and Methyl Vinyl Carbonyl Oxide. *J. Phys. Chem. A* **2010**, *114*, 9192-9204.
28. Vereecken, L.; Novelli, A.; Taraborrelli, D., Unimolecular Decay Strongly Limits the Atmospheric Impact of Criegee Intermediates. *Phys. Chem. Chem. Phys.* **2017**, *19*, 31599-31612.
29. Anglada, J. M.; Gonzalez, J.; Torrent-Sucarrat, M., Effects of the Substituents on the Reactivity of Carbonyl Oxides. A Theoretical Study on the Reaction of Substituted Carbonyl Oxides with Water. *Phys. Chem. Chem. Phys.* **2011**, *13*, 13034-13045.
30. Anglada, J. M.; Sole, A., Impact of the Water Dimer on the Atmospheric Reactivity of Carbonyl Oxides. *Phys. Chem. Chem. Phys.* **2016**, *18*, 17698-17712.
31. Aplincourt, P.; Anglada, J. M., Theoretical Studies on Isoprene Ozonolysis under Tropospheric Conditions. 1. Reaction of Substituted Carbonyl Oxides with Water. *J. Phys. Chem. A* **2003**, *107*, 5798-5811.
32. Samanta, K.; Beames, J. M.; Lester, M. I.; Subotnik, J. E., Quantum dynamical investigation of the simplest Criegee intermediate CH₂OO and its O-O photodissociation channels. *J. Chem. Phys.* **2014**, *141*, 134303.
33. Sheps, L., Absolute Ultraviolet Absorption Spectrum of a Criegee Intermediate CH₂OO. *J. Phys. Chem. Lett.* **2013**, *4*, 4201-5.
34. Ting, W.-L.; Chen, Y.-H.; Chao, W.; Smith, M. C.; Lin, J. J.-M., The UV absorption spectrum of the simplest Criegee intermediate CH₂OO. *Phys. Chem. Chem. Phys.* **2014**, *16*, 10438-43.
35. Sheps, L.; Scully, A. M.; Au, K., UV Absorption Probing of the Conformer-Dependent Reactivity of a Criegee Intermediate CH₃CHOO. *Phys. Chem. Chem. Phys.* **2014**, *16*, 26701-26706.
36. Smith, M. C.; Ting, W. L.; Chang, C. H.; Takahashi, K.; Boering, K. A.; Lin, J. J., UV absorption spectrum of the C2 Criegee intermediate CH₃CHOO. *J. Chem. Phys.* **2014**, *141*, 074302.
37. Chang, Y.-P.; Chang, C.-H.; Takahashi, K.; Lin, J. J.-M., Absolute UV Absorption Cross Sections of Dimethyl Substituted Criegee Intermediate (CH₃)₂COO. *Chem. Phys. Lett.* **2016**, *653*, 155-160.
38. Foreman, E. S.; Kapnas, K. M.; Jou, Y.; Kalinowski, J.; Feng, D.; Gerber, B. R.; Murray, C., High resolution absolute absorption cross sections of the B¹A' ← X¹A' transition of the CH₂OO biradical. *Phys. Chem. Chem. Phys.* **2015**, *17*, 32539-32546.
39. Vansco, M. F.; Li, H.; Lester, M. I., Prompt release of O ¹D products upon UV excitation of CH₂OO Criegee intermediates. *J. Chem. Phys.* **2017**, *147*, 013907.
40. Dawes, R.; Jiang, B.; Guo, H., UV absorption spectrum and photodissociation channels of the simplest Criegee intermediate (CH₂OO). *J. Am. Chem. Soc.* **2015**, *137*, 50-3.
41. Meng, Q.; Meyer, H. D., A full-dimensional multilayer multiconfiguration time-dependent Hartree study on the ultraviolet absorption spectrum of formaldehyde oxide. *J. Chem. Phys.* **2014**, *141*, 124309.
42. Ahrens, J.; Carlsson, P. T. M.; Hertl, N.; Olzmann, M.; Pfeifle, M.; Wolf, J. L.; Zeuch, T., Infrared Detection of Criegee Intermediates Formed during the Ozonolysis of β-Pinene and Their Reactivity towards Sulfur Dioxide. *Angew. Chem. Int. Ed.* **2014**, *53*, 715-719.
43. Womack, C. C.; Martin-Drumel, M. A.; Brown, G. G.; Field, R. W.; McCarthy, M. C., Observation of the simplest Criegee intermediate CH₂OO in the gas-phase ozonolysis of ethylene. *Science Advances* **2015**, *1* (e1400105).
44. Giorio, C.; Campbell, S. J.; Bruschi, M.; Tampieri, F.; Barbon, A.; Toffoletti, A.; Tapparo, A.; Paijens, C.; Wedlake, A. J.; Grice, P.; Howe, D. J.; Kalberer, M., Online Quantification of Criegee Intermediates of α-Pinene Ozonolysis by Stabilization with Spin Traps and Proton-Transfer Reaction Mass Spectrometry Detection. *J. Am. Chem. Soc.* **2017**, *139*, 3999-4008.
45. Berndt, T.; Herrmann, H.; Kurtén, T., Direct Probing of Criegee Intermediates from Gas-Phase Ozonolysis Using Chemical Ionization Mass Spectrometry. *J. Am. Chem. Soc.* **2017**, *139*, 13387-13392.
46. Su, M.-N.; Lin, J. J. M., Note: A transient absorption spectrometer using an ultra bright laser-driven light source. *Rev. Sci. Instrum.* **2013**, *84*, 086106.
47. Sheps, L.; Chandler, D. W. *Time-resolved broadband cavity-enhanced absorption spectroscopy for chemical kinetics SAND2013-2664*; Sandia National Laboratories: Livermore, CA, 2013.
48. Armarego, W.; Christina, C., Purification of Laboratory Chemicals. Elsevier: Kidlington, UK, 2012; p 114.
49. Karagoz, E. S.; Kus, M.; Akpınar, G. E.; Artok, L., Regio- and stereoselective synthesis of 2,3,5-trienoates by palladium-catalyzed alkoxy-carbonylation of conjugated enyne carbonates. *J. Org. Chem.* **2014**, *79*, 9222-30.
50. Menche, D.; Fassfeld, J.; Li, J.; Rudolph, S., Total Synthesis of Archazolid A. *J. Am. Chem. Soc.* **2007**, *129*, 6100-6101.
51. Chandrasekhar, B.; Athe, S.; Reddy, P. P.; Ghosh, S., Synthesis of fully functionalized aglycone of lycoperdinoside A and B. *Org. Biomol. Chem.* **2015**, *13*, 115-24.
52. Barbatti, M.; Granucci, G.; Persico, M.; Ruckebauer, M.; Vazdar, M.; Eckert-Maksić, M.; Lischka, H., The on-the-fly surface-hopping program system Newton-X: Application to ab initio simulation of the nonadiabatic photodynamics of benchmark systems. *J. Photochem. Photobiol. A* **2007**, *190*, 228-240.
53. Barbatti, M.; Aquino, A. J. A.; Lischka, H., The UV absorption of nucleobases: semi-classical ab initio spectra simulations. *Phys. Chem. Chem. Phys.* **2010**, *12*, 4959-4967.
54. Barbatti, M.; Ruckebauer, M.; Plasser, F.; Pittner, J.; Granucci, G.; Persico, M.; Lischka, H., Newton-X: a surface-hopping program for nonadiabatic molecular dynamics. *Wiley Interdiscip. Rev. Comput. Mol. Sci.* **2014**, *4*, 26-33.
55. Karsili, T. N. V.; Marchetti, B.; Ashfold, M. N. R., Mechanistic insights into excited state intramolecular proton transfer in isolated and metal chelated supramolecular chemosensors. *Dalton Trans.* **2016**, *45*, 18921-18930.
56. Karsili, T. N. V.; Thodika, M.; Nguyen, L.; Matsika, S., The origin of fluorescence in DNA thioanalogues. *Chem. Phys.* **2018**, *515*, 434-440.

57. Lehman, J. H.; Li, H.; Beames, J. M.; Lester, M. I., Communication: Ultraviolet photodissociation dynamics of the simplest Criegee intermediate CH₂OO. *J. Chem. Phys.* **2013**, *139*, 141103.
58. Li, H.; Fang, Y.; Beames, J. M.; Lester, M. I., Velocity Map Imaging of O-atom Products from UV Photodissociation of the CH₂OO Criegee Intermediate. *J. Chem. Phys.* **2015**, *142*, 214312.
59. Li, H.; Fang, Y.; Kidwell, N. M.; Beames, J. M.; Lester, M. I., UV Photodissociation Dynamics of the CH₃CHOO Criegee Intermediate: Action Spectroscopy and Velocity Map Imaging of O-Atom Products. *J. Phys. Chem. A* **2015**, *119*, 8328-8337.
60. Mordaunt, D. H.; Osborn, D. L.; Neumark, D. M., Nonstatistical unimolecular dissociation over a barrier. *J. Chem. Phys.* **1998**, *108*, 2448-2457.
61. Hunziker, H. E.; Wendt, H. R., Electronic absorption spectra of organic peroxy radicals in the near infrared. *J. Chem. Phys.* **1976**, *64*, 3488.
62. Blanksby, S. J.; Ramond, T. M.; Davico, G. E.; Nimlos, M. R.; Kato, S.; Bierbaum, V. M.; Lineberger, C. W.; Ellison, B. G.; Okumura, M., Negative-Ion Photoelectron Spectroscopy, Gas-Phase Acidity, and Thermochemistry of the Peroxyl Radicals CH₃CHOO and CH₃CH₂OO. *J. Am. Chem. Soc.* **2001**, *123*, 9585-9596.
63. Fu, H. B.; Hu, Y. J.; Bernstein, E. R., Generation and detection of alkyl peroxy radicals in a supersonic jet expansion. *J. Chem. Phys.* **2006**, *125*, 014310.
64. Chung, C.-Y.; Cheng, C.-W.; Lee, Y.-P.; Liao, H.-Y.; Sharp, E. N.; Rupper, P.; Miller, T. A., Rovibronic bands of the A-X transition of CH₃OO and CD₃OO detected with cavity ringdown absorption near 1.2-1.4 μm. *J. Chem. Phys.* **2007**, *127*, 044311.
65. Copan, A. V.; Schaefer, H. F.; Agarwal, J., Examining the ground and first excited states of methyl peroxy radical with high-level coupled-cluster theory. *Mol. Phys.* **2015**, *113*, 2992-2998.
66. Zhang, D.; Lei, W.; Zhang, R., Mechanism of OH Formation From Ozonolysis of Isoprene: Kinetics and Product Yields. *Chem. Phys. Lett.* **2002**, *358*, 171-179.
67. Zhang, D.; Zhang, R., Mechanism of OH Formation from Ozonolysis of Isoprene: A Quantum-Chemical Study. *J. Am. Chem. Soc.* **2002**, *124*, 2692-2703.
68. Hansen, R. F.; Lewis, T. R.; Graham, L.; Whalley, L. K.; Seakins, P. W.; Heard, D. E.; Blitz, M. A., OH production from the photolysis of isoprene-derived peroxy radicals: cross-sections, quantum yields and atmospheric implications. *Phys. Chem. Chem. Phys.* **2017**, *19*, 2332.
69. Holmes, J. L.; Terlouw, J. K.; Vijfhuizen, P. C.; A'Campo, C., Metastable ion studies. XII-Molecular and fragment ion structures for isomeric C₄H₆O₂ acids. *Org. Mass Spectrom.* **1979**, *14*, 204-212.
70. Burkhardt, I.; Lauterbach, L.; Brock, N. L.; Dickschat, J. S. Chemical differentiation of three DMSP lyases from the marine *Reseobacter* group. *Org. Biomol. Chem.* **2017**, *15*, 4432-4439.

CHAPTER 5

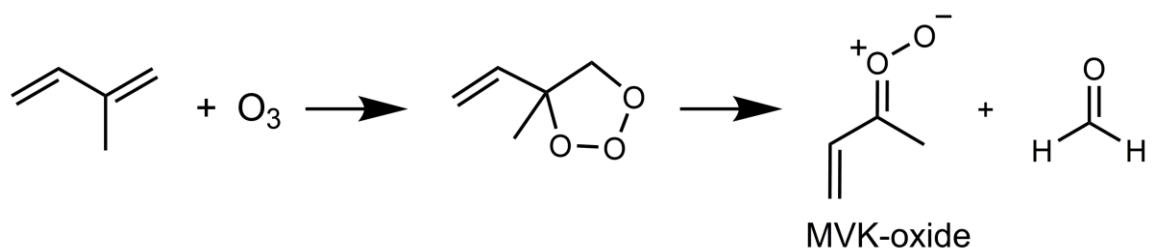
FIRST DIRECT KINETIC MEASUREMENTS AND THEORETICAL PREDICTIONS OF AN ISOPRENE-DERIVED CRIEGEE INTERMEDIATE

This research has been previously published in the *Proceedings of the National Academy of Sciences*, **117**, 9733 (2020) and reproduced with the permission of PNAS. The experimental research was performed with researchers Rebecca Caravan (*NASA Postdoctoral Program Fellow, NASA Jet Propulsion Laboratory, Combustion Research Facility, Sandia National Laboratories, Chemical Sciences and Engineering Division, Argonne National Laboratory*), Kendrew Au (*Combustion Research Facility, Sandia National Laboratories*), Yu-Lin Li (*Institute for Atomic and Molecular Sciences*), Frank Winiberg (*NASA Jet Propulsion Laboratory, California Institute of Technology*), Kristen Zuraski (*NASA Postdoctoral Program Fellow, NASA Jet Propulsion Laboratory*), Yen-Hsiu Lin (*Institute for Atomic and Molecular Sciences*), Wen Chao (*Institute for Atomic and Molecular Sciences*), David Osborn (*Combustion Research Facility, Sandia National Laboratories*), Carl Percival (*NASA Jet Propulsion Laboratory, California Institute of Technology*), Jim Jr-Min Lin (*Institute for Atomic and Molecular Sciences*), Leonid Sheps (*Combustion Research Facility, Sandia National Laboratories*), Craig Taatjes (*Combustion Research Facility, Sandia National Laboratories*), and Marsha Lester (*Department of Chemistry, University of Pennsylvania*). Synthetic work was performed by graduate student Nisalak Trongsiwat and Patrick J. Walsh (*Department of Chemistry, University of Pennsylvania*). Theoretical research was performed in collaboration with Stephen J. Klippenstein (*Chemical Sciences and Engineering Division, Argonne National Laboratory*). Atmospheric modeling was performed in collaboration with Anwar Khan and Dudley Shallcross (*School of Chemistry, University of Bristol*).

Introduction/background

Isoprene is a five carbon, doubly unsaturated hydrocarbon with the highest emission into Earth's atmosphere of any non-methane hydrocarbon. Its sources are predominantly biogenic, totaling 530 Tg per year ¹, with abundances peaking between the tropics over the landmass where most of the Earth's biomass is located (e.g., the Amazon). An important sink of tropospheric isoprene (~10% ²) is reaction with ozone, proceeding via 1,3-cycloaddition of ozone to either of the two C=C double bonds to give a primary ozonide (POZ). The POZ subsequently decomposes to form a carbonyl species and a carbonyl oxide – a zwitterionic reactive intermediate, known as a Criegee intermediate (CI) ³. Depending on the double bond to which ozone adds, and how the POZ decomposes, four pairs of reaction products are possible: formaldehyde oxide (CH₂OO) + methyl vinyl ketone, formaldehyde oxide + methacrolein, methacrolein oxide (HC(OO)C(CH₂)CH₃) + formaldehyde, or methyl vinyl ketone oxide (MVK-oxide, CH₃C(OO)CHCH₂) + formaldehyde (Scheme 1). The resulting chemically activated Criegee intermediate can undergo either rapid unimolecular decomposition or can be thermalized through collisions to form so-called stabilized Criegee intermediates, that can subsequently undergo unimolecular and bimolecular reactions. Here, we report the first direct measurements of unimolecular and bimolecular reactions of stabilized MVK-oxide at 298 K.

Global and local CI concentrations have previously been estimated via chemistry and transport models, using databases of alkene emissions ⁴. Concentration maxima are predicted in forested regions such as the Amazon, correlating with high isoprene emissions. With steady state CI concentrations $\leq 10^4 \text{ cm}^{-3}$ ⁴⁻⁸, two orders of magnitude lower than that of the principal tropospheric oxidant OH, reactivity of CIs with key



Scheme 1. Reaction scheme illustrating the generation of MVK-oxide + formaldehyde from the ozonolysis of isoprene.

pollutants needs to be substantial to impact tropospheric lifetimes in comparison to OH-initiated processing. Low steady-state concentrations of CIs, resulting from slow production via ozonolysis and rapid subsequent decomposition, had until recently inhibited study of CI reactivity. Direct methods to photolytically generate simple CIs with carbon backbones containing up to three carbons⁹⁻¹² have enabled studies that revealed CI reactivity to be far greater than previously thought. Consequently the flux of pollutant species, such as SO₂, through reaction with Criegee intermediates could be significant.

The reaction of CH₂OO with the critical tropospheric pollutant SO₂ was shown to be 10,000 times faster than inferred from ozonolysis studies¹¹ and leads to the formation of SO₃ – a critical sulfuric acid precursor in the troposphere that results in sulfate aerosol production¹³⁻¹⁶. Subsequent chemistry and transport modelling suggests that tropospheric processing of SO₂ to SO₃ by CIs is comparable to SO₂ removal by OH in areas where CI concentrations are largest⁴. CI + SO₂ reactions can account for as much as 46% of sulfuric acid production at ground level¹⁵ – increasing modelled particle nucleation rates by up to 820%¹⁷ and thus, impacting air quality, climate and human health.

Reactions of CIs with organic acids have also been implicated in the formation of aerosols^{18, 19}. Fast removal of CIs by reaction with a number of organic acids has been measured¹⁸⁻²⁰. Global chemistry and transport modelling reveals that these reactions could significantly reduce modelled organic acid concentrations¹⁸, with the greatest impacts over the Amazon area where CI concentrations are the highest¹⁸. Through a combination of experimental and theoretical work for reactions of simple 1-3 carbon CIs, a mechanism has been identified whereby the CI inserts into the acidic O-H bond¹⁸⁻²⁰, leading to highly oxygenated, lower volatility, functionalized organic hydroperoxides.

Due to the relatively high abundance of water in the troposphere, CI removal by reactions with water monomer and dimer can dominate over other reactive loss processes even for modest rate coefficients, constraining CI availability for other bimolecular reactions. However, through experimental work and theoretical studies, the rate coefficients for reaction of CIs with both water monomer and dimer have been shown to vary by orders of magnitude, depending on substituents and conformer of the CI. For example, a combination of experimental and theoretical studies of the two-carbon CI, acetaldehyde oxide, has shown that reactivity of the *syn*- and *anti*-conformers with water could differ by as much as five orders of magnitude^{4, 10, 21-28}. Therefore, the potential tropospheric impact of CIs is highly dependent on their structures.

MVK-oxide, a resonance-stabilized, four-carbon CI, is estimated to be produced from 21-23% of isoprene ozonolysis reactions under tropospheric conditions^{2, 29}. At present, local and global chemical models of the atmosphere represent the reactivity of four-carbon and higher, functionalized CIs based on direct measurements of the smaller H- or alkyl-substituted CIs. In MVK-oxide, the Criegee intermediate COO functional group is resonance stabilized with the vinyl side chain, potentially influencing reactivity, and thus, its role as a tropospheric oxidant. No direct measurements²² have been performed on the reactions of resonance stabilized CIs.

Like acetaldehyde oxide, MVK-oxide exists as distinct *syn*- and *anti*-conformers that do not interconvert at 298 K; *syn* and *anti* refer to the orientation of the terminal CI oxygen with respect to the methyl group of the carbon backbone. Each MVK-oxide conformer comprises two further configurations for the orientation of the vinyl group, *cis* and *trans*, that rapidly interconvert by rotation about the C-C bond at ~ 298 K (⁶, see SI). Until recently, no synthetic methods for the isolated production of MVK-oxide were known – preventing the direct study of the reactivity of either conformer. Barber *et al.*³⁰

recently reported a scheme for the selective production of MVK-oxide and employed this method to record an IR-action spectrum. The same scheme was used by Vansco *et al.*³¹ to obtain a UV-Vis depletion spectrum, which displayed broad absorption features from 300-450 nm, consistent with both *syn*- and *anti*-conformers. Both studies generated MVK-oxide via 248 nm photolysis of 1,3 diiodobut-2-ene in O₂/Ar carrier gas that was sampled following supersonic expansion (T~ 10 K) under collision free conditions. Vansco *et al.*³¹ recorded the UV-Vis induced depletion of the MVK-oxide photoionization signal (at 10.5 eV) on the m/z 86 (parent ion of MVK-oxide) mass channel. Additional studies indicated that MVK-oxide rapidly dissociates upon UV-Vis excitation to O(¹D) products, providing evidence that the depletion measurements can be directly related to absorption.

For MVK-oxide, theory predicts relatively slow loss of both *syn*- and *anti*-conformers by reactions with water monomer and dimers – leading to first order loss rates of $\leq 1 \text{ s}^{-1}$ in the troposphere^{6, 32}. However, rapid unimolecular decay represents a potentially significant competitive loss process: thermal unimolecular loss rates at 298 K of 33 s^{-1} and 2140 s^{-1} for *syn*- and *anti*-MVK-oxide conformers, respectively, have been calculated³⁰. Experimental observations to substantiate these unimolecular and water reaction loss rates, and to determine bimolecular reaction rate coefficients with key pollutant species, are therefore needed to evaluate the role of MVK-oxide in the troposphere.

The present study builds on the work of Vansco *et al.*³¹ and reports direct absorption spectra of MVK-oxide at 298 K, obtained using two separate experiments³³⁻³⁵. Using the characterized direct UV-Vis absorption spectra, we have employed broadband absorption spectroscopy to conduct direct bimolecular kinetics studies of MVK-oxide with key tropospheric species: SO₂, formic acid and water. Complementary

experiments using multiplexed photoionization mass spectrometry (MPIMS) and *ab initio* kinetic studies have been conducted to identify products resulting from reaction with SO₂ and formic acid and infer mechanisms. The implications of MVK-oxide reactivity on global sulfate aerosol formation and formic acid removal have been evaluated by a global 3-dimensional chemistry and transport model, STOCHEM-CRI.

Results/discussion

Spectroscopy and unimolecular decay

MVK-oxide spectroscopy

The MVK-oxide electronic spectra recorded by direct absorption at 298 K using both the Sandia³⁴ and IAMS³⁵ experimental apparatus span the same spectral range (300-450 nm) as that reported recently by Vansco *et al.*³¹ using a depletion method under jet-cooled conditions (Figure 1). The 298 K spectrum has a broad symmetric absorption from 300-450 nm, peaking at 370 nm with FWHM of 80 nm. The electronic spectrum obtained by Vansco *et al.*³¹ has a similarly broad, but asymmetric profile peaked at 388 nm. We anticipate that the MVK-oxide conformer distribution may differ significantly at 298 K and under jet-cooled experimental conditions. We propose that this difference originates from the fast unimolecular decay of *anti*-conformers compared to *syn*-conformers at 298 K, discussed herein, and the rapid interconversion of *cis* and *trans* configurations. The unimolecular decay mechanisms, transition state (TS) barriers, and thermal unimolecular decay rate coefficients for the *syn*- and *anti*-conformers of MVK-oxide differ considerably from one another. For *syn*-MVK-oxide conformers, unimolecular decay follows a 1,4 H-atom transfer mechanism that eventually releases OH radicals

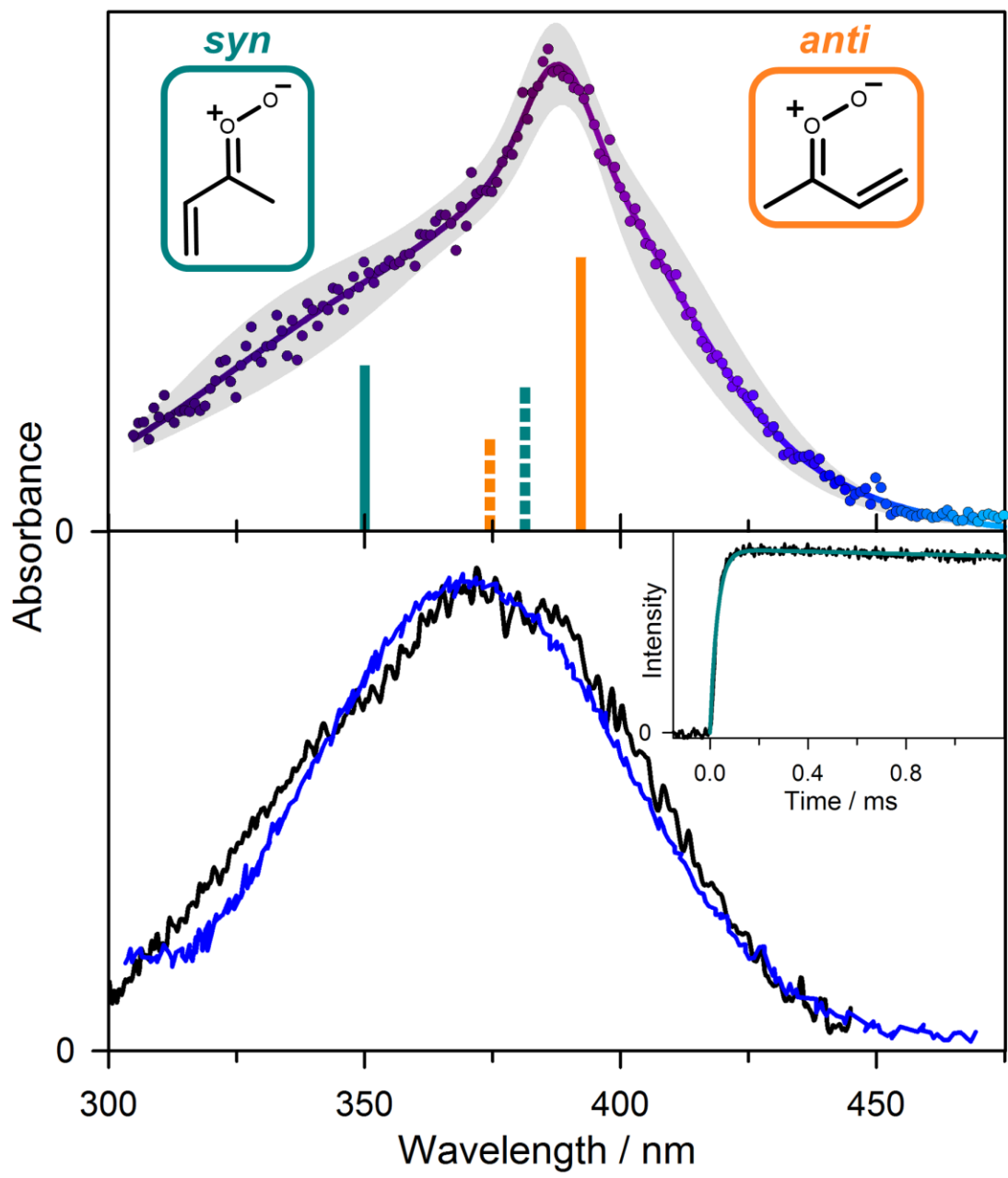
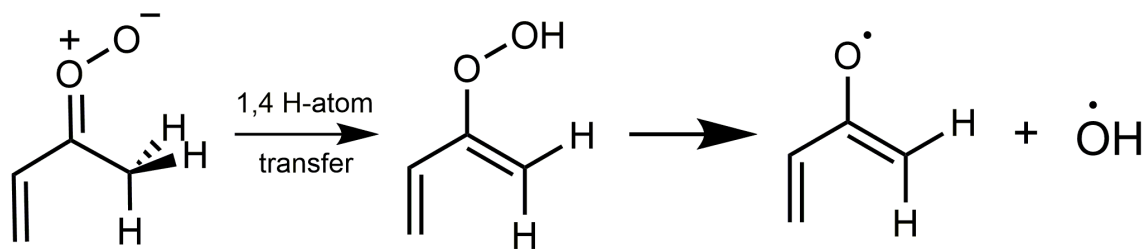


Figure 1. (Upper panel) Electronic spectrum of MVK-oxide recorded under jet-cooled conditions by the UV-Vis induced depletion method from Vansco *et al.* ³¹. Data are reproduced from Vansco MF, Marchetti B, & Lester MI (2018) Electronic spectroscopy of methyl vinyl ketone oxide: a four-carbon unsaturated Criegee intermediate from isoprene ozonolysis. *The Journal of Chemical Physics* 149(24):244309, with the permission of AIP Publishing. (Lower panel, main) Direct absorption spectra obtained for MVK-oxide at 298 K using the Sandia broadband multi-pass transient absorption spectrometer (black) and IAMS absorption instrument (blue). Vertical excitation energies and associated oscillator strengths (bars, upper panel) computed for the first $\pi^* \leftarrow \pi$ transition of MVK-oxide are shown for *syn*- (cyan) and *anti*- (orange) conformers; solid and dashed lines further distinguish between *trans* and *cis* configurations, respectively, which rapidly interconvert at 298 K. (Lower panel, inset) Kinetic time trace for MVK-oxide from the Sandia experiment (under 298 K, 10 Torr He; black) integrated between 330-367 nm compared with the simulated thermal unimolecular decay for *syn*-conformers to 2-hydroperoxybuta-1,3-diene (cyan) with $k(T) = 33 \text{ s}^{-1}$. Thermal rates are computed using *ab initio* master equation modeling in the high-pressure limit ³⁰. The simulations include an experimental rise time for MVK-oxide appearance of 30 μs from the reaction of the iodoalkenyl radical with O_2 (see SI).

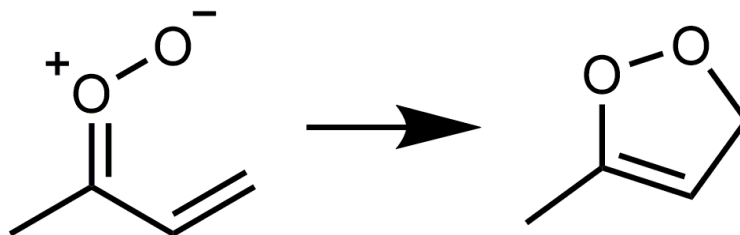
(Scheme 2). Thus, bimolecular reactions that compete with unimolecular decay in the troposphere will intercept OH production, and may impact the oxidizing capacity of the troposphere.

The thermal decay rate for *syn*-MVK-oxide was experimentally benchmarked by the rate of appearance of OH products upon IR-activation of *syn*-MVK-oxide, which agreed with an RRKM calculation based on an *ab initio* predicted TS barrier of 18.0 kcal mol⁻¹ ³⁰. Master equation calculations predicted a thermal unimolecular decay rate for *syn*-MVK-oxide of 33 s⁻¹ (298 K, 1 atm, with ~10% reduction at 10 torr), which includes substantial contribution from H-atom tunneling. By contrast, theory predicts that *anti*-MVK-oxide conformers decay via a 1,5 electrocyclic ring closure process that forms a cyclic peroxide (Scheme 3), known as dioxole ^{6, 30, 36}, with a TS barrier of only 12.0 kcal mol⁻¹ and thermal decay rate of 2140 s⁻¹ (298 K, 1 atm) ³⁰.

The transient absorption time trace for MVK-oxide obtained at 298 K in the Sandia experiment reveals a slow decay on the millisecond timescale as shown in Figure 1 (lower panel, inset, and reproduced larger in the SI). The experimental time profile agrees with a simulation using the predicted rate coefficient for *syn*-MVK-oxide of 33 s⁻¹ (298 K), shown as a cyan line in the inset of Figure 1 ^{30, 36}. Based on the theoretically predicted thermal decay rate coefficient for *anti*-MVK-oxide of 2140 s⁻¹ (298 K) ³⁰, the time-resolved experiments should also exhibit a fast decay component, which is not observed. This suggests a faster decay rate possibly due to initial internal excitation of *anti*-MVK-oxide and/or low yield of the stabilized *anti*-conformer in the present 298 K experiments. This differs from prior studies under jet-cooled conditions with short delay-times (20 μs) between generation and probing, where spectroscopic features attributed to both *syn*- and *anti*-conformers of MVK-oxide were observed ^{30, 31}.



Scheme 2. Reaction mechanism for production of OH from *syn*-MVK oxide via 1,4 H-atom transfer to 2-hydroperoxybuta-1,3-diene.



Scheme 3. Unimolecular isomerization of *anti*-MVK-oxide to the cyclic peroxide, dioxole, via 1,5 electrocyclic ring closure.

Comparison of the direct absorption and depletion measurements of the MVK-oxide electronic spectrum indicates that they match in the shorter wavelength region, suggesting that *syn*-conformers likely dominate at $\lambda < 375$ nm in both experiments. At $\lambda > 375$ nm, a combination of *syn*- and *anti*-conformers appear to contribute to the jet cooled spectrum, while predominantly *syn*-conformers give rise to the spectrum at 298 K. Theoretical calculations predict vertical transitions for the more stable *syn-trans*-conformer at shorter wavelengths (350 nm) and *anti-trans*-conformer at longer wavelengths (381 nm), although the computed electronic spectra³¹ suggest they will be broad and overlapping. Rapid removal of *anti*-conformers at 298 K is consistent with the observed spectral changes, and suggests that bimolecular reactions with the *anti*-conformer are unlikely to compete with unimolecular decay in the troposphere.

SO₂ Scavenging Experiments

Previous measurements of simple CIs have demonstrated rapid reaction with SO_2 ^{10, 11, 37, 38}. To substantiate the assignment of the broad spectral feature to MVK-oxide, SO_2 was added to act as a scavenger for MVK-oxide in the IAMS experiments. Sufficient SO_2 was added to reduce the lifetime of MVK-oxide to < 0.03 ms, assuming that the rate coefficient for MVK-oxide + SO_2 was comparable to that for $\text{CH}_2\text{OO} + \text{SO}_2$ ^{11, 38}. Time-resolved spectra in the absence of SO_2 (Figure 2, upper panel), show the broad absorption feature assigned to MVK-oxide at 370 nm and its decay due to various experimental loss processes (i.e., wall loss and reactions with I atoms). The transient absorption spectra also show depletion signals at $\lambda < 320$ nm due to the precursor, structured features due to IO ($\lambda \sim 410\text{-}450$ nm)³⁹ and a broad feature from I_2 side-product ($\lambda \sim 450\text{-}600$ nm)⁴⁰. Note that even in the absence of SO_2 , the decay in the IAMS experiment is more rapid than that observed in the Sandia absorption experiment

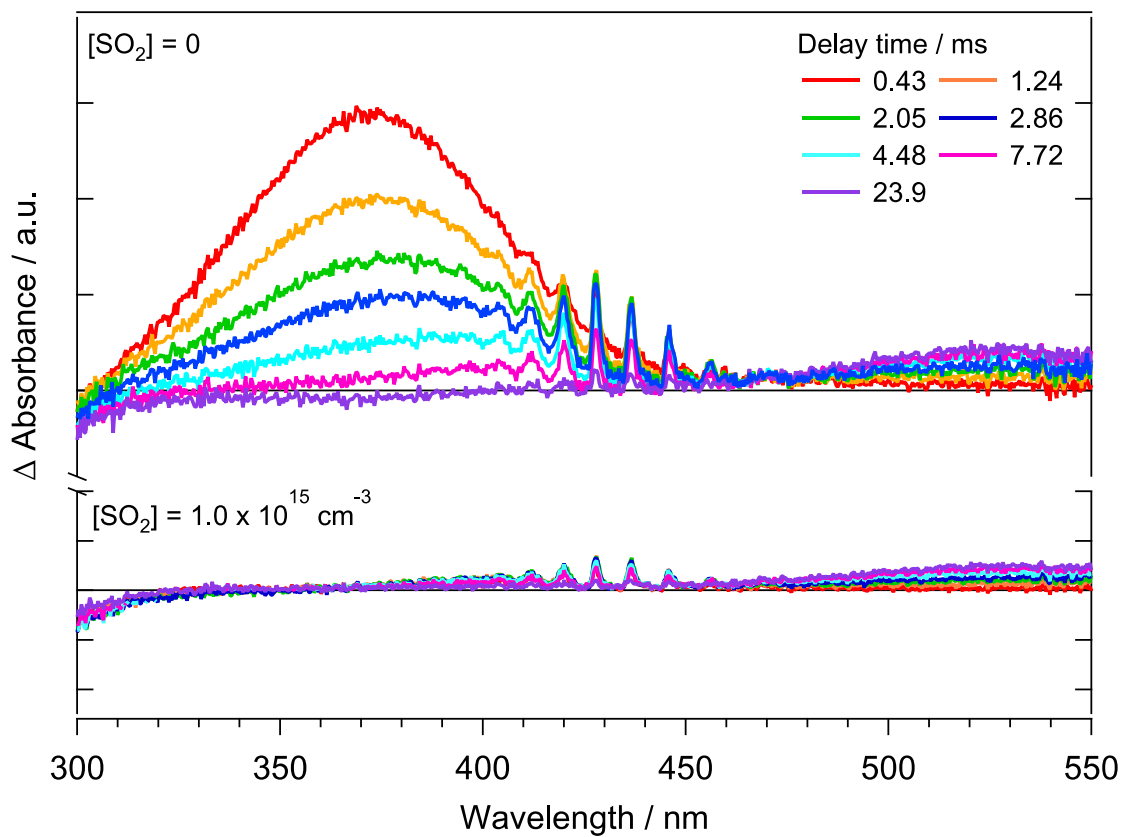


Figure 2. Time-resolved difference absorption spectra recorded at 298 K and 7.4 Torr in the IAMS experiment resulting from (upper panel) the photolysis of 1,3-diiodobut-2-ene in the presence of O₂ and (lower panel) subsequent addition of [SO₂] = 1.0 × 10¹⁵ cm⁻³. In addition to MVK-oxide, the transient spectra contain the spectral signatures of side-products including IO and I₂ (see main text).

(Figure 1, lower panel, inset and SI). In the latter, the experimental conditions were optimized to minimize bimolecular loss channels in order to observe unimolecular decay. In the presence of SO₂ (Figure 2, lower panel), the broad spectral feature centered at λ ~370 nm is absent – providing further evidence that this feature is due to MVK-oxide. Furthermore, the complete removal of this feature in <0.5 ms indicates that the bimolecular rate coefficient for MVK-oxide + SO₂ is rapid, as detailed below. By subtraction of the spectra in Figure 2 (lower panel from those in the upper panel), the features due to MVK-oxide are obtained, as shown in Figure 1. Note, this subtraction process does not perfectly remove spectral components due to IO, and so residual signal due to IO absorption at longer wavelengths has been manually removed to obtain the IAMS data presented in Figure 1. **Bimolecular Kinetics**

Using the direct UV-Vis absorption spectrum of *syn*-MVK-oxide, bimolecular kinetics with SO₂ and formic acid were investigated via broadband absorption spectroscopy. These experiments reveal that *syn*-MVK-oxide reactivity towards these species is similar to that of the smaller, H/alkyl-substituted CIs. Preliminary experiments also provide an upper limit for the very slow reaction of *syn*-MVK-oxide with water. The experimental observations are supported by high-level *ab initio* calculations that reveal much slower removal with water than for smaller CIs. Complementary investigations using MPIMS were undertaken to probe the products of the *syn*-MVK-oxide + SO₂ and formic acid reactions and further mechanistic insight is provided through high level *ab initio* kinetics calculations. Additional MPIMS experiments were performed to obtain the formation kinetics of MVK-oxide from the reaction of the iodoalkenyl radical with O₂, the results of which are discussed in the supporting information (SI).

MVK-oxide + SO₂

Rapid removal of *syn*-MVK-oxide in the presence of SO₂ was observed from both the Sandia (10 Torr He/O₂) and IAMS (7 Torr N₂/O₂) experiments (Figure 3). The pressure-dependence of the *syn*-MVK-oxide + SO₂ rate coefficient across the total pressure range 4-700 Torr N₂ was investigated using the IAMS direct absorption experiment and no significant dependence on pressure was observed. A rate coefficient of $(4.2 \pm 0.6) \times 10^{-11} \text{ cm}^3\text{s}^{-1}$ (95% confidence limit error bar) at 298 K across the total pressure range 300-700 Torr N₂ is derived. This rate coefficient is supported by high-level computational kinetics calculations, is comparable with that reported for smaller CIs 4, 10, 11, 27, 33, 37, 38, 41, 42, and is consistent with barrierless addition of MVK-oxide to SO₂, initially forming a secondary ozonide (SOZ) structure (Figure 4 and Scheme 4). *Ab initio* calculations along the reaction coordinate reveal that the transition state (TS) barrier(s) are comparatively higher for MVK-oxide + SO₂ vs. CH₂OO + SO₂ due to disruption of the extended conjugation of MVK-oxide. However, because the CH₂OO and MVK-oxide (Figure 4) reactions proceed through strongly submerged barriers relative to the reactants, this results in minimal perturbation of the overall bimolecular rate coefficients.

Interrogation of the reaction products was undertaken through complementary MPIMS experiments at 10 Torr: SO₃ production was observed, with rise times consistent with CI loss kinetics, confirming SO₃ as a direct reaction product from *syn*-MVK-oxide + SO₂ (Figure 3). Through rapid reaction of SO₃ with water in the troposphere, this reaction could represent a significant source of atmospheric sulfuric acid. Under the low-pressure conditions of these experiments, there was no substantive evidence for stabilized SOZ. To explore the pressure-dependent branching between SOZ stabilization and SO₃ + MVK formation, we implemented an *ab initio* transition state theory-based master equation (AITSTME) model for the overall kinetic process. At 10

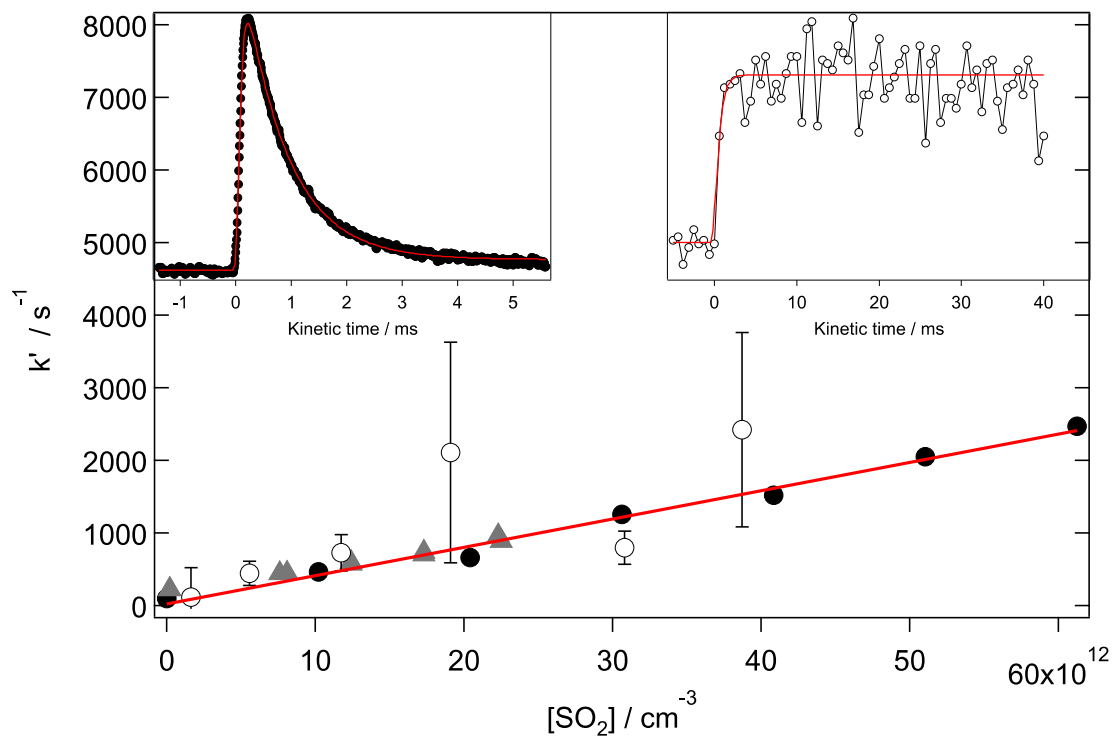


Figure 3. First order rate coefficients for the reaction of *syn*-MVK-oxide with SO₂ as a function of [SO₂], obtained from the decay of *syn*-MVK-oxide using the Sandia absorption experiment (black closed circles, 10 Torr total pressure with He bath gas, 95% confidence limit error bars), the IAMS absorption experiment (grey closed triangles, 4.1 Torr total pressure with O₂ bath gas, 340 nm probe wavelength, 95% confidence limit error bars) and SO₃ growth from the Sandia MPIMS experiment (open black circles, 10 Torr total pressure with He bath gas, 1σ error bars). Note that error bars for the black closed circles and grey closed triangles are smaller than the symbols. The red line is a linear fit to the Sandia absorption data, weighted by the 95% confidence limit error bars, obtaining a bimolecular rate coefficient of $(3.9 \pm 0.5) \times 10^{-11} \text{ cm}^3 \text{ s}^{-1}$. Inset are typical time-resolved traces from the reaction of *syn*-MVK-oxide with SO₂: *syn*-MVK-oxide (Sandia absorption, 330-367 nm, top left) and SO₃ (Sandia MPIMS, 13 eV ionization energy, top right).

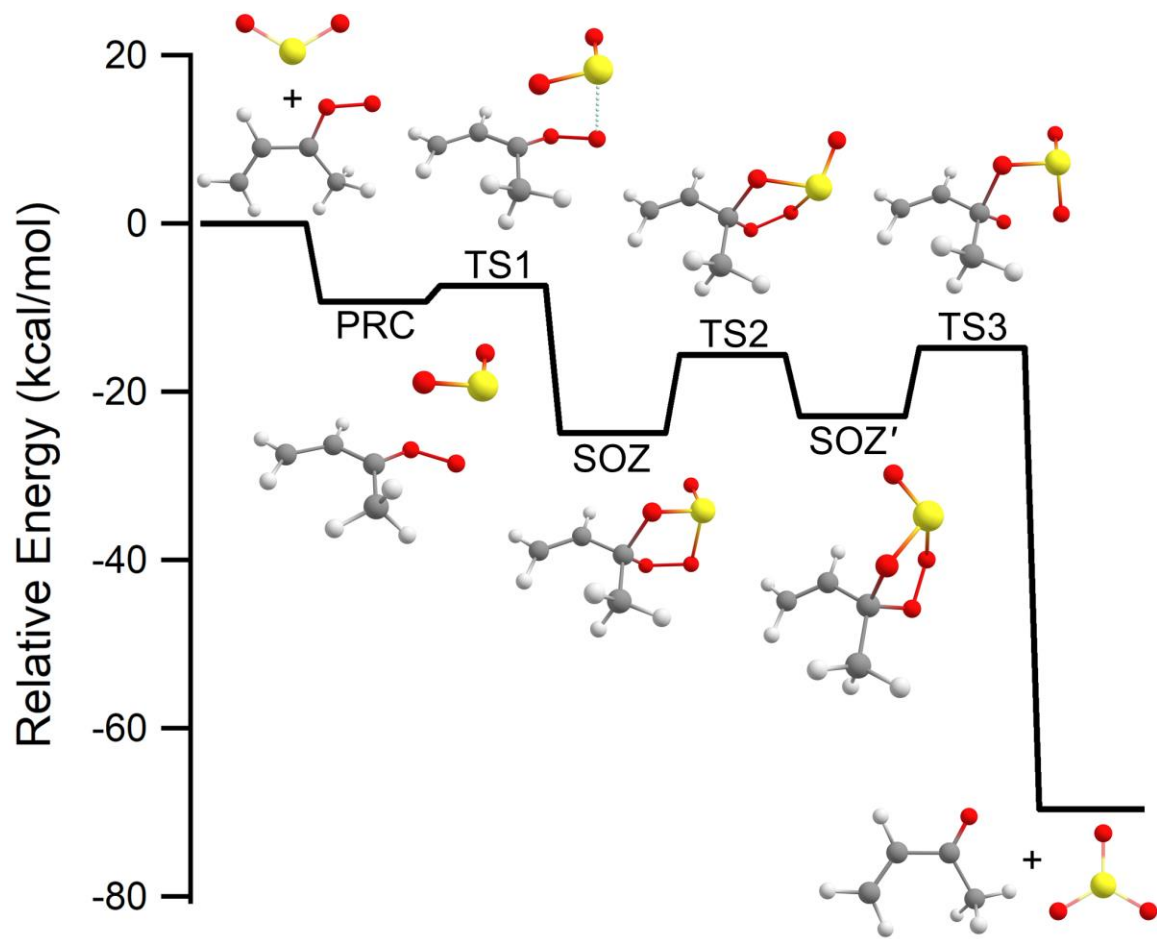
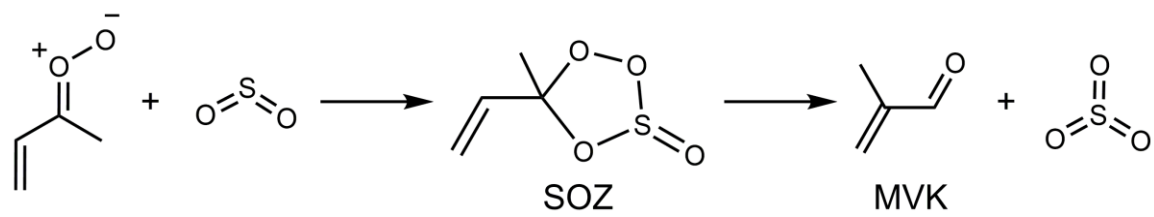


Figure 4. Computed reaction coordinate of the *syn-trans;endo* path for the reaction *syn*-MVK-oxide with SO₂ at the CCSD(T)/CBS//B2PLYP-D3/cc-pVTZ level with estimated T(A) corrections (see SI). The reaction proceeds through a pre-reactive complex (PRC) that forms secondary ozonides (SOZ and SOZ') via submerged barriers (TS1 and TS2). The SOZ subsequently decomposes in an exothermic reaction via TS3 to MVK + SO₃ products.



Scheme 4. Mechanism for the reaction of *syn*-MVK-oxide with SO_2 , leading to the formation of methyl vinyl ketone + SO_3 via a secondary ozonide (SOZ).

Torr, the AITSTME model demonstrates minimal stabilization of the SOZ (see SI), supporting the experimental observations. Under tropospheric conditions, the higher density of states in the SOZ formed from larger CI reactions with SO₂ is predicted to result in increased SOZ lifetime³², and third body collisions are expected to form stabilized SOZ. At 300 K and 1 atm, *ab initio* kinetics calculations predict a ~5 % yield of SOZ. However, the tropospheric fate of the SOZ remains uncertain with respect to decomposition or further reaction. The total rate coefficient is predicted to be effectively pressure-independent, with no back reaction from the SOZ to the reactants. However, there is predicted to be a fairly strong temperature-dependence due to the effect of TS1 connecting the pre-reactive complexes and SOZ (see SI).

MVK-oxide + formic acid

The kinetics of *syn*-MVK-oxide + formic acid were measured using the Sandia absorption experiment, yielding a rate coefficient of $(3.0 \pm 0.1) \times 10^{-10} \text{ cm}^3 \text{ s}^{-1}$ (Figure 5). Reaction near the gas kinetic limit is consistent with the rapid reaction of smaller CIs with organic acids reported previously^{18,19}. High level *ab initio* calculations confirm the barrierless insertion of the CI into the O-H bond of formic acid (Figure 6 and Scheme 5), leading to a functionalized hydroperoxide, hydroperoxybut-3-en-2-yl formate (HPBF). However the resonance-stabilization in MVK-oxide significantly alters the potential energy surface of this reaction, compared to the CH₂OO case⁴³. For the CH₂OO reaction, Vereecken *et al.*⁶ found that the primary reaction pathway involves H-transfer from the acid to the CI in concert with CO bond formation, followed by stabilization of the resulting functionalized hydroperoxide species. The functionalized hydroperoxide is much more weakly bound in the MVK-oxide reaction than in its CH₂OO analogue (30 versus 44 kcal mol⁻¹⁴³), due to the additional resonance stabilization present in MVK-

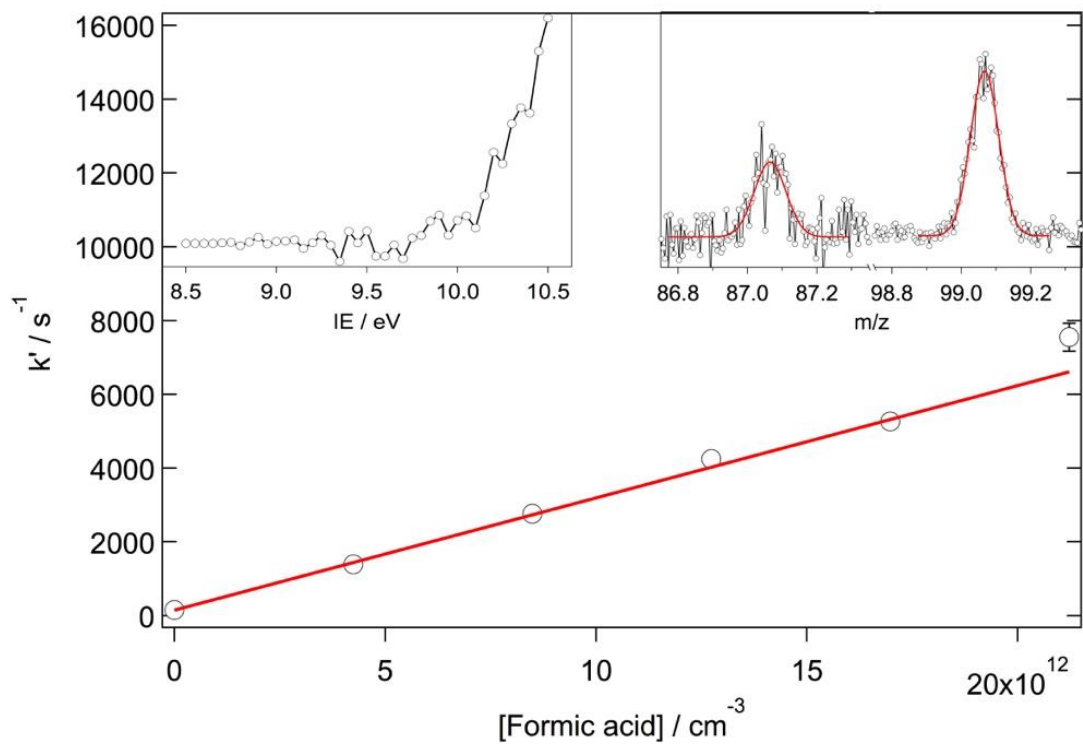
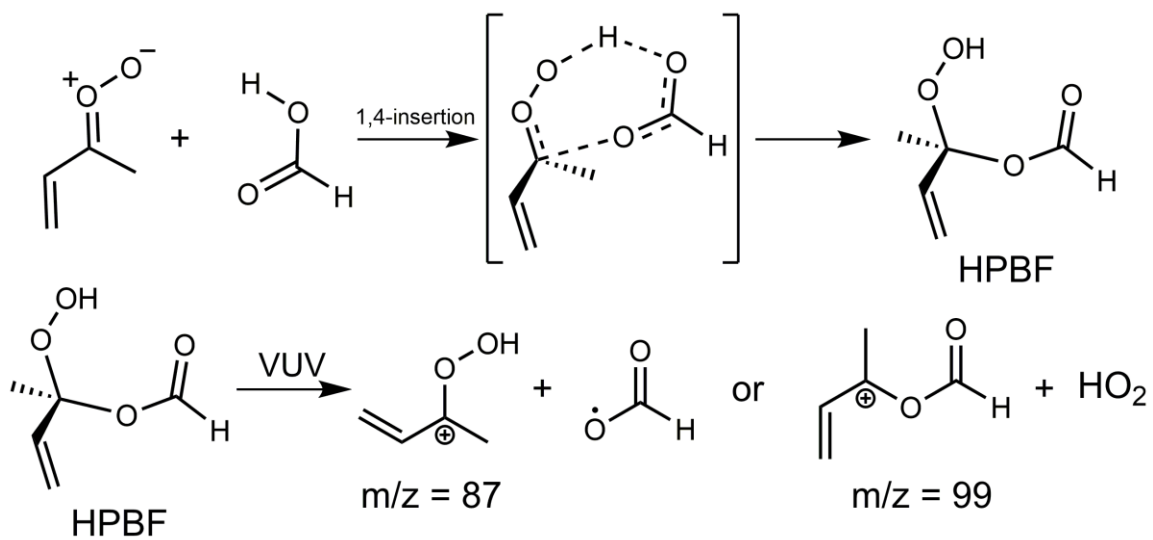


Figure 5. First order rate coefficients for the reaction of *syn*-MVK-oxide with formic acid as a function of formic acid concentration, obtained from the decay of *syn*-MVK-oxide using the Sandia absorption experiment. The red line is a linear fit to the absorption data, weighted by the 95% confidence limit error bars, obtaining a bimolecular rate coefficient of $(3.0 \pm 0.1) \times 10^{-10} \text{ cm}^3 \text{ s}^{-1}$. Note that some of the error bars are smaller than the symbols. Inset (left) is the photoionization spectrum for *m/z* 99, and (right) the mass spectrum of the proposed daughter ion (DI) products, both obtained using MPIMS. Gaussian fits to the mass peaks yield exact masses of (87.042 ± 0.004) and (99.044 ± 0.001) amu, consistent with the exact masses of 87.045 (MVK-oxide + H, HCO₂-loss DI) and 99.045 (HO₂-loss DI), respectively.

Figure 6. Schematic plot of the reaction pathway for the addition of formic acid to MVK-oxide. Stationary point energies are from CCSD(T)-F12/cc-pVTZ-F12//B2PLYPD3/cc-pVTZ calculations including ZPEs.



Scheme 5. 1,4-insertion of MVK-oxide into the O-H bond of formic acid, leading to the formation of a functionalized hydroperoxide reaction product.

oxide. In the CH₂OO case, stabilization of the adduct is predicted to dominate over bimolecular product formation, even though there is an exothermic exit channel arising from OO bond fission of the functionalized hydroperoxide. In the MVK-oxide case, the functionalized hydroperoxide is also favored over dissociation to produce OH + an alkoxy radical, which is now significantly endothermic relative to reactants. Despite these differences, the overall kinetics are predicted to be quite similar, with the reaction dominated by direct addition to form the functionalized hydroperoxide, HPBF in the case of MVK-oxide (discussed in further detail in the SI).

This reaction mechanism is supported by complementary MPIMS experiments that reveal the formation of species at exact masses corresponds to C₄H₇O₂ and C₅H₇O₂ (Figure 5, top right inset). These products are consistent with characteristic HCO₂-loss (= protonated Cl) and HO₂-loss daughter ions (DIs) from the dissociative photoionization of the predicted functionalized hydroperoxide reaction product, HPBF^{18, 19, 44}. The formation of the hydroperoxide product is further evidenced by the agreement between the observed and calculated vertical ionization energies and appearance energies for the m/z 99 daughter ion (further details in SI).

Master equation-based predictions for the temperature- and pressure-dependencies of the *syn*-MVK-oxide + formic acid recombination rate coefficient are illustrated in Figure 7. Notably, near room temperatures, at pressures near 10 Torr (0.013 bar), the predicted rate coefficient is essentially identical to the experimentally observed value and strongly pressure-dependent. Although the present calculations were performed for N₂ as a collider, the variation between N₂ and He, should be quite modest. Importantly, at atmospheric pressure, the pressure-dependence is greatly reduced with the rate coefficient effectively determined by the capture rate. At 1 bar, the predicted temperature-dependence is well represented by the expression $7.7 \times 10^6 T^{-5.86}$

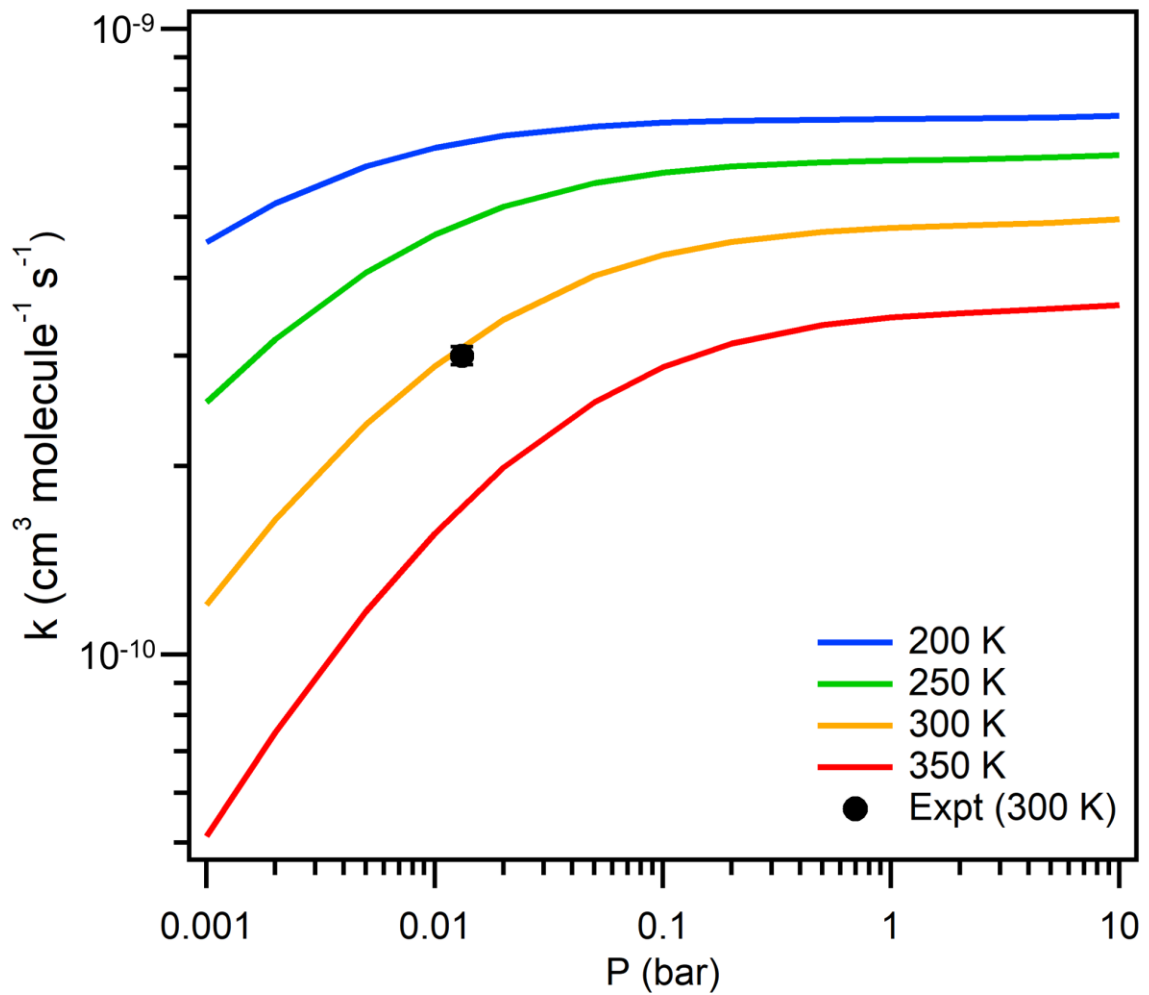


Figure 7. Temperature- and pressure-dependencies of the *syn*-MVK-oxide + formic acid recombination rate coefficient computed based on *ab initio* TST-based master equation modeling. The experimental rate coefficient obtained in this work (solid black circle) is shown for comparison.

$\exp(-1170/T) \text{ cm}^3 \text{ s}^{-1}$ over the 200 to 400 K temperature region, with a predicted value of $4.9 \times 10^{-10} \text{ cm}^3 \text{ s}^{-1}$ at room temperature.

MVK-oxide + water

Slow removal of *syn*-MVK-oxide in the presence of water vapor (where $[\text{H}_2\text{O}] \leq 5.7 \times 10^{17} \text{ cm}^{-3}$, $[(\text{H}_2\text{O})_2] \leq 7.9 \times 10^{14} \text{ cm}^{-3}$) was observed experimentally and upper limits of $4.0 \times 10^{-17} \text{ cm}^3 \text{ s}^{-1}$ and $3.0 \times 10^{-14} \text{ cm}^3 \text{ s}^{-1}$ are derived from IAMS absorption experiments. These results are consistent with previous theoretical predictions of $9.5 \times 10^{-20} \text{ cm}^3 \text{ s}^{-1}$ and $9.0 \times 10^{-17} \text{ cm}^3 \text{ s}^{-1}$ for the water monomer and dimer reaction rate coefficients^{6, 45}, respectively (or $8.1 \times 10^{-20} \text{ cm}^3 \text{ s}^{-1}$ and $3.1 \times 10^{-16} \text{ cm}^3 \text{ s}^{-1}$, respectively, following adjustments made by Vereecken *et al.* to account for the level of theory used, see SI). Higher level kinetics calculations performed herein (see SI for further details) return a rate coefficient of $1.1 \times 10^{-19} \text{ cm}^3 \text{ s}^{-1}$ for the *syn*-MVK-oxide + water monomer reaction, supporting the literature theoretical values^{6, 45} and experimental upper limits reported here. By contrast, CH_2OO reacts rapidly with water and water dimer, with bimolecular rate coefficients of 2.4×10^{-16} and $6.6 \times 10^{-12} \text{ cm}^3 \text{ s}^{-1}$, respectively, reported in the literature^{46, 47}, and thus these reactions are a significant atmospheric sink of CH_2OO . We attribute the smaller reactivity of MVK-oxide vs. CH_2OO with water vapor to a higher transition state (TS) barrier arising from disruption of the extended conjugation of *syn*-MVK-oxide in reaction leading to the hydroperoxide adduct. A pre-reactive complex exists for both reactions and both have similar stabilities ($-6.52 \text{ kcal mol}^{-1}$ for CH_2OO vs. $-6.11 \text{ kcal mol}^{-1}$ for MVK-oxide). At the TS, the carbonyl oxide moiety begins bending out of plane, indicating that the extended conjugation is disrupted in the case of MVK-oxide. As a result, the TS barrier for the MVK-oxide + H_2O reaction is significantly higher ($10.53 \text{ kcal mol}^{-1}$ for MVK-oxide vs. $3.12 \text{ kcal mol}^{-1}$ for CH_2OO), which

dramatically lowers the reaction rate compared to $\text{CH}_2\text{OO} + \text{H}_2\text{O}$. Reaction with water will therefore not be an important sink of *syn*-MVK-oxide in the troposphere, and thus, MVK-oxide will survive high-humidity environments; this implies a relatively high tropospheric concentration of *syn*-MVK-oxide.

Atmospheric modelling

The role of MVK-oxide in the troposphere has been evaluated through comparison of two model integrations, detailed herein. STOCHEM-CI0 represents our best current understanding of CI chemistry. It includes the reactions of MVK-oxide with SO_2 , formic acid, water and water dimer, in addition to unimolecular loss. STOCHEM-CI1 is a base-case scenario model wherein the reactions of MVK-oxide with SO_2 and formic acid are omitted (but still includes unimolecular decay and reactions with water and water dimer). In the model, *syn*- and *anti*-MVK-oxide are assumed to be produced from isoprene ozonolysis with yields of 0.14 and 0.07, respectively²⁹. The kinetic parameters utilized in both model integrations are detailed in the SI.

Evaluation of STOCHEM-CI0 reveals that, globally, MVK-oxide has the largest modelled steady-state concentration of all stabilized CIs (33% of the total CI molecules, 49% by weight). This is due to large isoprene emissions over forested regions, and slow tropospheric removal through unimolecular decomposition and reactions with water and water dimer. If removal with SO_2 and formic acid are neglected (STOCHEM-CI1), the steady-state concentration of MVK-oxide increases slightly (36% of total CI molecules, 54% by weight). The slow removal via bimolecular reactions with water and water dimer, and via unimolecular decomposition (33 s^{-1} at 298 K for *syn*-MVK-oxide³⁰ vs. ca. 300 s^{-1} for acetone oxide^{37, 48, 49}) means that MVK-oxide will survive in high humidity environments and thus other bimolecular reactions may be important.

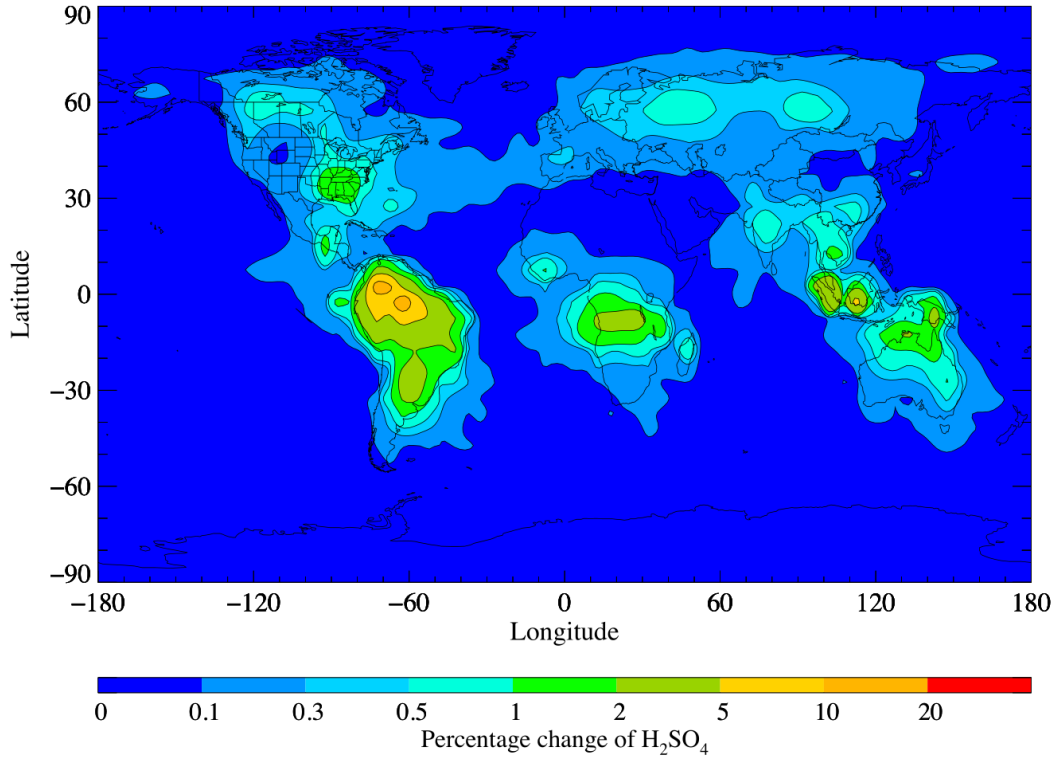
We find that MVK-oxide plays a role in the tropospheric conversion of SO₂ to sulfuric acid (Figure 8a), the removal of formic acid (Figure 8b) and potentially, particulate formation. Evaluation of STOCHEM-CI0 reveals that the reaction with SO₂ increases the SO₃ formation flux by 93% compared with the base-case scenario (STOCHEM-CI1), despite reaction with SO₂ accounting for only ~2% of the total tropospheric loss of MVK-oxide. Previous modelling work has indicated that CIs are responsible for between 10-70% of all SO₂-initiated oxidation to sulfuric acid^{15, 16, 50, 51}. Neglecting the reaction of MVK-oxide + SO₂ leads to an 11% decrease in the tropospheric concentration of SO₃ globally, significantly impacting modelled sulfuric acid. For example, over the Amazon region, where isoprene emissions and subsequently MVK-oxide concentrations are highest, the reaction of MVK-oxide + SO₂ contributes up to 20% of sulfuric acid production. This source has modest implications for sulfate aerosol formation (see SI).

The present work demonstrates that the reaction of the globally dominant and resonance stabilized CI, *syn*-MVK-oxide, with formic acid, is rapid. Evaluation of STOCHEM-CI0 reveals that reaction with MVK-oxide leads to up to 20% reduction in modelled formic acid globally (Figure 8b). Furthermore, the reactions of organic acids with CIs may contribute to the production of secondary organic aerosols via the formation of low volatility, highly oxygenated products¹⁹.

Conclusions

The direct UV-Vis absorption spectrum of the four-carbon, resonance-stabilized CI, MVK-oxide, has been recorded at 298 K in two independent experiments. We observe broad absorption centered around 370 nm in both experiments, in good agreement with the work of Vansco *et al.*³¹, with differences attributed to the different

(a)



(b)

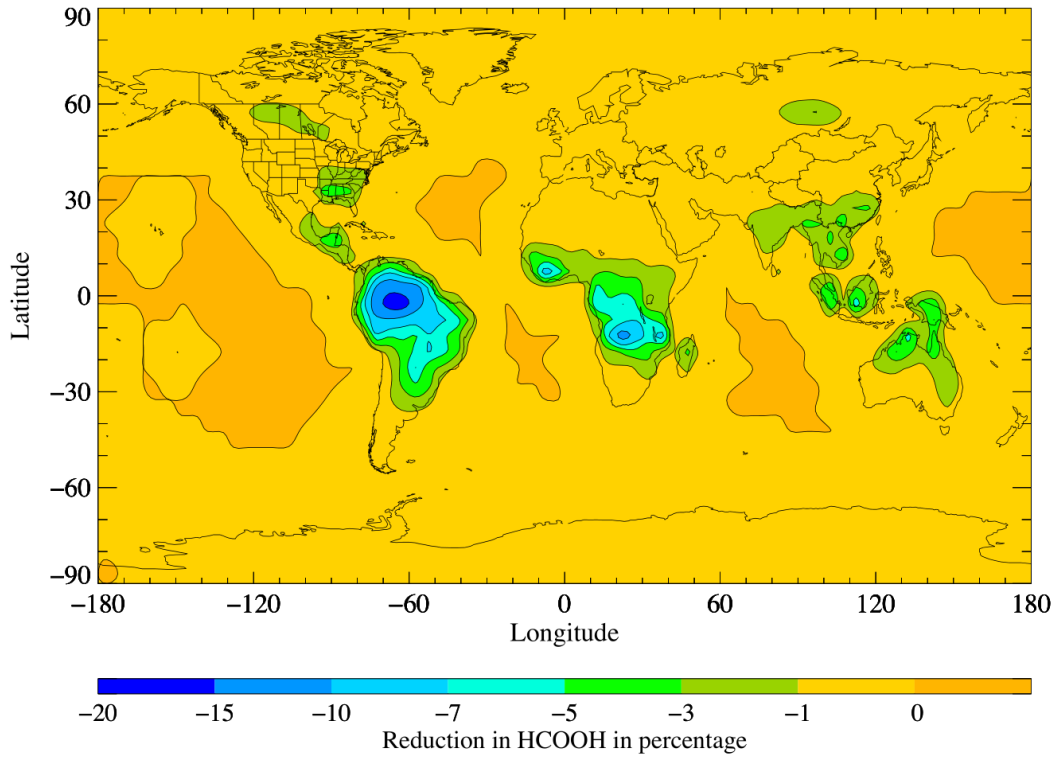


Figure 8. Modelled implications of (a) MVK-oxide reaction with SO₂ on global sulfuric acid and (b) MVK-oxide reaction with formic acid on global formic acid evaluated using the global chemistry and transport model STOCHEM-CRI. Model evaluations presented result from comparison of our best current understanding of CI reactions (STOCHEM-CI0) with a case neglecting the contribution of MVK-oxide reactions with SO₂ and formic acid, but including unimolecular decomposition, reactions with water and water dimer and unimolecular and bimolecular reactions of all other CIs (STOCHEM-CI1). Further details are given in the SI.

conformer distribution in the 298 K and jet-cooled experiments. The different conformer distribution observed in the 298 K experiments suggest a low yield of stabilized *anti*-MVK-oxide and/or faster *anti*-MVK-oxide decomposition possibly due to internal excitation. The experimentally observed lifetime of MVK-oxide in the 298 K experiments is consistent with *syn*-conformers and substantiates rapid removal of *anti*-conformers as indicated by calculations of Barber *et al.* ^{6,30}.

Computation and direct experimental kinetic measurements of bimolecular reactions of *syn*-MVK-oxide demonstrate slow *syn*-MVK-oxide removal in the presence of water, confirming recent theoretical predictions ^{6,45}. Rapid reactivity with SO₂ and formic acid were observed and predicted theoretically, similar to C1-C3 alkyl substituted CIs ^{10, 11, 18, 19, 37}. Complementary MPIMS measurements of the products from SO₂ and formic acid reactions with MVK-oxide indicate the potential role of these reactions in tropospheric particulate formation. SO₃ is observed from the reaction of *syn*-MVK-oxide with SO₂; global chemistry and transport modelling reveal a modest impact on predicted particle nucleation events due to the formation of sulfuric acid. The formation of a highly oxygenated organic hydroperoxide species, resulting from insertion of the CI into the acidic O-H bond, was observed from the reaction of MVK-oxide with formic acid – recent chamber work has implicated similar species in the formation of secondary organic aerosols ⁵².

Methods and Materials

UV-Vis absorption spectra and bimolecular rate coefficients for MVK-oxide were recorded using two independent transient absorption experiments, both of which have been described in detail previously. Further details of both the Sandia and IAMS experiments are given in the SI. Complementary experiments to identify the products of

the MVK-oxide + SO₂ and formic acid reactions, and to obtain the kinetics for MVK-oxide formation were undertaken using multiplexed photoionization mass spectrometry, described previously and in the SI. For all the work reported herein, MVK-oxide was generated using the method of Barber *et al.*³⁰ using 1,3-diiodobut-2-ene photolysis in the presence of excess O₂. All experiments were performed under pseudo-first-order conditions, such that [O₂] >> [1,3-diiodobut-2-ene], and for bimolecular kinetics investigations, [co-reactant] >> [MVK-oxide]. *Ab initio* kinetics calculations were performed to supplement each of the experimental observations. They were based on a combination of density functional theory based rovibrational analyses, coupled cluster-based energy evaluations, variational transition state theory, and master equation analyses that explicitly treat hindered rotational motions. Further details are provided in the SI. Modelling work was undertaken using STOCHEM-CRI which comprises a global chemistry transport model (STOCHEM) coupled with the common representative intermediate mechanism (CRI). This has been described previously and detailed further in the SI.

Acknowledgements

This material is based upon work supported by the Division of Chemical Sciences, Geosciences and Biosciences, Office of Basic Energy Sciences (BES), U.S. Department of Energy (USDOE). Sandia National Laboratories is a multimission laboratory managed and operated by National Technology and Engineering Solutions of Sandia, LLC., a wholly owned subsidiary of Honeywell International, Inc., for the USDOE's National Nuclear Security Administration under contract DE-NA0003525. This paper describes objective technical results and analysis. Any subjective views or opinions that might be expressed in the paper do not necessarily represent the views of

the USDOE or the United States Government. This material is based in part on research at Argonne supported by the U.S. Department of Energy, Office of Science, Office of Basic Energy Sciences, Division of Chemical Sciences, Geosciences, and Biosciences under Contract No. DE-AC02-06CH11357. The Advanced Light Source is supported by the Director, Office of Science, BES/USDOE under Contract DE- AC02-05CH11231 at Lawrence Berkeley National Laboratory. This research was carried out in part by the Jet Propulsion Laboratory, California Institute of Technology, under contract with the National Aeronautics and Space Administration (NASA), supported by the Upper Atmosphere Research and Tropospheric Chemistry program. The contributions of RLC and KLZ were in part supported by appointments to the NASA Postdoctoral Program at the NASA Jet Propulsion Laboratory, administered by Universities Space Research Association under contract with NASA. This research was also supported by the U.S. Department of Energy-Basic Energy Sciences under grant DE-FG02-87ER13792 (MIL). PJW thanks the NSF (CHE-1902509). Y.-L.L., Y.-H.L., W.C. and J.J.-M.L. were supported by Academia Sinica and Ministry of Science and Technology, Taiwan (MOST 106-2113-M-001-026-MY3 (JL)). DES and MAHK thank NERC (grant codes- NE/K004905/1), Bristol ChemLabS and Primary Science Teaching Trust under whose auspices various aspects of this work was funded. We gratefully acknowledge Stanley Sander for useful discussions. © 2019, California Institute of Technology. © 2019. All rights reserved.

References

1. C. Wiedinmyer, X. Tie, A. Guenther, R. Neilson and C. Granier, *Earth Interact* **10** (3), 1-19 (2006).
2. T. B. Nguyen, G. S. Tyndall, J. D. Crouse, A. P. Teng, K. H. Bates, R. H. Schwantes, M. M. Coggon, L. Zhang, P. Feiner and D. O. Miller, *Phys Chem Chem Phys* **18** (15), 10241-10254 (2016).
3. R. Criegee, *Angew Chem Int Ed Engl* **14** (11), 745-752 (1975).
4. M. Khan, C. Percival, R. Caravan, C. Taatjes and D. Shallcross, *Environ Sci: Process Impacts* **20** (3), 437-453 (2018).
5. A. Novelli, K. Hens, C. Tatum Ernest, M. Martinez, A. C. Nölscher, V. Sinha, P. Paasonen, T. Petäjä, M. Sipilä and T. Elste, *Atmos Chem Phys* **17** (12), 7807-7826 (2017).

6. L. Vereecken, A. Novelli and D. Taraborrelli, *Phys Chem Chem Phys* **19** (47), 31599-31612 (2017).
7. M. A. H. Khan, W. C. Morris, M. Galloway, Beth M. A. Shallcross, C. J. Percival and D. E. Shallcross, *Int J Chem Kinet* **49** (8), 611-621 (2017).
8. R. Chhantyal-Pun, M. A. H. Khan, R. Martin, N. Zachhuber, Z. J. Buras, C. J. Percival, D. E. Shallcross and A. J. Orr-Ewing, *ACS Earth Space Chem* **3**, 2363-2371 (2019).
9. C. A. Taatjes, G. Meloni, T. M. Selby, A. J. Trevitt, D. L. Osborn, C. J. Percival and D. E. Shallcross, *J Am Chem Soc* **130** (36), 11883-11885 (2008).
10. C. A. Taatjes, O. Welz, A. J. Eskola, J. D. Savee, A. M. Scheer, D. E. Shallcross, B. Rotavera, E. P. F. Lee, J. M. Dyke, D. K. W. Mok, D. L. Osborn and C. J. Percival, *Science* **340** (6129), 177-180 (2013).
11. O. Welz, J. D. Savee, D. L. Osborn, S. S. Vasu, C. J. Percival, D. E. Shallcross and C. A. Taatjes, *Science* **335** (6065), 204-207 (2012).
12. F. Liu, J. M. Beames, A. M. Green and M. I. Lester, *J Phys Chem A* **118** (12), 2298-2306 (2014).
13. R. Cox and S. Penkett, *J Chem Soc Faraday Trans* **68**, 1735-1753 (1972).
14. R. A. Cox and S. A. Penkett, *Nature* **230** (5292), 321-322 (1971).
15. M. Boy, D. Mogensen, S. Smolander, L. Zhou, T. Nieminen, P. Paasonen, C. Plass-Dülmer, M. Sipilä, T. Petäjä and L. Mauldin, *Atmos. Chem. Phys.* **12** (10), 27693-27736 (2012).
16. R. Mauldin, T. Berndt, M. Sipilä, P. Paasonen, T. Petäjä, S. Kim, T. Kurtén, F. Stratmann, V.-M. Kerminen and M. Kulmala, *Nature* **488** (7410), 193 (2012).
17. C. J. Percival, O. Welz, A. J. Eskola, J. D. Savee, D. L. Osborn, D. O. Topping, D. Lowe, S. R. Utembe, A. Bacak and G. McFiggans, *Faraday Discuss* **165**, 45-73 (2013).
18. O. Welz, A. J. Eskola, L. Sheps, B. Rotavera, J. D. Savee, A. M. Scheer, D. L. Osborn, D. Lowe, A. Murray Booth, P. Xiao, M. A. H. Khan, C. J. Percival, D. E. Shallcross and C. A. Taatjes, *Angew Chem* **53** (18), 4547-4550 (2014).
19. R. Chhantyal-Pun, B. Rotavera, M. R. McGillen, M. A. H. Khan, A. J. Eskola, R. L. Caravan, L. Blacker, D. P. Tew, D. L. Osborn, C. J. Percival, C. A. Taatjes, D. E. Shallcross and A. J. Orr-Ewing, *ACS Earth Space Chem* **2** (8), 833-842 (2018).
20. C. A. Taatjes, M. A. H. Khan, A. J. Eskola, C. J. Percival, D. L. Osborn, T. J. Wallington and D. E. Shallcross, *Environ Sci Technol* **53** (3), 1245-1251 (2019).
21. B. Long, J. L. Bao and D. G. Truhlar, *J Am Chem Soc* **138** (43), 14409-14422 (2016).
22. M. J. Newland, A. R. Rickard, L. Vereecken, A. Muñoz, M. Ródenas and W. J. Bloss, *Atmos. Chem. Phys.* **15** (16), 9521-9536 (2015).
23. L.-C. Lin, H.-T. Chang, C.-H. Chang, W. Chao, M. C. Smith, C.-H. Chang and K. Takahashi, *Phys Chem Chem Phys* **18** (6), 4557-4568 (2016).
24. J. Anglada, J. Gonzalez and M. Torrent-Sucarrat, *Phys Chem Chem Phys* **13** (28), 13034-13045 (2011).
25. J. M. Anglada, P. Aplincourt, J. M. Bofill and D. Cremer, *ChemPhysChem* **3** (2), 215-221 (2002).
26. A. B. Ryzhkov and P. A. Ariya, *Phys Chem Chem Phys* **6** (21), 5042-5050 (2004).
27. L. Sheps, A. M. Scully and K. Au, *Phys Chem Chem Phys* **16** (48), 26701-26706 (2014).
28. L.-C. Lin, W. Chao, C.-H. Chang and K. Takahashi, *Phys Chem Chem Phys* **18** (40), 28189-28197 (2016).
29. D. Zhang, W. Lei and R. Zhang, *Chem Phys Lett* **358** (3), 171-179 (2002).
30. V. P. Barber, S. Pandit, A. M. Green, N. Trongsiwiat, P. J. Walsh, S. J. Klippenstein and M. I. Lester, *J Am Chem Soc* **140** (34), 10866-10880 (2018).
31. M. F. Vansco, B. Marchetti and M. I. Lester, *J Chem Phys* **149** (24), 244309 (2018).
32. L. Vereecken, H. Harder and A. Novelli, *Phys Chem Chem Phys* **14** (42), 14682-14695 (2012).
33. L. Sheps, *J Phys Chem Lett* **4** (24), 4201-4205 (2013).
34. L. Sheps and D. W. Chandler, (Sandia National Laboratories (SNL-CA), Livermore, CA (United States), 2013).
35. M.-N. Su and J. J.-M. Lin, *Rev Sci Instrum* **84** (8), 086106 (2013).
36. K. T. Kuwata, L. C. Valin and A. D. Converse, *J Phys Chem A* **109** (47), 10710-10725 (2005).
37. R. Chhantyal-Pun, O. Welz, J. D. Savee, A. J. Eskola, E. P. F. Lee, L. Blacker, H. R. Hill, M. Ashcroft, M. A. H. Khan, G. C. Lloyd-Jones, L. Evans, B. Rotavera, H. Huang, D. L. Osborn, D. K. W. Mok, J. M. Dyke, D. E. Shallcross, C. J. Percival, A. J. Orr-Ewing and C. A. Taatjes, *J Phys Chem A* **121** (1), 4-15 (2017).
38. D. Stone, M. Blitz, L. Daubney, N. U. Howes and P. Seakins, *Phys Chem Chem Phys* **16** (3), 1139-1149 (2014).
39. P. Spietz, J. C. G. Martin and J. P. Burrows, *J Photochem Photobiol A* **176** (1-3), 50-67 (2005).
40. J. Burkholder, S. Sander, J. Abbatt, J. Barker, R. Huie, C. Kolb, M. Kurylo, V. Orkin, D. Wilmouth and P. Wine, 2015.
41. Y. Liu, F. Liu, S. Liu, D. Dai, W. Dong and X. Yang, *Phys Chem Chem Phys* **19** (31), 20786-20794 (2017).
42. H.-L. Huang, W. Chao and J. J.-M. Lin, *Proc Natl Acad Sci* **112** (35), 10857-10862 (2015).
43. L. Vereecken, *Phys Chem Chem Phys* **19** (42), 28630-28640 (2017).
44. R. Chhantyal-Pun, R. J. Shannon, D. P. Tew, R. L. Caravan, M. Duchi, C. Wong, A. Ingham, C. Feldman, M. R. McGillen and M. A. H. Khan, *Phys Chem Chem Phys* **21**, 14042-14052 (2019).
45. J. M. Anglada and A. Solé, *Phys Chem Chem Phys* **18** (26), 17698-17712 (2016).
46. L. Sheps, B. Rotavera, A. J. Eskola, D. L. Osborn, C. A. Taatjes, K. Au, D. E. Shallcross, M. A. H. Khan and C. J. Percival, *Phys Chem Chem Phys* **19** (33), 21970-21979 (2017).
47. W. Chao, J.-T. Hsieh, C.-H. Chang and J. J.-M. Lin, *Science* **347** (6223), 751-754 (2015).
48. Y. Fang, V. P. Barber, S. J. Klippenstein, A. B. McCoy and M. I. Lester, *J Chem Phys* **146** (13), 134307 (2017).
49. M. C. Smith, W. Chao, K. Takahashi, K. A. Boering and J. J.-M. Lin, *J Phys Chem A* **120** (27), 4789-4798 (2016).

50. G. Sarwar, H. Simon, K. Fahey, R. Mathur, W. S. Goliff and W. R. Stockwell, *Atmos Environ* **85**, 204-214 (2014).
51. J. Li, Q. Ying, B. Yi and P. Yang, *Atmos Environ* **79**, 442-447 (2013).
52. Y. Sakamoto, S. Inomata and J. Hirokawa, *J Phys Chem A* **117** (48), 12912-12921 (2013).

CHAPTER 6

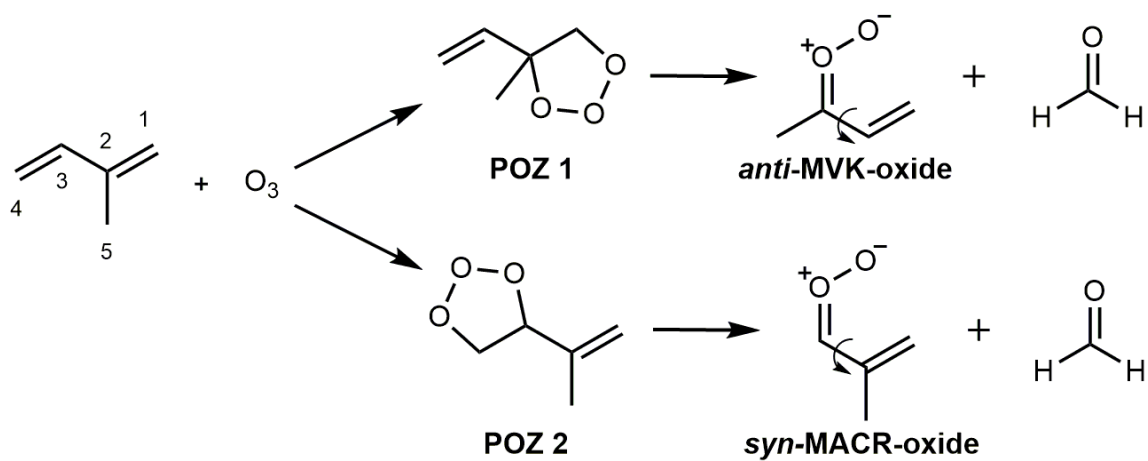
EXPERIMENTAL EVIDENCE OF DIOXOLE UNIMOLECULAR DECAY PATHWAY FOR ISOPRENE-DERIVED CRIEGEE INTERMEDIATES

This research has been previously published in the *Journal of Physical Chemistry A*, **124**, 3542 (2020) and reproduced with the permission of the American Chemical Society. The experimental research was performed with researchers Rebecca Caravan (*NASA Postdoctoral Program Fellow, NASA Jet Propulsion Laboratory, Combustion Research Facility, Sandia National Laboratories, Chemical Sciences and Engineering Division, Argonne National Laboratory*), Kristen Zuraski (*NASA Postdoctoral Program Fellow, NASA Jet Propulsion Laboratory*), Frank Winiberg (*NASA Jet Propulsion Laboratory, California Institute of Technology*), Kendrew Au (*Combustion Research Facility, Sandia National Laboratories*), David Osborn (*Combustion Research Facility, Sandia National Laboratories*), Carl Percival (*NASA Jet Propulsion Laboratory, California Institute of Technology*), Craig Taatjes (*Combustion Research Facility, Sandia National Laboratories*), and Marsha Lester (*Department of Chemistry, University of Pennsylvania*). Synthetic work was performed by graduate student Nisalak Trongsirawat and Patrick J. Walsh (*Department of Chemistry, University of Pennsylvania*). Atmospheric modeling was performed in collaboration with Anwar Khan and Dudley Shallcross (*School of Chemistry, University of Bristol*).

I. Introduction

Isoprene (2-methyl-1,3-butadiene) is the most abundant volatile organic compound (VOC) emitted into the Earth's atmosphere after methane, with global emissions estimated at ca. 600 Tg year⁻¹.¹ Ozonolysis is an important sink of atmospheric isoprene (ca. 10% globally) that generates reactive carbonyl oxide species called Criegee intermediates.² Unimolecular decay of Criegee intermediates is a significant non-photolytic source of OH radicals, accounting for ca. 1/3 of OH radicals formed in the daytime and essentially all of the OH radicals at night.³⁻⁶ Criegee intermediates have been found to be important tropospheric oxidants themselves, supplementing the oxidation chemistry initiated by OH radicals.⁷ Two four-carbon unsaturated Criegee intermediates, methyl vinyl ketone oxide ((CH₂=CH)(CH₃)COO, MVK-oxide) and methacrolein oxide ((CH₂=C(CH₃))CHO, MACR-oxide) along with formaldehyde co-product are generated from isoprene ozonolysis via distinct primary ozonide (POZ) intermediates as depicted in Scheme 1. In addition, the simplest Criegee intermediate formaldehyde oxide (CH₂OO) and either methyl vinyl ketone ((CH₂=CH)(CH₃)CO) or methacrolein ((CH₂=C(CH₃))CHO) are generated from isoprene ozonolysis. The substantial abundance of isoprene in the atmosphere makes understanding the atmospheric fate of MVK-oxide and MACR-oxide of considerable importance. The yields of MVK-oxide and MACR-oxide from isoprene are estimated at 23% and 19%, respectively.²

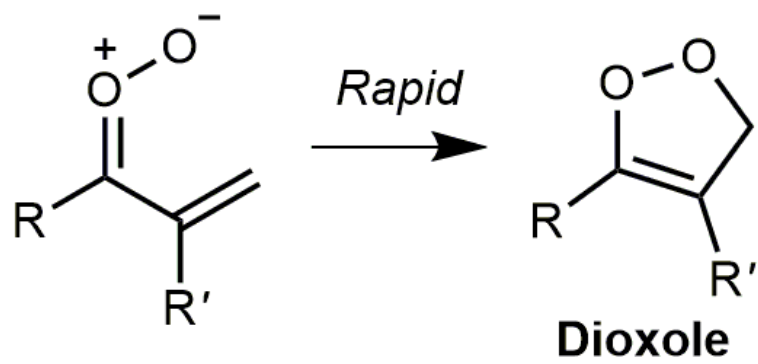
The MVK-oxide and MACR-oxide Criegee intermediates are isomers, both having vinyl and methyl substituents, but differing in the position of the methyl groups. Both have extended conjugation involving six π electrons across the vinyl (CH₂=C) and carbonyl oxide (C=O⁺-O⁻) functional groups.⁸⁻⁹ They are distinctly different than simple



Scheme 1. Formation of MVK-oxide and MACR-oxide Criegee intermediates from isoprene ozonolysis.

saturated carbonyl oxides, such as formaldehyde oxide (CH₂OO) and alkyl-substituted Criegee intermediates, which have four π electron systems (C=O⁺-O⁻).⁸⁻¹⁶ In addition, MVK-oxide and MACR-oxide each have four conformational forms with similar predicted ground state energies (within ca. 3 kcal mol⁻¹). The four conformational forms are separated into two groups based on: (1) the orientation of the terminal oxygen with respect to the vinyl group (*syn* and *anti*), and (2) the orientation of the vinyl group with respect to the C=O group (*cis* and *trans*). Under thermal conditions (298 K), the *cis* and *trans* conformations will rapidly interconvert by rotation about the C-C bond (indicated by the curved arrow in Scheme 1).¹⁵⁻¹⁷ The *syn* and *anti* configurations do not interconvert at ambient temperature due to high barriers for rotation about the C=O bond and are treated as distinct chemical species with different unimolecular and in some cases bimolecular reaction pathways.^{15, 17-19} The product branching from isoprene ozonolysis has been investigated using master equation modeling,¹⁸⁻²⁰ yielding results that differ depending on the theoretical method used. The most recent calculations give relative abundances for *syn* and *anti* conformers of MVK-oxide and MACR-oxide of ca. 1:1 and 1:4 (298 K, 760 torr), respectively.¹⁸⁻¹⁹

Several unimolecular decay pathways are predicted for MVK-oxide and MACR-oxide, which are highly dependent on their conformational forms.^{15, 17-19, 21} Thus far, only the 1,4 H-atom transfer pathway for *syn*-MVK-oxide to OH products has been experimentally observed.¹⁵ Here, we identify the unimolecular decay pathway predicted for the specific conformations displayed in Scheme 1, in which the terminal oxygen is oriented toward the vinyl group (*anti*-MVK-oxide and *syn*-MACR-oxide).¹⁸⁻¹⁹ For these conformers, the extended conjugation facilitates rapid electrocyclic ring closure that forms a 5-membered cyclic peroxide, known as a dioxole. The ring closure mechanism is illustrated in Scheme 2. Here, R and R' indicate the position of the methyl group in



Scheme 2. Electrocyclic ring closure of *anti*-MVK-oxide and *syn*-MACR-oxide to dioxole intermediates.

MVK-oxide and MACR-oxide, respectively, and in the dioxole product resulting from rapid isomerization. This novel mechanism is predicted to be rapid under thermal conditions for both *anti*-MVK-oxide and *syn*-MACR-oxide. (2140 s^{-1} and 2500 s^{-1} , respectively, 298 K, 760 torr).^{15, 17} These thermal decay rates are representative of a Boltzmann distribution of *cis* and *trans* conformers due to their rapid interconversion.¹⁵⁻¹⁷

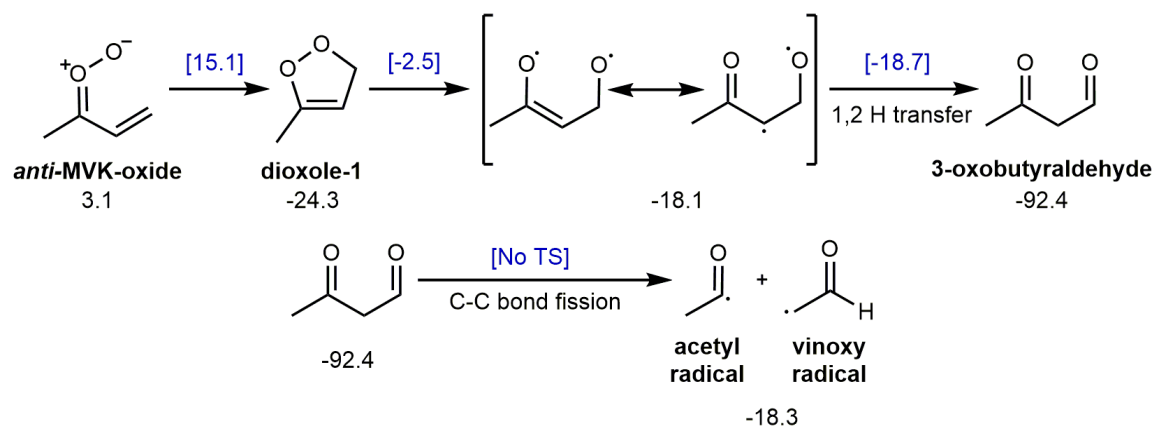
Rapid unimolecular decay via the dioxole pathway is expected to dominate the atmospheric loss of the *anti*-MVK-oxide and *syn*-MACR-oxide Criegee intermediates. The bimolecular chemistry of *anti*-MVK-oxide and *syn*-MACR-oxide is predicted to be similar to that of *syn*-MVK-oxide, which has been recently investigated through direct measurements and theory with H₂O, formic acid, and SO₂ co-reactants.¹⁶ *Syn*-MVK-oxide was found to react slowly with water monomer and dimer (with upper limits of $4.0 \times 10^{-17}\text{ cm}^3\text{ s}^{-1}$ and $3.0 \times 10^{-14}\text{ cm}^3\text{ s}^{-1}$ determined, respectively),¹⁶ in agreement with theoretical predictions.^{16-17, 22} In contrast, *syn*-MVK-oxide reacts rapidly with formic acid ($3.0 \times 10^{-10}\text{ cm}^3\text{ s}^{-1}$) and SO₂ ($4.2 \times 10^{-11}\text{ cm}^3\text{ s}^{-1}$), similar to simple Criegee intermediates.²³⁻²⁶ Typical atmospheric concentrations of H₂O, formic acid, and SO₂ are not large enough for bimolecular reactions to compete with rapid unimolecular decay via the dioxole pathway. Moreover, master equation modeling indicates that isomerization to dioxole under atmospheric conditions (298 K, 760 torr) will account for 42% and 25% of MVK-oxide and MACR-oxide loss, respectively, making the dioxole pathway a significant sink for the four-carbon unsaturated Criegee intermediates formed from isoprene ozonolysis.¹⁸⁻¹⁹ Thus, when evaluating the impact of MVK-oxide and MACR-oxide Criegee intermediates on the atmosphere it is important to characterize the dioxole pathway experimentally, including the final product formed. This study reports the first experimental evidence of products formed from the unimolecular decay of *anti*-MVK-

oxide and *syn*-MACR-oxide Criegee intermediates via the dioxole pathway. Dioxole is predicted to undergo further rapid unimolecular decay to radical products (Section II).¹⁵ Under thermal conditions (298 K), and in the presence of excess O₂, these radical products will rapidly add O₂ to form peroxy radicals (ROO) that subsequently undergo unimolecular decay to stable products along with the formation of an OH or HO₂ radical co-product.²⁷⁻³⁰ The stable products are identified using multiplexed photoionization mass spectrometry (MPIMS) (Section IV). The origin of the identified products is further interrogated via experiments using formic acid as a Criegee intermediate scavenger. The potential atmospheric impact of the dioxole pathway (Section V) is discussed in light of the present experimental findings.

II. Background

Theoretical studies indicate that electrocyclic ring closure to dioxole is the dominant sink for *anti*-MVK-oxide and *syn*-MACR-oxide Criegee intermediates.¹⁸⁻¹⁹ The full multistep reaction is shown in Scheme 3 for *anti*-MVK-oxide. In Scheme 3, the energies (kcal mol⁻¹) are given relative to *syn-trans*-MVK-oxide (CCSD(T)-F12/CBS-F12(TZ-F12,QZ-F12)//B2PLYP-D3/cc-pVTZ) as reported by Barber *et al.*¹⁵

Electrocyclic ring closure forms a 5-membered cyclic peroxide, 3-methyl-4H-1,2-dioxole (dioxole-1). This step is predicted to have a low transition state (TS) barrier (12.0 kcal mol⁻¹) and a fast thermal decay rate (2140 s⁻¹, 298 K, 760 torr).¹⁵ Dioxole-1 is generated with sufficient internal excitation to undergo further rapid unimolecular processes via submerged barriers. Homolytic cleavage of the O-O bond of dioxole-1 forms a diradical, which can rearrange to a closed shell β-dicarbonyl (3-oxobutyraldehyde) through a highly exothermic (-74.3 kcal mol⁻¹) intramolecular 1,2 H-

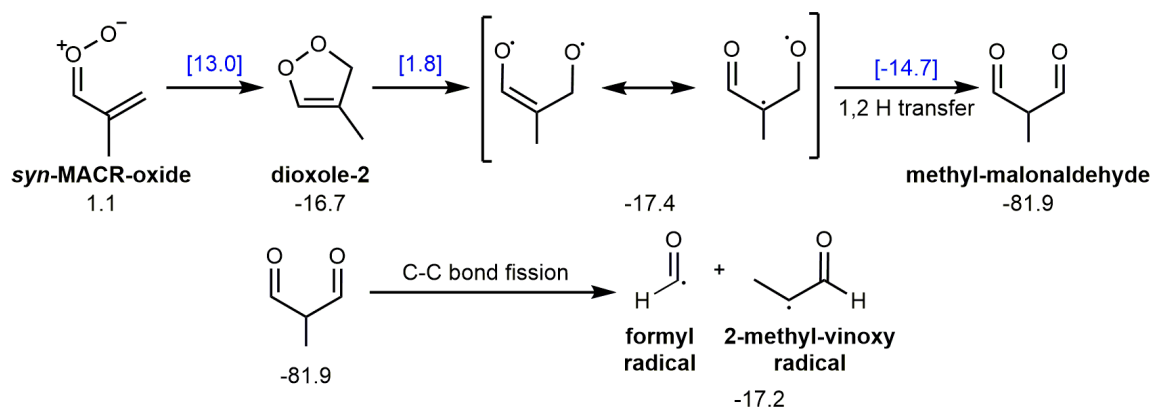


Scheme 3. Unimolecular decay of *anti*-MVK-oxide via electrocyclic ring closure to dioxole-1 and subsequent decay to vinyloxy and acetyl radicals. Energies are reported in kcal mol⁻¹ by Barber *et al.*¹⁵

atom transfer. This is followed by barrierless C-C bond fission to acetyl radical and vinoxy radical products.¹⁵

An analogous isomerization pathway to dioxole is predicted for *syn*-MACR-oxide, which generates 4-methyl-3H-1,2-dioxole (dioxole-2) as shown in Scheme 4.¹⁹ In Scheme 4, energies (kcal mol⁻¹) are reported by Kuwata *et al.*¹⁹ relative to the lowest energy *anti-trans*-MACR-oxide conformer (CBS-QB3// B3LYP/6-311G(d,p)). Electrocyclic ring closure for *syn*-MACR-oxide is also predicted to have a low TS barrier (11.9 kcal mol⁻¹) and rapid thermal decay rate (2500 s⁻¹, 298 K, 760 torr).¹⁷ Dioxole-2 is expected to undergo similar ring opening and intramolecular isomerization processes that form methylmalonaldehyde in an exothermic reaction (ca. -65.2 kcal mol⁻¹). In the case of dioxole-2, C-C bond fission results in the formation of formyl radical and 2-methyl-vinoxy radical products. C-C bond fission was not investigated previously.¹⁹ Additional calculations (see SI Sec. S1) demonstrate that sufficient energy is available for dissociation to radical products in an analogous mechanism as that predicted for *anti*-MVK-oxide.

In this study, MVK-oxide and MACR-oxide are generated under thermal conditions (298 K, 10 torr) in the presence of excess O₂. Under these experimental conditions, the radical products formed through unimolecular decay of MVK-oxide and MACR-oxide via the dioxole channel will rapidly react with O₂ to form ROO.^{28, 31-33} ROO intermediates are predicted to decay rapidly to closed-shell species along with an OH or HO₂ radical co-product via a hydroperoxyalkyl radical (QOOH) intermediate.²⁸⁻³⁰ Rapid unimolecular decay of ROO is facilitated by internal excitation of the radical products formed in the dioxole pathway, along with exothermic O₂ addition and submerged subsequent barriers that lead to stable products. *Ab initio* theoretical studies have examined the radical + O₂ reaction pathways.²⁷⁻³⁰ The mechanisms for product formation from the acetyl radical +

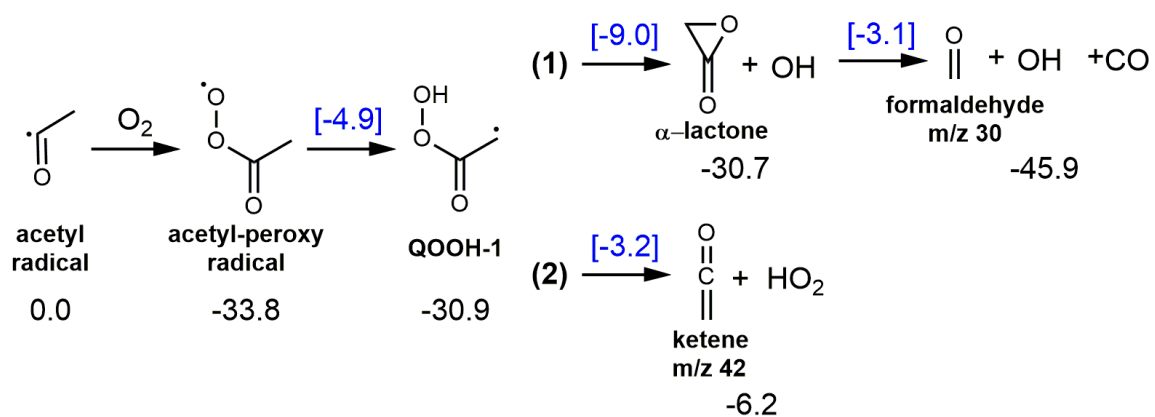


Scheme 4. Unimolecular decay of *syn*-MACR-oxide via electrocyclic ring closure to dioxole-2 and subsequent decay to formyl and 2-methyl-vinoxy radicals. Energies are reported in kcal mol⁻¹ by Kuwata *et al.*¹⁸

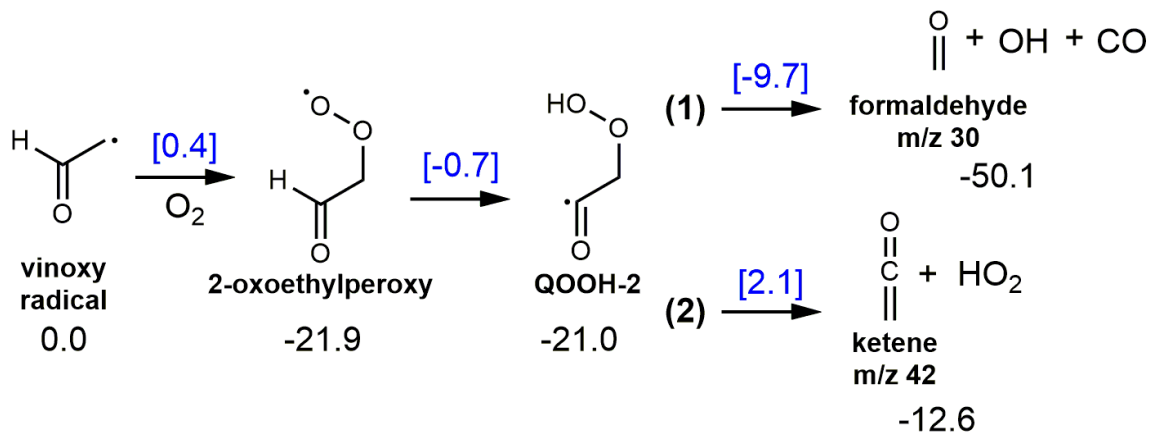
O₂ and vinoxy radical + O₂ reaction are shown in Scheme 5 and 6, respectively. For the acetyl radical, O₂ addition generates the acetyl-peroxy radical in an exothermic reaction (-33.8 kcal mol⁻¹).

The exothermicity of the acetyl radical + O₂ reaction facilitates a 1,4 H-atom transfer from the methyl group to the terminal oxygen atom and results in the formation of QOOH-1. The most energetically favorable decay pathway for QOOH-1 is via a submerged TS barrier (21.9 kcal mol⁻¹) to the cyclic intermediate, α -lactone, and OH co-product. Master equation modeling indicates significant fragmentation of α -lactone to formaldehyde + CO products under low pressure conditions.²⁸ Although the asymptotic energy for the formaldehyde + OH + CO product channel (Scheme 5) was not reported by Carr *et al.*,²⁸ additional calculations (see SI Sec. S1) demonstrate that this is the thermodynamically favored channel. OH yields measured experimentally and predicted using master equation modelling reported in a number of publications together with the low yield of α -lactone directly detected by Chen and Lee support the dominance of unimolecular decomposition channel over α -lactone stabilization.³⁴⁻⁴³ Ketene + HO₂ products are also energetically accessible, but are expected to be minor due to a higher barrier (27.7 kcal mol⁻¹) to formation. Furthermore, the OH-yield is demonstrated to approach unity at low-pressures (<10 Torr).^{28, 35-37, 39-40} Thus, formaldehyde (along with OH and CO) is expected to be the primary product channel under low pressure conditions.²⁸

The unpaired electron of vinoxy radicals in the ground state is primarily localized on the carbon,^{29-30, 44-46} which facilitates rapid reaction with O₂ to form ROO.⁴⁷⁻⁴⁸ The vinoxy radical + O₂ reaction generates the 2-oxoethylperoxy radical as shown in Scheme 6. A recent high-level theoretical study of the vinoxy + O₂ reaction predicts formaldehyde + OH + CO to be the dominant product channel, noting other pathways may be minor.²⁹



Scheme 5. Reaction of acetyl radical with O₂ and subsequent decay to formaldehyde + OH + CO or ketene + HO₂ products via the QOOH-1 intermediate. Energies are reported by Carr *et al.*, supplemented by the present work, in kcal mol⁻¹.²⁸



Scheme 6. Reaction of vinoxy radical with O₂ and subsequent decay to formaldehyde + OH + CO or ketene + HO₂ via the QOOH-2 intermediate. Energies (kcal mol⁻¹) are reported by Weidman *et al.*²⁹ (CCSD(T)/CBS).

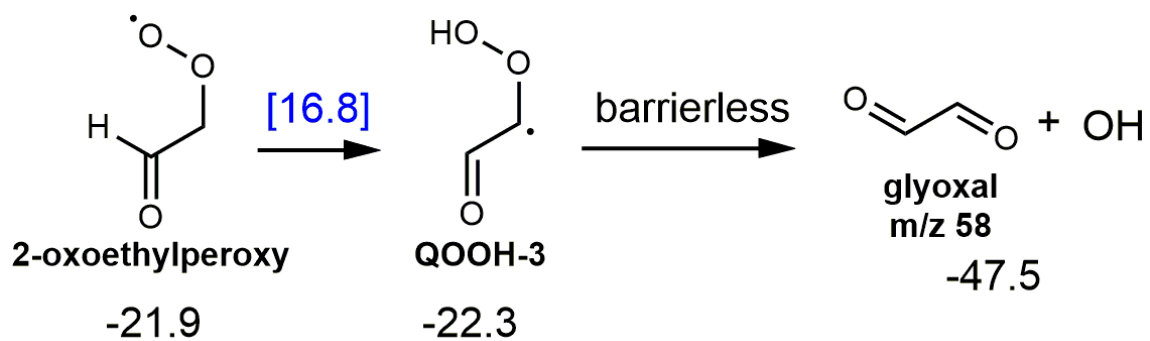
The proposed mechanism is shown in Scheme 6 and proceeds by O₂ addition to the vinoxy radical via a low barrier (0.4 kcal mol⁻¹) to form the 2-oxoethylperoxy radical in an exothermic reaction (-21.9 kcal mol⁻¹).

The 2-oxoethylperoxy radical is formed with sufficient energy (21.9 kcal mol⁻¹) to isomerize via a H-atom transfer from the neighboring aldehyde and yield QOOH-2, which can promptly decay via a submerged barrier (11.3 kcal mol⁻¹) to formaldehyde + CO + OH. QOOH-2 can also decay via a higher lying TS barrier (23.1 kcal mol⁻¹) to form ketene + HO₂, which is predicted to be a minor product channel. Alternatively, 2-oxoethylperoxy radical can undergo a 1,3 H-atom transfer via a large barrier (38.7 kcal mol⁻¹) to form QOOH-3, which will promptly decompose to glyoxal + OH (Scheme 7). Glyoxal formation is unlikely given the large TS barrier to formation of QOOH-3.

Fewer experimental studies have been conducted to investigate the products from the vinoxy radical + O₂ reaction compared with the corresponding acetyl reaction. Zhu *et al.*⁴⁹ reported that glyoxal may be a reaction product, however the disappearance rate of the vinoxy radical did not match the appearance rate of glyoxal, suggesting that is produced from the decomposition of the 2-oxoethylperoxy radical. Their preliminary results also suggested formaldehyde + CO + OH is a primary product channel.

Unimolecular decay of *syn*-MACR-oxide via the dioxole pathway results in formation of formyl radical and 2-methyl-vinoxy radical (Scheme 4), which are both predicted to undergo barrierless addition of O₂ to form the formyl-peroxy radical and 1-oxo-2-propylperoxy radical, respectively. Formyl-peroxy radical is known to undergo prompt decomposition to CO + HO₂,^{27, 50} whereas the products from the 1-oxo-2-propylperoxy radical are less well known.

A recent high-level theoretical study has predicted the products from the 2-methyl-vinoxy + O₂ reaction (Scheme 8 and 9).³⁰ The calculations indicate that 1-oxo-2-



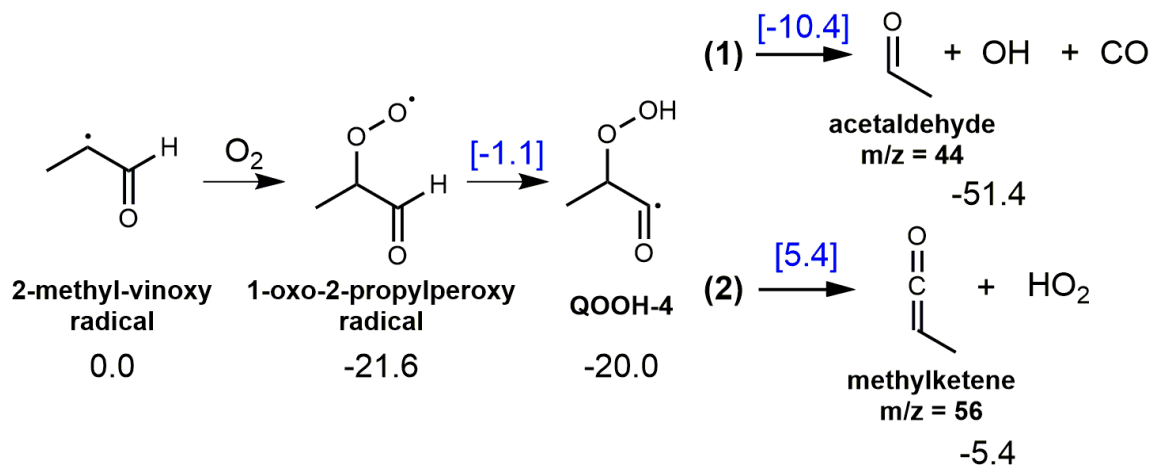
Scheme 7. Alternative decay pathway for 2-oxoethylperoxy radical (formed from vinoxy radical + O₂) to glyoxal + OH via the QOOH-3 intermediate. Energies (kcal mol⁻¹) are reported by Weidman *et al.*²⁹ (CCSD(T)/CBS).

propylperoxy will undergo a 1,4 H-atom transfer from the neighboring aldehyde via a submerged barrier ($20.5 \text{ kcal mol}^{-1}$) to form QOOH-4 (Scheme 8). QOOH-4 is anticipated to decompose primarily to acetaldehyde + OH + CO via a submerged barrier ($9.6 \text{ kcal mol}^{-1}$). Methylketene + HO₂ products are expected to be a minor channel due to a larger TS barrier to products ($25.4 \text{ kcal mol}^{-1}$). Alternatively, 1-oxo-2-propylperoxy radical can undergo direct unimolecular decay to acrolein + HO₂ via a barrier of $27.4 \text{ kcal mol}^{-1}$ (Scheme 9).

III. Methods

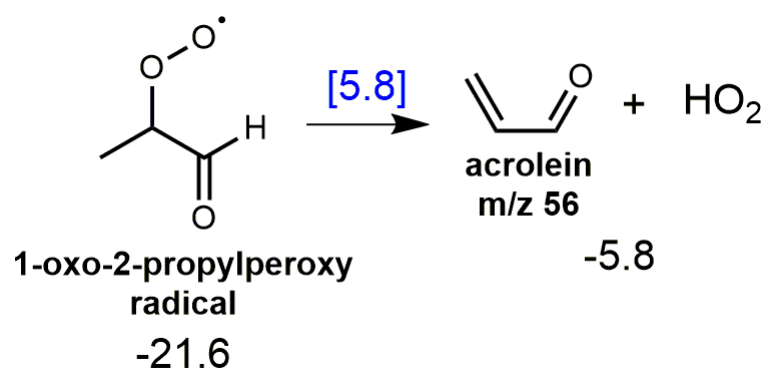
Experiments are performed using the Sandia Multiplexed Photoionization Mass Spectrometer (MPIMS) apparatus interfaced with the tunable-VUV radiation of the Chemical Dynamics Beamline (9.0.2) of the Advanced Light Source (Lawrence Berkeley National Laboratory).⁵¹⁻⁵² MVK-oxide and MACR-oxide Criegee intermediates are generated in separate experiments from the (Z/E)-1,3-diiodobut-2-ene or 1,3-diiodo-2-methylprop-1-ene precursor, respectively, as described by Barber *et al.*¹⁵ and Vansco *et al.*⁹.

The relevant precursor is entrained in a He flow using a pressure- and temperature-controlled glass bubbler (298 K, 100 torr). The precursor ($\sim 2\text{-}3 \times 10^{13} \text{ cm}^{-3}$), O₂, ($\sim 6.4 \times 10^{16} \text{ cm}^{-3}$), deuterated formic acid and bath gas (He) are delivered to a halocarbon wax-coated quartz reactor tube maintained at 298 K and 10 torr. Calibrated mass flow controllers are used to obtain specific mixing ratios of reactants. The gaseous mixture is photolyzed along the length of the quartz reactor tube with the 248 nm output of a KrF excimer laser (248 nm, 4 Hz). The laser energy is attenuated (to 100 mJ/pulse at laser output, $\sim 20 \text{ mJ/pulse}$ through the reactor) using fine meshes in order to reduce the Criegee intermediate concentration (max. $\sim 1 \times 10^{12} \text{ cm}^{-3}$) so that side removal



Scheme 8. Reaction of 2-methyl-vinoy radical with O₂ and subsequent decay to acetaldehyde + OH + CO, or methylketene + HO₂ via the QOOH-4 intermediate.

Energies (kcal mol⁻¹) are reported by Davis *et al.*³⁰ (CCSD(T)/CBS).



Scheme 9. Direct unimolecular decay of 1-oxo-2-propylperoxy radical (formed from 2-methyl-vinoy radical + O₂) to acrolein + HO₂. Energies (kcal mol⁻¹) are reported by Davis *et al.*³⁰ (CCSD(T)/CBS).

processes are minimized and the unimolecular reactions of the Criegee intermediates can be examined. The total gas flow rate through the reactor is sufficient such that the gas-mixture is entirely replenished between laser pulses. Pulsed UV-photolysis of the precursors generates a resonance-stabilized monoiodoalkenyl radical that subsequently reacts with O₂ to produce the Criegee intermediates.^{9, 15} The gas mixture is continuously sampled through an orifice on the side of the reactor tube and the resultant molecular beam is intercepted orthogonally with the tunable VUV radiation. The ions generated by VUV-ionization are pulse-extracted, accelerated orthogonally, and detected via time-of-flight mass spectrometry. Products resulting from MVK-oxide and MACR-oxide unimolecular decay and subsequent reaction with O₂ are investigated through experiments at a fixed ionization energy of 10.5 eV and photoionization efficiency (PIE) scans (9.0-11 eV). High-resolution mass spectrometry is utilized to identify stable products. For scavenger experiments, sufficient formic acid is added to the reactor tube such that bimolecular reaction with *anti*-MVK-oxide would compete with its unimolecular decay and prevent unimolecular decay products from being formed. Pseudo-first-order conditions were maintained throughout: [O₂] >> [(Z/E)-1,3-diiodobut-2-ene] and [deuterated formic acid] >> [MVK-oxide].

IV. Results

A. MVK-oxide

Specific conformers of MVK-oxide (*anti*) and MACR-oxide (*syn*) are predicted to rapidly decay via the dioxole pathway and generate radical products that include acetyl and vinyloxy (MVK-oxide, Scheme 3), and formyl and 2-methyl-vinyloxy radicals (MACR-oxide, Scheme 4). These radicals react rapidly with O₂ to form ROO (rate constants ca. 10⁻¹³-10⁻¹² cm³ s⁻¹, 298 K).^{28, 31-33} Typical concentrations of O₂ used in the experiment (ca.

6.4×10^{16} molecules cm^{-3}) facilitate rapid ROO formation (ca. μs) compared to the experimental time resolution.⁵¹ The resultant internally excited ROO are expected to undergo rapid unimolecular decay to closed-shell products along with transient OH or HO₂ radical co-products.^{27-30, 33} Stable products anticipated from MVK-oxide decay via the dioxole pathway (and subsequent reaction with O₂) include formaldehyde, ketene, glyoxal, and α -lactone (Section II, Schemes 5-7). Those expected from MACR-oxide decay via the dioxole pathway (and subsequent reaction with O₂) include acetaldehyde, methylketene, and acrolein (Section II, Schemes 8 and 9). The stable products are identified using MPIMS via a combination of high-resolution time-of-flight mass spectrometry, temporal profiles, and spectroscopically via photoionization efficiency (PIE) curves. Addition of a second O₂, following RO₂ isomerization to QOOH, is not anticipated to be substantial under our experimental conditions. Thus, we do not consider subsequent autoxidation products from any of the RO₂ discussed herein.

After photolytic generation of MVK-oxide, formaldehyde (m/z 30), ketene (m/z 42), and glyoxal (m/z 58) are identified as stable products in the MPIMS experiments. The temporal profile associated with m/z 30 (integrated over 8.4-11.0 eV) shows a fast rise followed by a constant photoionization signal consistent with the rapid formation of a stable product (Figure 1, top panel).

A Gaussian fit to m/z 30 of the mass spectrum (Figure 1, top panel inset) yields an exact mass of 30.011 ± 0.003 amu, consistent with the mass of formaldehyde (30.011 amu). The PIE curve of m/z 30 (open circles) integrated over the full kinetic time window (0-80 ms) is shown in the bottom panel of Figure 1. The appearance energy (10.88 eV)⁵⁴ and shape of the m/z 30 photoionization spectrum matches the absolute photoionization spectrum of formaldehyde (black line),⁵³ confirming its formation in the experiment. The experimental data is fit to the absolute photoionization spectrum of formaldehyde (black

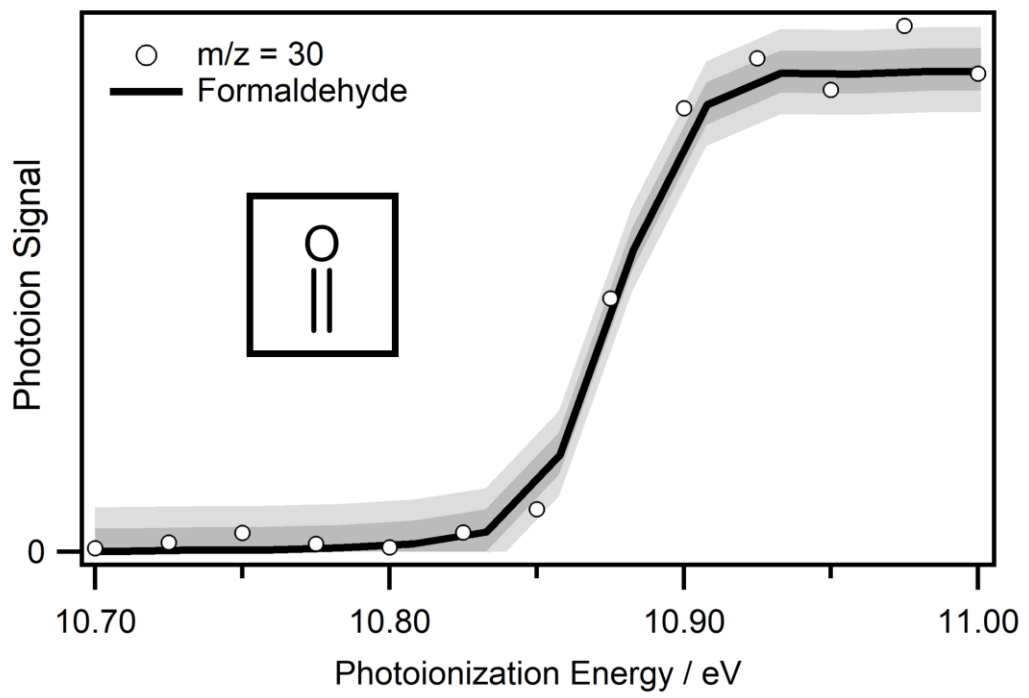
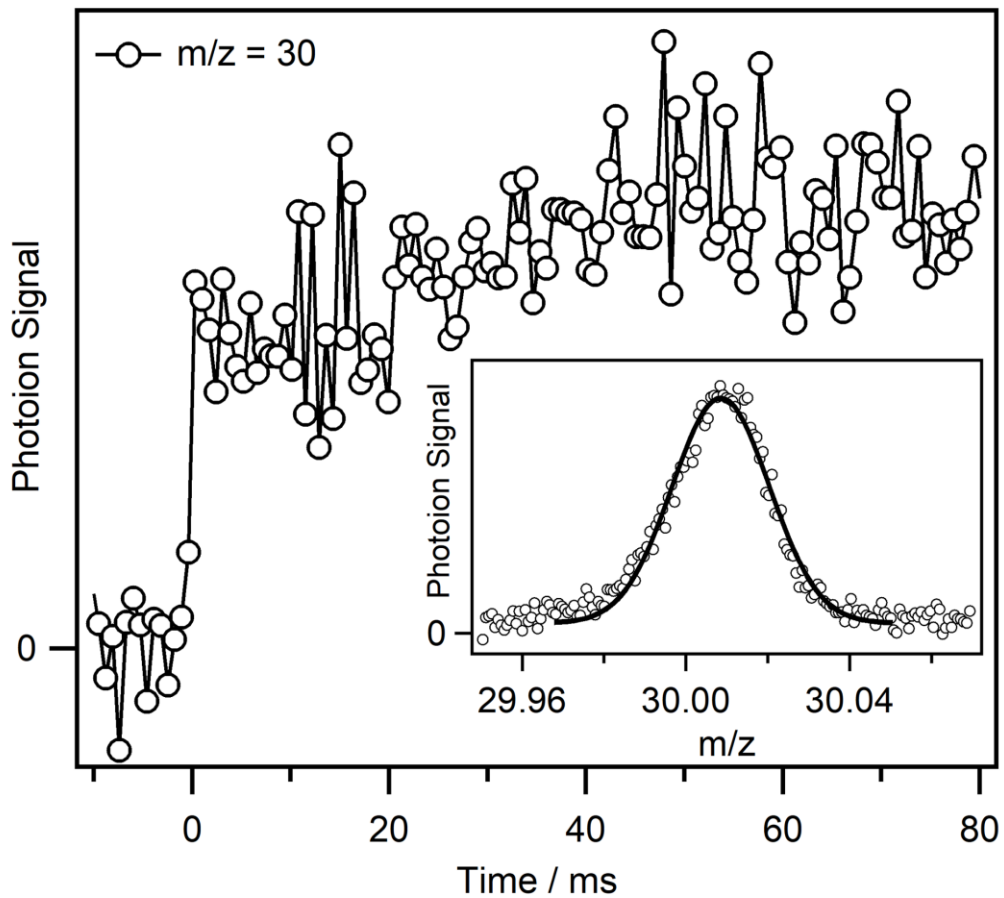


Figure 1. (Top) Temporal profile of m/z 30 mass channel integrated over the 8.0-11.0 eV photoionization energy range. (Inset) High resolution mass spectrum of the m/z 30 signal integrated over the full kinetic time window (0-80 ms) and photoionization energies (8.0-11.0 eV). (Bottom) PIE curve of m/z 30 (open circles) integrated over the full kinetic time window (0-80 ms) compared with the absolute photoionization spectrum of formaldehyde (black line).⁵³ The black lines shows the result of a least squares fit of the absolute photoionization spectrum of formaldehyde to the experimental m/z 30 data. The darker and lighter grey shaded regions represents 1σ and 2σ uncertainty in the fit, respectively.

line) via a least squares method. The uncertainty in the fit ($\pm \sigma$, $\pm 2\sigma$) is represented by shaded regions.

Ketene (m/z 42) is expected to be a minor product in the proposed mechanism. The temporal profile and high resolution mass spectrum of the m/z 42 mass channel (8.4-11.0 eV) is shown in Figure 2. The temporal profile shows rapid formation of a stable species upon photolysis. The width and asymmetry of the m/z 42 feature in the mass spectrum is indicative of multiple ionized species with the same nominal mass but different numbers of C and O atoms that results in partially resolved peaks. A sum of two Gaussian functions is used to fit the feature (black line) to extract the exact mass of each component. The fit yields an exact mass of 42.014 ± 0.004 amu (green line) and 42.050 ± 0.003 amu (blue line) consistent with the mass of ketene (42.011 amu) and C_3H_6 (42.047 amu), respectively. PIE curves associated with the two different mass regions are shown in Figure 3 (41.95-42.00 and 42.04-42.08 amu) to differentiate between the two species contributing to the m/z 42 photoionization signal.

The resultant PIE curves are distinctly different. The appearance energy and shape of the PIE curve associated with the lower mass region (bottom panel, green open circles, ca. 9.6 eV) matches the absolute photoionization spectrum of ketene (dark green line) below 10.5 eV.⁵⁵⁻⁵⁶ At higher photoionization energy (≥ 10.5 eV) the PIE curve changes due to photoionization of an interfering species. Integration of the higher mass region (42.04-42.08, top panel) results in a PIE curve that matches the interfering signal observed in the top panel. The mass of the interfering species (42.049 ± 0.003) is consistent with the chemical makeup of C_3H_6 (42.047) and is attributed to dissociative ionization of a larger species.

Glyoxal and α -lactone (m/z 58) products are predicted for the vinoxy radical + O_2 and acetyl radical + O_2 reactions, respectively. Glyoxal formation is unlikely given a high

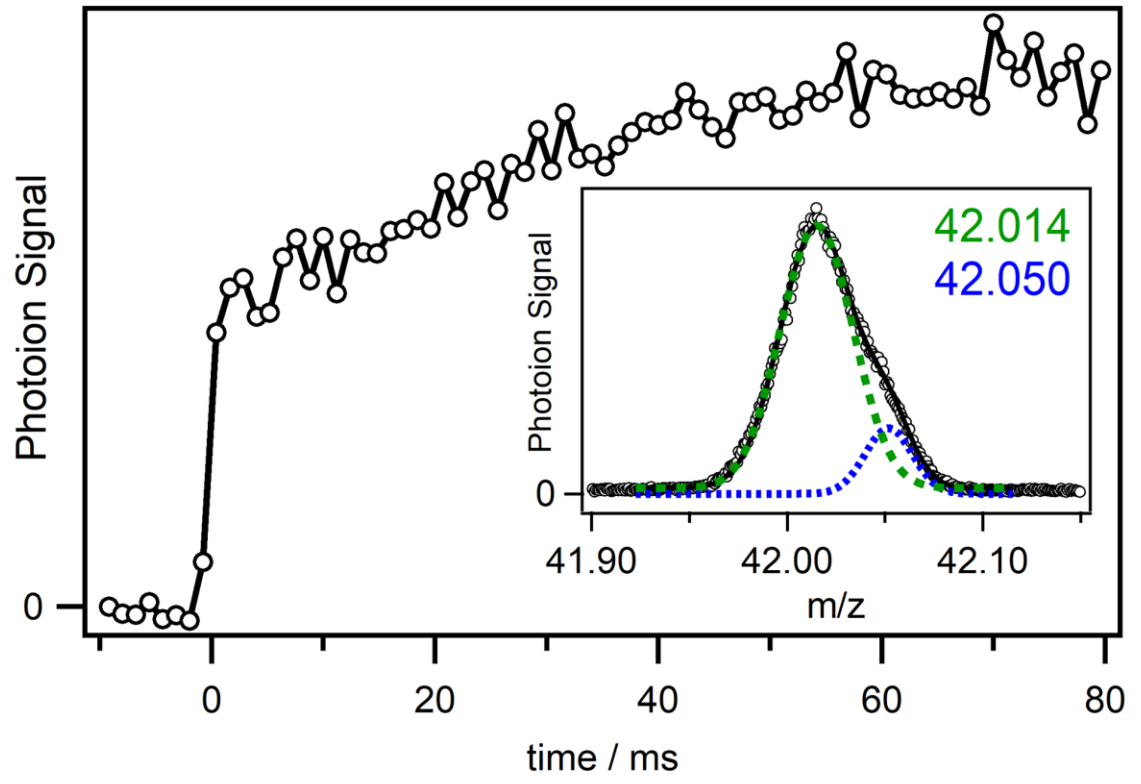


Figure 2. (Inset) High resolution mass spectrum integrated over the full kinetic time window (0-80 ms) and photoionization energies (8.0-11.0 eV) showing a partially resolved feature at m/z 42. The corresponding temporal profile (10.5 eV) shows rapid formation of a stable product following photolytic generation of MVK-oxide.

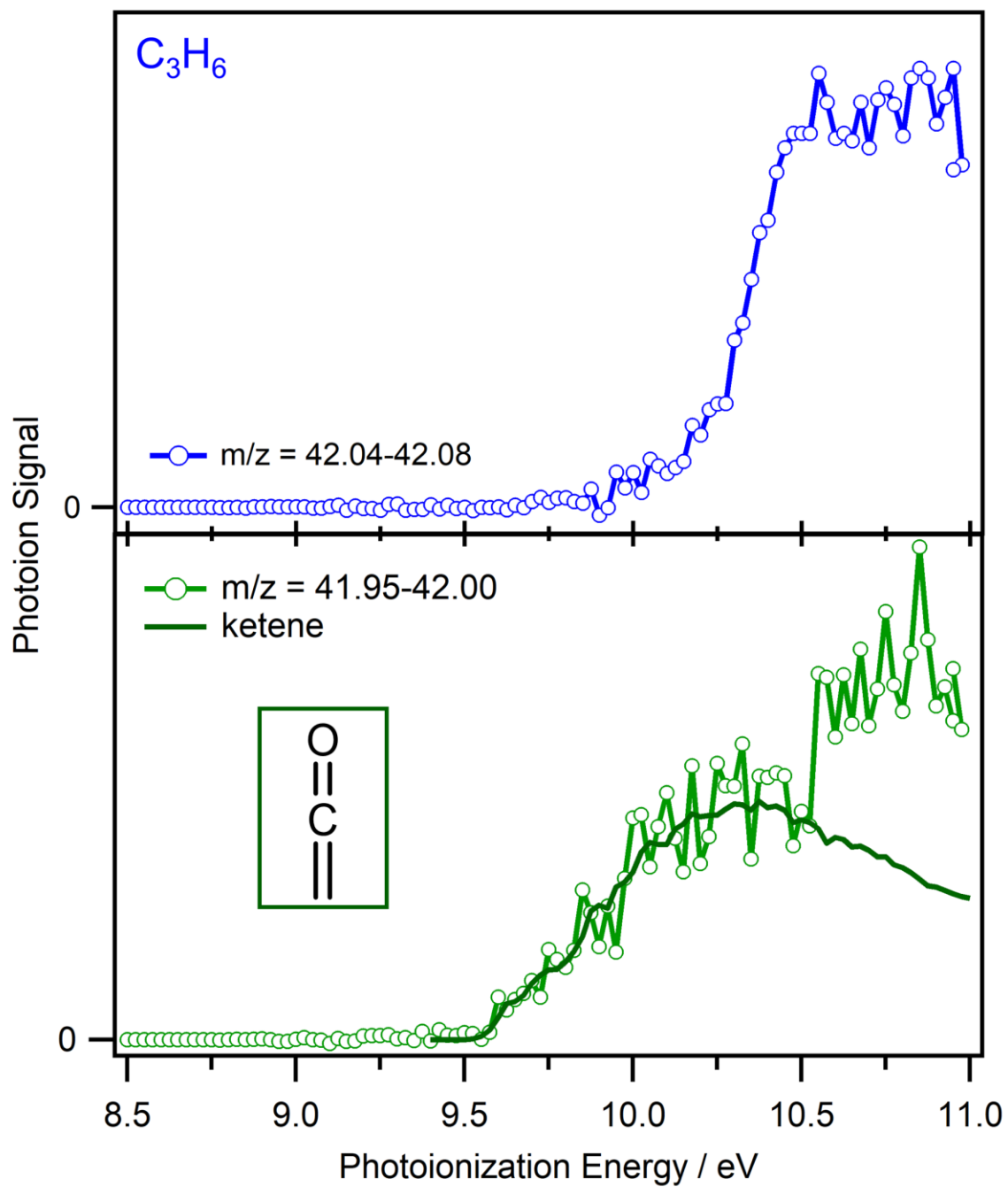


Figure 3. (Top) PIE curve associated with the 42.04-42.08 mass window (blue open circles). All traces are generated by integrating over the full kinetic time window (0-80 ms). (Lower panel) The PIE curve of the 41.95-42.00 mass window (green open circles) is consistent with the known PI spectrum of ketene is shown for comparison (dark green line).⁵⁵ Interference from an unidentified daughter ion is observed at higher photoionization energy (ca. 10.5 eV).

barrier to formation ($38.7 \text{ kcal mol}^{-1}$), while significant fragmentation of α -lactone to formaldehyde + CO is expected due to the exothermicity of the proposed mechanism. Nevertheless, a weak signal matching the exact mass of glyoxal and α -lactone (58.005) is observed. The temporal profile, high-resolution mass spectrum, and PIE curve of m/z 58 is shown in Figure 4. The width and asymmetry of the m/z 58 feature in the mass spectrum is indicative of multiple species with the same nominal mass but different numbers of C and O atoms contributing to the photoionization signal. A sum of two Gaussian functions is used to fit the feature (black line) and extract the exact mass of each component. The fit yields a peak position of $58.010 \pm 0.005 \text{ amu}$ (red line) and $58.043 \pm 0.003 \text{ amu}$ (purple line) consistent with the mass of glyoxal/ α -lactone (58.005 amu) and $\text{C}_3\text{H}_6\text{O}$ (58.042 amu), respectively. A PIE curve is associated with the lower mass region (57.95-58.00) is shown in the upper panel of Figure 4. The resultant PIE curve matches the onset (ca. 10.2 eV) and shape of the previously measured PI spectrum of glyoxal (black line).⁵⁵ No evidence of α -lactone is discernable in the PIE curve, consistent with the low yield of stabilization previously reported.^{28, 35-37, 39-40, 42}

B. MACR-oxide

Acetaldehyde (m/z 44), methylketene (m/z 56), and acrolein (m/z 56) are anticipated to be final products generated from the unimolecular decay of *syn*-MACR-oxide via the dioxole pathway and subsequent reaction of the radical products with O_2 (Section II, Schemes 8 and 9). The fast appearance of signal on the m/z 44 channel is consistent with rapid product formation, as shown in the temporal profile of m/z 44 (9.0-11.0 eV) in the top panel of Figure 5. The photoionization signal is constant at long reaction times indicating a stable spectral carrier. A high-resolution mass spectrum of m/z 44 is shown in the inset of Figure 5. A Gaussian fit to the feature yields a single peak at $44.028 \pm$

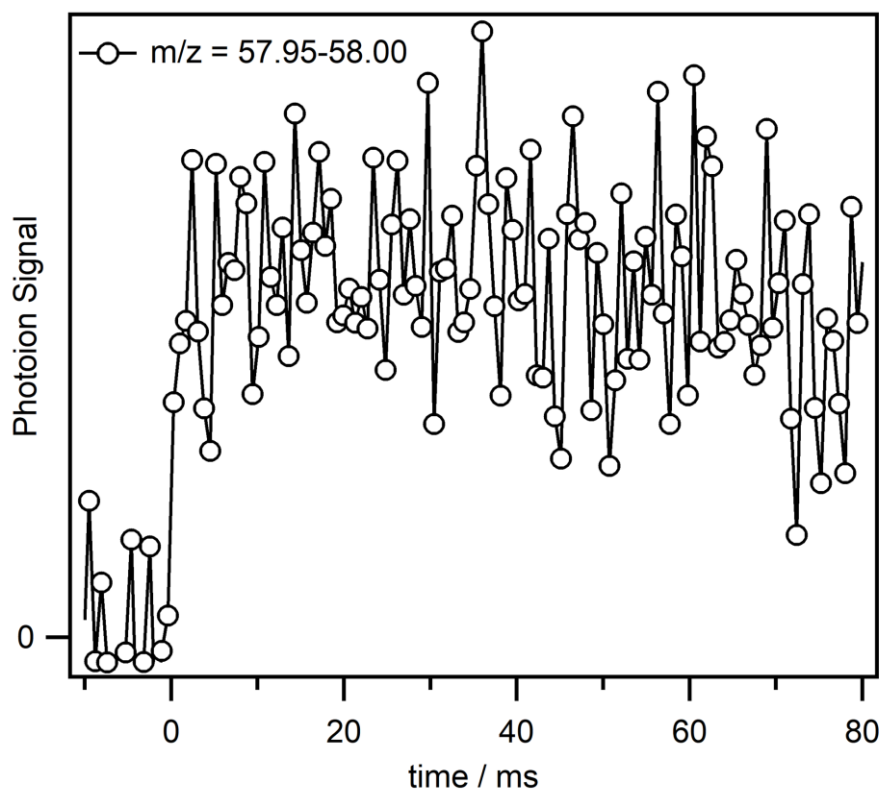
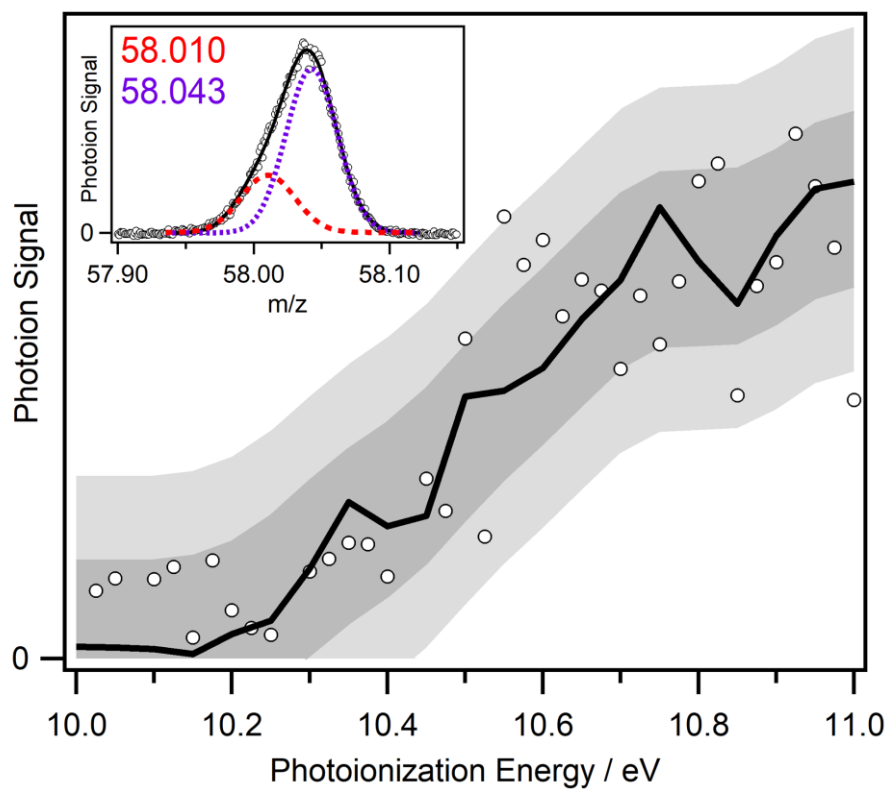


Figure 4. (Top, inset) High-resolution mass spectrum of the m/z 58 signal integrated over the full kinetic time window (0-80 ms) and photoionization energies (8.0-11.0 eV). (Top) Photoionization efficiency curve of m/z 58 (open circles) integrated over 57.95-58.00 amu and the full kinetic time window (0-80 ms) compared with the known photoionization spectrum of glyoxal (black line). (Bottom) Temporal profile of the m/z 57.95-58.00 mass region integrated over the 8.0-11.0 eV photoionization energy range.

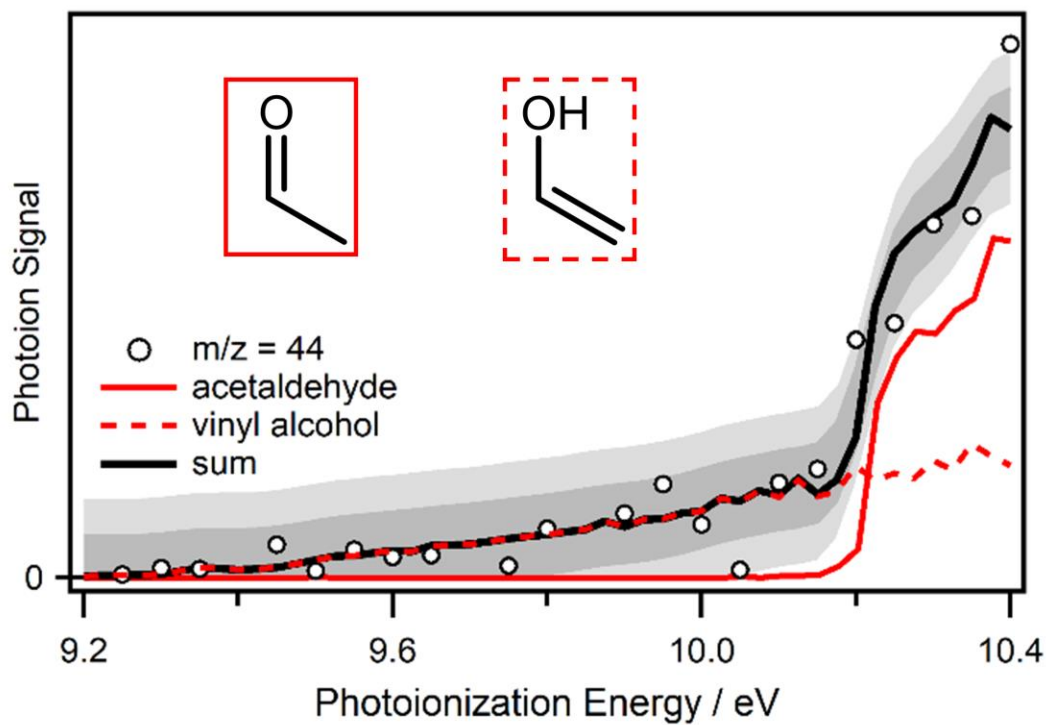
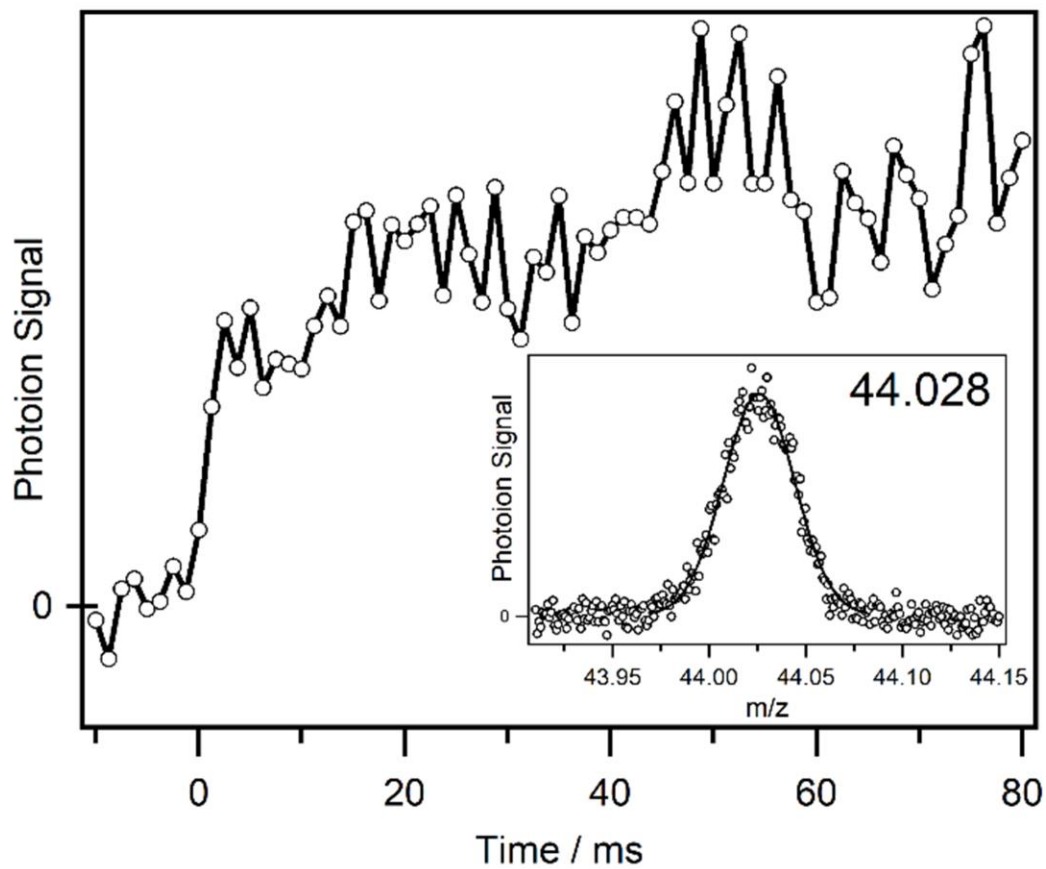


Figure 5. (Top, inset) High-resolution mass spectrum of the m/z 44 signal integrated over the full kinetic time window (0-80 ms) and photoionization energies (9.0-10.7 eV). (Top) Temporal profile of the m/z 44 over the 9.0-10.7 eV photoionization energy range. (Bottom) PIE curve of m/z 44 (open circles) integrated over the full kinetic time window (0-80 ms). The onset and shape of the spectrum at lower energies is consistent with the absolute photoionization spectrum of vinyl alcohol (red dashed line).⁵⁷ At higher energies (ca. 10.2 eV) a higher intensity feature is observed that is consistent with the absolute photoionization spectrum of acetaldehyde (red solid line).⁵⁸ The black line results from a least squares fit of the absolute photoionization spectra to the experimental $m/z = 44$ data. The darker and lighter grey shaded regions represent 1σ and 2σ uncertainty in the fit, respectively.

0.003, in accord with the chemical composition of acetaldehyde (CH_3CHCO , 44.026). Figure 5 (bottom) shows the PIE curve of m/z 44 integrated over the full kinetic time window (open circles, 0-80 ms), which reveals low and high energy components indicative of multiple species contributing to the photoionization signal.

Since only a single peak is observed in the high-resolution mass spectrum (44.028 amu), the species contributing to the PIE spectrum must have the same chemical composition and therefore are isomers. The onset (ca. 10.2 eV)⁵⁹ and shape of the higher energy component is consistent with the absolute photoionization spectrum of acetaldehyde (red solid line),⁵⁸ confirming its formation. The appearance energy (ca. 9.3 eV) and shape of the lower intensity feature agrees well with the absolute photoionization spectrum of vinyl alcohol (red dashed line).⁵⁷ Vinyl alcohol is likely generated directly from the exothermic unimolecular decay of QOOH-4 as the barrier for isomerization of acetaldehyde to vinyl alcohol is large (ca. 70 kcal mol⁻¹).⁶⁰ The experimental PIE curve is fit to the absolute spectra of acetaldehyde and vinyl alcohol by a least squares method and the resultant fit is shown in Figure 5 (black line). Uncertainty in the fit ($\pm \sigma$, $\pm 2\sigma$) is indicated by the shaded regions.

Rapid product formation is also observed on the m/z 56 mass channel. The temporal profile persists to long reaction times although it shows a slow decay after formation likely due to secondary chemistry (9.0-11.0 eV, Figure 6, top panel). A high-resolution mass spectrum of m/z 56 is shown in the inset of the top panel of Figure 6. A Gaussian fit to the feature results in a peak center of 56.029 ± 0.003 , which is consistent with the chemical composition of methylketene and acrolein ($\text{C}_3\text{H}_4\text{O}$, 56.026 amu). The corresponding PIE curve integrated over the full kinetic time window (0-80 ms) is shown in Figure 6 (bottom panel).

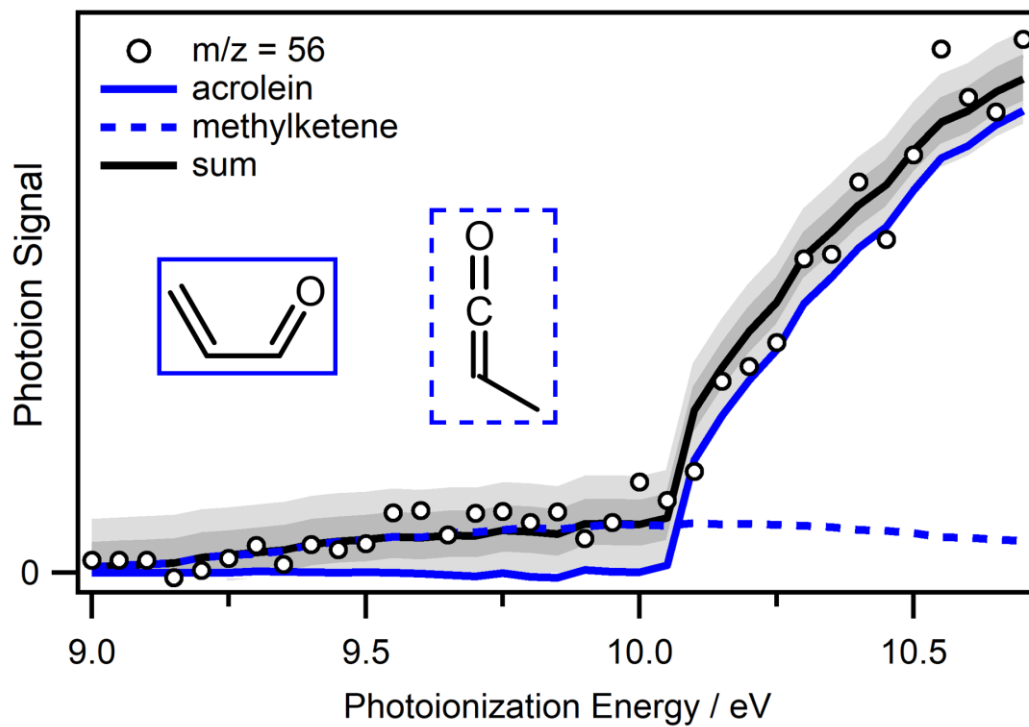
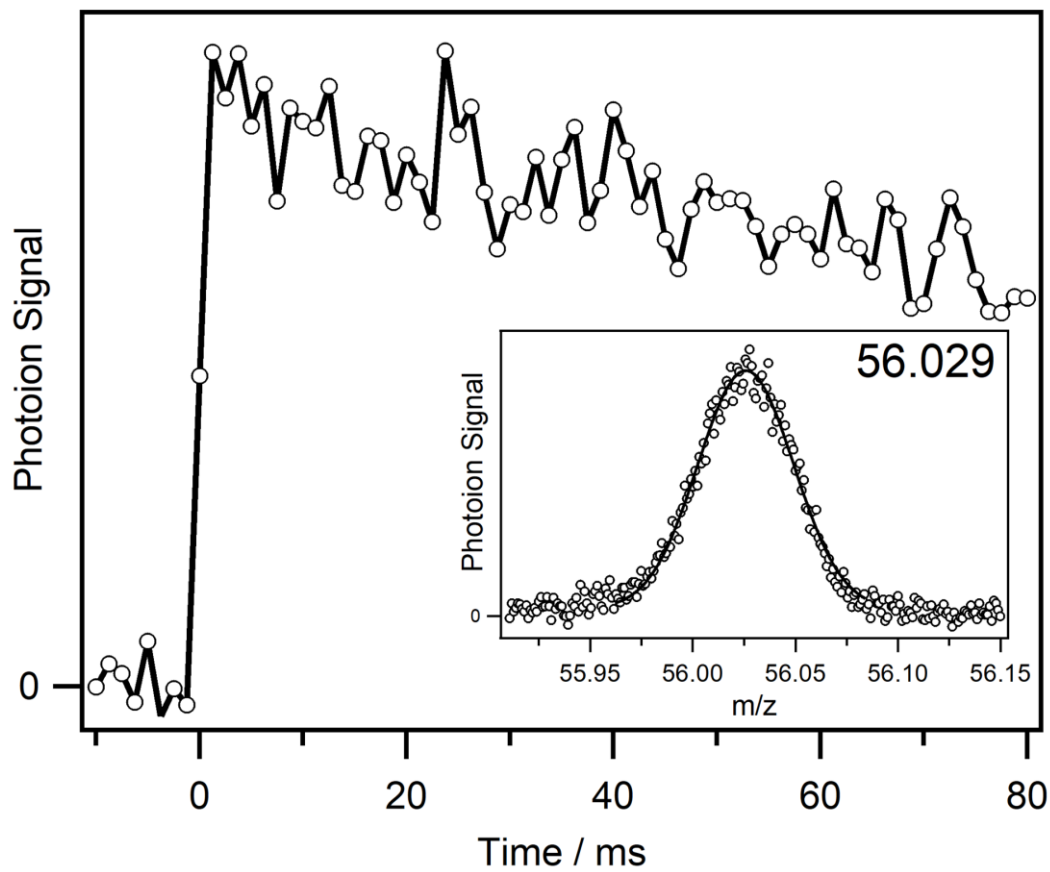


Figure 6. (Top, inset) High-resolution mass spectrum of the m/z 56 signal integrated over the full kinetic time window (0-80 ms) and photoionization energies (9.0-10.7 eV). (Top) Temporal profile of the m/z m/z 56 over the 9.0-10.7 eV photoionization energy range. (Bottom) PIE curve of m/z 56 (open circles) integrated over the full kinetic time window (0-80 ms). The appearance energy of the photoionization spectrum is consistent with the absolute photoionization spectrum of methylketene alcohol (blue dashed line). At higher energies (ca. 10.1 eV) a higher intensity feature is observed that is consistent with the absolute spectrum of acrolein (blue solid line). The black line shows the result of a least squares fit of the absolute photoionization spectra of acrolein and methylketene to the experimental m/z 56 data. The darker and lighter grey shaded regions represent 1σ and 2σ uncertainty in the fit, respectively.

Two components are apparent in the PIE curve: a lower intensity component at low photoionization energies and a higher intensity component at high photoionization energies. The lower intensity component and higher intensity component matches the onset and shape of the absolute PI spectra of methylketene (9.0 eV, blue dashed line)⁵⁵ and acrolein (10.1 eV, blue solid line),^{58, 61} respectively. The experimental data is fit to a sum of the methylketene and acrolein absolute photoionization spectra via a least squares method (black line). Uncertainty in the fit ($\pm \sigma$, $\pm 2\sigma$) is indicated by the shaded regions.

V. Discussion

A. Product Yields

High level *ab initio* calculations show that the unimolecular decay of the *anti*-MVK-oxide Criegee intermediate via the dioxole channel results in the generation of acetyl and vinyloxy radical products.¹⁵ An analogous pathway is predicted for *syn*-MACR-oxide leading to formyl and 2-methyl-vinyloxy radical products. Previous experimental and theoretical studies indicate that under the present experimental conditions, the radical products will rapidly undergo O₂ addition to generate ROO.²⁸⁻³⁰ These ROO are predicted to decay to closed shell products (Section II), which are identified using MPIMS (Section IV), along with transient OH or HO₂ radical co-products.

A quantitative analysis is conducted to determine the relative yields of the product channels identified from unimolecular decay of *anti*-MVK-oxide and *syn*-MACR-oxide to radical products, and subsequent ROO chemistry. The known absolute photoionization spectra of the products are scaled to fit the experimental PIE curves via a least squares method (Sec. IV and Figures S1-S3).^{53, 55, 57-58, 62} The resultant scaling factors correspond to the relative observed abundance of each product channel. Uncertainties

in the fits, and ultimately the relative product yields, are obtained by propagating the error associated with the least squares fitting method. Additional details of the analysis are provided in the Supporting Information (SI, Sec. S2, Figures S1-S3).

For the unimolecular decay of *anti*-MVK-oxide via the dioxole channel and subsequent ROO chemistry, formaldehyde, ketene and glyoxal are identified as principal products. The results from the product analysis indicate that formaldehyde + OH + CO is the dominant product channel ($88\% \pm 5\%$) with ketene + HO₂ and glyoxal + OH as minor product channels ($9\% \pm 1\%$ and $3\% \pm 1\%$, respectively). The resultant trend in product yields agrees well with theoretical predictions for the acetyl radical + O₂ and vinyloxy radical + O₂ reactions.²⁸⁻²⁹

For the unimolecular decay of *syn*-MACR-oxide via the dioxole channel and subsequent reaction of 2-methyl-vinyloxy radical product with O₂, acetaldehyde, vinyl alcohol, methylketene, and acrolein products are identified as main products (Figure 5 and 6). The minimum energy pathway predicted theoretically leads to acetaldehyde + CO + OH products. The total branching to this product channel, including the formation of vinyl alcohol ($9\% \pm 1\%$) is $46\% \pm 7\%$. Methylketene + HO₂ is found to be a minor product channel ($2\% \pm 1\%$), while acrolein + HO₂ is found to be the principal product channel ($52\% \pm 5\%$). This is the most direct route to products as acrolein + HO₂ is generated directly from the 1-oxo-2-propylperoxy radical (Scheme 9) and does not proceed through the QOOH intermediate. Master equation modeling of the 2-methyl-vinyloxy + O₂ reaction (Section C) indicates the acrolein product channel will not have an appreciable yield due to the high barrier (Scheme 9, 27.4 kcal mol⁻¹) for its formation. This suggests there may be a lower barrier pathway to acrolein + HO₂ products that has not been identified or an additional source of acrolein in the experiment. In the latter case, acetaldehyde + CO + OH would be the dominant product channel (ca. 96%).

B. Scavenger experiments

Additional experiments were conducted to robustly determine whether the stable products observed are generated from the dioxole pathway followed by reaction with O₂. These studies were conducted for the MVK-oxide Criegee intermediate only, for which the reaction rate coefficient with formic acid has recently been determined.¹⁶ Formic acid was introduced into the flow cell at sufficient concentration for its bimolecular reaction rate with MVK-oxide to surpass the predicted thermal unimolecular decay rate for *anti*-MVK-oxide (2140 s⁻¹, 298 K, 760 torr). As a result, *anti*-MVK-oxide will react more quickly with formic acid than undergo unimolecular decay, resulting in a decrease in the product yields from the dioxole pathway. We assume that *anti*-MVK-oxide reacts with formic acid at a similar rate to *syn*-MVK-oxide and alkyl-substituted Criegee intermediates (ca. 10⁻¹⁰ cm³ s⁻¹).^{16, 63}

Figure 7 shows temporal profiles of the m/z 30 channel (formaldehyde) measured using a photoionization energy of 11.0 eV. The temporal profile shows prompt formation of m/z 30 followed by a slow growth in signal. Upon introduction of formic acid, the m/z 30 signal is significantly reduced, leaving a prompt signal that persists to long kinetic time. The fraction of the m/z 30 signal remaining upon introduction of formic acid at specific concentrations is shown in the top panel of Figure 7 (solid circles). This is obtained by normalizing the integrated m/z 30 signal by the integrated I-atom (m/z 127) signal to account for experimental fluctuations, e.g. laser power or precursor concentration. Further, the integrated m/z 30 signal recorded in the absence of formic acid is set to 1 (black solid circle). A simple model is used to predict the fraction *f* of m/z 30 that would remain with increasing formic acid concentration (dashed line, top panel) according to equation (1):

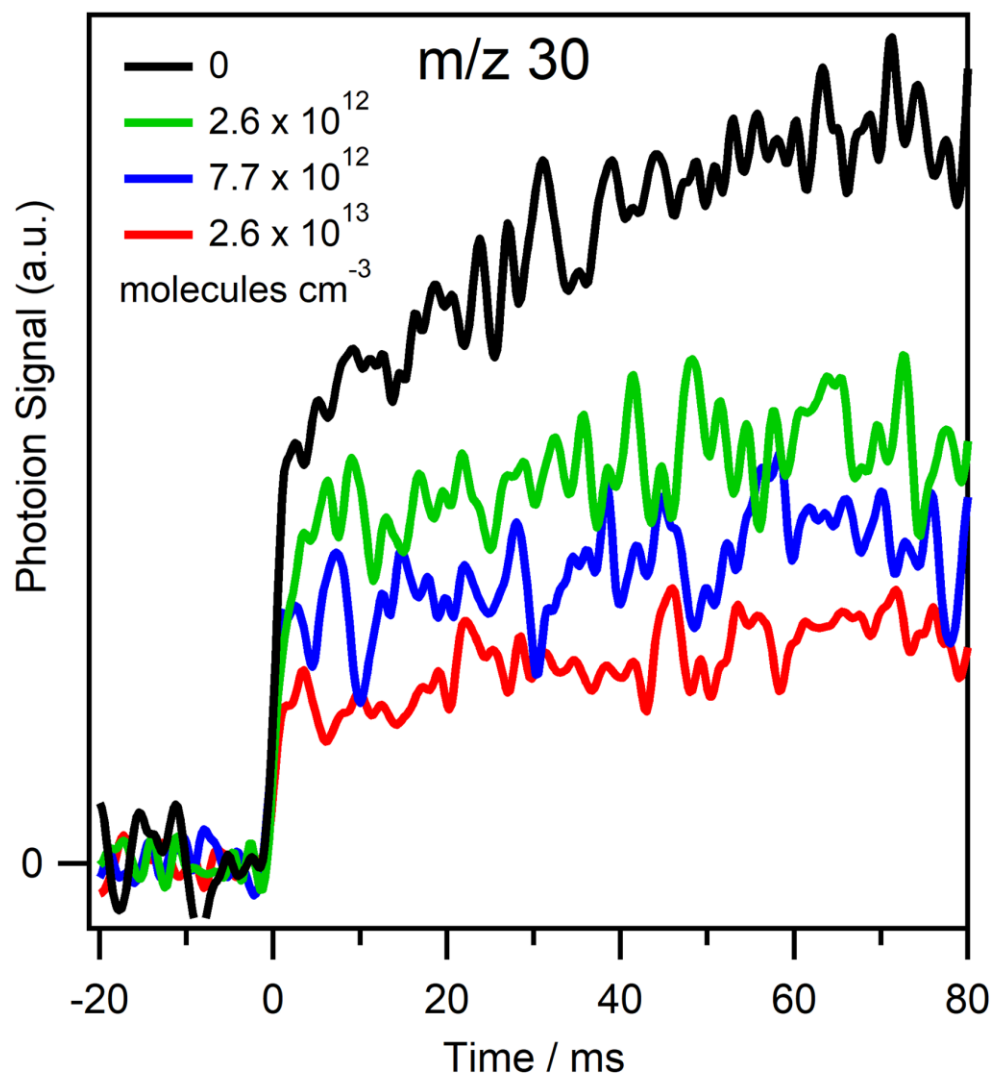
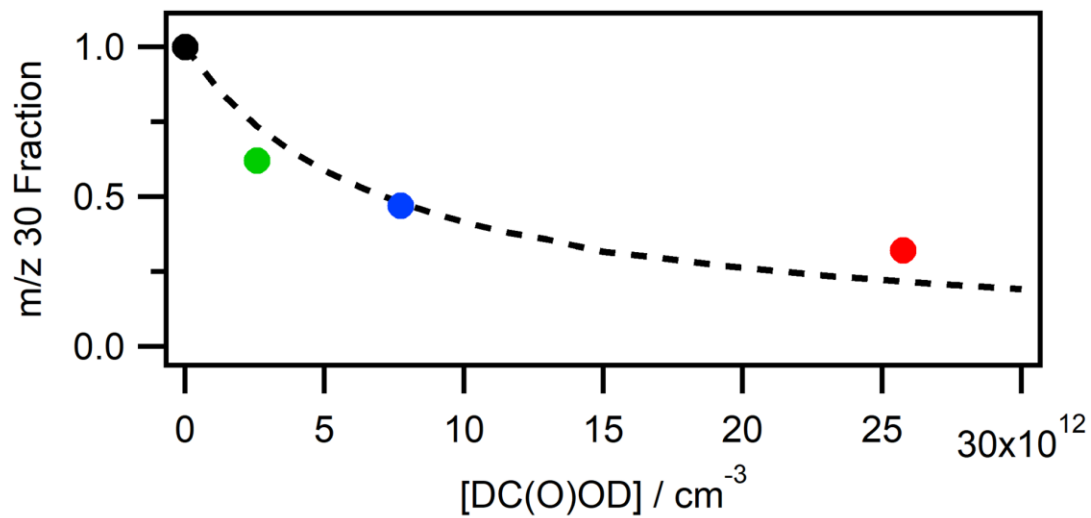


Figure 7. (Bottom) Temporal profiles of m/z 30 (11.0 eV) measured at varying formic acid concentrations. (Top) Fraction of m/z 30 signal remaining versus formic acid concentration compared to a kinetic model (dashed line).

$$(1) \quad f = \frac{r_{uni}}{r_{uni} + r_{acid}}$$

Here, r_{uni} is the thermal decay rate for *anti*-MVK-oxide (2140 s^{-1})¹⁵ and r_{acid} is the effective rate of reaction between *anti*-MVK-oxide and formic acid at a specific concentration. The model assumes that *m/z* 30 arises solely from unimolecular decay of *anti*-MVK-oxide to radical products and subsequent peroxy radical chemistry, the thermal decay rate (298 K) of *anti*-MVK-oxide is 2140 s^{-1} , and the rate constant for the reaction of *anti*-MVK-oxide with formic acid is the same as that for *syn*-MVK-oxide ($3.0 \times 10^{-10} \text{ cm}^3 \text{ s}^{-1}$). The results obtained agree reasonably well with the simple model.

There may be an additional source of formaldehyde that gives rise to the slow growth in signal on the *m/z* 30 channel. One possibility is that secondary chemistry associated with products from unimolecular decay of *syn*-MVK-oxide may produce formaldehyde. However, even at the lowest formic acid concentration used in the experiment ($2.6 \times 10^{12} \text{ molecules cm}^{-3}$, green), more than 95% of *syn*-MVK-oxide is expected to undergo bimolecular reaction with acid rather than unimolecular decay.

If there is another source of formaldehyde, the product yield to the formaldehyde + OH + CO channel would be overestimated. For example, if 50% of the *m/z* 30 signal is from a different source, the formaldehyde + OH + CO channel will be less dominant, but still the major product channel ($79 \pm 3\%$), while the ketene + HO₂ and glyoxal + OH product channels would become more significant ($16 \pm 1\%$ and $5 \pm 1\%$, respectively). Unfortunately, addition of formic acid results in formation of a daughter ion at energies above the ionization energy of ketene on the *m/z* 42 mass channel that precludes scavenger studies of the ketene product channel.

C. Atmospheric implications

Rapid unimolecular decay of *anti*-MVK-oxide and *syn*-MACR-oxide to dioxole (2150 and 2500 s⁻¹, respectively; 298 K, 760 torr)^{15, 17} and subsequent formation of radical products is expected to be the dominant sink for these Criegee intermediates under atmospheric conditions.¹⁶ Under our low pressure experimental conditions (298 K, 10 torr), the radical products react with O₂ to form ROO, which undergoes further unimolecular decay via QOOH intermediates to yield stable carbonyl products that are detected and an OH or HO₂ radical co-product.²⁷⁻³⁰ The radical products are expected to have a similar fate under atmospheric conditions (298 K, 760 torr) in pristine locations (low NO_x concentrations).⁶⁴⁻⁶⁵ Again, the radicals will react rapidly with O₂ to form ROO, which can undergo unimolecular decay to stable carbonyl products with an OH or HO₂ radical co-product. Alternatively, the ROO can be collisionally stabilized and thermally decay on a longer timescale (minutes), and/or undergo bimolecular reactions.⁶⁶⁻⁶⁷

Previous experiment and theory has shown that the acetyl radical + O₂ reaction exhibits a significant pressure dependence.²⁸ The OH yield drops from near unity at low pressure to ~4% at atmospheric pressure as a result of collisional stabilization of ROO at higher pressures.²⁸ A similar pressure dependence has been predicted theoretically by Kuwata *et al.*⁶⁸ for the vinoxy and 2-methyl-vinoxy + O₂ reactions, resulting in OH yields at atmospheric pressure of 25% and 5%, respectively.⁶⁸ More recent high-level electronic structure calculations by Weidman *et al.*²⁹ and Davis *et al.*³⁰ predict higher barriers for ROO dissociation back to reactants (vinoxy radical + O₂) than earlier calculations⁶⁸ and similar barriers for H-atom transfer leading to the QOOH intermediates. The higher barriers suggest that the previously computed OH yields⁶⁸ for these reactions may be overestimated. Therefore, we carried out master equation simulations (MESMER, SI Sec. S3)⁶⁹ to reinvestigate the OH yields from these reactions

under atmospheric conditions. We find that the higher barriers^{29,30} result in lower OH yields from the vinoxy + O₂ (5%) and 2-methyl-vinoxy + O₂ (2%) reactions under atmospheric conditions (298 K, 760 torr).

Given the large abundance of isoprene emitted into the atmosphere, we wanted to assess the potential atmospheric yield of OH radicals arising from the dioxole pathway and subsequent reaction of its radical products with O₂. Specifically, we estimate the OH yield derived from unimolecular decay of *anti*-MVK-oxide and *syn*-MACR-oxide, and subsequent peroxy radical chemistry under atmospheric conditions. This is then compared to the total OH yield from isoprene ozonolysis. The OH yield from isoprene ozonolysis has been reported from a variety of indirect methods that include the use of OH scavengers and tracers such as methylcyclohexane,⁷⁰ cyclohexane,⁷¹⁻⁷⁴ CO,⁷⁵⁻⁷⁶ trimethylbenzene,^{74, 77-78} as well as a limited number of direct OH measurements by laser-induced fluorescence,^{74, 79} and a comprehensive model that used experimental measurements as constraints in determining the OH yield.² The reported OH yields vary considerably (19% to 68%). Here, we compare to the IUPAC recommended OH yield from isoprene ozonolysis of 25%.⁸⁰

The OH yield from the dioxole pathway and subsequent peroxy radical chemistry is estimated by combining the yields of MVK-oxide and MACR-oxide from isoprene ozonolysis (23% and 19%, respectively),² the predicted reactive fluxes through the dioxole channel (42% and 25%, respectively),¹⁸⁻¹⁹ and the predicted OH yields from the respective radical + O₂ reactions under atmospheric conditions (see above). The resultant OH yield accounts for only ca. 4% of the total OH radicals produced from isoprene ozonolysis under atmospheric conditions. This estimate assumes that the radicals generated from the exothermic dioxole pathway are fully thermalized prior to reaction with O₂ and formation of ROO. If ROO is formed internally excited, the

estimated OH yield from the dioxole pathway may be underestimated. Thus, we conclude that dominant source of OH radicals from isoprene ozonolysis under atmospheric conditions is thermal unimolecular decay of *syn*-MVK-oxide via a 1,4 H-atom transfer mechanism (33 s^{-1} at 298 K, 760 torr).^{2, 15, 17}

Current atmospheric models utilizing the Master Chemical Mechanism (MCM)⁸¹ for tropospheric degradation of primary emitted volatile organic compounds indicate that decomposition of Criegee intermediates derived from isoprene ozonolysis is a substantial source of OH radicals, even when compared to all atmospheric sources of OH production. The OH production is predicted to be greatest over heavily forested regions including the Amazon, in particular at nighttime.⁷ The present work on the dioxole unimolecular pathway and subsequent bimolecular reactions of the radicals produced with molecular oxygen may extend the possible sources of atmospheric OH radicals. While the stabilization and bimolecular reactions of ROO with NO_x , HO_2 and other RO_2 are included in the current MCM, the unimolecular decay processes discussed in this work are not. Future work will assess if inclusion of these reaction mechanisms significantly impacts the generation of OH radicals from isoprene ozonolysis.

In addition, the production of ketene and methyl ketene may be substantial from ozonolysis of isoprene, and are estimated to be on the order of 2 Gg and 0.5 Gg, respectively. Given a rough estimate for the atmospheric lifetime of ketene (e.g. 5-15 hours) and its rate of reaction with OH (ca. $10^{-11} \text{ cm}^3 \text{ molecule}^{-1} \text{ s}^{-1}$),⁸² we anticipate that ketene and methylketene will be elevated close to the emission source of isoprene. Thus, ketene emission is a potential marker for ozonolysis of isoprene and other dialkenes, including acyclic monoterpenes, ocimene, and myrcene. In addition, ketene

has a well-defined IR absorption spectrum and can be a useful tracer in chamber studies.⁸³

VI. Conclusions

MVK-oxide and MACR-oxide, the four-carbon unsaturated Criegee intermediates generated in isoprene ozonolysis, have been photolytically generated in a flow cell (298 K, 10 torr) in the presence of O₂. Specific conformational forms of MVK-oxide (*anti*) and MACR-oxide (*syn*) with the vinyl substituent adjacent to the terminal O atom can rapidly isomerize via an exothermic electrocyclic ring closure mechanism to form a 5-membered cyclic peroxide, known as dioxole.^{15, 17-19} Dioxole is formed with sufficient internal excitation to undergo rapid unimolecular decay to oxygenated hydrocarbon radicals, producing acetyl and vinoxy radicals from MVK-oxide and formyl and 2-methyl-vinoxy radicals from MACR-oxide. In the presence of O₂ under our laboratory conditions, the newly formed radicals quickly react with O₂ in a barrierless, exothermic reaction that yields peroxy radicals.²⁷⁻³⁰ The peroxy radicals undergo H-atom transfer to form QOOH intermediates, which decay via submerged barriers to form closed shell carbonyl species.²⁸⁻³⁰ The resultant stable carbonyl products are detected by MPIMS, providing the first experimental evidence of the dioxole unimolecular decay pathway for the four-carbon unsaturated Criegee intermediates from isoprene ozonolysis. The main products identified in the unimolecular decay of *anti*-MVK-oxide and subsequent reaction of acetyl and vinoxy radicals with O₂ are formaldehyde (88 ± 5%), ketene (9 ± 1%) and glyoxal (3 ± 1%). Those identified from the unimolecular decay of *syn*-MACR-oxide and subsequent reaction of 2-methyl-vinoxy radicals with O₂ are acetaldehyde (37 ± 7%), vinyl alcohol (9 ± 1%), methylketene (2 ± 1%), and acrolein (52 ± 6%). In separate experiments, sufficient formic acid is added to ensure that its bimolecular reaction with

anti-MVK-oxide competes with unimolecular decay, thereby reducing the yield of products arising from unimolecular decay and subsequent reaction with O₂. Bimolecular reaction with formic acid is shown to decrease the yield of formaldehyde products arising from unimolecular decay of MVK-oxide. In addition to the stable carbonyl products that are observed, the peroxy chemistry also results in OH or HO₂ radical co-products with pressure-dependent yields.

Supporting Information

Supporting information includes computed stationary point geometries and zero point corrected energies, detailed description of the product branching analysis, and MESMER input files.

Acknowledgements

This research was supported by the U.S. Department of Energy-Basic Energy Sciences under grant DE-FG02-87ER13792 (MIL). This material is also based upon work supported by the Division of Chemical Sciences, Geosciences and Biosciences, Office of Basic Energy Sciences (BES), U.S. Department of Energy (USDOE). Sandia National Laboratories is a multimission laboratory managed and operated by National Technology and Engineering Solutions of Sandia, LLC., a wholly owned subsidiary of Honeywell International, Inc., for the USDOE's National Nuclear Security Administration under contract DE-NA0003525. This paper describes objective technical results and analysis. Any subjective views or opinions that might be expressed in the paper do not necessarily represent the views of the USDOE or the United States Government. This material is based in part on research at Argonne supported by the U.S. Department of Energy, Office of Science, Office of Basic Energy Sciences, Division of Chemical Sciences, Geosciences, and Biosciences under Contract No. DE-AC02-06CH11357.

The Advanced Light Source is supported by the Director, Office of Science, BES/USDOE under Contract DE- AC02-05CH11231 at Lawrence Berkeley National Laboratory. This research was carried out in part by the Jet Propulsion Laboratory, California Institute of Technology, under contract with the National Aeronautics and Space Administration (NASA), supported by the Upper Atmosphere Research and Tropospheric Chemistry program. The contributions of RLC and KLZ were in part supported by appointments to the NASA Postdoctoral Program at the NASA Jet Propulsion Laboratory, administered by Universities Space Research Association under contract with NASA. PJW thanks the NSF (CHE-1902509). DES and MAHK thank NERC (grant codes-NE/K004905/1), Bristol ChemLabS and Primary Science Teaching Trust under whose auspices various aspects of this work was funded. California Institute of Technology. © 2019. All rights reserved.

References

1. Sindelarova, K.; Granier, C.; Bouarar, I.; Guenther, A.; Tilmes, S.; Stavrou, T.; Müller, J. F.; Kuhn, U.; Stefani, P.; Knorr, W. Global Data Set of Biogenic VOC Emissions calculated by the MEGAN Model Over the Last 30 years. *Atmos. Chem. Phys.* **2014**, *14*, 9317-9341.
2. Nguyen, T. B.; Tyndall, G. S.; Crouse, J. D.; Teng, A. P.; Bates, K. H.; Schwantes, R. H.; Coggon, M. M.; Zhang, L.; Feiner, P.; Miller, D. O., et al. Atmospheric fates of Criegee intermediates in the ozonolysis of isoprene. *Phys. Chem. Chem. Phys.* **2016**, *18*, 10241-10254.
3. Finlayson-Pitts, B. J.; Pitts, J. N., *Chemistry of the Upper and Lower Atmosphere*. Academic Press: San Diego, 2000.
4. Lester, M. I.; Klippenstein, S. J. Unimolecular Decay of Criegee Intermediates to OH Radical Products: Prompt and Thermal Decay Processes. *Acc. Chem. Res.* **2018**, *51*, 978-985.
5. Emmerson, K. M.; Carslaw, N.; Carslaw, D. C.; Lee, J. D.; McFiggans, G.; Bloss, W. J.; Gravestock, T.; Heard, D. E.; Hopkins, J.; Ingham, T., et al. Free radical modelling studies during the UK TORCH Campaign in Summer 2003. *Atmos. Chem. Phys.* **2007**, *7*, 167-181.
6. Emmerson, K. M.; Carslaw, N. Night-time radical chemistry during the TORCH campaign. *Atmos. Environ.* **2009**, *43*, 3220-3226.
7. Khan, M. A. H.; Percival, C. J.; Caravan, R. L.; Taatjes, C. A.; Shallcross, D. E. Criegee intermediates and their impacts on the troposphere. *Environ. Sci.: Process. Impacts* **2018**, *20*, 437-453.
8. Vansco, M. F.; Marchetti, B.; Lester, M. I. Electronic spectroscopy of methyl vinyl ketone oxide: A four-carbon unsaturated Criegee intermediate from isoprene ozonolysis. *J. Chem. Phys.* **2018**, *149*, 244309.
9. Vansco, M. F.; Marchetti, B.; Trongsiwat, N.; Wang, G.; Bhagde, T.; Walsh, P. J.; Klippenstein, S. J.; Lester, M. I. Synthesis, electronic spectroscopy and photochemistry of methacrolein oxide: A four carbon unsaturated Criegee intermediate from isoprene ozonolysis. *J. Am. Chem. Soc.* **2019**, *141*, 15058-15069.
10. Welz, O.; Savee, J. D.; Osborn, D. L.; Vasu, S. S.; Percival, C. J.; Shallcross, D. E.; Taatjes, C. A. Direct Kinetic Measurements of Criegee Intermediate (CH₂OO) Formed by Reaction of CH₂I with O₂. *Science* **2012**, *335*, 204-207.
11. Beames, J. M.; Liu, F.; Lu, L.; Lester, M. I. Ultraviolet Spectrum and Photochemistry of the Simplest Criegee Intermediate CH₂OO. *J. Am. Chem. Soc.* **2012**, *134*, 20045-20048.
12. Taatjes, C. A.; Welz, O.; Eskola, A. J.; Savee, J. D.; Scheer, A. M.; Shallcross, D. E.; Rotavera, B.; Lee, E. P. F.; Dyke, J. M.; Mok, D. K. W., et al. Direct Measurements of Conformer-Dependent Reactivity of the Criegee Intermediate CH₃CHOO. *Science* **2013**, *340*, 177-180.

13. Beames, J. M.; Liu, F.; Lu, L.; Lester, M. I. UV spectroscopic characterization of an alkyl substituted Criegee intermediate CH_3CHOO . *J. Chem. Phys.* **2013**, *138*, 244307.
14. Liu, F.; Beames, J. M.; Green, A. M.; Lester, M. I. UV Spectroscopic Characterization of Dimethyl- and Ethyl-Substituted Carbonyl Oxides. *J. Phys. Chem. A* **2014**, *118*, 2298-2306.
15. Barber, V. P.; Pandit, S.; Green, A. M.; Trongsrirawat, N.; Walsh, P. J.; Klippenstein, S. J.; Lester, M. I. Four-Carbon Criegee Intermediate from Isoprene Ozonolysis: Methyl Vinyl Ketone Oxide Synthesis, Infrared Spectrum, and OH Production. *J. Am. Chem. Soc.* **2018**, *140*, 10866-10880.
16. Caravan, R. L.; Vansco, M. F.; Au, K.; Khan, M. A. H.; Li, Y.-L.; Winberg, F. A. F.; Zuraski, K.; Lin, Y.-H.; Chao, W.; Trongsrirawat, N., et al. First direct kinetic measurements and theoretical predictions of an isoprene-derived Criegee intermediate. *Proc. Natl. Acad. Sci.* **2020**, *117*, 9733-9740.
17. Vereecken, L.; Novelli, A.; Taraborrelli, D. Unimolecular decay strongly limits the atmospheric impact of Criegee intermediates. *Phys. Chem. Chem. Phys.* **2017**, *19*, 31599-31612.
18. Kuwata, K. T.; Valin, L. C.; Converse, A. D. Quantum Chemical and Master Equation Studies of the Methyl Vinyl Carbonyl Oxides Formed in Isoprene Ozonolysis. *J. Phys. Chem. A* **2005**, *109*, 10725.
19. Kuwata, K. T.; Valin, L. C. Quantum Chemical and RRKM/Master Equation Studies of Isoprene Ozonolysis: Methacrolein and Methacrolein Oxide. *Chem. Phys. Lett.* **2008**, *451*, 186-191.
20. Zhang, D.; Lei, W.; Zhang, R. Mechanism of OH formation from ozonolysis of isoprene: kinetics and product yields. *Chem. Phys. Lett.* **2002**, *358*, 171-179.
21. Stephenson, T. A.; Lester, M. I. Unimolecular decay dynamics of Criegee intermediates: Energy-resolved rates, thermal rates, and their atmospheric impact. *Int. Rev. Phys. Chem.* **2020**, *39*, 1-33.
22. Anglada, J. M.; Solé, A. Impact of the water dimer on the atmospheric reactivity of carbonyl oxides. *Phys. Chem. Chem. Phys.* **2016**, *18*, 17698-17712.
23. Welz, O.; Eskola, A. J.; Sheps, L.; Rotavera, B.; Savee, J. D.; Scheer, A. M.; Osborn, D. L.; Lowe, D.; Murray Booth, A.; Xiao, P., et al. Rate Coefficients of C1 and C2 Criegee Intermediate Reactions with Formic and Acetic Acid Near the Collision Limit: Direct Kinetics Measurements and Atmospheric Implications. *Angew. Chem. Int. Ed.* **2014**, *53*, 4547-4550.
24. Chhantyal-Pun, R.; Davey, A.; Shallcross, D. E.; Percival, C. J.; Orr-Ewing, A. J. A kinetic study of the CH_2OO Criegee intermediate self-reaction, reaction with SO_2 and unimolecular reaction using cavity ring-down spectroscopy. *Phys. Chem. Chem. Phys.* **2015**, *17*, 3617-3626.
25. Vereecken, L.; Harder, H.; Novelli, A. The reaction of Criegee intermediates with NO , RO_2 , and SO_2 , and their fate in the atmosphere. *Phys. Chem. Chem. Phys.* **2012**, *14*, 14682-14695.
26. Vereecken, L. The reaction of Criegee intermediates with acids and enols. *Phys. Chem. Chem. Phys.* **2017**, *19*, 28630-28640.
27. Martínez-Ávila, M.; Peiró-García, J.; Ramírez-Ramírez, V. M.; Ignacio, N.-G. Ab initio study on the mechanism of the $\text{HCO} + \text{O}_2 \rightarrow \text{HO}_2 + \text{CO}$ reaction. *Chem. Phys. Lett.* **2003**, *370*, 313-318.
28. Carr, S. A.; Glowacki, D. R.; Liang, C.-H.; Baeza-Romero, M. T.; Blitz, M. A.; Pilling, M. J.; Seakins, P. W. Experimental and Modeling Studies of the Pressure and Temperature Dependences of the Kinetics and the OH Yields in the Acetyl + O_2 Reaction. *J. Phys. Chem. A* **2011**, *115*, 1069-1085.
29. Weidman, J. D.; Allen, R. T.; Moore III, K. B.; Schaefer III, H. F. High-level theoretical characterization of the vinyloxy radical ($^+\text{CH}_2\text{CHO}$) + O_2 reaction. *J. Chem. Phys.* **2018**, *148*, 184308.
30. Davis, M. M.; Weidman, J. D.; Abbott, A. S.; Douberly, G. E.; Turney, J. M.; Schaefer III, H. F. Characterization of the 2-methylvinyloxy radical + O_2 reaction: A focal point analysis and composite multireference study. *J. Chem. Phys.* **2019**, *151*, 124302.
31. Gleason, J. F.; Stief, L. J. Temperature Dependence of the Rate Constant for the Reaction $\text{HCO} + \text{O}_2 \rightarrow \text{HO}_2 + \text{CO}$ at $T = 200$ - 398 K. *J. Phys. Chem. A* **1999**, *103*, 3038-3043.
32. Ninomiya, Y.; Goto, M.; Hashimoto, S.; Kagawa, Y.; Yoshizawa, K.; Kawasaki, M. Cavity Ring-Down Spectroscopy and Relative Rate Study of Reactions of HCO Radicals with O_2 , NO , NO_2 , and Cl_2 at 295 K. *J. Phys. Chem. A* **2000**, *104*, 7556-7564.
33. Hanoune, B.; Dusanter, S.; ElMaimouni, L.; Devolder, P.; Lemoine, B. Rate constant determinations by laser photolysis/diode laser infrared absorption: examples of $\text{HCO} + \text{O}_2 \rightarrow \text{HCH(O)} + \text{HO}_2$ reactions at 294 K. *Chem. Phys. Lett.* **2001**, *343*, 527-534.
34. Michael, J. V.; Keil, D. G.; Klemm, R. B. Rate constants for the reaction of hydroxyl radicals with acetaldehyde from 244-528 K. *J. Chem. Phys.* **1985**, *83*, 1630.
35. Tyndall, G. S.; Orlando, J. J.; Wallington, T. J.; Hurley, M. D. Pressure dependence of the rate coefficients and product yields for the reaction of CH_3CO radicals with O_2 . *Int. J. Chem. Kinet.* **1997**, *29*, 655-663.
36. Blitz, M. A.; Heard, D. E.; Pilling, M. J. OH formation from $\text{CH}_3\text{CO} + \text{O}_2$: a convenient experimental marker for the acetyl radical. *Chem. Phys. Lett.* **2002**, *365*, 374-379.
37. Hou, H.; Li, A.; Hu, H.; Li, Y.; Li, H.; Wang, B. Mechanistic and kinetic study of the $\text{CH}_3\text{CO} + \text{O}_2$ reaction. *J. Chem. Phys.* **2005**, *122*, 224304.
38. Devolder, P.; Dusanter, S.; Lemoine, B.; Fittschen, C. About the co-product of the OH radical in the reaction of acetyl with O_2 below atmospheric pressure. *Chem. Phys. Lett.* **2006**, *417*, 154-158.
39. Kovács, G.; Zádor, J.; Farkas, E.; Nádasdi, R.; Szilágyi, I.; Dóbbé, S.; Bérces, T.; Márta, F.; Lendvay, G. Kinetics and mechanism of the reactions of CH_3CO and $\text{CH}_3\text{C(O)CH}_2$ radicals with O_2 . Low-pressure discharge flow experiments and quantum chemical computations. *Phys. Chem. Chem. Phys.* **2007**, *9*, 4142-4154.
40. Carr, S. A.; Baeza-Romero, M. T.; Blitz, M. A.; Pilling, M. J.; Heard, D. E.; Seakins, P. W. OH yields from the $\text{CH}_3\text{CO} + \text{O}_2$ reaction using an internal standard. *Chem. Phys. Lett.* **2007**, *445*, 108-112.

41. Maranzana, A.; Barker, J. R.; Tonachini, G. Master equation simulations of competing unimolecular and bimolecular reactions: application to OH production in the reaction of acetyl radical with O₂. *Phys. Chem. Chem. Phys.* **2007**, *9*, 4129-4141.
42. Chen, S.-Y.; Lee, Y.-P. Transient infrared absorption of *t*-CH₃C(O)OO, *c*-CH₃C(O)OO, and α -lactone recorded in gaseous of CH₃CO and O₂. *J. Chem. Phys.* **2010**, *132*, 114303.
43. Seakins, P. W.; Blitz, M. A. Developments in Laboratory Studies of Gas-Phase Reactions for Atmospheric Chemistry with Applications to Isoprene Oxidation and Carbonyl Chemistry. *Annu. Rev. Phys. Chem.* **2011**, *62*, 351-373.
44. Inoue, G.; Akimoto, H. Laser-induced fluorescence of the C₂H₃O radical. *J. Chem. Phys.* **1981**, *74*, 425-433.
45. Dupuis, M.; Wendoloski, J. J.; Lester, W. A. J. Electronic structure of vinoxy radical CH₂CHO. *J. Chem. Phys.* **1982**, *76*, 488-492.
46. Jacox, M. E. The reaction of F atoms with acetaldehyde and ethylene oxide. Vibrational spectra of the CH₃CO and CH₂CHO free radicals trapped in solid argon. *Chem. Phys.* **1982**, *69*, 407-422.
47. Oguchi, T.; Miyoshi, A.; Koshi, M.; Matsui, H.; Washida, N. Kinetic Study on Reactions of 1- and 2-Methylvinoxy Radicals with O₂. *J. Phys. Chem. A* **2001**, *105*, 378-382.
48. Delbos, E.; Fittschen, C.; Hippler, H.; Krasteva, N.; Olzmann, M.; Viskolcz, B. Rate Coefficients and Equilibrium Constant for the CH₂CHO + O₂ Reaction System. *J. Phys. Chem. A* **2006**, *110*, 3238-3245.
49. Zhu, L.; Johnston, G. Kinetics and Products of the Reaction of the Vinoxy Radical with O₂. *J. Phys. Chem.* **1995**, *99*, 15114-15119.
50. Si-Ok, R.; Shin, K. S.; Hwang, S. M. Determination of the Rate Coefficients of the CH₄ + O₂ → HO₂ + CH₃ and HCO + O₂ ⇌ HO₂ + CO Reactions at High Temperatures. *Bull. Korean. Chem. Soc.* **2017**, *38*, 228-236.
51. Osborn, D. L.; Zou, P.; Johnsen, H.; Hayden, C. C.; Taatjes, C. A.; Knyazev, V. D.; North, S. W.; Peterka, D. S.; Ahmed, M.; Leone, S. R. The multiplexed chemical kinetic photoionization mass spectrometer: A new approach to isomer-resolved chemical kinetics. *Rev. Sci. Instrum.* **2008**, *79*, 104103.
52. Taatjes, C. A.; Meloni, G.; Selby, T. M.; Trevitt, A. J.; Osborn, D. L.; Percival, C. J.; Shallcross, D. E. Direct Observation of the Gas-Phase Criegee Intermediate (CH₂OO). *J. Am. Chem. Soc.* **2008**, *130*, 11883-11885.
53. Dodson, L. G.; Shen, L.; Savee, J. D.; Eddingsas, N. C.; Welz, O.; Taatjes, C. A.; Osborn, D. L.; Sander, S. P.; Okumura, M. VUV Photoionization Cross Sections of HO₂, H₂O₂, and H₂CO. *J. Phys. Chem. A* **2015**, *119*, 1279-1291.
54. Niu, D.; Shirley, D. A.; Bai, Y. High resolution photoelectron spectroscopy and femtosecond intramolecular dynamics of H₂CO⁺ and D₂CO⁺. *J. Chem. Phys.* **1993**, *98*, 4377.
55. Goulay, F.; Derakhshan, A.; Maher, E.; Trevitt, A. J.; Savee, J. D.; Scheer, A. M.; Osborn, D. L.; Taatjes, C. A. Formation of dimethylketene and methacrolein by reaction of the CH radical with acetone. *Phys. Chem. Chem. Phys.* **2013**, *15*, 4049-4058.
56. Vogt, J.; Williamson, A. D.; Beauchamp, J. L. Properties and Reactions of Ketene in the Gas Phase by Ion Cyclotron Resonance Spectroscopy and Photoionization Mass Spectrometry. Proton Affinity, Site Specificity of Protonation, and Heat of Formation of Ketene. *J. Am. Chem. Soc.* **1978**, *100*, 3478.
57. Osborn, D. L. Personal communication. Sandia National Laboratories, Livermore, CA 2020.
58. Welz, O.; Zádor, J.; Savee, J. D.; Ng, M. Y.; Meloni, G.; Fernandez, R. X.; Sheps, L.; Simmons, B. A.; Lee, T. S.; Osborn, D. L., et al. Low-temperature combustion chemistry of biofuels: pathways in the initial low-temperature (550 K–750 K) oxidation chemistry of isopentanol. *Phys. Chem. Chem. Phys.* **2012**, *14*, 3112-3127.
59. Traeger, J. C.; McLoughlin, R. G.; Nicholson, A. J. C. Heat of formation for acetyl cation in the gas phase. *J. Am. Chem. Soc.* **1982**, *104*, 5318-5322.
60. Heazlewood, B. R.; Maccarone, A. T.; Andrews, D. U.; Osborn, D. L.; Harding, L. B.; Klippenstein, S. J.; Jordan, M. J. T.; Kable, S. H. Near-threshold H/D exchange in CD₃CHO photodissociation. *Nat. Chem.* **2011**, *3*, 443-448.
61. Ohno, K.; Okamura, K.; Yamakado, H.; Hoshino, S.; Takami, T.; Yamauchi, M. Penning Ionization of HCHO, CH₂CH₂, and CH₂CHCHO by Collision with He*(2³S) Metastable Atoms. *J. Phys. Chem.* **1995**, *99*, 14247-14253.
62. Egolfopoulos, F. N.; Hansen, N.; Ju, Y.; Kohse-Höinghaus, K.; Law, C. K.; Qi, F. Advances and challenges in laminar flame experiments and implications for combustion chemistry. *Prog. Energy Combust. Sci.* **2014**, *43*, 36-67.
63. Chhantyal-Pun, R.; Rotavera, B.; McGillen, M. R.; Khan, M. A. H.; Eskola, A. J.; Caravan, R. L.; Blacker, L.; Tew, D. P.; Osborn, D. L.; Percival, C. J., et al. Criegee Intermediate Reactions with Carboxylic Acids: A Potential Source of Secondary Organic Aerosol in the Atmosphere. *ACS Earth and Space Chem.* **2018**, *2*, 833-842.
64. Kroll, J. H.; Seinfeld, J. H. Chemistry of secondary organic aerosol: Formation and evolution of low-volatility organics in the atmosphere. *Atmos. Environ.* **2008**, *42*, 3593-3624.
65. Zhao, Y.; Saleh, R.; Saliba, G.; Presto, A. A.; Gordon, T. D.; Drozd, G. T.; Goldstein, A. H.; Donahue, N. M.; Robinson, A. L. Reducing secondary organic aerosol formation from gasoline vehicle exhaust. *Proc. Natl. Acad. Sci.* **2017**, *114*, 6984-6989.
66. Glowacki, D. R.; Pilling, M. J. Unimolecular Reactions of Peroxy Radicals in Atmospheric Chemistry and Combustion. *ChemPhysChem* **2010**, *11*, 3836-3843.
67. Atkinson, R. Atmospheric chemistry of VOCs and NO_x. *Atmos. Environ.* **2000**, *34*, 2063-2101.
68. Kuwata, K. T.; Hasson, A. S.; Dickinson, R. V.; Peterson, E. B.; Valin, L. C. Quantum Chemical and Master Equation Simulations of the Oxidation and Isomerization of Vinoxy Radicals. *J. Phys. Chem. A* **2005**, *109*, 2514-2524.
69. Glowacki, D. R.; Liang, C.-H.; Morley, C.; Pilling, M. J.; Robertson, S. H. MESMER: An open-source Master Equation Solver for Multi-Energy Well reactions. *J. Phys. Chem. A* **2012**, *116*, 9545-9560.
70. Paulson, S. E.; Flagan, R. C.; Seinfeld, J. H. Atmospheric photooxidation of isoprene part II: The ozone-isoprene reaction. *Int. J. Chem. Kinet.* **1992**, *24*, 103-125.
71. Atkinson, R.; Aschmann, S. M.; Arey, J.; Shorees, B. Formation of OH Radicals in the Gas Phase Reactions of O₃ With a Series of Terpenes. *J. Geophys. Res.* **1992**, *97*, 6065-6073.

72. Grosjean, D.; Williams, E. L. I.; Grosjean, E. Atmospheric Chemistry of Isoprene and Its Carbonyl Products. *Environ. Sci. Technol.* **1993**, *27*, 830-840.
73. Neeb, P.; Moortgat, G. Formation of OH Radicals in the Gas-Phase Reaction of Propene, Isobutene, and Isoprene with O₃: Yields and Mechanistic Implications. *J. Phys. Chem. A* **1999**, *103*, 9003-9012.
74. Malkin, T. L.; Goddard, A.; Heard, D. E.; Seakins, P. W. Measurements of OH and HO₂ yields from the gas phase ozonolysis of isoprene. *Atmos. Chem. Phys.* **2010**, *10*, 1441-1459.
75. Gutbrod, R.; Kraka, E.; Schindler, R. N.; Cremer, D. Kinetic and theoretical investigation of the gas-phase ozonolysis of isoprene: Carbonyl oxides as an important source for OH radicals in the atmosphere. *J. Am. Chem. Soc.* **1997**, *119*, 7330-7342.
76. Gutbrod, R.; Meyer, S.; Rahman, M. M.; Schindler, R. N. On the use of CO as Scavenger for OH radicals in the Ozonolysis of Simple Alkenes and Isoprene. *Int. J. Chem. Kinet.* **1997**, *29*, 717-723.
77. Paulson, S. E.; Chung, M.; Sen, A. D.; Orzechowska, G. Measurement of OH radical formation from the reaction of ozone with several biogenic alkenes. *J. Geophys. Res.* **1998**, *103*, 25533-25539.
78. Rickard, A. R.; Johnson, D.; McGill, C. D.; Marston, G. OH Yields in the Gas-Phase Reactions of Ozone with Alkenes. *J. Phys. Chem A* **1999**, *103*, 7656-7664.
79. Donahue, N. M.; Kroll, J. H.; Anderson, J. G.; Demerjian, K. L. Direct observation of OH production from the ozonolysis of olefins. *Geophys. Res. Lett.* **1998**, *25*, 59-62.
80. Atkinson, R.; Baulch, D. L.; Cox, R. A.; Crowley, J. N.; Hampson, R. F.; Hynes, R. G.; Rossi, M. J.; Troe, J.; Subcommittee, I. Evaluated kinetic and photochemical data for atmospheric chemistry: Volume 2 – gas phase reactions of organic species. *Atmos. Chem. Phys.* **2006**, *6*, 3625-4055.
81. Master chemical mechanism, MCM v3.2. <http://mcm.leeds.ac.uk/MCM>. (accessed March 10, 2020).
82. Baulch, D. L.; Cobos, C. J.; Cox, R. A.; Esser, C.; Frank, P.; Just, T.; Kerr, J. A.; Pilling, M. J.; Troe, J.; Walker, R. W., et al. Evaluated Kinetic Data for Combustion Modelling. *J. Phys. Chem. Ref. Data* **1992**, *21*, 411-734.
83. Maity, S.; Kaiser, R. I.; Jones, B. M. Formation of Ketene (H₂CCO) in Interstellar Analogous Methane (CH₄)-Carbon Monoxide (CO) Ices: A Combined FTIR and Reflectron Time-of-Flight Mass Spectroscopic Study. *Astrophys. J.* **2014**, *789*, 1-13.

CHAPTER 7

FORMIC ACID CATALYZED ISOMERIZATION AND ADDUCT FORMATION OF AN ISOPRENE-DERIVED CRIEGEE INTERMEDIATE: EXPERIMENT AND THEORY

The experimental research was performed with researchers Rebecca Caravan (*NASA Postdoctoral Program Fellow, NASA Jet Propulsion Laboratory, Combustion Research Facility, Sandia National Laboratories, Chemical Sciences and Engineering Division, Argonne National Laboratory*), Shubhrangshu Pandit (*Department of Chemistry, University of Pennsylvania, Department of Chemistry and Biochemistry, University of California San Diego*), Kristen Zuraski (*NASA Postdoctoral Program Fellow, NASA Jet Propulsion Laboratory*), Frank Winiberg (*NASA Jet Propulsion Laboratory, California Institute of Technology*), Kendrew Au (*Combustion Research Facility, Sandia National Laboratories*), Trisha Bhagde (*Department of Chemistry, University of Pennsylvania*), David Osborn (*Combustion Research Facility, Sandia National Laboratories*), Carl Percival (*NASA Jet Propulsion Laboratory, California Institute of Technology*), Craig Taatjes (*Combustion Research Facility, Sandia National Laboratories*), and Marsha Lester (*Department of Chemistry, University of Pennsylvania*). Synthetic work was performed by graduate student Nisalak Trongsiwat and Patrick J. Walsh (*Department of Chemistry, University of Pennsylvania*).

I. Introduction

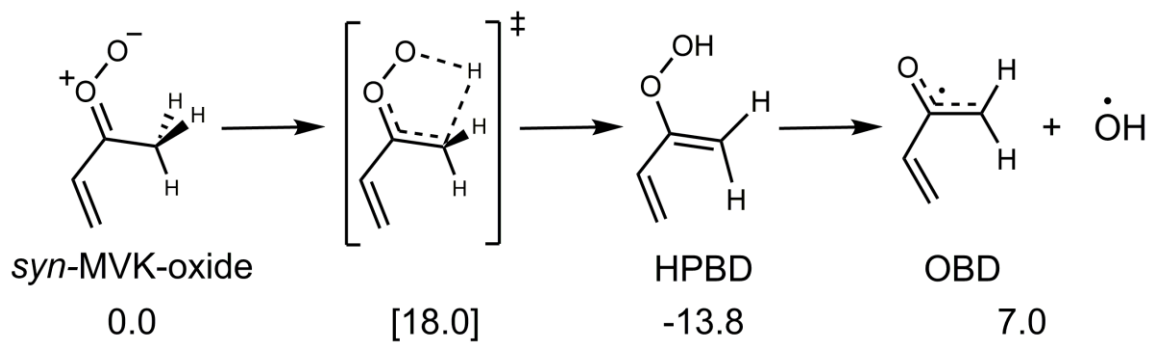
Criegee intermediates are reactive carbonyl oxide ($R_1R_2C=O^+O^-$) species generated from alkene ozonolysis. The reactions of Criegee intermediates formed from isoprene ozonolysis (ca. 10% of isoprene loss) are of particular interest due to the large amount of isoprene emitted into the atmosphere (ca. 600 Tg year⁻¹) from biogenic sources.¹ An important unimolecular decomposition pathway of Criegee intermediates with an alkyl group adjacent to the carbonyl oxide group is isomerization to a vinyl hydroperoxide (VHP) intermediate. This VHP is generated with sufficient internal excitation to decay to hydroxyl (OH) and vinoxy radical products.²⁻⁶ While the products from the unimolecular decomposition of Criegee intermediates via the VHP intermediate have been detected,²⁻¹² validating the decomposition mechanism, studies reporting the direct detection of the VHP intermediate have been extremely limited.^{13, 14} The products from the decomposition of the VHP intermediate have substantial atmospheric impact. The OH radical is the predominant tropospheric oxidant and initiates the atmospheric processing of a broad range of pollutants.¹⁵ Vinoxy radicals primarily exist as carbon-centered radicals¹⁶⁻²⁰ that undergo rapid reaction with O₂ to form peroxy radicals.¹⁹⁻²³ Peroxy radicals can undergo a subsequent H-atom transfer and further reaction with O₂ to form low volatility, highly oxygenated molecules.²⁴⁻²⁷ These autoxidation mechanisms have been implicated in the tropospheric formation of secondary organic aerosols.²⁸⁻³²

There are numerous examples in the literature in which the kinetics and branching fractions of gas-phase bimolecular reactions are shown to be influenced by the presence of additional species, for example, the water catalyzed reactions of aldehydes with OH and bimolecular reactions of Criegee intermediates.³³⁻⁴⁰ In addition, molecular catalysis has been shown to be operative in the unimolecular isomerization of Criegee

intermediates to VHPs with catalysts such as water, organic acids and alcohols.^{14, 41-45}

In this study, we investigate the formic acid catalyzed isomerization of methyl vinyl ketone oxide ((CH₂=CH)(CH₃)COO, MVK-oxide), the more abundant four-carbon unsaturated Criegee intermediate produced from isoprene ozonolysis.⁴⁶ From this pathway, the VHP intermediate, 2-hydroperoxybuta-1,3-diene (HPBD), formed upon a double H-atom transfer and isomerization of MVK-oxide, is directly detected for the first time.

Calculations have revealed that MVK-oxide has four conformational forms with similar ground state energies (within ca. 3 kcal mol⁻¹), which are separated into two groups based on the orientation of the terminal oxygen with respect to the methyl group (*syn* and *anti*) and the orientation of the vinyl group with respect to the C=O group (*cis* and *trans*).⁶ Under thermal conditions (298 K), the *cis* and *trans* configurations rapidly interconvert by rotation about the C-C bond, whereas interconversion between *syn* and *anti* configurations is restricted due to large barriers (ca. 30 kcal mol⁻¹).^{45, 47, 48} *Syn* and *anti* conformers of MVK-oxide have very different unimolecular and bimolecular reactivity and are therefore treated as distinct chemical species.^{6, 48} Previous experimental and theoretical studies have shown that *syn*-MVK-oxide undergoes slow thermal unimolecular decay (calculated to be 33 s⁻¹ at 298 K, 1 atm) via a 1,4 H-atom transfer mechanism to form HPBD, as shown in Scheme 1.⁶ Unimolecular decay requires surmounting (or tunneling through) the relatively high barrier (TS1, 18.0 kcal mol⁻¹) associated with 1,4-H atom transfer from the methyl group to the terminal O-atom of the unsaturated, four-carbon Criegee intermediate. HPBD is generated with significant internal excitation, which results in rapid homolytic cleavage of the O-O bond to form OH and 2-oxibuta-1,3-diene (OBD) radical products. OBD and OH may also follow a roaming mechanism to form 1-hydroxybut-3-en-2-one (HB).⁶



Scheme 1. Unimolecular decay mechanism of *syn*-MVK-oxide. Energies (kcal mol⁻¹) are relative to *syn*-MVK-oxide.

By contrast, *anti*-MVK-oxide is predicted to decay very rapidly (2140 s^{-1} at 298 K, 1 atm) under thermal conditions. Decay occurs via an electrocyclic ring closure mechanism to generate a 5-membered cyclic peroxide known as dioxole that subsequently undergoes C-C bond scission to generate two radical products.^{6, 47, 48} Experimental evidence of the dioxole unimolecular decay pathway has recently been reported.⁴⁹ Although unimolecular decay via a H-atom transfer mechanism has also been considered for *anti* conformers of MVK-oxide, generating 3-hydroperoxybuta-1,2-diene (HPBD-2),⁴⁷ this involves transfer of a vinyl H-atom and has a substantially higher barrier than that for formation of dioxole. As a result, the vinyl H-atom transfer pathway is not expected to be an important unimolecular decay process for *anti*-MVK-oxide.

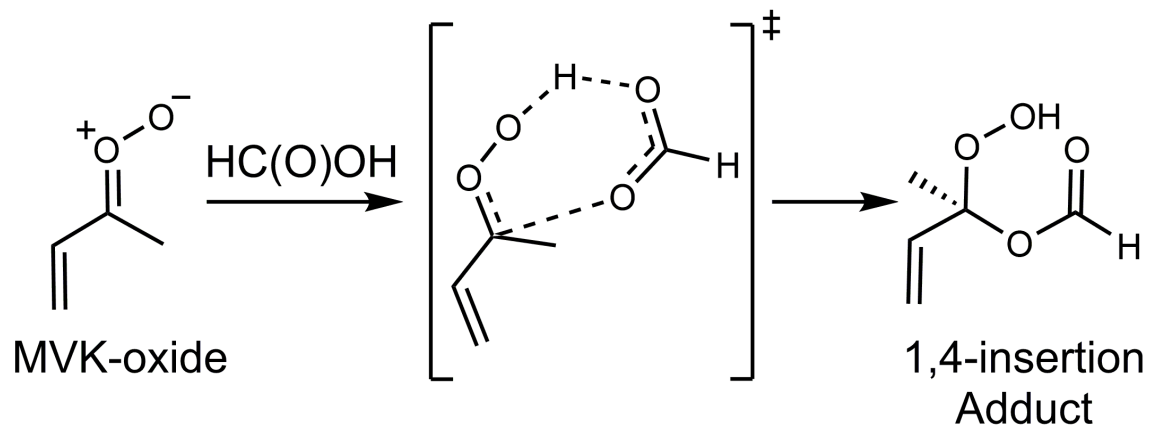
It is anticipated that unimolecular decay via the dioxole mechanism will be the dominant fate of *anti*-MVK-oxide in the troposphere, whereas the slow thermal unimolecular decay of *syn*-MVK-oxide suggests that its bimolecular reactions with key atmospheric species may also be important. This has been substantiated by direct kinetic measurements of *syn*-MVK-oxide with water vapor, formic acid, and SO_2 recorded via transient absorption spectroscopy using the strong $\pi^* \leftarrow \pi$ transition of MVK-oxide.^{45, 50}

In accord with theoretical predictions, reaction of *syn*-MVK-oxide with water vapor is found to be remarkably slow ($\leq 4 \times 10^{-17} \text{ cm}^3 \text{ s}^{-1}$ and $\leq 3 \times 10^{-14} \text{ cm}^3 \text{ s}^{-1}$ for water monomer and dimer, respectively),^{45, 48, 51} such that reaction with water is not a significant tropospheric sink of *syn*-MVK-oxide. By contrast, reaction with other key atmospheric species, including formic acid and SO_2 , is found to be rapid ($3.0 \times 10^{-10} \text{ cm}^3 \text{ s}^{-1}$ and $3.9 \times 10^{-11} \text{ cm}^3 \text{ s}^{-1}$, respectively), comparable with observations for smaller Criegee intermediates. Global modelling reveals the reaction of *syn*-MVK-oxide with

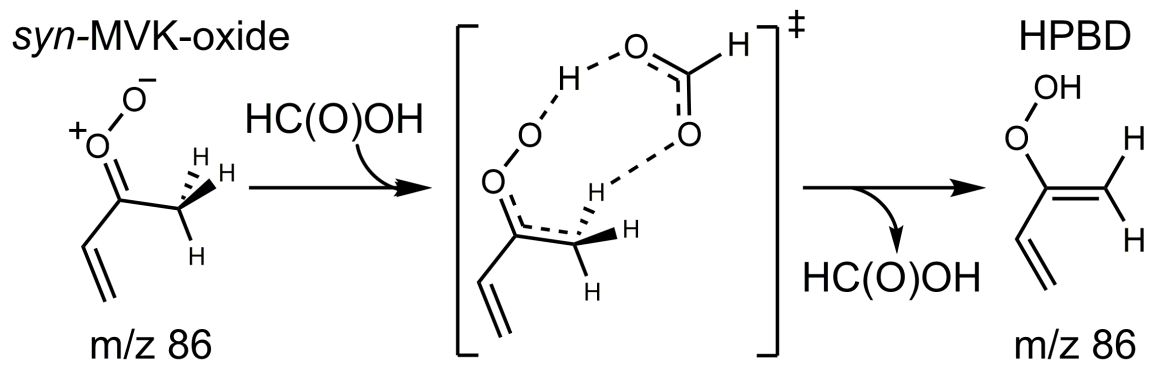
formic acid is a potentially important sink of formic acid.⁴⁵ Mass spectrometric product investigations together with high level theory demonstrate a reaction pathway leading to the formation of a functionalized hydroperoxide adduct (2-hydroperoxybut-3-en-2-yl formate, HPBF) via the 1,4-insertion of the Criegee intermediate into formic acid (Scheme 2), consistent with mechanisms observed in the reactions of smaller Criegee intermediates with organic acids.⁵²⁻⁵⁹

For MVK-oxide (and other Criegee intermediates having an α -H atom with respect to the carbonyl oxide group), an additional mechanism has been proposed for reaction with formic acid: catalyzed isomerization via a double H-atom transfer mechanism that forms a VHP intermediate (Scheme 3).⁴¹ Such functionalized hydroperoxide products have been postulated as potential precursors for the formation of secondary organic aerosols in the troposphere.⁵⁶

Prior experiments investigating the reaction of MVK-oxide with formic acid using photoionization mass spectrometry by Caravan *et al.*⁴⁵ demonstrated that the 1,4-insertion mechanism is operative. However, the acid-catalyzed mechanism producing HPBD is difficult to verify using this technique; HPBD is an isomer of MVK-oxide (and other potential products with m/z 86) and both are predicted to have similar photoionization thresholds.^{6, 60} Previously, Lester and coworkers demonstrated that reaction of deuterated organic acids (RC(O)OD) with *syn*-alkyl-substituted Criegee intermediates, specifically *syn*-CH₃CHOO, (CH₃)₂COO, and CH₃CH₂CHOO, results in formation of partially deuterated vinyl hydroperoxide species that are distinguishable by mass from the Criegee intermediates.¹⁴ Here, we utilize a similar approach with deuterated formic acid (D₂-formic acid) to reveal the acid-catalyzed isomerization of MVK-oxide (m/z 86) to partially deuterated HPBD (2-deuteroperoxy butadiene, DPBD) products (m/z 87). Moreover, we show that the observed threshold for photoionization of



Scheme 2. Mechanism for the 1,4-insertion of MVK-oxide into formic acid.



Scheme 3. Proposed mechanism for the formic acid catalyzed isomerization of *syn*-MVK-oxide.

DPBD agrees with high level adiabatic ionization energy (AIE) calculations,⁶ thereby providing spectroscopic identification of the vinyl hydroperoxide product (HPBD) from the acid-catalyzed reaction. Finally, we provide a comprehensive theoretical examination of possible reaction pathways for *syn*- and *anti*-conformers of MVK-oxide with formic acid.

II. Experimental

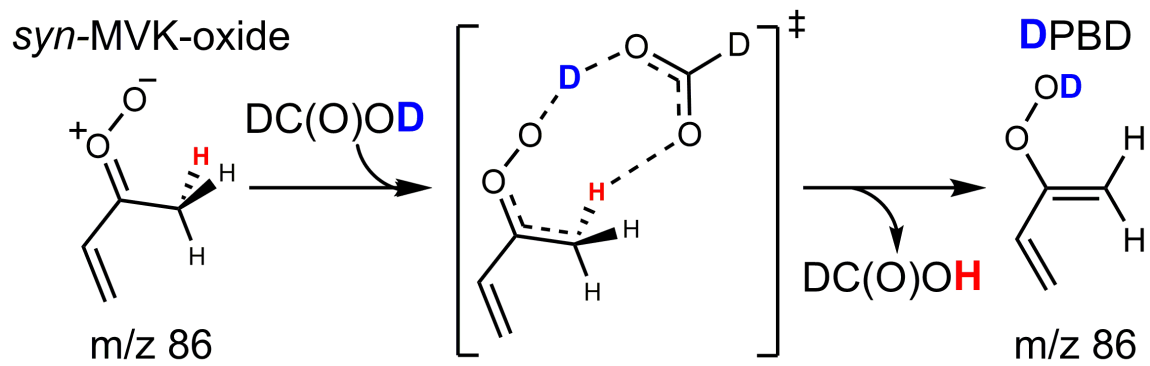
Experiments are carried out using the Sandia Multiplexed Photoionization Mass Spectrometer (MPIMS) apparatus interfaced with the tunable VUV radiation of the Chemical Dynamics Beamline (9.0.2) of the Advanced Light Source (Lawrence Berkeley National Laboratory).⁶¹ MVK-oxide is generated in the laboratory by the reaction of photolytically generated iodoalkenyl radicals with O₂ as described previously.^{6, 45, 50} Specifically, vapor of the (Z/E)-1,3-diiodobut-2-ene precursor is entrained in a He flow using a pressure and temperature controlled glass bubbler (100 torr, 298 K) and mixed with O₂ ($\sim 6.4 \times 10^{16} \text{ cm}^{-3}$) and deuterated formic acid (D₂-formic acid, 95% in D₂O, Fisher Scientific, $6.4 \times 10^{12} \text{ cm}^{-3}$) using calibrated mass flow controllers. The gas mixture is flowed through a halocarbon wax-coated quartz reactor tube (10 torr, 298 K), and photolyzed along the length of the tube with the 248 nm output of a KrF excimer laser (100 mJ/pulse at the laser exit, ~ 20 mJ/pulse through the reactor). The total gas flow rate through the reactor is set such that the gas-mixture is replenished between laser pulses. The gas mixture is continuously sampled through an orifice in the reactor tube and the resultant free jet expansion is skimmed and intercepted with tunable VUV radiation. Ions generated are pulse extracted and detected using an orthogonally accelerated time-of-flight mass spectrometer. Products resulting from the MVK-oxide + D₂-formic acid reaction are investigated either by fixed ionization energy (10.5 eV) to obtain mass spectra or by scanning the photoionization energy to generate

photoionization efficiency (PIE) curves (8.5-10.5 eV, 50 meV steps). Analogous experiments are conducted for the reaction of MVK-oxide with H₂-formic acid (3.2 × 10¹² cm⁻³ to 1.9 × 10¹³ cm⁻³, 99% Fisher Scientific) for comparison (see Supplementary Information (SI) Sec. I). The amount of H/D exchange of D₂-formic acid (m/z 48) that forms D₁-formic acid (m/z 47) is investigated under the experimental conditions by fixed ionization energy (11.5 eV) in the absence of 248 nm photolysis, and the potential impact of H/D exchange is considered in Sec. IV and SI.

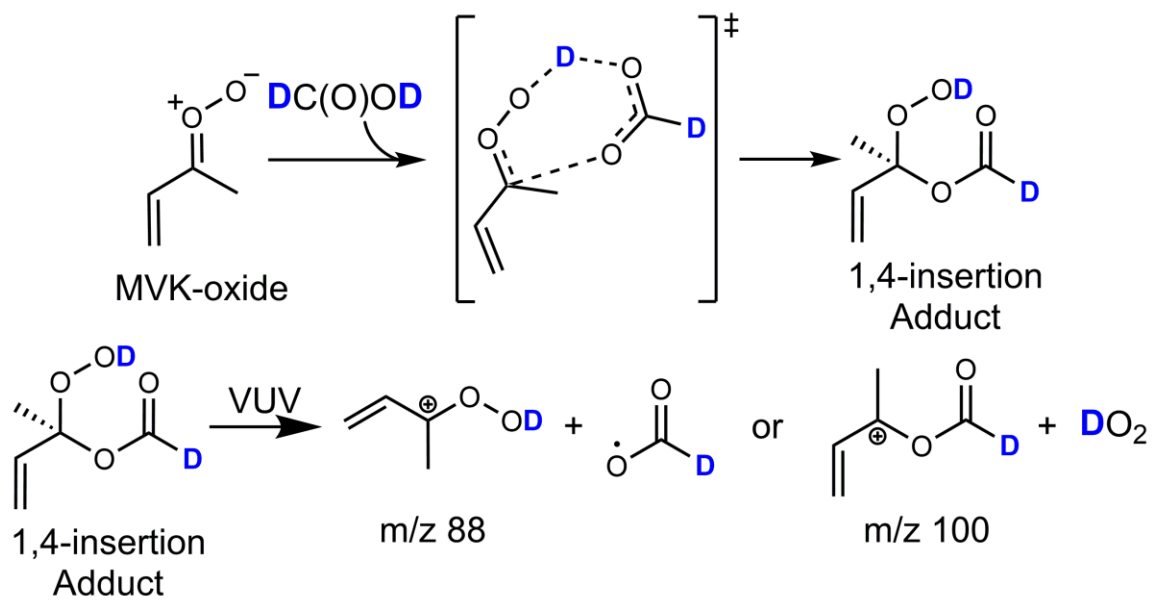
III. Results

The multiple reaction pathways between MVK-oxide and formic acid were investigated using D₂-formic acid via MPIMS at 298 K and 10 torr. Both the VHP product from the D₂-acid catalyzed isomerization of MVK-oxide and HPBF adduct from the 1,4-insertion pathway are observed. As explained below, only *syn*-MVK-oxide conformers are expected to generate appreciable DPBD via the acid catalyzed pathway depicted in Scheme 4, which is distinguishable by mass from MVK-oxide. Both *syn* and *anti* conformers of MVK-oxide are expected to react rapidly with D₂-formic acid (ca. 3 × 10⁻¹⁰ cm³s⁻¹)⁴⁵ via the 1,4-insertion mechanism to form a partially deuterated HPBF adduct (Scheme 5). For *anti* conformers of MVK-oxide, the bimolecular reaction with formic acid (ca. 1900 s⁻¹ under the present experimental conditions) must also compete with its rapid unimolecular decay (2140 s⁻¹).

Representative mass spectra obtained from the reaction of MVK-oxide with protic (H₂-formic acid) formic acid (top panel, Ref. 45) and D₂-formic acid (bottom panel) are shown in Figure 1. The 1,4-insertion product generated from the MVK-oxide + formic acid reaction undergoes fragmentation upon 10.5 eV photoionization to generate daughter ions at m/z 87 (-HCO₂) and m/z 99 (-HO₂).⁴⁵ For the MVK-oxide + D₂-formic



Scheme 4. D₂-formic acid catalyzed isomerization of *syn*-MVK-oxide to DPBD.



Scheme 5. Formation of the partially deuterated 1,4-insertion product from reaction between *syn*-MVK-oxide and D_2 -formic acid. Photoionization with VUV radiation results in the appearance of two daughter ions (m/z 88 and 100).

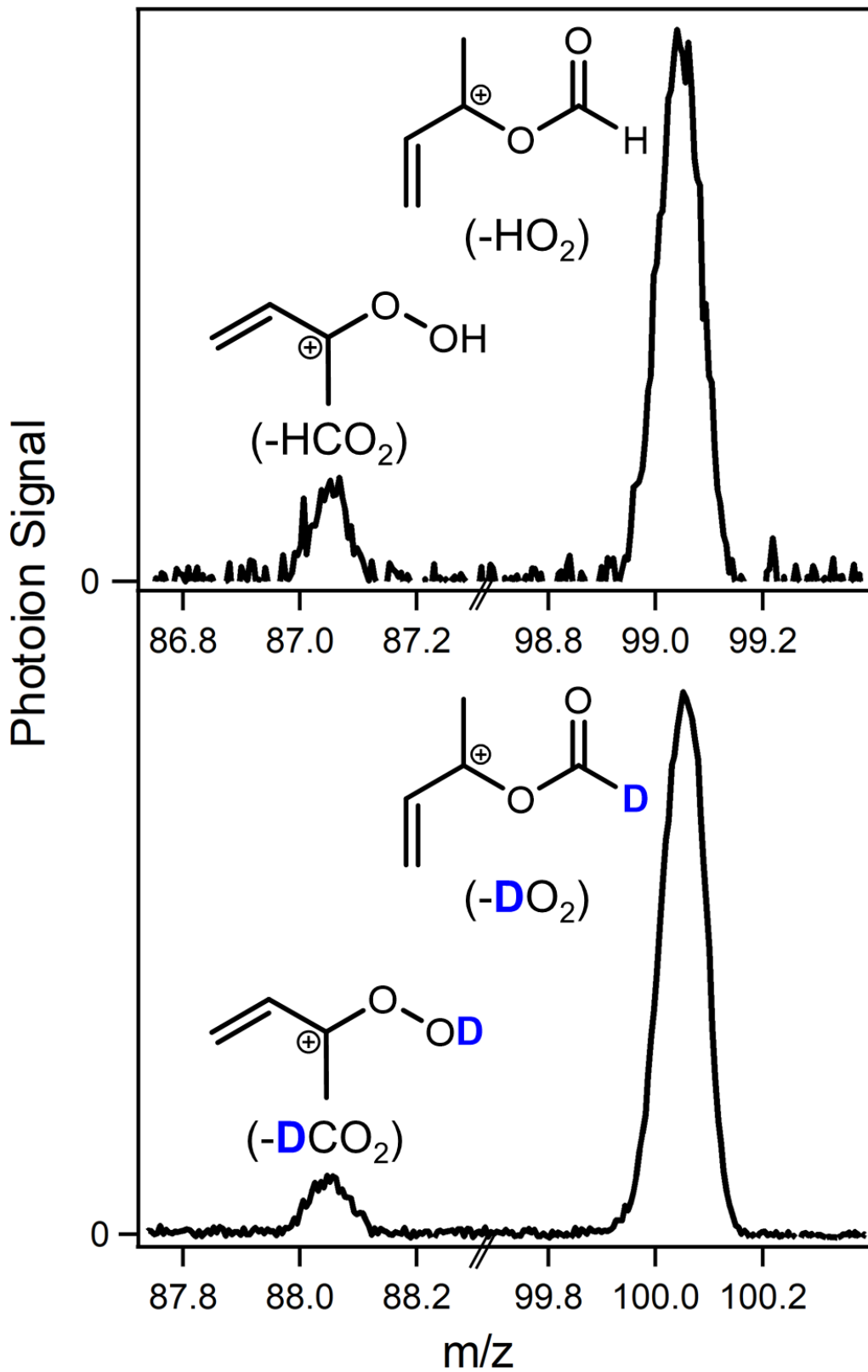


Figure 1. Comparison of daughter ions observed in mass spectra following reaction of MVK-oxide with H₂-formic acid (top panel) and D₂-formic acid (bottom panel) using MPIMS with 10.5 eV photoionization ($6.4 \times 10^{12} \text{ cm}^{-3}$ formic acid). For H₂-formic acid (top panel), mass channels m/z 87 and 99 are attributed to –HCO₂ and –HO₂ daughter ions from the 1,4-insertion HPBF adduct, respectively. For D₂-formic acid (bottom panel), partially deuterated analogs of the daughter ions from the 1,4-insertion product are observed at m/z 88 and 100, consistent with –DCO₂ and –DO₂ loss, respectively. Data in top panel is reproduced from Caravan et al., *Proc. Natl. Acad. Sci.*, 2020, **117**, 9733-9740 (Ref. 45).

acid reaction, deuterated analogs of the daughter ions from the 1,4-insertion product are observed (m/z 88 and 100) consistent with $-DCO_2$ and $-DO_2$ loss, respectively (Scheme 5), in accord with Caravan *et al.*⁴⁵ Gaussian fits to the m/z 88 and 100 mass peaks yield exact masses of 88.053 ± 0.002 and 100.053 ± 0.002 , respectively. The peak positions are consistent with the chemical composition expected daughter ions from the 1,4-insertion product ($C_4H_6O_2D$ 88.052, and $C_5H_6O_2D$ 100.052, respectively).

The DPBD product of the D_2 -formic acid catalyzed isomerization of MVK-oxide is computed to have a much lower adiabatic ionization energy (AIE)⁶ of 8.7 eV compared to those for the $-H/DO_2$ and $-H/DCO_2$ daughter ions (ca. 9.8 eV and 10.0 eV) from the adduct channel.⁴⁵ In order to identify the DPBD product, a mass spectrum is obtained by integration of the photoionization signal in the 8.5-9.8 eV energy range (MPIMS, 50 meV steps) as shown in Figure 2. Daughter ions at m/z 88 and 100 from the HPBF adduct (shown in Figure 1) are not detected because of their higher ionization energies. The observed m/z 87 mass peak in Figure 2 is consistent with the formation of DPBD from the D_2 -formic acid catalyzed isomerization of MVK-oxide (Scheme 4). A Gaussian fit to the m/z 87 mass peak yields an exact mass of 87.043 ± 0.003 , in agreement with the chemical composition of DPBD ($C_4H_5O_2D$ 87.045). Additional support for the acid-catalyzed reaction mechanism from *syn*-MVK-oxide to HPBD is provided in SI (Sec. 1, Figure S1), where a growth in the photoionization signal on the m/z 86 mass channel is observed at long kinetic times with increasing H_2 -formic acid concentration.

Figure 3 shows the PIE curve of m/z 87 (open circles) integrated over the full kinetic time window (0-80 ms) for each VUV photon energy (8.5-10.5 eV, 50 meV steps), which reveals low and high energy components suggestive of multiple species contributing to the photoionization signal. The onset of the photoionization spectrum agrees very well with the adiabatic ionization energy computed for HPBD (8.7 eV)⁶ as shown by the

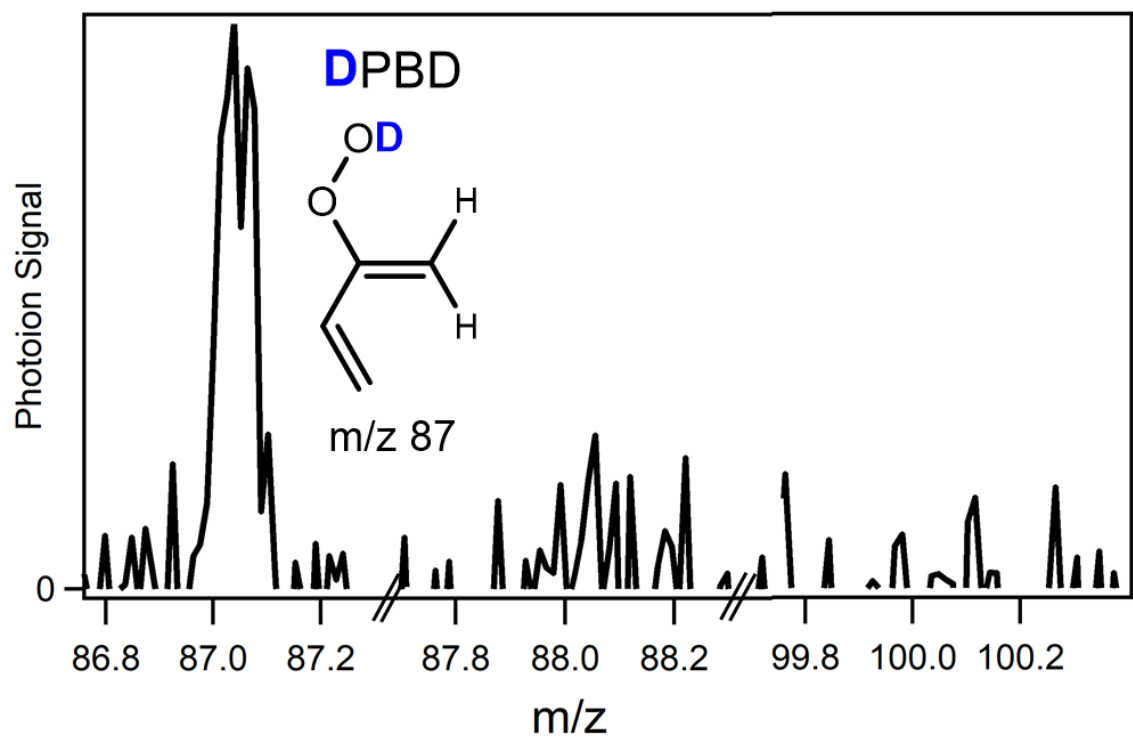


Figure 2. Mass spectrum of the DPBD (AIE 8.7 eV) product from the acid-catalyzed reaction of MVK-oxide with D₂-formic acid ($6.4 \times 10^{12} \text{ cm}^{-3}$) observed by photoionization in the 8.5-9.8 eV energy range (MPIMS, 50 meV steps). Daughter ions from the HPBF adduct product channel (shown in Figure 1) are not detected due to their higher ionization energies (AIE ~9.8-10 eV).⁴⁵

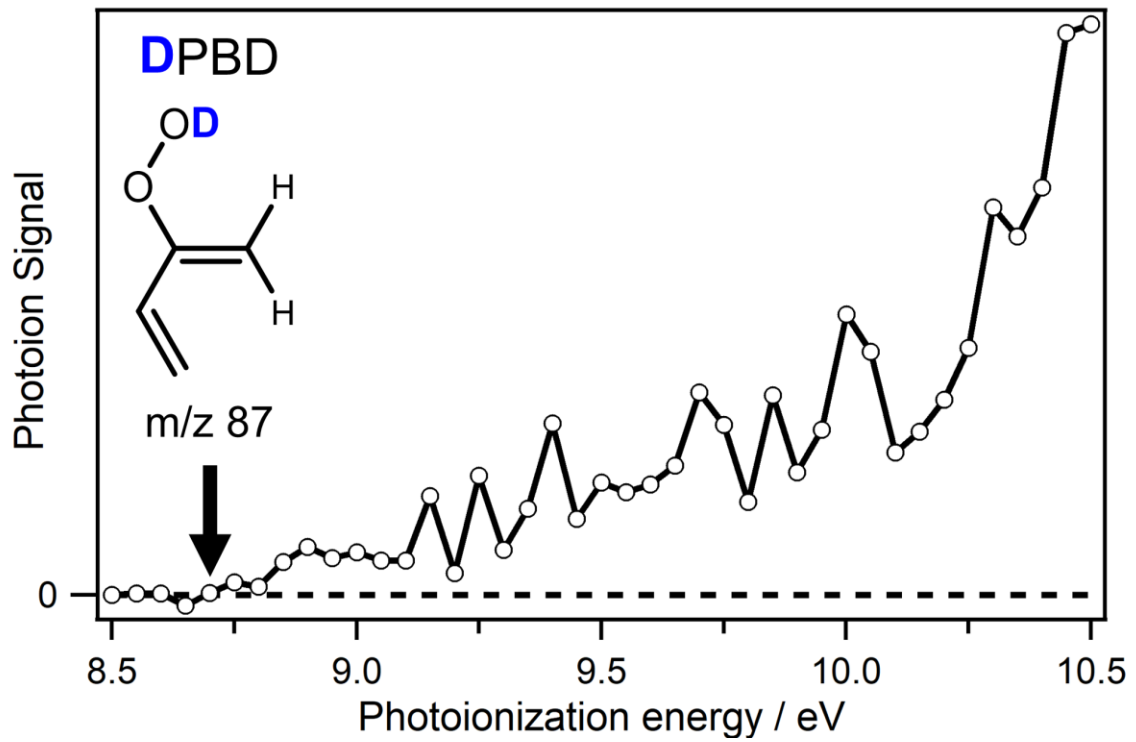


Figure 3. Photoionization efficiency curve of m/z 87 obtained by integration over the full kinetic time window (0-80 ms) using a D_2 -formic acid concentration of $6.4 \times 10^{12} \text{ cm}^{-3}$. The onset of photoionization signal agrees well with the adiabatic ionization energy of 8.7 eV (black arrow) computed for HPBD.⁶ An additional contribution is observed at higher energies (≥ 10.3 eV) that is likely due to an isomer of HPBD.

arrow in Figure 3. At higher energies (≥ 10.3 eV), an additional contribution to the PIE curve emerges. The origin of this signal is discussed in Sec. IV.

High level *ab initio* calculations investigating the formic acid catalyzed isomerization of *syn*-MVK-oxide are carried out at the CCSD(T)-F12/CBS(TZ-F12,QZ-F12)//B2PLYP-D3/cc-pVTZ level of theory (CCSD(T)-F12/CBS). A crude estimate of the CCSDT(Q) correction for higher order excitations in the coupled cluster expansion is also incorporated. Our prior theoretical calculations to characterize the unimolecular decomposition of MVK-oxide (Scheme 1)⁶ and the reaction of MVK-oxide with formic acid via the 1,4-insertion mechanism,⁴⁵ were performed at a slightly different level of theory and so those energies are redetermined here to enable a proper direct comparison of the reaction pathways (Figure 4). The formic acid catalyzed isomerization pathway has been investigated previously at the CCSD(T)/aug-cc-pVTZ//M06-2X/aug-cc-pVTZ level of theory and is compared with the present results in Sec. S2 of SI.⁴¹

The current calculations indicate that both the acid catalyzed isomerization (blue) and 1,4-insertion (green) pathways begin with barrierless formation of a 7-membered cyclic pre-reactive complex (PRC, MVK-oxide...FA) that is submerged (-14.3 kcal mol⁻¹) relative to reactants. Rapid interconversion between *cis* and *trans* conformational forms of MVK-oxide within the PRC structure is expected due to its low barrier with a submerged TS (TS_{int,cat}, Figure S2). Acid catalyzed isomerization then proceeds via a 9-membered cyclic TS (TS2, blue) with an energy below the reactant asymptote (-3.8 kcal mol⁻¹). The intermolecular interactions at the TS facilitate a concerted movement of H atoms, in which a methyl H-atom of *syn*-MVK-oxide shifts to the carbonyl O-atom of formic acid, while the carboxylic H-atom of formic acid transfers to the terminal O-atom of MVK-oxide. A hydrogen bonded complex (HPBD...FA, -21.2 kcal mol⁻¹) is formed in

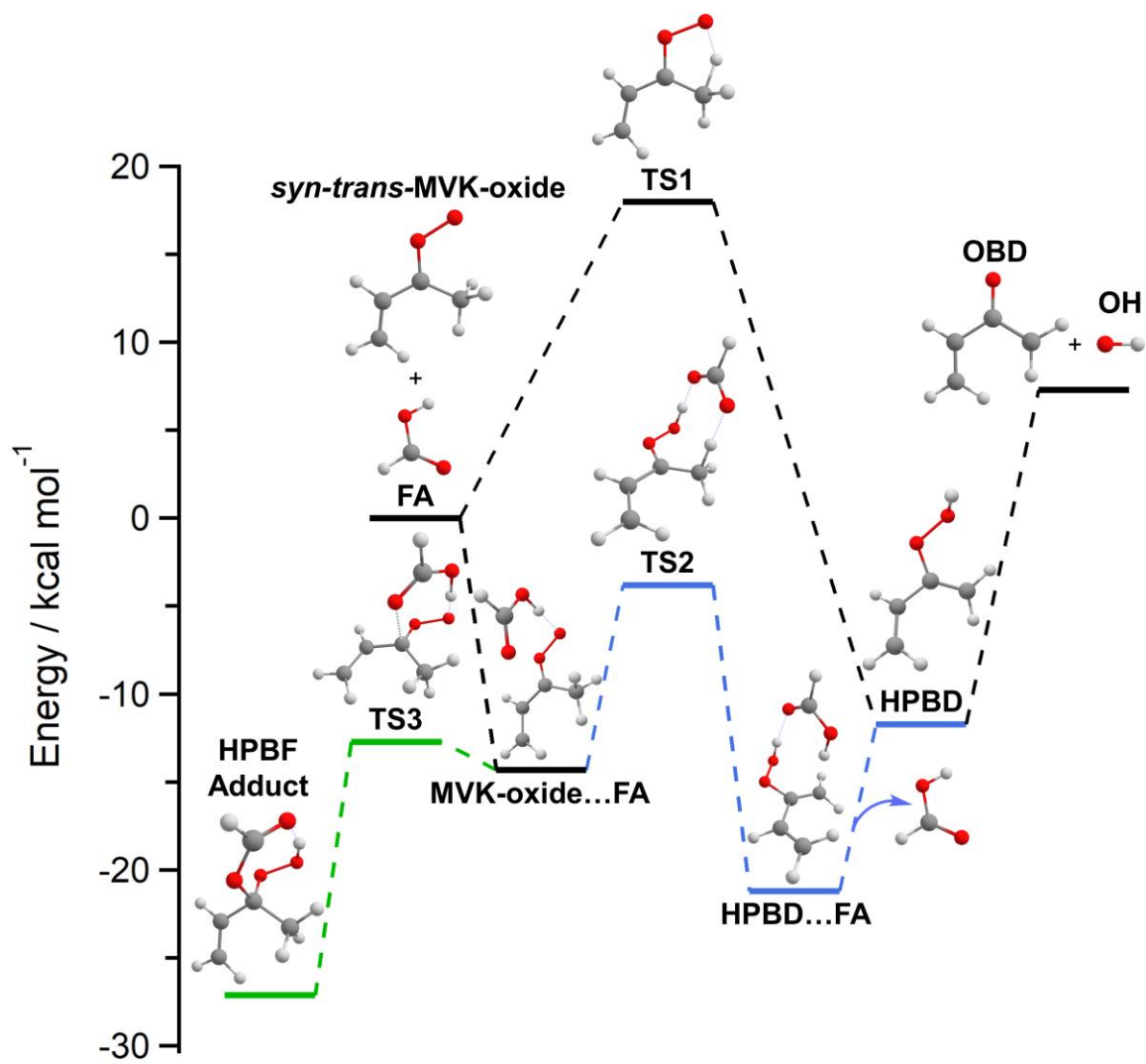


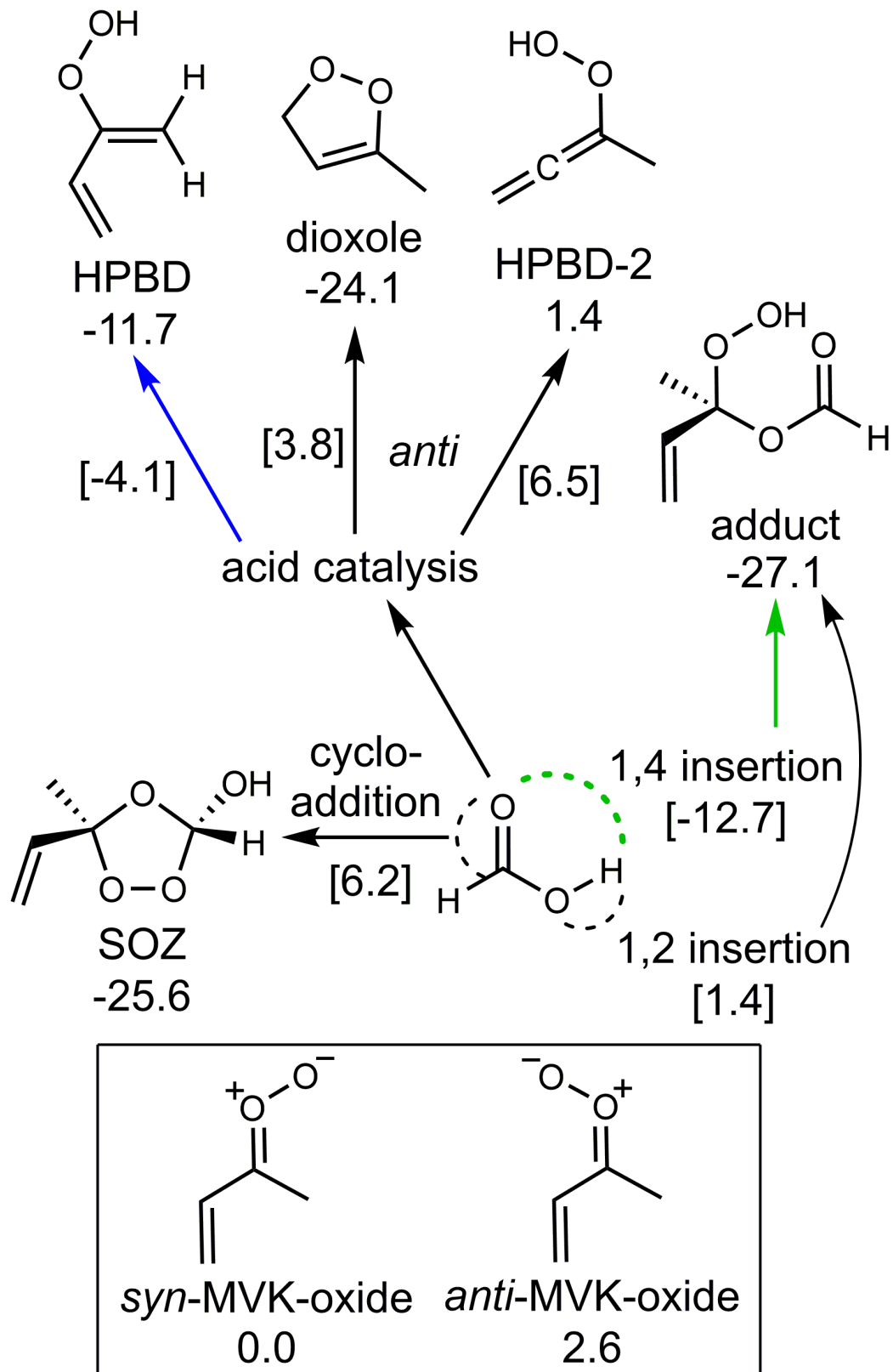
Figure 4. Reaction coordinate plot showing the unimolecular decay of *syn-trans*-MVK-oxide (black),⁶ formic acid catalyzed isomerization of *syn*-MVK-oxide (blue), and HPBF adduct formation from the 1,4-insertion reaction of *syn*-MVK-oxide with formic acid (green) at the CCSD(T)-F12/CBS level of theory with an estimate of the CCSDT(Q) correction. The adduct formation pathway is reproduced from Caravan et al., *Proc. Natl. Acad. Sci.*, 2020, **117**, 9733-9740 (Ref. 45).

the exit channel before completing the catalytic reaction with separation of the HPBD and formic acid products (-11.7 kcal mol⁻¹).

HPBF adduct formation is found to be the minimum energy reaction pathway for both *syn* (Figure 4) and *anti* (Figure S3) conformers of MVK-oxide. The TS associated with HPBF adduct formation from *syn*-MVK-oxide with formic acid is highly submerged (TS3, -12.7 kcal mol⁻¹) with a similar structure and energy as the PRC; an analogous TS is found for *anti*-MVK-oxide. This facilitates rapid formation of the HPBF adduct and is predicted to be a significant reaction pathway for *syn* and *anti*-MVK-oxide.⁴⁵ In Sec. IV, we utilize master equation modeling to evaluate the product branching for the primary channels, acid-catalyzed reaction and adduct formation, in the MVK-oxide + formic acid reaction.

Several additional pathways for reaction of MVK-oxide with formic acid have been investigated theoretically. These pathways are illustrated in Scheme 6 with corresponding stationary point energies relative to *syn-trans*-MVK-oxide. Additional information about the electronic structure calculations, energetics, and reaction coordinates are provided in the SI (Sec. S2, Tables S1-S6 and Figures S3-S9). The additional pathways include the acid catalyzed isomerization of *anti*-MVK-oxide (Figures S3-S5), HPBF adduct formation via a 1,2-insertion mechanism (Figure S6), secondary ozonide (SOZ) formation (Figure S7), and spectator catalysis of *syn*-MVK-oxide (Figure S8).

The acid catalyzed isomerization of *anti*-MVK-oxide can lead to formation of dioxole, HPBD, and HPBD-2 products (Figures S3-S5). The favorable interaction between *anti*-MVK-oxide and formic acid significantly reduces the TS barrier to dioxole formation from 12.4 kcal mol⁻¹ (uncatalyzed) to nearly thermoneutral (1.0 kcal mol⁻¹; acid catalyzed) relative to reactants (Figure S4). A similar low TS barrier is found for the acid catalyzed



Scheme 6. Pathways for the reaction of MVK-oxide with formic acid examined theoretically with stationary point energies and transition state barriers given in kcal mol⁻¹.

isomerization of *anti*-MVK-oxide to HPBD ($-1.0 \text{ kcal mol}^{-1}$) relative to reactants (Figure S3). The reactive flux through these acid-catalyzed pathways is predicted to be small compared to rapid thermal unimolecular decay of *anti*-MVK-oxide to dioxole (2140 s^{-1}) and the far more favorable bimolecular reaction with acid leading to HPBF adduct formation (ca. 1900 s^{-1} under the present experimental conditions). Finally, the formic acid catalyzed isomerization of *anti*-MVK-oxide to HPBD-2 (Figure S5) is unfavorable due to a higher TS barrier for vinyl H-atom transfer ($3.8 \text{ kcal mol}^{-1}$) relative to reactants. Additional pathways via 1,2-insertion to the HPBF adduct (Figure S6) and cycloaddition to the SOZ (Figure S7) are similarly unfavorable for MVK-oxide due to their relatively higher barriers ($1.4 \text{ kcal mol}^{-1}$ and $6.2 \text{ kcal mol}^{-1}$, respectively).

IV. Discussion

Two mechanisms are relevant for the reaction of *syn*-MVK-oxide with formic acid: acid catalyzed isomerization to yield a vinyl hydroperoxide (HPBD, m/z 86) and HPBF adduct formation arising from 1,4 insertion of the Criegee intermediate into formic acid. For *anti*-conformers of MVK-oxide, only HPBF adduct formation is predicted to be significant due to the higher barriers associated with its acid catalyzed isomerization process. Deuterated formic acid is utilized in this work to reveal the acid catalyzed isomerization process for *syn*-MVK-oxide. The DPBD (m/z 87) product arising from the D_2 -formic acid catalyzed reaction is observed using MPIMS (above 8.7 eV); the experimental threshold energy for ionization is consistent with the theoretical adiabatic ionization energy for H/DPBD.⁶ This provides experimental validation of the acid catalyzed mechanism originally proposed by Thompson and coworkers.⁴¹ In addition, this confirms that *syn*-conformers of MVK-oxide are generated and observed under thermal conditions.^{6, 45} The product branching for the primary channels in the *syn*-MVK-

oxide + formic acid reaction, acid-catalyzed reaction and adduct formation, are examined with master equation modeling (Figures S10 and S11). Finally, this observation extends earlier studies of the acid catalyzed reaction for simple alkyl-substituted Criegee intermediates.¹⁴

Appearance of daughter ions on the m/z 88 ($-\text{DCO}_2$) and m/z 100 ($-\text{DO}_2$) channels is consistent with the formation of the HPBF adduct arising from the 1,4-insertion reaction of MVK-oxide with D_2 -formic acid. Analogous daughter ions, m/z 87 ($-\text{HCO}_2$) and m/z 99 ($-\text{HO}_2$), are observed for the reaction with formic acid.⁴⁵ The PIE curves associated with the $-\text{H}/\text{DO}_2$ daughter ion are indistinguishable from one another (Figure S12) and both are in excellent agreement with the theoretically predicted onset for ionization (9.82 eV).⁴⁵ Thus, products from both the acid catalyzed and 1,4-insertion pathways for *syn*-MVK-oxide with formic acid are identified in the current work. Prior studies have identified the adducts formed from the 1,4-insertion reaction of simple Criegee intermediates (CH_2OO and CH_3CHOO) with formic acid using MPIMS⁵⁴ and microwave spectroscopy.⁵⁷⁻⁵⁹

Previously, the (uncatalyzed) unimolecular decay of *syn*-MVK-oxide has been investigated under jet-cooled, collision-free conditions using infrared (IR) action spectroscopy.^{6, 62} IR activation of *syn*-MVK-oxide with two quanta of CH stretch provides sufficient energy to surmount the transition state barrier for 1,4 H-atom transfer and generate HPBD (Scheme 1, Figure 4). The HPBD is formed with sufficient internal excitation to rapidly dissociate to OH and OBD radical products. Under thermal conditions (298K, 1 atm), (uncatalyzed) unimolecular decay of *syn*-MVK-oxide follows the same reaction pathway, albeit more slowly (33 s^{-1}).^{6, 45} An analogous (uncatalyzed) unimolecular decay process has been observed for d_3 -*syn*-MVK-oxide to OD products.⁶² In contrast, the acid catalyzed isomerization of *syn*-MVK-oxide under thermal conditions

will again form HPBD, but it is unlikely to have sufficient energy to dissociate to OH + OBD products. The same would occur for reaction with D₂-formic acid, yielding DPBD, but unlikely to form OD + OBD products. The formic acid leaving group will accept and carry away excess energy following generation of H/DPBD. Under atmospheric conditions, HPBD formed from the acid catalyzed pathway may eventually release OH/D + OBD radical products.⁶³⁻⁶⁶ HPBD is similar to other functionalized hydroperoxide compounds generated from Criegee intermediate chemistry and may undergo further reactions that can lead to secondary organic aerosol (SOA) formation.^{45, 54, 56}

A. H/D Exchange

An increase in the PIE curve at higher energies (≥ 10.3 eV) is apparent in Figure 3 and suggests that more than one species contributes to the photoionization signal at m/z 87. The narrowness of the m/z 87 peak in the mass spectrum recorded at 10.5 eV (Figure S13) indicates that the interfering species has the same chemical composition as DPBD (C₄H₅O₂D 87.045) and is therefore an isomer. A plausible explanation originates from reaction of MVK-oxide with partially deuterated formic acid (D₁-formic acid). Although the D₂-formic acid from the vendor had high isotopic purity (95%), we found evidence of H/D exchange following introduction of D₂-formic acid into the flow cell (see SI, Scheme S1, Figures S13-S15, Table S7). Even with the complication arising from H/D exchange, formation of DPBD from the acid catalyzed isomerization of MVK-oxide + D₂-formic acid is clearly evident from the 8.7 eV onset of the m/z 87 PIE curve and absence of daughter ions from dissociative ionization of the HPBF adduct at photoionization energies from 8.5 to 9.8 eV.

Additional electronic structure calculations and master equation modeling were carried out to assess the possible role of H/D exchange between HPBD and D₂-formic

acid under our experimental conditions. As shown in Figure S9, the barrier for isotopic exchange is significant and the associated rate constants indicate that isotopic exchange would be negligible.

B. Product Branching

The product branching to DPBD can be estimated by comparing the integrated photoionization signals (10.5 eV) of the acid catalyzed and adduct formation pathways. This analysis assumes the photoionization cross section of each product is similar. In addition, it assumes that all products and daughter ions have been identified. Integration of the m/z 88 and 100 mass channels yields the photoionization signal associated with adduct formation from the MVK-oxide + D₂-formic acid reaction. Integration of the m/z 87 mass channel provides an estimate of the DPBD signal from the acid catalyzed reaction. Corrections are then made to account for contributions to the m/z 87 mass channel due to daughter ions from MVK-oxide + DC(O)OH adducts as detailed in SI.

The product branching analysis shows that HPBF adduct formation is the dominant product channel (ca. 94%), while DPBD is a minor product (ca. 6%) assuming equal populations of *syn* and *anti*-MVK-oxide under the present experimental conditions. If only *syn*-MVK-oxide is present (e.g. because of rapid unimolecular decay of *anti*-MVK-oxide), HPBF adduct formation will still be the dominant product channel (97%) compared to the acid catalyzed pathway (3%).

Thermal rate constants for the reaction of MVK-oxide with formic acid are also predicted from *ab initio* transition state theory-based master equation calculations, which are detailed in SI. We focus on the resultant product branching for *syn*-conformers of MVK-oxide between the acid-catalyzed pathway to HPBD with release of formic acid and the addition pathway that forms the HPBF adduct. For the experimental (T, P)

conditions of 298 K and 10 torr He, the theoretical product branching ratio for the acid-catalyzed pathway is estimated to be ca. 0.3%. The product branching ratio is predicted to be strongly dependent on pressure and temperature (SI Sec. S2, Figures S10 and S11), since increased pressure and lower temperature favor stabilization of the HPBF adduct.

Notably, our calculations also indicate that the product branching ratio differs considerably for *syn-cis* and *syn-trans* conformers. Although the *syn-cis* conformer is less stable than *syn-trans* MVK-oxide, their pre-reactive complexes with formic acid will rapidly equilibrate (Figure S2). As a result, the reaction of formic acid with *syn-cis* MVK-oxide will have an effectively lower submerged TS2 barrier than that for *syn-trans* MVK-oxide, resulting in enhanced acid-catalyzed reaction and reduced stabilization of the HPBF adduct (Figures S10 and S11). For *anti*-conformers of MVK-oxide, the acid-catalyzed reaction is predicted to be negligibly slow due to the higher barrier (TS2) for this pathway (Figure S3), and thus the HPBF adduct will be the dominant product channel. The barriers for other pathways (depicted in Scheme 6, Table S1) are too high to contribute significantly to the thermal reaction rate or product branching.

While both experiment and theory predict that the adduct formation channel will dominate, master-equation modeling predicts a smaller contribution from the acid-catalyzed channel than experiment. Many possible uncertainties in the theoretical predictions are considered in SI. On the experimental side, the assumption of equivalent photoionization cross sections for the products detected may be an over simplification. Deviations in photoionization cross sections among related species have been predicted theoretically,⁶⁷ but are not available for the products detected in this study.

C. Comparison of MVK-oxide and CH₂OO reactions with formic acid

In addition to the primary 1,4-insertion pathway for HPBF adduct formation for *syn-trans*-MVK-oxide with formic acid considered thus far, we have characterized the 1,2-insertion pathway for HPBF adduct formation and a cycloaddition pathway to secondary ozonide formation theoretically (Figures S7 and S8). The analogous reactions have been investigated for the simplest Criegee intermediate (CH₂OO) with formic acid by Vereecken at the CCSD(T)/aug-cc-pVTZ//M06-2X/aug-cc-pVTZ level of theory.⁵⁵ For *syn-trans*-MVK-oxide + formic acid, the 1,4-insertion mechanism is predicted to be substantially more favorable than 1,2-insertion because of the higher TS barrier (-12.7 and 1.4 kcal mol⁻¹, respectively), as found previously for the reaction of CH₂OO with formic acid. However, the HPBF adduct formed from the *syn*-MVK-oxide + formic acid reaction is much less stable than its CH₂OO analog (-27.4 kcal mol⁻¹ vs -44.4 kcal mol⁻¹, respectively, Tables S3 and S4) due to disruption of the resonance stabilization present in MVK-oxide.⁴⁵

SOZ generation from the cycloaddition reaction of *syn*-MVK-oxide with formic acid further demonstrates the impact of resonance stabilization of MVK-oxide on its reactivity. The PRC formed between *syn-trans*-MVK-oxide and formic acid is more strongly bound than its CH₂OO analog (-14.3 vs -6.0 kcal mol⁻¹, respectively, Table S5), likely due to stronger dispersion forces in the MVK-oxide PRC. However, disruption of the resonance stability of MVK-oxide at the transition state results in a much higher barrier for SOZ formation than found for CH₂OO (6.2 vs -1.7 kcal mol⁻¹, respectively). Moreover, the SOZ formed from the reaction of *syn-trans*-MVK-oxide with formic acid is much less stable than its CH₂OO analog (-26.7 vs -40.2 kcal mol⁻¹, respectively, Table S5). Overall, HPBF adduct formation from the 1,4-insertion mechanism is the primary reaction pathway for both *syn*- and *anti*-conformers of MVK-oxide with formic acid;

formic acid catalyzed isomerization provides an alternate but less favorable pathway for *syn*-MVK-oxide.

V. Conclusion

High level *ab initio* calculations predict two active mechanisms for reaction of MVK-oxide with formic acid: (1) bimolecular reaction of formic acid with both *syn*- and *anti*-conformers of MVK-oxide via a 1,4-insertion mechanism that generates a functionalized hydroperoxide⁴⁵ and (2) formic acid catalyzed isomerization of *syn*-MVK-oxide via a barrierless double H-atom transfer mechanism to form vinyl hydroperoxide (HPBD) with regeneration of formic acid.⁴¹ In this study, we demonstrate that reaction of deuterated formic acid with MVK-oxide in a flow cell (298 K, 10 Torr) with photoionization (MPIMS) detection enables identification of both the adduct formation and acid catalyzed reaction pathways. Previously, the HPBF adduct was shown to be a primary product of the reaction of MVK-oxide with formic acid.⁴⁵ Specifically, dissociative photoionization of the HPBF adduct was observed by identification of daughter ions associated with -HCO_2 and -HO_2 loss processes. Here, the partially deuterated HPBF adduct from reaction of MVK-oxide with D_2 -formic acid is observed through analogous daughter ions (-DCO_2 at m/z 88 and -DO_2 at m/z 100) associated with dissociative photoionization. The PIE curves for the daughter ions from reaction with D_2 -formic acid agree with those reported previously for reaction with formic acid,⁴⁵ providing further support for the formation of the partially deuterated HPBF adduct in the MVK-oxide + D_2 -formic acid reaction.

In addition, the formic acid catalyzed isomerization pathway is revealed using D_2 -formic acid, which is identified for the first time. D-atom transfer from the acid to *syn*-MVK-oxide yields a partially deuterated vinyl hydroperoxide (DPBD), which is identified through MPIMS by its distinct mass (m/z 87) and photoionization threshold. The

analogous pathway with H₂-formic acid would appear at m/z 86. The onset energy at ca. 8.7 eV observed for photoionization of the DPBD products (m/z 87) from the acid catalyzed isomerization of *syn*-MVK-oxide is in good accord with a prior high level theoretical calculation of the adiabatic ionization energy of HPBD (8.7 eV).⁶ The product branching is estimated from the magnitude of the ionization signals (assuming similar photoionization cross sections). This indicates that the HPBF adduct is the dominant product channel (94%) and the acid catalyzed isomerization to DPBD is a minor channel (6%), assuming equal populations of *syn* and *anti*-MVK-oxide are generated under the present experimental conditions. High-level *ab initio* calculations indicate HPBF adduct formation is strongly favored compared to acid catalyzed isomerization, consistent with the experimental results.

Acknowledgements

This research was supported by the U.S. Department of Energy-Basic Energy Sciences under grant DE-FG02-87ER13792 (MIL). This material is also based upon work supported by the Division of Chemical Sciences, Geosciences and Biosciences, Office of Basic Energy Sciences (BES), U.S. Department of Energy (USDOE). Sandia National Laboratories is a multimission laboratory managed and operated by National Technology and Engineering Solutions of Sandia, LLC., a wholly owned subsidiary of Honeywell International, Inc., for the USDOE's National Nuclear Security Administration under contract DE-NA0003525. This paper describes objective technical results and analysis. Any subjective views or opinions that might be expressed in the paper do not necessarily represent the views of the USDOE or the United States Government. This material is based in part on research at Argonne supported by the U.S. Department of Energy, Office of Science, Office of Basic Energy Sciences, Division of Chemical

Sciences, Geosciences, and Biosciences under Contract No. DE-AC02-06CH11357. The Advanced Light Source is supported by the Director, Office of Science, BES/USDOE under Contract DE- AC02-05CH11231 at Lawrence Berkeley National Laboratory. This research was carried out in part by the Jet Propulsion Laboratory, California Institute of Technology, under contract with the National Aeronautics and Space Administration (NASA), supported by the Upper Atmosphere Research and Tropospheric Chemistry program. The contributions of RLC and KLZ were in part supported by appointments to the NASA Postdoctoral Program at the NASA Jet Propulsion Laboratory, administered by Universities Space Research Association under contract with NASA. PJW thanks the NSF (CHE-1902509). California Institute of Technology. © 2020. All rights reserved. We are grateful to Lenoid Sheps (Sandia) and Ahren Jasper (Argonne) for useful discussions.

References

1. K. Sindelarova, C. Granier, I. Bouarar, A. Guenther, S. Tilmes, T. Stavrakou, J. F. Müller, U. Kuhn, P. Stefani and W. Knorr, *Atmos. Chem. Phys.*, 2014, **14**, 9317-9341.
2. F. Liu, J. M. Beames, A. S. Petit, A. B. McCoy and M. I. Lester, *Science*, 2014, **345**, 1596-1598.
3. F. Liu, J. M. Beames and M. I. Lester, *J. Chem. Phys.*, 2014, **141**, 234312.
4. Y. Fang, F. Liu, S. J. Klippenstein and M. I. Lester, *J. Chem. Phys.*, 2016, **145**, 044312.
5. Y. Fang, F. Liu, V. P. Barber, S. J. Klippenstein, A. B. McCoy and M. I. Lester, *J. Chem. Phys.*, 2016, **144**, 061102.
6. V. P. Barber, S. Pandit, A. M. Green, N. Trongsiriwat, P. J. Walsh, S. J. Klippenstein and M. I. Lester, *J. Am. Chem. Soc.*, 2018, **140**, 10866-10880.
7. Y. Fang, F. Liu, V. P. Barber, S. J. Klippenstein, A. B. McCoy and M. I. Lester, *J. Chem. Phys.*, 2016, **145**, 234308.
8. Y. Fang, V. P. Barber, S. J. Klippenstein, A. B. McCoy and M. I. Lester, *J. Chem. Phys.*, 2017, **146**, 134307.
9. V. P. Barber, S. Pandit, V. J. Esposito, A. B. McCoy and M. I. Lester, *J. Phys. Chem. A*, 2019, **123**, 2559-2569.
10. V. P. Barber, V. J. Esposito, T. Trabelsi, A. S. Hansen, T. A. McHenry, J. S. Francisco and M. I. Lester, *Chem. Phys. Lett.*, 2020, **751**, 137478.
11. M. I. Lester and S. J. Klippenstein, *Acc. Chem. Res.*, 2018, **51**, 978-985.
12. T. A. Stephenson and M. I. Lester, *Int. Rev. Phys. Chem.*, 2020, **39**, 1-33.
13. A. Bagchi, Y. Yu, J.-H. Huang, C.-C. Tsai, W.-P. Hu and C. C. Wang, *Phys. Chem. Chem. Phys.*, 2020, **22**, 6528-6537.
14. F. Liu, Y. Fang, M. Kumar, W. H. Thompson and M. I. Lester, *Phys. Chem. Chem. Phys.*, 2015, **17**, 20490-20494.
15. B. J. Finlayson-Pitts and J. N. Pitts, *Chemistry of the Upper and Lower Atmosphere*, Academic Press, San Diego, 2000.
16. G. Inoue and H. Akimoto, *J. Chem. Phys.*, 1981, **74**, 425-433.
17. M. Dupuis, J. J. Wendoloski and W. A. Lester Jr., *J. Chem. Phys.*, 1982, **76**, 488-492.
18. M. E. Jacox, *Chem. Phys.*, 1982, **69**, 407-422.
19. J. D. Weidman, R. T. Allen, K. B. Moore III and H. F. Schaefer III, *J. Chem. Phys.*, 2018, **148**, 184308.
20. M. M. Davis, J. D. Weidman, A. S. Abbott, G. E. Douberly, J. M. Turney and H. F. Schaefer III, *J. Chem. Phys.*, 2019, **151**, 124302.
21. T. Oguchi, A. Miyoshi, M. Koshi, H. Matsui and N. Washida, *J. Phys. Chem. A*, 2001, **105**, 378-382.

22. M. Hassouna, E. Delbos, P. Devolder, B. Viskolcz and C. Fittschen, *J. Phys. Chem. A*, 2006, **110**, 6667-6672.
23. E. Delbos, C. Fittschen, H. Hippler, N. Krasteva, M. Olzmann and B. Viskolcz, *J. Phys. Chem. A*, 2006, **110**, 3238-3245.
24. J. J. Orlando and G. S. Tyndall, *Chem. Soc. Rev.*, 2012, **41**, 6294-6317.
25. K. H. Møller, K. H. Bates and H. G. Kjaergaard, *J. Phys. Chem. A*, 2019, **123**, 920-932.
26. E. Praske, R. V. Otkjaer, J. D. Crouse, J. C. Hethcox, B. M. Stoltz, H. G. Kjaergaard and P. O. Wennberg, *J. Phys. Chem. A*, 2019, **123**, 590-600.
27. R. V. Otkjaer, H. H. Jakobsen, C. M. Tram and H. G. Kjaergaard, *J. Phys. Chem. A*, 2018, **122**, 8665-8673.
28. F. Paulot, J. D. Crouse, H. G. Kjaergaard, A. Kürten, J. M. St Clair, J. H. Seinfeld and P. O. Wennberg, *Science*, 2009, **325**, 730-733.
29. J. D. Crouse, L. B. Nielsen, S. Jørgensen, H. G. Kjaergaard and P. O. Wennberg, *J. Phys. Chem. Lett.*, 2013, **4**, 3513-3520.
30. M. Ehn, J. A. Thornton, E. Kleist, M. Sipilä, H. Junninen, I. Pullinen, M. Springer, F. Rubach, R. Tillmann, B. Lee, F. Lopez-Hilfiker, S. Andres, I.-H. Acir, M. Rissanen, T. Jokinen, S. Schobesberger, J. Kangasluoma, J. Kontkanen, T. Nieminen, T. Kurtén, L. B. Nielsen, S. Jørgensen, H. G. Kjaergaard, M. Canagaratna, M. D. Maso, T. Berndt, T. Petäjä, A. Wahner, V.-M. Kerminen, M. Kulmala, D. R. Worsnop, J. Wildt and T. F. Mentel, *Nature*, 2014, **506**, 476.
31. T. Jokinen, M. Sipilä, S. Richters, V.-M. Kerminen, P. Paasonen, F. Stratmann, D. R. Worsnop, M. Kulmala, M. Ehn, H. Herrmann and T. Berndt, *Angew. Chem. Int. Ed.*, 2014, **53**, 14596-14600.
32. K. C. Barsanti, J. H. Kroll and J. A. Thornton, *J. Phys. Chem. Lett.*, 2017, **8**, 1503-1511.
33. E. Vöhringer-Martinez, B. Hansmann, H. Hernandez, J. S. Francisco, J. Troe and B. Abel, *Science*, 2007, **315**, 497-501.
34. W. Zhang, B. Du and Z. Qin, *J. Phys. Chem. A*, 2014, **118**, 4797-4807.
35. T. R. Lewis, M. A. Blitz, D. E. Heard and P. W. Seakins, *Phys. Chem. Chem. Phys.*, 2015, **17**, 4859-4863.
36. L. Sheps, B. Rotavera, A. J. Eskola, D. L. Osborn, C. A. Taatjes, K. Au, D. E. Shallcross, M. A. H. Khan and C. J. Percival, *Phys. Chem. Chem. Phys.*, 2017, **19**, 21970-21979.
37. T. A. Burd, X. Shan and D. C. Clary, *Phys. Chem. Chem. Phys.*, 2018, **20**, 25224-25234.
38. M. Kumar, A. Sinha and J. S. Francisco, *Acc. Chem. Res.*, 2016, **49**, 877-883.
39. W. Chao, C. Yin, K. Takahashi and J. J. M. Lin, *Phys. Chem. Chem. Phys.*, 2019, **21**, 22589-22597.
40. W. Chao, C. T. Yin, K. Takahashi and J. J. M. Lin, *J. Phys. Chem. A*, 2019, **123**, 8336-8348.
41. M. Kumar, D. H. Busch, B. Subramaniam and W. H. Thompson, *Phys. Chem. Chem. Phys.*, 2014, **16**, 22968-22973.
42. B. Long, J. L. Bao and D. G. Truhlar, *J. Am. Chem. Soc.*, 2016, **138**, 14409-14422.
43. M. Monge-Palacios, M. P. Rissanen, Z. Wang and S. M. Sarathy, *Phys. Chem. Chem. Phys.*, 2018, **20**, 10806-10814.
44. N. A. I. Watson, J. A. Black, T. M. Stonelake, P. J. Knowles and J. M. Beames, *J. Phys. Chem. A*, 2019, **123**, 218-229.
45. R. L. Caravan, M. F. Vansco, K. Au, M. A. H. Khan, Y.-L. Li, F. A. F. Winiberg, K. Zuraski, Y.-H. Lin, W. Chao, N. Trongsiwiat, P. J. Walsh, D. L. Osborn, C. J. Percival, J. J.-M. Lin, D. E. Shallcross, L. Sheps, S. J. Klippenstein, C. A. Taatjes and M. I. Lester, *Proc. Natl. Acad. Sci.*, 2020, **117**, 9733-9740.
46. T. B. Nguyen, G. S. Tyndall, J. D. Crouse, A. P. Teng, K. H. Bates, R. H. Schwantes, M. M. Coggon, L. Zhang, P. Feiner, D. O. Miller, K. M. Skog, J. C. Rivera-Rios, M. Dorris, K. F. Olson, A. Koss, R. J. Wild, S. S. Brown, A. H. Goldstein, J. A. de Gouw, W. H. Brune, F. N. Keutsch, J. H. Seinfeld and P. O. Wennberg, *Phys. Chem. Chem. Phys.*, 2016, **18**, 10241-10254.
47. K. T. Kuwata, L. C. Valin and A. D. Converse, *J. Phys. Chem. A*, 2005, **109**, 10725.
48. L. Vereecken, A. Novelli and D. Taraborrelli, *Phys. Chem. Chem. Phys.*, 2017, **19**, 31599-31612.
49. M. F. Vansco, R. L. Caravan, K. Zuraski, F. A. F. Winiberg, K. Au, N. Trongsiwiat, P. J. Walsh, D. L. Osborn, C. J. Percival, M. A. H. Khan, D. E. Shallcross, C. A. Taatjes and M. I. Lester, *J. Phys. Chem. A*, 2020, **124**, 3542-3554.
50. M. F. Vansco, B. Marchetti and M. I. Lester, *J. Chem. Phys.*, 2018, **149**, 244309.
51. J. M. Anglada and A. Solé, *Phys. Chem. Chem. Phys.*, 2016, **18**, 17698-17712.
52. P. Aplincourt and M. F. Ruiz-López, *J. Phys. Chem. A*, 2000, **104**, 380-388.
53. B. Long, J.-R. Cheng, X.-f. Tan and W.-j. Zhang, *J. Mol. Struct-THEOCHEM*, 2009, **916**, 159-167.
54. O. Welz, A. J. Eskola, L. Sheps, B. Rotavera, J. D. Savee, A. M. Scheer, D. L. Osborn, D. Lowe, A. Murray Booth, P. Xiao, M. Anwar H. Khan, C. J. Percival, D. E. Shallcross and C. A. Taatjes, *Angew. Chem. Int. Ed.*, 2014, **53**, 4547-4550.
55. L. Vereecken, *Phys. Chem. Chem. Phys.*, 2017, **19**, 28630-28640.
56. R. Chhantyal-Pun, B. Rotavera, M. R. McGillen, M. A. H. Khan, A. J. Eskola, R. L. Caravan, L. Blacker, D. P. Tew, D. L. Osborn, C. J. Percival, C. A. Taatjes, D. E. Shallcross and A. J. Orr-Ewing, *ACS Earth and Space Chem.*, 2018, **2**, 833-842.
57. J. P. Porterfield, K. L. K. Lee, V. Dell'Isola, P. B. Carroll and M. C. McCarthy, *Phys. Chem. Chem. Phys.*, 2019, **21**, 18065-18070.
58. C. Cabezas and Y. Endo, *Phys. Chem. Chem. Phys.*, 2019, **21**, 18029-18408.
59. C. Cabezas and Y. Endo, *Phys. Chem. Chem. Phys.*, 2020, **22**, 446-454.
60. C. A. Taatjes, F. Liu, B. Rotavera, M. Kumar, R. Caravan, D. L. Osborn, W. H. Thompson and M. I. Lester, *J. Phys. Chem. A*, 2017, **121**, 16-23.

61. D. L. Osborn, P. Zou, H. Johnsen, C. C. Hayden, C. A. Taatjes, V. D. Knyazev, S. W. North, D. S. Peterka, M. Ahmed and S. R. Leone, *Rev. Sci. Instrum.*, 2008, **79**, 104103.
62. A. S. Hansen, Z. Liu, S. Chen, M. G. Schumer, P. J. Walsh and M. I. Lester, *J. Phys. Chem A*, 2020, **124**, 4929-4938.
63. N. M. Donahue, G. T. Drozd, S. A. Epstein, A. A. Presto and J. H. Kroll, *Phys. Chem. Chem. Phys.*, 2011, **13**, 10848-10857.
64. G. T. Drozd, J. Kroll and N. M. Donahue, *J. Phys. Chem. A*, 2011, **115**, 161-166.
65. T. Kurten and N. M. Donahue, *J. Phys. Chem. A*, 2012, **116**, 6823-6830.
66. K. T. Kuwata, L. Luu, A. B. Weberg, K. Huang, A. J. Parsons, L. A. Peebles, N. B. Rackstraw and M. J. Kim, *J. Phys. Chem. A*, 2018, **122**, 2485-2502.
67. C. Huang, B. Yang and F. Zhang, *J. Chem. Phys.*, 2019, **150**, 164305.

APPENDIX I
PROMPT RELEASE OF O ¹D PRODUCTS UPON
UV EXCITATION OF CH₂OO CRIGEE INTERMEDIATES
SUPPLEMENTARY MATERIAL

This appendix has been previously published as online supplementary material in *The Journal of Chemical Physics*, **147**, 013907 (2017) and reproduced with the permission of AIP Publishing. It is a supplement to Chapter 2 of this thesis. Supplementary research was performed with graduate student Hongwei Li and Marsha I. Lester (*Department of Chemistry, University of Pennsylvania*).

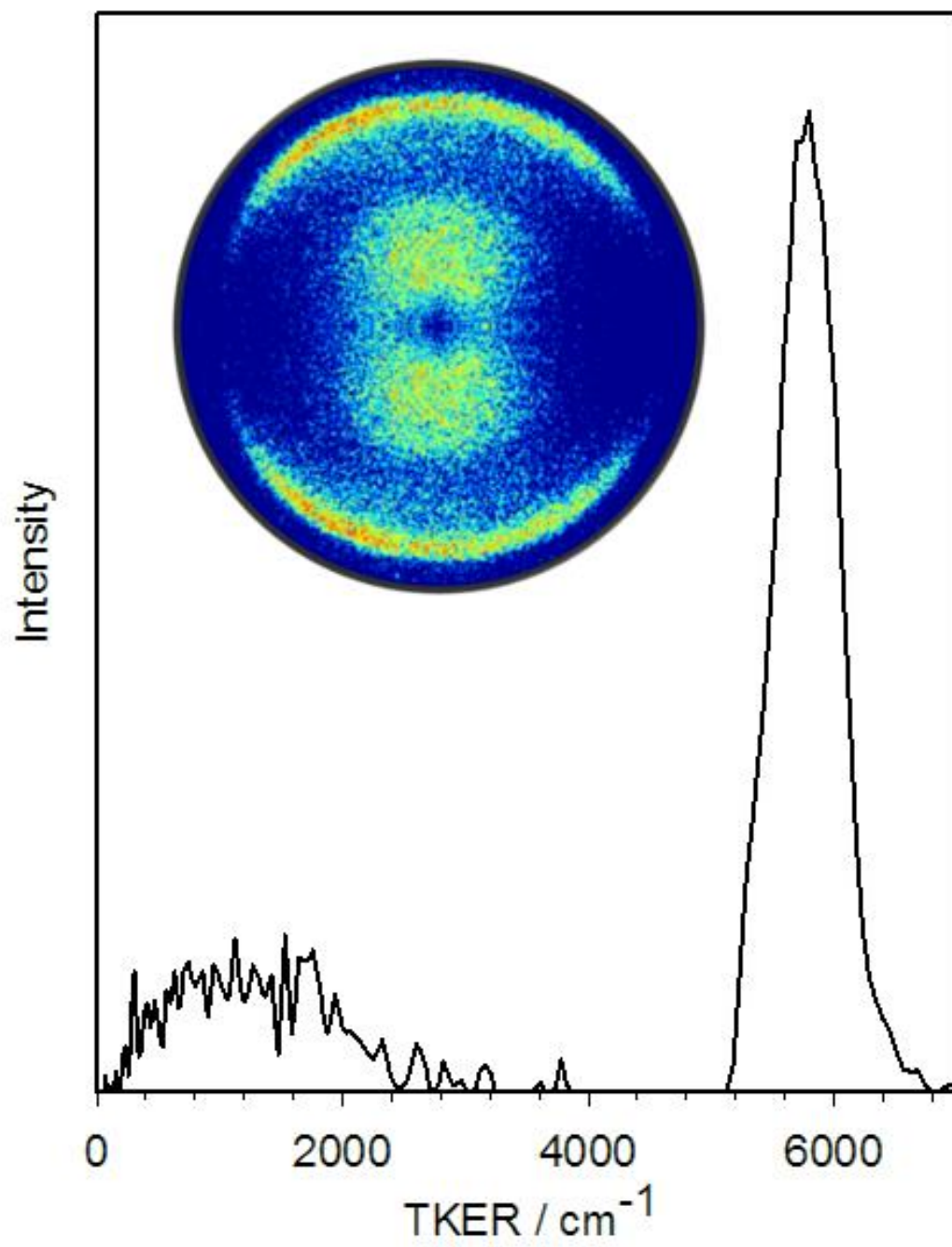


Figure S1. Velocity map image of O ¹D products following UV excitation of IO, a side product formed in reaction of CH₂I + O₂, and 2+1 REMPI detection of O ¹D products in a one-color experiment at 205 nm. The distinct ring in the image and sharply peaked TKER distribution are utilized to determine the energy resolution ($\Delta E/E$) of ~10%. The majority of products from IO dissociation (Ref. 1) are released with high total kinetic energy (TKER); the origin of minor TKER component at low energies is not known.

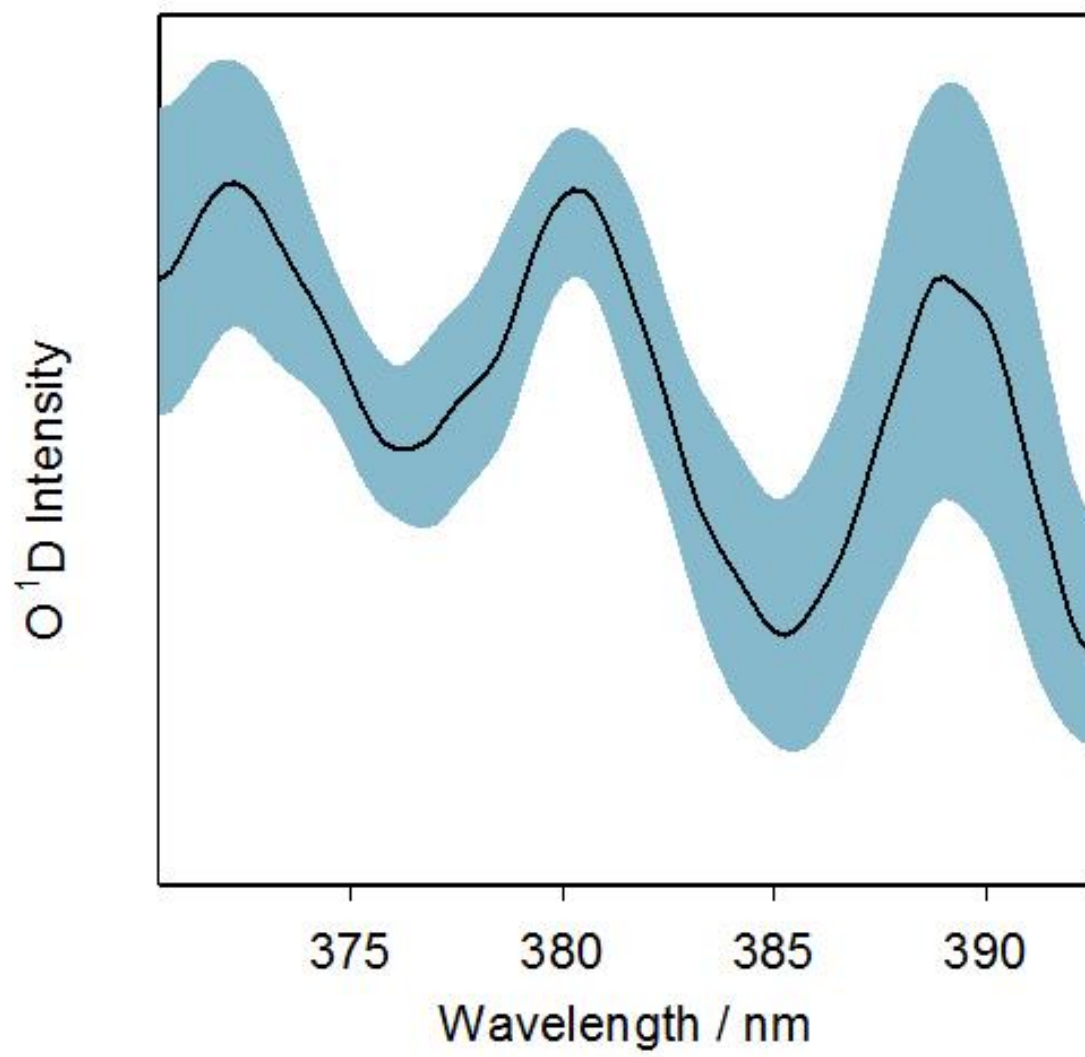


Figure S2. A portion of the UV O ¹D action spectrum of jet-cooled CH₂OO obtained by scanning a frequency-doubled dye (LDS 765 dye) laser across the spectral region from 371 to 392 nm with O ¹D detection by 2+1 REMPI at 205 nm. The oscillatory black curve is the average of several scans with the blue shaded region representing $\pm 1\sigma$ uncertainty; the data is normalized for UV laser power across the dye curve. The peak positions and shape of the broad oscillatory structure in the UV O ¹D action spectrum are similar to those seen previously in direct absorption measurements of Refs. 2-4. Specifically, peaks were reported at 372.0, 380.7, and 389.2 nm in Ref. 3 and at 372.2, 380.3, and 389.2 nm in Ref. 4. Other segments of the UV O ¹D action spectrum in the 390 to 420 nm range (not shown) exhibit analogous broad oscillatory structure as that reported previously.

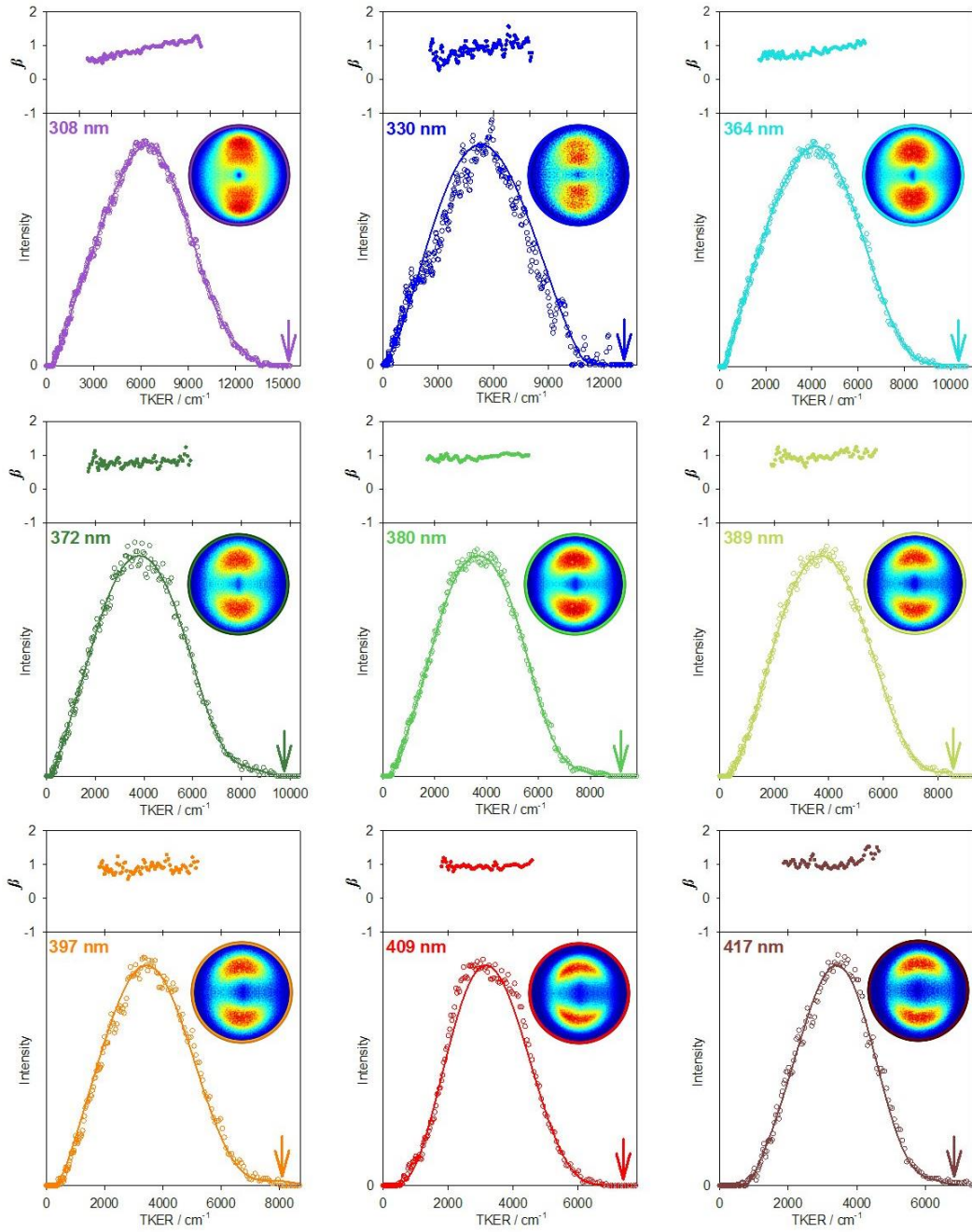


Figure S3. Velocity map images (symmetrized) of O ¹D products following UV excitation of CH₂OO X¹A' at distinct wavelengths from 308 to 417 nm. In each case, the reconstructed image yields the anisotropy parameter β and the total kinetic energy release (TKER) distribution to H₂CO X¹A₁ + O ¹D products with polynomial fit. The energy available (E_{avl}) to the recoiling products is indicated by an arrow. The data and fit at 308 and 330 nm are reproduced from Ref. 5.

Table S1. CH₂OO excitation wavelength and properties derived from velocity map images of O ¹D products: peak, average (avg.), breadth (FWHM), and span (E_{T,max}) of total kinetic energy distribution (TKER), average internal energy of H₂CO X¹A₁ co-product, and average anisotropy parameter β .

Wavelength / nm	Peak / cm ⁻¹	TKER			E _{T,max} / cm ⁻¹	H ₂ CO X ¹ A ₁ avg. internal energy / cm ⁻¹	$\langle \beta \rangle^a$
		Avg. / cm ⁻¹	FWHM / cm ⁻¹				
308	6380	6340	6790	14000	7610	0.79 ± 0.36	
330	5550	5200	5660	11700	6530	0.84 ± 0.29	
364	4130	4140	4850	9200	5020	0.82 ± 0.14	
372	3830	3920	4420	9000	5100	0.80 ± 0.12	
380	3650	3730	3970	8100	4370	0.94 ± 0.07	
389	3720	3800	3990	7900	4090	0.96 ± 0.13	
397	3510	3570	3580	7400	3820	0.92 ± 0.17	
409	3160	3280	2820	6500	3220	0.96 ± 0.08	
417	3400	3400	2670	6800	3410	1.00 ± 0.11	

^a The β parameter is related to the angle χ between the transition dipole moment and the velocity recoil vector in the molecular frame. Previous electronic structure calculations at the (EOM-CCSD)/6-311++G(2d,2p) level theory as implemented in the Molpro computational suite yielded $\chi=29.9^\circ$ and $\beta=1.25$.⁵ The same level of theory implemented in Gaussian 09 yields $\chi=35.8^\circ$ and $\beta=0.97$.

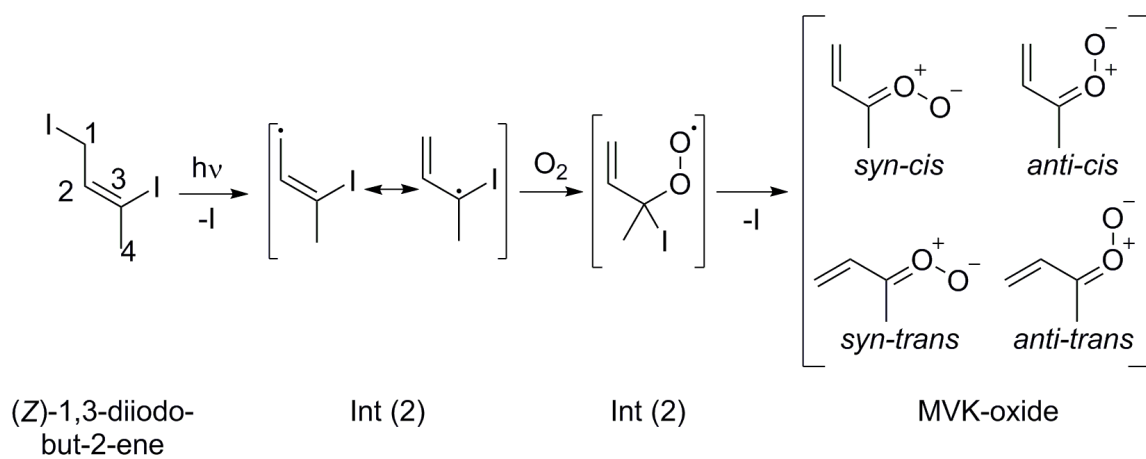
References

1. K. S. Dooley, J. N. Geidosch and S. W. North, *Chem. Phys. Lett.* **457**, 303 (2008).
2. L. Sheps, *J. Phys. Chem. Lett.* **4**, 4201 (2013).
3. W.-L. Ting, Y.-H. Chen, W. Chao, M. C. Smith and J. J.-M. Lin, *Phys. Chem. Chem. Phys.* **16**, 10438 (2014).
4. E. S. Foreman, K. M. Kapnas, Y. Jou, J. Kalinowski, D. Feng, R. B. Gerber and C. Murray, *Phys. Chem. Chem. Phys.* **17**, 32539 (2015).
5. J. H. Lehman, H. Li, J. M. Beames and M. I. Lester, *J. Chem. Phys.* **139**, 141103 (2013).

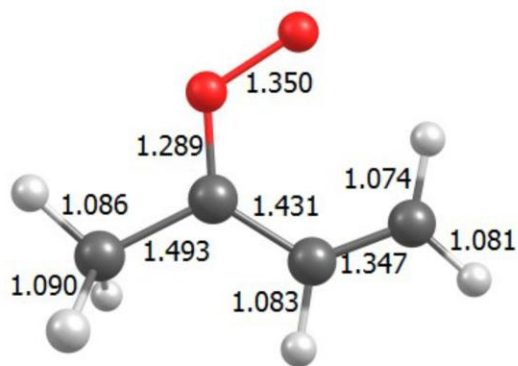
APPENDIX II

**ELECTRONIC SPECTROSCOPY OF METHYL VINYL KETONE
OXIDE: A FOUR-CARBON UNSATURATED CRIEGEE
INTERMEDIATE FROM ISOPRENE OZONOLYSIS
SUPPLEMENTARY MATERIAL**

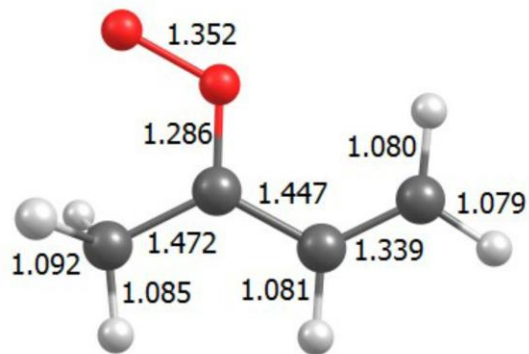
This appendix has been previously published as online supplementary material in *The Journal of Chemical Physics*, **149**, 244309 (2018) and reproduced with the permission of AIP publishing. It is a supplement to Chapter 3 of this thesis. Supplementary work was performed with postdoctoral researcher Barbara Marchetti and Marsha I. Lester (*Department of Chemistry, University of Pennsylvania*).



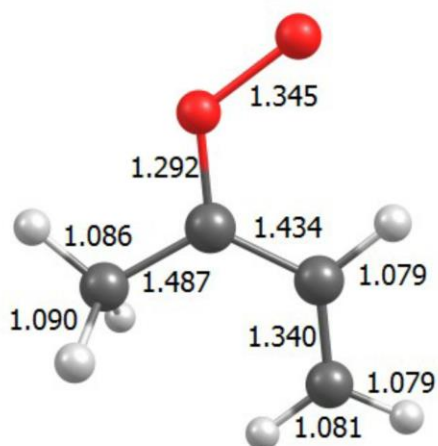
Scheme S1. Alternate synthetic route to MVK-oxide.



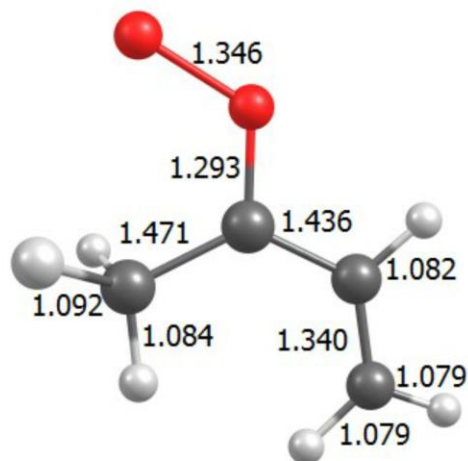
anti-cis
(3.05)



syn-cis
(1.76)



anti-trans
(2.57)



syn-trans
(0.00)

Figure S1. Optimized structures and zero-point corrected energies (kcal mol⁻¹) computed for the four conformers of the methyl vinyl ketone oxide (MVK-oxide) Criegee intermediate in the ground electronic state. Geometries are optimized at the B2PLYP-D3/VTZ level of theory. Energies are calculated at the ANL0-B2F level of theory.

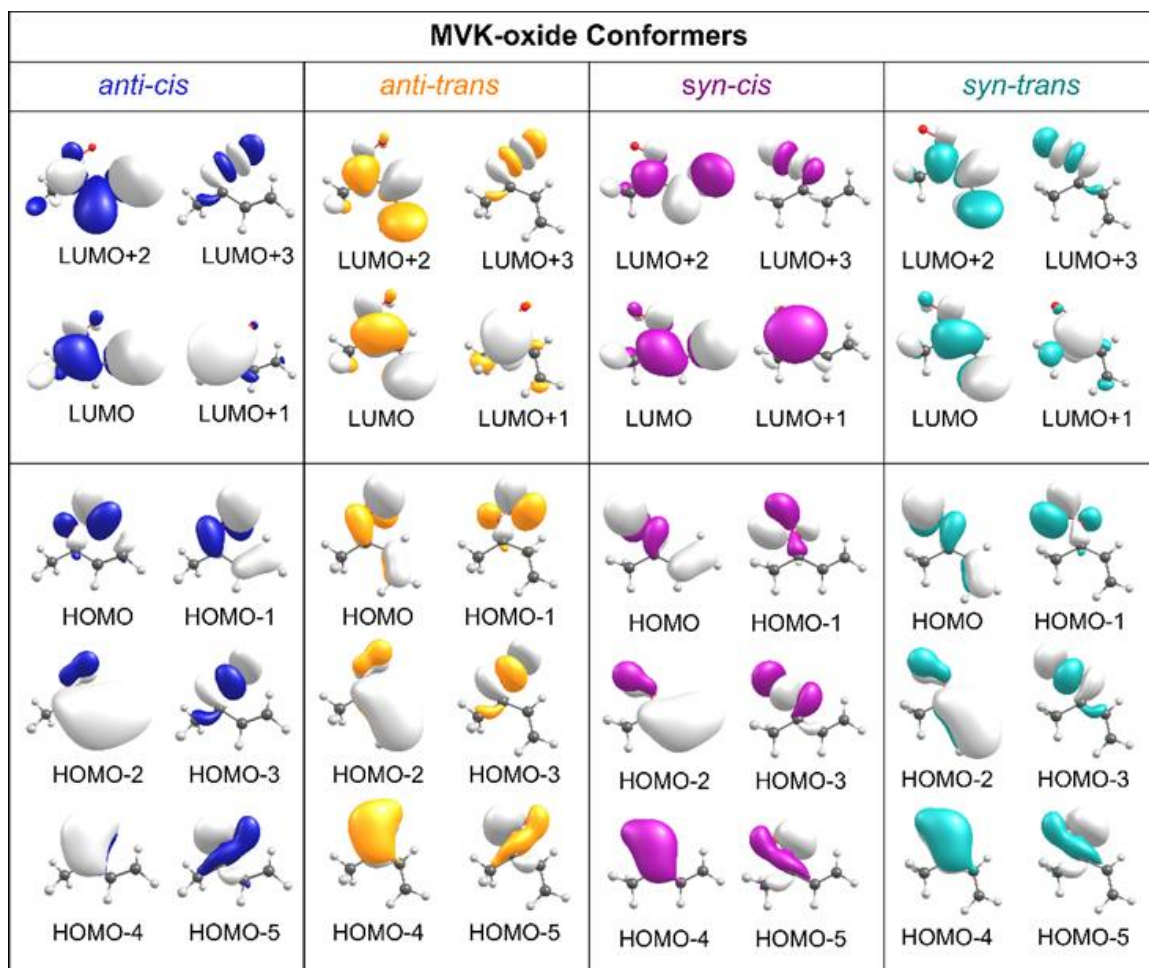


Figure S2. Full set of orbitals chosen for the CASSCF/CASPT2 calculations performed for the four conformers of methyl vinyl ketone oxide (MVK-oxide). The energetic ordering of the excited states for the four conformers (Table S2) can be qualitatively understood by considering steric interactions between the different functional groups. In particular, it is helpful to focus on the electron distribution of the LUMO (π^*) orbital. For *syn-trans*, *syn-cis*, and *anti-cis* conformers, the carbonyl oxide group is oriented toward a CH_3 or CH_2 group, causing a repulsive interaction between the adjacent C-H and terminal oxygen moieties, and resulting in destabilization of the $1^1\pi\pi^*$ excited state. The *syn-trans* conformer likely has an additional destabilizing interaction between the vinyl and methyl substituents. The *anti-trans* conformer has the lowest vertical excitation energy by virtue of stabilizing hyperconjugation in the excited π^* state between the vinyl and methyl group.

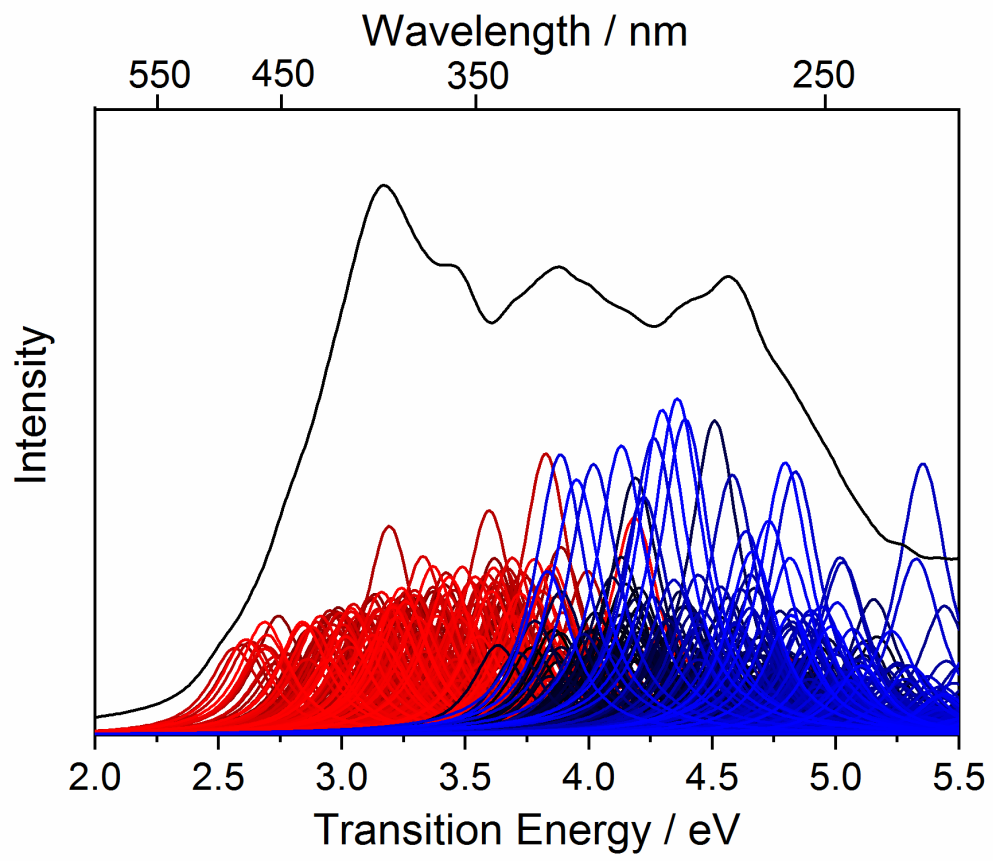


Figure S3. Simulated UV-vis spectrum of *syn-trans* conformer of MVK-oxide (black line). The computed spectrum is evaluated by summing an ensemble of vertical transitions originating from 300 (*N*) initial geometries that contribute to absorption bands associated with the $1^1\pi\pi^*$ (red lines) and $2^1\pi\pi^*$ (blue lines) states. Each of the individual transitions is broadened with a Lorentzian line shape function (0.25 eV FWHM).

Table S1. Zero-point corrected energies for the ground states of the four conformers of MVK-oxide evaluated at the ANOL-B2F level of theory.^{a,b}

Conformer	Relative Energy / kcal mol ⁻¹ (cm ⁻¹)
<i>syn-trans</i>	0.00
<i>syn-cis</i>	1.76 (616)
<i>anti-trans</i>	2.57 (899)
<i>anti-cis</i>	3.05 (1067)

^a V. P. Barber, S. Pandit, A. M. Green, N. Trongsiwat, P. J. Walsh, S. R. Klippenstein and M. I. Lester, *J. Am. Chem. Soc.* **140**, 10866-80 (2018).

^b CASPT2/AVDZ calculations (at the optimized structures, Figure S1) predict very similar ZPE-corrected energies for *syn* conformers, and slightly higher energies (by ca. 1-2 kcal mol⁻¹) and reverse ordering for *anti-cis* and *anti-trans* conformers.

Table S2. CASPT2(12,10)/ AVDZ vertical excitation energies (VEE, eV) and oscillator strengths (f) associated with lowest six singlet electronic transitions for the four conformers of MVK-oxide. The dominant excitation character associated with each electronic transition is indicated (parenthesis) and the strong $\pi^* \leftarrow \pi$ transitions are highlighted (bold).

Conformer of MVK-oxide ^a							
<i>anti-cis</i>		<i>anti-trans</i>		<i>syn-cis</i>		<i>syn-trans</i>	
VEE	f	VEE	f	VEE	f	VEE	f
2.08 ($n\pi^*$)	0.000	2.07 ($n\pi^*$)	0.000	2.14 ($n\pi^*$)	0.000	2.27 ($n\pi^*$)	0.000
3.31 ($\pi\pi^*$)	0.071	3.16 ($\pi\pi^*$)	0.211	3.25 ($\pi\pi^*$)	0.111	3.54 ($\pi\pi^*$)	0.128
4.68 ($\pi\pi^*$)	0.043	5.40 ($n3s$)	0.011	4.52 ($\pi\pi^*$)	0.091	4.52 ($\pi\pi^*$)	0.109
5.31 ($n3s$)	0.015	5.55 ($\pi\pi^*$)	0.345	5.41 ($\pi3s$)	0.002	5.43 ($\pi3s$)	0.003
5.38 ($\pi3s$)	0.000	5.71 ($n\pi^*$)	0.002	5.47 ($n\pi^*$)	0.000	5.53 ($n\pi^*$)	0.000
5.50 ($n\pi^*$)	0.000	7.86 ($\pi3s$)	0.050	5.64 ($n3s$)	0.002	5.58 ($n3s$)	0.013

^a The vertical excitation energies and energetic ordering of the $1^1\pi\pi^*$ and $2^1\pi\pi^*$ states differ considerably for the four conformers of MVK-oxide.

Table S3. Lowest spin-allowed product asymptotes^a and zero-point corrected dissociation energies for the four conformers of MVK-oxide.

MVK-oxide Conformer → Product Asymptote ^b	Dissociation Energy ^{c, d}		
<i>anti-cis</i> → <i>cis</i> -MVK X ¹ A' + O ¹ D	2.11 eV	17037 cm ⁻¹	587 nm
<i>anti-trans</i> → <i>trans</i> -MVK X ¹ A' + O ¹ D	2.14 eV	17267 cm ⁻¹	579 nm
<i>syn-cis</i> → <i>cis</i> -MVK X ¹ A' + O ¹ D	2.17 eV	17482 cm ⁻¹	572 nm
<i>syn-trans</i> → <i>trans</i> -MVK X ¹ A' + O ¹ D	2.25 eV	18180 cm ⁻¹	550 nm

^a *cis*↔*trans* energy splitting of MVK product (84 cm⁻¹) evaluated at B2PLYP-D3/VTZ level of theory.

^b The *trans*-MVK + O structure was optimized at the B2PLYP-D3/VTZ level of theory with O-O bond distance and C-O-O angle fixed to aid in convergence.

^c CASPT2(12,10)/AVDZ level of theory.

^d The zero-point corrected energy required for the lowest bond cleavage channel (O-O bond fission) of *syn-trans*- MVK-oxide was evaluated for spin allowed dissociation on singlet surfaces, leading to *trans*-MVK X ¹A' + O ¹D. The O-O dissociation energies for the other conformers are evaluated by accounting for their relative ground state energies (Table S1) and the *cis*↔*trans* energy splitting between the two MVK conformer products.

Table S4. CASPT2(12,10)/ AVDZ vertical excitation energies (VEE, eV), corresponding wavelengths (λ , nm), and oscillator strengths (f) for the lowest six singlet electronic transitions of possible isomers of MVK-oxide. Transitions predicted to have appreciable oscillator strength are highlighted (bold).

5-methyl-3H-1,2-dioxole (dioxole)		1-hydroxybut-3-en-2-one (HB)	
VEE / eV (λ /nm)	f	VEE / eV (λ /nm)	f
4.12 (301)	0.001	3.90 (318)	0.000
5.87 (211)	0.230	6.05 (205)	0.275
6.00 (207)	0.004	7.08 (175)	0.000
7.76 (160)	0.002	7.14 (174)	0.002
8.10 (153)	0.129	7.58 (164)	0.042
9.16 (135)	0.005	7.92 (156)	0.019
<i>trans</i> -2-hydroperoxybuta-1,3-diene (<i>trans</i> -HPBD)		<i>cis</i> -2-hydroperoxybuta-1,3-diene (<i>cis</i> -HPBD)	
VEE / eV (λ /nm)	f	VEE / eV (λ /nm)	f
5.68 (218)	0.001	5.72 (217)	0.029
5.94 (209)	0.058	5.83 (213)	0.236
6.07 (204)	0.646	6.16 (201)	0.058
7.57 (164)	0.000	6.48 (191)	0.026
7.39 (168)	0.097	7.73 (160)	0.072
9.03 (137)	0.002	7.93 (156)	0.038
3-hydroxybut-2-enal (enol)		3-oxobutanal (β -dicarbonyl)	
VEE / eV (λ /nm)	f	VEE / eV (λ /nm)	f
3.92 (316)	0.000	4.01 (309)	0.001

4.71 (263)	0.259	4.22 (294)	0.000
5.87 (211)	0.111	6.37 (195)	0.006
6.00 (207)	0.008	6.49 (191)	0.017
6.74 (184)	0.001	6.50 (191)	0.005
7.30 (170)	0.054	7.22 (172)	0.016

Table S5. Characteristics of the total kinetic energy release (TKER) and anisotropic angular distributions derived from reconstructed images of O ¹D products following electronic excitation of MVK-oxide on the 1¹ $\pi\pi^*$ transition at 390 and 420 nm. For TKER, the parameters include the average $\langle \text{TKER} \rangle$ and most probable (Peak) kinetic energy, and the full width at half maximum (FWHM). The anisotropy parameter β is derived from the angular distributions.

	O ¹ D	
	390 nm	420 nm
$\langle \text{TKER} \rangle / \text{cm}^{-1}$	2136	2085
Peak / cm^{-1}	2058	1785
FWHM / cm^{-1}	1734	1790
β	0.69(15)	0.86(39)
$E_{\text{avl}} / \text{cm}^{-1}$	7460 ^a	5630 ^a

^a Estimated from laser excitation energy and zero-point corrected dissociation energy for *syn-trans* conformer of MKV-oxide (Table S3). Higher energy conformers have lower dissociation energies, suggesting an increase in E_{avl} by as much as 1140 cm^{-1} (*anti-cis*).

APPENDIX III

**SYNTHESIS, ELECTRONIC SPECTROSCOPY AND
PHOTOCHEMISTRY OF METHACROLEIN OXIDE: A FOUR-
CARBON UNSATURATED CRIEGEE INTERMEDIATE FROM
ISOPRENE OZONOLYSIS
SUPPORTING INFORMATION**

This appendix has been previously published as online supplementary material and reproduced with permission from *The Journal of the American Chemical Society*, **141**, 15058 (2018). It is a supplement to Chapter 4 of this thesis. Supplementary experimental work was performed with graduate students Trisha Bhagde, and Guanghan Wang, and postdoctoral researchers Barbara Marchetti and Marsha I. Lester (*Department of Chemistry, University of Pennsylvania*). Synthetic work was performed by graduate student Nisalak Trongsiwat and Patrick J. Walsh (*Department of Chemistry, University of Pennsylvania*). Theoretical research was performed by postdoctoral researcher Barbara Marchetti (*Department of Chemistry, University of Pennsylvania*) and in collaboration with Stephen J. Klippenstein (*Chemical Sciences and Engineering Division, Argonne National Laboratory*).

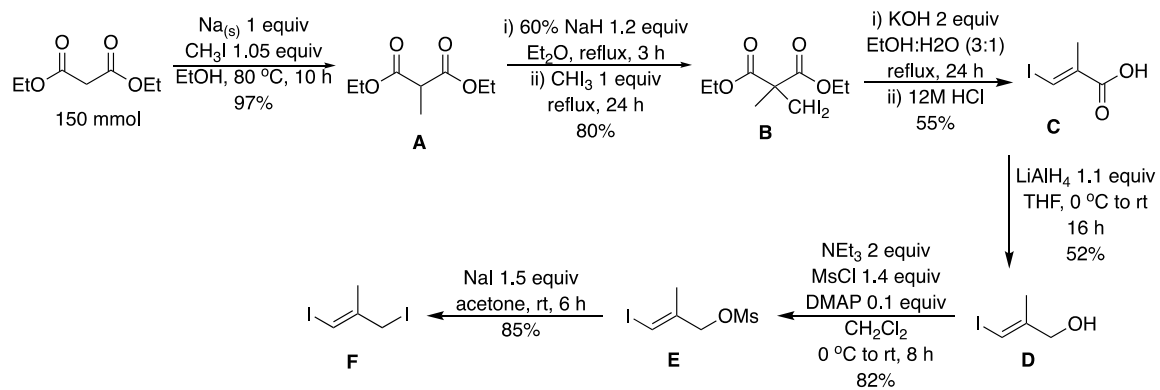
Section S1. Synthesis of (*E*)-1,3-diiodo-2-methylprop-1-ene

S1.1. Overview of (*E*)-1,3-diiodo-2-methylprop-1-ene precursor synthesis

An overview of the (*E*)-1,3-diiodo-2-methylprop-1-ene precursor synthesis is given in the main text (Scheme 1) and further details are provided here. Based on Artok's procedure,¹ diethyl malonate was methylated with methyl iodide in the presence of sodium ethoxide in ethanol to provide diethyl methylmalonate **A** in 97% yield. Following Rudolph's protocol,² deprotonation of **A** in the presence of NaH in diethyl ether was followed by alkylation with iodoform to generate diiodide **B** in 80% yield. Diiodide **B**, used without purification, was subjected to base, hydrolyzed, and eliminated under refluxing conditions to provide 55% yield of the carboxylic acid **C** as a single stereoisomer. Reduction of the carboxylic acid **C** was performed with lithium aluminum hydride at room temperature for 16 h to afford alcohol **D** in 52% yield. Using a modified version of Ghosh's procedure³ alcohol **D** was treated with methanesulfonyl chloride (MsCl), triethylamine, and catalytic 4-dimethylaminopyridine (DMAP) to provide mesylated **E** in 82% yield. The highly reactive allylic mesylate **E** was used without further purification. In the final step, mesylate **E** was reacted with sodium iodide in acetone at room temperature. The substitution reaction was conducted in the absence of light because the product is light sensitive. After 6 h of reaction time, the desired yellow oil **F** was obtained in 85% yield as a single diastereomer. The detailed procedures and full characterization are described below.

S1.2. Diethyl methylmalonate¹

Anhydrous ethanol (70 mL, 298 K) was added to a dry two-neck round bottom flask equipped with a reflux condenser and purged with N₂. Under the N₂ purge, small



Scheme S1. Synthesis of (*E*)-1,3-diiodo-2-methylprop-1-ene.

pieces of metallic sodium (3.48 g, 150 mmol) were added very carefully to the stirred solution with effervescence observed. After all the sodium had reacted, diethyl malonate (23.0 mL, 150 mmol) was added dropwise to the colorless solution. The room temperature reaction mixture was treated with iodomethane (9.80 mL, 157 mmol) by dropwise addition over 5 min and the pale-yellow mixture was heated to reflux at 80 °C. After 10 h, the mixture was allowed to cool to room temperature and the reaction mixture was concentrated under reduced pressure and diluted with Et₂O and water. The aqueous layer was extracted with Et₂O (3 x 20 mL). The combined organic layers were dried over Na₂SO₄ and concentrated under reduced pressure to afford a colorless oil (25.4 g, 97%). ¹H NMR (500 MHz, CDCl₃) δ 4.28-4.10 (m, 4H), 3.42 (q, *J* = 7.3 Hz, 1H), 1.42 (d, *J* = 7.3 Hz, 3H), 1.27 (t, *J* = 7.1 Hz, 6H). ¹³C{¹H} NMR (125 MHz, CDCl₃) δ 170.0, 61.2, 46.1, 13.9, 13.4. The spectroscopic data were identical to a previous report.⁴ The crude product was used in the next step without further purification.

S1.3. Diethyl 2-(diiodomethyl)-2-methylmalonate²

Under an N₂ atmosphere, a dry two-neck 250 mL round-bottom flask was loaded with NaH (60% dispersion in oil, 1.65 g, 69.0 mmol) and dry Et₂O (50 mL) at room temperature (23 °C). Diethyl methylmalonate (10.0 g, 57.4 mmol) was added dropwise by syringe with vigorous stirring and the resulting thick mixture was refluxed at 40 °C for 3 h. After being cooled to room temperature, the yellow solid CHI₃ (22.6 g, 57.4 mmol) was added in one portion and the yellow mixture was refluxed under N₂ for another 24 h. The reaction vessel was cooled to 0 °C and opened to air. 10% aqueous HCl solution (50 mL) was added dropwise over 20 min and the orange homogeneous solution stirred for 30 min at 0 °C. The organic layer was separated and the residual organic material from the aqueous layer was extracted with Et₂O (3 x 20 mL). The combined organic

layers were dried over Na₂SO₄, decanted, and concentrated under reduced pressure. The yellow residue was redissolved in petroleum ether (30 mL) and the precipitated CHI₃ was removed by filtration. The filtrate was concentrated under reduced pressure to afford the title compound (20.2 g, 80%) as a dark orange oil. The product was used directly for the next step without any further purification.

S1.4. (*E*)-3-Iodo-2-methylprop-2-enoic acid²

A solution of crude diethyl diiodomethylmethylmalonate (20.2 g, 45.9 mmol), KOH (5.14 g, 91.8 mmol) and EtOH/H₂O (3:1, 80 mL) was added to a round-bottom flask (250 mL) and refluxed under air at 85 °C for 24 h. After cooling to room temperature, the light-orange mixture was concentrated under vacuum. The residue was then redissolved in 10% aqueous K₂CO₃ (60 mL) and the mixture was washed with CH₂Cl₂ (3 x 20 mL), acidified with 12 M HCl (80 mL), and extracted with CH₂Cl₂ (10 x 20 mL). The organic layer was dried over Na₂SO₄ and concentrated in vacuum. The remaining thick oil was purified by column chromatography on silica gel (hexanes: EtOAc = 10:1, 0.5% AcOH, R_f = 0.25) to provide the carboxylic acid (5.33 g, 55%) as a white solid. ¹H NMR (300 MHz, CDCl₃) δ 9.51-10.7 (br s, 1H), 8.03 (s, 1H), 2.06 (s, 3H). ¹³C{¹H} NMR (125 MHz, CDCl₃) δ 169.3, 139.2, 102.2, 19.9. The spectroscopic data were identical to those previously reported.⁵

S1.5. (*E*)-3-Iodo-2-methylprop-2-en-1-ol²

A solution of carboxylic acid (1.36 g, 6.42 mmol) in THF (25 mL) was added to a 100 mL Schlenk flask under N₂ atmosphere. The colorless solution was cooled to 0 °C for 15 min. LiAlH₄ (270 mg, 7.10 mmol) was added as a solid into the reaction mixture in three portions over a 30 min period to form a gray heterogeneous mixture. The reaction mixture was allowed to warm to room temperature (RT) and stirred for 16 h. The reaction

mixture was then cooled to 0 °C, opened to air and quenched by dropwise addition of saturated aqueous Na₂SO₄ (2 mL) over 5 min. The reaction mixture was diluted with Et₂O (10 mL) and 2M aqueous H₂SO₄ (10 mL). The mixture was next extracted with CH₂Cl₂ (3 x 15 mL). The combined organic layers were concentrated under reduced pressure and the remaining oil dissolved in CH₂Cl₂ (10 mL) and washed with 10% aqueous K₂CO₃ (10 mL). The aqueous layer was extracted with CH₂Cl₂ (3 x 10 mL). The combined organic layers were dried over Na₂SO₄ and concentrated under reduced pressure. The crude oil product was purified by column chromatography on silica gel (hexanes: EtOAc = 4:1, R_f = 0.2) to afford the alcohol (0.66 g, 52%) as a pale-yellow oil. ¹H NMR (500 Mz, CDCl₃) δ 6.28 (s, 1H), 4.09 (d, *J* = 5.1 Hz, 2H), 3.52(t, *J* = 5.5 Hz, 1H), 1.77 (s, 3H). ¹³C{H} NMR (125 MHz, CDCl₃) δ 147.2, 76.8, 66.5, 21.4. The spectroscopic data were identical to those previous reported.⁵

S1.6. (*E*)-3-Iodo-2-methylallyl methanesulfonate³

Et₃N (0.59 mL, 6.66 mmol) and methanesulfonyl chloride (0.39 mL, 4.50 mmol) followed by DMAP (40.7 mg, 0.333 mmol) was added to a solution of the alcohol (0.660 g, 3.33 mmol) in dry CH₂Cl₂ (10 mL) at 0 °C under an N₂ atmosphere. After the addition was complete, the pale yellow mixture was warmed to room temperature and stirred for 8 h. The reaction mixture was filtered through a short pad of silica, the silica was washed with CH₂Cl₂ (2 x 5 mL) and the solvent was removed under reduced pressure to give the mesylated compound (0.754 g, 82%) as a yellow oil. The crude oil was used in the next step without further purification.

S1.7. (*E*)-1,3-Diiodo-2-methylprop-1-ene³

Acetone (10 mL) and NaI (0.614 g, 4.10 mmol) were added to a solution of mesylated compound (0.754 g, 2.73 mmol) at room temperature in a dark fume hood

under air. The yellow reaction mixture was wrapped with aluminum foil (to exclude light) and stirred for 6 h. The reaction mixture was then filtered through a short pad of silica and then the silica was washed with CH₂Cl₂ (2 x 10 mL). The filtrate was washed with saturated aqueous Na₂S₂O₃ solution (2 x 10 mL). The combined organic layers were dried over Na₂SO₄ and concentrated under reduced pressure. The crude product was purified via column chromatography on silica gel (hexanes: EtOAc = 4:1, R_f = 0.8) to afford a yellow oil (0.714 g, 85%). ¹H NMR (500 MHz, CDCl₃) δ 6.48 (d, *J* = 0.9 Hz, 1H), 4.11 (d, *J* = 0.8 Hz, 2H), 1.96 (d, *J* = 1.1 Hz, 3H). ¹³C{¹H} NMR (125 MHz, CDCl₃) δ 143.3, 82.0, 48.6, 21.8. HRMS (EI): *m/z* calculated for C₄H₆I₂ 307.8580, found: 307.8559. The full ¹H and ¹³C NMR spectra are shown in Figure S1. Spectroscopic data for this compound was not previously reported.⁵

(*E*)-1,3-diiodo-2-methylprop-1-ene was characterized via UV-vis spectroscopy and compared to the UV-vis spectrum of CH₂I₂. Dilute solutions of (*E*)-1,3-diiodo-2-methylprop-1-ene (0.08 mmol/L) and CH₂I₂ (0.19 mmol/L) in hexanes were prepared and the UV-vis spectra shown in Figure S2 were recorded with a spectrophotometer (Jasco V-650). A previous study of the UV-vis spectra of CH₂I₂ in both polar and nonpolar solvents indicated virtually no shift in peak absorption wavelengths compared to the gas phase UV spectrum.⁶ By analogy, the peak UV absorption of (*E*)-1,3-diiodo-2-methylprop-1-ene in the gas phase is expected to be similar to that shown in hexanes solvent in Figure S2.

In addition, the FTIR spectrum of (*E*)-1,3-diiodo-2-methylprop-1-ene on a KBr plate was obtained with an FTIR spectrometer (Thermo Scientific, Nicolet iS5), and is presented in Figure S3. A complementary theoretical calculation of the optimized structure and fundamental frequencies of the (*E*)-1,3-diiodo-2-methylprop-1-ene precursor are reported in Figure S4 and Table S1, respectively.

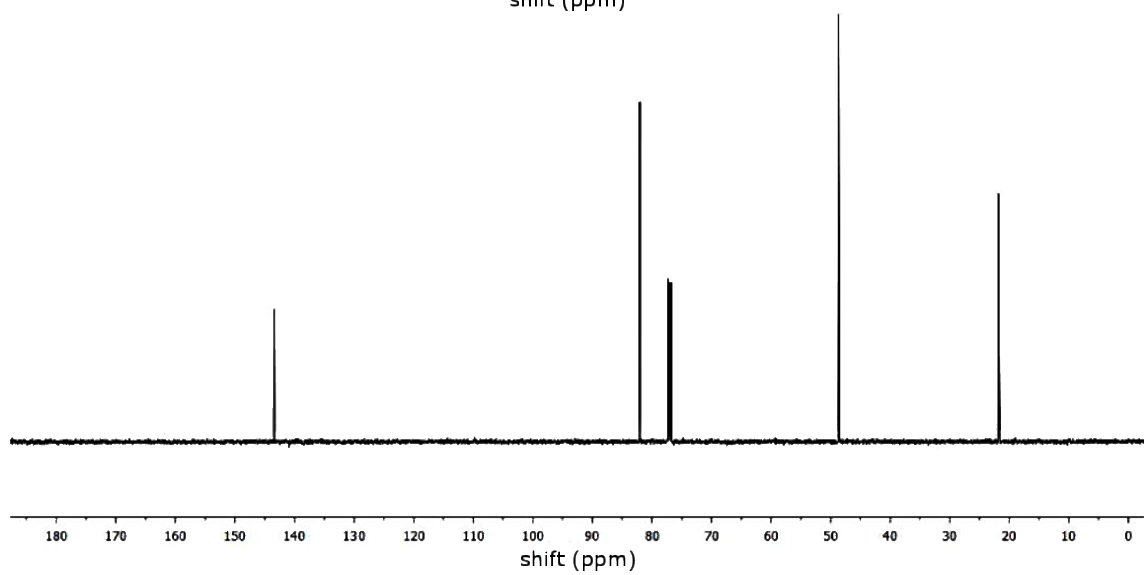
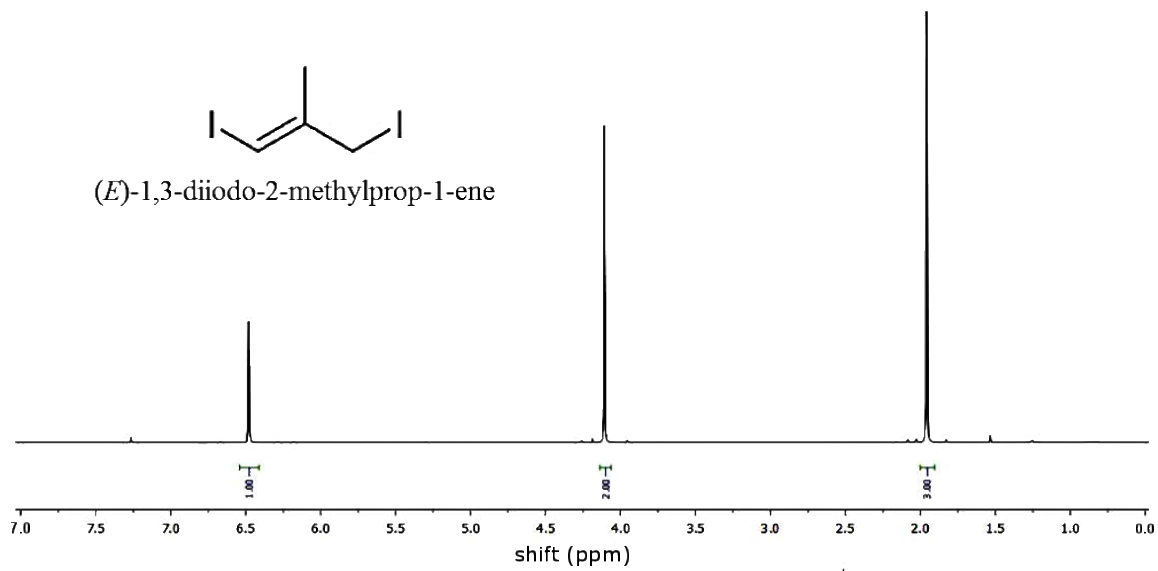
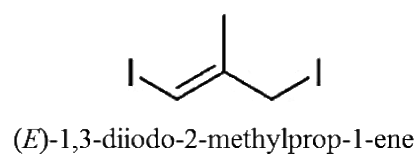


Figure S1. (*E*)-1,3-diiodo-2-methylprop-1-ene characterization via 500 MHz ^1H NMR in CDCl_3 (top panel) and 125 MHz $^{13}\text{C}\{^1\text{H}\}$ NMR in CDCl_3 (lower panel).

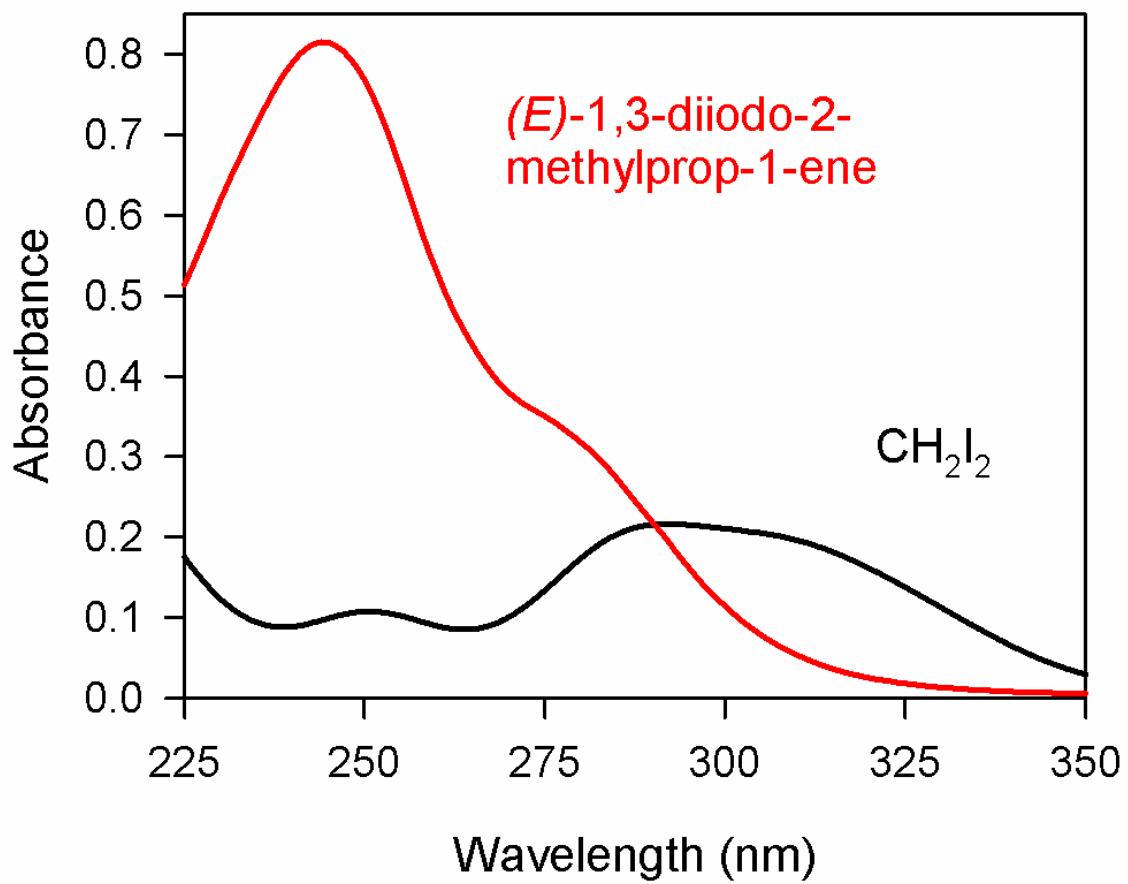


Figure S2. UV spectrum of the (*E*)-1,3-diiodo-2-methylprop-1-ene precursor (red solid line) compared to the UV spectrum of CH₂I₂ (black solid line).

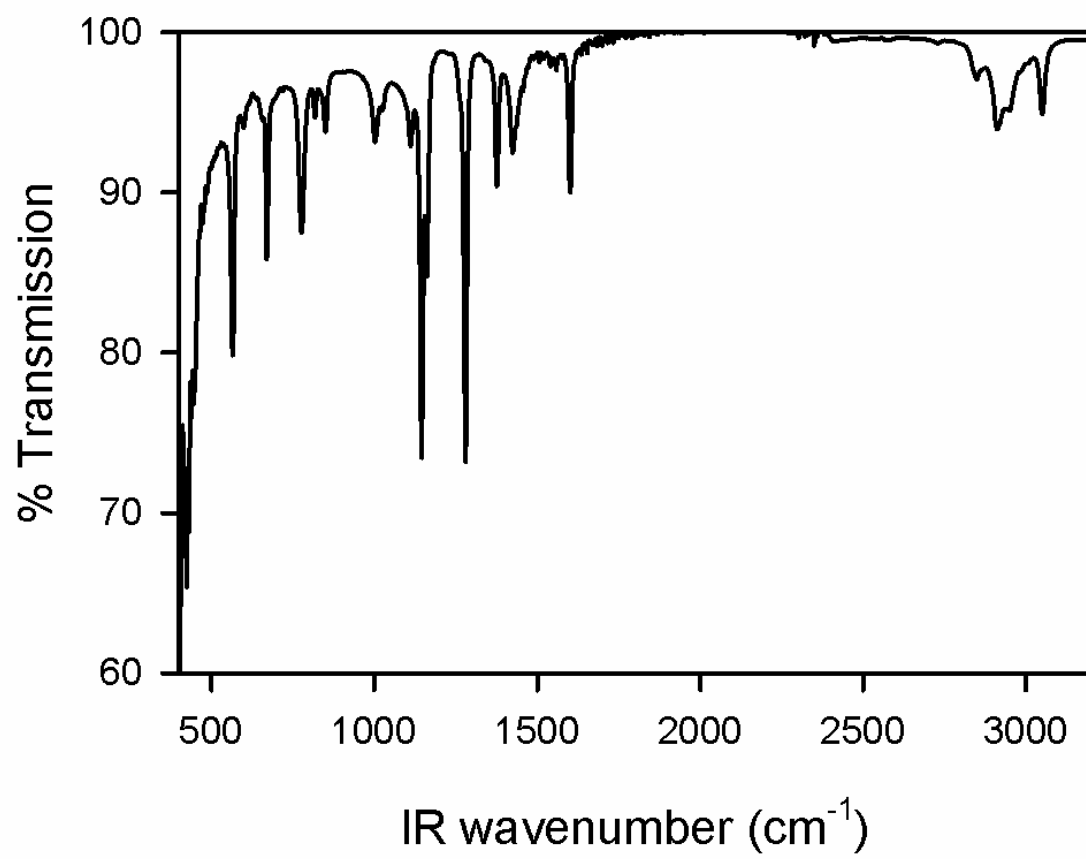


Figure S3. FTIR spectrum of (E)-1,3-diiodo-2-methylprop-1-ene on a KBr plate from 400-3200 cm^{-1} . High frequency vibrations (ca. 2800-3200 cm^{-1}) are assigned to the alkyl CH stretches. CH scissor and CH wag vibrational modes appear in the 1000-1500 cm^{-1} energy region. The sharp features at ca. 1150 and 1280 cm^{-1} are attributed to CH wag vibrational modes. The very strong C-I stretches appear at ca. 450 cm^{-1} .

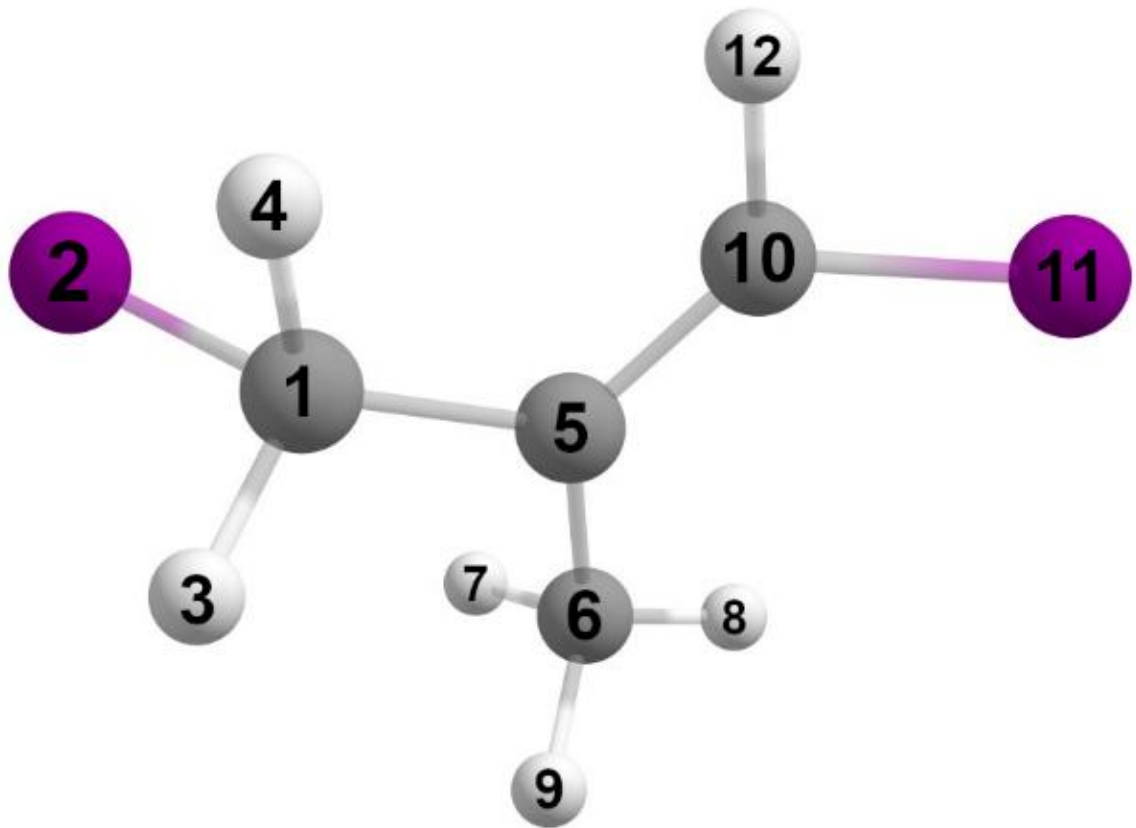


Figure S4. (*E*)-1,3-diiodo-2-methylprop-1-ene precursor geometry with number labelling of atoms for vibrational mode assignment (Table S1).

Table S1. Calculated vibrational modes of (*E*)-1,3-diiodo-2-methylprop-1-ene at the B3LYP/6-311+G(d,p) level of theory. Labelling is based on the numbering of atoms in Figure S4.

Mode	Harmonic Frequency (cm ⁻¹)	Description
v ₁	3204	Methine C ₍₁₀₎ H ₍₁₂₎ stretch
v ₂	3180	Out-of-phase C ₍₁₎ H ₍₃₎ H ₍₄₎ stretch
v ₃	3136	Methyl C ₍₆₎ H ₍₇₎ stretch
v ₄	3107	In-phase C ₍₁₎ H ₍₃₎ H ₍₄₎ stretch
v ₅	3076	Out-of-phase C ₍₆₎ H ₍₈₎ H ₍₉₎ stretch
v ₆	3027	In-phase methyl CH stretch
v ₇	1656	Alkene C ₍₅₎ -C ₍₁₀₎ stretch
v ₈	1490	Methyl C ₍₆₎ H ₍₈₎ H ₍₉₎ scissor
v ₉	1484	Methyl C ₍₆₎ H ₍₇₎ H ₍₉₎ scissor
v ₁₀	1472	Alkyl C ₍₁₎ H ₍₃₎ H ₍₄₎ scissor
v ₁₁	1417	Methyl umbrella
v ₁₂	1312	Methine C ₍₁₀₎ H ₍₁₂₎ wag
v ₁₃	1189	Alkyl C ₍₁₎ H ₍₃₎ H ₍₄₎ wag
v ₁₄	1178	C ₍₁₎ -C ₍₅₎ stretch
v ₁₅	1144	Alkyl C ₍₁₎ H ₍₃₎ H ₍₄₎ twist
v ₁₆	1057	Methyl C ₍₆₎ H ₍₇₎ wag
v ₁₇	1018	Methyl rock
v ₁₈	868	C ₍₁₎ C ₍₅₎ C ₍₁₀₎ bend
v ₁₉	828	C ₍₅₎ -C ₍₆₎ stretch
v ₂₀	809	Methine C ₍₁₀₎ H ₍₁₂₎ twist

V21	676	$C_{(10)}I_{(11)}$ stretch
V22	561	$C_{(5)}C_{(6)}C_{(10)}$ rock
V23	436	$C_{(9)}I_{(12)}$ stretch
V24	409	$C_{(1)}I_{(2)}$ stretch
V25	300	Alkyl $C_{(1)}H_{(3)}H_{(4)}$ rock
V26	199	$C_{(6)}C_{(5)}C_{(10)}I_{(11)}$ bend
V27	185	$C_{(6)}C_{(5)}C_{(10)}$ twist
V28	119	$C_{(6)}C_{(5)}C_{(1)}I_{(2)}$ bend
V29	80	Methyl rotor
V30	41	Alkyl $C_{(1)}H_{(3)}H_{(4)}I_{(2)}$ rotor

Section S2. Ground state energies and vertical excitation

energies of MACR-oxide

The ground state minimum energy geometries of the four conformers of MACR-oxide are optimized using the B2PLYP-D3 functional in Density Functional Theory coupled with Dunning's correlation consistent basis set of triple ζ quality (cc-pVTZ) using the Gaussian09 computational package (Figure S5, Table S2).⁷ High level ab initio calculations are carried out to characterize the energies of each MACR-oxide conformer using a slightly modified version of the ANL0-F12 approach described previously.⁸ This approach is based on CCSD(T)-F12/CBS(TZ-F12,QZ-F12)//B2PLYP-D3/cc-pVTZ calculations. The energies obtained by the various methods used in this study are compared to a previous study (Table S3).⁹ Ground state normal mode harmonic wavenumbers are computed at the same level of theory (Table S4) to evaluate zero-point energy (ZPE) corrections to the relative ground state energies. A similar approach is used to evaluate the vertical ionization energies (VIE) and adiabatic ionization energies (AIE) for each conformer, but for these energies we include a correction for higher order excitations [from CCSDT(Q)/cc-pVDZ calculations] and for core-valence interactions [CCSD(T)/CBS(cc-pcVTZ,cc-pcVQZ) calculations] to account for the significantly different bonding in the neutral and the ions. For simplicity this correction is presumed to be the same for each of the conformers and is taken equal to the average of the correction for the four conformers of CH₂CHCHO, which is 1.7 kcal mol⁻¹.

Qualitatively, the relative stabilities of the conformers can be explained by inspection of orbital interactions between the carbonyl oxide and adjacent functional groups. The most stable conformation (*anti-trans*) has the least electronic repulsion between the in-plane carbonyl O-atom and out-of-plane H-atoms of the adjacent methyl

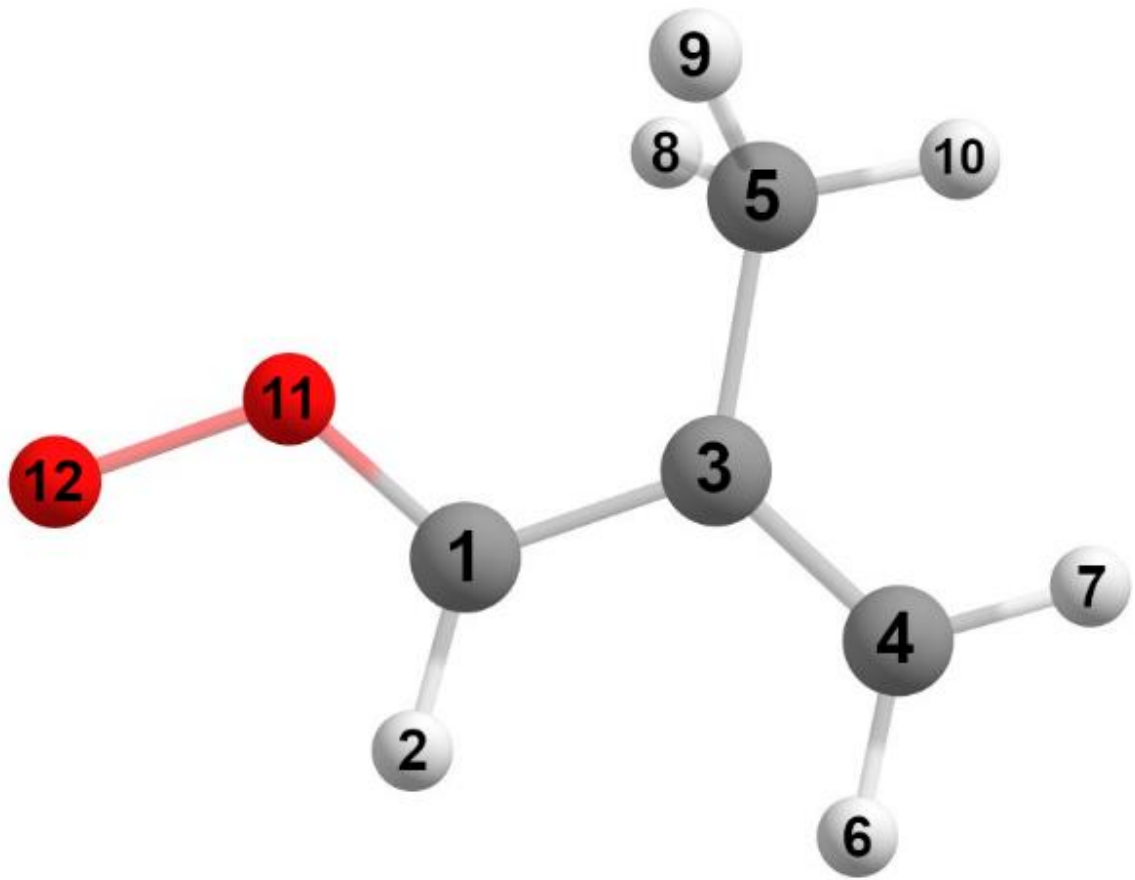


Figure S5. Representative geometry and atomic labelling of *anti-cis*-MACR-oxide for vibrational mode assignment (Table S4).

Table S2. Stationary point geometries of the four conformers of MACR-oxide calculated at the B2PLYP-D3/cc-pVTZ level of theory.

Single-Reference Stationary Points			
Minima			
<i>syn-trans</i> -MACR-oxide			
C	-0.53804	2.10943	0.00000
H	-1.60792	2.26229	0.00000
H	0.08834	2.98874	0.00000
C	0.00000	0.87276	0.00000
C	1.48566	0.65054	0.00000
H	1.99551	1.61205	0.00000
H	1.79014	0.07336	0.86827
H	1.79014	0.07336	-0.86827
C	-0.9543	-0.20543	0.00000
H	-2.0140	0.01019	0.00000
O	-0.7474	-1.47014	0.00000
O	0.49717	-1.97784	0.00000
<i>syn-cis</i> -MACR-oxide			
C	-1.35044	0.76018	0.00000
H	-1.87332	-0.17789	0.00000
H	-1.90564	1.68862	0.00000
C	0.00000	0.80376	0.00000
C	0.75673	2.11049	0.00000
H	0.06606	2.94922	0.00000
H	1.39541	2.19703	0.87907
H	1.39541	2.19703	-0.87907
C	0.83282	-0.35823	0.00000
H	1.91038	-0.26665	0.00000
O	0.49458	-1.60131	0.00000
O	-0.79744	-1.95926	0.00000
<i>anti-trans</i> -MACR-oxide			
C	2.21517	-0.19956	0.00000
H	2.59720	0.81126	0.00000
H	2.93423	-1.00461	0.00000
C	0.89225	-0.44694	0.00000
C	0.31011	-1.83037	0.00000
H	1.10092	-2.57522	0.00000
H	-0.31956	-1.98459	0.87510

H	-0.31956	-1.98459	-0.87510
C	0.00000	0.67388	0.00000
H	0.31870	1.70903	0.00000
O	-1.26263	0.46245	0.00000
O	-2.08951	1.51837	0.00000
<i>anti-cis-MACR-oxide</i>			
C	-0.03285	-1.84885	0.00000
H	1.04564	-1.89286	0.00000
H	-0.57598	-2.78155	0.00000
C	-0.68829	-0.67659	0.00000
C	-2.19010	-0.58186	0.00000
H	-2.63701	-1.57204	0.00000
H	-2.54808	-0.04419	0.87830
H	-2.54808	-0.04419	-0.87830
C	0.00000	0.59309	0.00000
H	-0.50933	1.54938	0.00000
O	1.27845	0.64304	0.00000
O	1.87659	1.84078	0.00000

Table S3. Harmonic zero-point energy corrected relative energies (ΔE_{ZPE}) for the four conformers of MACR-oxide calculated at the CCSD(T)-F12/CBS(TZ-F12,QZ-F12)//B2PLYP-D3/cc-pVTZ, B2PLYP-D3/cc-pVTZ, CASPT2(12,10)/AVDZ and CBS-QB3 levels of theory.

MACR-oxide conformer	CCSD(T)-F12 cm ⁻¹ (kcal mol ⁻¹)	B2PLYP-D3 cm ⁻¹ (kcal mol ⁻¹)	CASPT2 cm ⁻¹ (kcal mol ⁻¹)	CBS-QB3 ^a cm ⁻¹ (kcal mol ⁻¹)
<i>anti-cis</i>	1112 (3.18)	1219 (3.49)	1001 (2.86)	1120 (3.2)
<i>anti-trans</i>	0 (0.00)	0 (0.00)	0 (0.00)	0 (0.00)
<i>syn-cis</i>	317 (0.91)	235 (0.67)	493 (1.41)	385 (1.1)
<i>syn-trans</i>	873 (2.50)	841 (2.40)	1023 (2.93)	945 (2.7)

^a Ref. 9.

Table S4. Fundamental harmonic and anharmonic vibrational frequencies and descriptions computed for *syn-trans*, *syn-cis*, *anti-trans*, and *anti-cis* MACR-oxide in C_s symmetry at the B2PLYP-D3/cc-pVTZ level of theory.

Mode	Symmetry	Harmonic Frequency (cm ⁻¹)	Anharmonic Frequency (cm ⁻¹)	Description
<i>syn-trans</i> -MACR-oxide				
V ₁	A'	3258	3119	Vinyl out-of-phase CH stretch
V ₂	A'	3204	3077	Methine C ₍₁₎ H ₍₂₎ stretch
V ₃	A'	3165	3025	Vinyl in-phase CH stretch
V ₄	A'	3152	3009	Methyl C ₍₅₎ H ₍₁₀₎ stretch
V ₅	A'	3071	2966	Methyl in-phase CH Stretch
V ₆	A'	1642	1599	Alkene C ₍₃₎ C ₍₄₎ stretch
V ₇	A'	1513	1479	Vinyl symmetric CH scissor
V ₈	A'	1480	1443	C ₍₁₎ C ₍₃₎ stretch
V ₉	A'	1446	1410	Methyl symmetric scissor
V ₁₀	A'	1425	1396	Methyl umbrella
V ₁₁	A'	1358	1323	Methine in-plane C ₍₆₎ H ₍₇₎ wag
V ₁₂	A'	1339	1304	C ₍₁₎ O ₍₁₁₎ stretch
V ₁₃	A'	1069	1048	Methyl in-plane rock
V ₁₄	A'	1004	984	Vinyl in-plane C ₍₄₎ H ₍₆₎ H ₍₇₎ rock
V ₁₅	A'	959	936	O ₍₁₁₎ O ₍₁₂₎ stretch
V ₁₆	A'	853	837	C ₍₃₎ C ₍₅₎ stretch
V ₁₇	A'	729	720	C ₍₁₎ C ₍₃₎ O ₍₁₁₎ in-plane bend
V ₁₈	A'	426	427	C ₍₃₎ C ₍₄₎ C ₍₅₎ bend
V ₁₉	A'	350	344	C ₍₁₎ O ₍₁₁₎ O ₍₁₂₎ in-plane bend
V ₂₀	A'	257	256	C ₍₁₎ C ₍₃₎ C ₍₅₎ O ₍₁₁₎ O ₍₁₂₎ ring closing
V ₂₁	A''	3155	3010	Methyl out-of-phase CH stretch
V ₂₂	A''	1481	1441	Methyl asymmetric scissor
V ₂₃	A''	1082	1057	Methyl out-of-plane CH wag
V ₂₄	A''	944	926	Vinyl out-of-plane C ₍₄₎ H ₍₆₎ H ₍₇₎ wag
V ₂₅	A''	858	842	Methine out-of-plane C ₍₁₎ H ₍₂₎ wag
V ₂₆	A''	700	683	Vinyl twist
V ₂₇	A''	556	549	C ₍₁₎ C ₍₃₎ O ₍₁₁₎ out-of-plane distortion

V ₂₈	A''	331	328	C ₍₁₎ C ₍₃₎ C ₍₄₎ O ₍₁₁₎ out-of-plane distortion
V ₂₉	A''	213	226	Methyl torsion
V ₃₀	A''	64	59	Vinyl torsion
<hr/> <i>syn-cis</i> -MACR-oxide <hr/>				
V ₁	A'	3310	3157	Vinyl out-of-phase CH stretch
V ₂	A'	3204	3081	Methine C ₍₁₎ H ₍₂₎ stretch
V ₃	A'	3166	3034	Vinyl in-phase CH stretch
V ₄	A'	3148	3012	Methyl C ₍₅₎ H ₍₁₀₎ stretch
V ₅	A'	3054	2965	Methyl in-phase CH Stretch
V ₆	A'	1629	1585	Alkene C ₍₃₎ C ₍₄₎ stretch
V ₇	A'	1517	1475	Methyl symmetric scissor
V ₈	A'	1497	1457	C ₍₁₎ C ₍₃₎ stretch
V ₉	A'	1439	1404	Vinyl symmetric CH scissor
V ₁₀	A'	1420	1391	Methyl umbrella
V ₁₁	A'	1350	1313	Methine in-plane C ₍₆₎ H ₍₇₎ wag
V ₁₂	A'	1273	1244	C ₍₁₎ O ₍₁₁₎ stretch
V ₁₃	A'	1051	1031	Vinyl in-plane C ₍₄₎ H ₍₆₎ H ₍₇₎ rock
V ₁₄	A'	1022	1003	Methyl rock
V ₁₅	A'	981	958	O ₍₁₁₎ O ₍₁₂₎ stretch
V ₁₆	A'	913	898	C ₍₁₎ C ₍₃₎ O ₍₁₁₎ in-plane bend
V ₁₇	A'	713	706	C ₍₃₎ C ₍₅₎ stretch
V ₁₈	A'	422	417	C ₍₃₎ C ₍₄₎ C ₍₅₎ in-plane bend
V ₁₉	A'	341	339	C ₍₁₎ O ₍₁₁₎ O ₍₁₂₎ in-plane bend
V ₂₀	A'	284	280	C ₍₁₎ C ₍₃₎ C ₍₅₎ O ₍₁₁₎ O ₍₁₂₎ ring closing
V ₂₁	A''	3111	2972	Methyl out-of-phase CH stretch
V ₂₂	A''	1499	1456	Methyl asymmetric scissor
V ₂₃	A''	1082	1057	Methyl out-of-plane CH wag
V ₂₄	A''	980	961	Vinyl out-of-plane C ₍₄₎ H ₍₆₎ H ₍₇₎ wag
V ₂₅	A''	861	850	Methine out-of-plane C ₍₁₎ H ₍₂₎ wag
V ₂₆	A''	710	692	Vinyl twist
V ₂₇	A''	542	535	C ₍₁₎ C ₍₃₎ O ₍₁₁₎ out-of-plane distortion
V ₂₈	A''	318	311	C ₍₁₎ C ₍₃₎ C ₍₄₎ O ₍₁₁₎ out-of-plane distortion
V ₂₉	A''	130	107	Methyl torsion
V ₃₀	A''	107	87	Vinyl torsion

<i>anti-cis-MACR-oxide</i>				
V ₁	A'	3268	3129	Vinyl out-of-phase CH stretch
V ₂	A'	3184	3052	Methine C ₍₁₎ H ₍₂₎ stretch
V ₃	A'	3175	3062	Vinyl in-phase CH stretch
V ₄	A'	3150	3014	Methyl C ₍₅₎ H ₍₁₀₎ stretch
V ₅	A'	3053	2965	Methyl in-phase CH Stretch
V ₆	A'	1663	1622	Alkene C ₍₃₎ C ₍₄₎ stretch
V ₇	A'	1410	1468	Methyl symmetric scissor
V ₈	A'	1472	1425	C ₍₁₎ C ₍₃₎ stretch
V ₉	A'	1456	1410	Vinyl symmetric CH scissor
V ₁₀	A'	1426	1393	Methyl umbrella
V ₁₁	A'	1318	1280	C ₍₁₎ O ₍₁₁₎ stretch
V ₁₂	A'	1278	1251	Methine in-plane C ₍₆₎ H ₍₇₎ wag
V ₁₃	A'	1077	1047	O ₍₁₁₎ O ₍₁₂₎ stretch
V ₁₄	A'	1033	1010	Vinyl in-plane C ₍₄₎ H ₍₆₎ H ₍₇₎ rock
V ₁₅	A'	1015	998	Methyl rock
V ₁₆	A'	912	894	C ₍₃₎ C ₍₅₎ stretch
V ₁₇	A'	562	552	C ₍₁₎ C ₍₃₎ O ₍₁₁₎ in-plane bend
V ₁₈	A'	466	462	C ₍₁₎ O ₍₁₁₎ O ₍₁₂₎ in-plane bend
V ₁₉	A'	370	367	C ₍₃₎ C ₍₄₎ C ₍₅₎ in-plane bend
V ₂₀	A'	199	196	C ₍₁₎ C ₍₃₎ C ₍₄₎ O ₍₁₁₎ ring closing
V ₂₁	A''	3109	2971	Methyl out-of-phase CH stretch
V ₂₂	A''	1496	1453	Methyl asymmetric scissor
V ₂₃	A''	1082	1055	Methyl out-of-plane CH wag
V ₂₄	A''	947	927	Vinyl out-of-plane C ₍₄₎ H ₍₆₎ H ₍₇₎ wag
V ₂₅	A''	922	904	Methine out-of-plane C ₍₁₎ H ₍₂₎ wag
V ₂₆	A''	686	669	Vinyl twist
V ₂₇	A''	501	497	C ₍₁₎ C ₍₃₎ O ₍₁₁₎ out-of-plane distortion
V ₂₈	A''	198	194	C ₍₁₎ C ₍₃₎ C ₍₅₎ O ₍₁₁₎ O ₍₁₂₎ ring distortion
V ₂₉	A''	149	140	Methyl torsion
V ₃₀	A''	91	90	Vinyl torsion
<i>anti-trans-MACR-oxide</i>				
V ₁	A'	3260	3121	Vinyl out-of-phase CH stretch
V ₂	A'	3189	3057	Methine C ₍₁₎ H ₍₂₎ stretch
V ₃	A'	3168	3034	Vinyl in-phase CH stretch

V ₄	A'	3154	3014	Methyl C ₍₅₎ H ₍₁₀₎ stretch
V ₅	A'	3064	2970	Methyl in-phase CH Stretch
V ₆	A'	1655	1611	Alkene C ₍₃₎ C ₍₄₎ stretch
V ₇	A'	1512	1471	Methyl symmetric scissor
V ₈	A'	1473	1436	C ₍₁₎ C ₍₃₎ stretch
V ₉	A'	1442	1401	Methyl umbrella
V ₁₀	A'	1422	1388	Vinyl symmetric CH scissor
V ₁₁	A'	1371	1334	C ₍₁₎ O ₍₁₁₎ stretch
V ₁₂	A'	1290	1262	Methine in-plane C ₍₆₎ H ₍₇₎ wag
V ₁₃	A'	1060	1035	Methyl rock
V ₁₄	A'	1046	1018	O ₍₁₁₎ O ₍₁₂₎ stretch
V ₁₅	A'	1004	987	Vinyl in-plane C ₍₄₎ H ₍₆₎ H ₍₇₎ rock
V ₁₆	A'	874	857	C ₍₃₎ C ₍₅₎ stretch
V ₁₇	A'	576	569	C ₍₁₎ C ₍₃₎ O ₍₁₁₎ in-plane bend
V ₁₈	A'	480	479	C ₍₁₎ O ₍₁₁₎ O ₍₁₂₎ in-plane bend
V ₁₉	A'	371	370	C ₍₃₎ C ₍₄₎ C ₍₅₎ in-plane bend
V ₂₀	A'	188	188	C ₍₁₎ C ₍₃₎ C ₍₄₎ O ₍₁₁₎ ring closing
V ₂₁	A''	3125	2987	Methyl out-of-phase CH stretch
V ₂₂	A''	1493	1448	Methyl asymmetric scissor
V ₂₃	A''	1080	1053	Methyl out-of-plane CH wag
V ₂₄	A''	941	921	Vinyl out-of-plane C ₍₄₎ H ₍₆₎ H ₍₇₎ wag
V ₂₅	A''	918	898	Methine out-of-plane C ₍₁₎ H ₍₂₎ wag
V ₂₆	A''	698	682	Vinyl twist
V ₂₇	A''	507	505	C ₍₁₎ C ₍₃₎ O ₍₁₁₎ out-of-plane distortion
V ₂₈	A''	230	221	C ₍₁₎ C ₍₃₎ C ₍₅₎ O ₍₁₁₎ O ₍₁₂₎ ring distortion
V ₂₉	A''	186	179	Vinyl torsion
V ₃₀	A''	151	140	Methyl torsion

group, whereas the least stable conformation (*anti-cis*) has significant in-plane repulsion between the carbonyl O-atom and adjacent H-atom of the vinyl group. In contrast, a weak stabilizing interaction occurs between the terminal oxygen and adjacent alkyl group for *syn*-conformers of MACR-oxide, as found previously for other *syn*-substituted Criegee intermediates.¹⁰ This weak stabilization effect is likely greater for *syn-cis* than *syn-trans* because the nearest H-atom is closer (2.08 vs. 2.58 Å), but is not sufficient for *syn*-conformers to be more stable than the sterically unhindered *anti-trans* conformer.

Vertical excitation energies (VEE) were then calculated starting from the B2PLYP-D3/cc-pVTZ optimized geometries, using a State-Averaged (SA) Complete Active Space with 2nd Order Perturbation Theory (CASPT2)¹¹⁻¹³ and an augmented valence double ζ basis set (AVDZ) method.¹⁴ The calculations are carried out using MOLPRO v2010.1.¹⁵ This was based on a CASSCF reference wavefunction including the lowest seven singlet states (state averaged, SA7) and an active space of 12 electrons distributed in 10 orbitals. The set of orbitals used for the calculations is depicted in Figure S6. The occupied orbitals included in the active space for the SA7-CASSCF(12,10)/CASPT2(12,10) calculations were 3 delocalized π orbitals (HOMO, HOMO-2, HOMO-4), the p_y and p_z oxygen lone pairs (HOMO-1, HOMO-5), and the σ orbital associated with the O-O bond (HOMO-3). The unoccupied orbitals included two π^* orbitals (LUMO and LUMO+2), the diffuse oxygen 3s Rydberg orbital (LUMO+1), and the σ^* orbital around the O-O bond (LUMO+3). The oscillator strengths were evaluated from the SA7-CASSCF(12,10)/AVDZ transition dipole moments (μ_{ij}) according to:

$$f_{ij} = \frac{2}{3} E_{ij} \sum_{a=x,y,z} |\mu_{ij}|_a^2$$

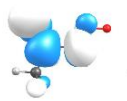
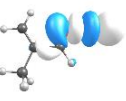
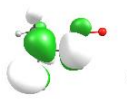
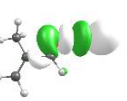
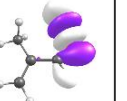
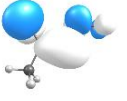
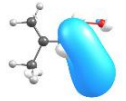
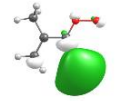
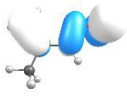
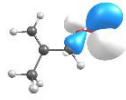
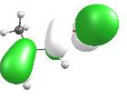
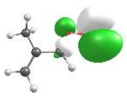
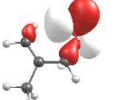
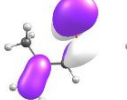
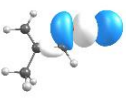
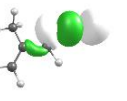
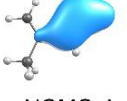
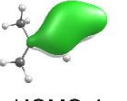
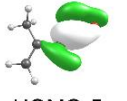
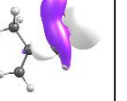
MACR-oxide Conformers							
<i>anti-cis</i>		<i>anti-trans</i>		<i>syn-cis</i>		<i>syn-trans</i>	
							
LUMO+2	LUMO+3	LUMO+2	LUMO+3	LUMO+2	LUMO+3	LUMO+2	LUMO+3
							
LUMO	LUMO+1	LUMO	LUMO+1	LUMO	LUMO+1	LUMO	LUMO+1
							
HOMO	HOMO-1	HOMO	HOMO-1	HOMO	HOMO-1	HOMO	HOMO-1
							
HOMO-2	HOMO-3	HOMO-2	HOMO-3	HOMO-2	HOMO-3	HOMO-2	HOMO-3
							
HOMO-4	HOMO-5	HOMO-4	HOMO-5	HOMO-4	HOMO-5	HOMO-4	HOMO-5

Figure S6. Complete active space used in the CASSCF(12,10)/CASPT2(12,10)/AVDZ calculations for vertical excitation energies of the four conformers of MACR-oxide. The occupied orbitals include three delocalized π (HOMO, HOMO-2, HOMO-4), the two p_y and p_z lone pairs localized on the oxygen atoms (HOMO-1 and HOMO-5) and the σ around the O-O bond (HOMO-3). The virtual orbitals are the two π^* (LUMO, LUMO+2), the 3s Rydberg orbital (LUMO+1) and the σ^* around the O-O moiety (LUMO+3). The lowest six singlet electronic transitions were computed using this active space for each of the conformers of MACR-oxide.

where E_{ij} are the vertical excitation energies between the initial and final electronic states i and j at the SA7-CASSCF(12,10)/CASPT2(12,10)/AVDZ level of theory. Vertical excitation energies and oscillator strengths for the lowest six singlet transitions of MACR-oxide are reported in Table S5.

Section S3. Spectroscopic Methods

The diiodo alkene precursor is seeded in a 20% O₂/Ar gas mixture (12 psig) as it passes through a heated (60 °C) solenoid valve (Parker-Hannifin General Valve series 9) into a quartz capillary reactor tube (25 mm length, 1 mm ID). The vapor pressure of the precursor is significantly increased by heating (Peltier thermoelectric heating module; Laird technology, PC4). The temperature is monitored using a digital thermometer (Cole Parmer Type K). The precursor is photolyzed by the 248 nm output of a KrF excimer laser (Coherent, COMPex 102, 10 Hz, 25 mJ pulse⁻¹), which is cylindrically focused along the length of the capillary tube. MACR-oxide is collisionally stabilized in the capillary and cooled in a supersonic jet expansion ($T_{\text{rot}} \sim 10$ K) as it passes into a collision free region.

For photoionization measurements, MACR-oxide is ionized using 10.5 eV (118 nm) vacuum ultraviolet (VUV) radiation after traveling ~4 cm downstream. The VUV radiation is generated by frequency tripling the third harmonic output of a Nd:YAG laser (Continuum Powerlite Series 9010, 10 Hz, ~35 mJ pulse⁻¹) in a phase matched Xe:Ar gas mixture. MACR-oxide is monitored on the $m/z=86$ mass channel of a Wiley McLaren linear time-of-flight mass spectrometer (TOF, RM Jordan).

Photoionization of the (*E*)-1,3-diiodo-2-methylprop-1-ene precursor is observed on the $m/z = 308$ parent mass channel as shown in the upper panel of Figure S7. Several other species present in the molecular beam are also ionized at 10.5 eV

Table S5. Vertical excitation energies (VEE, eV), corresponding wavelengths (λ/nm), and oscillator strengths (f) computed at the CASPT2(12,10)/AVDZ level of theory for the lowest six singlet electronic transitions of the four conformers of MACR-oxide. The transitions with the highest oscillator strengths (in bold) are of $\pi^* \leftarrow \pi$ nature.

MACR-oxide conformer							
<i>anti-cis</i>		<i>anti-trans</i>		<i>syn-cis</i>		<i>syn-trans</i>	
VEE/eV (λ/nm)	f						
1.99 (623)	0.00	2.11(588)	0.000	2.04 (609)	0.000	2.05 (583)	0.000
3.26 (380)	0.093	3.31 (374)	0.116	3.62 (342)	0.057	3.29 (377)	0.094
4.07 (304)	0.083	4.31 (288)	0.082	4.36 (285)	0.062	5.23 (237)	0.000
5.21 (238)	0.000	5.30 (234)	0.000	5.31 (234)	0.000	5.43 (228)	0.110
5.65 (220)	0.001	5.53 (224)	0.000	5.71 (217)	0.015	5.43 (228)	0.000
5.85 (212)	0.021	5.68 (218)	0.010	5.79 (214)	0.001	5.45 (227)	0.024

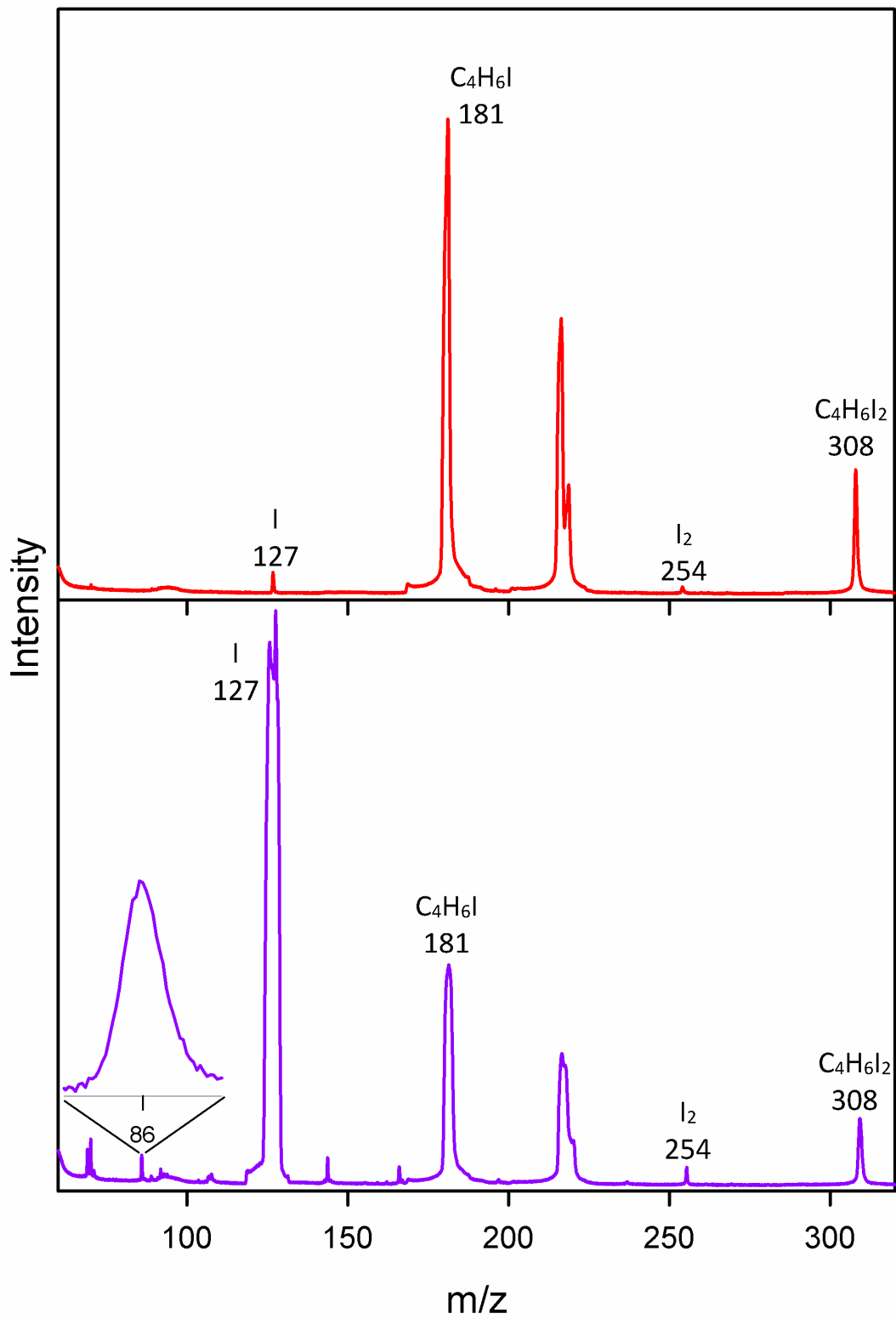


Figure S7. TOF mass spectrum of (*E*)-1,3-diiodo-2-methylprop-1-ene precursor (upper panel) recorded upon photoionization at 118 nm (10.5 eV). The precursor was heated to a temperature of 60 °C to increase the vapor pressure. Mass channels result from photoionization of the precursor ($m/z = 308$ C₄H₆I₂) and its fragmentation ($m/z = 254$ I₂, $m/z = 181$ C₄H₆I, $m/z = 127$ I). (Lower) TOF mass spectrum of (*E*)-1,3-diiodo-2-methylprop-1-ene precursor in a 20% O₂/Ar carrier gas obtained by photolysis of the precursor at 248 nm prior to the 118 nm photoionization. The inset shows the $m/z = 86$ mass channel assigned to MACR-oxide⁺.

including I ($m/z = 127$), C_4H_6I ($m/z = 181$), and I_2 ($m/z = 254$). The lower panel of Figure S7 shows a representative TOF-MS when 248 nm radiation is cylindrically focused along the length of the quartz capillary reactor. Photolysis at 248 nm results in prompt dissociation of the precursor to produce an internally excited allylic monoiodoalkene radical (C_4H_6I) and I atoms. Its subsequent reaction with O_2 generates MACR-oxide. This is demonstrated in the lower panel of Figure S7 by the decrease in $m/z = 308$ intensity with a corresponding increase in intensity of I ($m/z = 127$) and C_4H_6I ($m/z = 181$), and appearance of MACR-oxide ($m/z = 86$). Other 248 nm dependent masses ($m/z = 69$ and $m/z = 70$) are also observed. These masses are tentatively assigned to formation of MACR ($m/z = 70$) from dissociation of the Criegee intermediate O-O bond and a radical product associated with loss of OH from MACR-oxide ($m/z = 69$).

UV-vis radiation is generated using a broadly tunable BBO-OPO (EKSPLA 342NT, 3-5 ns pulse width, $< 5 \text{ cm}^{-1}$ linewidth, 5 Hz). The signal output of the OPO was used in the 410-500 nm spectral region and sum frequency generation (SFG) of the signal + 1064 nm Nd:YAG fundamental was used between 315 and 409 nm. The OPO wavelength (vacuum) is calibrated using a wavemeter (Coherent WaveMaster). The OPO power is carefully maintained near 2.5 mJ/pulse using a power meter (Gentec TPM3/300) to ensure linear scaling with power (Figure S8).

For UV-vis depletion measurements, counter-propagating UV-vis radiation is introduced ~50 ns prior to VUV photoionization. The UV-vis is loosely focused (30 cm focal length) and spatially overlapped with the 118 nm radiation in the ionization region of the TOF. The BBO-OPO is operated at half the repetition rate (5 Hz) of the 118 nm radiation (10 Hz) to obtain the fractional depletion $[(UV\text{-vis off} - UV\text{-vis on}) / (UV\text{-vis off})]$ of the $m/z=86$ photoionization signal on alternating laser shots.

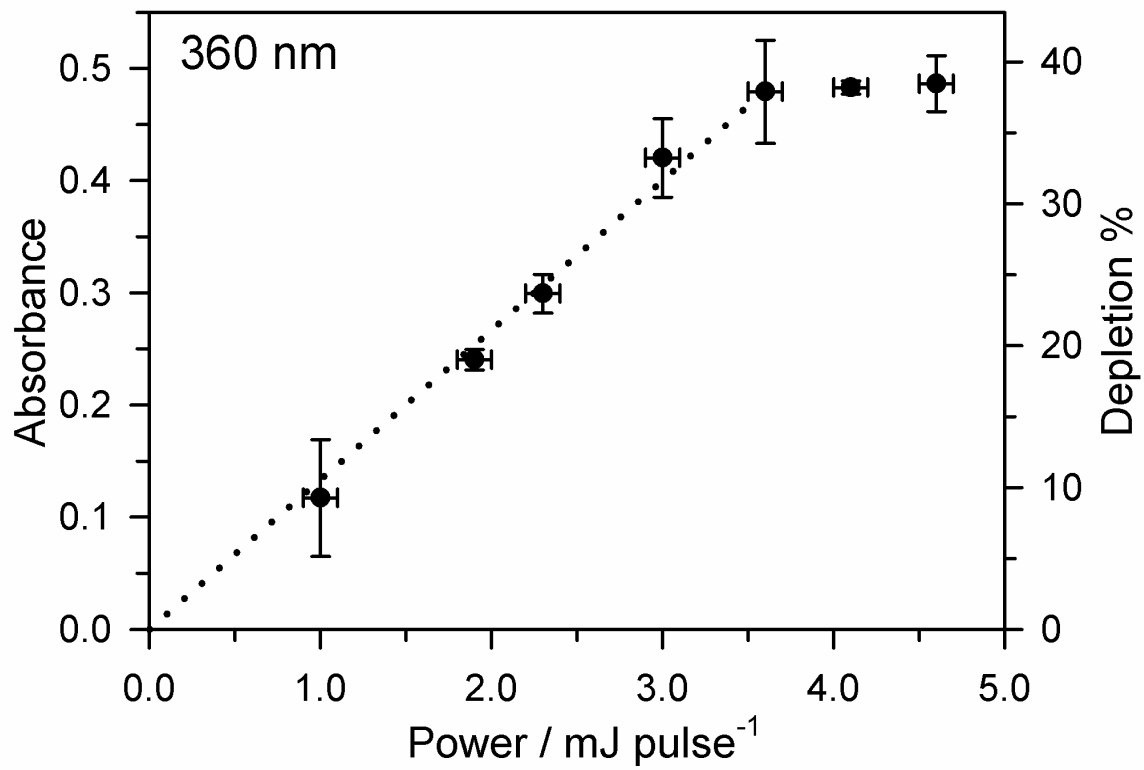


Figure S8. Percentage depletion of the $m/z = 86$ (MACR-oxide⁺) ion signal as a function of the laser power at 360 nm. The percentage depletion is evaluated as $(N_0 - N)/N_0 \cdot 100\%$ with N_0 and N being the ground state populations of MACR-oxide before and after irradiation. The error bars represent the standard deviation ($\pm 1\sigma$) derived from repeated measurements. The corresponding absorbance ($-\ln(N/N_0)$) follows a linear dependence (dashed line) at excitation energies up to 3.6 mJ/pulse indicating a one-photon process

The UV-vis excitation of MACR-oxide also results in O ¹D products, which were investigated using the velocity-map imaging (VMI) technique as described previously.¹⁶⁻²⁰ For these measurements, MACR-oxide is electronically excited using focused (70 cm focal length) UV-vis radiation from the BBO-OPO source (~3.5 mJ/pulse SFG, ~5 mJ/pulse Signal). The polarization of the BBO-OPO radiation is set parallel to the detection plane. After a 50 ns delay, the O ¹D products are ionized by 2+1 resonance enhanced multiphoton ionization (REMPI) using a counter-propagating, spatially overlapped, and focused (70 cm focal length) probe laser at 205.47 nm.²¹ The probe radiation is generated by frequency tripling the output of a Nd:YAG (Continuum Powerlite 8010, 10 Hz) pumped dye laser (Continuum, ND6000, Rh 610) and scanned over the O-atom Doppler profile ($\pm 0.4 \text{ cm}^{-1}$). O⁺ ²D ions formed in the interaction region are velocity mapped onto a spatially sensitive detector comprised of dual MCPs coupled with a phosphor screen (Photek). A CCD camera (Sydor Instruments) selectively records the O ¹D images by gating on the m/z = 16 mass channel. The central region of the MCP detector is protected from ions with low translational energy (<150 cm⁻¹) using a physical beam block. The resultant image was analyzed to obtain angular and velocity information using the pBASEX inversion method.²²

Section S4. Details of Lorentzian fitting to MACR-oxide electronic spectrum

A nonlinear curve fitting was carried out using Lorentzian functions to extract best fit parameters for the weak oscillatory structure in the long wavelength region of the experimental spectrum (Figure 7, where an empirical smoothed curve is shown through the dataset). The experimental data points (recorded in 0.5 nm steps) were fit from 345

to 500 nm using four Lorentzian functions in Origin.²³ The Lorentzian functions had the form

$$y = \frac{2A}{\pi} \frac{w}{4(x - x_c)^2 + w^2}$$

for lineshapes of intensity y as a function of wavelength x with center position x_c , FWHM w , and area A . The best fit consisted of a broad component centered at 374.8 nm with 88.7% of the signal that gives the overall broad shape of the spectrum. Three much smaller Lorentzian components are needed to represent the weak oscillatory structure. The smaller components are centered at 416.4 nm (8%), 430.9 nm (0.8%), and 448.1 nm (2.2%), with percentage contributions to the total signal in parentheses. The four Lorentzian components and the sum are superimposed on the experimental data in Figure S9. The full set of parameters and associated standard errors describing the four Lorentzian functions that contribute to the best fit are given in Table S6.

Section S5. Details of theoretical absorption profile calculations and dissociation energies

S5.1. Theoretical absorption profiles

For each MACR-oxide conformer, an ensemble of 300 initial ground state configurations was generated by sampling a Wigner distribution based on the ground state normal mode harmonic wavenumbers (evaluated with the Becke, 3-parameter, Lee-Yang-Parr functional in DFT with Pople's 6-311+G(d,p) basis set²⁴). VEEs and oscillator strengths for each of the initial geometries were then calculated at the SA7-CASSCF(12,10/CASPT2(12,10)/AVDZ level of theory. Each transition was then fitted to a Lorentzian line shape with an assumed broadening factor of 0.25 eV. The sum of the ensemble of 300 transition yields an absorption spectrum for a single conformer of

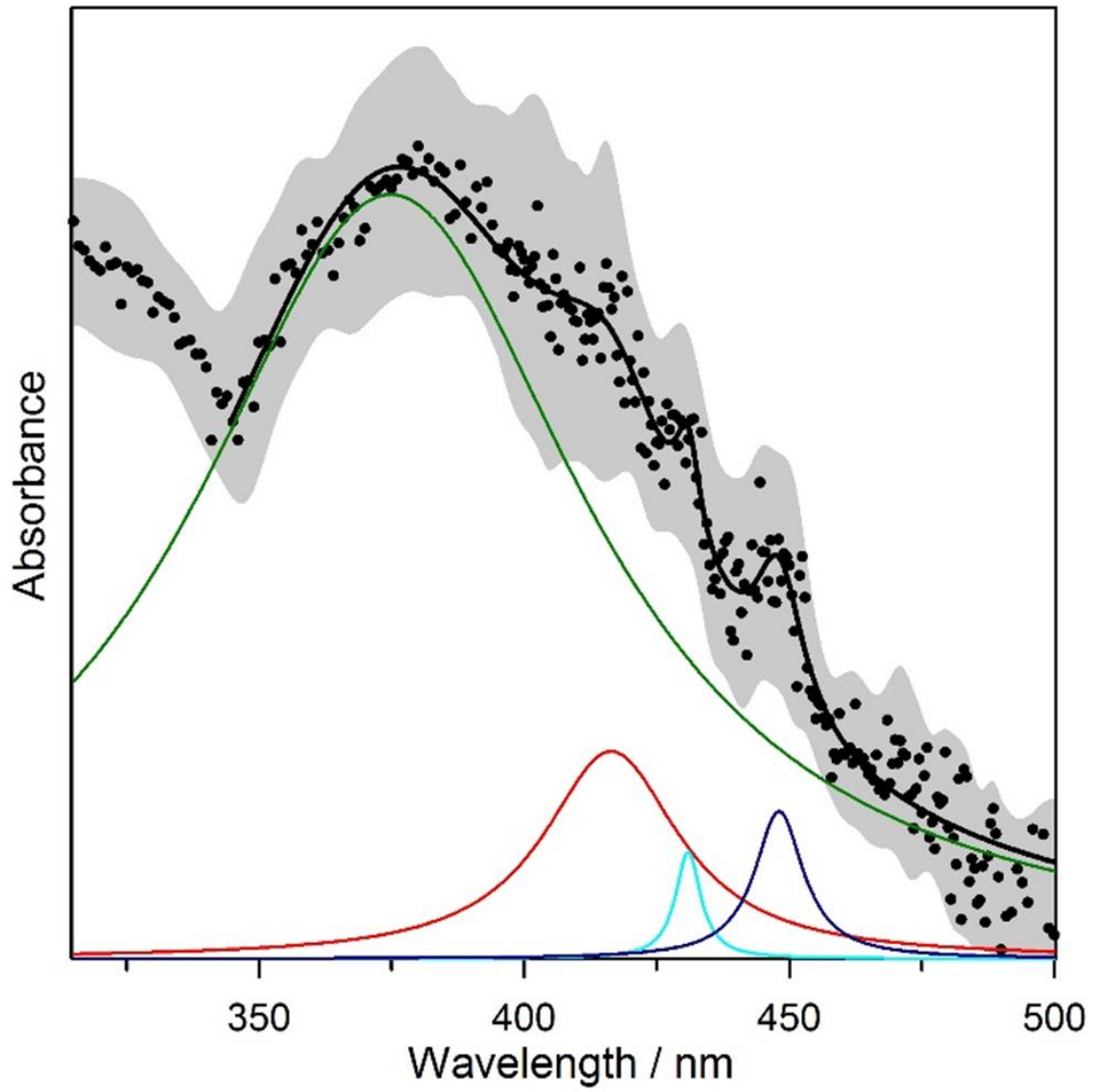


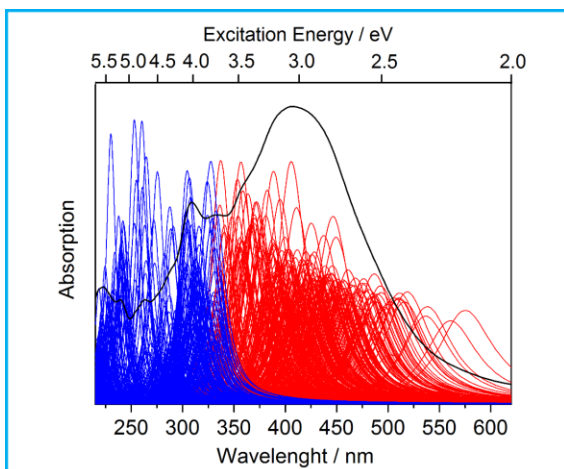
Figure S9. Weak oscillatory structure in the long wavelength region of the experimental UV-vis spectrum of MACR-oxide (points) is simulated using four Lorentzian functions superimposed on a broad Lorentzian peaked at 374.8 nm (green), the latter of which accounts for most of the spectral intensity. The oscillatory structure is fit to Lorentzian functions (416.4 nm, red; 430.9 nm, cyan; 448.1 nm, dark blue) as detailed in Table S6, and the overall fit (black) is the sum of the Lorentzian functions. The shaded region represents the experimental uncertainty from repeated measurements.

Table S6. Simulation of MACR-oxide electronic spectrum using Lorentzian fits of the broad UV-vis absorption profile from 340-500 nm and superimposed weak oscillatory structure. The overall simulation and Lorentzian components are superimposed on the experimental data in Figure S9.

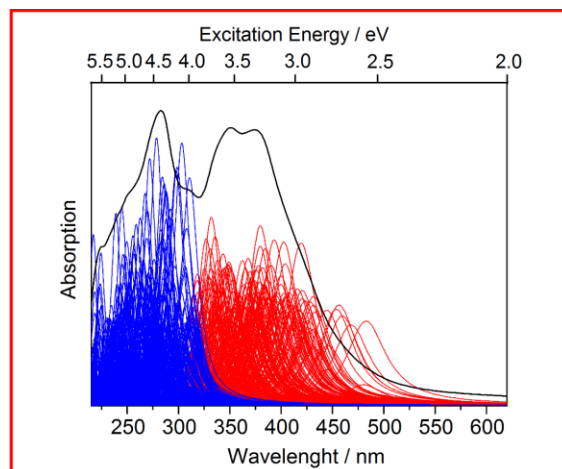
Band center	Area (A)	FWHM (w) / cm^{-1}	Spacing / cm^{-1}
374.8 ± 1.1	0.886 ± 0.036	6520 ± 310	
416.4 ± 1.2	0.084 ± 0.027	1810 ± 580	
430.9 ± 0.5	0.008 ± 0.004	310 ± 180	810 ± 70
448.1 ± 0.5	0.022 ± 0.004	560 ± 130	890 ± 40

MACR-oxide. The vertical transitions derived from the 300 sampled ground state configurations for each conformer of MACR-oxide are displayed in Figure S10. The transitions with high oscillator strength contribute to the two absorption bands associated with the $1^1\pi\pi^* \leftarrow S_0$ (red) and $2^1\pi\pi^* \leftarrow S_0$ (blue) transitions. The first excited electronic state is predominately of $n\pi^*$ character, as found previously for other Criegee intermediates.^{20, 25-30} Vertical excitation to this $n\pi^*$ state has negligible oscillator strength due to poor orbital overlap.

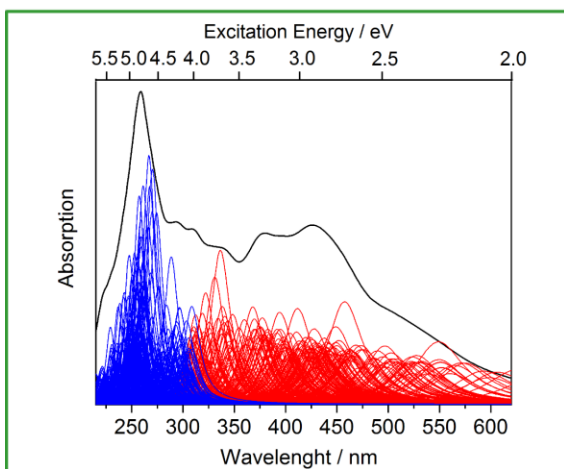
As shown in Figure S10, the ensemble of transitions to the $1^1\pi\pi^*$ states are predicted to have largest contributions in the 370-440 nm region for the *anti-cis* (390-435 nm), *anti-trans* (380-440 nm), and *syn-trans* (370-425 nm) conformers of MACR-oxide. The analogous ensemble for the *syn-cis* conformer peaks in the 355-380 nm region and falls off more rapidly to longer wavelength than other conformers. Excitation to the $2^1\pi\pi^*$ state of the *anti-trans* conformer is most distinctive with a narrow Franck-Condon profile peaked at ca. 260 nm, while that for the *syn-cis* conformer peaks at ca. 280 nm. The breadth of the two absorption bands for each conformer originates primarily from the Franck-Condon profiles associated with the initial ground state configurations sampled. The profiles associated with the second $\pi^* \leftarrow \pi$ transitions of the *anti-cis* and *syn-trans* conformers are broader and overlap to a greater extent with their first $\pi^* \leftarrow \pi$ transitions. The distinctive vertical transition to the $2^1\pi\pi^*$ state of the *syn-trans* conformer at 228 nm has a broad Franck-Condon profile that shifts the peak absorbance of its second $\pi^* \leftarrow \pi$ transition to considerably longer wavelength.



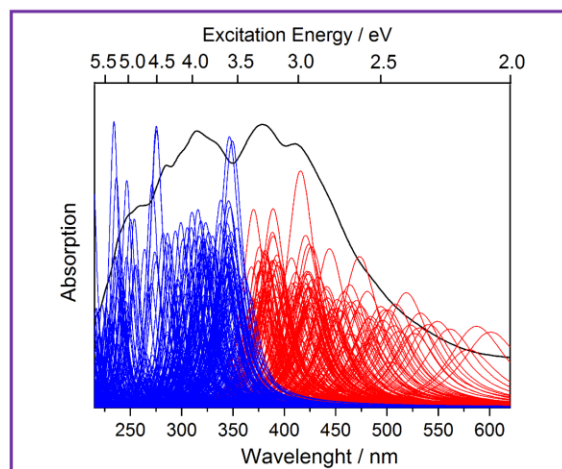
anti-cis



syn-cis



anti-trans



syn-trans

Figure S10. CASSCF(12,10)/CASPT2(12,10)/AVDZ UV-vis spectra of MACR-oxide (black line) obtained as a sum of an ensemble of vertical transitions for each of the four conformers starting from 300 (N) initial ground state geometries. The singlet transitions with high oscillator strengths to the $1^1\pi\pi^*$ and $2^1\pi\pi^*$ states contribute to the first (red lines) and second (blue lines) absorption bands, respectively. Each of the individual transitions is broadened with a Lorentzian line shape function (0.25 eV FWHM). Spectra for the four conformers of MACR-oxide are color-coded as follows: *anti-trans* (green), *syn-trans* (purple), *syn-cis* (red), and *anti-cis* (cyan).

S5.2. Dissociation energies

The zero-point energy (ZPE) corrected dissociation energy of *anti-trans*-MACR-oxide to *trans*-MACR X $^1A'$ + O 1D is evaluated as follows. First, the geometry associated with the *trans*-MACR X $^1A'$ + O 1D product asymptote is approximated by extending the O-O bond length of *anti-trans*-MACR-oxide to 3.0 Angstrom. The C-O-O bond angle is fixed at 118.4° , while optimizing the other degrees of freedom at the B2PLYP-D3/cc-pVTZ level of theory to facilitate convergence (Table S7). Next, the energy of the optimized structure with elongated O-O bond length is evaluated at the CASPT2(12,10)/AVDZ level of theory. The residual fragment-fragment interaction may change the computed dissociation energy by ≤ 0.1 eV. The purely electronic dissociation energy is then evaluated by subtracting the minimum energy computed for *anti-trans*-MACR-oxide (CASPT2(12,10)/AVDZ). The ZPE-corrected dissociation energy is obtained by considering the change in ZPE between *anti-trans*-MACR-oxide and *trans*-MACR. The dissociation energies of the other MACR-oxide conformers are obtained by considering the minimum energies of the MACR-oxide conformers (CCSD(T)-F12/CBS(TZ-F12, QZ-F12)//B2PLYP-D3/cc-pVTZ), the *cis* \leftrightarrow *trans* energy splitting of MACR product (1242 cm^{-1} , B2PLYP-D3/cc-pVTZ), and ZPE corrections (B2PLYP-D3/cc-pVTZ). The resultant ZPE-corrected dissociation energies for the four conformers of MACR-oxide are reported in Table S8.

Section S6. Excitation of MACR-oxide on its second $\pi^* \leftarrow \pi$ transition and VMI background subtraction

Excitation of MACR-oxide at 205 nm accesses its second $\pi^* \leftarrow \pi$ transition, which is also found to yield a significant amount of O 1D products. Additional O 1D products

Table S7. Geometry from a relaxed optimization of *trans*-MACR X ¹A' + O ¹D at a fixed large O-O separation (3.0 Angstrom) and C-O-O angle (118.4°) calculated at the B2PLYP-D3/cc-pVTZ level of theory.

<i>trans</i> -MACR X ¹ A' + O ¹ D			
C	-2.47797	3.22477	-1.27950
H	-2.69102	4.28511	-1.29996
H	-2.69072	2.65942	-2.17514
C	-1.97198	2.65120	-0.18269
C	-1.64059	1.19943	-0.04356
H	-0.58613	1.07231	0.19809
H	-2.20171	0.75942	0.77982
H	-1.86456	0.65614	-0.95788
C	-1.72259	3.52244	0.98025
H	-1.98073	4.58911	0.83909
O	-0.85438	5.10074	4.25103
O	-1.26610	3.12278	2.03334

Table S8. Lowest spin-allowed product asymptotes^{a,b} and zero-point corrected dissociation energies for the four conformers of MACR-oxide.

MACR-oxide conformer → Product Asymptote	Dissociation Energy ^c		
<i>anti-cis</i> -MACR-oxide → <i>cis</i> -MACR X ¹ A' + O ¹ D	2.09 eV	48.1 kcal mol ⁻¹	595 nm
<i>anti-trans</i> -MACR-oxide → <i>trans</i> -MACR X ¹ A' + O ¹ D	2.08 eV	47.9 kcal mol ⁻¹	597 nm
<i>syn-cis</i> -MACR-oxide → <i>cis</i> -MACR X ¹ A' + O ¹ D	2.18 eV	50.3 kcal mol ⁻¹	568 nm
<i>syn-trans</i> -MACR-oxide → <i>trans</i> -MACR X ¹ A' + O ¹ D	1.97 eV	45.4 kcal mol ⁻¹	630 nm

^a *cis*↔*trans* energy splitting of MACR product (1242 cm⁻¹) evaluated at B2PLYP-D3/cc-pVTZ level of theory.

^b The *trans*-MACR X ¹A' + O ¹D structure was evaluated at the B2PLYP-D3/cc-pVTZ level of theory with O-O bond distance and C-O-O angle fixed (3.0 Angstrom and 118.4°) to aid in geometry optimization (Table S7). The residual fragment-fragment interaction may change the computed dissociation energy by ≤ 0.1 eV.

^c See SI Sec. S5.2.

are generated from electronic excitation of IO at 205 nm.³¹ The O ¹D signal produced from 205 nm excitation is significant. These O ¹D background signals are removed by an active background subtraction where the BBO-OPO pump laser and 205 nm probe laser is operated at 5 Hz and 10 Hz, respectively. To further reduce contribution from the background signal in the image associated with the first $\pi^* \leftarrow \pi$ transition of MACR-oxide, the probe laser polarization is set perpendicular to the plane of the detector. This setup results in an isotropic distribution of ions generated from the 205 nm probe laser, which enables a more uniform background subtraction in the image (Figure S11).

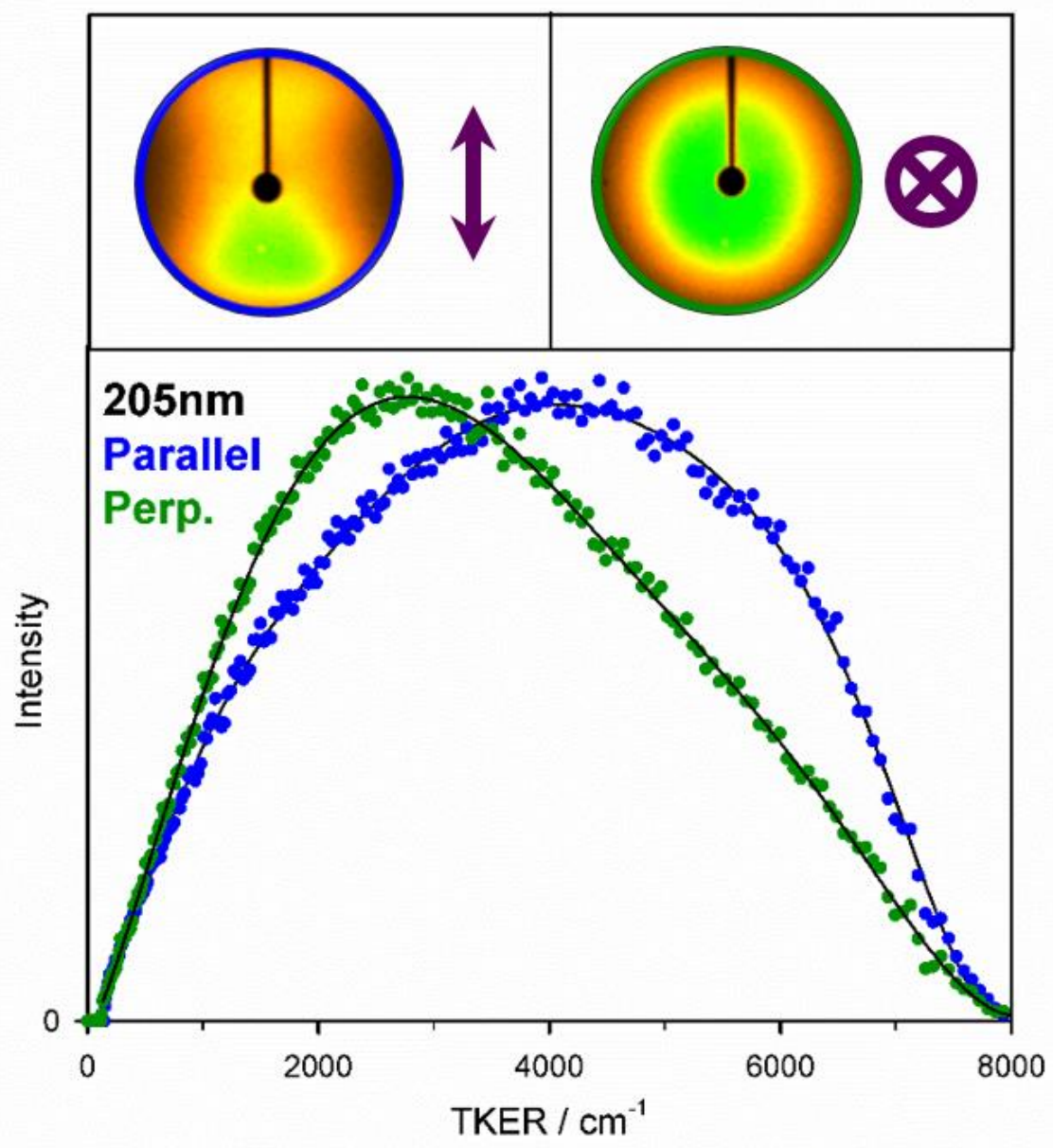


Figure S11. One color O ¹D background images arising from 205 nm photodissociation of IO and MACR-oxide on its second $\pi^* \leftarrow \pi$ transition, and subsequent 2 + 1 REMPI ionization with the same laser. Images are recorded when the polarization of the 205 nm probe laser is set parallel and perpendicular to the plane of the detector. The intensity distribution of the image obtained from perpendicular 205 nm laser polarization enables more uniform subtraction in the high kinetic energy release region of the detector.

Table S9. Characteristics of the total kinetic energy release (TKER) and anisotropic angular distributions derived from reconstructed images of O ¹D products following electronic excitation of MACR-oxide on the first $\pi^* \leftarrow \pi$ transition at discrete wavelengths from 385 to 471 nm. For TKER, the parameters include the average $\langle \text{TKER} \rangle$ and most probable (Peak) kinetic energy, and the full width at half maximum (FWHM). The anisotropy parameter β is derived from the angular distributions as the average value over the FWHM of the TKER distribution ($\pm 1\sigma$).

	O ¹ D				
	385 nm	416nm	430nm	447nm	471 nm
$\langle \text{TKER} \rangle / \text{cm}^{-1}$	2465	2761	2865	2892	2502
Peak / cm^{-1}	1999	2243	2265	2218	1842
FWHM / cm^{-1}	2729	3175	3356	3361	2628
β	0.60(38)	0.67(31)	0.74(44)	0.66(30)	0.58(39)

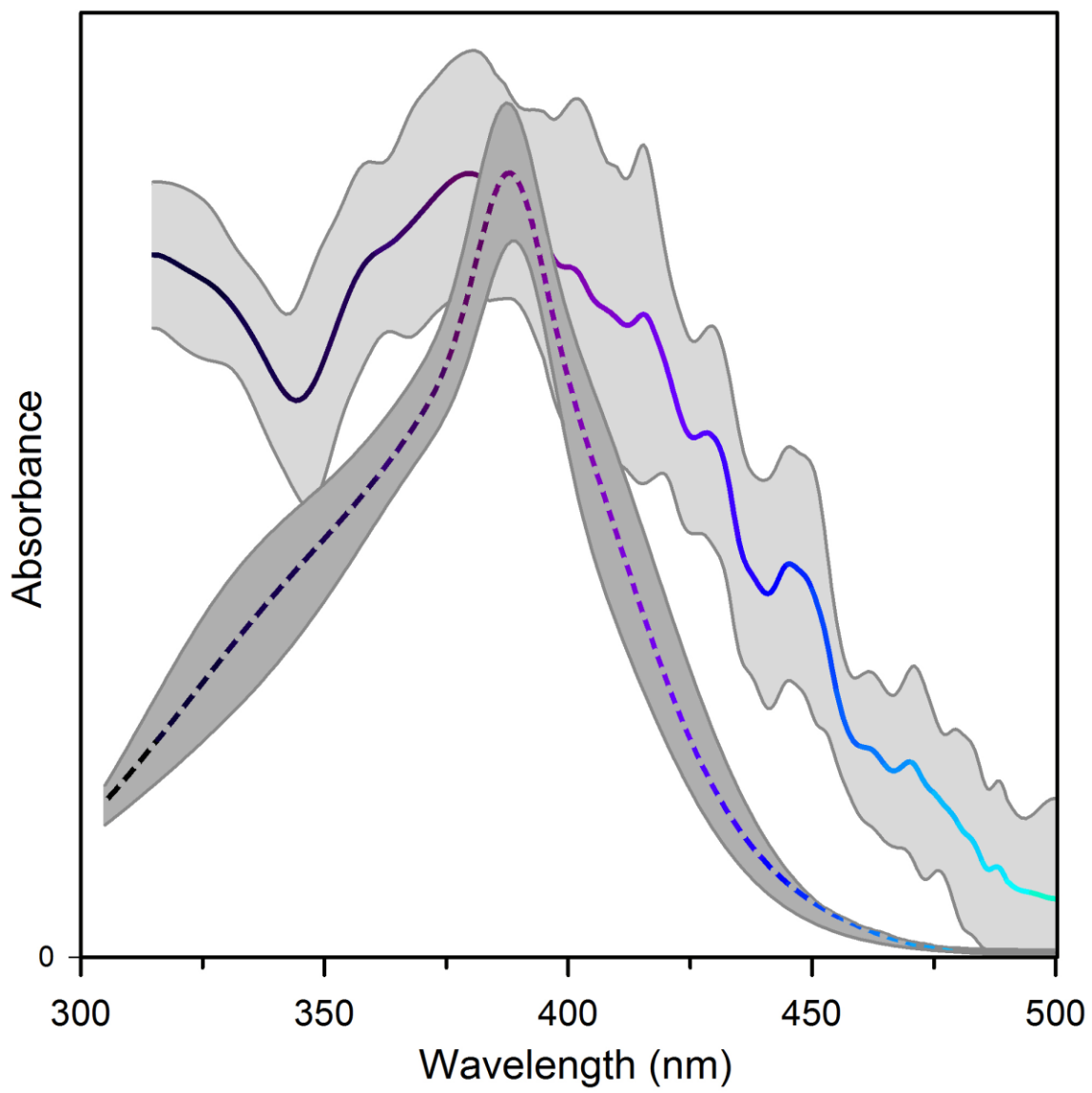


Figure S12. Comparison of the MACR-oxide (solid colored line) and MVK-oxide (dashed colored line; adapted from Ref. 20) experimental absorption spectra derived from UV-vis induced depletion of the associated photoionization signals. The shaded regions illustrate the uncertainties derived from repeated measurements. The maximum absorbance for MACR-oxide (at 380 nm) is set equal to that for MVK-oxide (at 388 nm) for comparison.

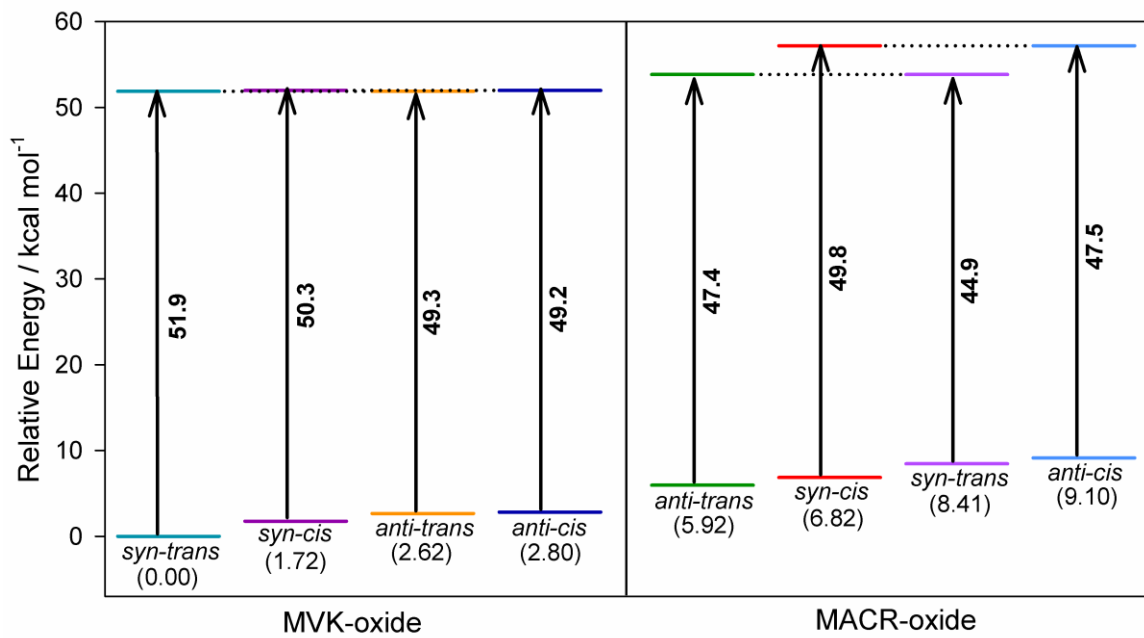
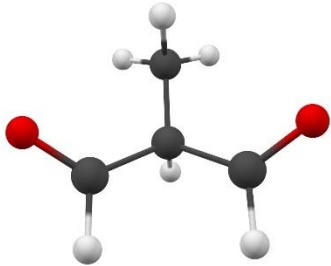
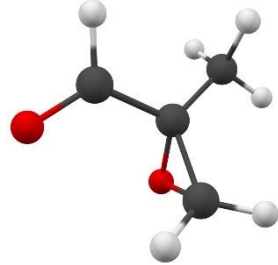


Figure S13. Relative energies of MACR-oxide and MVK-oxide conformers with respect to the most stable *syn-trans* conformer of MVK-oxide (kcal mol⁻¹). Ground state energies are evaluated at the CCSD(T)-F12/CBS(TZ-F12,QZ-F12)//B2PLYP-D3/cc-pVTZ level of theory. The energies required for dissociation of MACR-oxide and MVK-oxide conformers to MACR (or MVK) X ¹A' + O ¹D products are shown (CASPT2(12,10)/AVDZ level of theory).

Table S10. CASPT2(12,10)/ AVDZ vertical excitation energies (VEE, eV), corresponding wavelengths (λ , nm), and oscillator strengths (f) for the lowest six singlet electronic transitions of possible isomers of MACR-oxide. Geometric optimizations of the isomers were calculated at the B2PLYP-D3/cc-VTZ level of theory. Transitions predicted to have appreciable oscillator strength are highlighted (bold).

4-methyl-3H-1,2-dioxole (dioxole)		3-(prop-1-en-2-yl)dioxirane (dioxirane)		2-Methylprop-2-enoic acid (methacrylic acid)	
VEE / eV (λ /nm)	f	VEE / eV (λ /nm)	f	VEE / eV (λ /nm)	f
4.10 (302)	0.003	4.13 (300)	0.002	4.77 (260)	0.012
5.08 (244)	0.160	6.52 (190)	0.001	6.75 (184)	0.019
5.56 (223)	0.930	6.86 (181)	0.029	7.24 (171)	0.338
5.67 (219)	0.002	7.00 (177)	0.349	7.30 (170)	0.277
6.14 (202)	0.002	7.14 (174)	0.089	7.42 (167)	0.187
7.45 (166)	0.034	7.38 (168)	0.001	7.54 (164)	0.008

2-methyl-3-oxopropanal (β -dicarbonyl)		1-2-epoxy-2-methyl-3-propanal (epoxide)	
			

VEE / eV (λ /nm)	f	VEE / eV (λ /nm)	f
3.97 (312)	0.001	3.83 (324)	0.001
4.06 (305)	0.001	6.12 (203)	0.033
6.39 (194)	0.080	6.91 (179)	1.205
6.56 (189)	0.006	7.16 (173)	0.006
7.19 (172)	0.204	7.63 (162)	0.062
8.08 (153)	0.002	7.91 (157)	0.033

Table S11. Stationary point geometries for MACR-oxide isomers evaluated at the B2PLYP-D3/cc-pVTZ level of theory.

Single-Reference Stationary Points			
Minima			
4-methyl-3H-1,2-dioxole (dioxole)			
C	-0.15931	-1.16268	0.00019
H	-0.01294	-1.78116	0.89195
H	-0.01275	-1.78116	0.89195
C	2.19425	0.02716	-0.00005
C	0.70783	0.06225	-0.00009
H	2.61000	1.03218	-0.00015
H	2.57747	-0.49613	0.87793
H	2.57747	-0.49613	-0.87793
C	-0.11447	1.10268	-0.00000
H	0.09174	2.16060	-0.00005
O	-1.44180	0.81457	0.00015
O	-1.50830	-0.66629	-0.00028
3-(prop-1-en-2-yl)dioxirane (dioxirane)			
C	0.94868	1.40908	0.00004
H	2.84747	-0.60514	0.00010
H	1.65227	-2.00992	-0.00006
C	0.80331	-0.07105	-0.00003
C	1.82130	-0.94208	0.00000
H	1.99723	1.69448	0.00018
H	0.46315	1.83913	0.87460
H	0.46315	1.83913	-0.87462
C	-0.57223	-0.63086	-0.00012
H	-0.65045	-1.71512	-0.00030
O	-1.54870	0.02654	0.75365
O	-1.54873	0.02680	-0.75355
2-Methylprop-2-enoic acid (methacrylic acid)			
C	1.05303	1.44588	0.24836
H	0.34672	2.23395	0.47737
H	2.09819	1.72388	0.27244
C	0.67814	0.19075	0.00305
C	-0.76862	-0.21533	0.03305
H	2.67297	-0.58135	-0.18222

H	1.47345	-1.40106	-1.19832
H	1.49590	-1.71200	0.52124
C	1.64414	-0.93311	-0.22690
H	-1.24301	1.53032	-0.59074
O	-1.12397	-1.32753	0.31311
O	-1.68658	0.73717	-0.26875
2-methyl-3-oxopropanal (β -dicarbonyl)			
C	0.00000	0.08844	0.54269
H	0.00002	0.03347	1.64218
H	-1.24271	-1.75514	0.44438
C	-1.23555	-0.69267	0.13518
C	0.00000	1.52546	0.06155
H	0.00003	1.56097	-1.02486
H	-0.88722	2.04325	0.41549
H	0.88721	2.04326	0.41552
C	1.23552	-0.69270	0.13511
H	1.24275	-1.75511	0.44449
O	-2.16241	-0.22137	-0.47406
O	2.16242	-0.22137	-0.47401
1-2-epoxy-2-methyl-3-propanal (epoxide)			
C	-0.33588	0.14300	-0.04710
H	-1.45666	-1.49656	-1.00125
H	0.37840	-1.71458	-1.00137
C	-0.49205	-1.21532	-0.59601
C	-1.47760	1.11863	-0.01759
H	-1.45198	1.76982	-0.89141
H	-1.42618	1.74411	0.87346
H	-2.42529	0.58702	-0.00780
C	1.05022	0.72821	-0.09082
H	1.08855	1.82023	-0.26580
O	-0.45626	-1.00117	0.81026
O	2.05939	0.08151	0.04016

Table S12. Adiabatic ionization energies (AIE) and vertical ionization energies (VIE) for isomers of MACR-oxide computed at the CCSD(T)/cc-pVTZ//B3LYP/cc-pVTZ level of theory.

MACR-oxide Isomer	AIE / eV	VIE / eV
4-methyl-3H-1,2-dioxole (dioxole)	8.27	8.46
3-(prop-1-en-2-yl)dioxirane (dioxirane)	10.04	10.35
2-methylprop-2-enoic acid (methacrylic acid)	9.82	
2-methyl-3-oxopropanal (β -dicarbonyl)	9.98	10.09
1-2-epoxy-2-methyl-3-propanal (epoxide)	9.68	10.08

References

1. Karagoz, E. S.; Kus, M.; Akpınar, G. E.; Artok, L., Regio- and stereoselective synthesis of 2,3,5-trienoates by palladium-catalyzed alkoxycarbonylation of conjugated enyne carbonates. *J. Org. Chem.* **2014**, *79*, 9222-30.
2. Menche, D.; Fassfeld, J.; Li, J.; Rudolph, S., Total Synthesis of Archazolid A. *J. Am. Chem. Soc.* **2007**, *129*, 6100-6101.
3. Chandrasekhar, B.; Athe, S.; Reddy, P. P.; Ghosh, S., Synthesis of fully functionalized aglycone of lycoperdinolide A and B. *Org. Biomol. Chem.* **2015**, *13*, 115-24.
4. Xu, Q.; Cheng, B.; Ye, X.; Zhai, H., SmI₂-Mediated Carbon-Carbon Bond Fragmentation in α -Aminomethyl Malonates. *Org. Lett.* **2009**, *18*, 4136-4138.
5. Yang, Z.; Xu, X.; Yang, C. H.; Tian, Y.; Chen, X.; Lian, L.; Pan, W.; Su, X.; Zhang, W.; Chen, Y., Total Synthesis of Nannocystin A. *Org. Lett.* **2016**, *18*, 5768-5770.
6. Kwok, W. M.; Phillips, D. L., Solvation and Solvent Effects on the Short-Time Photodissociation Dynamics of CH₂I₂ from Resonance Raman Spectroscopy. *J. Chem. Phys.* **1996**, *104*, 2529-2540.
7. Frisch, M. J.; Trucks, G. W.; Schlegel, H. B.; Scuseria, G. E.; Robb, M. A.; Cheeseman, J. R.; Scalmani, G.; Barone, V.; Mennucci, B.; Petersson, G. A.; Nakatsuji, H.; Caricato, M.; Li, X.; Hratchian, H. P.; Izmaylov, A. F.; Bloino, J.; Zheng, G.; Sonnenberg, J. L.; Hada, M.; Ehara, M.; Toyota, K.; Fukuda, R.; Hasegawa, J.; Ishida, M.; Nakajima, T.; Honda, Y.; Kitao, O.; Nakai, H.; Vreven, T.; Montgomery Jr., J. A.; Peralta, J. E.; Ogliaro, F.; Bearpark, M.; Heyd, J. J.; Brothers, E.; Kudin, K. N.; Staroverov, V. N.; Kobayashi, R.; Normand, J.; Raghavachari, K.; Rendell, A.; Burant, J. C.; Iyengar, S. S.; Tomasi, J.; Cossi, M.; Rega, N.; Millam, J. M.; Klene, M.; Knox, J. E.; Cross, J. B.; Bakken, V.; Adamo, C.; Jaramillo, J.; Gomperts, R.; Stratmann, R. E.; Yazyev, O.; Austin, A. J.; Cammi, R.; Pomelli, C.; Ochterski, J. W.; Martin, R. L.; Morokuma, K.; Zakrzewski, V. G.; Voth, G. A.; Salvador, P.; Dannenberg, J. J.; Dapprich, S.; Daniels, A. D.; Farkas, O.; Foresman, J. B.; Ortiz, J. V.; Cioslowski, J.; Fox, D. J. *Gaussian 09*, Revision A.03, Gaussian, Inc.: Wallingford CT, 2009.
8. Barber, V. P.; Pandit, S.; Green, A. M.; Trongsiwat, N.; Walsh, P. J.; Klippenstein, S. R.; Lester, M. I., Four carbon Criegee intermediate from isoprene ozonolysis: Methyl vinyl ketone oxide synthesis, infrared spectrum, and OH production. *J. Am. Chem. Soc.* **2018**, *140*, 10866-10880.
9. Kuwata, K. T.; Valin, L. C., Quantum Chemical and RRKM/Master Equation Studies of Isoprene Ozonolysis: Methacrolein and Methacrolein Oxide. *Chem. Phys. Lett.* **2008**, *451*, 186-191.
10. Cabezas, C.; Endo, Y., The reactivity of the Criegee intermediate CH₃CHOO with water probed by FTMW spectroscopy. *J. Chem. Phys.* **2018**, *148*, 014308.
11. Roos, B. O.; Linse, P.; Siegbahn, P. E. M.; Blomberg, M. R. A., A simple method for the evaluation of the second-order-perturbation energy from external double-excitations with a CASSCF reference wavefunction. *Chem. Phys.* **1982**, *66*, 197-207.
12. Andersson, K.; Malmqvist, P. A.; Roos, B. O.; Sadlej, A. J.; Wolinski, K., Second-order perturbation theory with a CASSCF reference function. *J. Phys. Chem.* **1990**, *94*, 5483-5488.
13. Andersson, K.; Malmqvist, P. Å.; Roos, B. O., Second-order perturbation theory with a complete active space self-consistent field reference function. *J. Chem. Phys.* **1992**, *96*, 1218-1226.
14. Dunning, T. H., Gaussian Basis Sets for Use in Correlated Molecular Calculations. I. The atoms Boron through Neon and Hydrogen. *J. Chem. Phys.* **1989**, *90*, 1007-1023.
15. Werner, H.-J.; Knowles, P. J.; Knizia, G.; Manby, F. R.; Schütz, M.; Celani, P.; Györfly, W.; Kats, D.; Korona, T.; Lindh, R.; Mitrushenkov, A.; Rauhut, G.; Shamasundar, K. R.; Adler, T. B.; Amos, R. D.; Bernhardsson, A.; Berning, A.; Cooper, D. L.; Deegan, M. J. O.; Dobbyn, A. J.; Eckert, F.; Goll, E.; Hampel, C.; Hesselmann, A.; Hetzer, G.; Hrenar, T.; Jansen, G.; Köppl, C.; Liu, Y.; Lloyd, A. W.; Mata, R. A.; May, A. J.; McNicholas, S. J.; Meyer, W.; Mura, M. E.; Nicklaß, A.; O'Neill, D. P.; Palmieri, P.; Peng, D.; Pflüger, K.; Pitzer, R.; Reiher, M.; Shiozaki, T.; Stoll, H.; Stone, A. J.; Tarroni, R.; Thorsteinsson, T.; Wang, M.; Welborn, MOLPRO, version 2015.1, a package of *ab initio* programs, 2015, see <http://www.molpro.net>.
16. Lehman, J. H.; Li, H.; Beames, J. M.; Lester, M. I., Communication: Ultraviolet photodissociation dynamics of the simplest Criegee intermediate CH₂OO. *J. Chem. Phys.* **2013**, *139*, 141103.
17. Li, H.; Fang, Y.; Beames, J. M.; Lester, M. I., Velocity Map Imaging of O-atom Products from UV Photodissociation of the CH₂OO Criegee Intermediate. *J. Chem. Phys.* **2015**, *142*, 214312.
18. Li, H.; Fang, Y.; Kidwell, N. M.; Beames, J. M.; Lester, M. I., UV Photodissociation Dynamics of the CH₃CHOO Criegee Intermediate: Action Spectroscopy and Velocity Map Imaging of O-Atom Products. *J. Phys. Chem. A* **2015**, *119*, 8328-8337.
19. Vansco, M. F.; Li, H.; Lester, M. I., Prompt release of O ¹D products upon UV excitation of CH₂OO Criegee intermediates. *J. Chem. Phys.* **2017**, *147*, 013907.
20. Vansco, M. F.; Marchetti, B.; Lester, M. I., Electronic spectroscopy of methyl vinyl ketone oxide: A four-carbon unsaturated Criegee intermediate from isoprene ozonolysis. *J. Chem. Phys.* **2018**, *149*, 244309.
21. Pratt, S. T.; Dehmer, P. M.; Dehmer, J. L., Double-Resonance Spectroscopy of Transitions between Autoionizing Levels of Atomic Oxygen. *Phys. Rev. A* **1991**, *43*, 4702-4711.
22. Garcia, G. A.; Nahon, L.; Powis, I., Two-dimensional charged particle image inversion using a polar basis function expansion. *Rev. Sci. Instrum.* **2004**, *75*, 4989-4996.
23. OriginLab Corporation *Origin(Pro)*, 2019b; OriginLab Corporation: Northhampton, MA, USA.
24. Krishnan, R.; Binkley, J. S.; Seeger, R.; Pople, J. A., Self-consistent molecular orbital methods. XX. A basis set for correlated wave functions. *J. Chem. Phys.* **1980**, *72*, 650-654.
25. Aplincourt, P.; Henon, E.; Bohr, F., Theoretical study of photochemical processes involving singlet excited states of formaldehyde carbonyl oxide in the atmosphere. *Chem. Phys.* **2002**, *285*, 221-231.
26. Beames, J. M.; Li, F.; Lu, L.; Lester, M. I., Ultraviolet Spectrum and Photochemistry of the Simplest Criegee Intermediate CH₂OO. *J. Am. Chem. Soc.* **2012**, *134*, 20045-20048.

27. Lee, E. P.; Mok, D. K.; Shallcross, D. E.; Percival, C. J.; Osborn, D. L.; Taatjes, C. A.; Dyke, J. M., Spectroscopy of the simplest Criegee intermediate CH_2OO : simulation of the first bands in its electronic and photoelectron spectra. *Chem. Eur. J.* **2012**, *18*, 12411-23.
28. Beames, J. M.; Liu, F.; Lu, L.; Lester, M. I., UV Spectroscopic Characterization of an Alkyl Substituted Criegee Intermediate CH_3CHOO . *J. Chem. Phys.* **2013**, *138*, 244307.
29. Liu, F.; Beames, J. M.; Green, A. M.; Lester, M. I., UV Spectroscopic Characterization of Dimethyl- and Ethyl-Substituted Carbonyl Oxides. *J. Phys. Chem. A* **2014**, *118*, 2298-2306.
30. Samanta, K.; Beames, J. M.; Lester, M. I.; Subotnik, J. E., Quantum dynamical investigation of the simplest Criegee intermediate CH_2OO and its O-O photodissociation channels. *J. Chem. Phys.* **2014**, *141*, 134303.
31. Dooley, K. S.; Geidosch, J. N.; North, S. W., Ion imaging study of IO radical photodissociation: Accurate bond dissociation energy determination. *Chem. Phys. Lett.* **2008**, *457*, 303-306.

APPENDIX IV

FIRST DIRECT KINETIC MEASUREMENTS AND THEORETICAL PREDICTIONS OF AN ISOPRENE-DERIVED CRIEGEE INTERMEDIATE

SUPPORTING INFORMATION

This appendix has been previously published as online supplementary information in the *Proceedings of the National Academy of Sciences*, **117**, 9733 (2020) and reproduced with the permission of PNAS. It is a supplement to Chapter 5 of this thesis. Supplementary experimental research was performed with researchers Rebecca Caravan (*NASA Postdoctoral Program Fellow, NASA Jet Propulsion Laboratory, Combustion Research Facility, Sandia National Laboratories, Chemical Sciences and Engineering Division, Argonne National Laboratory*), Kendrew Au (*Combustion Research Facility, Sandia National Laboratories*), Yu-Lin Li (*Institute for Atomic and Molecular Sciences*), Frank Winiberg (*NASA Jet Propulsion Laboratory, California Institute of Technology*), Kristen Zuraski (*NASA Postdoctoral Program Fellow, NASA Jet Propulsion Laboratory*), Yen-Hsiu Lin (*Institute for Atomic and Molecular Sciences*), Wen Chao (*Institute for Atomic and Molecular Sciences*), David Osborn (*Combustion Research Facility, Sandia National Laboratories*), Carl Percival (*NASA Jet Propulsion Laboratory, California Institute of Technology*), Jim Jr-Min Lin (*Institute for Atomic and Molecular Sciences*), Leonid Sheps (*Combustion Research Facility, Sandia National Laboratories*), Craig Taatjes (*Combustion Research Facility, Sandia National Laboratories*), and Marsha Lester (*Department of Chemistry, University of Pennsylvania*). Synthetic work was performed by graduate student Nisalak Trongsirawat and Patrick J. Walsh (*Department of Chemistry, University of Pennsylvania*). Theoretical research was performed in collaboration with Stephen J. Klippenstein (*Chemical Sciences and Engineering Division, Argonne National Laboratory*). Atmospheric modeling was performed in collaboration with Anwar Khan and Dudley Shallcross (*School of Chemistry, University of Bristol*).

1. Methods

1.1 Sandia transient absorption experiment

The UV-Vis spectra of methyl vinyl ketone oxide (MVK-oxide) and kinetics measurements with co-reactant SO₂ or formic acid were obtained using the Sandia broadband multi-pass transient absorption experiment as described previously^{1,2}. Following the method of Barber *et al.*³, MVK-oxide was produced by the 266 nm laser flash photolysis of 1,3-diiodobut-2-ene in the presence of excess O₂. The vapor of 1,3-diiodobut-2-ene was entrained into a He flow using a pressure- and temperature-controlled glass bubbler. Reactants (1,3-diiodobut-2-ene, O₂ and SO₂ or formic acid) and bath gases (He) were delivered via a set of calibrated mass flow controllers to the reactor (operated at 300 K and 10 Torr). Continuous broadband radiation was provided by a Xe arc lamp, leading to an effective path length in the range 30-40 m across the 300-450 nm spectral range. Time-resolved broadband spectra were obtained for each laser shot and were analyzed by a custom-built spectrometer. Experiments were performed under pseudo-first-order conditions such that [O₂] >> [1,3-diiodobut-2-ene]. For bimolecular kinetics investigations, [co-reactant] >> [MVK-oxide]. Spectral analysis was performed by subtracting overlapping absorptions due to MVK and IO from the spectrum at long kinetic times, as discussed in the main text. Kinetic data were extracted by integrating over 330-367 nm to avoid perturbations from IO appearance at longer kinetic times. Analysis was conducted for wavelength ranges across the whole spectral range, and the resultant kinetics were consistent. The time traces were fitted with a single-exponential growth, single-exponential decay expression convolved with the instrument response function.

1.2 Sandia MPIMS

Complementary experiments to examine the kinetics of the iodoalkenyl + O₂ reaction and the products of *syn*-MVK-oxide + SO₂ and formic acid were performed using the Sandia Multiplexed Photoionization Mass Spectrometer (MPIMS) instrument ⁴. The MPIMS was interfaced with the tunable-VUV ionizing radiation of the Chemical Dynamics Beamline (9.0.2) of the Advanced Light Source (Lawrence Berkeley National Laboratory). 1,3-diiodobut-2-ene, O₂, He and SO₂ or formic acid were delivered to a halocarbon wax-coated quartz reactor (298 K, 10 Torr) as described above. MVK-oxide was produced using the method of Barber *et al.* ³, using a 248 nm excimer laser aligned along the length of the reactor. Reactants, intermediates and products were continuously sampled from a pinhole orifice in the reactor sidewall. The resultant molecular beam generated from expansion of the sampled gas into vacuum was intercepted orthogonally by the tunable-VUV radiation. The resultant ions were subsequently detected via orthogonal acceleration time-of-flight mass spectrometry. Experiments were performed at a photoionization energy of 8 eV in the absence of co-reactant, varying [O₂] to establish the bimolecular rate coefficient for the iodoalkenyl radical + O₂ reaction (see section 3.1). The iodoalkenyl time profiles were fitted with a single exponential decay convolved with the instrument response function. Using the measured bimolecular rate coefficient for iodoalkenyl + O₂, experimental conditions were designed such that pseudo-first-order conditions were maintained: [O₂] >> [1,3-diiodobut-2-ene] and [SO₂ or formic acid] >> [MVK-oxide]. Investigations of SO₃ production from the reaction of MVK-oxide with SO₂ were performed using a photoionization energy of 13 eV, above the ionizing threshold of 12.80 eV ⁵. High resolution mass spectrometry was utilized to identify SO₃ via its exact mass. SO₃ time traces were fitted with a single-exponential growth single-exponential decay (to account for wall and diffusional loss) expression

convolved with an instrument response function. Products of the MVK-oxide + formic acid reaction were investigated through experiments at a fixed ionization energy of 10.5 eV in addition to photoionization efficiency scans at ionization energies between 8.50 and 10.50 eV at 0.05 eV increments. High resolution mass spectrometry was utilized to identify product formation at m/z 87 and 99.

1.3 IAMS transient absorption experiment

UV-Vis absorption spectra and kinetics were also recorded using the IAMS transient absorption experiment, detailed previously^{6,7}. MVK-oxide was generated using the method of Barber *et al.*³ via the 248 nm laser photolysis of 1,3-diiodobut-2-ene. The vapor pressure of 1,3-diiodobut-2-ene (heated to ~307 K) was entrained in O₂ or N₂, then mixed with O₂ prior to entering the photolysis reactor. A set of calibrated mass flow controllers were used to deliver N₂, O₂, 1,3-diiodobut-2-ene and SO₂ (or humidified N₂) to the reactor, which was held at 298 K. Pseudo-first-order conditions were maintained such that [O₂] \gg [1,3-diiodobut-2-ene], and for bimolecular investigations, [SO₂] or [water] \gg [MVK-oxide]. Prior to mixing, the concentrations of 1,3-diiodobut-2-ene and SO₂ were monitored in separate absorption cells by their UV absorption spectra. Absolute SO₂ concentrations were derived by comparing the integrated absorbance to the integrated cross section⁸ within 200-250 nm. The concentration of SO₂ was also measured in the photolysis reactor using UV absorption for some experiments to confirm the concentration calculation. The error from this calibration process is ~8%, including uncertainties in the spectrum measurement, pressure measurement, and uncertainty of the mass flow controllers. The error in [SO₂] from the reported absolute cross section is about 5–10%⁸. Thus, the total error of [SO₂] is estimated to be 11–14%. [water] was derived in a similar manner with a humidity-temperature sensor. To prevent

contamination of the reactor windows, slow flows of N₂ were used to purge the inner surfaces of the windows. To enhance the sensitivity of the absorption measurement, the probe light was focused and passed through the reactor 6 times using a spherical mirror and a SiO₂ prism resulting in an effective absorption length of ~ 426 cm. The spectra were acquired by using a grating spectrometer (Andor SR303i) and an electron-multiplying charge-coupled device (EMCCD, Andor Newton970, DU970N-UVB). The absorption change (after the photolysis pulse) at 340 or 375 nm (selected by a 10 nm bandpass filter) was monitored in real time by using a balanced photodiode detector and recorded by an oscilloscope.

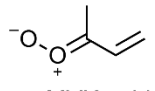
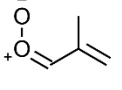
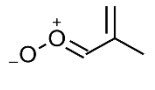
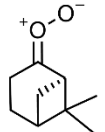
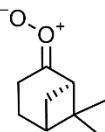
1.4 Global atmospheric modelling

Model simulation were conducted to quantify the impact of the MVK-oxide reactions with SO₂ and formic acid on the troposphere using the 3-dimensional global chemistry transport model, STOCHEM-CRI. STOCHEM is based upon a Lagrangian approach, with the chemical outputs being mapped onto a 5° latitude by 5° longitude Eulerian grid with 9 vertical layers. The Lagrangian approach has been used as it allows the advection of the 50,000 air parcels to be uncoupled from the chemical processes within these parcels. It is an 'offline' model with the radiation codes and transport driven by archived meteorological data, produced by the UKMO Unified Model (UM) at a grid resolution of 1.25° longitude, 0.8333° latitude, and 12 unevenly spaced (with respect to altitude) vertical levels with an upper boundary of 100 hPa⁹. More details about the meteorological parameterizations in STOCHEM can be found in Collins *et al.*¹⁰ and Derwent *et al.*¹¹. The chemical mechanism used in STOCHEM, is the common representative intermediates mechanism version 2 and reduction 5 (CRI v2-R5), referred to as 'STOCHEM-CRI'¹²⁻¹⁵. The mechanism consists of 229 chemical species and 627

reactions. The emissions data employed in the STOCHEM model were adapted from the Precursor of Ozone and their Effects in the Troposphere (POET) inventory (http://accent.aero.jussieu.fr/database_table_inventories.php). The surface emissions from biomass burning, vegetation, oceanic and soil are distributed using monthly two-dimensional source maps at a resolution of 5° longitude × 5° latitude ¹⁶. The anthropogenic surface emissions have been distributed using the method developed by the International Institute for Applied Systems Analysis (IIASA) ¹⁷. The surface emissions of isoprene are emitted at a rate proportional to the cosine of the solar zenith angle during the day, with no emissions at night. More details about the emissions data of CO, NO_x, SO₂, CH₄ and non-methane volatile organic compounds are given by Khan *et al.* ¹⁸.

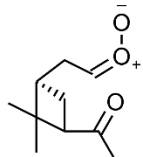
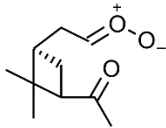
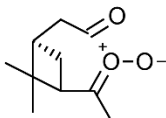
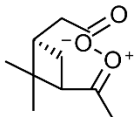
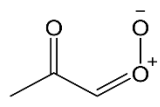
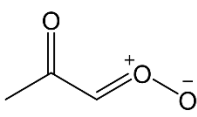
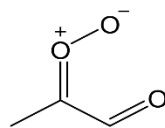
The improved CRI v2-R5 mechanism of STOCHEM-CRI utilized in this study incorporates Criegee intermediates (CIs) formed from the ozonolysis reactions of six alkenes: ethene, propene, *trans*-but-2-ene, isoprene, α-pinene and β-pinene. Individual CIs are accounted for with their explicit formation and loss processes in the model. The chemical loss processes of unimolecular decomposition and/or reaction with water monomer and water dimer strongly dominate, which result in very short atmospheric lifetimes of CIs. The detailed information about the formation and loss processes of CIs used in the model can be found in McGillen *et al.* ¹⁹ and Chhantyal-Pun *et al.* ²⁰. The loss of MVK-oxide by unimolecular decay, reactions with water monomer and dimer, and with SO₂ have been updated from the study McGillen *et al.* ¹⁹ and Chhantyal-Pun *et al.* ²⁰ with the rate coefficients detailed in Table S1. Reactions of other functionalized CIs with SO₂ and formic acid have also been included. The reaction products from CH₂OO + water dimer have been updated, following recent experimental characterization by Sheps *et al.* ²¹ that revealed little formic acid production from this reaction. As a result of this, global

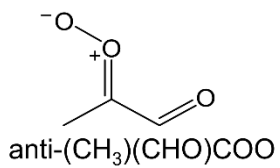
Table S1. Reactions of Criegee intermediates and associated rate coefficients accounted for in the atmospheric model utilized in this work. The rate coefficients in bold font are those updated from previous work ^{19, 20}.

Criegee intermediate	Rate coefficients ^a	References
 CH ₂ OO	$k_{(\text{H}_2\text{O})_2}: 3.92 \times 10^{-16} \exp(2930/T)$	Smith <i>et al.</i> ²²
 <i>syn</i> -CH ₃ CHOO	$k_{\text{uni}}: 2.76 \times 10^{-73} T^{27.88} \exp(3978/T)$ $k_{\text{SO}_2}: 2.4 \times 10^{-11}$ $k_{\text{HCOOH}}: 2.5 \times 10^{-10}$	Fang <i>et al.</i> ²³ Taatjes <i>et al.</i> ²⁴ Welz <i>et al.</i> ²⁵
 <i>anti</i> -CH ₃ CHOO	$k_{\text{H}_2\text{O}}: 1.3 \times 10^{-14} \text{ cm}^3 \text{ s}^{-1}$ $k_{(\text{H}_2\text{O})_2}: 5.23 \times 10^{-20} \exp(6124/T)$ $k_{\text{SO}_2}: 6.7 \times 10^{-11}$ $k_{\text{HCOOH}}: 5.0 \times 10^{-10}$	Lin <i>et al.</i> ²⁶ Lin <i>et al.</i> ²⁶ Taatjes <i>et al.</i> ²⁴ Welz <i>et al.</i> ²⁵
 <i>syn</i> -MVK oxide	$k_{\text{uni}}^{\text{b}}: 2.46 \times 10^{-76} T^{29.09} \exp(3545/T)$ $k_{\text{H}_2\text{O}}: 3.4 \times 10^{-19}$ $k_{(\text{H}_2\text{O})_2}: 9.2 \times 10^{-16}$ $k_{\text{SO}_2}: 3.9 \times 10^{-11} \text{ cm}^3 \text{ s}^{-1}$ $k_{\text{HCOOH}}: 3.0 \times 10^{-10} \text{ cm}^3 \text{ s}^{-1}$	Barber <i>et al.</i> ³ Anglada and Solé ²⁷ Anglada and Solé ²⁷ This study This study
 <i>anti</i> -MVK oxide	$k_{\text{uni}}: 1.94 \times 10^{12} \exp(-6150/T)$	Barber <i>et al.</i> ³
 <i>syn</i> -MACR oxide	$k_{\text{uni}}: 1.59 \times 10^{11} T^{0.44} \exp(-6102/T)$	Vereecken <i>et al.</i> ²⁸
 <i>anti</i> -MACR oxide	$k_{\text{H}_2\text{O}}: 2.13 \times 10^{-19} T^{1.74} \exp(-929/T)$ $k_{(\text{H}_2\text{O})_2}: 2.24 \times 10^{-19} T^{1.73} \exp(1313/T)$ $k_{\text{uni}}: 5.93 \times 10^8 T^{1.46} \exp(-7832/T)$	Vereecken <i>et al.</i> ²⁸ Vereecken <i>et al.</i> ²⁸ Vereecken <i>et al.</i> ²⁸
 <i>syn</i> -nopinone oxide	$k_{\text{uni}}: 1.9 \times 10^9 T^{1.33} \exp(-8425/T)$ $k_{\text{H}_2\text{O}}: 8.46 \times 10^{-23} T^{2.64} \exp(121/T)$	Vereecken <i>et al.</i> ²⁸ Vereecken <i>et al.</i> ²⁸
 <i>anti</i> -nopinone oxide	$k_{\text{uni}}: 2.76 \times 10^{-73} T^{27.88} \exp(3978/T)$	Same k_{uni} as used for <i>syn</i> -CH ₃ CHOO

^aThe units of the unimolecular and bimolecular rate coefficient are s⁻¹ and cm³ s⁻¹, respectively.

^bNote that OH produced from the unimolecular decomposition of stabilized *syn*-MVK-oxide is omitted from the model. This is a relatively minor source of OH and is anticipated to have minimal perturbation on the reactions assessed herein.

Criegee intermediate	Rate coefficients ^a	References
 <i>syn</i> -pinonaldehyde oxide	$k_{\text{uni}}: 2.76 \times 10^{-73} T^{27.88} \exp(3978/T)$	Same k_{uni} as used for <i>syn</i> -CH ₃ CHOO
 <i>anti</i> -pinonaldehyde oxide	$k_{\text{H}_2\text{O}}: 1.3 \times 10^{-14} \text{ cm}^3 \text{ s}^{-1}$ $k_{(\text{H}_2\text{O})_2}: 5.23 \times 10^{-20} \exp(6124/T)$ $k_{\text{SO}_2}: 6.7 \times 10^{-11}$ $k_{\text{HCOOH}}: 5.0 \times 10^{-10}$	Same $k_{\text{H}_2\text{O}}$, $k_{(\text{H}_2\text{O})_2}$, k_{SO_2} and k_{HCOOH} as used for <i>anti</i> -CH ₃ CHOO
 <i>anti</i> -isopinonaldehyde oxide	$k_{\text{uni}}: 2.76 \times 10^{-73} T^{27.88} \exp(3978/T)$	Same k_{uni} as used for <i>syn</i> -CH ₃ CHOO
 <i>syn</i> -isopinonaldehyde oxide	$k_{\text{uni}}: 6.95 \times 10^{-66} T^{25.7} \exp(2391/T)$	Vereecken <i>et al.</i> ²⁸
 <i>syn</i> -CH ₃ C(O)CHOO	$k_{\text{H}_2\text{O}}: 2.18 \times 10^{-19} T^{1.43} \exp(1268/T)$ $k_{(\text{H}_2\text{O})_2}: 2.26 \times 10^{-19} T^{1.43} \exp(3279/T)$ $k_{\text{SO}_2}: 2.4 \times 10^{-11}$ $k_{\text{HCOOH}}: 2.5 \times 10^{-10}$	Vereecken <i>et al.</i> ²⁸ Vereecken <i>et al.</i> ²⁸ Same k_{SO_2} and k_{HCOOH} as used for <i>syn</i> -CH ₃ CHOO
 <i>anti</i> -CH ₃ C(O)CHOO	$k_{\text{H}_2\text{O}}: 1.3 \times 10^{-14} \text{ cm}^3 \text{ s}^{-1}$ $k_{(\text{H}_2\text{O})_2}: 5.23 \times 10^{-20} \exp(6124/T)$ $k_{\text{SO}_2}: 6.7 \times 10^{-11}$ $k_{\text{HCOOH}}: 5.0 \times 10^{-10}$	Same $k_{\text{H}_2\text{O}}$, $k_{(\text{H}_2\text{O})_2}$, k_{SO_2} and k_{HCOOH} as used for <i>anti</i> -CH ₃ CHOO
 <i>syn</i> -(CH ₃)(CHO)COO	$k_{\text{uni}}: 2.76 \times 10^{10} T^{0.78} \exp(-5162/T)$ $k_{\text{H}_2\text{O}}: 7.81 \times 10^{-20} T^{1.68} \exp(757/T)$ $k_{(\text{H}_2\text{O})_2}: 8.07 \times 10^{-20} T^{1.67} \exp(2828/T)$	Vereecken <i>et al.</i> ²⁸ Vereecken <i>et al.</i> ²⁸ Vereecken <i>et al.</i> ²⁸



$$k_{\text{uni}}: 2.76 \times 10^{-73} T^{27.88} \exp(3978/T)$$

Same k_{uni} as used for *syn*-CH₃CHOO

^aThe units of the unimolecular and bimolecular rate coefficient are s⁻¹ and cm³ s⁻¹, respectively.

^bNote that OH produced from the unimolecular decomposition of stabilized *syn*-MVK-oxide is omitted from the model. This is a relatively minor source of OH and is anticipated to have minimal perturbation on the reactions assessed herein.

modelled formic acid concentrations are reduced by 3% compared with previous model evaluations. Following the inclusion of the CI field, each air parcel contains 248 species that compete in 786 chemical reactions and utilize a time-step of 5 minutes.

1.5 Computational kinetics and mechanistic investigations

Coupled cluster calculations were performed using MOLPRO²⁹, with the CCSDT(Q) calculations employing Kállay's MRCC supplement³⁰. Density functional theory calculations were performed using G09³¹. The master equation calculations were undertaken with the MESS code^{32,33}, and the variable reaction coordinate transition state theory (TST) calculations were performed with VaReCoF³⁴.

2. Computational MVK-oxide isomerization kinetics

As discussed in the main text, there are four low lying conformers of MVK-oxide. A proper analysis of the experimental observations requires some understanding of the timescales for isomerization between these conformers. A high-level *ab initio* kinetics analysis for the unimolecular dissociation rates of *syn*- and *anti*-MVK-oxide was reported by Barber *et al.*³. This previous analysis is readily adapted to predict the rates of isomerization between the four conformers under temperature and pressure conditions of relevance to Earth's atmosphere.

The focus of Barber *et al.*³ involved dissociation of MVK-oxide at specific excitation energies (ca. 6000 cm⁻¹) obtained through direct IR-excitation. At these energies, isomerizations between the *cis* and *trans* forms of *syn*-MVK-oxide (and similarly *cis*- and *trans-anti*-MVK-oxide) are rapid relative to the dissociation timescale. Thus, the two *cis* and *trans* conformers were treated as merged species for both the *syn* and *anti* forms. For the present analysis, we instead treat all four conformers as distinct

species within the master equation and directly explore both the *cis-trans* and *syn-anti* isomerizations.

This analysis indicates that: (i) all four conformers are kinetically stable (i.e., their isomerization rate coefficients are smaller than the collisional relaxation rates), (ii) the *cis-trans* isomerization rates are fast on the timescale of the present experiments, and (iii) the *syn-anti* isomerization rates are slow on the timescale of experiment. The first finding indicates that, at least in principle, one can properly derive bimolecular rate coefficients separately for each of the individual conformers. However, the second finding indicates that the experimental observations cannot resolve the *cis* and *trans* conformers as separate species and so the observed reactive decays will instead correspond to the Boltzmann weighted average of the rate coefficients for the *cis* and *trans* pair of species. Meanwhile, the third finding indicates that the *syn-* and *anti-* conformers should exhibit distinct decays.

The underlying energies for this master equation analysis of the isomerization are as reported by Barber *et al.*³. They were largely obtained from CCSD(T)-F12b/CBS(cc-pVTZ-F12,cc-pVQZ-F12)//B2PLYPD3/cc-pVTZ evaluations coupled with CCSDT(Q)/cc-pVDZ corrections for higher order excitations, CCSD(T)/CBS(cc-pcVTZ,cc-pcVQZ) core-valence corrections, and B2PLYP-D3/cc-pVTZ anharmonicity corrections. For the two *syn-* to *anti-* torsional saddle points, the barrier heights were instead based on CASPT2 analyses due to the presence of significant multireference effects arising from the breaking of the O=O double bond in the zwitterionic resonant form of MVK-oxide. To facilitate interpretation of the present isomerization kinetics analysis, these conformer energies and isomerization barriers are reported again in Table S2.

Table S2. Stationary point energies (kcal mol⁻¹) for MVK-oxide isomerization.

Species	CCSD(T)-F12b				T(Q)	T(Q)	Core	E0	Anh.	Total ^a
	DZ- F12	TZ- F12	QZ- F12	CBS	Corr. DZ	Corr. 6- 31G*	Val. CBS TZ- QZ	B2 TZ	B2 TZ	
<i>syn-trans</i>	0.0	0	0	0	0	0	0	0	0	0
<i>syn-cis</i>	1.93	1.94	1.94	1.94	0.01	0.04	0.05	0.19	0.00	1.76
<i>anti-trans</i>	2.70	2.72	2.74	2.75	-0.07	-0.03	0.01	0.10	0.03	2.57
<i>anti-cis</i>	2.84	2.79	2.79	2.78	0.20	0.21	0.01	0.03	0.01	3.05
<i>syn-cis to syn-trans</i>	8.09	8.17	8.17	8.17	0.45	0.41	0.01	0.63	0.03	7.97
<i>anti-cis to anti-trans</i>	11.4	11.5	11.5	11.5	0.41	0.37	0.01	0.71	0.03	11.25
<i>syn-trans to anti-trans^a</i>	-	-	-	-	-	-	-	-	-	30.93 ^a
<i>syn-cis to anti-cis^a</i>	-	-	-	-	-	-	-	-	-	30.63 ^a

^aThe total energies for the *syn-anti* zero-point corrected barriers are derived from CASPT2(4e,4o)/cc-pVTZ calculations of the singlet-triplet splitting at the saddle point coupled with CCSD(T)-F12 based evaluations of the triplet energy as described in detail by Barber *et al.*³. Also, as reported by Barber *et al.*³ the total energy includes a minor (≤ 0.01 kcal mol⁻¹) contribution from relativistic effects.

In the present master equation analysis, the CH₃ groups were again treated as 1-dimensional hindered rotors with the torsional potentials as described by Barber *et al.*³. For the C₂H₃ rotors, with our current codes, there is some difficulty in assigning the state density from the quantized hindered rotor states for the overall torsional motion to specific conformational states. Here we considered two simple approximations and found that the predicted rates agreed to within ~10%. In particular, the simplest approximation involved the treatment of these modes as harmonic oscillators. An alternative treatment replaced the full torsional potential with a symmetrized potential that roughly corresponds to restricting the range of torsional space for that rotor to +/- 90 degrees from the given conformer. The isomerization rates predicted with the harmonic separation approximation are reported in Table S3. The *syn-anti* and *anti-syn* rates are too small to be kinetically relevant (10⁻³ s⁻¹ or less) and so are not reported here. For comparison purposes, the corresponding conformer-specific unimolecular dissociation rate coefficients are also reported therein. The bath gas for these calculations was presumed to be N₂, although minimal bath gas dependence is anticipated. The conformer-specific partition functions and Boltzmann thermal probabilities reported in Table S4 allow for the conversion of these conformer-specific isomerization and dissociation rate coefficients to more averaged quantities such as the *syn-* and *anti-* rate coefficients.

In summary, *syn-anti* isomerization of MVK-oxide will be negligibly slow due to the high barriers (Table S2) associated with rotation about C=O bond, and thus *syn-* and *anti-* conformers of MVK-oxide can be treated as distinct species. By contrast, the theoretical analysis demonstrates the rapid rate for *cis-trans* isomerization (ca. 10⁷ s⁻¹, Table S3) for both *syn-* and *anti-* conformers of MVK-oxide due to the much lower barriers (Table S2) associated with rotation about the C-C single bond. The

Table S3. Predicted MVK-oxide *cis-trans* isomerization rate coefficients (s⁻¹) and conformer-specific dissociation rate coefficients (s⁻¹) for a range of temperatures and pressures.

T/K	P/atm	<i>syn-trans</i> <i>syn-cis</i>	<i>syn-cis</i> <i>syn-trans</i>	<i>anti-trans</i> <i>anti-cis</i>	<i>anti-cis</i> <i>anti-trans</i>	<i>syn-</i> <i>trans</i>	<i>syn-cis</i>	<i>anti-trans</i>	<i>anti-cis</i>
225	0.01	4.1e3	1.3e5	1.9e3	5.1e3	-	-	2.1	3.7
250		1.6e4	3.4e5	9.0e3	2.2e4	1.6	8.6	28	45
275		4.6e4	6.8e5	3.0e4	6.5e4	6.3	31	230	330
298		1.0e5	1.1e6	7.0e4	1.4e5	22	110	1.1e3	1.5e3
350		3.7e5	2.6e6	2.8e5	5.1e5	240	1.9e3	1.4e4	1.8e4
400		-	-	6.7e5	1.2e6	4.0e3	-	7.7e5	9.8e4
225	0.1	2.1e4	6.6e5	7.1e3	1.9e4	-	-	2.6	4.7
250		9.0e4	1.9e6	3.8e4	9.1e4	1.7	6.4	39	63
275		2.8e5	4.1e6	1.4e5	3.1e5	6.5	29	350	520
298		6.4e5	7.3e6	3.6e5	7.4e5	23	110	1.8e3	2.6e3
350		2.6e6	1.8e7	1.7e6	3.1e6	320	1.9e3	3.2e4	4.2e4
400		-	-	4.5e6	7.7e6	5.6e3	-	2.2e5	2.8e5
225	1	6.5e4	2.1e6	1.6e4	4.1e4	-	-	2.4	6.0
250		3.2e5	6.7e6	9.7e4	2.3e5	1.6	7.3	38	78
275		1.1e6	1.7e7	4.1e5	9.0e5	6.5	29	360	650
298		2.9e6	3.3e7	1.2e6	2.5e6	24	102	2.1e3	3.3e3
350		1.3e7	9.6e7	7.0e6	1.3e7	390	1.6e3	4.3e4	6.0e4
400		3.8e7	1.9e8	2.2e7	3.8e7	3.3e3	2.1e4	3.6e5	4.7e5

^aAt 298 K and 1 atm, the average decay rate for the *syn*-conformers is 33 s⁻¹ based on a Boltzmann average $[Q_1k_1 + Q_2k_2]/(Q_1+Q_2)$, where Q_i is the partition function for conformer i (*cis* or *trans*), c.f. Table S4. Similarly, the Boltzmann averaged decay rate for *anti*-conformers is 2140 s⁻¹.

Table S4. MVK-oxide partition functions and thermal probabilities.^a

T/K	Partition Functions (cm ³) ^b				P _{trans}		P _{syn} ^e
	<i>syn-trans</i>	<i>syn-cis</i>	<i>anti-trans</i>	<i>anti-cis</i>	<i>syn</i> ^b	<i>anti</i> ^d	
225	2.5e32	4.1e32	3.8e32	4.2e32	0.969	0.725	0.994
250	4.8e32	7.9e32	7.3e32	8.1e32	0.954	0.705	0.988
275	8.9e32	1.5e33	1.4e33	1.5e33	0.937	0.687	0.981
298	1.5e33	2.6e33	2.5e33	2.6e33	0.919	0.674	0.973
350	5.1e33	9.0e33	8.2e33	8.7e33	0.877	0.651	0.949
400	1.5e34	2.8e34	2.5e34	2.6e34	0.835	0.635	0.922

^aNote that the thermal probabilities reported here (P_{trans}, P_{syn}, etc.) are for an equilibrium distribution of MVK-oxide conformers and do not reflect the nascent or time-dependent populations from the experiments.

^bPartition functions defined relative to their conformer-specific ground state energy.

^cThermal probability of the *trans* conformer within *trans*- and *cis-syn*-MVK-oxide.

^dThermal probability of the *trans* conformer within *trans*- and *cis-anti*-MVK-oxide.

^eThermal probability of the *syn*- conformer of MVK-oxide.

corresponding timescale for *cis-trans* isomerization is sub-microsecond, which is significantly faster than the experimental timescale of milliseconds. As a result, the *cis* and *trans* forms will rapidly interconvert with population of the lower energy *trans* form strongly favored over the higher energy *cis* form under thermal conditions.

3. MVK-oxide kinetics and reaction mechanisms

3.1 MVK-oxide formation and unimolecular decay

Iodoalkenyl + O₂ kinetics for MVK-oxide formation

To establish the rate of formation of MVK-oxide from the iodoalkenyl ($\cdot\text{C}_4\text{H}_6\text{I}$) + O₂ reaction, the rate coefficient for the reaction was measured by direct monitoring of the iodoalkenyl radical at m/z 181 using MPIMS at a photoionization energy of 8 eV. This energy was chosen such that it was below the threshold for dissociative ionization of the photolytic precursor (C₄H₆I₂) appearing at the mass of the iodoalkenyl radical. A bimolecular rate coefficient of $(1.70 \pm 0.07) \times 10^{-13} \text{ cm}^3 \text{ s}^{-1}$ for the reaction of C₄H₆I + O₂ is established (Figure S1) – around an order of magnitude slower than for the equivalent CH₂OO formation reaction (CH₂I + O₂)³⁵. This is rationalized by the resonance stabilization of the iodoalkenyl radical in the present case – comparisons can be drawn with R + O₂ reactions, where the rate coefficients are typically an order of magnitude slower for resonance stabilized R, due to the loss of resonance stabilization on addition of O₂.

3.2 MVK-oxide + SO₂

Further experimental evidence for SO₃ formation

Using the bimolecular rate coefficient measured via the Sandia transient absorption experiment, and assuming a first order loss rate of 300 s⁻¹ (based on the

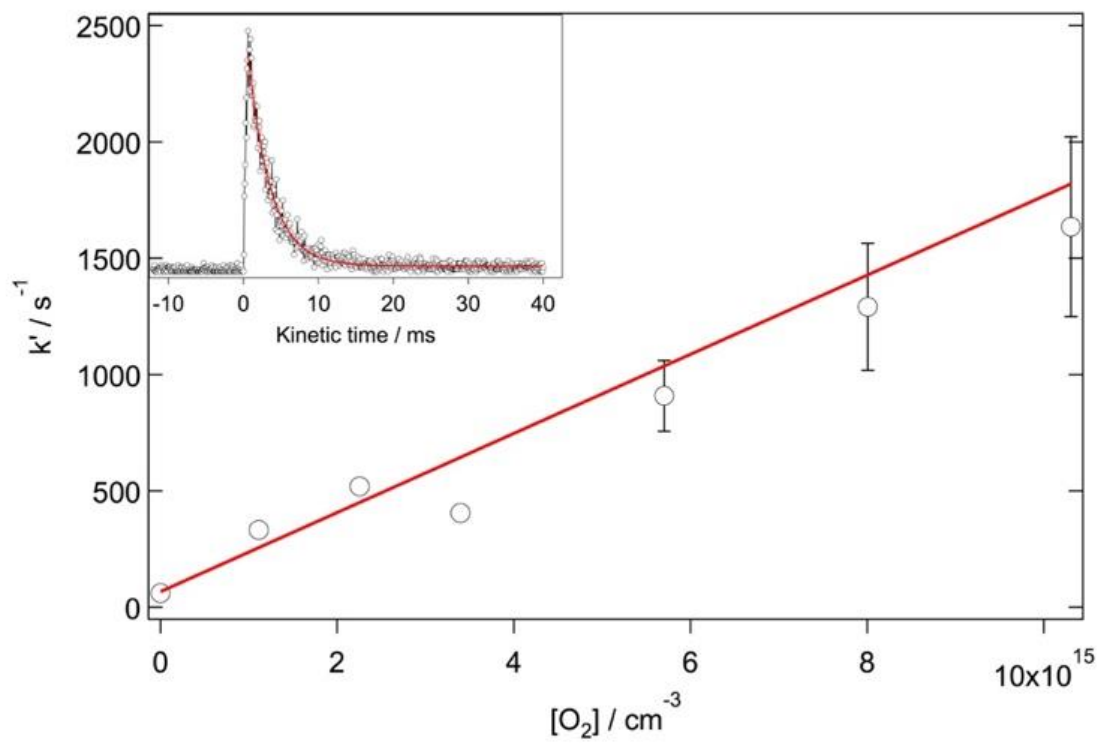


Figure S1. First order rate coefficient for the loss of the iodoalkenyl radical as a function of $[O_2]$, recorded at a photoionization energy of 8 eV using the Sandia MPIMS experiment. An example kinetic trace of the iodoalkenyl radical is inset. Kinetic traces are fitted with a single exponential decay expression convolved with the instrument response function. The bimolecular rate coefficient is obtained from a linear fit to k' vs. $[O_2]$, weighted to the 95% confidence limit error bars (note that the error bars for the first four points are smaller than the symbols). From this a bimolecular rate coefficient of $(1.70 \pm 0.07) \times 10^{-13} \text{ cm}^{-3} \text{ s}^{-1}$ is obtained.

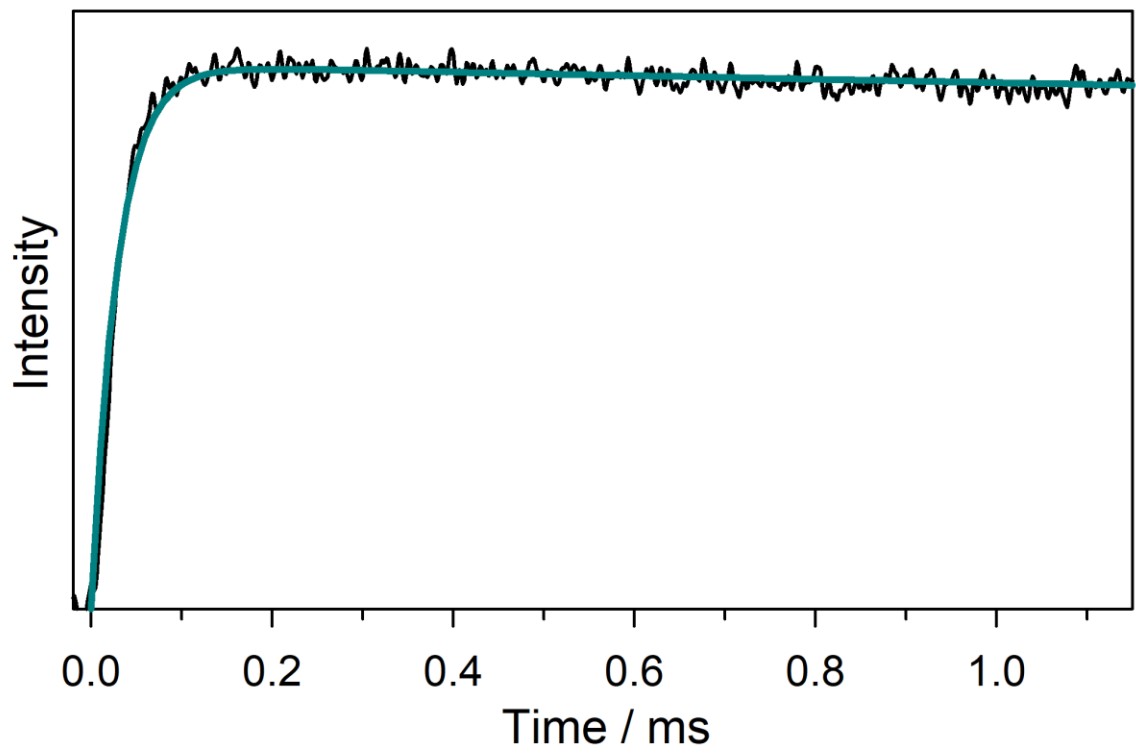


Figure S2. Enlarged inset from Figure 1 (lower panel) from the main text. Kinetic time trace for MVK-oxide from the Sandia experiment (black) integrated between 330-367 nm compared with the simulated thermal unimolecular decay for *syn*-conformers to 2-hydroperoxyl-buta-1,3-diene (cyan) with $k(T) = 33 \text{ s}^{-1}$ ($T = 298 \text{ K}$). Thermal rates are computed using *ab initio* master equation modeling in the high-pressure limit³. The simulations include an experimental rise time for MVK-oxide appearance of 30 μs from the reaction of the iodoalkenyl radical + O_2 .

transient absorption measured first order loss, and consistent with previous smaller CI first order losses in the MPIMS experiments), the signal appearing at the exact mass of SO_3 ($m/z = 79.96$) at 13 eV can be evaluated versus the fraction of MVK-oxide undergoing reaction with SO_2 . A linear increase in the amplitude of the signal at m/z 79.96 is observed with increasing fraction of MVK-oxide undergoing reaction with SO_2 (Figure S3). This, together with the exact mass determination (Figure S3, inset) and the bimolecular rate coefficient for formation (main text, Figure 3) provides further experimental evidence that SO_3 is a direct product of the MVK-oxide + SO_2 reaction. ***Ab initio calculations, computational kinetics and mechanistic investigations.***

For the reaction of MVK-oxide with SO_2 , *ab initio* kinetics calculations were performed in order to gain a better understanding of the expected temperature- and pressure-dependencies of both the rate coefficient and product branching. The experimental observation that the rate coefficient is independent of pressure suggests that the rate is governed by the capture rate for the formation of the initial complex. However, there may still be strong temperature- and pressure-dependencies to the branching between stabilization of this complex and formation of bimolecular products (primarily SO_3 + methyl vinyl ketone (MVK)). This branching has significant ramifications for the net SO_3 formation rate.

To our best knowledge, there are no prior theoretical studies of the reaction of SO_2 with MVK-oxide. However, there is considerable prior work on the reaction of SO_2 with CH_2OO ³⁶⁻⁴⁰ and many of the conclusions from those studies are relevant to the reaction with MVK-oxide. These prior studies examined a great variety of possible pathways, with the quantitative analysis of the kinetics complicated by the present of both diradical and concerted pathways. Unfortunately, quantitative predictions for such

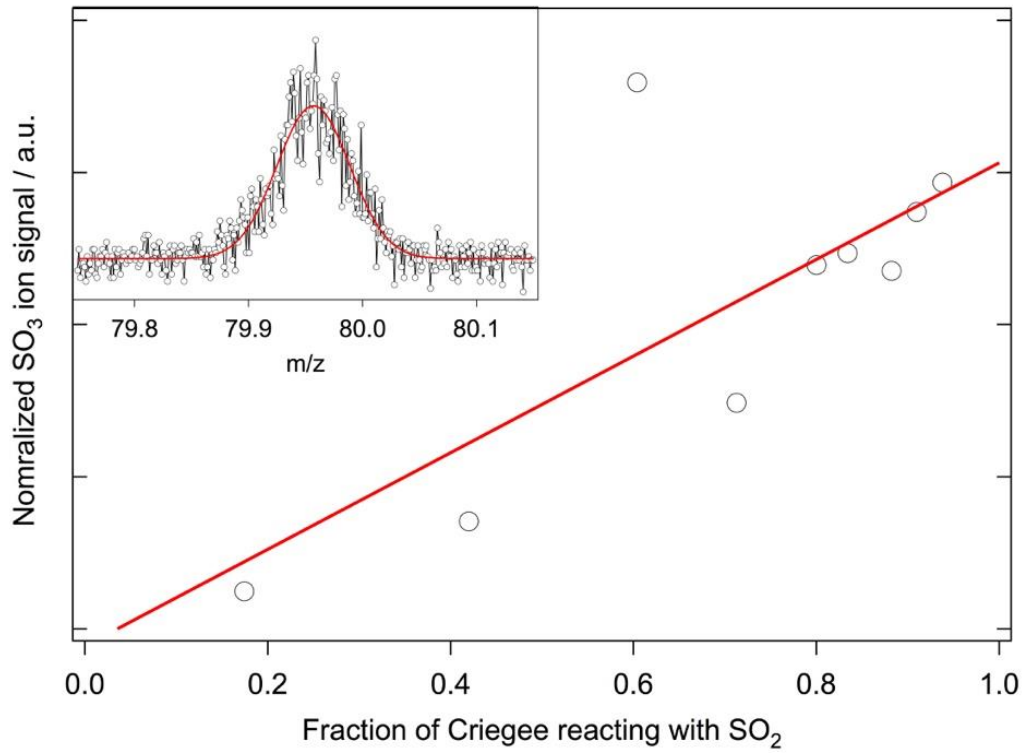


Figure S3. Linear relationship of SO₃ amplitude, (summed over the kinetic time of 0-60 ms), and the estimated fraction of MVK-oxide reacting with SO₂. SO₃ data were obtained via MPIMS at a photoionization energy of 13 eV, using the absorption experiment bimolecular rate coefficient of $3.9 \times 10^{-11} \text{ cm}^{-3} \text{ s}^{-1}$ and assuming a first-order loss of 300 s^{-1} , consistent with the Sandia broadband multi-pass transient absorption experiment data and previous MPIMS experiments of Criegee intermediate chemistry. A Gaussian fit to m/z 80 to determine the exact mass is shown in the inset. The Gaussian fit retrieved a mass value of $(79.957 \pm 0.007) \text{ amu}$ consistent with the exact m/z of SO₃ (79.95683 amu).

diradical channels generally require multi-reference electronic structure treatments. A similar competition between diradical and concerted pathways arises in the ozonolysis of Criegee intermediates, as discussed for example in the recent analysis of the dynamics of Criegee intermediate stabilization for the ozonolysis of ethylene by Pfeifle *et al.*⁴¹.

A particularly detailed exploration of the kinetics was provided in the recent study of Kuwata *et al.*⁴⁰. For simplicity, in this first analysis, we restrict our attention to the analogue of the dominant pathway from their study. In particular, we consider the addition to form both *endo* and *exo* van der Waals complexes (MVKO...SO₂) (3a/3b in the notation of Kuwata *et al.*), the conversion of these complexes to secondary ozonides (SOZ) (via TS-4a/TS-4b to 5a/5b), the interconversion of *endo/exo* forms (via TS-6), but with the loss of symmetry now yielding different secondary ozonides (SOZ'), and then dissociation of SOZ' to SO₃ + MVK (via TS7a/TS7b). (Again, MVK-oxide is often denoted in shorthand as MVKO.)

The energetics along these pathways were calculated for both *syn-trans*- and *syn-cis*-MVK-oxide at the CCSD(T)/CBS//B2PLYP-D3/cc-pVTZ level. The CBS extrapolation is based on calculations with Dunning's tight d supplemented correlated consistent basis sets [cc-pV(n+d)Z]⁴². A correction for higher order electronic excitation was estimated from CCSDT(Q)/6-31G* calculations for related aspects of the CH₂OO + SO₂ system. In particular, we estimate higher level corrections of 0.41, 0.80, 1.49, -0.72, and 1.23 kcal mol⁻¹ for the van der Waals minima, the transition state from the van der Waals minima to the SOZ, the SOZ, the transition state from the SOZ to SO₃ + MVK, and the products SO₃ + MVK, respectively. The calculated stationary point energies are reported in Table S5 and a schematic illustration of the reaction pathways is provided in Figure S4.

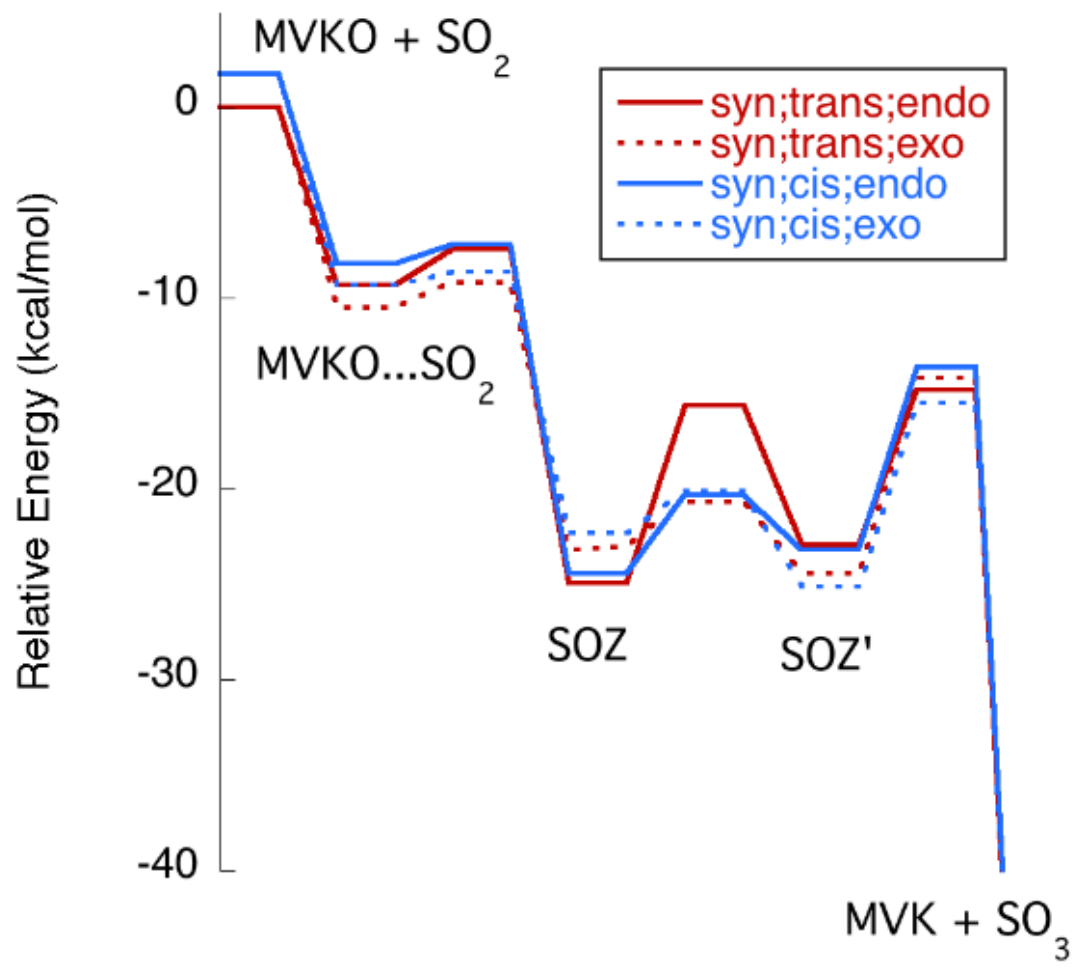


Figure S4. Schematic plot of the expected lowest energy path for the reaction of MVK-oxide (denoted MVKO here) with SO₂ (cf., Table S5). Note that the *exo/endo* labeling is based on the structures of the first two complexes. The conversion to the SOZ' actually reverses this labeling, which is not accounted for in this plot. In particular, for SOZ and SOZ' the *endo* forms are lower in energy.

Table S5. Stationary point energies (kcal mol⁻¹) for the reaction of SO₂ with *syn*-MVK-oxide.^a

Species	B2PLY P-D3 ^b		CCSD(T) ^c			E ₀ ^d	Total ^e	Total ^f	T1 ^g
	TZ	DZ	TZ	QZ	CBS	B2/TZ		+Corr	
<i>syn-trans</i> + SO ₂	0.0	0.0	0.0	0.0	0.0	0.0	0.0	0.0	0.035 0.022
<i>trans; endo^h</i>									
MVKO;st...SO ₂	-12.4	-9.4	-9.8	10.6	-11.1	1.4	-9.7	-9.3	0.027
MVKO;st ...SO ₂ = SOZ	-11.1	-7.4	-8.4	-9.3	-10.0	1.8	-8.2	-7.4	0.024
SOZ	-26.1	25.8	28.9	29.1	-29.2	2.9	-26.4	-24.9	0.017
SOZ=SOZ'	-16.5	14.7	18.5	19.0	-19.4	2.4	-17.0	-15.6	0.017
SOZ'	-24.6	24.6	27.0	27.1	-27.2	2.8	-24.4	-22.9	0.018
SOZ' = MVK + SO ₃	-12.8	11.0	14.3	15.0	-15.4	1.3	-14.1	-14.8	0.026
MVK + SO ₃	-64.3	64.2	70.3	71.3	-72.0	1.1	-70.8	-69.6	0.014 0.019
<i>trans; exo^h</i>									
MVKO;st ...SO ₂	-14.1	11.1	11.4	12.0	-12.4	1.6	-10.9	-10.5	0.027
MVKO;st ...SO ₂ = SOZ	-13.1	-9.9	10.7	11.4	-11.9	1.9	-10.0	-9.2	0.024
SOZ	-24.9	24.7	27.3	27.5	-27.6	2.8	-24.7	-23.2	0.017
SOZ=SOZ'	-21.9	21.6	24.6	24.7	-24.8	2.6	-22.2	-20.7	0.017
SOZ'	-25.6	25.6	28.4	28.6	-28.7	2.8	-25.9	-24.4	0.017
SOZ' = MVKO + SO ₃	-12.2	10.7	13.8	14.5	-14.9	1.4	-13.5	-14.2	0.026
MVKO + SO ₃	-64.3	64.2	70.3	71.3	-72.0	1.1	-70.8	-69.6	0.014
<i>syn-cis</i> + SO ₂	2.3	1.3	1.8	2.0	2.02	-0.2	1.8	-	0.037
<i>cis; endo^h</i>									
MVKO;sc ...SO ₂	-11.5	-8.8	-8.9	-9.5	-10.0	1.4	-8.6	-8.2	0.028
MVKO;sc ...SO ₂ = SOZ	-10.9	-8.0	-8.4	-9.1	-9.6	1.6	-8.0	-7.2	0.024
SOZ	-25.6	25.7	28.5	28.6	-28.6	2.7	-25.9	-24.4	0.017
SOZ=SOZ'	-21.4	20.9	24.1	24.2	-24.2	2.5	-21.8	-20.3	0.017
SOZ'	-24.7	24.4	27.0	27.3	-27.4	2.6	-24.7	-23.2	0.017
SOZ' = MVKO + SO ₃	-11.4	10.0	13.1	13.7	-14.2	1.3	-12.9	-13.6	0.026
MVKO + SO ₃	-64.0	64.5	70.0	70.8	-71.4	1.0	-70.4	-69.2	0.014
<i>cis; exo^h</i>									
MVKO;sc ...SO ₂	-12.6	10.0	10.1	10.7	-11.2	1.4	-9.7	-9.3	0.028
MVKO;sc ...SO ₂ = SOZ	-12.2	-9.3	-9.9	10.6	-11.1	1.7	-9.4	-8.6	0.025
SOZ	-23.9	24.0	26.4	26.5	-26.5	2.7	-23.8	-22.3	0.017
SOZ=SOZ'	-21.3	21.2	24.1	24.1	-24.2	2.5	-21.6	-20.1	0.017

SOZ'	-26.2	26.1	29.0	29.2	-29.3	2.7	-26.6	-25.1	0.017
SOZ' = MVKO + SO ₃	-13.6	12.3	15.2	15.8	-16.2	1.4	-14.8	-15.5	0.026
MVKO + SO ₃	-64.0	64.5	70.0	70.8	-71.4	1.0	-70.4	-69.2	0.014

^aAll energies are relative to *syn-trans*-MVK-oxide + SO₂.

^bB2PLYP-D3/cc-pVTZ electronic energies.

^cCCSD(T) electronic energies for the cc-pVDZ, cc-pVTZ, cc-pVQZ and an estimate of the CBS limit.

^dB2PLYP-D3/cc-pVTZ vibrational zero-point energy.

^eThe total energy taken as the sum of the CCSD(T)/CBS//B2PLYP-D3/cc-pVTZ energy and the B2PLYP-D3/cc-pVTZ zero-point energy.

^fThe total energy corrected by estimated T(Q) corrections obtained from CCSDT(Q)/6-31G* calculations for related geometries in the CH₂OO + SO₂ system.

^gThe T1 diagnostic. ^hThe pathways are labeled as *exo/endo* according to the initial van der Waals complex (MVKO...SO₂) and SOZ. The transition from SOZ to SOZ' converts between the *endo* and *exo* forms.

Species	B2PLYP-D3 ^b		CCSD(T) ^c			E ₀ ^d	Total ^e	Total ^f	T1 ^g
	TZ	DZ	TZ	QZ	CBS	B2/TZ		+Corr	
<i>syn,trans = syn,cis;</i> <i>endo^h</i>									
MVKO...SO ₂	-5.6	-3.9	-3.6	-4.4	-4.9	1.0	-3.8	-3.4	0.024
MVKO...SO ₂ ; geom. B	-4.5	-2.6	-2.7	-3.4	-3.9	0.7	-3.2	-2.8	0.024
SOZ	-23.6	23.4	26.5	26.7	26.8	2.5	-24.3	-22.8	0.017
SOZ; geom. B	-23.9	23.8	26.7	27.0	27.1	2.5	-24.6	-23.1	0.017
<i>syn,trans = syn,cis;</i> <i>exo^h</i>									
MVKO...SO ₂	-7.4	-5.8	-5.6	-6.3	-6.7	1.1	-5.6	-5.2	0.024
SOZ	-23.1	23.0	25.5	-25.7	-25.8	2.6	-23.2	-21.7	0.018
SOZ; geom. B	-23.2	23.2	25.7	-25.8	-25.9	2.6	-23.3	-21.9	0.017

^aAll energies are relative to *syn-trans*-MVK-oxide (denoted MVKO) + SO₂.

^bB2PLYP-D3/cc-pVTZ electronic energies.

^cCCSD(T) electronic energies for the cc-pVDZ, cc-pVTZ, cc-pVQZ and an estimate of the CBS limit.

^dB2PLYP-D3/cc-pVTZ vibrational zero-point energy.

^eThe total energy taken as the sum of the CCSD(T)/CBS//B2PLYP-D3/cc-pVTZ energy and the B2PLYP-D3/cc-pVTZ zero-point energy.

^fThe total energy corrected by estimated T(Q) corrections obtained from CCSDT(Q)/6-31G* calculations for related geometries in the CH₂OO + SO₂ system.

^gThe T1 diagnostic.

^hThe pathways are labeled as *exo/endo* according to the initial van der Waals complex (MVKO...SO₂) and SOZ. The transition from SOZ to SOZ' converts between the *endo* and *exo* forms.

For the $\text{SO}_2 + \text{CH}_2\text{OO}$ system, there has been some debate as to whether or not there is a saddle point for the formation of the long-range van der Waals complex. We examined this question herein via calculations along the minimum energy path determined at the $\omega\text{B97XD/cc-pVTZ}$ level. Interestingly, calculations at the $\text{CCSD(T)/CBS//}\omega\text{B97XD/cc-pVTZ}$ level show no saddle point, even with the inclusion of a CCSDT(Q)/6-31G^* correction. This finding strongly suggests that there is no saddle point for this reaction.

Notably, the resonance stabilization in MVK-oxide changes the picture for reaction with SO_2 (Figure S5). In particular, we now find a saddle point with an imaginary frequency in the $100\text{-}200\text{ cm}^{-1}$ range for each of the $\omega\text{B97XD/6-31+G}^*$, $\omega\text{B97XD/cc-pVTZ}$, and B2PLYP-D3/cc-pVTZ methods for both *syn-trans* and *syn-cis* isomers and for *endo* and *exo* pathways (Table S5). The resonance stabilization also decreases the depth of the SOZ and SOZ' wells relative to reactants from $\sim 35\text{ kcal mol}^{-1}$ for CH_2OO to $\sim 24\text{ kcal mol}^{-1}$ for MVK-oxide.

We used direct sampling *ab initio* variable reaction coordinate transition state theory (VRC-TST) to explore the rate coefficient for forming the van der Waals complex. For this VRC-TST analysis, we considered four separate electronic structure methods (MP2/cc-pVDZ , MP2/cc-pVTZ , $\omega\text{B97XD/6-31+G}^*$, and $\omega\text{B97XD/cc-pVTZ}$) finding only modest variation ($\sim 20\%$ near room temperature) in the predicted long-range capture rate coefficient, as illustrated in Figure S6. The reaction coordinate was presumed to be defined by the separation between the two centers-of-mass of the two fragments and the separation was constrained to 4.2 \AA and larger. A dynamical correction factor of 0.85, based on reference comparisons of trajectories and TST⁴³ is included.

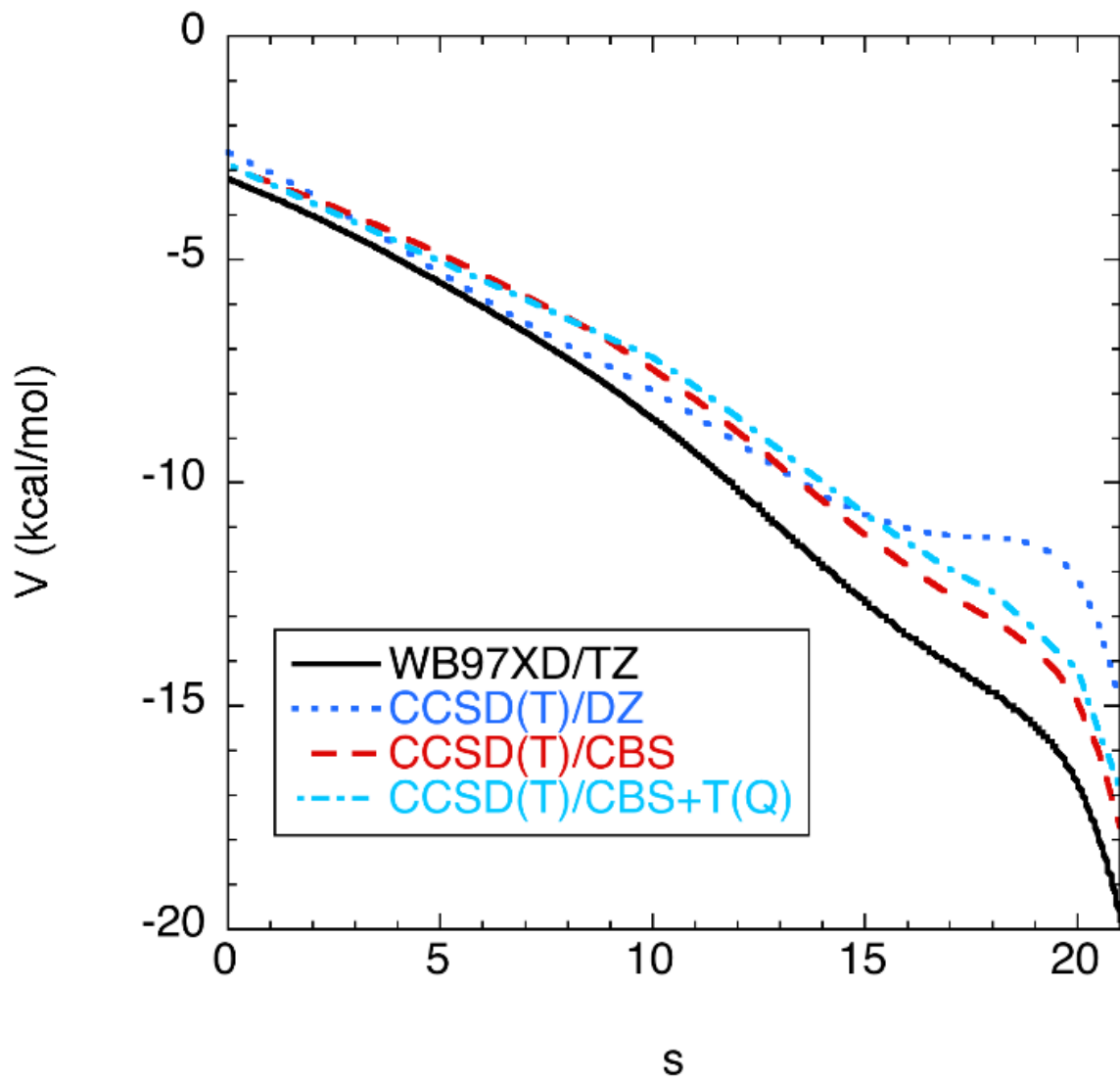


Figure S5. Plot of the minimum energy path (MEP) potential for the addition of SO₂ to *syn-trans*-MVK-oxide evaluated at various levels, all along the ω B97XD/cc-pVTZ minimum energy potential (MEP).

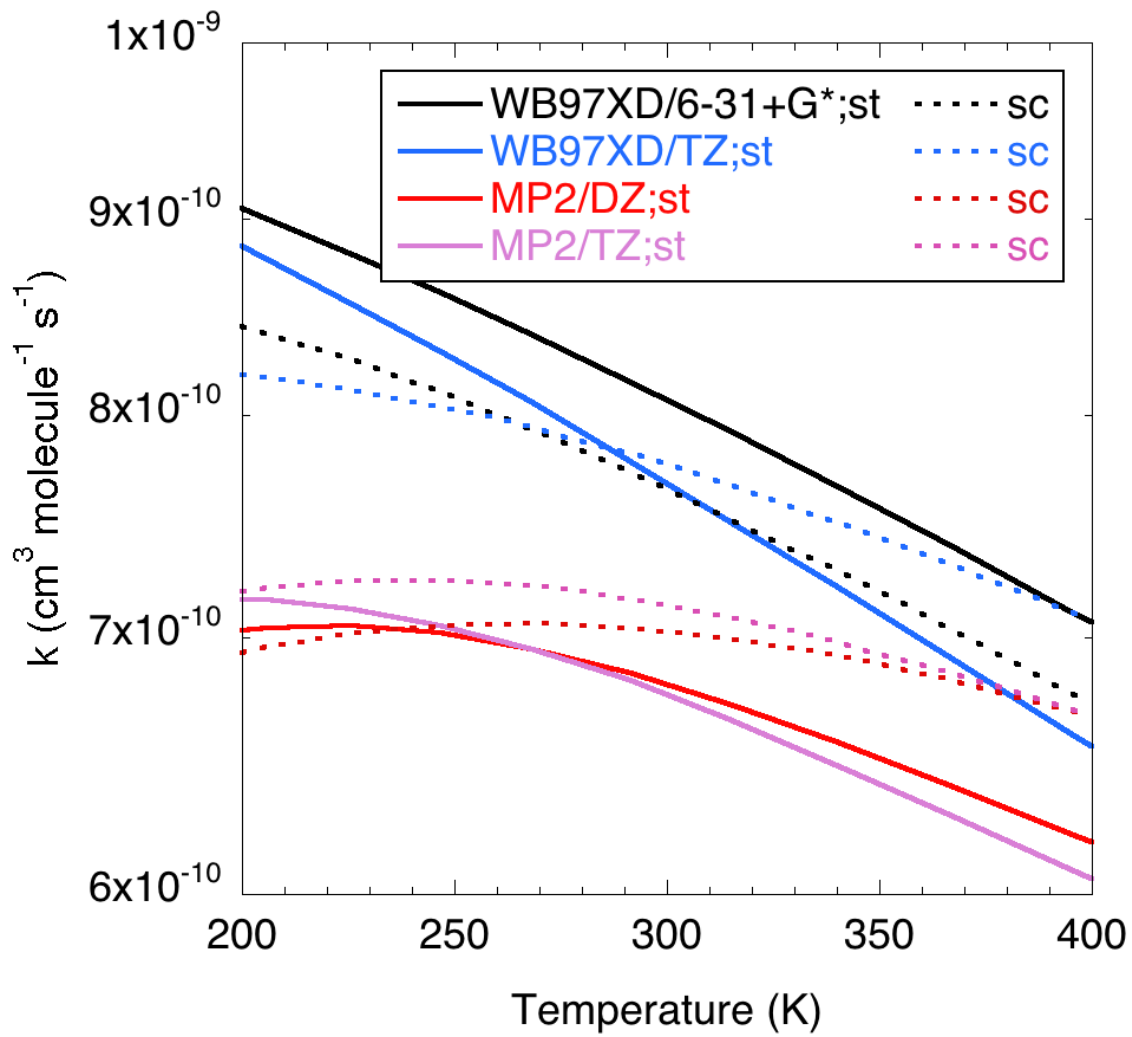
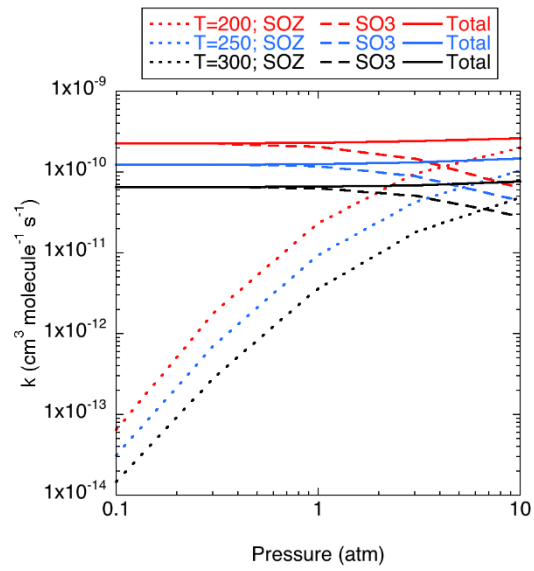


Figure S6. Plot of the VRC-TST predicted rate coefficient for the high-pressure addition of SO₂ to *syn-trans* (st) and *syn-cis* (sc) MVK-oxide evaluated with four different *ab initio* methods.

(a)



(b)

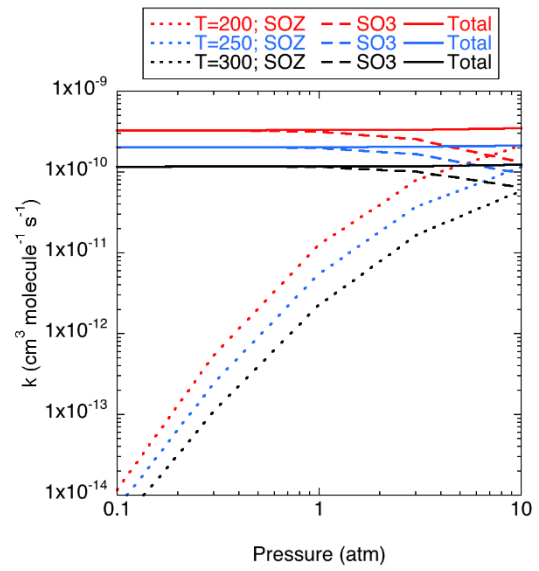


Figure S7. The predicted temperature- and pressure-dependencies of the total rate coefficient, the rate coefficient to form any of the SOZ, and the rate coefficient to form SO₃ + MVK for the reaction of (a) *syn-trans*-MVK-oxide with SO₂ and (b) *syn-cis*-MVK-oxide with SO₂.

The pressure-dependence of branching between stabilization and SO₃ + MVK formation was explored through an *ab initio* transition state theory-based master equation (AITSTME) model for the overall kinetic process. This master equation model employs standard exponential down energy transfer probabilities, with a temperature-dependent expression for the average downwards energy transferred given by $\langle \Delta E_{\text{down}} \rangle = 400 (T/298)^{0.85} \text{ cm}^{-1}$ and a Lennard-Jones collision rate appropriate for collision with N₂. As part of this analysis we presume rapid equilibration of the *endo* and *exo* forms of both the MVKO;st ...SO₂ and MVKO;sc ...SO₂ van der Waals complexes. The entrance channel flux is obtained from the MP2/cc-pVTZ VRC-TST calculations, while the flux for the other channels are obtained from the T(Q) corrected CCSD(T)/CBS//B2PLYP-D3/cc-pVTZ analysis employing rigid-rotor harmonic oscillator (RRHO) treatments for all but the CH₃ rotors, which are treated as one-dimensional hindered rotors.

The AITSTME predictions for the SO₂ + MVK-oxide rate coefficients are illustrated in Figures S7 (a) and (b) for the *syn,trans*- and *syn,cis*- forms of MVK-oxide, respectively. As noted in the main text, the total rate coefficient is predicted to be effectively pressure-independent, with no back reaction from the SOZ to the reactants. However, there is predicted to be a fairly strong temperature-dependence due to the effect of the TS connecting the van der Waals complexes and the SOZ. The total rate coefficients for the *syn,trans*- and *syn,cis*- forms are well reproduced by the expressions $2.3 \times 10^9 T^{-7.28} \exp(-1031/T)$ and $2.5 \times 10^{10} T^{-7.50} \exp(-1202/T) \text{ cm}^3 \text{ s}^{-1}$ for temperatures ranging from 200 to 400 K. At 300 K the *syn,trans*- and *syn,cis*- rates coefficients are predicted to be 6.5×10^{-11} and $1.2 \times 10^{-10} \text{ cm}^3 \text{ s}^{-1}$, respectively.

The total rate coefficient predicted for the *syn,trans* isomer is a factor of 1.7 larger than the value observed experimentally for the thermal average ($3.9 \times 10^{-11} \text{ cm}^3 \text{ s}^{-1}$). This modest overprediction may indicate either the need for a variational treatment of

the TS from the van der Waals complex to SOZ, or shortcomings in the electronic energies of that saddle point. The former may be quite significant because the submerged nature of the saddle point implies that the variational deviation from the saddle point can be quite significant even at low temperature. Furthermore, this TS effectively corresponds to that for an addition process, which commonly have significant variational effects. Meanwhile, a simple increase by 0.5 kcal mol⁻¹ for each of the saddle point energies (roughly the expected uncertainty) for the TSs connecting the van der Waals complexes to the SOZ reduces the predicted *syn,trans* rate coefficient to 4.6×10^{11} cm³ s⁻¹ at room temperature and 1 atm. Further explorations of the reason for this modest overprediction are left for future work.

Both the decreased stability of the SOZ, and the additional vibrational degrees of freedom decreases the possibility for stabilization prior to decomposition to SO₃. Nevertheless, for pressures below 1 atm the branching to stabilized SOZ is predicted to be negligible, while by 10 atm the stabilization amounts to ~50% of the overall reaction. Ambiguity in the energy transfer parameters suggests that even at 1 atm there may be some stabilization of the SOZ.

3.3 MVK-oxide + formic acid

Ionization energy calculations of the reaction product

A variety of theoretical calculations were performed to complement the experimental observations of the ionization of the MVK-oxide + formic acid reaction product. These analyses included density functional theory (DFT) based conformational analyses of C₅H₈O₄, CCSD(T) based calculations of the vertical ionization energies for the different conformers, DFT evaluations of the relaxation energies for the vertically excited ions (and thus adiabatic ionization energies), a DFT mapping of an ion

dissociation path, and a CCSD(T) based calculation of the daughter appearance energy for the ground conformer.

In analogy with calculations for the $\text{CH}_2\text{OO} + \text{formic acid}$ reaction, the reaction product was presumed to be 2-hydroperoxybut-3-en-2-yl formate ($\text{CH}_2\text{CHC}(\text{CH}_3)\text{OCHO}$, HPBF), as shown in Scheme 5 of the main text ⁴⁴. The low energy conformers of this species were determined through random sampling of 200 sets of the 6 torsional angles followed by $\omega\text{B97XD/6-31+G}^*$ ⁴⁵ geometry optimizations for each starting geometry. This optimization was performed in two steps, with first just the torsional angles optimized, and then the full set of internal coordinates optimized. The resulting set of 9 conformers that had energies within $3.5 \text{ kcal mol}^{-1}$ of the ground state conformer were then reoptimized at the B2PLYP-D3/cc-pVTZ level ⁴⁶. The vertical ionization energies for the set of 9 conformers with energies within 3 kcal mol^{-1} of the ground state were evaluated as the sum: $\text{CCSD(T)-F12b/cc-pVDZ-F12} + \text{MP2-F12/cc-pVTZ-F12} - \text{MP2-F12/cc-pVDZ-F12}$, which is meant to approximate the $\text{CCSD(T)-F12b/cc-pVTZ-F12//B2PLYP-D3/cc-pVTZ}$ level ⁴⁷. These values are reported in Table S6. For the ground conformer, the appearance energy for the daughter ion (obtained by simply pulling off the HO_2 and then allowing the $\text{C}_5\text{H}_7\text{O}_2^+$ structure to relax) is predicted to be 9.82 eV using the methodology above to approximate the $\text{CCSD(T)-F12b/cc-pVTZ-F12//B2PLYP-D3/cc-pVTZ}$ level of theory.

The relaxation of the HPBF^+ ions was explored for each of the 9 lowest neutral conformers through B2PLYP-D3/cc-pVTZ optimizations of the ion initiated at the neutral geometry. In each case the calculated relaxation energy exceeds 29 kcal mol^{-1} and the relaxation involves substantial geometrical transformations. For the ground state, the relaxation energy is 33 kcal mol^{-1} . For such large relaxations, adiabatic ionization will have very poor Franck-Condon overlaps resulting in low experimental signals at the

Table S6. Energies of relevance to the ionization of HPBF.

HPBF conformer	Conformer energy (kcal mol ⁻¹) ^a	Vertical excitation (eV) ^b	Relaxation energy (kcal mol ⁻¹)
1	0.0	10.41 (10.70)	33.1
2	0.6	10.37 (10.80)	31.5
3	1.0	10.31 (10.47)	29.6
4	1.7	10.48 (10.71)	36.1
5	2.2	10.13 (10.39)	54.5
6	3.	10.10	35.9
7	3.1	10.52	42.6
8	3.1	10.76	48.4
9	3.2	10.14	36.8

^aB2PLYP-D3/cc-pVTZ calculated zero-point corrected energy of the given conformer relative to the ground conformer.

^bB2PLYP-D3/cc-pVTZ and approximate CCSD(T)-F12b/cc-pVTZ-F12 vertical electronic excitation energies for the given conformer. The latter energies are given in parentheses, and were obtained from the sum: CCSD(T)-F12b/cc-pVDZ-F12 + MP2-F12/cc-pVTZ-F12 – MP2-F12/cc-pVDZ-F12, all evaluated at the B2PLYP-D3/cc-pVTZ geometries.

^cB2PLYP-D3/cc-pVTZ calculated relaxation energies for the parent cation (from the vertically excited geometry to the optimized geometry).

adiabatic threshold. Instead, the ionization process is likely to be dominated by nearly vertical transitions.

Notably, the vertical ionization states have energies that substantially exceed the threshold for C-O fission to produce $\text{HO}_2 + \text{CH}_2\text{CHC}(\text{CH}_3)\text{OCHO}^+$. A schematic plot of the minimum energy path for dissociation of one conformer of the HPBF^+ ions is provided in Figure S8. This minimum energy path was mapped through constrained optimizations (with the CO distance fixed) at the $\omega\text{B97XD}/6\text{-}31\text{+G}^*$ level. For this conformer, the daughter ion is 16 kcal mol^{-1} below the vertical excitation energy. Furthermore, CO fission from the adiabatic minimum requires only 13 kcal mol^{-1} , suggesting that the dissociation of that parent ion should be rapid. At the B2PLYP-D3/cc-pVTZ level the HPBF^+ vertical excitation states for the 9 lowest conformers range from 17 to 33 kcal mol^{-1} higher than the ground state of $\text{HO}_2 + \text{CH}_2\text{CHC}(\text{CH}_3)\text{OCHO}^+$. Thus, it is expected that the ionization process will directly produce $\text{CH}_2\text{CHC}(\text{CH}_3)\text{OCHO}^+$ (HO_2 -loss) daughter ions, as is observed experimentally (Figure 5, main text). The correlation between the energy of the observed rise in the daughter ion signal and the calculated vertical ionization energies further suggests that the ionization process primarily involves nearly vertical transitions.

Kinetics calculations of MVK-oxide + formic acid

For the reaction of MVK-oxide with formic acid, it is interesting to ponder why the experimentally observed rate coefficient is so large and yet not quite as large as what one would predict on the basis of long-range capture theory. Understanding this behavior has important ramifications for the expected temperature- and pressure-dependencies of the rate coefficient. One possibility is that this reduction from the long-range capture rate is indicative of the effect of entropic loss in the transition state for

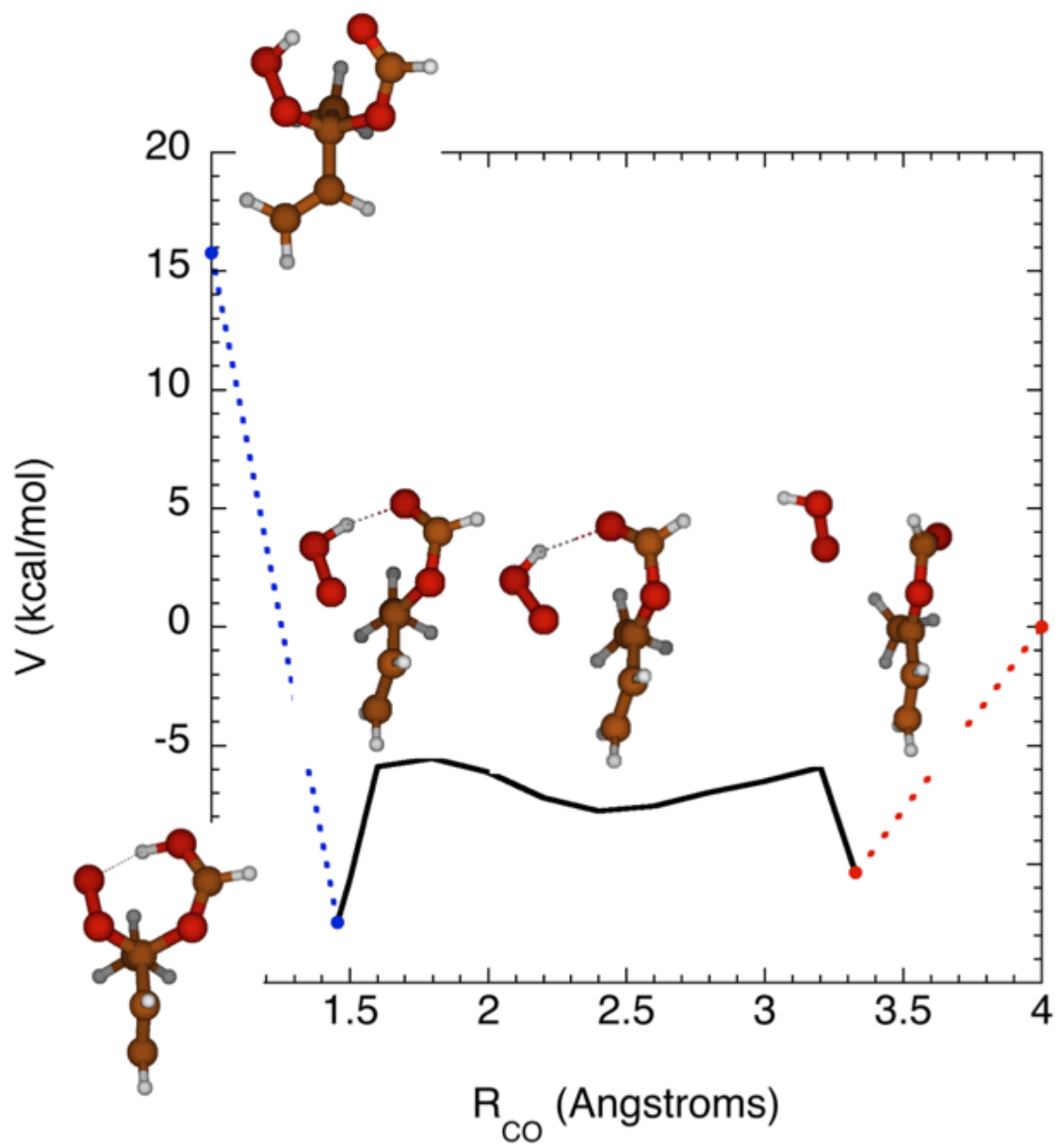


Figure S8. Schematic plot of the process from vertical excitation of HPBF^+ through to CO fission to product $\text{HO}_2 + \text{CH}_2\text{CHC}(\text{CH}_3)\text{OCHO}^+$.

formation of the initial chemically bound complex. In this case, one would expect the rate coefficient to be nearly independent of temperature and pressure. Alternatively, the reduction may arise from redissociation of the initial formed complex back to reactants. This would culminate in significant temperature- and pressure-dependencies. To interrogate these possibilities, we must examine in detail both the overall reaction pathway as well as the minimum energy path potential for the initial formation of the complex.

There are a variety of possible reaction channels for the reaction of formic acid with CIs, as discussed, for example, in a recent study by Vereecken ⁴⁴, where the reaction of CH₂OO with formic acid was considered in detail. Vereecken found that the primary reaction pathway involves H-transfer from the acid to the CI in concert with CO bond formation, followed by stabilization of the resulting functionalized hydroperoxide, hydroperoxymethyl formate (HPMF). Notably, even though there are exothermic exit channels arising from OO bond fission of the complex, stabilization was predicted to dominate over bimolecular product formation. Addition over the C=O bond to form a cyclic ozonide was found to have a submerged barrier, however, the TS for this pathway was very tight, and the corresponding addition rate was predicted to be quite small ($\sim 10^{-13} \text{ cm}^3 \text{ s}^{-1}$). By contrast, *ab initio* variational TST calculations predicted the pathway to form the functionalized hydroperoxide has a rate coefficient of $1.0 \times 10^{-10} \text{ cm}^3 \text{ s}^{-1}$ - in excellent accord with the experimentally observed value of $1.1 \times 10^{-10} \text{ cm}^3 \text{ s}^{-1}$ ²⁵.

For the reaction of MVK-oxide with formic acid we restricted our attention to the analogue of Vereecken's predicted primary reaction pathway for CH₂OO based on the previous work described above. We find that, notably, the resonance stabilization in MVK-oxide leads to a significant destabilization of the functionalized hydroperoxide pathway relative to reactants. A schematic illustration of the CCSD(T)-F12/cc-pVTZ-

F12//B2PLYPD3/cc-pVTZ predicted reaction path energies is shown in the main text (Figure 6) and the corresponding energies are provided in Table S7.

The initial approach along the reaction co-ordinate leads to a planar van der Waals complex, which is a minimum at some levels of theory and a saddle point at others (see Table S7). Proceeding on from there leads to a clear long-range minimum followed by a well-defined (imaginary frequency of 598 cm^{-1}), but strongly submerged, saddle point that separates the global long-range minimum from the functionalized hydroperoxide product, HPBF. As discussed in the main text, HPBF is much more weakly bound than in its CH_2OO analogue (30 vs. 44 kcal mol^{-1} ⁴⁴), due to the additional resonance stabilization present in MVK-oxide. Correspondingly, the OO fission pathway of HPBF to produce OH + an alkoxy radical is now significantly endothermic relative to initial reactants. Nevertheless, as discussed below, the overall kinetics is predicted to be quite similar, with the reaction dominated by direct addition to form the functionalized hydroperoxide species.

There are now three distinct regions of the potential energy surface that may provide the kinetic bottleneck for the addition process, as illustrated in Figure S9. The longer-range portion of the MEP (labelled A in Figure S9) was derived from the minimum center-of-mass constrained sampling of random orientations of the two reactants. The two shorter ranged portions (B and C in Figure S9) of the MEPs were derived from reaction path following initiated at the larger of the separations on that portion of the curve. At low temperatures, the longest ranged portion (A in Figure S9) of the curve provides the greatest bottleneck, while at higher temperatures the saddle point region (C in Figure S9), which occurs at a CO separation of 2.27 \AA , should provide the dominant bottleneck due to its lower entropy. However, the deeply submerged nature of this saddle point (i.e., with a ZPE corrected energy of $-13.5\text{ kcal mol}^{-1}$) suggests that this

Table S7. Reaction path energies for the reaction of *syn-trans*-MVK-oxide with formic acid.^a

Species	R _{CO} (Å)	B2PLYP-D3 ^b TZ	E0 ^c B2/TZ	CCSD(T)-F12 ^d cc-pVTZ-F12	Total ^e	T1 ^f
<i>syn-trans</i> + OCHOH	-	0.0	0.0	0.0	0.0	-
<i>syn-trans</i> ...OCHOH (long-range C _s)	5.68	-11.7	0.9	-10.8	-9.9	0.027
<i>syn-trans</i> ...OCHOH (short-range C ₁)	2.89	-17.0	1.1	-15.8	-14.7	0.024
<i>syn-trans</i> ...OCHOH= vinyl hydroperoxideHPBF	2.26	-14.5	-0.9	-12.6	-13.5	0.020
HPBF	1.48	-30.8	2.8	-33.0	-30.3	0.015
alkoxy + OH	-	17.7	-2.7	16.6	13.4	0.019

^a All energies are in kcal mol⁻¹ relative to *syn-trans*-MVK-oxide + formic acid.

^b Stationary point electronic energy from B2PLYP-D3//cc-pVTZ calculations.

^c Zero-point energy (ZPE) from B2PLYP-D3//cc-pVTZ calculations.

^d CCSD(T)-F12b/cc-pVTZ-F12 B2PLYP-D3//cc-pVTZ electronic energies.

^e Sum of CCSD(T)-F12b/cc-pVTZ-F12// B2PLYP-D3//cc-pVTZ energies and B2PLYP-D3//cc-pVTZ ZPEs.

^f T1 diagnostic for the CCSD(T)-F12b/cc-pVTZ-F12// B2PLYP-D3//cc-pVTZ calculations.

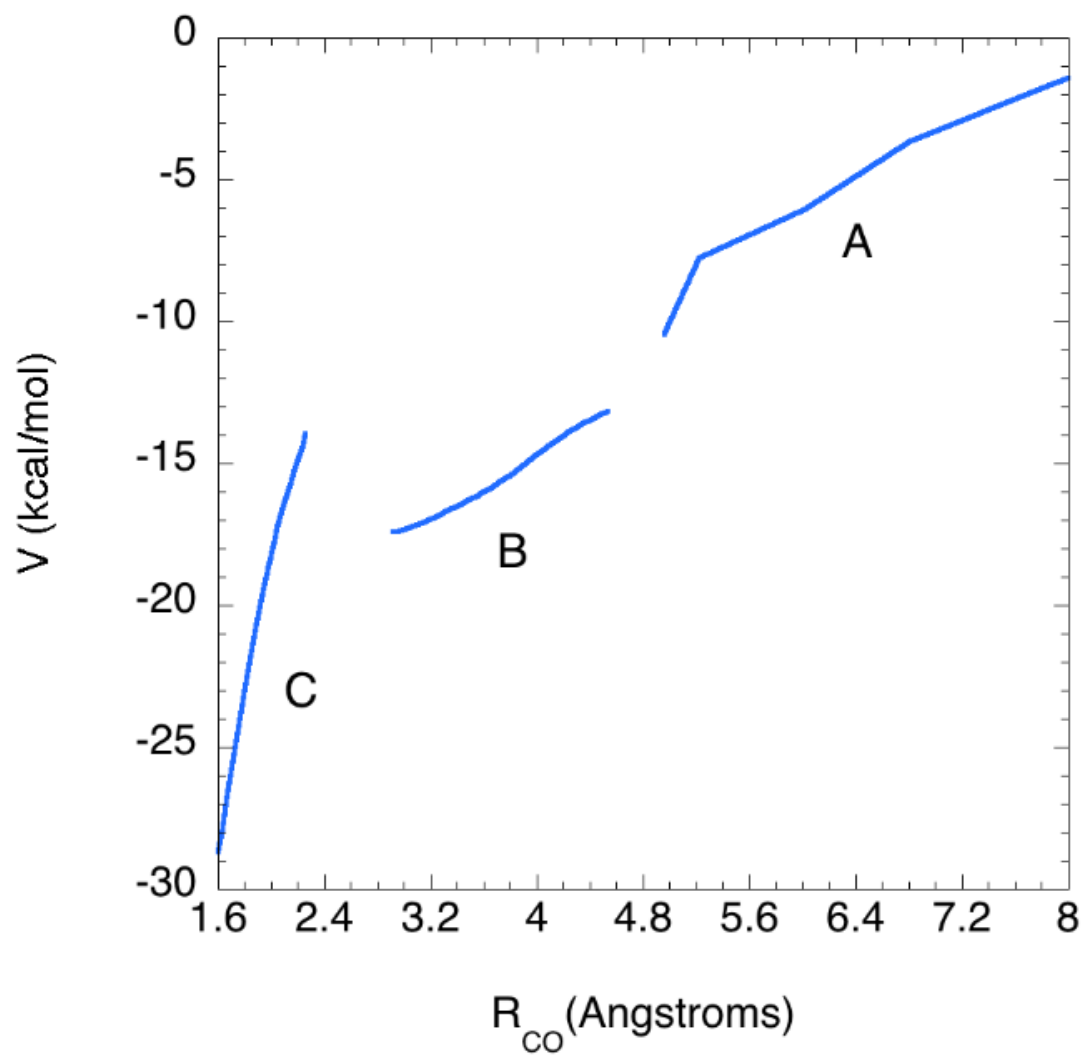


Figure S9. The ω B97XD/6-31+G* calculated minimum energy path (MEP) for the addition of formic acid to the syn-trans form of MVK-oxide. The three disjoint curves correspond to physically distinct aspects of the addition process.

bottleneck may only become important at quite high temperature. The intermediate regime (B in Figure S9) may also provide an important bottleneck at intermediate temperatures.

We have used direct sampling *ab initio* variable reaction coordinate transition state theory to explore the effect of the long-range bottleneck on the addition kinetics. For this VRC-TST analysis, we considered four separate electronic structure methods (MP2/cc-pVDZ, MP2/cc-pVTZ, ω B97XD/6-31+G*, and ω B97XD/cc-pVTZ) finding only modest variation (~10% near room temperature) in the predicted long-range capture rate coefficient, as illustrated in Figure S10. For these calculations, the reaction coordinate was presumed to be defined by the separation between the two centers-of-mass of the two fragments and the separation was constrained to 4.2 Å and larger. A dynamical correction factor of 0.85, based on reference comparisons of trajectories and TST⁴³, is also included.

Notably, the predicted room-temperature long-range capture rate coefficient of $\sim 8 \times 10^{-10} \text{ cm}^3 \text{ s}^{-1}$ is considerably greater than what might be expected on the basis of dipole-dipole capture theory. This is likely due to additional contributions from dispersion interactions. Furthermore, this value is about 3 times larger than that observed experimentally ($(3.0 \pm 0.1) \times 10^{-10} \text{ cm}^3 \text{ s}^{-1}$). Related calculations for addition to *syn-cis*-MVK-oxide yield essentially identical predictions for the capture rate (i.e., differing by 10% or less).

From our experience, we would expect uncertainties in the VRC-TST predictions to be on the order of 10-20%. Thus, the apparent overprediction of the rate coefficient suggests that some other bottleneck is operative. The effect of the two inner transition state regions (B and C in Figure S9) were included here through microcanonical (E-resolved) variational TST implementing ω B97XD/6-31+G* based evaluations of the

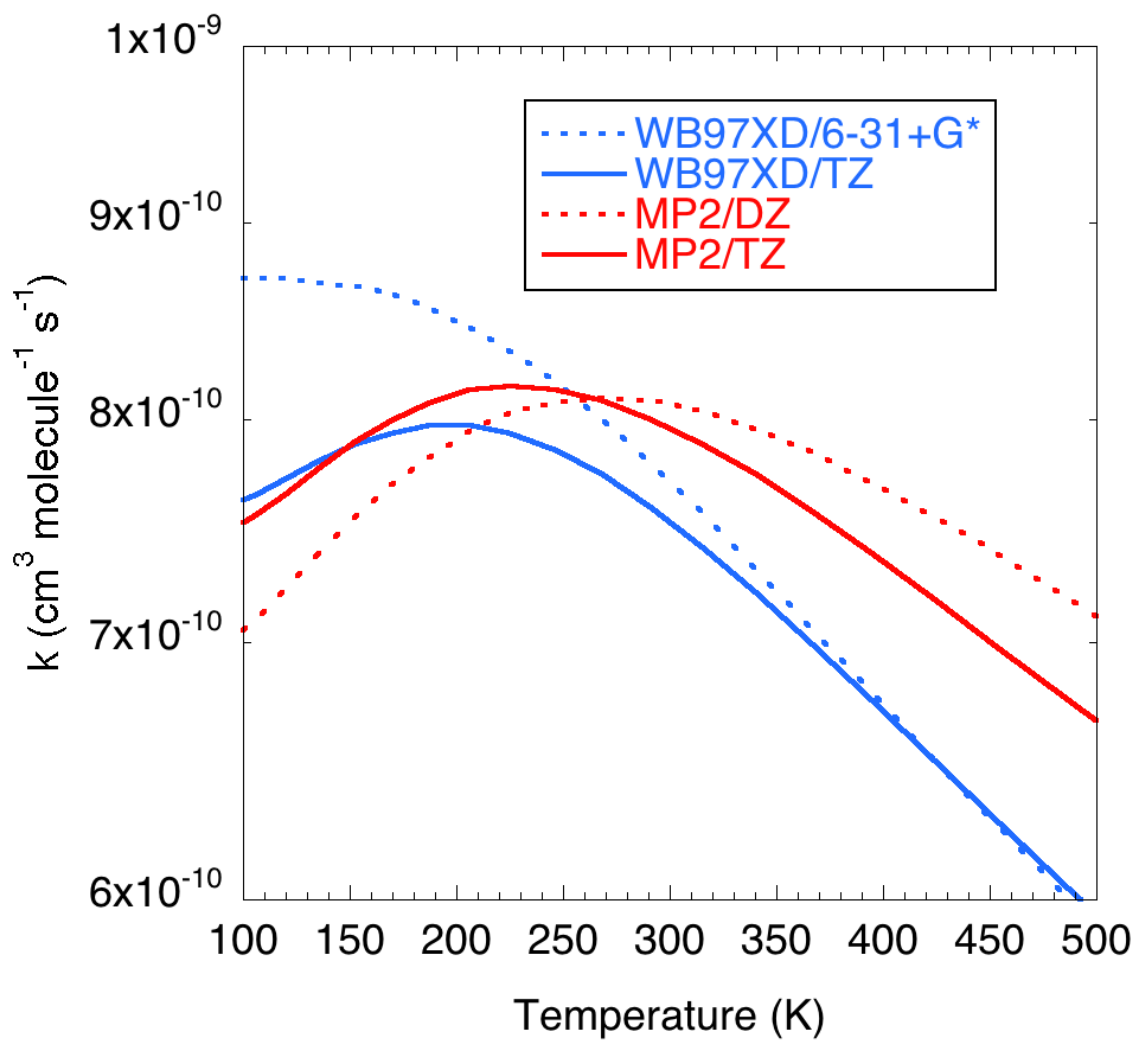


Figure S10. Temperature-dependence of the predicted VRC-TST rate coefficients for capture to form the van der Waals complex, calculated using four different levels of theory.

minimum energy path properties coupled with CCSD(T)-F12/cc-pVTZ-F12 evaluation of the energy for the starting point on the path. For simplicity, the vibrational modes were all treated as harmonic oscillators, aside from the CH₃ rotor, which was treated as a 1-dimensional hindered rotor in both the reactants and the transition. The inclusion of such variational TST treatments for the two separate inner bottlenecks leads to only a modest reduction in the predicted formation rate coefficient for HPBF. For example, at 300 K the predicted recombination rate coefficient at 10 bar is now $5.0 \times 10^{-10} \text{ cm}^3 \text{ s}^{-1}$.

Although, there is considerably greater uncertainty in our estimate of the effect of these inner transition state regions, it still appears that there must be another bottleneck to HPBF formation. One possibility is that there is substantial back dissociation of the initially formed HPBF. To explore this issue, we have implemented an *ab initio* transition state theory-based master equation model for the overall kinetic process. This master equation model employs standard exponential down energy transfer probabilities with a temperature dependent expression for the average downwards energy transferred given by $\langle \Delta E_{\text{down}} \rangle = 300 (T/298)^{0.85} \text{ cm}^{-1}$, and Lennard-Jones collision rate appropriate for N₂. For HPBF, we have optimized 100 randomly sampled sets of torsional angles to estimate the lowest torsional conformer, and then performed one-dimensional mappings of the 6 hindered rotor modes. The resultant master equation-based predictions for the temperature- and pressure-dependencies of the recombination rate coefficient are shown in Figure 7 of the main text and the results discussed therein.

3.4 MVK-oxide + water monomer

Ab initio calculations, computational kinetics and mechanistic investigations

For the reaction of MVK-oxide with water, the present experimental analysis is only able to obtain an upper bound to the rate coefficient. Thus, it is interesting to

consider what theory predicts for the actual rate coefficient for this reaction. This reaction has been the subject of previous theoretical studies by Anglada and coworkers^{27, 48, 49}, Kuwata *et al.*⁵⁰ and Vereecken *et al.*²⁸ (based on the results of Anglada and Solé²⁷). The recent study of Anglada and Solé²⁷ was based on CCSD(T)/aug-cc-pVTZ//B3LYP/6-311++G(2df,2p) energetic analyses, while that of Kuwata *et al.* employed MCG3///QCISD/6-31G* energies. A recent survey by Vereecken *et al.*²⁸ suggested that the rates predicted by Anglada and Solé should be reduced by a factor of 7.1 on the basis of comparisons of related calculations for CH₃CHOO + H₂O. This rate reduction was correlated with an increase in the barrier height by 1.16 kcal mol⁻¹, which apparently was needed due to the lack of post-CCSD(T) calculations.

Here, we proceed beyond these earlier works with higher level calculations of the energies. We also explore the role of one additional form of H₂O-catalysis, where the water molecule is simply a spectator molecule that lowers the isomerization barriers relative to isolated MVK-oxide + H₂O. For example, this spectator catalysis can enhance the rate of the internal H-transfer from MVK-oxide to form a vinyl hydroperoxide-type species. It also catalyzes the transformation from the *cis* to *trans* forms of MVK-oxide.

The present *ab initio* evaluations begin with a B2PLYP-D3/cc-pVTZ density functional-based analysis of the rovibrational properties of the stationary points. Our prior kinetic analyses of CI isomerization reactions have indicated good performance for this double-hybrid functional. At these geometries, we determine CCSD(T)/CBS limit energies from CCSD(T)-F12 calculations for the cc-pVTZ-F12 and cc-pVQZ-F12 basis sets. We also evaluate CCSDT(Q)/6-31G* corrections for high order excitations, core-valence corrections from the CBS limit of CCSD(T) for the cc-pcVTZ and cc-pcVQZ bases, and anharmonicity corrections evaluated with B2PLYP-D3/cc-pVTZ based

vibrational perturbation theory. For validation purposes, we also perform a closely related analysis for the reaction of CH₂OO with H₂O.

An initial study of CH₂OO + H₂O provides some validation for the present approach for MVK-oxide + H₂O. Various components of the stationary point energies for CH₂OO + H₂O are provided in Table S8. The 0.1 kcal mol⁻¹ difference in the T(Q) correction for the 6-31G* and cc-pVDZ bases provides some indication of the basis set dependence of this correction. For the MVK-oxide + H₂O reaction our computational resources constrain us to the 6-31G* basis set. Notably, the differences between the deviations in the B2PLYP-D3 and CCSD(T) calculated ZPEs decrease quite substantially with increasing basis set. Nevertheless, at the complete basis set (CBS) limit the two values likely still differ by about 0.2 kcal mol⁻¹ for the TS. This difference may simply be a result of the significant multireference effects in CH₂OO, which can yield different errors in the B2PLYP-D3 and CCSD(T) estimates. It is not clear *a priori* which is correct. Overall, it seems reasonable to expect high accuracy for the present scheme, with overall uncertainties of ~ 0.3 kcal mol⁻¹ ⁵¹.

Long *et al.* ⁵² also examined the CH₂OO + H₂O reaction in detail, finding similar results to the present work, but with 0.4 kcal mol⁻¹ higher saddle point energies. The higher barriers predicted by Long *et al.* appear to arise primarily from their use of a scaling-based relation to treat the anharmonic ZPE, in contrast with the explicit spectroscopic perturbation theory evaluations performed herein. The method used by Long *et al.* limits the ZPE change from reactants to TS to fairly small numbers due to the cancellation in TS and reactant effects. Additionally, the present analysis also employs a somewhat more direct treatment of the higher order excitations and improved treatment of other aspects such as the geometries and frequencies.

Table S8. Stationary Point Energies (kcal mol⁻¹) for CH₂OO + H₂O.^a

Species	CCSD(T)-F12b				T(Q) Corr.	Core Val.	ZPE Harm.	ZPE Anh.	Total ^b	
	DZ- F12	TZ- F12	QZ- F12	6- 31G*	DZ					
CH ₂ OO + H ₂ O	0.0	0.0	0.0	0.0	0.00	0.0	0.0	0.0	0.0	
CH ₂ OO...H ₂ O	-8.34	-8.41	-8.40	0.26	0.14	0.00	2.28	2.61,2 .39	-0.14	-6.11 (-6.27)
TS; tau a	-0.03	-0.18	-0.22	0.81	0.72	0.25	2.78	3.35,3 .14	-0.39	3.12 (3.48)
TS; tau b	0.92	0.76	0.73	0.82	0.73	0.25	2.70	3.23,3 .06	-0.43	3.97 (4.35)
OHCH ₂ OOH	47.62	47.65	47.73	1.47	1.43	0.11	5.27	5.73,5 .60	-0.13	-41.09 (-40.93)

Ab initio transition state theory calculations utilizing these energies combined with an Eckart tunneling model and rigid rotor harmonic oscillator state counts (employing the anharmonic fundamental frequencies) yield a predicted room temperature rate coefficient of $4.4 \times 10^{-16} \text{ cm}^3 \text{ s}^{-1}$ for the $\text{CH}_2\text{OO} + \text{H}_2\text{O}$ reaction. For comparison, the most recent experimental measurement of $(3.2 \pm 1.2) \times 10^{-16} \text{ cm}^3 \text{ s}^{-1}$ ⁵³ falls more or less midway between the present prediction and that of Long *et al.* ($2.4 \times 10^{-16} \text{ cm}^3 \text{ s}^{-1}$), with the experimental error bars encompassing both theoretical predictions. Notably, the primary cause for the variation in the theoretical results appears to be the difference in the predicted barrier heights, with a $0.4 \text{ kcal mol}^{-1}$ room temperature Boltzmann factor essentially identical to the ratio of the two predictions. It is perhaps worth noting that, due to the relatively low tunneling frequency ($\sim 500 \text{ cm}^{-1}$), tunneling has only a modest effect on the rate predictions; simply removing tunneling lowers our rate prediction by only 20%, while reducing the tunneling frequency by 20% only lowers the rate coefficient by 8%. Thus, the physically more meaningful small curvature tunneling treatment of Long *et al.* is unlikely to have much bearing on the discrepancy in the rate predictions.

Prior work has examined four separate types of TSs for the reaction of MVK-oxide + H_2O ^{27, 48-50}. The primary transition state involves OH-insertion across COO. Here, this insertion was studied for both *exo* and *endo* orientations and for all 4 conformers of MVK-oxide. Another key transition state involves direct catalysis of the H-transfer from the CH_3 group to the terminal O via a bridging H_2O . Although the barriers for this pathway are considerably larger, the imaginary frequency is also much larger, which dramatically increases the tunneling rate⁵⁴. In the end, the rates for the two pathways are fairly comparable. A pathway involving OH-insertion across the CH_2CHCOO group has barriers that are of similar magnitude to those for the H_2O -

catalyzed H-transfer from CH₃ to O. Finally, the barriers for an H₂O-catalyzed H transfer from the CH group to the terminal O were found to be too high for this pathway to be relevant.

The present calculations of these stationary point energies for the reaction of all four isomers of MVK-oxide with H₂O are reported in Table S9. Then, in Table S10 we report the stationary point energies for a few of the spectator H₂O processes, again for all four isomers. For simplicity, the latter calculations focus on spectator catalysis related to the *trans* to *cis* isomerization process and the Cl to vinyl hydroperoxide isomerization in the *syn* conformers. These processes are chosen due to their direct relevance to the present discussion, although others, such as a catalysis of the decomposition of the anti-forms may also be occurring.

A schematic plot of the key reaction pathways for the *syn-trans* conformer is provided in Figure S11. Notably, although the pathway for formation of the C₂H₃C(OH)(CH₃)OOH species has the lowest barriers, the imaginary frequencies for the direct and spectator-catalyzed pathways to the C₂H₃C(CH₂)OOH + H₂O products are about twice as large. Thus, it is not clear which pathway will contribute most to the kinetics.

Predicted rate coefficients for the reaction of water with each of the conformer of MVK-oxide were obtained from AITSTME calculations implementing the energies in Table S9 and S10 together with an Eckart tunneling model, rigid rotor harmonic oscillator state counts employing the anharmonic fundamental frequencies, and one-dimensional torsional treatments for the methyl rotors. The predictions are not sensitive to the energy transfer parameters for the relevant region of temperature and pressure. They are also not sensitive to the rate for forming the van der Waals complexes. Thus, these parameters are not described here. Suffice it to say, that we use physically realistic

Table S9. Stationary point energies (kcal mol⁻¹) for MVK-oxide + H₂O. All energies are relative to the *syn-trans* conformer of MVK-oxide + H₂O.

Species	Label	CCSD(T)-F12b			T(Q)	Core Val.	E0	Anh.	Total
		DZ-F12	TZ-F12	CBS	6-31G*				
<i>syn-trans</i>	1a	0.0	0.0	0.0	0.0	0.0	0.0	0.0	0.0
<i>syn-trans</i> ...H ₂ O	2a	-8.82	-8.89	-8.92	0.39	-0.01	2.09	-0.07	-6.52
2a = 3a		7.22	7.16	7.12	0.93	0.23	1.10	-0.42	8.97
VHPOH; <i>trans</i>	3a	32.55	32.44	32.38	1.60	0.13	3.99	-0.10	26.76
2a = 3a'		8.76	8.70	8.67	0.96	0.23	1.11	-0.43	10.53
VHPOH; <i>trans</i> '	3a'	32.36	32.23	32.17	1.60	0.13	3.88	-0.09	26.64
2a = 4a		13.08	12.86	12.75	0.82	-0.01	-1.64	0.24	12.16
VHP; <i>trans</i> ...H ₂ O	4a	20.76	20.61	20.54	1.31	-0.09	2.26	-0.09	17.21
2a = 4a'		12.85	12.63	12.51	0.83	-0.01	-1.60	0.21	11.94
VHP; <i>trans</i> ...H ₂ O	4a'	21.18	21.03	20.95	1.31	-0.09	2.30	-0.22	17.66
<i>syn-cis</i>	1b	1.93	1.94	1.94	0.04	0.0	-0.19	0.00	1.79
<i>syn-cis</i> ...H ₂ O	2b	-6.96	-7.02	-7.05	0.48	-0.01	1.88	-0.09	-4.79
2b = 3b		7.44	7.39	7.37	1.00	0.23	1.21	-0.64	9.17
VHPOH; <i>cis</i>	3b	33.24	33.15	33.11	1.64	0.11	3.99	-0.10	27.40
2b = 3a'		9.04	8.99	8.97	1.00	0.23	0.97	-0.45	10.72
VHPOH; <i>trans</i> '	3a'	32.36	32.23	32.17	1.60	0.13	3.88	-0.09	26.64
2b = 4b		13.36	13.14	13.03	0.87	-0.02	-1.61	0.05	12.32
VHP; <i>cis</i> ...H ₂ O	4b	22.66	22.53	22.47	1.32	-0.10	2.36	-0.18	19.06
2b = 4b'		13.14	12.91	12.80	0.88	-0.02	-1.54	-0.04	12.07
VHP; <i>cis</i> ...H ₂ O'	4b'	23.30	23.16	23.09	1.32	-0.10	2.46	-0.27	19.68
<i>anti-trans</i>	1c	2.70	2.72	2.74	-0.03	0.01	-0.10	-0.03	2.60
<i>anti-trans</i> ...H ₂ O	2c	-6.26	-6.28	-6.29	0.47	0.02	2.00	-0.17	-3.96
2c = 3c		7.97	7.92	7.89	0.93	0.23	0.96	-0.51	9.50
VHPOH; <i>trans</i>	3c	32.21	32.10	34.76	1.62	0.12	3.98	-0.07	26.38
2c = 3c'		7.43	7.35	7.32	0.90	0.22	1.04	-0.66	8.81
VHPOH; <i>trans</i> '	3c'	34.20	34.11	34.06	1.64	0.11	3.92	-0.15	28.54
2c = 5c		24.19	24.02	23.94			-2.30	0.04	21.68
AHP...H ₂ O	5c								-6.91
2c = 5c'		23.82	23.65	23.57			-2.30	0.02	21.29
AHP;tau'...H ₂ O	5c'								-6.61
<i>anti-cis</i>	1d	2.84	2.79	2.78	0.21	0.05	0.03	-0.01	3.06
<i>anti-cis</i> ...H ₂ O	2d	-5.06	-5.15	-5.19	0.56	0.05	2.00	-0.30	-2.88
2d = 3d		9.31	9.24	9.20	1.03	0.24	1.00	-0.61	10.86
VHPOH; <i>cis</i>	3d	32.71	32.61	32.57	1.63	0.12	3.97	-0.14	26.98
2d = 3d'		9.52	9.43	9.38	1.00	0.24	0.97	-0.60	11.00
VHPOH; <i>cis</i> '	3d'	33.63	33.53	33.48	1.63	0.11	3.98	-0.07	27.83
2d = 6d		9.53	9.32	9.22	0.71	0.21	2.17	-0.57	11.74
VHPOH'	6d	27.34	27.31	27.30	1.48	0.04	5.27	-0.15	20.65
2d = 6d'		9.90	9.70	9.59	0.74	0.21	1.84	-0.73	11.65
VHPOH';tau'	6d'	25.97	25.92	25.90	1.49	0.04	5.16	-0.18	19.39

Table S10. Stationary point energies (kcal mol⁻¹) describing effect of spectator H₂O on MVK-oxide transformations. All energies are relative to the *syn-trans* conformer of MVK-oxide + H₂O.

Species	Label	CCSD(T)-F12b			T(Q)	Core Val.	E0	Anh.	Total
		DZ-F12	TZ-F12	CBS	Corr.				
<i>syn-trans</i>	1a	0.0	0.0	0.0	0.0	0.0	0.0	0.0	0.0
<i>syn-trans</i> ...H ₂ O =	stcH ₂ O	-1.60	-1.58	-1.56	0.72	-0.00	1.47	-0.22	0.41
<i>syn-cis</i> ...H ₂ O									
<i>syn-trans</i> ...H ₂ O =	stcH ₂ O'	-2.07	-2.05	-2.04	0.73	0.00	1.55	-0.40	-0.17
<i>syn-cis</i> ...H ₂ O									
<i>syn-trans</i> ...H ₂ O =	stVHPH	13.78	13.73	13.70	0.79	0.02	-0.95	-0.23	13.33
VHP...H ₂ O;a									
<i>syn-trans</i> ...H ₂ O =	stVHPH'	12.89	12.79	12.74	0.80	0.02	-0.60	-0.11	12.86
VHP...H ₂ O;a;gb									
VHP...H ₂ O;a	VHPHt	16.95	-16.73	16.62	1.30	-0.09	1.32	-0.14	-14.22
VHP...H ₂ O;a;gb	VHPHt'	16.92	-16.74	16.65	1.33	-0.08	1.50	-0.30	-14.19
<i>syn-cis</i>	1b	1.93	1.94	1.94	0.04	0.0	-0.19	0.0	1.79
<i>syn-cis</i> ...H ₂ O =	scVHPH	14.69	14.62	14.58	0.85	0.03	-0.82	-0.09	14.55
VHP...H ₂ O;b									
<i>syn-cis</i> ...H ₂ O =	scVHPH'	14.10	13.99	13.93	0.83	0.01	-0.63	-0.24	13.89
VHP...H ₂ O;b;gb									
VHP...H ₂ O;b	VHPHc	18.99	-18.77	18.67	1.33	-0.09	1.39	-0.10	-16.15
VHP...H ₂ O;b;gb	VHPHc'	18.93	-18.78	18.70	1.34	-0.09	1.63	-0.25	-16.07
<i>anti-trans</i>	1c	2.70	2.72	2.74	-0.03	0.01	-0.10	-0.03	2.60
<i>anti-trans</i> ...H ₂ O	atcH ₂ O	0.87	0.88	0.89	0.72	0.01	1.52	-0.18	2.97
= <i>anti-cis</i> ...H ₂ O									
<i>anti-trans</i> ...H ₂ O	atcH ₂ O'	1.25	1.29	1.30	0.72	0.01	1.34	-0.19	3.19
= <i>anti-cis</i> ...H ₂ O									

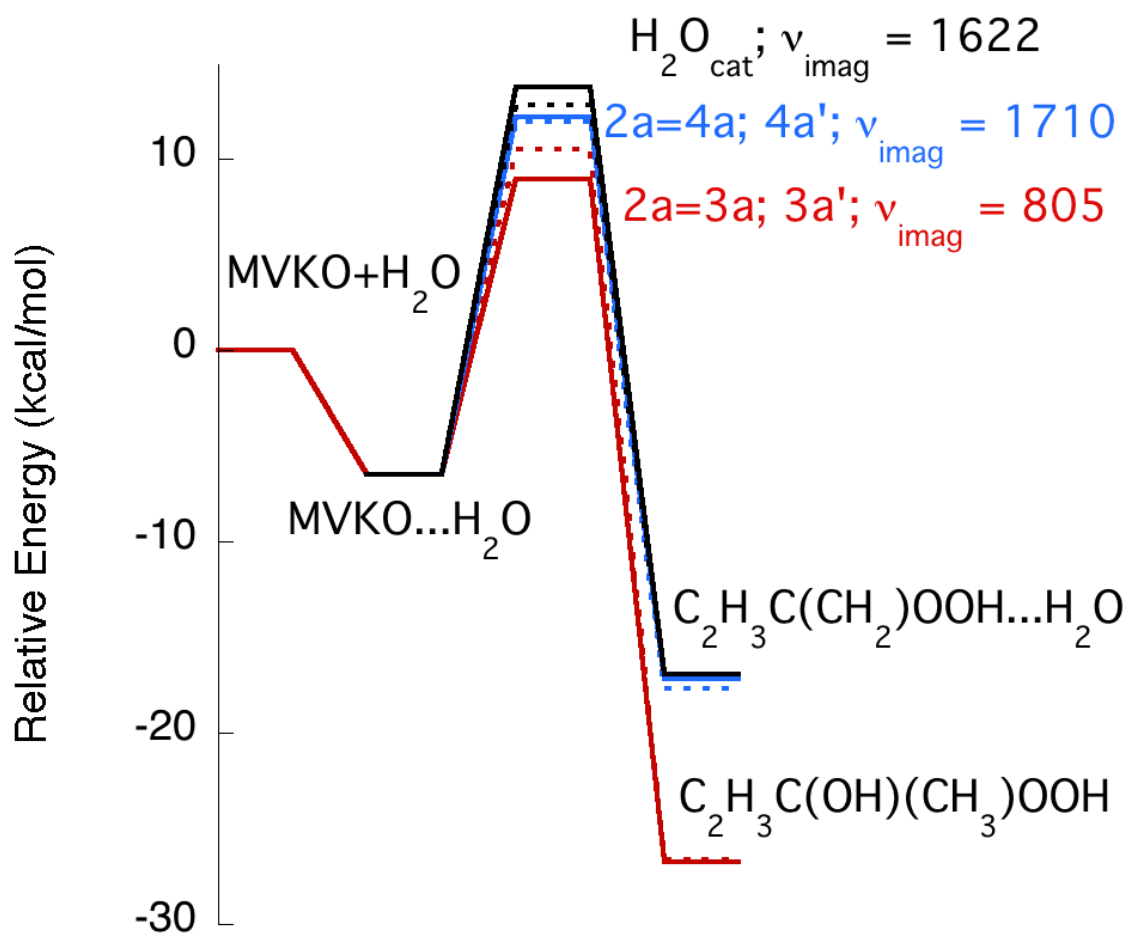


Figure S11. Schematic plot of the reaction pathways for the reaction of H₂O with *syn-trans*-MVK-oxide (denoted MVKO here).

values. The rate coefficients are obtained from two separate master equations: one treating the *syn-trans*- and *syn-cis*- conformers, and one treating the *anti-trans*- and *anti-cis*- conformers. For simplicity, we ignore the coupling of the *syn*- and *anti*- conformers, which we do not expect to be significant. The most significant shortcoming in this analysis is in the use of the Eckart model to predict the tunneling rates. This shortcoming may affect our predictions of which pathway is of greatest significance kinetically.

The AITSTME-predicted rate coefficients for the chemically significant reactions are summarized in Table S11. For simplicity, we do not report the rate coefficients for formation of the van der Waals wells, which are chemically irrelevant since the branching from those wells onto chemical products does not contribute significantly to the overall flux to chemical products. Similarly, we do not report the rate coefficients for isomerization between *cis* and *trans* conformers, since that process has already been calculated to happen rapidly enough to yield thermal distributions of the *cis* and *trans* conformers, as discussed in section 2 of the SI.

The total rate coefficient for the reaction of the thermal distribution of *syn*-conformers, *syn*(thermal), is predicted to be $1.1 \times 10^{-19} \text{ cm}^3 \text{ s}^{-1}$, while that for the thermal distribution of *anti*- isomers, *anti*(thermal), is predicted to be $8 \times 10^{-19} \text{ cm}^3 \text{ s}^{-1}$. Interestingly, for the *syn*(thermal) case, the spectator catalysis pathway has the largest contribution to the rate coefficient, but all pathways make a significant contribution. The rate coefficient determined in the present work is in accord with the previous work by Anglada and Solé ($3.4 \times 10^{-19} \text{ cm}^3 \text{ s}^{-1}$)²⁷, and the adjusted value of Anglada and Solé by Vereecken *et al.* ($9.5 \times 10^{-20} \text{ cm}^3 \text{ s}^{-1}$)²⁸, but the value obtained herein was achieved without empirical adjustment of the barrier height or other parameters.

Table S11: Conformer-specific AITSTME predicted rate coefficients ($\text{cm}^3 \text{s}^{-1}$) for the MVK-oxide.

Reactants\Products^a	W2	P2	P3	W3	Total
<i>Syn-trans</i>	1.4×10^{-20}	9.3×10^{-21}	7.9×10^{-20}	-	1.0×10^{-19}
<i>Syn-cis</i>	1.2×10^{-19}	8.4×10^{-20}	4.2×10^{-20}	-	2.5×10^{-19}
<i>Syn(thermal)</i>	2.3×10^{-20}	1.5×10^{-20}	7.6×10^{-20}	-	1.1×10^{-19}
<i>Anti-trans</i>	1.1×10^{-18}	-	-	$<1 \times 10^{-23}$	1.1×10^{-18}
<i>Anti-cis</i>	2×10^{-19}	-	-	1.3×10^{-20}	2×10^{-19}
<i>Anti(thermal)</i>	8×10^{-19}	-	-	4.2×10^{-21}	8×10^{-19}

^a W2 denotes $\text{C}_2\text{H}_3\text{C}(\text{OH})(\text{CH}_3)\text{OOH}$; P2 denotes $\text{C}_2\text{H}_3\text{C}(\text{CH}_2)\text{OOH} \dots \text{H}_2\text{O}$ via direct H_2O catalysis; P3 denotes $\text{C}_2\text{H}_3\text{C}(\text{CH}_2)\text{OOH} \dots \text{H}_2\text{O}$ via spectator H_2O catalysis; W3 denotes $\text{C}_2\text{H}_3\text{C}(\text{OH})(\text{CH}_3)\text{OOH}$ via the pathway leading to the 6d isomers in Table S10.

4. Global chemical modelling evaluation of particulate formation from MVK-oxide + SO₂

The implications for the reaction of MVK-oxide with SO₂ on particle nucleation have been modelled with nucleation coefficients of 2 (55) and 1.5 (56) for H₂SO₄, and the results presented in Figures S12 and S13, respectively.

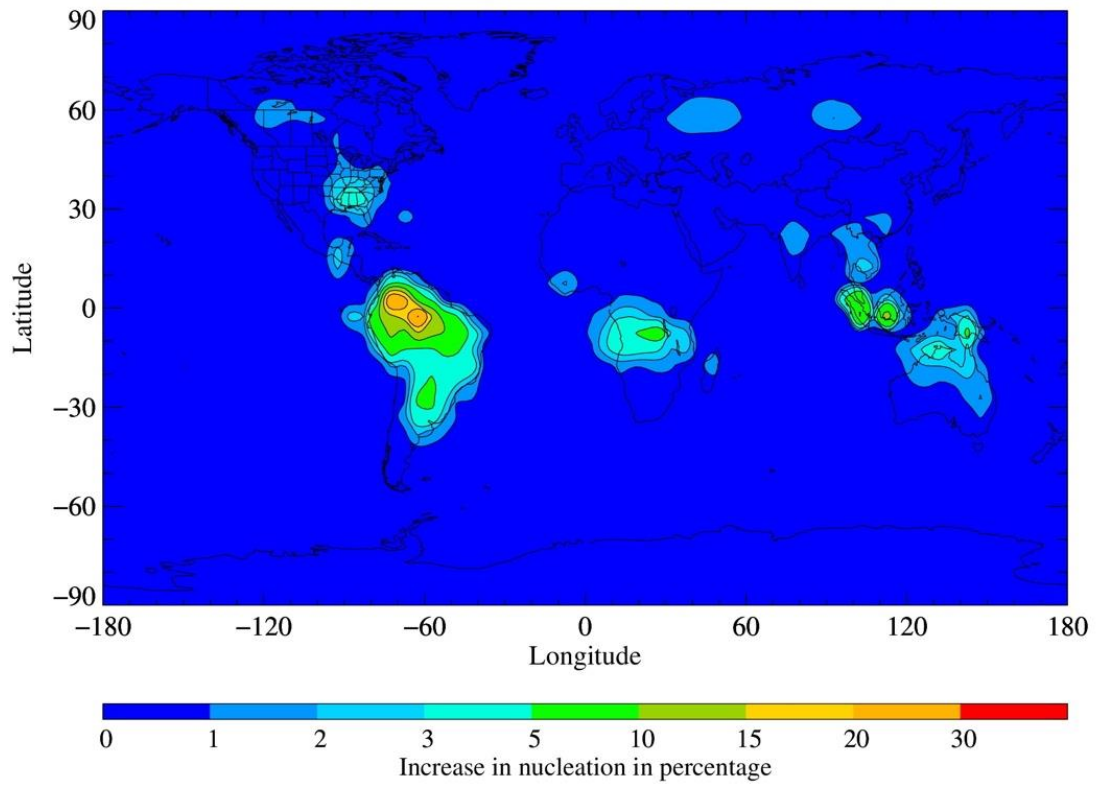


Figure S12. The impact of the MVK-oxide reaction with SO₂ on particulate nucleation, using a nucleation coefficient for sulfuric acid of 2.

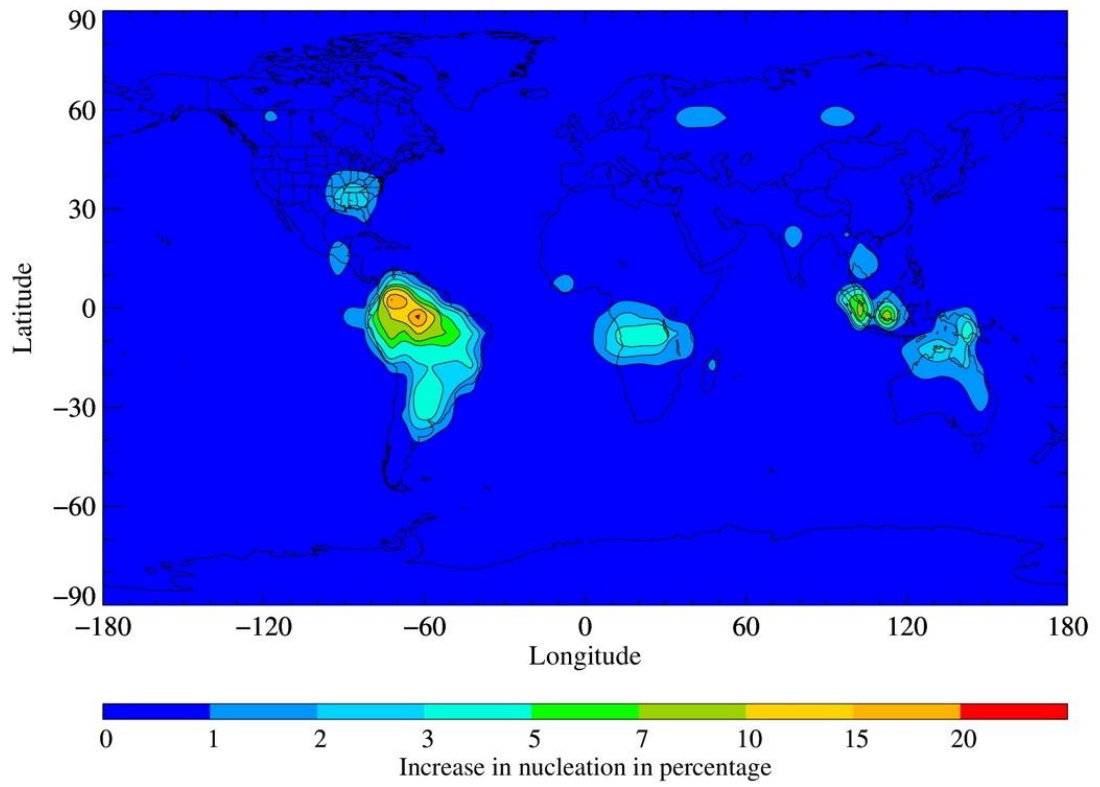


Figure S13: The impact of the MVK-oxide reaction with SO₂ on particulate nucleation, using a nucleation coefficient for sulfuric acid of 1.5.

5. *Ab initio* optimized geometries and frequencies

5.1 MVK-oxide

Syn-trans

Relative energy = 0.0 kcal mol⁻¹

1	6	0	-0.281002	-2.428825	0.000000
2	6	0	0.489860	-1.332579	0.000000
3	6	0	0.000000	0.017627	0.000000
4	6	0	-1.397431	0.477385	0.000000
5	8	0	0.934365	0.910720	0.000000
6	8	0	0.561182	2.203583	0.000000
7	1	0	-1.359012	-2.376515	0.000000
8	1	0	0.163693	-3.411629	0.000000
9	1	0	1.567972	-1.424436	0.000000
10	1	0	-2.098829	-0.348501	0.000000
11	1	0	-1.553379	1.122502	0.866535
12	1	0	-1.553379	1.122502	-0.866535
Frequencies --	119.9147		198.1647		256.1167
Frequencies --	283.2193		331.6966		459.4209
Frequencies --	496.8539		609.8350		682.4911
Frequencies --	814.7146		950.8478		998.3597
Frequencies --	1026.7698		1041.7510		1047.8678
Frequencies --	1076.4570		1292.3767		1337.6406
Frequencies --	1400.1620		1449.9665		1453.0141
Frequencies --	1472.8403		1504.9644		1662.0030
Frequencies --	3052.6351		3097.5438		3178.5451
Frequencies --	3186.9118		3194.4379		3270.2727

Syn-cis

Relative energy = 3.05 kcal mol⁻¹

1	6	0	-2.181296	-0.839531	0.000000
2	6	0	-1.445765	0.279851	0.000000
3	6	0	0.000000	0.334288	0.000000
4	6	0	0.795556	1.572979	0.000000
5	8	0	0.625731	-0.789133	0.000000
6	8	0	1.976736	-0.749625	0.000000
7	1	0	-1.722960	-1.817168	0.000000
8	1	0	-3.258737	-0.787750	0.000000
9	1	0	-1.934488	1.244081	0.000000
10	1	0	0.161642	2.453346	0.000000
11	1	0	1.461921	1.566019	0.865256
12	1	0	1.461921	1.566019	-0.865256
Frequencies --	66.4658		206.2188		228.8220
Frequencies --	275.2111		327.6923		442.9534
Frequencies --	485.9721		623.2547		665.9256
Frequencies --	815.8805		971.1810		992.1262
Frequencies --	1024.2898		1041.0284		1044.4521

Frequencies --	1108.3087	1286.3487	1340.7090
Frequencies --	1397.3938	1418.9712	1451.4392
Frequencies --	1475.0005	1500.5024	1669.4449
Frequencies --	3044.5296	3088.3513	3171.9026
Frequencies --	3177.8055	3200.0465	3272.9201

Syn-trans=syn-cis

Relative energy = 7.97 kcal mol⁻¹

1	6	0	2.327858	-0.267919	0.425627
2	6	0	1.381300	-0.133215	-0.497496
3	6	0	-0.027092	0.153355	-0.167281
4	6	0	-0.602629	1.490867	0.045170
5	8	0	-0.796694	-0.864200	-0.093452
6	8	0	-2.103652	-0.635657	0.189406
7	1	0	2.105556	-0.189953	1.480296
8	1	0	3.351766	-0.466552	0.146356
9	1	0	1.626162	-0.217122	-1.550508
10	1	0	-1.070284	1.516480	1.033036
11	1	0	-1.432790	1.629417	-0.652467
12	1	0	0.145734	2.268058	-0.060451
Frequencies --	-155.8236	160.3454	206.9403		
Frequencies --	272.9053	318.6863	393.4493		
Frequencies --	519.1815	618.1650	677.8188		
Frequencies --	801.6223	973.9469	989.5462		
Frequencies --	996.7350	1008.2812	1048.2105		
Frequencies --	1090.0645	1299.6607	1324.2466		
Frequencies --	1397.9023	1440.7421	1448.6849		
Frequencies --	1456.7181	1494.5998	1693.0250		
Frequencies --	3035.8504	3076.2762	3155.4400		
Frequencies --	3168.9422	3179.8447	3258.5054		

Anti-trans

Relative energy = 2.57 kcal mol⁻¹

1	6	0	-1.894146	-1.185090	0.000000
2	6	0	-0.571837	-0.965527	0.000000
3	6	0	0.000000	0.349961	0.000000
4	6	0	-0.769734	1.622704	0.000000
5	8	0	1.282506	0.506388	0.000000
6	8	0	2.101575	-0.560185	0.000000
7	1	0	-2.612894	-0.378124	0.000000
8	1	0	-2.286939	-2.190359	0.000000
9	1	0	0.144815	-1.772424	0.000000
10	1	0	-0.083752	2.464487	0.000000
11	1	0	-1.409789	1.687253	0.880050
12	1	0	-1.409789	1.687253	-0.880050
Frequencies --	113.8309	150.9705	244.3138		
Frequencies --	280.5671	326.0586	377.0466		
Frequencies --	479.0748	640.2948	718.3130		
Frequencies --	798.5875	977.2758	985.0386		

Frequencies --	1021.2924	1049.6643	1057.6112
Frequencies --	1065.0237	1281.3674	1373.2418
Frequencies --	1391.3621	1436.2627	1469.0936
Frequencies --	1486.0836	1512.5356	1657.6094
Frequencies --	3054.8184	3111.1078	3162.1730
Frequencies --	3170.5660	3228.1091	3261.6980

Anti-cis

Relative energy = 3.05 kcal mol⁻¹

1	6	0	-1.352990	-1.521124	0.000000
2	6	0	-1.214381	-0.180848	0.000000
3	6	0	0.000000	0.576665	0.000000
4	6	0	-0.021963	2.069054	0.000000
5	8	0	1.191358	0.084982	0.000000
6	8	0	1.382201	-1.251687	0.000000
7	1	0	-0.494812	-2.166647	0.000000
8	1	0	-2.348757	-1.942692	0.000000
9	1	0	-2.104292	0.435798	0.000000
10	1	0	0.990778	2.459965	0.000000
11	1	0	-0.547687	2.442365	0.879064
12	1	0	-0.547687	2.442365	-0.879064
Frequencies --	116.7361	165.5085	285.0024		
Frequencies --	305.2060	339.0183	368.0726		
Frequencies --	411.2073	640.2272	717.5908		
Frequencies --	823.6757	990.3387	1004.8285		
Frequencies --	1029.1718	1053.3593	1054.9509		
Frequencies --	1099.6379	1269.7395	1340.3444		
Frequencies --	1418.9240	1438.3092	1463.9237		
Frequencies --	1487.0283	1508.1717	1640.9833		
Frequencies --	3054.6683	3110.9627	3165.1107		
Frequencies --	3167.2660	3181.8932	3314.1293		

Anti-trans=anti-cis

Relative energy = 11.25 kcal mol⁻¹

1	6	0	2.007829	-0.418699	-0.342971
2	6	0	0.984974	-0.461235	0.502459
3	6	0	-0.412755	-0.301218	0.080860
4	6	0	-1.331026	-1.454707	-0.099639
5	8	0	-0.925829	0.850993	-0.119854
6	8	0	-0.181649	1.963910	0.046691
7	1	0	1.863784	-0.218324	-1.394427
8	1	0	3.019565	-0.567451	0.002037
9	1	0	1.146198	-0.648731	1.558247
10	1	0	-2.328717	-1.110049	-0.356799
11	1	0	-1.377214	-2.045749	0.816530
12	1	0	-0.957925	-2.113760	-0.884538
Frequencies --	-172.4811	152.1270	208.0108		
Frequencies --	231.6809	294.2586	330.2831		
Frequencies --	521.8294	599.3025	696.2792		

Frequencies --	802.6304	974.6524	982.0157
Frequencies --	993.4085	1013.3162	1031.6387
Frequencies --	1096.0715	1286.3799	1328.8923
Frequencies --	1414.9866	1434.1413	1473.1757
Frequencies --	1478.4513	1514.3980	1695.7927
Frequencies --	3046.9529	3100.6707	3156.9139
Frequencies --	3158.0516	3173.6061	3263.0241

5.2 MVK-oxide + H₂O

All energies are relative to the *syn-trans* conformer of MVK-oxide + H₂O.
syn,trans...H₂O

Relative energy = -6.52 kcal mol⁻¹

1	6	0	0.489007	0.264516	0.167706
2	8	0	-0.336591	1.153141	-0.251510
3	8	0	-1.577619	1.195747	0.327256
4	8	0	-2.306706	-1.265045	-0.649351
5	1	0	-2.721363	-1.216477	-1.512131
6	1	0	-2.264989	-0.342001	-0.331686
7	6	0	1.751470	0.296037	-0.529991
8	6	0	2.762595	-0.549002	-0.298507
9	1	0	1.836135	1.061648	-1.289087
10	1	0	2.703200	-1.329584	0.444164
11	1	0	3.678923	-0.475719	-0.863409
12	6	0	0.100681	-0.642904	1.258049
13	1	0	-0.415836	-0.058942	2.019359
14	1	0	0.957059	-1.164312	1.669279
15	1	0	-0.628323	-1.357237	0.868810
Frequencies --	44.9318	93.9248	113.8528		
Frequencies --	148.0790	209.4653	225.2281		
Frequencies --	259.7891	310.6386	351.0015		
Frequencies --	410.5464	464.0009	493.3084		
Frequencies --	601.9423	690.2681	758.4837		
Frequencies --	815.3560	958.3834	978.0073		
Frequencies --	1015.8055	1030.3811	1055.7593		
Frequencies --	1072.2687	1304.8934	1342.0402		
Frequencies --	1401.5251	1450.9373	1471.2367		
Frequencies --	1490.9252	1510.5859	1665.5925		
Frequencies --	1671.7086	3050.9581	3111.8539		
Frequencies --	3179.8565	3186.4210	3200.7510		
Frequencies --	3272.6727	3517.4754	3899.8520		

syn,cis...H₂O

Relative energy = -4.79 kcal mol⁻¹

1	6	0	0.482794	0.413398	-0.218287
2	8	0	0.044784	-0.676190	-0.719244
3	8	0	-1.240344	-0.677599	-1.215796
4	8	0	-2.354573	-0.265627	1.250537
5	1	0	-2.586255	-1.076662	1.705565

6	1	0	-2.140465	-0.534429	0.334956
7	6	0	1.823278	0.368578	0.340056
8	6	0	2.541485	-0.747768	0.503219
9	1	0	2.223477	1.324114	0.646605
10	1	0	2.152041	-1.714733	0.221869
11	1	0	3.533280	-0.706893	0.925958
12	6	0	-0.352026	1.624801	-0.233754
13	1	0	-0.834194	1.706409	-1.207879
14	1	0	0.236074	2.504747	0.005606
15	1	0	-1.156078	1.498725	0.495949
Frequencies --		32.9371	76.5633	94.9279	
Frequencies --		132.2298	197.4039	226.9238	
Frequencies --		238.2559	309.3540	341.8078	
Frequencies --		415.7916	448.5863	489.0176	
Frequencies --		611.1751	670.6446	768.7060	
Frequencies --		816.5299	943.1330	996.1371	
Frequencies --		1023.4833	1034.5872	1052.8533	
Frequencies --		1104.9161	1283.8398	1342.4179	
Frequencies --		1401.5507	1444.1634	1454.9261	
Frequencies --		1496.2033	1508.2471	1666.4515	
Frequencies --		1677.4319	3043.2697	3104.8767	
Frequencies --		3171.1756	3178.4725	3208.2614	
Frequencies --		3274.0038	3499.0217	3900.5198	

*syn,trans...H₂O=**syn,cis...H₂O*

Geometry a

Relative energy = 0.41 kcal mol⁻¹

1	6	0	-2.880802	-0.049482	-0.250076
2	6	0	-1.657458	-0.463922	-0.559184
3	6	0	-0.447285	-0.007237	0.151529
4	6	0	0.079441	-0.630814	1.374894
5	8	0	0.149436	0.972956	-0.390681
6	8	0	1.333044	1.393574	0.189844
7	1	0	-3.054975	0.665315	0.541436
8	1	0	-3.741856	-0.413030	-0.790043
9	1	0	-1.491233	-1.180144	-1.355249
10	1	0	0.434330	0.156667	2.040266
11	1	0	0.961090	-1.219379	1.104128
12	1	0	-0.668603	-1.265176	1.837324
13	1	0	2.296332	-0.038523	-0.323660
14	8	0	2.473161	-0.973300	-0.554529
15	1	0	3.056417	-0.942845	-1.314258
Frequencies --		-144.9212	46.0741	103.9866	
Frequencies --		128.5973	171.3865	211.5284	
Frequencies --		253.0168	275.8132	337.9782	
Frequencies --		387.2042	442.1334	525.8062	
Frequencies --		620.9468	669.0667	774.3546	
Frequencies --		803.3119	921.7968	988.7619	
Frequencies --		995.4181	1009.7640	1040.3556	

Frequencies --	1096.3749	1296.7309	1319.6798
Frequencies --	1392.2818	1447.3971	1467.5752
Frequencies --	1486.7451	1512.9638	1671.3128
Frequencies --	1696.1287	3037.5917	3100.0800
Frequencies --	3165.3029	3173.6130	3179.4224
Frequencies --	3260.9581	3483.9766	3901.7777

Geometry b

Relative energy = -0.17 kcal mol⁻¹

1	6	0	-2.279697	0.982306	-0.266373
2	6	0	-1.838890	-0.269776	-0.204644
3	6	0	-0.432410	-0.564433	0.130695
4	6	0	0.098045	-0.593244	1.502423
5	8	0	0.320806	-0.783591	-0.865900
6	8	0	1.669941	-0.963834	-0.607926
7	1	0	-1.614501	1.816222	-0.091944
8	1	0	-3.310818	1.197532	-0.502666
9	1	0	-2.493472	-1.113315	-0.386002
10	1	0	0.653299	0.334399	1.669393
11	1	0	0.823017	-1.403018	1.581226
12	1	0	-0.707523	-0.676043	2.224105
13	1	0	1.919619	0.786143	-0.201781
14	8	0	1.681904	1.677294	0.128239
15	1	0	2.066888	2.290007	-0.500239
Frequencies --	-146.2612	52.1943	112.8834		
Frequencies --	142.5367	178.9859	209.4953		
Frequencies --	248.4925	277.1258	337.6150		
Frequencies --	391.8617	439.5577	542.9273		
Frequencies --	606.7060	668.0224	782.7031		
Frequencies --	806.2161	918.8306	987.8445		
Frequencies --	1000.1376	1005.9314	1047.9252		
Frequencies --	1101.3053	1293.0978	1325.9385		
Frequencies --	1392.4906	1448.9594	1463.0891		
Frequencies --	1487.0840	1515.9956	1675.3110		
Frequencies --	1688.1794	3040.1213	3104.6560		
Frequencies --	3165.0939	3176.6070	3176.9574		
Frequencies --	3262.2919	3474.5887	3899.8450		

syn-trans...H₂O = VHPOH

Geometry a

Relative energy = 8.97 kcal mol⁻¹

1	6	0	0.096795	0.004807	-0.275680
2	8	0	-0.842261	-0.766000	-0.754394
3	8	0	-2.127980	-0.227189	-0.370471
4	8	0	-0.725808	0.079180	1.554832
5	1	0	-0.583657	-0.790042	1.946386
6	1	0	-1.602700	-0.037664	0.859505
7	6	0	1.377145	-0.701605	-0.195220
8	6	0	2.536563	-0.108681	0.087187

9	1	0	1.319500	-1.768604	-0.361240
10	1	0	2.606455	0.952441	0.272096
11	1	0	3.449323	-0.681477	0.149333
12	6	0	0.037925	1.489363	-0.427360
13	1	0	-0.994569	1.812091	-0.442100
14	1	0	0.514369	1.740427	-1.376576
15	1	0	0.569104	1.981601	0.379287
Frequencies --			-806.5569	84.1812	184.9313
Frequencies --			211.2148	257.8291	313.1670
Frequencies --			342.9059	402.6911	471.3653
Frequencies --			498.2204	573.8569	601.3477
Frequencies --			680.0268	707.6429	788.8630
Frequencies --			898.6793	956.7308	987.6368
Frequencies --			1002.8543	1035.4158	1070.3564
Frequencies --			1106.5912	1305.3303	1336.5641
Frequencies --			1397.3269	1445.8988	1461.3039
Frequencies --			1505.8700	1509.4564	1601.4307
Frequencies --			1691.5810	1801.1955	3066.5856
Frequencies --			3161.1164	3178.8631	3200.7703
Frequencies --			3210.7818	3269.2248	3817.1273

Geometry b

Relative energy = 10.53 kcal mol⁻¹

1	6	0	0.103536	-0.013306	-0.245140
2	8	0	-0.817370	-0.793650	-0.734748
3	8	0	-2.117430	-0.231700	-0.425306
4	8	0	-0.775030	-0.035873	1.550089
5	1	0	-1.637472	-0.081893	0.831802
6	1	0	-0.780862	0.844114	1.938907
7	6	0	1.375923	-0.717161	-0.072217
8	6	0	2.553002	-0.106230	0.052532
9	1	0	1.295142	-1.793937	-0.040268
10	1	0	2.648733	0.968963	0.031579
11	1	0	3.459806	-0.676776	0.183327
12	6	0	0.056207	1.465045	-0.471549
13	1	0	-0.974845	1.789186	-0.525408
14	1	0	0.544807	1.666803	-1.426620
15	1	0	0.591320	2.003239	0.304652
Frequencies --			-803.9253	89.1490	198.1131
Frequencies --			232.4033	249.7559	312.9024
Frequencies --			337.6056	411.8848	456.5700
Frequencies --			492.9717	565.7829	619.9861
Frequencies --			672.4764	715.7811	798.8568
Frequencies --			895.4729	949.0614	984.5613
Frequencies --			1000.1212	1035.2495	1066.5264
Frequencies --			1104.1322	1310.7011	1332.0434
Frequencies --			1394.1137	1437.9090	1464.7692
Frequencies --			1505.1144	1512.8790	1516.7876
Frequencies --			1693.5497	1878.6334	3062.7141

Frequencies --	3143.4079	3178.0814	3203.9525
Frequencies --	3213.6932	3266.9008	3841.4265

VHPOH

Geometry a

Relative energy = -26.76 kcal mol⁻¹

1	6	0	0.020989	0.026262	0.156928
2	8	0	-0.865799	-0.609365	-0.769894
3	8	0	-2.202317	-0.086467	-0.572193
4	8	0	-0.415309	-0.258740	1.479554
5	1	0	-0.188513	-1.173939	1.676847
6	1	0	-2.387080	-0.406142	0.323900
7	6	0	1.325600	-0.666074	-0.133761
8	6	0	2.488688	-0.069546	-0.361328
9	1	0	1.260053	-1.748513	-0.137088
10	1	0	2.589484	1.005022	-0.381339
11	1	0	3.382045	-0.650006	-0.536527
12	6	0	0.024121	1.530367	0.009457
13	1	0	-0.966596	1.912145	0.230255
14	1	0	0.288013	1.802094	-1.008646
15	1	0	0.733606	1.969865	0.705093
Frequencies --	69.7971	149.1262	229.3361		
Frequencies --	236.1173	291.2859	315.2939		
Frequencies --	351.1442	402.2086	425.4415		
Frequencies --	443.5173	500.7283	623.4160		
Frequencies --	689.5235	781.0899	894.8016		
Frequencies --	937.1683	951.2917	980.5495		
Frequencies --	1024.1114	1035.0427	1145.5435		
Frequencies --	1169.0051	1196.1006	1331.0266		
Frequencies --	1388.0185	1405.7064	1444.1300		
Frequencies --	1463.5143	1506.7559	1507.7273		
Frequencies --	1711.9751	3087.3529	3158.9796		
Frequencies --	3165.8071	3177.3391	3180.8342		
Frequencies --	3260.5345	3723.5227	3805.882		

Geometry b

Relative energy = -26.64 kcal mol⁻¹

1	6	0	0.030843	0.089208	0.209106
2	8	0	-0.756425	-0.738745	-0.673282
3	8	0	-2.134789	-0.270440	-0.594456
4	8	0	-0.467702	0.018331	1.520913
5	1	0	-2.521566	-1.006508	-0.103769
6	1	0	-1.276349	0.540392	1.543603
7	6	0	1.352053	-0.627576	0.223052
8	6	0	2.451299	-0.233838	-0.406336
9	1	0	1.340614	-1.537943	0.806720
10	1	0	2.486929	0.670390	-0.995229
11	1	0	3.359558	-0.814596	-0.346054
12	6	0	0.054305	1.517581	-0.300845

13	1	0	-0.958279	1.915260	-0.303202
14	1	0	0.430458	1.555510	-1.319532
15	1	0	0.678967	2.132090	0.342213
Frequencies --	62.1506		143.7477		189.9464
Frequencies --	253.7147		259.8264		293.5761
Frequencies --	351.3994		397.9616		437.1932
Frequencies --	462.6130		501.3034		617.0535
Frequencies --	676.7290		780.9787		883.7850
Frequencies --	911.0227		966.8616		978.5326
Frequencies --	1034.2065		1041.8784		1129.4282
Frequencies --	1153.4620		1223.1173		1330.2207
Frequencies --	1355.9002		1403.4147		1425.9346
Frequencies --	1466.3463		1504.2881		1520.7190
Frequencies --	1714.6837		3074.3526		3150.2909
Frequencies --	3160.6100		3172.8632		3197.4643
Frequencies --	3258.7111		3781.4294		3815.6786

syn-trans...H₂O = *VHP...H₂O*

Geometry a

Relative energy = 12.16 kcal mol⁻¹

1	6	0	0.026254	0.979209	0.829133
2	6	0	-0.438225	-0.193280	0.208507
3	8	0	0.336152	-1.213066	-0.044070
4	8	0	1.697094	-1.068073	0.366731
5	6	0	-1.764129	-0.411668	-0.364713
6	6	0	-2.805521	0.398811	-0.174064
7	1	0	0.961596	1.294094	-0.049447
8	1	0	-0.721674	1.731460	1.029025
9	1	0	0.726908	0.788151	1.636374
10	1	0	2.016119	-0.046645	-0.270412
11	8	0	2.026235	1.020553	-0.786263
12	1	0	2.790270	1.513493	-0.470245
13	1	0	-1.861072	-1.305408	-0.965125
14	1	0	-3.760971	0.181580	-0.626388
15	1	0	-2.737305	1.289526	0.431854
Frequencies --	-1715.1668		73.6559		131.7662
Frequencies --	254.6795		264.3027		328.9123
Frequencies --	440.4471		475.9273		483.4808
Frequencies --	539.4930		576.1226		637.3117
Frequencies --	679.2480		713.9916		778.2489
Frequencies --	878.0055		922.1894		929.3425
Frequencies --	993.8413		1031.4964		1035.2753
Frequencies --	1067.0307		1094.4327		1313.0413
Frequencies --	1329.9010		1356.8597		1408.6694
Frequencies --	1451.5531		1475.2206		1567.4922
Frequencies --	1608.5694		1690.1443		1838.4171
Frequencies --	3124.7152		3178.8874		3204.4247
Frequencies --	3233.5887		3269.6241		3835.9575

Geometry b

Relative energy = 11.94 kcal mol⁻¹

1	6	0	0.017561	0.979653	0.831745
2	6	0	-0.437134	-0.193406	0.208458
3	8	0	0.346570	-1.203232	-0.056867
4	8	0	1.702657	-1.063612	0.372186
5	6	0	-1.762855	-0.420361	-0.363536
6	6	0	-2.808885	0.385031	-0.176117
7	1	0	0.955620	1.304888	-0.040800
8	1	0	-0.732918	1.726291	1.041317
9	1	0	0.737971	0.800914	1.624553
10	1	0	2.038690	-0.022582	-0.234005
11	8	0	2.110272	1.076252	-0.644381
12	1	0	2.038345	1.090183	-1.604273
13	1	0	-1.856471	-1.318329	-0.958422
14	1	0	-3.763891	0.159187	-0.625186
15	1	0	-2.745445	1.278690	0.426014
Frequencies --			-1704.6546	73.5736	135.2417
Frequencies --			253.9871	266.8284	327.0986
Frequencies --			448.0507	465.5533	479.3773
Frequencies --			529.5039	573.0349	642.8930
Frequencies --			663.0429	742.4472	784.2410
Frequencies --			864.9158	923.6307	928.7932
Frequencies --			993.5743	1031.5957	1036.8219
Frequencies --			1075.7109	1131.2404	1312.7019
Frequencies --			1355.5910	1363.0013	1430.5355
Frequencies --			1474.4650	1523.4621	1579.7225
Frequencies --			1592.1540	1689.4874	1711.9249
Frequencies --			3125.3620	3178.6245	3202.3754
Frequencies --			3236.7281	3269.4890	3832.7224

VHP...H₂O

Geometry a

Relative energy = -17.21 kcal mol⁻¹

1	6	0	0.181948	-0.635330	1.242252
2	6	0	0.489801	0.140066	0.194460
3	8	0	-0.295599	1.132987	-0.325585
4	8	0	-1.541648	1.264757	0.384997
5	6	0	1.707406	0.046237	-0.623933
6	6	0	2.892433	-0.351740	-0.165837
7	1	0	-1.534739	-1.484385	-0.297638
8	1	0	0.868493	-1.412189	1.533466
9	1	0	-0.698928	-0.455598	1.833045
10	1	0	-2.054653	0.546034	-0.042733
11	8	0	-2.355073	-1.151484	-0.685960
12	1	0	-3.052897	-1.677380	-0.287283
13	1	0	1.595279	0.349109	-1.656808
14	1	0	3.745804	-0.418558	-0.823347
15	1	0	3.040679	-0.612502	0.872026

Frequencies --	58.7952	84.2872	115.4096
Frequencies --	159.5406	204.2848	229.2551
Frequencies --	254.6363	328.1704	359.2160
Frequencies --	424.8692	428.0981	508.6751
Frequencies --	591.0468	687.6844	753.2525
Frequencies --	762.6515	840.0211	867.1096
Frequencies --	926.5550	969.7516	990.3591
Frequencies --	1029.7465	1088.3186	1253.4371
Frequencies --	1333.8494	1421.4485	1469.2171
Frequencies --	1532.4440	1648.7185	1678.3021
Frequencies --	1696.0539	3169.0329	3188.2244
Frequencies --	3202.7754	3260.0955	3301.3985
Frequencies --	3501.1082	3738.0065	3893.0082

Geometry b

Relative energy = -17.66 kcal mol⁻¹

1	6	0	-0.210776	0.510265	1.320295
2	6	0	-0.481730	-0.159872	0.193469
3	8	0	0.340506	-1.073175	-0.412277
4	8	0	1.567478	-1.262266	0.318127
5	6	0	-1.688694	-0.017277	-0.633525
6	6	0	-2.886167	0.333874	-0.169276
7	1	0	1.551801	1.543583	-0.089286
8	1	0	-0.921730	1.235522	1.678301
9	1	0	0.667860	0.297365	1.903575
10	1	0	2.077684	-0.490741	-0.011252
11	8	0	2.378931	1.245669	-0.490758
12	1	0	2.277218	1.419632	-1.430217
13	1	0	-1.559153	-0.244840	-1.683799
14	1	0	-3.729028	0.437647	-0.835426
15	1	0	-3.055777	0.518070	0.881586
Frequencies --	58.8468	77.4634	108.8680		
Frequencies --	160.6063	216.8647	229.7746		
Frequencies --	257.0245	287.0584	360.3984		
Frequencies --	422.0656	461.9540	508.2914		
Frequencies --	588.1264	728.0656	751.9346		
Frequencies --	786.2670	848.8605	866.6547		
Frequencies --	926.0643	969.0438	989.2951		
Frequencies --	1029.1321	1087.6721	1250.8469		
Frequencies --	1334.7156	1422.3986	1469.9034		
Frequencies --	1513.4219	1646.8323	1680.3985		
Frequencies --	1696.5475	3169.3860	3184.9715		
Frequencies --	3203.0888	3260.5771	3301.2142		
Frequencies --	3487.7504	3742.9802	3889.7963		

syn-trans...H₂O = VHP...H₂O; spectator

Geometry a

Relative energy = 13.33 kcal mol⁻¹

1	6	0	-2.930724	-0.787681	0.220770
---	---	---	-----------	-----------	----------

2	6	0	-1.654916	-0.904493	-0.154089
3	6	0	-0.732938	0.213944	-0.151998
4	6	0	-0.793171	1.447695	0.516853
5	8	0	0.424719	-0.070353	-0.711769
6	8	0	1.338249	0.976023	-0.443746
7	1	0	-3.344569	0.162601	0.524279
8	1	0	-3.586964	-1.644309	0.230951
9	1	0	-1.248280	-1.852519	-0.478760
10	1	0	0.559711	1.401142	0.539903
11	1	0	-0.655640	2.333809	-0.097706
12	1	0	-1.547993	1.549526	1.281948
13	1	0	2.715570	-0.210671	0.225273
14	8	0	3.248646	-0.937737	0.577960
15	1	0	3.685748	-1.299829	-0.194656
Frequencies --	-1623.8460		11.1229		41.2886
Frequencies --	87.2978		114.7241		168.5606
Frequencies --	246.9054		280.3284		314.7069
Frequencies --	470.7153		488.8173		557.6282
Frequencies --	613.5770		634.1574		742.5515
Frequencies --	760.3229		901.7057		932.4415
Frequencies --	952.4302		999.5443		1027.1984
Frequencies --	1038.1109		1069.4271		1294.8528
Frequencies --	1332.7958		1352.5309		1466.8781
Frequencies --	1472.6696		1554.6363		1678.9579
Frequencies --	1683.3409		1822.6553		3116.6088
Frequencies --	3175.5300		3201.0990		3227.7275
Frequencies --	3269.2147		3700.7887		3901.3284

Geometry b

Relative energy = 12.86 kcal mol⁻¹

1	6	0	2.842589	-0.738115	-0.255600
2	6	0	1.966605	0.260018	-0.389128
3	6	0	0.600034	0.170898	0.088609
4	6	0	0.014999	-0.690530	1.026894
5	8	0	-0.143951	1.192582	-0.294159
6	8	0	-1.369216	1.166109	0.415969
7	1	0	2.562082	-1.675809	0.200850
8	1	0	3.858683	-0.635924	-0.604630
9	1	0	2.241778	1.187748	-0.872242
10	1	0	-0.837486	0.329887	1.295141
11	1	0	-0.877046	-1.222294	0.695759
12	1	0	0.691416	-1.276894	1.630796
13	1	0	-2.450495	-0.153437	-0.415841
14	8	0	-2.746203	-1.043237	-0.668696
15	1	0	-3.659347	-1.090543	-0.379395
Frequencies --	-1619.7920		40.4798		92.9244
Frequencies --	120.7195		147.0689		182.0655
Frequencies --	249.2568		287.3693		389.6724
Frequencies --	474.4114		502.3374		584.1612

Frequencies --	622.1154	646.6367	747.8941
Frequencies --	773.7153	911.4622	937.2180
Frequencies --	957.8210	999.0272	1027.4762
Frequencies --	1043.2972	1071.3300	1291.0009
Frequencies --	1327.6510	1354.5021	1467.5326
Frequencies --	1473.7311	1561.0778	1679.3621
Frequencies --	1683.7954	1817.5718	3080.9513
Frequencies --	3175.1911	3198.6914	3221.3979
Frequencies --	3268.9692	3639.8589	3897.2997

VHP,trans...H₂O

Geometry a

Relative energy = -14.22 kcal mol⁻¹

1	6	0	-2.685189	-0.770786	0.346657
2	6	0	-1.868960	0.280972	0.349671
3	6	0	-0.540005	0.296512	-0.274838
4	6	0	-0.165615	-0.361384	-1.372960
5	8	0	0.262290	1.128807	0.470052
6	8	0	1.568971	1.232610	-0.157960
7	1	0	-2.394755	-1.711573	-0.097878
8	1	0	-3.666411	-0.710878	0.791985
9	1	0	-2.165534	1.198849	0.840627
10	1	0	1.872616	2.033779	0.288238
11	1	0	0.833673	-0.305526	-1.765128
12	1	0	-0.902967	-0.944110	-1.898243
13	1	0	2.328571	-0.627562	0.385954
14	8	0	2.430080	-1.571786	0.542455
15	1	0	1.562691	-1.921913	0.326895
Frequencies --	18.8629	62.6694	83.1228		
Frequencies --	96.6136	119.9030	168.4570		
Frequencies --	178.2037	243.3064	289.5296		
Frequencies --	348.5398	408.5999	421.6917		
Frequencies --	500.8707	586.6265	730.2464		
Frequencies --	741.7971	842.6029	864.2300		
Frequencies --	916.8610	968.7429	981.8101		
Frequencies --	1024.8529	1090.1636	1250.2508		
Frequencies --	1334.0461	1390.7864	1445.1525		
Frequencies --	1472.9841	1677.4963	1694.0508		
Frequencies --	1701.2668	3169.8590	3185.6676		
Frequencies --	3210.6659	3261.8643	3308.9523		
Frequencies --	3792.4662	3804.9132	3903.9729		

Geometry b

Relative energy = -14.19 kcal mol⁻¹

1	6	0	2.938903	-0.772898	-0.363353
2	6	0	2.124956	0.229502	-0.038415
3	6	0	0.680516	0.082433	0.182241
4	6	0	0.054587	-0.981823	0.685862
5	8	0	0.080039	1.271413	-0.194042

6	8	0	-1.335040	1.262729	0.059949
7	1	0	2.568065	-1.775664	-0.518305
8	1	0	3.998854	-0.608408	-0.482922
9	1	0	2.513735	1.234276	0.065338
10	1	0	-1.365997	1.451075	1.010024
11	1	0	-1.015431	-1.042365	0.783287
12	1	0	0.652285	-1.821747	0.997802
13	1	0	-2.679898	-0.188801	-0.445728
14	8	0	-3.293670	-0.912039	-0.274389
15	1	0	-3.076020	-1.568473	-0.939648
Frequencies --	30.0012		81.5532		90.1021
Frequencies --	119.6322		136.3285		176.5566
Frequencies --	184.9440		252.6182		302.6837
Frequencies --	358.6996		412.8368		460.4775
Frequencies --	507.6841		596.5048		742.0151
Frequencies --	757.7345		867.6883		882.2439
Frequencies --	922.5481		968.5072		982.6309
Frequencies --	1026.7891		1090.3249		1233.7579
Frequencies --	1333.1302		1390.2259		1440.9317
Frequencies --	1472.7418		1668.3157		1692.9582
Frequencies --	1698.4573		3169.3909		3185.7531
Frequencies --	3201.8314		3261.1948		3298.0041
Frequencies --	3731.6328		3778.9128		3906.2494

syn-cis...H₂O = VHPOH

Geometry a

Relative energy = 9.17 kcal mol⁻¹

1	6	0	0.076443	0.343639	-0.222305
2	8	0	-0.279064	-0.783420	-0.764280
3	8	0	-1.688818	-1.003933	-0.498672
4	8	0	-0.816056	-0.064608	1.544625
5	1	0	-0.265599	-0.740835	1.954992
6	1	0	-1.434025	-0.593689	0.795269
7	6	0	1.520157	0.469064	0.022322
8	6	0	2.354578	-0.569880	-0.016738
9	1	0	1.877909	1.465077	0.239726
10	1	0	1.993135	-1.565998	-0.224602
11	1	0	3.412755	-0.438554	0.150696
12	6	0	-0.721484	1.590456	-0.408857
13	1	0	-1.772759	1.357662	-0.510082
14	1	0	-0.360663	2.062194	-1.326594
15	1	0	-0.557412	2.270160	0.420681
Frequencies --	-663.2814		84.2144		188.5574
Frequencies --	200.4108		222.8651		309.6968
Frequencies --	331.2155		392.3162		473.1180
Frequencies --	505.8716		573.1798		608.1536
Frequencies --	677.5527		699.0772		796.5091
Frequencies --	896.8130		982.3474		1016.8755
Frequencies --	1028.6415		1032.6439		1079.3518

Frequencies --	1154.8919	1271.7814	1340.1440
Frequencies --	1405.4248	1437.8650	1468.7964
Frequencies --	1499.2398	1515.9329	1612.9980
Frequencies --	1688.2184	1825.4816	3051.7700
Frequencies --	3151.2596	3175.7266	3208.2582
Frequencies --	3214.3332	3271.2382	3820.2684

Geometry b

Relative energy = 10.72 kcal mol⁻¹

1	6	0	0.076567	0.366363	-0.218684
2	8	0	-0.299432	-0.713357	-0.840192
3	8	0	-1.693006	-0.970608	-0.525976
4	8	0	-0.645585	-0.328771	1.526931
5	1	0	-1.353808	-0.739461	0.756408
6	1	0	-1.126392	0.352549	2.006803
7	6	0	1.528029	0.482429	-0.052944
8	6	0	2.320570	-0.586817	0.010720
9	1	0	1.925418	1.483456	0.037436
10	1	0	1.908308	-1.582951	-0.042442
11	1	0	3.388632	-0.482499	0.127326
12	6	0	-0.738915	1.617774	-0.276881
13	1	0	-1.793759	1.383269	-0.330011
14	1	0	-0.442704	2.148182	-1.185708
15	1	0	-0.519019	2.260845	0.570827
Frequencies --	-778.7290	75.6379	205.7397		
Frequencies --	217.5452	228.7024	307.9544		
Frequencies --	326.5040	404.1722	460.3552		
Frequencies --	507.1050	579.3972	617.1243		
Frequencies --	668.3553	700.9135	801.9431		
Frequencies --	899.7381	945.7280	1000.6411		
Frequencies --	1017.4813	1018.8314	1068.4232		
Frequencies --	1112.6826	1267.1694	1341.3092		
Frequencies --	1400.5293	1436.2913	1463.3959		
Frequencies --	1498.6358	1508.2548	1514.1600		
Frequencies --	1689.4044	1873.3174	3049.7893		
Frequencies --	3133.2123	3177.6426	3202.8972		
Frequencies --	3206.4094	3274.9449	3840.5095		

VHPOH

Geometry a

Relative energy = 27.40 kcal mol⁻¹

1	6	0	-0.005013	0.341376	0.038973
2	8	0	-0.420685	-1.012154	-0.105800
3	8	0	-1.864638	-1.047694	-0.157160
4	8	0	-0.501348	0.854664	1.269009
5	1	0	0.000751	0.434303	1.976302
6	1	0	-2.081678	-0.755572	0.741079
7	6	0	1.500000	0.308830	0.058301
8	6	0	2.260281	-0.762311	-0.137807

9	1	0	1.945726	1.274459	0.261593
10	1	0	1.831860	-1.729823	-0.348117
11	1	0	3.336779	-0.686503	-0.096153
12	6	0	-0.543207	1.236464	-1.060475
13	1	0	-1.624643	1.295908	-0.994827
14	1	0	-0.263365	0.828401	-2.027879
15	1	0	-0.124425	2.234147	-0.954340
Frequencies --	56.8928		144.5237		208.8953
Frequencies --	236.0355		298.0344		318.0550
Frequencies --	341.6076		395.4223		449.5740
Frequencies --	476.3087		541.6937		586.2015
Frequencies --	705.8692		778.5015		901.7022
Frequencies --	950.1916		960.6471		983.9387
Frequencies --	1035.7976		1048.2743		1110.2349
Frequencies --	1170.8587		1251.0122		1328.5902
Frequencies --	1373.3061		1411.8717		1423.9101
Frequencies --	1464.0146		1498.0495		1503.7572
Frequencies --	1704.1868		3081.4192		3159.2936
Frequencies --	3170.6931		3175.3728		3184.3036
Frequencies --	3267.1688		3724.0059		3798.5698

syn-cis...H₂O = VHP...H₂O

Geometry a

Relative energy = 12.32 kcal mol⁻¹

1	6	0	-0.499055	1.296463	-0.683845
2	6	0	0.418244	0.280551	-0.357324
3	8	0	0.089437	-0.974666	-0.285207
4	8	0	-1.291598	-1.259071	-0.543523
5	6	0	1.792620	0.560679	0.059298
6	6	0	2.630785	-0.359543	0.539832
7	1	0	-1.332822	1.109067	0.312575
8	1	0	-0.070087	2.283009	-0.783191
9	1	0	-1.218555	1.011619	-1.445543
10	1	0	-1.839036	-0.540092	0.339258
11	8	0	-2.124681	0.333934	1.063396
12	1	0	-3.050273	0.559693	0.925651
13	1	0	2.104516	1.588599	-0.053833
14	1	0	3.640052	-0.094958	0.815816
15	1	0	2.325374	-1.387406	0.664167
Frequencies --	-1677.2913		51.8937		144.3724
Frequencies --	231.1471		248.9179		330.7382
Frequencies --	436.7246		453.7879		507.8745
Frequencies --	538.0216		582.2478		630.0122
Frequencies --	679.5402		721.6996		774.3263
Frequencies --	871.4765		924.3257		940.2022
Frequencies --	1007.1516		1025.3979		1045.2410
Frequencies --	1086.5071		1101.7038		1321.0917
Frequencies --	1357.4213		1367.0415		1404.6809
Frequencies --	1458.0239		1463.5304		1552.9322

Frequencies --	1604.4416	1692.3058	1839.0213
Frequencies --	3121.8912	3178.4399	3209.9399
Frequencies --	3228.0063	3273.7666	3835.9199

Geometry b

Relative energy = 12.07 kcal mol⁻¹

1	6	0	-0.491504	1.299606	-0.681344
2	6	0	0.417691	0.281625	-0.343843
3	8	0	0.080840	-0.970005	-0.254291
4	8	0	-1.291751	-1.259911	-0.550994
5	6	0	1.792297	0.560232	0.075783
6	6	0	2.647392	-0.367793	0.509331
7	1	0	-1.340301	1.118961	0.303040
8	1	0	-0.061269	2.284617	-0.787463
9	1	0	-1.223149	1.015159	-1.431870
10	1	0	-1.880498	-0.524754	0.301016
11	8	0	-2.257045	0.372083	0.932660
12	1	0	-2.053239	0.237915	1.863995
13	1	0	2.092336	1.595025	-0.002573
14	1	0	3.656067	-0.101432	0.785756
15	1	0	2.358435	-1.404837	0.589541
Frequencies --	-1659.8567	54.2417	147.4361		
Frequencies --	231.5930	250.0026	328.8234		
Frequencies --	431.0516	464.5993	495.2850		
Frequencies --	529.5229	582.0860	640.2210		
Frequencies --	650.7053	740.1933	794.6366		
Frequencies --	859.3922	922.9021	942.8757		
Frequencies --	1005.8419	1027.4319	1046.3525		
Frequencies --	1096.6992	1153.4891	1323.9984		
Frequencies --	1354.6651	1359.2454	1449.9170		
Frequencies --	1459.7587	1544.6848	1560.7880		
Frequencies --	1599.2501	1692.5124	1704.9322		
Frequencies --	3122.4702	3177.9713	3208.8211		
Frequencies --	3230.7335	3273.0327	3832.0606		

VHP...H₂O

Geometry a

Relative energy = -19.06 kcal mol⁻¹

1	6	0	-0.199658	1.441808	-0.817304
2	6	0	0.488350	0.380121	-0.370220
3	8	0	0.054874	-0.914006	-0.386677
4	8	0	-1.254450	-1.034476	-0.974156
5	6	0	1.820564	0.486077	0.224090
6	6	0	2.537175	-0.537614	0.689529
7	1	0	-1.676544	0.830724	1.147424
8	1	0	0.259414	2.414592	-0.756187
9	1	0	-1.155679	1.338582	-1.298763
10	1	0	-1.807053	-0.818365	-0.193138
11	8	0	-2.327582	0.131984	1.291293

12	1	0	-3.178854	0.576376	1.270483
13	1	0	2.214779	1.492341	0.261902
14	1	0	3.518338	-0.375053	1.108811
15	1	0	2.164287	-1.549564	0.659213
Frequencies --	47.8616		93.7149		128.1673
Frequencies --	169.0544		182.4060		225.8452
Frequencies --	244.7701		323.4094		366.1745
Frequencies --	417.1388		468.4122		490.8694
Frequencies --	583.9379		683.9367		749.9291
Frequencies --	773.6256		839.4133		857.5646
Frequencies --	930.8243		963.7070		994.6559
Frequencies --	1022.4231		1072.6067		1326.5761
Frequencies --	1333.5519		1417.4114		1466.7914
Frequencies --	1535.1374		1642.3979		1649.4228
Frequencies --	1708.9027		3176.9886		3194.5157
Frequencies --	3202.2470		3270.5188		3302.1174
Frequencies --	3506.9285		3755.5070		3895.4757

Geometry b

Relative energy = -19.68 kcal mol⁻¹

1	6	0	0.170765	1.689933	0.192702
2	6	0	-0.472576	0.513215	0.206915
3	8	0	0.012672	-0.653124	0.726951
4	8	0	1.323327	-0.479436	1.298519
5	6	0	-1.803713	0.324219	-0.368274
6	6	0	-2.480609	-0.825032	-0.378764
7	1	0	1.683513	0.382663	-1.396280
8	1	0	-0.324431	2.541382	-0.243829
9	1	0	1.129955	1.821210	0.661323
10	1	0	1.867041	-0.572603	0.486482
11	8	0	2.291656	-0.358684	-1.281748
12	1	0	1.912302	-1.068801	-1.806883
13	1	0	-2.234190	1.216198	-0.802457
14	1	0	-3.464480	-0.878884	-0.819185
15	1	0	-2.074152	-1.725214	0.055583
Frequencies --	44.9263		89.3525		128.2721
Frequencies --	173.1129		202.8612		228.0720
Frequencies --	246.3972		298.4040		365.6868
Frequencies --	447.6155		468.8739		491.1726
Frequencies --	584.2631		726.2253		770.0856
Frequencies --	787.4620		847.8675		861.2585
Frequencies --	930.4261		961.8039		993.1874
Frequencies --	1024.3212		1072.0825		1326.0816
Frequencies --	1332.2698		1417.6698		1466.9057
Frequencies --	1514.5512		1641.4916		1652.0266
Frequencies --	1708.7184		3176.6255		3194.4279
Frequencies --	3202.1493		3269.6624		3301.6066
Frequencies --	3491.2443		3757.6946		3888.1530

syn-cis...H₂O = VHP...H₂O; spectator

Geometry a

Relative energy = 14.55 kcal mol⁻¹

1	6	0	1.481827	1.696796	-0.147649
2	6	0	1.772232	0.402019	0.009845
3	6	0	0.733772	-0.616735	-0.054147
4	6	0	0.531846	-1.726875	0.780324
5	8	0	-0.266886	-0.315440	-0.848219
6	8	0	-1.386619	-1.136105	-0.532343
7	1	0	0.462749	2.019973	-0.307175
8	1	0	2.255553	2.447226	-0.081055
9	1	0	2.772513	0.066408	0.242049
10	1	0	-0.778427	-1.492734	0.614598
11	1	0	0.343642	-2.676351	0.284534
12	1	0	1.163902	-1.795617	1.653138
13	1	0	-2.065358	0.648193	0.105604
14	8	0	-1.926631	1.528585	0.484657
15	1	0	-2.631556	1.635354	1.125310
Frequencies --			-1610.8587	41.6251	64.9473
Frequencies --			80.8787	125.8768	171.5352
Frequencies --			219.9222	290.8253	386.6796
Frequencies --			446.8301	533.1061	562.0907
Frequencies --			589.2097	623.2465	718.0198
Frequencies --			744.7442	901.7159	923.5264
Frequencies --			940.6928	1018.8397	1033.3920
Frequencies --			1042.0176	1090.4185	1313.9961
Frequencies --			1336.1702	1363.2248	1440.9053
Frequencies --			1479.2665	1541.4499	1674.8181
Frequencies --			1679.5495	1830.4941	3112.2610
Frequencies --			3166.9518	3207.1640	3225.1584
Frequencies --			3267.7036	3697.4471	3906.9090

Geometry b

Relative energy = 13.89 kcal mol⁻¹

1	6	0	2.772155	-0.460193	0.613818
2	6	0	1.966132	0.529855	0.222269
3	6	0	0.577018	0.345171	-0.163675
4	6	0	-0.329191	1.323088	-0.596079
5	8	0	0.176292	-0.902418	-0.289602
6	8	0	-1.100778	-0.917670	-0.909354
7	1	0	2.431957	-1.484393	0.646766
8	1	0	3.786587	-0.257057	0.920391
9	1	0	2.309364	1.554140	0.213001
10	1	0	-0.912610	0.351812	-1.315616
11	1	0	-1.281541	1.365195	-0.066026
12	1	0	0.091547	2.289866	-0.832257
13	1	0	-2.365642	-0.466964	0.419279
14	8	0	-2.851098	0.096167	1.044819
15	1	0	-3.771672	0.011248	0.789565

Frequencies --	-1615.0701	34.2583	79.7759
Frequencies --	111.3066	150.1824	176.3081
Frequencies --	235.5029	283.6266	394.4130
Frequencies --	483.2131	498.3378	577.4891
Frequencies --	637.2685	651.5047	736.1667
Frequencies --	769.1469	909.4509	940.7370
Frequencies --	957.1199	997.3684	1025.3350
Frequencies --	1041.8259	1084.7334	1314.4620
Frequencies --	1333.1704	1367.8817	1436.6193
Frequencies --	1486.2579	1546.8586	1679.9654
Frequencies --	1687.5295	1821.0748	3072.6479
Frequencies --	3178.0501	3208.6378	3215.1417
Frequencies --	3272.6954	3629.8532	3896.5430

VHP, cis...H₂O

Geometry a

Relative energy = -16.15 kcal mol⁻¹

1	6	0	1.775810	1.719398	0.301535
2	6	0	1.849955	0.496614	-0.226932
3	6	0	0.830123	-0.541268	-0.112105
4	6	0	0.916426	-1.742261	-0.687561
5	8	0	-0.223824	-0.099598	0.659119
6	8	0	-1.278757	-1.089266	0.689024
7	1	0	0.921706	2.041230	0.877213
8	1	0	2.579476	2.425974	0.162881
9	1	0	2.717649	0.201281	-0.800444
10	1	0	-1.340187	-1.228984	1.643507
11	1	0	0.140398	-2.480303	-0.599503
12	1	0	1.793486	-1.967153	-1.271073
13	1	0	-2.524862	0.310280	-0.253041
14	8	0	-2.813695	1.127254	-0.670816
15	1	0	-1.991346	1.595661	-0.827778
Frequencies --	9.2016	26.6217	97.4239		
Frequencies --	126.0226	136.5129	160.0549		
Frequencies --	182.5184	232.5979	255.4877		
Frequencies --	360.1208	429.5917	450.1572		
Frequencies --	489.3924	578.6185	729.2227		
Frequencies --	765.8449	851.5971	863.4689		
Frequencies --	923.6757	956.6147	979.0578		
Frequencies --	1023.6906	1069.1968	1319.2068		
Frequencies --	1327.6300	1379.4509	1426.2499		
Frequencies --	1470.6070	1653.8693	1674.2874		
Frequencies --	1718.7794	3177.9083	3197.5566		
Frequencies --	3208.8633	3269.0984	3310.8547		
Frequencies --	3778.6400	3813.3351	3915.1257		

Geometry b

Relative energy = 16.07 kcal mol⁻¹

1	6	0	-2.972277	-0.290171	-0.372847
---	---	---	-----------	-----------	-----------

2	6	0	-2.055182	0.635098	-0.086673
3	6	0	-0.636063	0.381440	0.147514
4	6	0	0.254566	1.339591	0.419638
5	8	0	-0.364014	-0.968085	0.057762
6	8	0	1.030535	-1.245275	0.265897
7	1	0	-2.720133	-1.335983	-0.454635
8	1	0	-4.001668	-0.009159	-0.534025
9	1	0	-2.335247	1.676922	-0.013598
10	1	0	1.069701	-1.327877	1.229880
11	1	0	1.303531	1.151305	0.566346
12	1	0	-0.100017	2.355969	0.469892
13	1	0	2.684342	-0.271024	-0.457974
14	8	0	3.471506	0.276853	-0.364030
15	1	0	3.449001	0.856157	-1.128717
Frequencies --	26.3764		80.2553		93.4152
Frequencies --	120.3937		152.5259		181.4691
Frequencies --	192.0226		241.8137		298.0946
Frequencies --	363.9711		439.4282		465.5648
Frequencies --	500.1938		581.9594		735.3764
Frequencies --	774.9849		856.1208		881.4772
Frequencies --	929.2280		958.1029		988.1722
Frequencies --	1022.7305		1069.5849		1317.6924
Frequencies --	1328.8220		1389.0893		1432.1536
Frequencies --	1475.3027		1652.1241		1667.0065
Frequencies --	1715.4983		3178.0457		3195.6407
Frequencies --	3201.0007		3270.1964		3298.2980
Frequencies --	3744.2286		3783.1508		3907.6372

anti,trans...H₂O

Relative energy = -3.96 kcal mol⁻¹

1	6	0	0.502759	-0.530908	-0.040525
2	8	0	-0.557746	-1.204586	-0.283864
3	8	0	-1.565217	-0.632306	-1.026483
4	8	0	-1.865696	1.189809	1.000324
5	1	0	-2.511715	0.878462	1.636905
6	1	0	-1.986430	0.602401	0.228125
7	6	0	0.700039	0.779689	-0.598049
8	6	0	1.794721	1.506221	-0.344643
9	1	0	-0.092263	1.135874	-1.235209
10	1	0	2.582188	1.158439	0.308080
11	1	0	1.919171	2.484508	-0.782971
12	6	0	1.475764	-1.233265	0.838470
13	1	0	1.115678	-2.233429	1.057719
14	1	0	1.589922	-0.684234	1.773165
15	1	0	2.453023	-1.295780	0.362849
Frequencies --	49.4309		69.1601		126.9246
Frequencies --	146.2738		162.4503		214.7714
Frequencies --	256.1720		308.5324		331.6080
Frequencies --	384.0414		405.0895		477.3556

Frequencies --	627.8561	722.8786	774.4368
Frequencies --	801.5273	934.0422	996.6085
Frequencies --	1001.7754	1049.3132	1057.4421
Frequencies --	1067.1525	1292.0431	1371.3492
Frequencies --	1430.2155	1434.0662	1470.9814
Frequencies --	1487.5212	1524.1467	1668.2012
Frequencies --	1678.2292	3063.0967	3126.1236
Frequencies --	3169.8606	3174.5228	3246.6946
Frequencies --	3267.5276	3506.6328	3891.2774

anti,cis...H₂O

Relative energy = -2.88 kcal mol⁻¹

1	6	0	0.492942	2.001152	0.040826
2	6	0	-0.555963	1.257901	-0.353437
3	6	0	-0.897727	-0.073605	0.057168
4	8	0	-0.244460	-0.812669	0.871531
5	8	0	0.953912	-0.371673	1.382346
6	6	0	-2.127248	-0.729000	-0.473605
7	8	0	1.935971	-0.814562	-1.201091
8	1	0	0.599021	3.003775	-0.349259
9	1	0	1.218535	1.617969	0.733413
10	1	0	-1.260002	1.679944	-1.058260
11	1	0	-2.017349	-0.882065	-1.547889
12	1	0	-2.284155	-1.688865	0.007583
13	1	0	-2.997395	-0.093158	-0.316379
14	1	0	1.824254	-0.679011	-0.243089
15	1	0	2.281685	-1.706045	-1.274127
Frequencies --	44.1500	66.0818	125.6064		
Frequencies --	142.2799	172.8292	194.7427		
Frequencies --	300.0454	312.1421	329.9431		
Frequencies --	368.6155	383.4176	413.4903		
Frequencies --	634.2084	715.9449	734.7861		
Frequencies --	818.1382	954.3371	1025.9549		
Frequencies --	1032.6593	1033.4561	1054.7801		
Frequencies --	1105.5990	1269.0253	1346.9081		
Frequencies --	1416.0047	1459.6556	1469.2495		
Frequencies --	1487.1046	1523.6652	1651.8002		
Frequencies --	1674.5818	3058.5127	3120.1840		
Frequencies --	3171.6983	3173.7647	3189.4565		
Frequencies --	3316.6378	3580.4946	3892.2086		

anti,trans...H₂O=anti,cis...H₂O

Geometry a

Relative energy = 2.97 kcal mol⁻¹

1	6	0	0.163221	2.016779	-0.114447
2	6	0	-0.689443	1.124935	-0.605383
3	6	0	-0.900523	-0.212897	-0.035092
4	6	0	-2.008865	-0.487804	0.913438
5	8	0	-0.193875	-1.214919	-0.349240

6	8	0	0.877192	-1.034809	-1.200961
7	1	0	0.825506	1.772397	0.702310
8	1	0	0.233200	2.998417	-0.558249
9	1	0	-1.329943	1.360660	-1.448599
10	1	0	-2.079190	-1.549448	1.130802
11	1	0	-2.950775	-0.126122	0.500633
12	1	0	-1.829912	0.066755	1.835683
13	1	0	1.937399	-0.377786	0.106745
14	8	0	2.213454	-0.006541	0.969978
15	1	0	2.633215	-0.740795	1.421361
Frequencies --		-156.8769	59.6181	126.7416	
Frequencies --		160.2462	173.7484	202.2182	
Frequencies --		235.2546	250.6306	313.5951	
Frequencies --		337.1840	403.4059	523.8421	
Frequencies --		614.4239	691.8397	795.5026	
Frequencies --		808.5329	918.1595	992.5158	
Frequencies --		1007.9969	1015.3548	1032.6755	
Frequencies --		1108.1189	1284.3942	1330.6004	
Frequencies --		1413.4804	1454.1093	1475.9875	
Frequencies --		1478.2113	1543.2840	1677.6597	
Frequencies --		1693.6016	3053.8027	3113.1901	
Frequencies --		3153.9258	3165.7002	3173.2901	
Frequencies --		3271.0651	3481.9512	3895.7840	

Geometry b

Relative energy = 3.19 kcal mol⁻¹

1	6	0	-1.410208	1.824285	0.014094
2	6	0	-0.693551	0.865838	-0.560421
3	6	0	-0.578340	-0.483883	0.008063
4	6	0	-1.368265	-1.621415	-0.524574
5	8	0	0.213131	-0.766137	0.955263
6	8	0	1.055931	0.214863	1.439151
7	1	0	-1.902529	1.675364	0.963950
8	1	0	-1.506085	2.794108	-0.449499
9	1	0	-0.171534	1.012741	-1.496436
10	1	0	-1.148627	-2.533229	0.022531
11	1	0	-1.119236	-1.759756	-1.578106
12	1	0	-2.432566	-1.393692	-0.471263
13	1	0	2.024410	0.185169	-0.096554
14	8	0	2.199222	0.025285	-1.046860
15	1	0	2.812077	0.718254	-1.298023
Frequencies --		-157.0894	48.1979	101.8422	
Frequencies --		137.8273	152.8159	203.6406	
Frequencies --		227.3128	257.8037	312.0105	
Frequencies --		328.9664	470.3643	523.4228	
Frequencies --		611.3910	693.7141	709.0625	
Frequencies --		799.9243	911.9615	975.0008	
Frequencies --		995.6496	1004.6362	1031.9230	
Frequencies --		1103.8764	1277.8132	1323.6416	

Frequencies --	1412.9140	1453.4750	1472.9391
Frequencies --	1478.6440	1544.1414	1695.4714
Frequencies --	1705.4387	3053.5222	3114.0954
Frequencies --	3167.5622	3170.9889	3194.4822
Frequencies --	3262.6214	3479.4929	3896.9657

anti,trans...H₂O=VHPOH

Geometry a

Relative energy = 9.50 kcal mol⁻¹

1	6	0	-0.060964	0.348874	-0.257893
2	8	0	1.104144	0.322443	-0.845143
3	8	0	1.775310	-0.892980	-0.423839
4	8	0	0.701112	-0.040932	1.549924
5	1	0	1.208043	0.740233	1.802977
6	1	0	1.368332	-0.593706	0.837969
7	6	0	-0.899577	-0.853879	-0.285482
8	6	0	-2.189293	-0.857695	0.045887
9	1	0	-0.392214	-1.739157	-0.634649
10	1	0	-2.693912	0.016126	0.430868
11	1	0	-2.777556	-1.757576	-0.050120
12	6	0	-0.666046	1.711249	-0.188051
13	1	0	0.116882	2.462255	-0.155407
14	1	0	-1.288423	1.792242	0.698268
15	1	0	-1.290405	1.880042	-1.064208
Frequencies --	-766.0672	76.9871	154.3111		
Frequencies --	185.7923	276.3150	292.3097		
Frequencies --	330.0388	404.9399	460.2178		
Frequencies --	480.1778	598.7133	611.1162		
Frequencies --	681.3080	716.3455	774.2926		
Frequencies --	885.5082	950.6225	985.5434		
Frequencies --	998.1127	1043.4725	1068.2890		
Frequencies --	1115.4939	1293.4962	1340.9066		
Frequencies --	1421.3128	1422.1262	1464.1920		
Frequencies --	1497.9532	1518.3014	1609.4665		
Frequencies --	1689.0270	1812.3004	3076.5471		
Frequencies --	3151.2677	3174.0378	3177.1669		
Frequencies --	3234.2172	3262.9730	3800.2828		

Geometry b

Relative energy = 8.81 kcal mol⁻¹

1	6	0	-0.049109	0.377978	-0.240168
2	8	0	1.126947	0.388183	-0.798726
3	8	0	1.792912	-0.850010	-0.447411
4	8	0	0.733872	-0.038785	1.548430
5	1	0	0.176333	-0.704826	1.963800
6	1	0	1.395115	-0.584810	0.834292
7	6	0	-0.883864	-0.824049	-0.364886
8	6	0	-2.178242	-0.861621	-0.047807
9	1	0	-0.366155	-1.676843	-0.776161

10	1	0	-2.695046	-0.018084	0.386214
11	1	0	-2.758985	-1.755870	-0.216151
12	6	0	-0.651197	1.732970	-0.089070
13	1	0	0.135311	2.461576	0.073332
14	1	0	-1.331641	1.744906	0.756808
15	1	0	-1.210309	1.987181	-0.988886
Frequencies --			-745.1645	98.5291	128.3402
Frequencies --			194.7012	274.9690	290.1252
Frequencies --			329.9074	410.0732	459.4679
Frequencies --			470.8369	595.8293	641.6124
Frequencies --			694.0950	719.1753	783.4741
Frequencies --			891.0935	957.4582	983.9842
Frequencies --			1001.3301	1046.8400	1070.7165
Frequencies --			1104.6322	1290.1523	1336.0323
Frequencies --			1419.1908	1426.2368	1460.3318
Frequencies --			1495.2773	1507.5237	1542.5180
Frequencies --			1683.1166	1875.6883	3076.8297
Frequencies --			3154.3186	3172.1687	3186.0913
Frequencies --			3227.7811	3260.6458	3832.2368

VHPOH

Geometry a

Relative energy = -26.38 kcal mol⁻¹

1	6	0	0.001754	0.347355	0.079629
2	8	0	1.051787	0.024753	-0.839713
3	8	0	1.782266	-1.118200	-0.334030
4	8	0	0.574729	0.682899	1.333042
5	1	0	0.996464	1.544131	1.240056
6	1	0	2.202669	-0.729864	0.447526
7	6	0	-0.887106	-0.836140	0.342141
8	6	0	-2.147870	-0.951168	-0.054476
9	1	0	-0.412260	-1.633597	0.893732
10	1	0	-2.656790	-0.177400	-0.609821
11	1	0	-2.715262	-1.842351	0.168318
12	6	0	-0.668586	1.541389	-0.571433
13	1	0	0.066826	2.331241	-0.717579
14	1	0	-1.464649	1.907590	0.070566
15	1	0	-1.076413	1.276020	-1.542358
Frequencies --			58.8681	156.1299	239.5871
Frequencies --			248.4048	288.6436	295.5697
Frequencies --			365.4981	388.6557	404.7531
Frequencies --			454.2048	497.3250	628.5350
Frequencies --			723.2871	762.0343	870.0899
Frequencies --			945.1639	953.4268	970.2892
Frequencies --			1032.0665	1039.5753	1130.1690
Frequencies --			1150.7350	1218.8760	1336.6346
Frequencies --			1394.7020	1406.2260	1426.3282
Frequencies --			1467.5029	1498.6449	1519.3882
Frequencies --			1714.0146	3071.3160	3146.1692

Frequencies --	3169.5006	3171.8245	3215.1879
Frequencies --	3255.8783	3730.8872	3803.7581

Geometry b

Relative energy = -28.54 kcal mol⁻¹

1	6	0	0.032573	0.409777	0.025494
2	8	0	1.329446	0.066005	-0.483071
3	8	0	1.574135	-1.323887	-0.127835
4	8	0	-0.003684	0.310457	1.420449
5	1	0	-0.024930	-0.630092	1.629284
6	1	0	2.277763	-1.198049	0.521191
7	6	0	-1.009151	-0.448695	-0.646571
8	6	0	-2.101219	-0.908592	-0.048255
9	1	0	-0.819681	-0.653808	-1.691858
10	1	0	-2.305128	-0.695446	0.991393
11	1	0	-2.824483	-1.502635	-0.586370
12	6	0	-0.103454	1.876792	-0.341807
13	1	0	0.699993	2.439694	0.126850
14	1	0	-1.060952	2.240390	0.019827
15	1	0	-0.054246	2.003651	-1.419824
Frequencies --	93.2146	136.8482	197.3803		
Frequencies --	218.2526	254.2255	293.6399		
Frequencies --	311.3784	382.2208	458.2974		
Frequencies --	501.9114	533.1771	602.3731		
Frequencies --	716.4808	773.6692	876.0991		
Frequencies --	937.6960	968.8371	976.2985		
Frequencies --	1040.2922	1048.1515	1102.0556		
Frequencies --	1171.2961	1263.8172	1319.8772		
Frequencies --	1359.9256	1385.0481	1422.5130		
Frequencies --	1458.0122	1496.6490	1501.7827		
Frequencies --	1703.6625	3077.6217	3161.2562		
Frequencies --	3165.8904	3167.6871	3191.8615		
Frequencies --	3255.2450	3781.7822	3803.4998		

anti,trans...H₂O=AHP...H₂O

Geometry a

Relative energy = 21.68 kcal mol⁻¹

1	6	0	0.303404	0.974816	0.038461
2	6	0	0.721753	-0.363217	0.033286
3	8	0	-0.051964	-1.360414	-0.260270
4	8	0	-1.314260	-1.032972	-0.861754
5	1	0	-0.901826	0.988992	0.565484
6	6	0	0.875077	2.033302	-0.534223
7	6	0	2.036767	-0.805764	0.580613
8	1	0	0.493652	3.029386	-0.356569
9	1	0	1.691124	1.951182	-1.244506
10	1	0	-1.808729	-0.332866	-0.079944
11	8	0	-2.124658	0.607173	0.704286
12	1	0	-2.277368	0.299361	1.603439

13	1	0	2.141304	-0.471189	1.610843
14	1	0	2.827595	-0.324473	0.003950
15	1	0	2.139292	-1.885511	0.530385
Frequencies --			-1617.1316	93.4341	117.5596
Frequencies --			156.1532	209.3185	266.2491
Frequencies --			295.0504	341.4218	469.3560
Frequencies --			513.9825	543.1889	602.5271
Frequencies --			638.5084	661.9232	752.1415
Frequencies --			820.5784	912.6893	991.3215
Frequencies --			1033.8029	1043.2842	1096.6395
Frequencies --			1245.0686	1308.4410	1381.8822
Frequencies --			1392.0930	1406.5819	1436.8604
Frequencies --			1479.1749	1489.8744	1534.4171
Frequencies --			1546.3747	1713.7599	1734.7203
Frequencies --			3060.6175	3122.2553	3128.8256
Frequencies --			3169.5414	3214.8391	3831.7935

Geometry b

Relative energy = 21.29 kcal mol⁻¹

1	6	0	0.283133	0.977742	0.030655
2	6	0	0.726868	-0.353668	0.029436
3	8	0	-0.024171	-1.366579	-0.265828
4	8	0	-1.303151	-1.062739	-0.842170
5	1	0	-0.905621	0.969589	0.580006
6	6	0	0.847140	2.039157	-0.544843
7	6	0	2.048331	-0.767424	0.581303
8	1	0	0.457560	3.033309	-0.372753
9	1	0	1.668587	1.962416	-1.249286
10	1	0	-1.789679	-0.384301	-0.046939
11	8	0	-2.078768	0.492468	0.839930
12	1	0	-2.754779	1.084097	0.494161
13	1	0	2.124963	-0.453197	1.620590
14	1	0	2.832246	-0.249426	0.027996
15	1	0	2.182611	-1.842534	0.511462
Frequencies --			-1579.1606	90.0409	123.4064
Frequencies --			157.6379	209.5987	266.6685
Frequencies --			294.7909	347.5860	455.0434
Frequencies --			526.7034	567.4724	582.2499
Frequencies --			634.0059	685.5202	746.8656
Frequencies --			824.8423	914.8717	985.9504
Frequencies --			1034.7025	1046.2654	1102.7353
Frequencies --			1199.5851	1260.8384	1311.7191
Frequencies --			1351.3159	1402.1852	1432.7856
Frequencies --			1478.6880	1489.9102	1536.7907
Frequencies --			1614.6585	1729.0537	1824.8393
Frequencies --			3061.5159	3122.5845	3129.5143
Frequencies --			3170.0530	3211.7163	3833.7874

AHP...H₂O

Geometry a

Relative energy = -6.91 kcal mol⁻¹

1	6	0	-0.624401	1.015594	0.112446
2	6	0	-0.838068	-0.272220	-0.011432
3	8	0	-0.019619	-1.265056	0.480104
4	8	0	1.016691	-0.712630	1.318904
5	1	0	1.437880	0.546875	-1.183862
6	6	0	-0.516771	2.305151	0.284470
7	6	0	-1.993133	-0.889772	-0.737307
8	1	0	0.025645	2.936970	-0.408967
9	1	0	-0.959780	2.797947	1.141972
10	1	0	1.673610	-0.467461	0.634004
11	8	0	2.279214	0.105767	-1.012504
12	1	0	2.290861	-0.640922	-1.617613
13	1	0	-1.639204	-1.544723	-1.533165
14	1	0	-2.620793	-0.115184	-1.166175
15	1	0	-2.584264	-1.490670	-0.047285
Frequencies --	51.8862		76.4725		146.2370
Frequencies --	149.3252		156.9621		179.0429
Frequencies --	223.6477		233.4389		283.4862
Frequencies --	295.0367		426.1347		444.3698
Frequencies --	477.3723		635.3040		654.5487
Frequencies --	761.0903		778.5411		923.2105
Frequencies --	930.7934		1012.9331		1041.7696
Frequencies --	1072.9719		1207.7811		1335.0640
Frequencies --	1416.8419		1485.5980		1493.4692
Frequencies --	1510.8598		1523.8538		1646.0169
Frequencies --	2049.9484		3058.6593		3119.6405
Frequencies --	3121.2609		3166.0610		3190.6588
Frequencies --	3517.0725		3762.6274		3890.1968

Geometry b

Relative energy = -6.61 kcal mol⁻¹

1	6	0	0.415322	1.067370	-0.181275
2	6	0	0.898486	-0.135078	0.022591
3	8	0	0.305726	-1.310940	-0.374304
4	8	0	-0.848575	-1.057362	-1.201633
5	1	0	-1.457498	0.286146	1.218656
6	6	0	0.043327	2.293374	-0.433067
7	6	0	2.167949	-0.438246	0.756979
8	1	0	-0.601963	2.850620	0.236544
9	1	0	0.363287	2.807794	-1.331718
10	1	0	-1.524717	-0.909587	-0.508296
11	8	0	-2.264835	-0.213564	1.043798
12	1	0	-2.922905	0.456118	0.838981
13	1	0	1.968488	-1.088860	1.607745
14	1	0	2.623666	0.481615	1.109145
15	1	0	2.862612	-0.953435	0.094687
Frequencies --	50.1646		87.0192		142.9584

Frequencies --	149.3477	158.7080	167.0358
Frequencies --	223.7866	234.6360	288.6377
Frequencies --	318.4374	418.3033	442.6383
Frequencies --	477.3767	632.9827	654.9138
Frequencies --	697.2521	778.8863	920.4341
Frequencies --	929.4444	1014.8930	1042.0460
Frequencies --	1073.3720	1210.0207	1335.2911
Frequencies --	1416.6933	1485.7834	1493.5879
Frequencies --	1523.2201	1533.2856	1650.6912
Frequencies --	2048.0531	3060.5511	3116.9570
Frequencies --	3122.8288	3166.5824	3185.3278
Frequencies --	3525.1606	3761.1085	3891.0181

anti,cis...H₂O=VHPOH

Geometry a

Relative energy = 10.86 kcal mol⁻¹

1	6	0	-0.388508	-0.350380	-0.210752
2	8	0	-0.311195	0.656681	-1.023936
3	8	0	0.601097	1.645685	-0.463307
4	8	0	-0.678676	0.806967	1.410648
5	1	0	-1.555363	1.198982	1.318992
6	1	0	-0.027221	1.412091	0.748594
7	6	0	0.772650	-1.023489	0.390931
8	6	0	2.037656	-0.802011	0.040803
9	1	0	0.518239	-1.797717	1.100519
10	1	0	2.291957	-0.006970	-0.641497
11	1	0	2.828880	-1.412160	0.450715
12	6	0	-1.621623	-1.174340	-0.395128
13	1	0	-2.430924	-0.569185	-0.790990
14	1	0	-1.908420	-1.609399	0.558707
15	1	0	-1.408009	-1.988985	-1.087403
Frequencies --	-674.5780	101.8342	148.5727		
Frequencies --	195.1035	268.4223	281.8501		
Frequencies --	314.7528	394.0978	396.6247		
Frequencies --	500.2505	605.5288	617.5990		
Frequencies --	664.3580	698.1845	791.3388		
Frequencies --	877.3650	990.8995	1009.3404		
Frequencies --	1018.1333	1021.4220	1089.3939		
Frequencies --	1159.3065	1250.3718	1344.9554		
Frequencies --	1409.2663	1451.0265	1465.6964		
Frequencies --	1493.0244	1536.3723	1609.0816		
Frequencies --	1689.2386	1824.0412	3068.0849		
Frequencies --	3141.3853	3174.9886	3176.1005		
Frequencies --	3203.7723	3280.3937	3804.9265		

Geometry b

Relative energy = 11.00 kcal mol⁻¹

1	6	0	-0.428855	-0.318181	-0.214489
2	8	0	-0.313221	0.702025	-1.004512

3	8	0	0.684613	1.612693	-0.461079
4	8	0	-0.673337	0.866203	1.388133
5	1	0	0.026316	1.433773	0.739005
6	1	0	-0.134718	0.530033	2.112040
7	6	0	0.706631	-1.096416	0.310396
8	6	0	1.985905	-0.906269	-0.011407
9	1	0	0.415112	-1.934469	0.929974
10	1	0	2.282551	-0.062393	-0.613191
11	1	0	2.739967	-1.596739	0.337253
12	6	0	-1.728696	-1.037255	-0.364871
13	1	0	-1.988267	-1.516079	0.575210
14	1	0	-1.625876	-1.811000	-1.126488
15	1	0	-2.509427	-0.341773	-0.651905
Frequencies --			-696.1114	103.3479	118.4113
Frequencies --			203.6312	272.2101	281.8229
Frequencies --			316.3765	393.6546	401.9063
Frequencies --			486.6747	614.5843	635.4449
Frequencies --			674.1498	699.6737	796.5493
Frequencies --			884.5974	983.6792	1013.6366
Frequencies --			1021.5052	1030.7381	1085.6974
Frequencies --			1132.4333	1246.3111	1344.4397
Frequencies --			1411.6678	1445.7731	1457.4424
Frequencies --			1491.9088	1506.4974	1570.4516
Frequencies --			1683.7050	1870.9907	3068.2243
Frequencies --			3144.8718	3170.5353	3184.8291
Frequencies --			3187.6561	3280.2180	3831.2141

VHPOH

Geometry a

Relative energy = -26.98 kcal mol⁻¹

1	6	0	-0.434176	-0.223139	0.049316
2	8	0	-0.160154	0.856789	-0.832798
3	8	0	0.630349	1.851133	-0.134189
4	8	0	-1.108875	0.267069	1.199004
5	1	0	-2.004795	0.501023	0.932304
6	1	0	0.059178	2.025786	0.630414
7	6	0	0.794731	-0.936398	0.544691
8	6	0	1.981395	-0.871087	-0.042331
9	1	0	0.632025	-1.554498	1.417612
10	1	0	2.144981	-0.238779	-0.901861
11	1	0	2.819228	-1.437488	0.335679
12	6	0	-1.326945	-1.138142	-0.775903
13	1	0	-2.234171	-0.610141	-1.070451
14	1	0	-1.593511	-2.010144	-0.183830
15	1	0	-0.803526	-1.463096	-1.670639
Frequencies --			97.3360	173.2096	221.3963
Frequencies --			238.3839	285.0856	306.4104
Frequencies --			327.0645	392.1530	449.3677
Frequencies --			457.3646	568.7384	601.2449

Frequencies --	697.1390	775.6259	882.3414
Frequencies --	943.5583	962.9693	977.3258
Frequencies --	1028.4957	1052.4216	1112.5386
Frequencies --	1180.3117	1204.4873	1320.9402
Frequencies --	1382.0702	1411.3412	1423.8875
Frequencies --	1460.7418	1493.7442	1508.8581
Frequencies --	1712.7621	3059.5616	3139.2879
Frequencies --	3163.6236	3171.4476	3191.4398
Frequencies --	3264.4236	3705.7594	3801.7305

Geometry b

Relative energy = -27.83 kcal mol⁻¹

1	6	0	-0.479325	-0.185478	0.054686
2	8	0	-0.043901	0.860097	-0.822213
3	8	0	0.824881	1.746865	-0.064732
4	8	0	-1.093485	0.345171	1.202741
5	1	0	0.230724	2.502545	0.028156
6	1	0	-0.387751	0.688009	1.761486
7	6	0	0.650511	-1.107595	0.437219
8	6	0	1.868978	-1.083358	-0.087795
9	1	0	0.387891	-1.836997	1.193870
10	1	0	2.139508	-0.357824	-0.839729
11	1	0	2.624074	-1.786888	0.230389
12	6	0	-1.551043	-0.894863	-0.751128
13	1	0	-1.889533	-1.771492	-0.204763
14	1	0	-1.149149	-1.205883	-1.711360
15	1	0	-2.390446	-0.220771	-0.902306
Frequencies --	104.1417	154.0731	208.2934		
Frequencies --	226.2055	251.2813	299.7956		
Frequencies --	325.5446	374.7833	438.7487		
Frequencies --	477.1720	561.6252	605.3659		
Frequencies --	705.1873	773.2915	882.3863		
Frequencies --	935.0130	968.1711	980.5835		
Frequencies --	1034.9798	1048.6518	1099.8717		
Frequencies --	1194.6209	1238.5412	1324.2960		
Frequencies --	1367.9514	1384.6870	1423.8268		
Frequencies --	1459.4309	1497.2096	1500.4669		
Frequencies --	1706.8475	3075.9029	3158.4723		
Frequencies --	3165.3588	3166.8158	3179.7441		
Frequencies --	3263.8458	3776.7739	3810.2997		

anti,cis...H₂O=VHPOH'

Geometry a

Relative energy = 11.74 kcal mol⁻¹

1	6	0	1.181696	-1.105939	-0.621422
2	6	0	-0.123216	-1.180428	-0.152020
3	6	0	-1.011849	-0.110341	-0.021072
4	8	0	-0.739039	1.154097	-0.083319
5	8	0	0.599650	1.560576	-0.359944

6	6	0	-2.459627	-0.341139	0.286392
7	8	0	2.227800	-0.005548	0.668072
8	1	0	1.775451	-2.008299	-0.617786
9	1	0	1.463794	-0.353269	-1.332398
10	1	0	-0.483472	-2.124135	0.229730
11	1	0	-2.578998	-1.209829	0.928832
12	1	0	-2.891005	0.532767	0.765251
13	1	0	-3.001900	-0.532278	-0.639758
14	1	0	1.549947	0.754006	0.378732
15	1	0	1.936864	-0.304869	1.537654
Frequencies --			-451.3264	65.0174	110.6201
Frequencies --			227.7562	278.6256	304.7792
Frequencies --			319.7197	408.6109	448.6185
Frequencies --			562.8341	613.3668	656.3177
Frequencies --			704.6316	739.7717	831.8753
Frequencies --			890.6157	991.4057	1040.1498
Frequencies --			1057.7057	1112.3887	1157.8441
Frequencies --			1229.5522	1258.1369	1290.5621
Frequencies --			1416.7735	1448.8475	1485.2244
Frequencies --			1493.4663	1541.9056	1565.1270
Frequencies --			1697.3704	2060.1566	3066.0558
Frequencies --			3134.0600	3168.0256	3188.4964
Frequencies --			3204.9873	3305.3259	3809.4140

Geometry b

Relative energy = 11.65 kcal mol⁻¹

1	6	0	1.176175	-1.119960	-0.598814
2	6	0	-0.134488	-1.181748	-0.143371
3	6	0	-1.015770	-0.108200	-0.022925
4	8	0	-0.739086	1.156601	-0.097632
5	8	0	0.611049	1.541843	-0.359195
6	6	0	-2.464637	-0.327176	0.288110
7	8	0	2.115162	-0.049638	0.772260
8	1	0	1.758732	-2.029269	-0.572430
9	1	0	1.459437	-0.382629	-1.325916
10	1	0	-0.495723	-2.115499	0.259617
11	1	0	-2.589570	-1.205918	0.915094
12	1	0	-2.882251	0.542530	0.786521
13	1	0	-3.014704	-0.493190	-0.638297
14	1	0	1.483994	0.741569	0.412075
15	1	0	3.015408	0.174462	0.501871
Frequencies --			-519.6163	53.1173	109.6619
Frequencies --			227.0268	285.2376	306.7603
Frequencies --			321.4268	417.5422	439.8591
Frequencies --			573.6071	613.3627	657.9144
Frequencies --			732.2839	740.1208	835.3925
Frequencies --			891.0237	983.4814	1040.2060
Frequencies --			1059.3293	1104.9590	1120.0779
Frequencies --			1207.9229	1254.7307	1292.0503

Frequencies --	1416.7748	1445.4571	1485.1901
Frequencies --	1493.8964	1537.9054	1551.6986
Frequencies --	1718.6760	1890.5637	3066.4609
Frequencies --	3135.6372	3168.8694	3184.9716
Frequencies --	3210.8343	3299.5086	3782.1838

VHPOH'

Geometry a

Relative energy = -20.65 kcal mol⁻¹

1	6	0	1.502722	-0.866820	-0.424407
2	6	0	0.028286	-1.103276	-0.299031
3	6	0	-0.942073	-0.215242	-0.032206
4	8	0	-0.834620	1.133058	0.142981
5	8	0	0.371928	1.700828	-0.412714
6	6	0	-2.375012	-0.588153	0.191714
7	8	0	2.042984	-0.075121	0.660001
8	1	0	2.017835	-1.826773	-0.458795
9	1	0	1.765791	-0.313658	-1.321493
10	1	0	-0.304730	-2.126605	-0.386805
11	1	0	-2.496462	-1.666392	0.158629
12	1	0	-2.712873	-0.225529	1.162021
13	1	0	-3.005813	-0.129206	-0.568223
14	1	0	1.056242	1.343666	0.193923
15	1	0	1.754139	-0.484672	1.482180
Frequencies --	116.9832	136.7951	170.9232		
Frequencies --	237.4197	272.5092	318.6126		
Frequencies --	356.1842	420.0098	486.2482		
Frequencies --	596.2211	679.0309	733.6570		
Frequencies --	769.3643	836.9906	914.3297		
Frequencies --	972.5143	1024.5142	1035.6495		
Frequencies --	1076.8781	1118.5148	1194.8865		
Frequencies --	1224.5794	1364.2247	1379.0228		
Frequencies --	1418.7083	1427.0220	1484.0339		
Frequencies --	1503.6347	1510.8655	1527.3541		
Frequencies --	1712.0466	3062.2105	3066.9710		
Frequencies --	3122.0853	3129.4466	3162.2357		
Frequencies --	3205.1317	3476.1743	3810.9337		

Geometry b

Relative energy = -19.39 kcal mol⁻¹

1	6	0	1.490886	-0.866167	-0.425176
2	6	0	0.023667	-1.098123	-0.255849
3	6	0	-0.958991	-0.213597	-0.032898
4	8	0	-0.886408	1.142335	0.080062
5	8	0	0.369535	1.697329	-0.364033
6	6	0	-2.385128	-0.603828	0.207766
7	8	0	1.999327	-0.121700	0.711889
8	1	0	1.992591	-1.832336	-0.470572
9	1	0	1.714718	-0.316972	-1.339932
10	1	0	-0.297312	-2.128072	-0.265130
11	1	0	-2.490620	-1.683769	0.181673
12	1	0	-2.717309	-0.240502	1.179539
13	1	0	-3.030243	-0.160094	-0.549227
14	1	0	0.998547	1.315318	0.284585
15	1	0	2.947393	-0.006993	0.592666
Frequencies --	114.1636		131.0879		164.6963
Frequencies --	231.3946		270.9307		319.2052
Frequencies --	362.3171		390.3695		483.7937
Frequencies --	592.0545		651.4890		697.8492
Frequencies --	765.7936		837.5721		918.0522
Frequencies --	988.3888		1025.9377		1061.2584
Frequencies --	1078.2323		1112.2956		1210.9950
Frequencies --	1241.9220		1283.1551		1387.3697
Frequencies --	1422.5277		1453.1533		1483.9119
Frequencies --	1505.1795		1521.8337		1531.5533
Frequencies --	1720.5676		3052.8464		3063.1287
Frequencies --	3092.5907		3123.0977		3163.6576
Frequencies --	3212.8775		3492.0836		3817.3314

5.3 MVK-oxide + SO₂

Syn-trans; endo

syn,trans...SO₂

1	6	0	1.311109	0.345350	-0.209375
2	8	0	0.362537	0.503429	-1.056591
3	8	0	-0.632142	1.399004	-0.710766
4	6	0	1.409318	1.217912	0.974013
5	6	0	2.242344	-0.684275	-0.604152
6	1	0	1.155129	2.232114	0.669745
7	1	0	0.660746	0.906862	1.700368
8	1	0	2.397493	1.173493	1.416686
9	1	0	1.999064	-1.194353	-1.525464
10	6	0	3.318454	-1.029680	0.110503
11	1	0	3.572002	-0.548981	1.042587
12	1	0	3.967801	-1.822831	-0.226365
13	16	0	-2.051709	-0.120369	0.400535
14	8	0	-0.930287	-0.777883	1.093355

15	8	0	-2.626639	-0.864081	-0.715005
Frequencies --	43.9908		59.0891		107.1044
Frequencies --	120.3070		151.7698		153.3231
Frequencies --	201.5872		270.5415		291.4578
Frequencies --	340.6993		359.4257		456.4786
Frequencies --	496.1234		526.9041		600.8922
Frequencies --	688.5251		809.4764		942.7130
Frequencies --	995.3231		1014.8939		1028.0444
Frequencies --	1049.5269		1071.1873		1106.3835
Frequencies --	1278.9453		1312.2044		1343.8888
Frequencies --	1398.1147		1454.0322		1471.3221
Frequencies --	1504.1864		1506.2464		1675.7023
Frequencies --	3074.6456		3138.7306		3182.0912
Frequencies --	3189.5210		3209.4786		3275.2279

syn-trans...SO₂ = SOZ

1	6	0	-1.048953	0.326164	0.232035
2	8	0	-0.167040	0.505860	1.168655
3	8	0	0.930174	1.285150	0.769924
4	6	0	-1.349697	1.366447	-0.783806
5	6	0	-1.954410	-0.760475	0.558780
6	1	0	-0.507744	2.036212	-0.890137
7	1	0	-1.580017	0.907446	-1.738432
8	1	0	-2.222431	1.924200	-0.436409
9	1	0	-1.641755	-1.390528	1.378690
10	6	0	-3.082346	-0.997546	-0.113981
11	1	0	-3.393034	-0.385517	-0.947113
12	1	0	-3.718728	-1.826951	0.153285
13	16	0	1.811584	-0.131809	-0.473040
14	8	0	0.483112	-0.516972	-1.065376
15	8	0	2.340104	-1.119471	0.463120
Frequencies --	-172.4600		72.5411		96.7084
Frequencies --	176.3007		188.1187		203.9954
Frequencies --	244.3385		277.0329		354.5020
Frequencies --	375.1692		427.1594		478.1019
Frequencies --	495.1429		552.4431		596.1116
Frequencies --	690.2365		801.6257		940.5472
Frequencies --	978.0869		1001.8076		1008.0748
Frequencies --	1028.9826		1068.6190		1077.9155
Frequencies --	1243.4173		1310.4264		1349.2203
Frequencies --	1401.5745		1443.9629		1464.9777
Frequencies --	1497.4740		1504.4880		1683.5791
Frequencies --	3058.6222		3161.8023		3181.6111
Frequencies --	3215.2830		3218.4911		3272.7976

SOZ

1	6	0	-0.810866	0.210377	-0.022436
2	8	0	-0.115855	0.371045	1.209972
3	8	0	1.142045	1.007981	0.821016

4	6	0	-1.420496	1.503020	-0.509191
5	6	0	-1.728288	-0.951062	0.204200
6	1	0	-0.645604	2.261924	-0.563145
7	1	0	-1.850944	1.365390	-1.497444
8	1	0	-2.191085	1.835134	0.181579
9	1	0	-1.216624	-1.851468	0.514245
10	6	0	-3.044724	-0.918906	0.041466
11	1	0	-3.566516	-0.026945	-0.270702
12	1	0	-3.641479	-1.801243	0.215963
13	16	0	1.739115	-0.003209	-0.404496
14	8	0	0.207454	-0.208514	-0.981424
15	8	0	2.180438	-1.269514	0.151336
Frequencies --	72.1395		83.9393		185.3454
Frequencies --	255.6892		287.8302		290.3490
Frequencies --	323.3446		383.4275		426.5892
Frequencies --	474.0264		485.8914		560.9295
Frequencies --	643.5201		651.0299		664.1314
Frequencies --	744.0322		788.4121		835.6166
Frequencies --	895.6685		934.7505		986.8967
Frequencies --	1034.2859		1036.2261		1117.0259
Frequencies --	1187.2859		1259.7703		1299.4224
Frequencies --	1332.1137		1421.2332		1461.7920
Frequencies --	1501.2734		1508.2993		1709.3089
Frequencies --	3081.2734		3162.8175		3168.5959
Frequencies --	3177.2524		3205.3243		3264.6000

SOZ = SOZ'

1	6	0	-0.847639	0.162309	-0.060086
2	16	0	1.700713	0.153586	-0.346480
3	8	0	1.138013	0.406572	1.241100
4	8	0	-0.302221	0.585166	1.238309
5	8	0	0.208035	-0.466602	-0.766873
6	6	0	-1.334630	1.398666	-0.782488
7	6	0	-1.865589	-0.890803	0.245541
8	1	0	-2.098553	1.900783	-0.194820
9	1	0	-1.739638	1.131311	-1.755411
10	1	0	-0.502821	2.084971	-0.922412
11	6	0	-3.163093	-0.797152	-0.016721
12	1	0	-1.448557	-1.762579	0.730602
13	1	0	-3.594198	0.067877	-0.497806
14	1	0	-3.837443	-1.597243	0.248066
15	8	0	2.615612	-0.965213	-0.260288
Frequencies --	-180.1149		54.0427		89.1287
Frequencies --	244.6280		271.3617		281.1275
Frequencies --	295.3848		366.1179		392.3921
Frequencies --	435.7800		468.1111		544.9621
Frequencies --	599.8537		656.1245		694.0788
Frequencies --	732.2315		810.4111		866.9843
Frequencies --	931.2864		949.9810		981.3546

Frequencies --	1030.7971	1042.1053	1113.1599
Frequencies --	1192.3260	1271.7153	1288.2060
Frequencies --	1331.2705	1422.6896	1461.8080
Frequencies --	1494.3423	1509.3856	1707.9555
Frequencies --	3074.2157	3153.6338	3161.6426
Frequencies --	3176.4577	3202.1638	3263.2218

SOZ'

1	6	0	0.848155	-0.372341	-0.050003
2	16	0	-1.700029	-0.127067	-0.332040
3	8	0	-1.015350	-0.443867	1.235632
4	8	0	0.269870	-1.072385	1.042397
5	8	0	-0.232607	-0.358200	-1.035797
6	6	0	1.946571	-1.254082	-0.587142
7	6	0	1.216625	1.033716	0.319336
8	1	0	2.732503	-1.362162	0.155517
9	1	0	2.362417	-0.814681	-1.488923
10	1	0	1.531517	-2.228815	-0.822522
11	6	0	2.407956	1.579909	0.108251
12	1	0	0.425099	1.603019	0.784636
13	1	0	3.219323	1.045240	-0.362458
14	1	0	2.603840	2.598932	0.405799
15	8	0	-2.045672	1.282993	-0.254989
Frequencies --	70.7843	112.9503	188.8152		
Frequencies --	216.0415	250.8206	299.2589		
Frequencies --	337.5532	360.2643	387.9994		
Frequencies --	437.6159	495.8934	547.4546		
Frequencies --	606.2036	667.1724	703.4317		
Frequencies --	757.4715	784.7002	832.5222		
Frequencies --	908.0846	947.0281	979.6173		
Frequencies --	1036.3545	1042.5875	1122.9048		
Frequencies --	1186.0015	1251.4788	1310.2085		
Frequencies --	1352.0258	1421.1886	1466.4078		
Frequencies --	1500.7091	1506.7893	1708.8968		
Frequencies --	3086.5516	3169.2442	3174.5349		
Frequencies --	3177.4720	3213.5355	3260.3609		

SOZ' = MVK + SO₃

1	8	0	0.268666	0.387733	1.287376
2	6	0	0.854924	0.245856	0.094638
3	8	0	-0.209985	-0.312955	-0.909070
4	16	0	-1.690468	-0.037483	-0.364985
5	8	0	-1.367533	1.082298	0.612173
6	8	0	-2.299841	-1.260266	0.130902
7	6	0	1.393812	1.503594	-0.542399
8	6	0	1.790829	-0.937246	0.239469
9	6	0	3.088824	-0.885572	-0.026553
10	1	0	0.596203	2.238434	-0.594597
11	1	0	1.772095	1.305811	-1.541350

12	1	0	2.191488	1.902718	0.079789
13	1	0	1.308823	-1.828074	0.612782
14	1	0	3.572867	0.007988	-0.389188
15	1	0	3.705215	-1.761415	0.110345
Frequencies --			-450.0671	78.7750	90.7688
Frequencies --			163.8373	254.1774	278.8818
Frequencies --			291.2274	311.7642	359.7220
Frequencies --			407.5348	434.9676	483.7795
Frequencies --			549.3286	556.3118	616.6765
Frequencies --			667.2262	775.1922	832.5499
Frequencies --			907.0316	948.6545	968.4700
Frequencies --			1020.6555	1042.7559	1090.9731
Frequencies --			1187.1692	1252.4011	1290.6189
Frequencies --			1327.4357	1417.1863	1448.0406
Frequencies --			1498.4711	1502.8134	1687.5787
Frequencies --			3079.7277	3159.8213	3172.1172
Frequencies --			3176.9569	3221.7848	3265.9236

MVK

1	6	0	-0.468498	-1.879311	0.000000
2	6	0	-0.887861	-0.614171	0.000000
3	6	0	0.000000	0.574545	0.000000
4	8	0	-0.490257	1.689933	0.000000
5	6	0	1.497998	0.373306	0.000000
6	1	0	0.581237	-2.134287	0.000000
7	1	0	-1.168614	-2.701731	0.000000
8	1	0	-1.942964	-0.375221	0.000000
9	1	0	1.980827	1.344719	0.000000
10	1	0	1.810871	-0.189581	0.878903
11	1	0	1.810871	-0.189581	-0.878903
Frequencies --			121.9725	130.7326	281.7531
Frequencies --			433.2220	489.3543	537.8415
Frequencies --			700.4204	769.8615	951.4588
Frequencies --			994.8900	1047.6423	1055.0048
Frequencies --			1077.8724	1280.3410	1314.1765
Frequencies --			1398.3095	1455.8343	1485.3347
Frequencies --			1492.8355	1679.8415	1738.4354
Frequencies --			3061.5825	3126.2050	3169.3574
Frequencies --			3173.3711	3196.0384	3256.1623

syn-trans; exo
syn-trans...SO₂

1	6	0	1.236440	0.390605	0.151715
2	8	0	0.531658	1.231267	-0.511902
3	8	0	-0.698475	1.566097	0.030360
4	6	0	0.853829	-0.015215	1.518422
5	6	0	2.440205	0.006535	-0.547209
6	1	0	0.373840	0.833874	2.001684
7	1	0	0.112485	-0.809683	1.476293

8	1	0	1.720614	-0.353260	2.075580
9	1	0	2.567783	0.448503	-1.525056
10	6	0	3.332282	-0.862677	-0.061322
11	1	0	3.213087	-1.333555	0.902154
12	1	0	4.204064	-1.132818	-0.636936
13	16	0	-1.981897	-0.265887	-0.441372
14	8	0	-0.833566	-1.076429	-0.884748
15	8	0	-2.456875	-0.535231	0.916114
Frequencies --	57.0917		72.7004		84.0406
Frequencies --	127.4748		152.7600		183.4696
Frequencies --	224.9502		265.0922		313.7244
Frequencies --	347.3043		366.5307		454.8247
Frequencies --	497.4793		524.0630		602.8360
Frequencies --	690.4562		809.0349		938.2261
Frequencies --	999.9873		1007.4196		1027.3797
Frequencies --	1051.0598		1072.4356		1101.9211
Frequencies --	1265.6009		1312.3075		1346.9207
Frequencies --	1400.8599		1451.5061		1470.9465
Frequencies --	1502.7602		1510.9854		1676.4860
Frequencies --	3079.0081		3147.2198		3180.5378
Frequencies --	3186.1877		3210.9597		3275.6186

syn-trans...SO₂ = SOZ

1	6	0	1.015510	0.302431	0.248281
2	8	0	0.388404	1.420436	0.019286
3	8	0	-0.942872	1.412902	0.449094
4	6	0	0.745309	-0.540890	1.442817
5	6	0	2.258943	0.236659	-0.500454
6	1	0	-0.251816	-0.367311	1.822691
7	1	0	0.854319	-1.590591	1.194434
8	1	0	1.485635	-0.277088	2.201787
9	1	0	2.375865	0.984563	-1.271158
10	6	0	3.192724	-0.691806	-0.285424
11	1	0	3.078440	-1.456637	0.467523
12	1	0	4.096171	-0.710615	-0.875189
13	16	0	-1.767337	-0.163050	-0.568130
14	8	0	-0.420516	-0.671740	-1.012252
15	8	0	-2.354532	-0.888083	0.558706
Frequencies --	-167.7993		91.1538		110.1131
Frequencies --	159.7578		187.1136		247.0902
Frequencies --	266.6364		284.8685		345.7335
Frequencies --	394.7844		410.2281		474.9027
Frequencies --	501.1198		537.0575		602.0049
Frequencies --	690.2732		801.1307		948.5216
Frequencies --	983.4073		1000.2142		1006.4490
Frequencies --	1028.6333		1066.6902		1080.4563
Frequencies --	1232.2081		1309.2590		1351.2467
Frequencies --	1407.1312		1438.6424		1464.6375
Frequencies --	1495.2816		1507.5699		1684.6645

Frequencies --	3055.7108	3161.6268	3182.1052
Frequencies --	3213.7608	3218.5836	3273.3685

SOZ

1	6	0	-0.796759	0.007833	0.094681
2	8	0	-0.321012	-1.084616	0.869362
3	8	0	1.097683	-0.838653	1.009361
4	6	0	-0.802549	1.314193	0.854941
5	6	0	-2.095677	-0.456136	-0.484579
6	1	0	0.184364	1.510115	1.260075
7	1	0	-1.072421	2.127871	0.187250
8	1	0	-1.518233	1.259142	1.671205
9	1	0	-2.021490	-1.380097	-1.040618
10	6	0	-3.252938	0.179585	-0.353186
11	1	0	-3.344714	1.104208	0.195975
12	1	0	-4.150914	-0.216053	-0.802877
13	16	0	1.693998	-0.232978	-0.505424
14	8	0	0.157025	0.063183	-1.012056
15	8	0	2.379677	0.991288	-0.123588
Frequencies --	71.8977	101.2198	193.7868		
Frequencies --	230.0141	257.3903	306.0574		
Frequencies --	344.3281	382.5171	385.3521		
Frequencies --	440.0113	498.3458	549.7680		
Frequencies --	619.0751	647.3337	662.0985		
Frequencies --	746.9057	790.1960	887.5937		
Frequencies --	897.4436	942.8491	991.9983		
Frequencies --	1031.1810	1034.3584	1118.5892		
Frequencies --	1187.8736	1248.3406	1311.2663		
Frequencies --	1332.2939	1427.3591	1462.2944		
Frequencies --	1504.4116	1511.8488	1710.5720		
Frequencies --	3084.0662	3162.3347	3178.0671		
Frequencies --	3181.2154	3204.8200	3266.0589		

SOZ = SOZ'

1	6	0	-0.771401	0.079359	0.081826
2	16	0	1.705098	-0.200138	-0.494836
3	8	0	1.146660	-1.153744	0.762592
4	8	0	-0.241030	-0.812745	1.099287
5	8	0	0.159946	0.018694	-1.016757
6	8	0	2.235585	1.049767	0.028730
7	6	0	-0.874703	1.481217	0.641405
8	6	0	-2.039774	-0.553881	-0.401717
9	1	0	-1.569386	1.490702	1.477379
10	1	0	-1.224381	2.165439	-0.127842
11	1	0	0.101665	1.804527	0.986063
12	6	0	-3.244508	-0.003603	-0.322052
13	1	0	-1.897695	-1.539807	-0.822492
14	1	0	-3.403850	0.977072	0.099911
15	1	0	-4.114903	-0.530051	-0.683232

Frequencies --	-128.6963	82.5424	136.2609
Frequencies --	248.9685	255.3495	295.3057
Frequencies --	352.5496	372.8959	388.6703
Frequencies --	411.7868	507.3882	598.7262
Frequencies --	641.4672	652.5990	689.8590
Frequencies --	745.2134	802.6924	849.4882
Frequencies --	886.9147	941.7272	985.4665
Frequencies --	1029.0111	1034.8454	1116.2608
Frequencies --	1182.5865	1244.6799	1290.5690
Frequencies --	1331.4208	1424.6902	1460.5608
Frequencies --	1503.5271	1509.7037	1708.3981
Frequencies --	3080.4549	3158.4946	3176.8937
Frequencies --	3180.8852	3200.6762	3264.4480

SOZ'

1	6	0	-0.787569	0.291556	0.096676
2	16	0	1.642177	-0.408203	-0.454036
3	8	0	0.871613	-1.005404	0.942438
4	8	0	-0.060773	0.059587	1.299220
5	8	0	0.210895	0.230810	-0.966674
6	8	0	2.525421	0.692026	-0.113254
7	6	0	-1.313489	1.702952	0.193916
8	6	0	-1.782312	-0.801371	-0.150581
9	1	0	-2.019966	1.785733	1.015723
10	1	0	-1.808761	1.973030	-0.734222
11	1	0	-0.476298	2.373112	0.361054
12	6	0	-3.072512	-0.614991	-0.399116
13	1	0	-1.366201	-1.798473	-0.105191
14	1	0	-3.515240	0.368479	-0.451773
15	1	0	-3.730327	-1.455672	-0.560219
Frequencies --	68.6685	88.5478	179.9058		
Frequencies --	230.5303	262.9262	297.1211		
Frequencies --	333.8729	369.9032	424.6329		
Frequencies --	466.1481	483.9051	554.3839		
Frequencies --	635.3846	662.1696	692.3499		
Frequencies --	763.4537	782.9097	848.0047		
Frequencies --	854.4974	945.3141	979.8726		
Frequencies --	1032.5001	1037.4845	1124.6301		
Frequencies --	1189.4902	1259.8852	1302.3925		
Frequencies --	1337.6638	1419.4249	1465.4764		
Frequencies --	1500.2241	1507.3283	1710.2486		
Frequencies --	3084.2149	3166.5541	3173.4626		
Frequencies --	3177.3086	3200.0141	3259.5848		

SOZ' = MVK + SO₃

1	8	0	-0.186754	0.192973	1.396827
2	6	0	-0.837553	0.295080	0.233370
3	8	0	0.224710	0.295761	-0.911001
4	16	0	1.598019	-0.362493	-0.406400

5	8	0	1.045713	-1.107803	0.804439
6	8	0	2.614303	0.656553	-0.204869
7	6	0	-1.415870	1.711510	0.133287
8	6	0	-1.756056	-0.847164	-0.075644
9	6	0	-3.007592	-0.729336	-0.501939
10	1	0	-0.625675	2.425789	0.337169
11	1	0	-2.211042	1.818450	0.864416
12	1	0	-1.806436	1.870237	-0.867181
13	1	0	-1.321978	-1.819286	0.113177
14	1	0	-3.468637	0.228894	-0.689570
15	1	0	-3.615890	-1.604613	-0.673224
Frequencies --		-473.4865	74.2209	96.4266	
Frequencies --		160.8422	250.7272	261.1170	
Frequencies --		285.6100	321.8525	356.5760	
Frequencies --		410.8617	439.1278	484.1888	
Frequencies --		550.4309	559.5446	620.4054	
Frequencies --		714.5322	776.5328	833.6393	
Frequencies --		896.7259	977.2618	981.8632	
Frequencies --		1002.5179	1033.9802	1076.8321	
Frequencies --		1200.8184	1252.2579	1281.5727	
Frequencies --		1329.7380	1395.5760	1463.9511	
Frequencies --		1494.6021	1505.6603	1704.4290	
Frequencies --		3087.7173	3173.3040	3176.9059	
Frequencies --		3186.7751	3202.0907	3259.1691	

syn-cis; endo

syn-cis...SO₂

1	6	0	-1.396102	-0.416273	-0.127917
2	8	0	-0.540530	-0.188874	-1.048961
3	8	0	0.480149	-1.133281	-1.173323
4	6	0	-1.486764	-1.735925	0.522970
5	6	0	-2.294559	0.687029	0.150232
6	1	0	-1.295027	-2.510968	-0.217227
7	1	0	-0.699473	-1.807794	1.271641
8	1	0	-2.454860	-1.855646	0.999713
9	16	0	1.892903	-0.070201	0.288799
10	8	0	0.873203	0.007544	1.351876
11	8	0	2.114468	1.181301	-0.434241
12	1	0	-3.266453	0.432495	0.547220
13	6	0	-1.907238	1.958682	0.003600
14	1	0	-0.902133	2.198807	-0.311735
15	1	0	-2.578839	2.771724	0.233492
Frequencies --		43.2671	70.2224	104.1838	
Frequencies --		134.6299	158.8260	169.6804	
Frequencies --		205.9363	241.2487	308.6136	
Frequencies --		341.5754	361.2506	442.9580	
Frequencies --		515.1565	532.0978	617.5337	
Frequencies --		666.9368	812.7348	929.5168	
Frequencies --		1006.0134	1027.1538	1033.5241	

Frequencies --	1036.5175	1101.2979	1105.6093
Frequencies --	1263.0818	1284.9026	1343.2089
Frequencies --	1395.4818	1453.2569	1458.6708
Frequencies --	1498.2911	1514.5928	1672.4294
Frequencies --	3069.0380	3138.0126	3171.8518
Frequencies --	3173.9184	3210.2599	3273.9748

syn-cis...SO₂ = SOZ

1	6	0	1.203998	-0.416266	0.117429
2	8	0	0.439098	-0.187720	1.137028
3	8	0	-0.701695	-1.011974	1.194873
4	6	0	1.398031	-1.768751	-0.454732
5	6	0	2.139276	0.664026	-0.151845
6	1	0	0.568948	-2.416370	-0.206011
7	1	0	1.517635	-1.701055	-1.531027
8	1	0	2.323953	-2.165313	-0.027205
9	1	0	3.096366	0.383683	-0.567964
10	6	0	1.799172	1.941646	0.037930
11	1	0	0.805490	2.204259	0.371847
12	1	0	2.495474	2.738171	-0.176115
13	16	0	-1.735547	-0.070347	-0.344503
14	8	0	-0.546041	-0.115784	-1.253828
15	8	0	-1.976610	1.260259	0.216405
Frequencies --	-129.5665	64.7575	104.4926		
Frequencies --	169.9394	190.3104	194.2593		
Frequencies --	237.0143	256.7082	349.0032		
Frequencies --	363.4854	432.7902	455.1087		
Frequencies --	525.1393	547.2784	612.8386		
Frequencies --	681.1048	809.8750	932.1484		
Frequencies --	981.2245	1010.1798	1027.1060		
Frequencies --	1032.5378	1066.4216	1094.6932		
Frequencies --	1229.5193	1292.0716	1346.1600		
Frequencies --	1409.7243	1420.0289	1477.7869		
Frequencies --	1490.4436	1497.8665	1675.8051		
Frequencies --	3043.4646	3150.8782	3171.6071		
Frequencies --	3206.2721	3219.4754	3272.1975		

SOZ

1	6	0	0.907295	-0.405427	-0.025360
2	8	0	0.190774	-0.594452	1.193233
3	8	0	-1.109741	-1.094304	0.746435
4	6	0	1.394320	-1.711856	-0.615207
5	6	0	2.009227	0.558704	0.304050
6	1	0	0.561199	-2.398470	-0.735995
7	1	0	1.850396	-1.525677	-1.584498
8	1	0	2.132902	-2.159123	0.046405
9	1	0	2.861998	0.119246	0.803097
10	6	0	1.966315	1.854067	0.022745
11	1	0	1.115177	2.290310	-0.476584

12	1	0	2.787212	2.502629	0.288658
13	16	0	-1.602317	0.056679	-0.400700
14	8	0	-0.045285	0.190147	-0.937642
15	8	0	-1.952593	1.310022	0.242067
Frequencies --	44.9461		78.5191		189.8789
Frequencies --	241.3992		251.7340		286.2888
Frequencies --	331.3636		364.6086		421.6027
Frequencies --	475.6638		546.6402		569.2323
Frequencies --	607.3737		649.3898		679.1661
Frequencies --	739.8702		801.4266		832.4554
Frequencies --	896.7450		939.2530		997.2198
Frequencies --	1018.4852		1045.0085		1137.7855
Frequencies --	1181.3033		1254.2441		1271.6650
Frequencies --	1332.7052		1418.0835		1457.5890
Frequencies --	1498.1322		1501.3975		1705.1443
Frequencies --	3074.1596		3153.8069		3164.8350
Frequencies --	3177.4631		3197.9810		3273.2407

SOZ = SOZ'

1	6	0	0.911327	-0.378097	-0.142746
2	16	0	-1.635035	-0.222030	-0.250163
3	8	0	-0.987060	-0.576716	1.256376
4	8	0	0.467849	-0.410597	1.230748
5	8	0	-0.231095	-0.716859	-0.954211
6	6	0	1.938869	-1.472741	-0.335160
7	6	0	1.429591	0.987001	-0.501228
8	1	0	2.772196	-1.303076	0.342328
9	1	0	2.309369	-1.456595	-1.357764
10	1	0	1.484812	-2.436986	-0.124481
11	6	0	1.557798	1.990066	0.355837
12	1	0	1.720789	1.092907	-1.538230
13	1	0	1.259404	1.885422	1.387439
14	1	0	1.950759	2.942716	0.035174
15	8	0	-1.794981	1.213011	-0.408173
Frequencies --	-120.1622		82.7292		128.5310
Frequencies --	218.2618		255.5735		285.7301
Frequencies --	300.8523		363.1113		385.3828
Frequencies --	480.4077		531.5594		575.0967
Frequencies --	612.1847		677.0763		712.8606
Frequencies --	736.0692		797.6061		856.6195
Frequencies --	879.9283		953.0834		987.1970
Frequencies --	1024.8840		1041.6467		1139.7834
Frequencies --	1177.9508		1237.2523		1262.4494
Frequencies --	1326.4300		1414.6795		1454.6557
Frequencies --	1493.6399		1496.7896		1707.8902
Frequencies --	3072.5768		3154.7555		3165.7878
Frequencies --	3175.5233		3189.8773		3271.0645

SOZ'

1	6	0	0.931326	-0.385516	-0.124795
2	16	0	-1.628327	-0.383650	-0.049333
3	8	0	-0.716347	0.154814	1.329453
4	8	0	0.616979	-0.406876	1.249533
5	8	0	-0.253763	-0.953088	-0.755124
6	6	0	2.071613	-1.356405	-0.329866
7	6	0	1.202454	0.985707	-0.675468
8	1	0	2.937279	-1.013712	0.231615
9	1	0	2.330764	-1.389564	-1.384874
10	1	0	1.776762	-2.346517	0.005686
11	6	0	1.481012	2.041177	0.076343
12	1	0	1.178911	1.050211	-1.754914
13	1	0	1.484456	1.975092	1.154018
14	1	0	1.692635	3.000023	-0.371416
15	8	0	-2.080119	0.849286	-0.669873
Frequencies --	77.6864		104.4866		171.3643
Frequencies --	207.8023		252.7274		293.5452
Frequencies --	303.9485		352.2568		386.0403
Frequencies --	457.7828		519.8118		562.0009
Frequencies --	605.7655		645.9559		707.9753
Frequencies --	746.8007		796.8104		842.6741
Frequencies --	899.6510		958.0061		982.9617
Frequencies --	1024.1320		1053.8698		1129.8241
Frequencies --	1204.2170		1251.8427		1269.6128
Frequencies --	1325.1640		1415.0838		1456.9714
Frequencies --	1495.4468		1496.9660		1708.3465
Frequencies --	3077.5080		3161.0416		3169.5402
Frequencies --	3174.5091		3195.2092		3266.9753

$$SOZ' = MVK + SO_3$$

1	8	0	0.482112	0.096044	1.192693
2	6	0	0.888782	0.387026	-0.046778
3	8	0	-0.273751	0.037489	-1.030527
4	16	0	-1.672792	-0.013135	-0.247270
5	8	0	-1.242972	0.775722	0.990566
6	8	0	-2.128139	-1.382450	-0.084597
7	6	0	1.228913	1.838015	-0.316405
8	6	0	1.959296	-0.586127	-0.497241
9	6	0	2.616486	-1.396176	0.321589
10	1	0	0.385361	2.468266	-0.049913
11	1	0	1.478920	1.987490	-1.363823
12	1	0	2.085294	2.108879	0.297519
13	1	0	2.168133	-0.546577	-1.556916
14	1	0	2.402830	-1.428247	1.378545
15	1	0	3.385258	-2.050516	-0.061156
Frequencies --	-503.0963		49.7067		114.2572
Frequencies --	167.4532		238.4033		245.8125
Frequencies --	278.7626		305.0201		349.8186
Frequencies --	426.6553		438.4999		506.6686

Frequencies --	559.1815	564.7677	620.5304
Frequencies --	695.2147	773.8967	833.3841
Frequencies --	884.3514	956.1887	987.0136
Frequencies --	1017.9460	1054.3601	1085.3504
Frequencies --	1208.7140	1238.4825	1259.3925
Frequencies --	1335.8924	1413.3947	1449.7609
Frequencies --	1493.8651	1498.2580	1691.5326
Frequencies --	3073.4758	3153.3649	3166.4758
Frequencies --	3176.1199	3203.1558	3271.4335

MVK

1	6	0	-0.602979	-1.916344	0.000000
2	6	0	0.344205	-0.980834	0.000000
3	6	0	0.000000	0.471355	0.000000
4	8	0	-1.152853	0.859147	0.000000
5	6	0	1.166490	1.427951	0.000000
6	1	0	-1.644059	-1.625329	0.000000
7	1	0	-0.364261	-2.969258	0.000000
8	1	0	1.392679	-1.248799	0.000000
9	1	0	0.809026	2.452241	0.000000
10	1	0	1.791571	1.252604	0.876727
11	1	0	1.791571	1.252604	-0.876727

Frequencies --	95.1011	131.0806	269.1744
Frequencies --	415.7426	462.4459	602.2285
Frequencies --	687.4931	785.7875	967.0014
Frequencies --	1013.9690	1033.2112	1051.5520
Frequencies --	1087.8778	1208.6350	1333.8510
Frequencies --	1393.9406	1447.6324	1477.1397
Frequencies --	1488.2154	1670.7956	1760.3327
Frequencies --	3051.0294	3111.7758	3165.6515
Frequencies --	3172.4552	3186.9241	3262.9738

syn-cis; exo
syn-cis...SO₂

1	6	0	-1.219190	0.620860	0.013608
2	8	0	-0.754735	0.166576	1.114975
3	8	0	0.541528	0.573857	1.432524
4	6	0	-0.568118	1.738745	-0.697170
5	6	0	-2.477938	0.038333	-0.409795
6	1	0	-0.118868	2.408720	0.034103
7	1	0	0.245201	1.360712	-1.313128
8	1	0	-1.291026	2.245408	-1.329957
9	16	0	1.802481	-0.662432	0.043243
10	8	0	0.644867	-1.135470	-0.741838
11	8	0	2.570187	0.423403	-0.568268
12	1	0	-3.085188	0.642949	-1.067294
13	6	0	-2.840666	-1.203969	-0.075669
14	1	0	-2.194285	-1.830054	0.520459
15	1	0	-3.774832	-1.619559	-0.421066

Frequencies --	56.1451	76.6191	93.8906
Frequencies --	117.4857	161.1770	185.9439
Frequencies --	212.7011	257.1847	316.8018
Frequencies --	345.8488	363.2753	438.7743
Frequencies --	507.8252	527.6101	618.6452
Frequencies --	667.4510	811.7390	928.9049
Frequencies --	1005.6513	1018.8100	1029.9406
Frequencies --	1040.2637	1097.3132	1102.8004
Frequencies --	1259.3446	1284.9025	1342.2884
Frequencies --	1400.0391	1450.5955	1457.1662
Frequencies --	1495.6403	1515.8685	1676.5034
Frequencies --	3070.6281	3141.6053	3169.2440
Frequencies --	3180.6319	3212.3966	3278.8832

syn-cis...SO₂ = SOZ

1	6	0	-1.036423	-0.569695	-0.091739
2	8	0	-0.683518	0.031185	-1.183873
3	8	0	0.677129	-0.108934	-1.494635
4	6	0	-0.408801	-1.826235	0.386972
5	6	0	-2.346039	-0.169360	0.401100
6	1	0	0.593102	-1.950930	0.001190
7	1	0	-0.390329	-1.835253	1.472045
8	1	0	-1.049273	-2.646082	0.046857
9	16	0	1.645514	0.703425	0.136307
10	8	0	0.388215	0.749438	0.954793
11	8	0	2.541390	-0.410744	0.448493
12	6	0	-2.854513	1.045537	0.185349
13	1	0	-2.298019	1.791904	-0.360689
14	1	0	-3.824660	1.317313	0.572167
15	1	0	-2.870130	-0.900793	0.999201
Frequencies --	-123.7674	74.4108	107.6976		
Frequencies --	160.6666	169.4768	209.1505		
Frequencies --	246.9406	288.5004	335.6721		
Frequencies --	389.0692	417.0246	450.8684		
Frequencies --	504.2118	535.0754	615.6071		
Frequencies --	682.2739	807.3926	938.8246		
Frequencies --	991.0806	1013.9062	1017.7537		
Frequencies --	1020.2132	1064.8532	1092.7112		
Frequencies --	1234.3351	1293.9499	1343.9756		
Frequencies --	1415.3087	1421.3805	1475.7465		
Frequencies --	1489.8036	1501.7213	1682.0705		
Frequencies --	3038.9938	3149.7618	3180.8647		
Frequencies --	3208.7517	3221.1247	3278.1294		

SOZ

1	6	0	-0.779585	0.384611	0.040320
2	8	0	-0.589124	-0.641560	0.992638
3	8	0	0.843265	-0.732371	1.142240
4	6	0	-0.464132	1.764846	0.580380

5	6	0	-2.165273	0.268516	-0.515729
6	1	0	0.536772	1.794889	0.998165
7	1	0	-0.529988	2.491539	-0.225891
8	1	0	-1.189834	2.019051	1.349825
9	1	0	-2.461803	1.095351	-1.146347
10	6	0	-2.994644	-0.736625	-0.265359
11	1	0	-2.708221	-1.564766	0.364084
12	1	0	-3.987500	-0.746076	-0.688885
13	16	0	1.572727	-0.539794	-0.428120
14	8	0	0.157383	0.030750	-1.030284
15	8	0	2.538319	0.525509	-0.209432
Frequencies --	36.1557		105.3336		175.9085
Frequencies --	231.8567		241.0284		273.8856
Frequencies --	324.7940		362.5611		405.7042
Frequencies --	455.2395		529.9198		539.6025
Frequencies --	605.7772		641.8940		670.6488
Frequencies --	755.3290		786.1635		886.0549
Frequencies --	915.8021		955.1147		994.7821
Frequencies --	1024.3631		1050.3633		1112.5466
Frequencies --	1199.6396		1249.0329		1289.5320
Frequencies --	1338.1200		1424.4544		1463.0970
Frequencies --	1501.1459		1504.3566		1706.9609
Frequencies --	3076.6809		3152.9606		3177.4554
Frequencies --	3178.1646		3198.5264		3271.0558

SOZ = SOZ'

1	6	0	-0.750870	0.425265	0.042461
2	16	0	1.596200	-0.450413	-0.467304
3	8	0	0.780782	-1.214376	0.788980
4	8	0	-0.509122	-0.571852	1.051037
5	8	0	0.175153	0.143042	-1.032326
6	8	0	2.414777	0.625546	0.070978
7	6	0	-0.518499	1.811236	0.613785
8	6	0	-2.134715	0.245429	-0.511245
9	1	0	-1.237852	1.990770	1.409681
10	1	0	-0.659901	2.557137	-0.165752
11	1	0	0.489889	1.892948	1.006593
12	6	0	-2.933819	-0.771690	-0.217300
13	1	0	-2.453715	1.035289	-1.178297
14	1	0	-2.620342	-1.555008	0.454932
15	1	0	-3.922574	-0.834843	-0.645858
Frequencies --	-133.2936		72.1887		142.1014
Frequencies --	216.8127		248.0823		275.0878
Frequencies --	326.4457		358.3408		391.6093
Frequencies --	462.0406		536.0663		585.6902
Frequencies --	610.0290		674.8926		684.2602
Frequencies --	752.9529		804.1265		863.5861
Frequencies --	898.1980		950.8904		996.1242
Frequencies --	1023.8946		1042.0366		1128.0166

Frequencies --	1170.1279	1247.7673	1266.3849
Frequencies --	1331.6613	1422.3919	1455.2068
Frequencies --	1499.6002	1502.1347	1705.9511
Frequencies --	3072.7861	3149.2641	3175.7037
Frequencies --	3176.5065	3193.3570	3272.4330

SOZ'

1	6	0	-0.791668	0.527932	-0.012448
2	16	0	1.563227	-0.448364	-0.429741
3	8	0	0.524135	-1.160350	0.710682
4	8	0	-0.308209	-0.052998	1.180502
5	8	0	0.345890	0.554797	-0.921788
6	8	0	2.562073	0.372741	0.229342
7	6	0	-1.172831	1.952046	0.329694
8	6	0	-1.891837	-0.256105	-0.667690
9	1	0	-1.977449	1.947522	1.061019
10	1	0	-1.519975	2.454752	-0.569402
11	1	0	-0.306641	2.472784	0.727433
12	6	0	-2.547812	-1.247738	-0.080676
13	1	0	-2.131355	0.062059	-1.673848
14	1	0	-2.299481	-1.566149	0.920738
15	1	0	-3.342954	-1.767477	-0.593274
Frequencies --	68.2866	103.6043	160.2137		
Frequencies --	218.1171	272.8290	299.2199		
Frequencies --	313.5158	356.4622	422.0825		
Frequencies --	454.8566	532.9197	584.1393		
Frequencies --	609.8676	658.9598	705.9982		
Frequencies --	745.0954	793.4774	843.6220		
Frequencies --	863.4891	954.1695	985.1935		
Frequencies --	1028.9074	1051.8352	1130.4946		
Frequencies --	1191.6050	1260.8896	1267.7118		
Frequencies --	1324.8389	1414.8872	1458.2459		
Frequencies --	1496.0492	1497.6730	1708.5752		
Frequencies --	3076.6143	3159.2269	3170.8591		
Frequencies --	3172.5961	3190.7577	3265.5691		

SOZ' = MVK + SO₃

1	8	0	-0.447442	0.071849	1.266523
2	6	0	-0.857914	0.503795	0.074448
3	8	0	0.358966	0.598592	-0.862650
4	16	0	1.532092	-0.393748	-0.366779
5	8	0	0.697451	-1.262461	0.565033
6	8	0	2.637288	0.376643	0.177886
7	6	0	-1.269315	1.981693	0.222449
8	6	0	-1.871802	-0.330398	-0.652632
9	6	0	-2.473618	-1.370723	-0.092318
10	1	0	-0.455653	2.540364	0.673219
11	1	0	-2.154854	2.027636	0.848700
12	1	0	-1.496560	2.379623	-0.762650

13	1	0	-2.097241	-0.016501	-1.662953
14	1	0	-2.231097	-1.669281	0.916754
15	1	0	-3.212284	-1.945054	-0.630622
Frequencies --			-447.2184	81.6922	108.8363
Frequencies --			148.0682	239.3886	274.9905
Frequencies --			288.8271	313.4491	344.0712
Frequencies --			412.0518	448.3199	506.0042
Frequencies --			554.9954	578.1282	651.6463
Frequencies --			703.5862	762.4105	837.8981
Frequencies --			897.4024	991.5857	993.4577
Frequencies --			1027.1804	1050.9033	1058.3022
Frequencies --			1103.8862	1253.0342	1297.1832
Frequencies --			1322.7889	1394.3247	1451.2759
Frequencies --			1489.4554	1498.5584	1702.4875
Frequencies --			3081.3797	3170.8131	3172.1865
Frequencies --			3184.0891	3193.7063	3266.4647

Endo

syn-trans...SO₂ = syn-cis...SO₂

geometry a

1	6	0	-1.273420	-0.513003	-0.143486
2	8	0	-0.402685	-0.696295	-1.053176
3	8	0	0.708753	-1.471228	-0.714010
4	6	0	-1.360321	-1.322892	1.087101
5	6	0	-2.326425	0.451536	-0.515511
6	1	0	-0.527774	-2.010361	1.157333
7	1	0	-1.386183	-0.659688	1.947609
8	1	0	-2.312399	-1.858843	1.054826
9	16	0	1.845490	0.149620	0.377155
10	8	0	0.621330	0.671981	1.032206
11	8	0	2.349667	0.968348	-0.720124
12	6	0	-2.334332	1.690946	-0.037388
13	1	0	-3.086395	0.093790	-1.199168
14	1	0	-1.550377	2.037002	0.619790
15	1	0	-3.114234	2.382208	-0.318343
Frequencies --			-137.3412	49.2487	83.9355
Frequencies --			113.8335	155.7416	165.5789
Frequencies --			205.5293	252.0622	285.1036
Frequencies --			345.5625	375.5006	405.4768
Frequencies --			526.2842	543.5276	605.0432
Frequencies --			661.5901	806.8491	923.8679
Frequencies --			990.9652	997.9811	1008.8129
Frequencies --			1015.0531	1081.7154	1103.3945
Frequencies --			1262.6065	1301.3353	1328.7103
Frequencies --			1402.7698	1428.1997	1465.8226
Frequencies --			1486.0751	1525.4642	1687.5889
Frequencies --			3052.0485	3138.4154	3170.8435
Frequencies --			3180.9613	3210.2552	3272.6398

syn-trans...SO₂ = syn-cis...SO₂

geometry b

1	6	0	-1.266771	0.268995	0.029727
2	8	0	-0.501188	-0.085406	0.978838
3	8	0	0.512342	0.808108	1.321553
4	6	0	-1.258435	1.637503	-0.517744
5	6	0	-2.197186	-0.783617	-0.419262
6	1	0	-0.930194	2.326887	0.256834
7	1	0	-0.527677	1.682586	-1.325353
8	1	0	-2.240873	1.881066	-0.910803
9	16	0	2.075935	0.063173	-0.234613
10	8	0	1.056567	-0.104028	-1.290300
11	8	0	2.545248	-1.172954	0.380938
12	6	0	-3.405966	-0.954173	0.102755
13	1	0	-1.818610	-1.413450	-1.214539
14	1	0	-3.776151	-0.327131	0.901211
15	1	0	-4.055059	-1.738731	-0.254629
Frequencies --			-143.2147	37.3977	47.3685
Frequencies --			80.0180	139.0395	155.3255
Frequencies --			192.9941	240.4993	277.9177
Frequencies --			323.9631	355.2652	412.9535
Frequencies --			516.4126	529.0533	617.9783
Frequencies --			669.6472	798.8716	918.1594
Frequencies --			988.8932	993.2423	1008.6899
Frequencies --			1029.3298	1087.6807	1105.8856
Frequencies --			1273.5181	1293.3621	1315.8431
Frequencies --			1390.4512	1444.4492	1465.9561
Frequencies --			1487.7166	1526.5271	1696.0014
Frequencies --			3066.8804	3135.4638	3169.9656
Frequencies --			3174.7734	3185.5434	3263.7766

SO₂; cis = trans

geometry a

1	6	0	-0.825407	0.343417	0.068557
2	8	0	-0.003366	0.714184	1.164955
3	8	0	1.241652	1.129348	0.534996
4	6	0	-1.370812	1.540569	-0.679878
5	6	0	-1.868915	-0.569714	0.646799
6	1	0	-0.554924	2.185322	-0.994976
7	1	0	-1.920711	1.202062	-1.554498
8	1	0	-2.045891	2.096189	-0.033477
9	1	0	-1.876912	-0.637968	1.725787
10	6	0	-2.719340	-1.262484	-0.098668
11	1	0	-2.699873	-1.216031	-1.178169
12	1	0	-3.448707	-1.915528	0.355223
13	16	0	1.645742	-0.189483	-0.469211
14	8	0	0.051310	-0.396470	-0.834280
15	8	0	2.075652	-1.321193	0.330158
Frequencies --			-96.9181	74.4658	182.5025

Frequencies --	220.9202	260.6107	278.6742
Frequencies --	316.0630	371.3625	443.3348
Frequencies --	467.8152	507.5954	545.2081
Frequencies --	601.5993	652.6251	682.3011
Frequencies --	739.8253	787.5621	863.4692
Frequencies --	898.1504	947.7932	977.4333
Frequencies --	1012.6638	1049.2440	1118.2157
Frequencies --	1191.4095	1260.7514	1273.5871
Frequencies --	1329.6238	1417.3744	1463.2934
Frequencies --	1494.7308	1499.9772	1706.0785
Frequencies --	3075.1257	3156.7556	3164.1626
Frequencies --	3170.2703	3200.0086	3260.6776

SOZ; cis = trans

geometry b

1	6	0	-0.811085	0.267181	-0.201655
2	8	0	-0.333841	0.032089	1.116251
3	8	0	0.958814	0.715487	1.124231
4	6	0	-1.298234	1.687901	-0.398387
5	6	0	-1.843209	-0.786249	-0.485868
6	1	0	-0.512466	2.392837	-0.140672
7	1	0	-1.585197	1.832768	-1.437135
8	1	0	-2.166250	1.860672	0.233273
9	1	0	-1.725135	-1.297950	-1.429676
10	6	0	-2.830102	-1.078940	0.351607
11	1	0	-2.939832	-0.576305	1.301801
12	1	0	-3.549631	-1.846545	0.110903
13	16	0	1.762687	0.073335	-0.232126
14	8	0	0.334793	0.042510	-1.065780
15	8	0	2.161646	-1.299859	0.010468
Frequencies --	-75.8958	75.7866	192.3321		
Frequencies --	209.1616	252.5286	286.2159		
Frequencies --	325.3928	364.0805	421.0991		
Frequencies --	484.6492	488.5934	561.4365		
Frequencies --	617.8284	649.1694	685.4120		
Frequencies --	736.1086	798.1539	838.8671		
Frequencies --	894.8477	946.7115	980.8125		
Frequencies --	1019.1964	1052.7240	1144.0676		
Frequencies --	1170.7977	1263.8802	1271.3226		
Frequencies --	1324.3798	1416.3232	1462.8996		
Frequencies --	1496.5251	1498.1685	1700.3838		
Frequencies --	3074.1907	3155.8792	3163.4417		
Frequencies --	3170.5592	3212.0804	3260.9346		

Exo

syn-trans...SO₂ = syn-cis...SO₂

1	6	0	-1.149908	-0.588714	0.112488
2	8	0	-0.582517	-0.934356	-0.975086
3	8	0	0.757829	-1.316590	-0.880511

4	6	0	-0.634704	-0.908268	1.459617
5	6	0	-2.507615	-0.041782	-0.079261
6	1	0	0.348627	-1.357838	1.416132
7	1	0	-0.605422	0.000615	2.054298
8	1	0	-1.359867	-1.581435	1.925265
9	16	0	1.751506	0.558706	-0.330879
10	8	0	0.473985	1.268003	-0.066013
11	8	0	2.456565	0.083986	0.859583
12	6	0	-2.750257	1.263475	-0.042303
13	1	0	-3.295077	-0.768182	-0.239628
14	1	0	-1.950096	1.973357	0.103918
15	1	0	-3.754255	1.637586	-0.172959
Frequencies --			-137.2454	63.5784	82.8236
Frequencies --			111.8508	161.8526	202.8914
Frequencies --			208.9994	277.7327	295.2521
Frequencies --			337.3578	379.4662	411.2342
Frequencies --			520.6840	544.5149	606.8125
Frequencies --			663.9245	807.1788	924.9610
Frequencies --			990.5460	998.8587	1010.3478
Frequencies --			1016.4557	1075.0346	1102.1108
Frequencies --			1249.5330	1300.8653	1329.1910
Frequencies --			1403.7664	1430.4841	1465.7504
Frequencies --			1481.3702	1525.6310	1689.6678
Frequencies --			3047.0326	3139.8321	3170.4656
Frequencies --			3180.5097	3210.4498	3274.3671

SOZ'; *cis = trans*
geometry a

1	6	0	0.802265	0.238964	0.176963
2	8	0	0.227223	1.471521	-0.219784
3	8	0	-1.189799	1.279027	-0.041198
4	6	0	0.716684	-0.011677	1.668587
5	6	0	2.193444	0.245563	-0.382838
6	1	0	-0.310755	0.052771	2.012100
7	1	0	1.101299	-1.004663	1.887015
8	1	0	1.326668	0.723316	2.188280
9	1	0	2.506097	1.180803	-0.826619
10	6	0	2.991468	-0.813592	-0.359609
11	1	0	2.674967	-1.756149	0.063717
12	1	0	3.982951	-0.769724	-0.783391
13	16	0	-1.586169	-0.333454	-0.573674
14	8	0	0.003626	-0.748263	-0.550434
15	8	0	-2.306759	-0.883116	0.563799
Frequencies --			-85.2953	108.2796	164.6015
Frequencies --			226.5849	247.3041	285.7631
Frequencies --			323.0215	367.6012	394.3238
Frequencies --			470.6404	506.7293	532.9293
Frequencies --			590.6467	640.9903	679.1629
Frequencies --			748.2718	783.7174	886.9478

Frequencies --	918.1605	958.4712	980.5447
Frequencies --	1013.7737	1050.6370	1116.2086
Frequencies --	1190.7427	1248.7770	1286.3933
Frequencies --	1329.5052	1424.2112	1464.4160
Frequencies --	1498.3918	1503.0747	1707.3309
Frequencies --	3079.1284	3156.7240	3170.4471
Frequencies --	3177.3317	3198.1728	3260.8380

SOZ'; *cis = trans*
geometry b

1	6	0	-0.776471	0.225102	-0.016391
2	8	0	-0.542500	-1.019942	0.625930
3	8	0	0.874359	-0.997109	0.918638
4	6	0	-0.663208	1.411817	0.919891
5	6	0	-2.097256	0.114034	-0.719034
6	1	0	0.302463	1.424109	1.415045
7	1	0	-0.781565	2.329649	0.349149
8	1	0	-1.457819	1.354279	1.659970
9	1	0	-2.083319	0.371506	-1.768108
10	6	0	-3.208192	-0.277765	-0.108239
11	1	0	-3.218239	-0.547389	0.938131
12	1	0	-4.139809	-0.351690	-0.648058
13	16	0	1.687166	-0.326453	-0.464242
14	8	0	0.262058	0.273024	-1.033948
15	8	0	2.512883	0.719484	0.117428
Frequencies --	-71.8617	102.0041	170.8726		
Frequencies --	218.3242	245.3680	294.2465		
Frequencies --	308.4214	361.3665	407.1019		
Frequencies --	452.6191	503.4032	541.2898		
Frequencies --	613.9883	643.8508	682.6372		
Frequencies --	742.6893	804.5322	878.0768		
Frequencies --	898.6595	952.1154	982.0569		
Frequencies --	1019.2087	1053.6853	1147.0870		
Frequencies --	1164.9783	1250.1096	1283.0711		
Frequencies --	1325.1509	1423.2133	1463.6601		
Frequencies --	1499.3624	1501.4061	1702.2779		
Frequencies --	3078.1819	3155.5483	3170.4671		
Frequencies --	3176.7499	3209.7600	3260.9465		

HPBF

Conformer 1

1	6	0	0.887132	1.833521	1.149484
2	6	0	1.033689	0.527588	0.972696
3	6	0	0.655613	-0.227145	-0.267388
4	6	0	1.835608	-0.472676	-1.191309
5	8	0	-0.260085	0.585337	-1.104488
6	6	0	-1.552793	0.721494	-0.833135
7	8	0	-2.195196	0.212668	0.056200
8	8	0	0.132622	-1.493107	-0.001688

9	8	0	-0.587135	-1.525235	1.253677
10	1	0	0.420651	2.462359	0.406039
11	1	0	1.231685	2.308060	2.055470
12	1	0	1.500777	-0.089177	1.726790
13	1	0	2.187882	0.473424	-1.590896
14	1	0	2.634065	-0.953481	-0.633335
15	1	0	1.526081	-1.122352	-2.006823
16	1	0	-1.997569	1.392848	-1.573025
17	1	0	-1.380709	-1.005674	1.004085
Frequencies --		76.1711	98.5487	202.2302	
Frequencies --		212.1820	245.8493	273.2042	
Frequencies --		294.7566	305.7585	332.8620	
Frequencies --		358.8855	474.2877	526.6551	
Frequencies --		574.6422	651.1098	692.8068	
Frequencies --		702.5734	816.1616	842.2435	
Frequencies --		933.2481	971.5763	989.7281	
Frequencies --		1026.8053	1051.0905	1054.6095	
Frequencies --		1135.3447	1177.4427	1242.9183	
Frequencies --		1267.6844	1327.9383	1415.4150	
Frequencies --		1422.0319	1461.0597	1496.5182	
Frequencies --		1499.6406	1508.0581	1708.5395	
Frequencies --		1757.0750	3077.5436	3079.7063	
Frequencies --		3160.6890	3172.7467	3174.6443	
Frequencies --		3210.0141	3262.9315	3497.3191	

Conformer 2

1	6	0	2.800298	-0.078238	-0.575578
2	6	0	1.782497	-0.747966	-0.051368
3	6	0	0.432501	-0.145439	0.222837
4	6	0	0.223710	0.169153	1.691010
5	8	0	-0.492656	-1.270099	-0.139905
6	6	0	-1.787283	-1.075385	-0.335491
7	8	0	-2.405703	-0.033684	-0.298248
8	8	0	0.282190	0.928971	-0.645465
9	8	0	-0.617024	1.935990	-0.127875
10	1	0	2.700249	0.953942	-0.873023
11	1	0	3.755913	-0.558716	-0.721603
12	1	0	1.877501	-1.784268	0.241133
13	1	0	-0.805109	0.443408	1.896868
14	1	0	0.490531	-0.707676	2.275645
15	1	0	0.871135	0.996327	1.967941
16	1	0	-2.264274	-2.035198	-0.552882
17	1	0	-1.470738	1.470002	-0.250589
Frequencies --		72.6077	109.6505	174.0443	
Frequencies --		228.3544	254.0508	270.5366	
Frequencies --		291.2392	294.2404	351.8090	
Frequencies --		383.7694	472.9525	504.0488	
Frequencies --		563.2571	652.0546	686.6383	
Frequencies --		723.4533	807.2726	833.4947	

Frequencies --	930.3300	980.5030	990.2689
Frequencies --	1030.8915	1052.6003	1062.0250
Frequencies --	1102.4706	1204.3290	1252.8101
Frequencies --	1280.8337	1329.9264	1419.0313
Frequencies --	1421.4803	1456.2740	1496.2891
Frequencies --	1500.3208	1502.3878	1707.3000
Frequencies --	1744.7778	3079.4897	3084.3109
Frequencies --	3163.5218	3176.6857	3180.1701
Frequencies --	3202.7073	3271.2215	3511.0775

Conformer 3

1	6	0	-2.700863	0.677522	-0.396425
2	6	0	-1.907555	-0.354897	-0.145113
3	6	0	-0.436016	-0.293236	0.160140
4	6	0	-0.115599	-0.828123	1.542376
5	8	0	-0.083298	1.144070	0.126040
6	6	0	1.168304	1.567049	0.019593
7	8	0	2.177512	0.909985	-0.102894
8	8	0	0.158020	-0.992693	-0.896774
9	8	0	1.411122	-1.612816	-0.519061
10	1	0	-2.330660	1.690002	-0.403682
11	1	0	-3.749164	0.522127	-0.602266
12	1	0	-2.291444	-1.365908	-0.148592
13	1	0	-0.705340	-0.277363	2.270200
14	1	0	-0.377204	-1.882051	1.586777
15	1	0	0.939547	-0.726421	1.769854
16	1	0	1.176309	2.659874	0.056525
17	1	0	1.981476	-0.818516	-0.470734
Frequencies --	70.9725	83.0563	183.1175		
Frequencies --	225.3040	248.2182	255.7482		
Frequencies --	281.4223	308.5218	352.2594		
Frequencies --	411.3527	443.2096	499.0019		
Frequencies --	581.2000	645.2795	689.4894		
Frequencies --	702.6669	820.9861	848.7920		
Frequencies --	924.5984	965.8192	982.8748		
Frequencies --	1029.9415	1050.2296	1052.6445		
Frequencies --	1135.8451	1187.7340	1245.4425		
Frequencies --	1273.9436	1330.7779	1419.6062		
Frequencies --	1422.4236	1459.7448	1490.5004		
Frequencies --	1498.5693	1501.6175	1709.8954		
Frequencies --	1752.1261	3081.3073	3085.3122		
Frequencies --	3163.9066	3179.2747	3182.0759		
Frequencies --	3199.4308	3274.0408	3533.6429		

Conformer 4

1	6	0	2.256691	0.310569	-1.343272
2	6	0	0.990230	0.369548	-0.951865
3	6	0	0.478134	-0.196689	0.339340
4	6	0	1.474675	-0.945423	1.195306

5	8	0	-0.507320	-1.274408	-0.025416
6	6	0	-1.723094	-1.009747	-0.476735
7	8	0	-2.252354	0.069999	-0.628895
8	8	0	-0.101405	0.735899	1.200238
9	8	0	-0.655706	1.876741	0.504841
10	1	0	3.031646	-0.140918	-0.742866
11	1	0	2.555588	0.729250	-2.292392
12	1	0	0.248588	0.838287	-1.578912
13	1	0	1.855298	-1.810345	0.661139
14	1	0	2.291198	-0.284501	1.468692
15	1	0	0.972995	-1.278056	2.099917
16	1	0	-2.229915	-1.950814	-0.708395
17	1	0	-1.450921	1.461696	0.110020
Frequencies --	66.3568		77.8885		190.0123
Frequencies --	230.3490		260.2765		270.6017
Frequencies --	295.5257		316.5064		332.6341
Frequencies --	385.9255		431.7643		497.2633
Frequencies --	555.9009		640.1973		673.5732
Frequencies --	747.1058		796.5578		827.1998
Frequencies --	929.0861		981.1652		987.1140
Frequencies --	1029.8110		1039.1963		1053.2775
Frequencies --	1098.1228		1196.3029		1249.1956
Frequencies --	1319.5007		1347.1306		1417.1866
Frequencies --	1423.5562		1465.3969		1500.1482
Frequencies --	1502.9957		1509.3740		1708.8388
Frequencies --	1743.1153		3079.0016		3086.9559
Frequencies --	3167.8822		3176.3493		3178.8435
Frequencies --	3227.3268		3263.0480		3515.1882

Conformer 5

1	6	0	1.862518	-1.184768	1.034523
2	6	0	1.028076	-0.154746	1.079421
3	6	0	0.442672	0.538891	-0.116905
4	6	0	1.240147	1.769321	-0.515581
5	8	0	-0.864598	1.141518	0.312323
6	6	0	-1.957120	0.419068	0.502308
7	8	0	-2.122102	-0.762068	0.290876
8	8	0	0.316997	-0.188064	-1.293753
9	8	0	-0.021816	-1.583978	-1.105457
10	1	0	2.116602	-1.670192	0.106395
11	1	0	2.296389	-1.572963	1.943961
12	1	0	0.779032	0.314646	2.021722
13	1	0	0.761089	2.250422	-1.365013
14	1	0	1.280144	2.466068	0.316859
15	1	0	2.246722	1.464274	-0.784319
16	1	0	-2.749873	1.063724	0.892065
17	1	0	-0.895706	-1.501825	-0.666180
Frequencies --	54.8229		92.8148		192.7587
Frequencies --	219.1158		241.3391		261.0966

Frequencies --	293.4826	303.5717	333.2831
Frequencies --	345.7920	456.9745	495.2362
Frequencies --	557.3205	649.4915	680.8286
Frequencies --	720.5705	794.9812	828.8467
Frequencies --	927.9457	982.7147	992.9715
Frequencies --	1026.7125	1054.9495	1063.3596
Frequencies --	1099.9610	1183.3088	1244.2319
Frequencies --	1292.9000	1334.9112	1413.6882
Frequencies --	1418.7588	1461.7528	1496.2354
Frequencies --	1498.4557	1528.3866	1706.7823
Frequencies --	1749.0698	3078.5776	3080.3184
Frequencies --	3162.1624	3174.5581	3176.6790
Frequencies --	3192.2964	3276.2387	3477.4975

Conformer 6

1	6	0	-1.674338	1.722750	-0.541696
2	6	0	-0.454659	1.238912	-0.347264
3	6	0	-0.171135	-0.034434	0.397970
4	6	0	0.358532	0.204850	1.800976
5	8	0	0.757458	-0.881697	-0.368160
6	6	0	2.001743	-0.471506	-0.646335
7	8	0	2.512511	0.572308	-0.337010
8	8	0	-1.287380	-0.858438	0.595436
9	8	0	-1.864228	-1.227222	-0.681641
10	1	0	-2.555267	1.189274	-0.220298
11	1	0	-1.814029	2.671058	-1.038620
12	1	0	0.421650	1.782799	-0.666625
13	1	0	0.638567	-0.743559	2.253615
14	1	0	1.220340	0.861903	1.760179
15	1	0	-0.424830	0.671901	2.391634
16	1	0	2.504292	-1.260193	-1.216057
17	1	0	-1.298470	-1.976214	-0.914732
Frequencies --	94.0340	103.6592	157.2415		
Frequencies --	190.1500	220.9352	240.4219		
Frequencies --	244.4562	249.4702	300.9962		
Frequencies --	333.4790	383.8830	444.1606		
Frequencies --	503.3586	582.5964	697.1762		
Frequencies --	732.8237	807.6844	863.5570		
Frequencies --	918.6703	975.7838	982.8918		
Frequencies --	1041.8929	1045.2582	1064.5126		
Frequencies --	1119.1812	1183.6051	1212.0479		
Frequencies --	1289.0441	1332.9549	1399.6695		
Frequencies --	1409.8760	1416.0447	1462.5033		
Frequencies --	1498.3652	1505.3240	1707.8531		
Frequencies --	1778.2308	3061.1112	3079.9520		
Frequencies --	3160.4578	3175.8834	3184.6688		
Frequencies --	3218.8248	3268.4147	3759.2248		

Conformer 7

1	6	0	-1.154950	2.330792	-0.297869
2	6	0	-0.166662	1.519720	0.059372
3	6	0	-0.284853	0.025600	0.181687
4	6	0	-0.069336	-0.470952	1.597731
5	8	0	0.660637	-0.634168	-0.742234
6	6	0	1.983137	-0.476287	-0.610022
7	8	0	2.562074	0.195441	0.202901
8	8	0	-1.538893	-0.317469	-0.339124
9	8	0	-1.755794	-1.737260	-0.177692
10	1	0	-2.137316	1.962781	-0.548197
11	1	0	-0.992013	3.397291	-0.341954
12	1	0	0.809941	1.902402	0.314622
13	1	0	-0.066720	-1.555864	1.619678
14	1	0	0.871984	-0.093347	1.982129
15	1	0	-0.886613	-0.103740	2.213683
16	1	0	2.479600	-1.069218	-1.385580
17	1	0	-1.347074	-2.065893	-0.990579
Frequencies --		43.5490	98.7842	129.3191	
Frequencies --		204.3070	220.6656	228.5749	
Frequencies --		257.1323	286.9489	310.2734	
Frequencies --		329.8679	409.7847	462.0348	
Frequencies --		494.7611	565.4119	673.7914	
Frequencies --		728.2247	811.0002	882.7275	
Frequencies --		926.8690	968.2530	986.9309	
Frequencies --		1044.4577	1049.5988	1062.7698	
Frequencies --		1112.4270	1195.7764	1234.0116	
Frequencies --		1276.9768	1336.0482	1399.0534	
Frequencies --		1413.0014	1416.2748	1463.8452	
Frequencies --		1500.1601	1508.0085	1704.9298	
Frequencies --		1776.6319	3058.8456	3087.0457	
Frequencies --		3167.7082	3177.0361	3185.7857	
Frequencies --		3221.5582	3270.1645	3756.4166	

Conformer 8

1	6	0	1.374023	2.111856	-0.111803
2	6	0	0.491501	1.311409	-0.693233
3	6	0	-0.326886	0.267698	0.010845
4	6	0	-0.264716	0.243469	1.519962
5	8	0	-0.004544	-1.053816	-0.554967
6	6	0	1.197586	-1.613519	-0.342556
7	8	0	2.104060	-1.171405	0.309191
8	8	0	-1.626102	0.517698	-0.476233
9	8	0	-2.552744	-0.439415	0.093444
10	1	0	1.583744	2.066793	0.945605
11	1	0	1.926988	2.833964	-0.693269
12	1	0	0.306226	1.365362	-1.757726
13	1	0	-0.653922	1.185063	1.898671
14	1	0	-0.884449	-0.565279	1.891787
15	1	0	0.755498	0.101316	1.856682

16	1	0	1.226826	-2.569634	-0.876707
17	1	0	-2.455328	-1.167558	-0.535813
Frequencies --	52.1622		89.8422		135.6378
Frequencies --	206.3076		224.1317		228.7328
Frequencies --	249.9107		294.4314		321.0038
Frequencies --	345.9323		416.8605		428.2077
Frequencies --	500.8694		576.9841		649.4785
Frequencies --	723.2063		814.0751		893.0125
Frequencies --	915.3274		948.4706		985.5456
Frequencies --	1028.1844		1034.5877		1043.4320
Frequencies --	1123.9488		1192.9246		1202.0943
Frequencies --	1309.1027		1335.3283		1390.6948
Frequencies --	1415.4315		1418.8487		1462.9530
Frequencies --	1504.6030		1516.2279		1713.2945
Frequencies --	1784.8432		3053.8729		3092.9023
Frequencies --	3172.8335		3177.1970		3193.3726
Frequencies --	3194.1770		3266.4829		3757.5812

Conformer 9

1	6	0	0.627628	2.218261	-0.568681
2	6	0	-0.196589	1.185170	-0.683224
3	6	0	-0.352857	0.093177	0.333459
4	6	0	0.191471	0.361097	1.719807
5	8	0	0.183918	-1.161909	-0.220115
6	6	0	1.501334	-1.305401	-0.436957
7	8	0	2.373677	-0.524157	-0.170905
8	8	0	-1.709244	-0.212846	0.568126
9	8	0	-2.374427	-0.506072	-0.683757
10	1	0	1.284994	2.345963	0.277405
11	1	0	0.673746	2.970015	-1.342422
12	1	0	-0.830933	1.074822	-1.549560
13	1	0	-0.336420	1.206486	2.151773
14	1	0	0.027127	-0.517213	2.338472
15	1	0	1.252867	0.572415	1.673367
16	1	0	1.665968	-2.283242	-0.902688
17	1	0	-2.154657	-1.443186	-0.779567
Frequencies --	50.6800		98.0937		141.9017
Frequencies --	203.3189		216.9084		237.9371
Frequencies --	259.0828		292.6021		311.8059
Frequencies --	369.4189		374.2639		428.9182
Frequencies --	498.3528		594.6826		660.0609
Frequencies --	731.4627		821.3215		853.9187
Frequencies --	920.3430		965.4445		980.6762
Frequencies --	1030.1599		1038.8639		1042.9657
Frequencies --	1123.0195		1192.0355		1207.5967
Frequencies --	1306.8671		1335.7605		1395.9644
Frequencies --	1414.2006		1417.6825		1465.4207
Frequencies --	1500.4944		1515.6410		1710.1232
Frequencies --	1783.9694		3054.5957		3088.6734

Frequencies --	3164.8523	3175.8920	3195.6310
Frequencies --	3220.5255	3263.3052	3757.8764

5.4 MVK-oxide + formic acid

Planar minimum

1	6	0	1.741217	0.130226	0.000189
2	8	0	0.555319	-0.358983	0.000568
3	8	0	-0.473966	0.542452	0.000064
4	8	0	-3.904313	0.798072	0.000785
5	6	0	-3.759207	-0.399502	-0.000162
6	8	0	-2.604470	-1.054101	-0.000957
7	1	0	-4.594850	-1.110732	-0.000285
8	1	0	-1.846557	-0.401643	-0.000741
9	6	0	1.899630	1.592252	-0.000496
10	6	0	2.776238	-0.871954	0.000469
11	6	0	4.087061	-0.601848	-0.000134
12	1	0	2.939955	1.892743	0.000320
13	1	0	1.372547	1.997505	0.864787
14	1	0	1.374324	1.996632	-0.867284
15	1	0	2.423735	-1.894328	0.001128
16	1	0	4.469782	0.407095	-0.000845
17	1	0	4.810873	-1.401840	0.000045
Frequencies --	-11.2128		28.0164		28.5450
Frequencies --	93.0419		114.4863		187.3679
Frequencies --	187.6019		202.7433		283.9468
Frequencies --	288.2781		374.3504		466.6073
Frequencies --	499.7103		613.3722		688.0206
Frequencies --	700.7362		816.1089		960.2787
Frequencies --	971.2524		981.8794		1023.7979
Frequencies --	1028.5016		1046.9966		1070.0874
Frequencies --	1078.7956		1223.0542		1307.2149
Frequencies --	1340.6752		1402.9329		1407.4447
Frequencies --	1452.4933		1462.4560		1478.6718
Frequencies --	1489.8396		1505.6518		1670.7873
Frequencies --	1790.6366		3027.2501		3058.1226
Frequencies --	3105.0973		3130.1696		3182.2002
Frequencies --	3195.2472		3202.5521		3274.2473

van der Waals minimum

1	6	0	0.000000	0.000000	0.000000
2	8	0	0.000000	0.000000	1.275955
3	8	0	1.245775	0.000000	1.892005
4	8	0	0.606398	-2.800437	0.381749
5	6	0	1.017466	-3.231013	1.441733
6	8	0	1.418780	-2.525602	2.475900
7	1	0	1.096188	-4.304566	1.647652
8	1	0	1.354816	-1.531258	2.273211
9	6	0	1.271230	0.075133	-0.735745

10	6	0	-1.329184	-0.043379	-0.564140
11	6	0	-1.585380	-0.054876	-1.875686
12	1	0	1.115967	0.238392	-1.795234
13	1	0	1.804535	-0.859772	-0.570167
14	1	0	1.877193	0.865388	-0.294599
15	1	0	-2.132100	-0.086121	0.158207
16	1	0	-0.802662	-0.028630	-2.617617
17	1	0	-2.601700	-0.103459	-2.234886
Frequencies --	46.8365		56.9407		93.3520
Frequencies --	126.3653		148.3550		156.9454
Frequencies --	221.9254		247.4525		269.3290
Frequencies --	338.2014		358.9841		455.7681
Frequencies --	493.3374		597.9164		688.1404
Frequencies --	708.0896		808.8531		926.4019
Frequencies --	991.7365		1019.5153		1028.1072
Frequencies --	1041.7520		1047.0099		1071.0999
Frequencies --	1116.5869		1260.2678		1313.3572
Frequencies --	1342.3675		1392.1696		1408.1414
Frequencies --	1457.3675		1471.1291		1492.7186
Frequencies --	1502.5265		1519.0126		1678.8845
Frequencies --	1747.2199		2799.5379		3051.0151
Frequencies --	3073.7270		3135.1225		3183.0650
Frequencies --	3193.5201		3207.7761		3275.1933

van der Waals minimum = HPBF

1	6	0	0.735502	0.454862	0.005429
2	8	0	-0.012061	1.158611	-0.764566
3	8	0	-1.165269	1.718647	-0.142895
4	8	0	-0.488945	-1.447803	0.047960
5	6	0	-1.725710	-1.379711	-0.017457
6	8	0	-2.456497	-0.330435	-0.094877
7	1	0	-2.299636	-2.314001	-0.008477
8	1	0	-1.862852	0.675446	-0.120004
9	6	0	0.665065	0.556642	1.481842
10	6	0	1.860444	-0.120030	-0.717072
11	6	0	2.908772	-0.687222	-0.120910
12	1	0	1.082850	-0.330317	1.941562
13	1	0	1.249719	1.432001	1.776493
14	1	0	-0.355806	0.708391	1.801768
15	1	0	1.796939	-0.048340	-1.793121
16	1	0	2.983701	-0.776058	0.951796
17	1	0	3.722827	-1.086513	-0.705978
Frequencies --	-598.0338		58.5295		83.8810
Frequencies --	142.1704		169.6873		192.1403
Frequencies --	250.3268		271.1921		305.4575
Frequencies --	345.1720		376.8882		461.5846
Frequencies --	484.5414		575.6331		662.7502
Frequencies --	706.2328		774.5847		819.0039
Frequencies --	939.2021		995.0411		1000.5989

Frequencies --	1028.5869	1060.3462	1066.7508
Frequencies --	1078.1853	1271.7963	1318.4128
Frequencies --	1346.0554	1354.1718	1403.3264
Frequencies --	1417.4923	1456.9270	1475.3778
Frequencies --	1496.8015	1526.9577	1669.0611
Frequencies --	1691.6501	1744.9004	3039.1798
Frequencies --	3057.8435	3169.0449	3183.6576
Frequencies --	3213.6016	3225.2961	3273.7312

HPBF

1	6	0	-0.883500	1.834737	1.149530
2	6	0	-1.034160	0.529419	0.971859
3	1	0	-1.227925	2.310005	2.055163
4	1	0	-0.413804	2.462367	0.407125
5	6	0	-0.655954	-0.226175	-0.267616
6	1	0	-1.504382	-0.086180	1.724944
7	6	0	-1.836046	-0.471726	-1.191482
8	8	0	0.260416	0.584631	-1.104752
9	8	0	-0.134272	-1.492675	-0.000581
10	1	0	-2.188107	0.474285	-1.591477
11	1	0	-1.526585	-1.121755	-2.006710
12	1	0	-2.634634	-0.952142	-0.633379
13	6	0	1.553524	0.719314	-0.833830
14	8	0	0.585099	-1.524915	1.255073
15	8	0	2.195498	0.210024	0.055430
16	1	0	1.998607	1.390186	-1.573964
17	1	0	1.379722	-1.006701	1.006175
Frequencies --	76.0580	98.5864	202.2503		
Frequencies --	212.1732	245.6072	272.8544		
Frequencies --	294.5828	305.7747	332.8314		
Frequencies --	358.7746	474.4106	526.5001		
Frequencies --	574.6054	651.3611	692.4755		
Frequencies --	702.5520	816.2610	842.2525		
Frequencies --	933.1789	971.4580	989.3940		
Frequencies --	1026.7452	1051.0041	1054.5359		
Frequencies --	1135.5926	1177.0500	1242.5607		
Frequencies --	1267.6093	1327.8929	1415.3733		
Frequencies --	1422.0245	1461.0687	1496.5053		
Frequencies --	1499.6251	1507.1182	1708.6714		
Frequencies --	1757.4064	3077.6396	3079.7797		
Frequencies --	3160.8343	3172.7541	3174.8347		
Frequencies --	3210.0886	3263.1153	3498.3543		

Alkoxy

1	6	0	2.372674	-1.020834	-0.081462
2	6	0	1.802909	0.171921	0.034423
3	1	0	3.448819	-1.110346	-0.098440
4	1	0	1.785744	-1.919485	-0.181417
5	6	0	0.297368	0.406274	0.068797

6	1	0	2.382535	1.074785	0.156943
7	6	0	-0.114558	1.570558	-0.832022
8	8	0	0.074864	0.636804	1.370559
9	8	0	-0.331173	-0.831697	-0.394272
10	1	0	0.095177	1.310963	-1.866845
11	1	0	0.457472	2.451934	-0.554932
12	1	0	-1.172513	1.773592	-0.706715
13	6	0	-1.655823	-0.957260	-0.204460
14	8	0	-2.399740	-0.137245	0.260446
15	1	0	-1.964267	-1.948301	-0.554118
Frequencies --	62.0861		107.9899		173.0780
Frequencies --	223.5841		239.7966		262.0089
Frequencies --	307.7685		348.7095		425.4105
Frequencies --	511.1594		545.8325		649.3337
Frequencies --	691.0476		828.4077		891.6562
Frequencies --	951.9134		987.3386		1018.9171
Frequencies --	1034.7477		1043.9681		1102.8519
Frequencies --	1162.2461		1169.2324		1230.4460
Frequencies --	1324.1390		1399.1923		1412.1628
Frequencies --	1443.1028		1491.2506		1513.5205
Frequencies --	1685.8150		1784.4604		3057.9617
Frequencies --	3078.6667		3160.3187		3178.1332
Frequencies --	3184.1275		3215.5311		3276.1918

APPENDIX V

EXPERIMENTAL EVIDENCE OF DIOXOLE UNIMOLECULAR DECAY PATHWAY FOR ISOPRENE-DERIVED CRIEGEE INTERMEDIATES SUPPORTING INFORMATION

This appendix has been previously published as online supplementary material in the *Journal of Physical Chemistry A*, **124**, 3542 (2020) and reproduced with the permission of the American Chemical Society. It is a supplement to Chapter 6 of this thesis. The experimental research was performed with researchers Rebecca Caravan (*NASA Postdoctoral Program Fellow, NASA Jet Propulsion Laboratory, Combustion Research Facility, Sandia National Laboratories, Chemical Sciences and Engineering Division, Argonne National Laboratory*), Kristen Zuraski (*NASA Postdoctoral Program Fellow, NASA Jet Propulsion Laboratory*), Frank Winiberg (*NASA Jet Propulsion Laboratory, California Institute of Technology*), Kendrew Au (*Combustion Research Facility, Sandia National Laboratories*), David Osborn (*Combustion Research Facility, Sandia National Laboratories*), Carl Percival (*NASA Jet Propulsion Laboratory, California Institute of Technology*), Craig Taatjes (*Combustion Research Facility, Sandia National Laboratories*), and Marsha Lester (*Department of Chemistry, University of Pennsylvania*). Synthetic work was performed by graduate student Nisalak Trongsiwat and Patrick J. Walsh (*Department of Chemistry, University of Pennsylvania*). Atmospheric modeling was performed in collaboration with Anwar Khan and Dudley Shallcross (*School of Chemistry, University of Bristol*).

Section S1. Product branching analysis

For the product branching analysis, the PIE curves that are analyzed are obtained by integrating over the full product mass and time window (0-80 ms). The known absolute photoionization spectra of the products are scaled to match the experimental PIE curves via a least squares method.¹⁻⁴ Examples are shown in the main text for mass channels where only the products contribute to the photoionization signal (Figures 1, 5, 6). For ketene (m/z 42) and glyoxal products (m/z 58), interfering species contribute to the photoionization signal of the associated mass channel (Figures 2 and 4). The interfering species have the same nominal mass but different numbers of C and O atoms that results in partially resolved features in the mass spectrum. The photoionization spectra of the interfering species are required to quantify the contribution of ketene and glyoxal in their respective PIE curve (m/z 42 and m/z 58, respectively). The mass resolution of the MPIMS experiment is sufficient to estimate the photoionization spectrum of each interfering species by integrating over a mass region where it is the dominant spectral carrier. An example is shown in Figure 3 of the main text for the ketene (m/z 42) product channel. Integration over the 42.04-42.08 mass region results in an estimated photoionization spectrum of the interfering species. The contributions to the PIE curve of the full m/z 42 mass and time window (Figure S1, open circles) can then be separated by a scaled sum (black line) of the absolute photoionization spectrum of ketene (green line)² and the estimated photoionization spectrum of the interfering species (blue line) by a least squares method to extract branching information for the ketene product channel.

For the glyoxal product channel, the same analysis was conducted to estimate the photoionization spectrum of the interfering species (Figure S2) and determine branching to the glyoxal product channel (Figure S3). The identity of the interfering specie(s) is

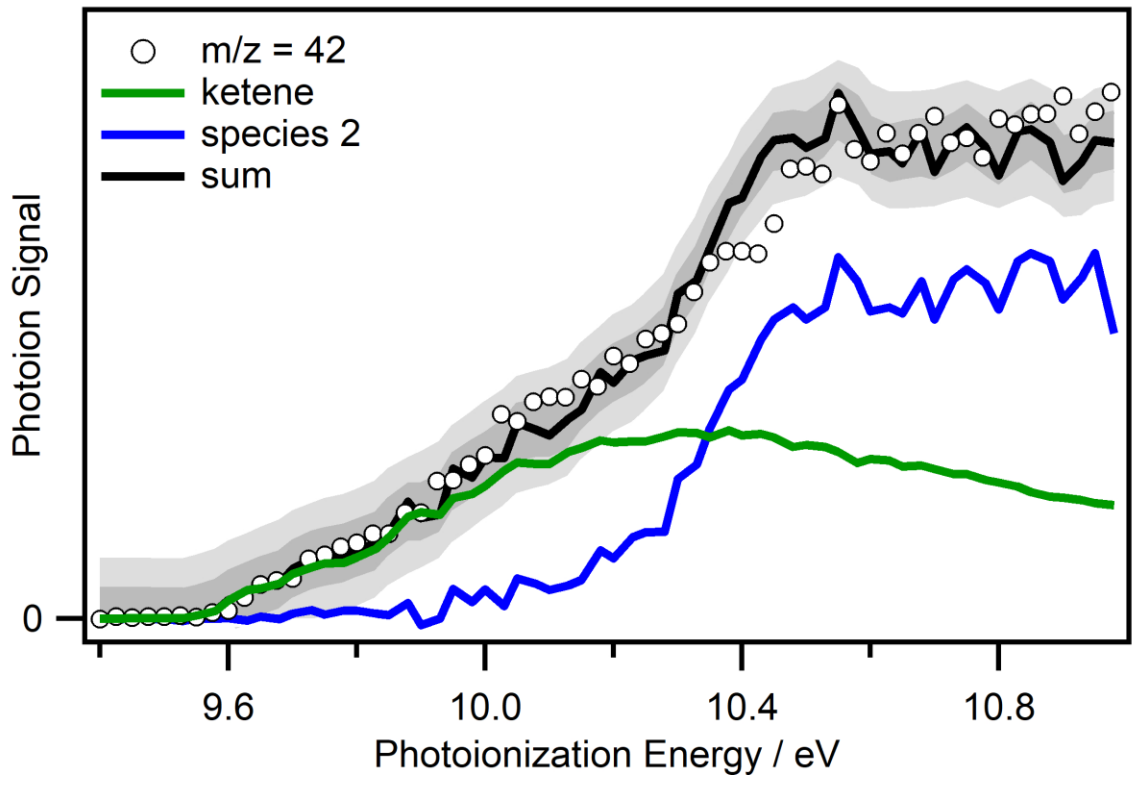


Figure S1. PIE curve of m/z 42 (open circles) integrated over the full kinetic time window (0-80 ms) and mass window (41.95-42.08 amu). The black lines shows the result of a least squares fit of the absolute photoionization spectrum of ketene and experimental photoionization spectrum of the interfering species (species 2) to the m/z 42 PIE curve. The darker and lighter grey shaded regions represents 1σ and 2σ uncertainty in the fit, respectively.

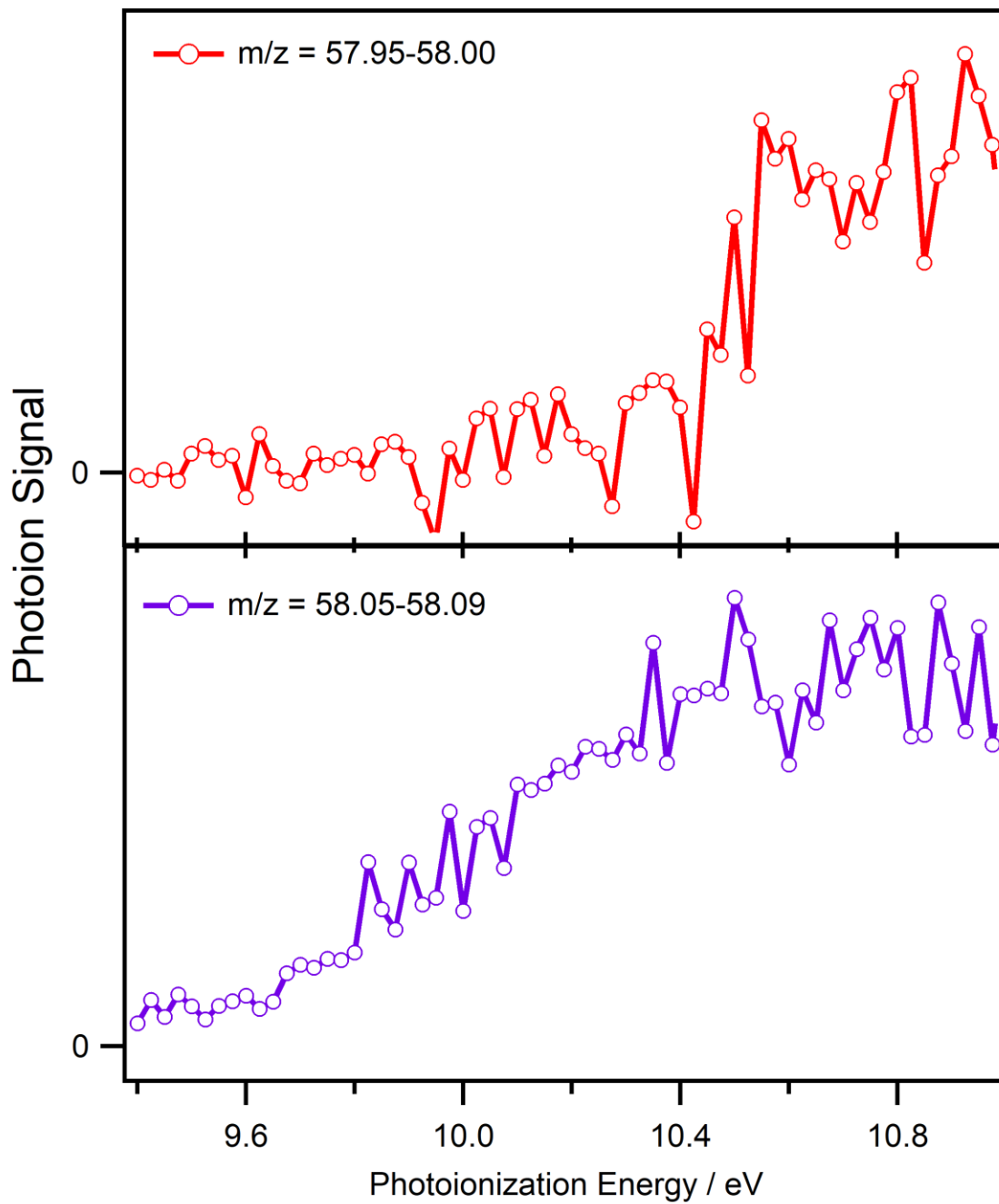


Figure S2. (Top) The PIE curve of the 57.95-58.00 mass window (red open circles) is consistent with the known PI spectrum of glyoxal.² (Lower panel) PIE curve associated with the 58.05-58.09 mass window (purple open circles). The PIE curves are generated by integrating over the full kinetic time window (0-80 ms).

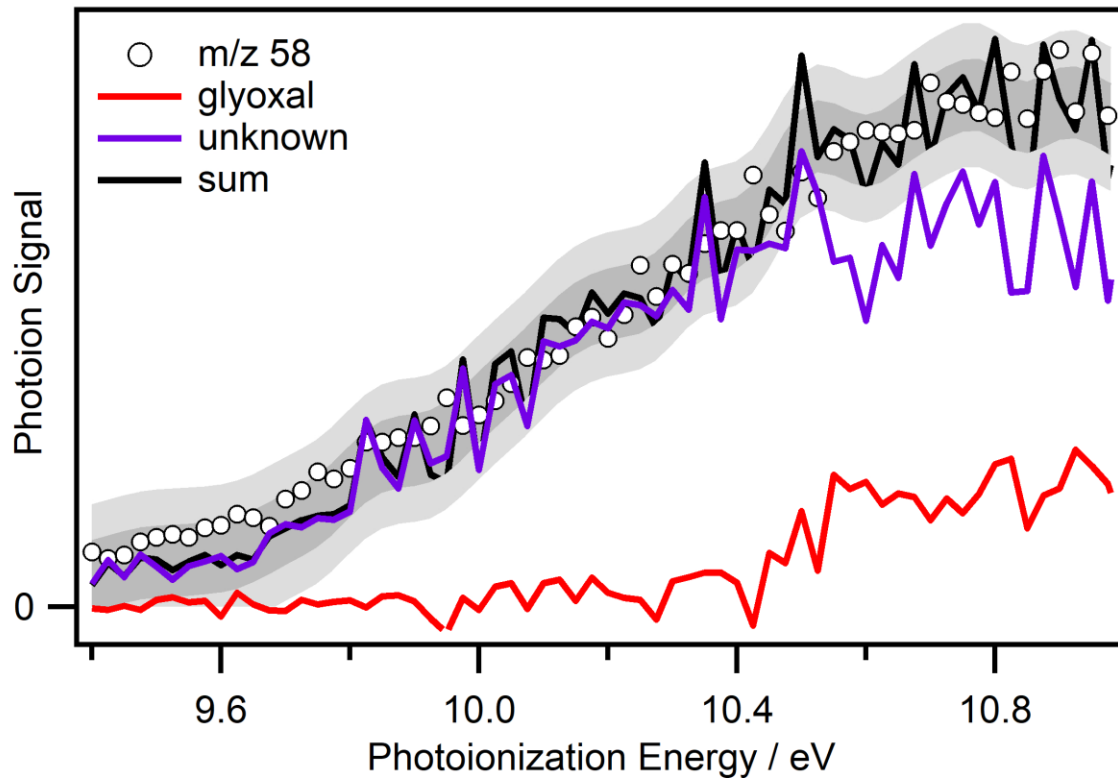


Figure S3. PIE curve of m/z 58 (open circles) integrated over the full kinetic time window (0-80 ms) and mass window (57.95-58.09 amu). The black lines shows the result of a least squares fit of the absolute photoionization spectrum of glyoxal and experimental photoionization spectrum of the interfering species (unknown) to the m/z 58 PIE curve. The darker and lighter grey shaded regions represents 1σ and 2σ uncertainty in the fit, respectively.

unknown. The chemical composition is consistent with acetone (IE = 9.70 eV)⁵ or 2-propen-1-ol (IE = 9.70 eV).⁶ However, photoionization signal is observed at lower ionization energies, potentially due to a daughter ion.

In this case, an assumption of the photoionization cross section of glyoxal is required because only the relative photoionization spectrum of glyoxal is known.³ We estimate the photoionization cross-section of glyoxal by drawing comparisons to similar molecules with known absolute spectra. Acrolein is chemically similar to glyoxal, only differing by a C=C vs C=O bond, respectively. It is well known that the photoionization cross section of molecules with C=O bonds are larger than those with C=C bonds.⁷ For example, the photoionization cross section of formaldehyde (H₂CO) at 11 eV is ca. 20% greater than that of ethylene (C₂H₄).^{1,8} Thus, to account for the difference in structure we scale the photoionization spectrum of glyoxal such that its cross-section at 11 eV is 20% greater than that of acrolein.⁴ The overall product branching is insensitive to the 20% change in the cross-section (± 1 %) used for the analysis of glyoxal on the m/z 58 mass channel and is within uncertainty of the analysis.

Section S2. Theoretical calculations

Additional calculations were carried out to supplement the results of previous theoretical studies in cases where the energies of specific products were not reported. Kuwata *et al.*⁹ reported the unimolecular decay of the *syn*-MACR-oxide Criegee intermediate via the dioxole channel (Scheme 4). C-C bond fission of methylmalonaldehyde was not investigated. We carried out theoretical calculations of methylmalonaldehyde and the predicted alkyl radical products (2-methyl-vinoxy and formyl radical) to demonstrate that sufficient energy is available for C-C bond fission. The energy in Scheme 4 is reported at the same level of theory used by Kuwata *et al.*⁹

(CBS/QB3//B3LYP/6-311G(d,p)), including harmonic zero point energy (ZPE) corrections. The stationary point geometry of methylmalonaldehyde, 2-methyl-vinoxy radical, and formyl radical are reported in Table S1 and the relative energies are reported in Table S2.

The acetyl radical + O₂ reaction was theoretically investigated by Carr *et al.*¹⁰ In this study, the barrier to the formaldehyde products from the decomposition of α -lactone was reported, but not the asymptotic product energy. We carried out theoretical calculations to demonstrate that formaldehyde + OH + CO is the thermodynamically favored product. The energy in Scheme 5 for formaldehyde + OH + CO is reported at the CCSD/cc-pVTZ//B2PLYP-D3/cc-pVTZ level of theory relative to α -lactone + OH, including harmonic ZPE corrections. The stationary point geometry of α -lactone, OH, CO, and formaldehyde are reported in Table S1; the relative energies are reported in Table S2.

Section S3. MESMER input file

The parameters used for the master equation modeling using the Master Equation Solver for Multi-Energy well Reactions (MESMER) are described briefly; the input files for the calculations are also provided below. Collisional energy transfer was described using an exponential down model $\Delta E_{\text{down}} = 130 \text{ cm}^{-1}$ in N₂. Lennard-Jones parameters were chosen based on those determined for similar molecules.¹⁰ Parameters from the high level electronic structure calculations carried out by Weidman *et al.*¹¹ and Davis *et al.*¹² were used as inputs for the vinoxy + O₂ and 2-methyl-vinoxy + O₂ simulations, respectively. This includes the energetics for each stationary point and vibrational frequencies. The inputs for the rotational constants of each species were

Table S1. Stationary point geometries of species discussed in Section S2.

Stationary Point Geometries			
Minima			
methyl-malonaldehyde ^a			
C	-0.75902	1.59477	-0.00040
H	-0.97651	1.58207	-1.06702
H	-1.70979	1.64517	0.52282
H	-0.18862	2.49388	0.22592
C	0.01060	0.35087	0.40497
H	0.24354	0.34149	1.47439
C	1.34846	0.20971	-0.30109
H	1.49592	0.87823	-1.16991
O	2.19247	-0.58912	0.02410
C	-0.77023	-0.93498	0.15931
H	-0.21731	-1.85719	0.40461
O	-1.89573	-0.96161	-0.27004
2-methyl-vinoxy radical ^a			
C	-1.50101	-0.41221	0.00012
H	-2.15872	-0.34593	0.87596
H	-0.99984	-1.37982	0.00146
H	-2.15679	-0.34783	-0.87742
C	-0.50778	0.67815	-0.00014
H	-0.85153	1.72006	-0.00028
C	0.90245	0.45293	0.00007
H	1.54651	1.35270	0.00048
O	1.40790	-0.67231	-0.00006
formyl radical ^a			
C	0.06231	0.58418	0.00000
H	-0.87235	1.21503	0.00000
O	0.06231	-0.59001	0.00000
α -lactone ^b			
C	-1.02255	0.59518	0.00008
H	-1.49203	0.90431	-0.92253
H	-1.49234	0.90466	0.92204
C	0.32406	0.06797	0.00048
O	-0.61119	-0.88163	-0.00006
O	1.50809	0.15815	-0.00018
OH ^b			
O	0.00000	0.00000	0.10786
H	0.00000	0.00000	-0.86290

Formaldehyde ^b			
C	-0.00001	0.52883	0.00000
H	0.93516	1.11372	0.00000
H	-0.93505	1.11393	0.00000
O	-0.00001	-0.67508	0.00000
CO ^b			
C	0.00000	0.00000	-0.64654
O	0.00000	0.00000	0.48490

^aB3LYP/6-311G(d,p)

^bB2PLYP-D3/cc-pVTZ

Table S2. Calculated energies and ZPE corrections of predicted product asymptotes.

Species	Relative Energy (kcal mol ⁻¹)	Relative ZPE (kcal mol ⁻¹)	Total Energy (kcal mol ⁻¹)
methyl-malonaldehyde ^a	0	0	0
2-methyl-vinoxy + formyl radical ^a	70.4	-5.7	64.7
α -lactone + OH ^b	0	0	0
formaldehyde + OH + CO ^b	-10.9	-4.3	-15.2

^aCBS/QB3//B3LYP/6-311G(d,p)^bCCSD/cc-pVTZ//B2PLYP-D3/cc-pVTZ

calculated at the CCSD(T)/cc-pVTZ level of theory using the stationary point geometries previously calculated.^{11, 12}

Vinoxy radical + O₂ MESMER input

```
<?xml version="1.0" encoding="utf-8" ?>
<?xml-stylesheet type='text/xsl' href='../mesmer2.xsl' media='other'?>
<?xml-stylesheet type='text/xsl' href='../mesmer1.xsl' media='screen'?>
<me:mesmer xmlns="http://www.xml-cml.org/schema"
  xmlns:me="http://www.chem.leeds.ac.uk/mesmer"
  xmlns:xsi="http://www.w3.org/2001/XMLSchema-instance">
  <me:title> Vinoxy O2 Association</me:title>
  <moleculeList>
    <molecule id="vinoxy" description="CH2CHO">
      <atomArray>
        <atom id="a1" elementType="C" />
        <atom id="a2" elementType="C" />
        <atom id="a3" elementType="H" />
        <atom id="a4" elementType="H" />
        <atom id="a5" elementType="O" />
        <atom id="a6" elementType="H" />
      </atomArray>
      <bondArray>
        <bond atomRefs2="a1 a2" order="1" />
        <bond atomRefs2="a1 a3" order="1" />
        <bond atomRefs2="a1 a4" order="1" />
        <bond atomRefs2="a2 a5" order="2" />
        <bond atomRefs2="a2 a6" order="1" />
      </bondArray>
      <propertyList>
        <property dictRef="me:ZPE">
          <scalar units="kcal/mol">0</scalar>
        </property>
        <property dictRef="me:rotConsts">
          <array units="cm-1">2.232601 0.380527 0.325114</array>
        </property>
        <property dictRef="me:symmetryNumber">
          <scalar>1</scalar>
        </property>
        <property dictRef="me:frequenciesScaleFactor">
          <scalar>1</scalar>
        </property>
        <property dictRef="me:vibFreqs">
          <array units="cm-1">3277 3159 2988 1573 1474 1403 1158 970 499 974 735 432
        </array>
        </property>
        <property dictRef="me:MW">
```

```

    <scalar units="amu">43</scalar>
  </property>
  <property dictRef="me:spinMultiplicity">
    <scalar>2</scalar>
  </property>
</propertyList>
<me:DOSCMethod xsi:type="ClassicalRotors"/>
</molecule>
<molecule id="O2" description="oxygen">
  <atomArray>
    <atom id="a1" elementType="O" />
    <atom id="a2" elementType="O" />
  </atomArray>
  <bondArray>
    <bond atomRefs2="a1 a2" order="2" />
  </bondArray>
  <propertyList>
    <property dictRef="me:ZPE">
      <scalar units="kcal/mol">0.0</scalar>
    </property>
    <property dictRef="me:rotConsts">
      <array units="cm-1">1.431782</array>
    </property>
    <property dictRef="me:symmetryNumber">
      <scalar>2</scalar>
    </property>
    <property dictRef="me:frequenciesScaleFactor">
      <scalar>1</scalar>
    </property>
    <property dictRef="me:vibFreqs">
      <array units="cm-1">1583</array>
    </property>
    <property dictRef="me:MW">
      <scalar units="amu">32</scalar>
    </property>
    <property dictRef="me:spinMultiplicity">
      <scalar>3</scalar>
    </property>
  </propertyList>
  <me:DOSCMethod xsi:type="ClassicalRotors"/>
</molecule>
<molecule id="OH" description="OH radical">
  <atomArray>
    <atom id="a1" elementType="O" />
    <atom id="a2" elementType="H" />
  </atomArray>
  <bondArray>
    <bond atomRefs2="a1 a2" order="1" />
  </bondArray>

```

```

<propertyList>
  <property dictRef="me:ZPE">
    <scalar units="kcal/mol">0.0</scalar>
  </property>
  <property dictRef="me:rotConsts">
    <array units="cm-1">18.86743</array>
  </property>
  <property dictRef="me:symmetryNumber">
    <scalar>1</scalar>
  </property>
  <property dictRef="me:frequenciesScaleFactor">
    <scalar>1</scalar>
  </property>
  <property dictRef="me:vibFreqs">
    <array units="cm-1">3718</array>
  </property>
  <property dictRef="me:MW">
    <scalar units="amu">17</scalar>
  </property>
  <property dictRef="me:spinMultiplicity">
    <scalar>2</scalar>
  </property>
  <property dictRef="me:eletronicExcitation">
    <array units="cm-1">139.7</array>
  </property>
</propertyList>
<me:DOSMethod xsi:type="ClassicalRotors"/>
</molecule>
<molecule id="PRa" description="peroxy vinoxy O2 adduct">
  <atomArray>
    <atom id="a1" elementType="C" />
    <atom id="a2" elementType="C" />
    <atom id="a3" elementType="O" />
    <atom id="a4" elementType="H" />
    <atom id="a5" elementType="O" />
    <atom id="a6" elementType="O" />
    <atom id="a7" elementType="H" />
    <atom id="a8" elementType="H" />
  </atomArray>
  <bondArray>
    <bond atomRefs2="a1 a2" order="1" />
    <bond atomRefs2="a1 a7" order="1" />
    <bond atomRefs2="a1 a8" order="1" />
    <bond atomRefs2="a1 a5" order="1" />
    <bond atomRefs2="a2 a3" order="2" />
    <bond atomRefs2="a2 a4" order="1" />
    <bond atomRefs2="a5 a6" order="1" />
  </bondArray>
</propertyList>

```

```

<property dictRef="me:ZPE">
  <scalar units="kcal/mol">-21.9</scalar>
</property>
<property dictRef="me:rotConsts">
  <array units="cm-1">0.552028 0.099531 0.089599</array>
</property>
<property dictRef="me:symmetryNumber">
  <scalar>1</scalar>
</property>
<property dictRef="me:frequenciesScaleFactor">
  <scalar>1</scalar>
</property>
<property dictRef="me:vibFreqs">
  <array units="cm-1">3150 3084 2977 1789 1451 1408 1333 1258 1145 1107
1046 969 742 584 439 295 148 54</array>
</property>
<property dictRef="me:MW">
  <scalar units="amu">75</scalar>
</property>
<property dictRef="me:spinMultiplicity">
  <scalar>2</scalar>
</property>
<property dictRef="me:epsilon">
  <scalar>473.17</scalar>
</property>
<property dictRef="me:sigma">
  <scalar>5.09</scalar>
</property>
</propertyList>
<me:energyTransferModel xsi:type="me:ExponentialDown">
  <me:deltaEDown units="cm-1">130</me:deltaEDown>
</me:energyTransferModel>
<me:DOSCMMethod xsi:type="ClassicalRotors"/>
</molecule>
<molecule id="TS1" description="TS1a: PRa -> QR1">
  <atomArray>
    <atom id="a1" elementType="C" />
    <atom id="a2" elementType="C" />
    <atom id="a3" elementType="O" />
    <atom id="a4" elementType="O" />
    <atom id="a5" elementType="O" />
    <atom id="a6" elementType="H" />
    <atom id="a7" elementType="H" />
    <atom id="a8" elementType="H" />
  </atomArray>
  <bondArray>
    <bond atomRefs2="a1 a2" order="1" />
    <bond atomRefs2="a1 a4" order="1" />
    <bond atomRefs2="a1 a6" order="1" />

```

```

    <bond atomRefs2="a1 a7" order="1" />
    <bond atomRefs2="a4 a5" order="1" />
        <bond atomRefs2="a2 a3" order="2" />
        <bond atomRefs2="a2 a8" order="1" />
</bondArray>
<propertyList>
  <property dictRef="me:ZPE">
    <scalar units="kcal/mol">-0.7</scalar>
  </property>
  <property dictRef="me:rotConsts">
    <array units="cm-1">0.444475 0.122314 0.099436</array>
  </property>
  <property dictRef="me:symmetryNumber">
    <scalar>1</scalar>
  </property>
  <property dictRef="me:frequenciesScaleFactor">
    <scalar>1</scalar>
  </property>
  <property dictRef="me:vibFreqs">
    <array units="cm-1">3151 3044 1921 1829 1453 1272 1221 1156 1046 929 885
797 682 538 395 380 184</array>
  </property>
  <property dictRef="me:MW">
    <scalar units="amu">75</scalar>
  </property>
  <property dictRef="me:spinMultiplicity">
    <scalar>2</scalar>
  </property>
  <property dictRef="me:imFreqs">
    <scalar units="cm-1">2130</scalar>
  </property>
</propertyList>
<me:DOSCMMethod xsi:type="ClassicalRotors"/>
</molecule>
<molecule id="TS2" description="PRa -> QR2">
  <atomArray>
    <atom id="a1" elementType="C" />
    <atom id="a2" elementType="C" />
    <atom id="a3" elementType="O" />
    <atom id="a4" elementType="H" />
    <atom id="a5" elementType="O" />
    <atom id="a6" elementType="H" />
    <atom id="a7" elementType="H" />
    <atom id="a8" elementType="O" />
  </atomArray>
  <bondArray>
    <bond atomRefs2="a1 a2" order="1" />
    <bond atomRefs2="a1 a5" order="1" />
    <bond atomRefs2="a1 a7" order="1" />

```

```

    <bond atomRefs2="a1 a6" order="1" />
    <bond atomRefs2="a5 a8" order="1" />
      <bond atomRefs2="a2 a4" order="1" />
      <bond atomRefs2="a2 a3" order="2" />
</bondArray>
<propertyList>
  <property dictRef="me:ZPE">
    <scalar units="kcal/mol">16.8</scalar>
  </property>
  <property dictRef="me:rotConsts">
    <array units="cm-1">0.619707 0.093273 0.089574</array>
  </property>
  <property dictRef="me:symmetryNumber">
    <scalar>1</scalar>
  </property>
  <property dictRef="me:frequenciesScaleFactor">
    <scalar>1</scalar>
  </property>
  <property dictRef="me:vibFreqs">
    <array units="cm-1">3138 2992 1992 1758 1400 1288 1134 1091 1085 1022 793
743 640 493 328 138 120 </array>
  </property>
  <property dictRef="me:MW">
    <scalar units="amu">75</scalar>
  </property>
  <property dictRef="me:spinMultiplicity">
    <scalar>2</scalar>
  </property>
  <property dictRef="me:imFreqs">
    <scalar units="cm-1">1897</scalar>
  </property>
</propertyList>
<me:DOSCMMethod xsi:type="ClassicalRotors"/>
</molecule>
<molecule id="ketene" description="CH2CO">
  <atomArray>
    <atom id="a1" elementType="C" />
    <atom id="a2" elementType="O" />
    <atom id="a3" elementType="C" />
    <atom id="a4" elementType="H" />
    <atom id="a5" elementType="H" />
  </atomArray>
  <bondArray>
    <bond atomRefs2="a1 a3" order="2" />
    <bond atomRefs2="a1 a2" order="2" />
    <bond atomRefs2="a3 a4" order="1" />
    <bond atomRefs2="a3 a5" order="1" />
  </bondArray>
</propertyList>

```

```

<property dictRef="me:ZPE">
  <scalar units="kcal/mol">-12.6</scalar>
</property>
<property dictRef="me:rotConsts">
  <array units="cm-1">9.428139 0.341214 0.329295</array>
</property>
<property dictRef="me:symmetryNumber">
  <scalar>1</scalar>
</property>
<property dictRef="me:frequenciesScaleFactor">
  <scalar>1</scalar>
</property>
<property dictRef="me:vibFreqs">
  <array units="cm-1">3307 3202 2202 1413 1152 991 595 522 436 </array>
</property>
<property dictRef="me:MW">
  <scalar units="amu">42</scalar>
</property>
<property dictRef="me:spinMultiplicity">
  <scalar>1</scalar>
</property>
</propertyList>
<me:DOSCMMethod xsi:type="ClassicalRotors"/>
</molecule>
<molecule id="HO2">
<atomArray>
  <atom id="a1" elementType="O" />
  <atom id="a2" elementType="H" />
  <atom id="a3" elementType="O" />
</atomArray>
<bondArray>
  <bond atomRefs2="a1 a2" order="1" />
  <bond atomRefs2="a1 a3" order="1" />
</bondArray>
<propertyList>
<property dictRef="me:ZPE">
  <scalar units="kcal/mol">0.0</scalar>
</property>
<property dictRef="me:rotConsts">
  <array units="cm-1">20.52618 1.113085 1.05583</array>
</property>
<property dictRef="me:symmetryNumber">
  <scalar>1</scalar>
</property>
<property dictRef="me:frequenciesScaleFactor">
  <scalar>1</scalar>
</property>
<property dictRef="me:vibFreqs">
  <array units="cm-1">3674 1434 1126</array>

```

```

    </property>
    <property dictRef="me:MW">
      <scalar units="amu">33</scalar>
    </property>
    <property dictRef="me:spinMultiplicity">
      <scalar>2</scalar>
    </property>
  </propertyList>
  <me:DOSCMMethod xsi:type="ClassicalRotors"/>
</molecule>
<molecule id="QR1" description="peroxide_isomer_opt">
  <atomArray>
    <atom id="a1" elementType="C" />
    <atom id="a2" elementType="C" />
    <atom id="a3" elementType="O" />
    <atom id="a4" elementType="H" />
    <atom id="a5" elementType="H" />
    <atom id="a6" elementType="O" />
    <atom id="a7" elementType="H" />
    <atom id="a8" elementType="O" />
  </atomArray>
  <bondArray>
    <bond atomRefs2="a1 a2" order="1" />
    <bond atomRefs2="a1 a5" order="1" />
    <bond atomRefs2="a1 a4" order="1" />
    <bond atomRefs2="a1 a3" order="1" />
    <bond atomRefs2="a3 a6" order="1" />
    <bond atomRefs2="a6 a7" order="1" />
    <bond atomRefs2="a2 a8" order="2" />
  </bondArray>
  <propertyList>
    <property dictRef="me:ZPE">
      <scalar units="kcal/mol">-21.0</scalar>
    </property>
    <property dictRef="me:rotConsts">
      <array units="cm-1">0.316736 0.148749 0.112639</array>
    </property>
    <property dictRef="me:symmetryNumber">
      <scalar>1</scalar>
    </property>
    <property dictRef="me:frequenciesScaleFactor">
      <scalar>1</scalar>
    </property>
    <property dictRef="me:vibFreqs">
      <array units="cm-1">3743 3130 3062 1894 1428 1397 1341 1275 1062 936 844
814 706 424 378 272 206 144</array>
    </property>
    <property dictRef="me:MW">
      <scalar units="amu">75</scalar>

```

```

</property>
<property dictRef="me:spinMultiplicity">
  <scalar>2</scalar>
</property>
<property dictRef="me:epsilon">
  <scalar>473.17</scalar>
</property>
<property dictRef="me:sigma">
  <scalar>5.09</scalar>
</property>
</propertyList>
<me:energyTransferModel xsi:type="me:ExponentialDown">
  <me:deltaEDown units="cm-1">130</me:deltaEDown>
</me:energyTransferModel>
<me:DOSCMETHOD xsi:type="ClassicalRotors"/>
</molecule>
<molecule id="TS4" description="TS QR1 -> CH2OOH_CO">
  <atomArray>
    <atom id="a1" elementType="C" />
    <atom id="a2" elementType="C" />
    <atom id="a3" elementType="O" />
    <atom id="a4" elementType="H" />
    <atom id="a5" elementType="H" />
    <atom id="a6" elementType="O" />
    <atom id="a7" elementType="H" />
    <atom id="a8" elementType="O" />
  </atomArray>
  <bondArray>
    <bond atomRefs2="a1 a3" order="1" />
    <bond atomRefs2="a1 a5" order="1" />
    <bond atomRefs2="a3 a6" order="1" />
    <bond atomRefs2="a6 a7" order="1" />
    <bond atomRefs2="a1 a4" order="1" />
    <bond atomRefs2="a2 a8" order="2" />
  </bondArray>
  <propertyList>
    <property dictRef="me:ZPE">
      <scalar units="kcal/mol">-9.7</scalar>
    </property>
    <property dictRef="me:rotConsts">
      <array units="cm-1">0.295498 0.127205 0.098056</array>
    </property>
    <property dictRef="me:symmetryNumber">
      <scalar>1</scalar>
    </property>
    <property dictRef="me:frequenciesScaleFactor">
      <scalar>1</scalar>
    </property>
    <property dictRef="me:vibFreqs">

```

```

    <array units="cm-1">3745 3251 3121 1964 1441 1393 1209 1144 973 846 605
477 364 323 200 134 99</array>
  </property>
  <property dictRef="me:MW">
    <scalar units="amu">75</scalar>
  </property>
  <property dictRef="me:spinMultiplicity">
    <scalar>2</scalar>
  </property>
  <property dictRef="me:imFreqs">
    <scalar units="cm-1">375</scalar>
  </property>
</propertyList>
<me:DOSCMETHOD xsi:type="ClassicalRotors"/>
</molecule>
  <molecule id="TS5" description="TS QR1 -> ketene_HO2">
<atomArray>
  <atom id="a1" elementType="O" />
  <atom id="a2" elementType="O" />
  <atom id="a3" elementType="H" />
  <atom id="a4" elementType="C" />
  <atom id="a5" elementType="H" />
  <atom id="a6" elementType="H" />
  <atom id="a7" elementType="C" />
  <atom id="a8" elementType="O" />
</atomArray>
<bondArray>
  <bond atomRefs2="a4 a5" order="1" />
  <bond atomRefs2="a4 a6" order="1" />
  <bond atomRefs2="a4 a7" order="1" />
  <bond atomRefs2="a7 a8" order="1" />
  <bond atomRefs2="a1 a2" order="1" />
  <bond atomRefs2="a2 a3" order="1" />
</bondArray>
<propertyList>
  <property dictRef="me:ZPE">
    <scalar units="kcal/mol">2.1</scalar>
  </property>
  <property dictRef="me:rotConsts">
    <array units="cm-1">0.326465 0.105935 0.085832</array>
  </property>
  <property dictRef="me:symmetryNumber">
    <scalar>1</scalar>
  </property>
  <property dictRef="me:frequenciesScaleFactor">
    <scalar>1</scalar>
  </property>
  <property dictRef="me:vibFreqs">

```

```

    <array units="cm-1">3754 3254 3159 2119 1399 1376 1056 1051 944 847 653
445 424 406 266 131 50</array>
  </property>
  <property dictRef="me:MW">
    <scalar units="amu">75</scalar>
  </property>
  <property dictRef="me:spinMultiplicity">
    <scalar>2</scalar>
  </property>
  <property dictRef="me:imFreqs">
    <scalar units="cm-1">695</scalar>
  </property>
</propertyList>
<me:DOSCMMethod xsi:type="ClassicalRotors"/>
</molecule>
<molecule id="H2CO">
  <atomArray>
    <atom id="a1" elementType="C" />
    <atom id="a2" elementType="O" />
    <atom id="a3" elementType="H" />
    <atom id="a4" elementType="H" />
  </atomArray>
  <bondArray>
    <bond atomRefs2="a1 a2" order="1" />
    <bond atomRefs2="a1 a3" order="1" />
    <bond atomRefs2="a1 a4" order="1" />
  </bondArray>
  <propertyList>
    <property dictRef="me:ZPE">
      <scalar units="kcal/mol">-50.1</scalar>
    </property>
    <property dictRef="me:rotConsts">
      <array units="cm-1">9.522858 1.287951 1.13451</array>
    </property>
    <property dictRef="me:symmetryNumber">
      <scalar>1</scalar>
    </property>
    <property dictRef="me:frequenciesScaleFactor">
      <scalar>1</scalar>
    </property>
    <property dictRef="me:vibFreqs">
      <array units="cm-1">3004 2937 1773 1537 1272 1188</array>
    </property>
    <property dictRef="me:MW">
      <scalar units="amu">30</scalar>
    </property>
    <property dictRef="me:spinMultiplicity">
      <scalar>1</scalar>
    </property>
  </propertyList>

```

```

        <property dictRef="me:epsilon">
          <scalar>473.17</scalar>
        </property>
        <property dictRef="me:sigma">
          <scalar>5.09</scalar>
        </property>
      </propertyList>
      <me:energyTransferModel xsi:type="me:ExponentialDown">
        <me:deltaEDown units="cm-1">130</me:deltaEDown>
      </me:energyTransferModel>
      <me:DOSCMETHOD xsi:type="ClassicalRotors"/>
    </molecule>
    <molecule id="CH2OOH">
      <atomArray>
        <atom id="a1" elementType="C" />
        <atom id="a2" elementType="H" />
        <atom id="a3" elementType="H" />
        <atom id="a4" elementType="O" />
        <atom id="a5" elementType="O" />
        <atom id="a6" elementType="H" />
      </atomArray>
      <bondArray>
        <bond atomRefs2="a1 a2" order="1" />
        <bond atomRefs2="a1 a3" order="1" />
        <bond atomRefs2="a1 a4" order="1" />
        <bond atomRefs2="a4 a5" order="1" />
        <bond atomRefs2="a5 a6" order="1" />
      </bondArray>
      <propertyList>
        <property dictRef="me:ZPE">
          <scalar units="kcal/mol">-15.1</scalar>
        </property>
        <property dictRef="me:rotConsts">
          <array units="cm-1">1.730428 0.376788 0.321947</array>
        </property>
        <property dictRef="me:symmetryNumber">
          <scalar>1</scalar>
        </property>
        <property dictRef="me:frequenciesScaleFactor">
          <scalar>1</scalar>
        </property>
        <property dictRef="me:vibFreqs">
          <array units="cm-1">3774 3284 3142 1441 1372 1204 1149 840 709 484 275
176</array>
        </property>
        <property dictRef="me:MW">
          <scalar units="amu">47</scalar>
        </property>
        <property dictRef="me:spinMultiplicity">

```

```

    <scalar>2</scalar>
  </property>
</propertyList>
<me:DOSCMethod xsi:type="ClassicalRotors"/>
</molecule>
  <molecule id="CO">
<atomArray>
  <atom id="a1" elementType="C" />
  <atom id="a2" elementType="O" />
</atomArray>
<bondArray>
  <bond atomRefs2="a1 a2" order="2" />
</bondArray>
<propertyList>
  <property dictRef="me:ZPE">
    <scalar units="kcal/mol">0</scalar>
  </property>
  <property dictRef="me:rotConsts">
    <array units="cm-1">1.905061</array>
  </property>
  <property dictRef="me:symmetryNumber">
    <scalar>2</scalar>
  </property>
  <property dictRef="me:frequenciesScaleFactor">
    <scalar>1</scalar>
  </property>
  <property dictRef="me:vibFreqs">
    <array units="cm-1">2146</array>
  </property>
  <property dictRef="me:MW">
    <scalar units="amu">28</scalar>
  </property>
  <property dictRef="me:spinMultiplicity">
    <scalar>1</scalar>
  </property>
</propertyList>
<me:DOSCMethod xsi:type="ClassicalRotors"/>
</molecule>
  <molecule id="QR2">
<atomArray>
  <atom id="a1" elementType="C" />
  <atom id="a2" elementType="C" />
  <atom id="a3" elementType="O" />
  <atom id="a4" elementType="H" />
  <atom id="a5" elementType="O" />
  <atom id="a6" elementType="H" />
  <atom id="a7" elementType="O" />
  <atom id="a8" elementType="H" />
</atomArray>

```

```

<bondArray>
  <bond atomRefs2="a1 a2" order="1" />
  <bond atomRefs2="a1 a5" order="1" />
  <bond atomRefs2="a1 a6" order="1" />
  <bond atomRefs2="a2 a4" order="1" />
  <bond atomRefs2="a2 a3" order="2" />
  <bond atomRefs2="a5 a7" order="1" />
  <bond atomRefs2="a7 a8" order="1" />
</bondArray>
<propertyList>
  <property dictRef="me:ZPE">
    <scalar units="kcal/mol">-22.3</scalar>
  </property>
  <property dictRef="me:rotConsts">
    <array units="cm-1">0.575612 0.099941 0.085156</array>
  </property>
  <property dictRef="me:symmetryNumber">
    <scalar>1</scalar>
  </property>
  <property dictRef="me:frequenciesScaleFactor">
    <scalar>1</scalar>
  </property>
  <property dictRef="me:vibFreqs">
    <array units="cm-1">3804 3233 3062 1574 1520 1412 1336 1235 1135 948 844
700 639 430 251 235 137 35</array>
  </property>
  <property dictRef="me:MW">
    <scalar units="amu">75</scalar>
  </property>
  <property dictRef="me:spinMultiplicity">
    <scalar>2</scalar>
  </property>
  <property dictRef="me:epsilon">
    <scalar>473.17</scalar>
  </property>
  <property dictRef="me:sigma">
    <scalar>5.09</scalar>
  </property>
</propertyList>
<me:energyTransferModel xsi:type="me:ExponentialDown">
  <me:deltaEDown units="cm-1">130</me:deltaEDown>
</me:energyTransferModel>
<me:DOSMethod xsi:type="ClassicalRotors"/>
</molecule>
  <molecule id="glyoxal">
<atomArray>
  <atom id="a1" elementType="C" />
  <atom id="a2" elementType="C" />
  <atom id="a3" elementType="O" />

```

```

    <atom id="a4" elementType="O" />
    <atom id="a5" elementType="H" />
      <atom id="a6" elementType="H" />
</atomArray>
<bondArray>
  <bond atomRefs2="a1 a2" order="1" />
  <bond atomRefs2="a1 a5" order="1" />
  <bond atomRefs2="a1 a4" order="2" />
  <bond atomRefs2="a2 a6" order="1" />
  <bond atomRefs2="a2 a3" order="2" />
</bondArray>
<propertyList>
  <property dictRef="me:ZPE">
    <scalar units="kcal/mol">-47.5</scalar>
  </property>
  <property dictRef="me:rotConsts">
    <array units="cm-1">1.861549 0.159348 0.146783</array>
  </property>
  <property dictRef="me:symmetryNumber">
    <scalar>1</scalar>
  </property>
  <property dictRef="me:frequenciesScaleFactor">
    <scalar>1</scalar>
  </property>
  <property dictRef="me:vibFreqs">
    <array units="cm-1">2996 2991 1776 1753 1383 1342 1095 1066 818 560 332
130</array>
  </property>
  <property dictRef="me:MW">
    <scalar units="amu">58</scalar>
  </property>
  <property dictRef="me:spinMultiplicity">
    <scalar>2</scalar>
  </property>
  <property dictRef="me:epsilon">
    <scalar>473.17</scalar>
  </property>
  <property dictRef="me:sigma">
    <scalar>5.09</scalar>
  </property>
</propertyList>
<me:energyTransferModel xsi:type="me:ExponentialDown">
  <me:deltaEDown units="cm-1">130</me:deltaEDown>
</me:energyTransferModel>
<me:DOSCMMethod xsi:type="ClassicalRotors"/>
</molecule>
</moleculeList>
<reactionList>
  <reaction id="R1">

```

```

<reactant>
  <molecule ref="vinoxy" role="deficientReactant" />
</reactant>
<reactant>
  <molecule ref="O2" role="excessReactant" />
</reactant>
<product>
  <molecule ref="PRa" role="modelled" />
</product>
<me:MCRCMethod xsi:type="me:MesmerILT">
  <me:preExponential units="cm3molecule-1s-1">1.04e-13</me:preExponential>
  <me:activationEnergy units="kcal/mol">0.4</me:activationEnergy>
  <me:TInfinity>298.0</me:TInfinity>
  <me:nInfinity>-0.5</me:nInfinity>
</me:MCRCMethod>
<me:excessReactantConc>4.90E18</me:excessReactantConc>
</reaction>
  <reaction id="R2">
<reactant>
  <molecule ref="PRa" role="modelled" />
</reactant>
<product>
  <molecule ref="QR1" role="modelled" />
</product>
<me:transitionState>
  <molecule ref="TS1" role="transitionState" />
</me:transitionState>
<me:tunneling name="Eckart"/>
<me:MCRCMethod name="RRKM"/>
</reaction>
  <reaction id="R3">
<reactant>
  <molecule ref="PRa" role="modelled" />
</reactant>
<product>
  <molecule ref="glyoxal" role="sink" />
</product>
  <product>
  <molecule ref="OH" role="sink" />
</product>
<me:transitionState>
  <molecule ref="TS2" role="transitionState" />
</me:transitionState>
<me:tunneling name="Eckart"/>
<me:MCRCMethod name="RRKM"/>
</reaction>
  <reaction id="R4">
<reactant>
  <molecule ref="QR1" role="modelled" />

```

```

</reactant>
<product>
  <molecule ref="H2CO" role="sink" />
</product>
  <product>
    <molecule ref="CO" role="sink" />
  </product>
  <product>
    <molecule ref="OH" role="sink" />
  </product>
<me:transitionState>
  <molecule ref="TS4" role="transitionState" />
</me:transitionState>
<me:MCRCMethod name="RRKM"/>
</reaction>
  <reaction id="R5">
<reactant>
  <molecule ref="QR1" role="modelled" />
</reactant>
<product>
  <molecule ref="ketene" role="sink" />
</product>
  <product>
    <molecule ref="HO2" role="sink" />
  </product>
<me:transitionState>
  <molecule ref="TS5" role="transitionState" />
</me:transitionState>
  <me:MCRCMethod name="RRKM"/>
</reaction>
</reactionList>
<me:conditions>
  <me:bathGas>N2</me:bathGas>
  <me:PTs>
    <me:PTpair units="Torr" P="760" T="298." />
    <!--<me:PTpair units="Torr" P="201.60" T="298." />-->
    <!--<me:PTpair units="Torr" P="10.06" T="298." />-->
    <!--<me:PTpair units="Torr" P="15.01" T="298." />-->
  </me:PTs>
</me:conditions>
<me:modelParameters>
  <!--Specify grain size directly...-->
  <me:grainSize units="cm-1">100</me:grainSize>
  <!--...or by the total number of grains
  <me:numberOfGrains> 500 </me:numberOfGrains>-->
  <!--Specify increased energy range
  <me:maxTemperature>6000</me:maxTemperature>-->
  <me:energyAboveTheTopHill>25.0</me:energyAboveTheTopHill>
</me:modelParameters>

```

```

<me:control>
  <me:testDOS />
  <me:printSpeciesProfile />
  <!--<me:testMicroRates />-->
  <me:testRateConstant />
  <me:printGrainDOS />
  <!--<me:printCellDOS />-->
  <!--<me:printReactionOperatorColumnSums />-->
  <!--<me:printTunnellingCoefficients />-->
  <me:printGrainkfE />
  <!--<me:printGrainBoltzmann />-->
  <me:printGrainkB E />
  <me:eigenvalues>0</me:eigenvalues>
  <!--<me:hideInactive/>-->
  <me:diagramEnergyOffset ref="R1">0</me:diagramEnergyOffset>
</me:control>
</me:mesmer>

```

2-methyl-vinoxy + O₂ MESMER input

```

<?xml version="1.0" encoding="utf-8" ?>
<?xml-stylesheet type='text/xsl' href='../mesmer2.xsl' media='other'?>
<?xml-stylesheet type='text/xsl' href='../mesmer1.xsl' media='screen'?>
<me:mesmer xmlns="http://www.xml-cml.org/schema"
  xmlns:me="http://www.chem.leeds.ac.uk/mesmer"
  xmlns:xsi="http://www.w3.org/2001/XMLSchema-instance">
  <me:title> 2-methyl-vinoxy O2 Association</me:title>
  <moleculeList>
    <molecule id="MVR">
      <atomArray>
        <atom id="a1" elementType="C" />
        <atom id="a2" elementType="H" />
        <atom id="a3" elementType="H" />
        <atom id="a4" elementType="H" />
        <atom id="a5" elementType="C" />
        <atom id="a6" elementType="H" />
        <atom id="a7" elementType="C" />
        <atom id="a8" elementType="H" />
        <atom id="a9" elementType="O" />
      </atomArray>
      <bondArray>
        <bond atomRefs2="a1 a2" order="1" />
        <bond atomRefs2="a1 a3" order="1" />
        <bond atomRefs2="a1 a4" order="1" />
        <bond atomRefs2="a1 a5" order="1" />
        <bond atomRefs2="a5 a6" order="1" />
        <bond atomRefs2="a5 a7" order="1" />
        <bond atomRefs2="a7 a8" order="1" />
        <bond atomRefs2="a7 a9" order="2" />
      </bondArray>
    </molecule>
  </moleculeList>
</me:mesmer>

```

```

</bondArray>
<propertyList>
  <property dictRef="me:ZPE">
    <scalar units="kcal/mol">0.0</scalar>
  </property>
  <property dictRef="me:rotConsts">
    <array units="cm-1">0.6583 0.19553 0.155021</array>
  </property>
  <property dictRef="me:symmetryNumber">
    <scalar>1</scalar>
  </property>
  <property dictRef="me:frequenciesScaleFactor">
    <scalar>1</scalar>
  </property>
  <property dictRef="me:vibFreqs">
    <array units="cm-1">102.7 273.4 300.2 640.2 700.3 890.9 957.9 1022.7 1068.9
1180.6 1396.8 1418.8 1431.5 1488.9 1500.4 1644.1 2964.9 3032.0 3074.7 3158.1 3194
</array>
  </property>
  <property dictRef="me:MW">
    <scalar units="amu">57</scalar>
  </property>
  <property dictRef="me:spinMultiplicity">
    <scalar>2</scalar>
  </property>
</propertyList>
<me:DOSCMMethod xsi:type="ClassicalRotors"/>
</molecule>
<molecule id="O2" description="oxygen">
  <atomArray>
    <atom id="a1" elementType="O" />
    <atom id="a2" elementType="O" />
  </atomArray>
  <bondArray>
    <bond atomRefs2="a1 a2" order="2" />
  </bondArray>
  <propertyList>
    <property dictRef="me:ZPE">
      <scalar units="kcal/mol">0.0</scalar>
    </property>
    <property dictRef="me:rotConsts">
      <array units="cm-1">1.431782</array>
    </property>
    <property dictRef="me:symmetryNumber">
      <scalar>2</scalar>
    </property>
    <property dictRef="me:frequenciesScaleFactor">
      <scalar>1</scalar>
    </property>
  </propertyList>

```

```

<property dictRef="me:vibFreqs">
  <array units="cm-1">1583</array>
</property>
<property dictRef="me:MW">
  <scalar units="amu">32</scalar>
</property>
<property dictRef="me:spinMultiplicity">
  <scalar>3</scalar>
</property>
</propertyList>
<me:DOSCMETHOD xsi:type="ClassicalRotors"/>
</molecule>
<molecule id="OH" description="OH radical">
  <atomArray>
    <atom id="a1" elementType="O" />
    <atom id="a2" elementType="H" />
  </atomArray>
  <bondArray>
    <bond atomRefs2="a1 a2" order="1" />
  </bondArray>
  <propertyList>
    <property dictRef="me:ZPE">
      <scalar units="kcal/mol">0.0</scalar>
    </property>
    <property dictRef="me:rotConsts">
      <array units="cm-1">18.86743</array>
    </property>
    <property dictRef="me:symmetryNumber">
      <scalar>1</scalar>
    </property>
    <property dictRef="me:frequenciesScaleFactor">
      <scalar>1</scalar>
    </property>
    <property dictRef="me:vibFreqs">
      <array units="cm-1">3718</array>
    </property>
    <property dictRef="me:MW">
      <scalar units="amu">17</scalar>
    </property>
    <property dictRef="me:spinMultiplicity">
      <scalar>2</scalar>
    </property>
    <property dictRef="me:eletronicExcitation">
      <array units="cm-1">139.7</array>
    </property>
  </propertyList>
  <me:DOSCMETHOD xsi:type="ClassicalRotors"/>
</molecule>
<molecule id="PRa" description="peroxy vinoxyl O2 adduct">

```

```

<atomArray>
  <atom id="a1" elementType="C" />
  <atom id="a2" elementType="C" />
  <atom id="a3" elementType="O" />
  <atom id="a4" elementType="H" />
  <atom id="a5" elementType="O" />
  <atom id="a6" elementType="O" />
  <atom id="a7" elementType="H" />
  <atom id="a8" elementType="C" />
  <atom id="a9" elementType="H" />
  <atom id="a10" elementType="H" />
  <atom id="a11" elementType="H" />
</atomArray>
<bondArray>
  <bond atomRefs2="a1 a2" order="1" />
  <bond atomRefs2="a1 a7" order="1" />
  <bond atomRefs2="a1 a8" order="1" />
  <bond atomRefs2="a1 a5" order="1" />
  <bond atomRefs2="a2 a3" order="2" />
  <bond atomRefs2="a2 a4" order="1" />
  <bond atomRefs2="a8 a9" order="1" />
  <bond atomRefs2="a8 a10" order="1" />
  <bond atomRefs2="a8 a11" order="1" />
  <bond atomRefs2="a5 a6" order="1" />
</bondArray>
<propertyList>
  <property dictRef="me:ZPE">
    <scalar units="kcal/mol">-21.5</scalar>
  </property>
  <property dictRef="me:rotConsts">
    <array units="cm-1">0.186276354 0.093111055 0.065640364</array>
  </property>
  <property dictRef="me:symmetryNumber">
    <scalar>1</scalar>
  </property>
  <property dictRef="me:frequenciesScaleFactor">
    <scalar>1</scalar>
  </property>
  <property dictRef="me:vibFreqs">
    <array units="cm-1">47.9 131.2 207.6 242.3 283.8 414.1 472.2 604 835.4 895.4
    928.5 1082.8 1094.0 1127.4 1182.3 1313 1335.8 1400 1417.1 1493.3 1503.6 1781.8
    2990.5 3067.2 3087 3160 3171.8</array>
  </property>
  <property dictRef="me:MW">
    <scalar units="amu">89</scalar>
  </property>
  <property dictRef="me:spinMultiplicity">
    <scalar>2</scalar>
  </property>

```

```

    <property dictRef="me:epsilon">
      <scalar>473.17</scalar>
    </property>
    <property dictRef="me:sigma">
      <scalar>5.09</scalar>
    </property>
  </propertyList>
  <me:energyTransferModel xsi:type="me:ExponentialDown">
    <me:deltaEDown units="cm-1">130</me:deltaEDown>
  </me:energyTransferModel>
  <me:DOSCMMethod xsi:type="ClassicalRotors"/>
</molecule>
<molecule id="TS1" description="TS1a: PRa -> QR1">
  <atomArray>
    <atom id="a1" elementType="C" />
    <atom id="a2" elementType="C" />
    <atom id="a3" elementType="O" />
    <atom id="a4" elementType="H" />
    <atom id="a5" elementType="O" />
    <atom id="a6" elementType="O" />
    <atom id="a7" elementType="C" />
    <atom id="a8" elementType="H" />
    <atom id="a9" elementType="H" />
    <atom id="a10" elementType="H" />
    <atom id="a11" elementType="H" />
  </atomArray>
  <bondArray>
    <bond atomRefs2="a1 a2" order="1" />
    <bond atomRefs2="a1 a8" order="1" />
    <bond atomRefs2="a1 a7" order="1" />
    <bond atomRefs2="a1 a5" order="1" />
    <bond atomRefs2="a5 a6" order="1" />
      <bond atomRefs2="a7 a9" order="1" />
      <bond atomRefs2="a7 a10" order="1" />
      <bond atomRefs2="a7 a11" order="1" />
      <bond atomRefs2="a2 a4" order="1" />
      <bond atomRefs2="a2 a3" order="2" />
  </bondArray>
  <propertyList>
    <property dictRef="me:ZPE">
      <scalar units="kcal/mol">-1.1</scalar>
    </property>
    <property dictRef="me:rotConsts">
      <array units="cm-1">0.153311532 0.115148817 0.069511665</array>
    </property>
    <property dictRef="me:symmetryNumber">
      <scalar>1</scalar>
    </property>
    <property dictRef="me:frequenciesScaleFactor">

```

```

    <scalar>1</scalar>
  </property>
  <property dictRef="me:vibFreqs">
    <array units="cm-1">149.7 204.4 233.3 288 414.3 506.6575.1136 674.8190
751.7762 870.3413 921.8204 990.4815 1103.1380 1132.0032 1179.6469 1272.4483
1333.7250 1414.0624 1488.1788 1501.2280 1828.7960 1911.8811 3048.9239
3064.8311 3158.5322 3162.7378 </array>
  </property>
  <property dictRef="me:MW">
    <scalar units="amu">89</scalar>
  </property>
  <property dictRef="me:spinMultiplicity">
    <scalar>2</scalar>
  </property>
  <property dictRef="me:imFreqs">
    <scalar units="cm-1">2171.7</scalar>
  </property>
</propertyList>
<me:DOSCMMethod xsi:type="ClassicalRotors"/>
</molecule>
  <molecule id="QR1">
    <atomArray>
      <atom id="a1" elementType="O" />
      <atom id="a2" elementType="C" />
      <atom id="a3" elementType="C" />
      <atom id="a4" elementType="O" />
      <atom id="a5" elementType="O" />
      <atom id="a6" elementType="H" />
      <atom id="a7" elementType="H" />
      <atom id="a8" elementType="C" />
      <atom id="a9" elementType="H" />
      <atom id="a10" elementType="H" />
      <atom id="a11" elementType="H" />
    </atomArray>
    <bondArray>
      <bond atomRefs2="a2 a1" order="2" />
      <bond atomRefs2="a2 a3" order="1" />
      <bond atomRefs2="a3 a8" order="1" />
      <bond atomRefs2="a3 a7" order="1" />
      <bond atomRefs2="a3 a4" order="1" />
      <bond atomRefs2="a8 a9" order="1" />
      <bond atomRefs2="a8 a10" order="1" />
      <bond atomRefs2="a8 a11" order="1" />
      <bond atomRefs2="a4 a5" order="1" />
      <bond atomRefs2="a5 a6" order="1" />
    </bondArray>
    <propertyList>
      <property dictRef="me:ZPE">
        <scalar units="kcal/mol">-20</scalar>

```

```

</property>
<property dictRef="me:rotConsts">
  <array units="cm-1">0.144487634 0.122939961 0.072846032 </array>
</property>
<property dictRef="me:symmetryNumber">
  <scalar>1</scalar>
</property>
<property dictRef="me:frequenciesScaleFactor">
  <scalar>1</scalar>
</property>
<property dictRef="me:vibFreqs">
  <array units="cm-1">119.4818161.8741      214.1119      244.0278
    311.5554      362.6836      409.2454      512.638      668.0661
    738.5844      837.2351      919.8197      1028.7648    1113.4922
    1165.3845     1298.2956     1333.3916     1382.1359    1408.6773
    1490.0535     1506.6147     1873.1 3065.7637 3070.3675    3158.9006
    3168.7117     3734.9548 </array>
</property>
<property dictRef="me:MW">
  <scalar units="amu">89</scalar>
</property>
<property dictRef="me:spinMultiplicity">
  <scalar>2</scalar>
</property>
<property dictRef="me:epsilon">
  <scalar>473.17</scalar>
</property>
<property dictRef="me:sigma">
  <scalar>5.09</scalar>
</property>
</propertyList>
<me:energyTransferModel xsi:type="me:ExponentialDown">
  <me:deltaEDown units="cm-1">130</me:deltaEDown>
</me:energyTransferModel>
<me:DOSCMMethod xsi:type="ClassicalRotors"/>
</molecule>
<molecule id="TS7" description="QR1 -> AA + OH">
  <atomArray>
    <atom id="a1" elementType="C" />
    <atom id="a2" elementType="C" />
    <atom id="a3" elementType="O" />
    <atom id="a4" elementType="H" />
    <atom id="a5" elementType="C" />
    <atom id="a6" elementType="O" />
    <atom id="a7" elementType="H" />
    <atom id="a8" elementType="O" />
    <atom id="a9" elementType="H" />
    <atom id="a10" elementType="H" />
    <atom id="a11" elementType="H" />
  </atomArray>

```

```

</atomArray>
<bondArray>
  <bond atomRefs2="a1 a4" order="1" />
  <bond atomRefs2="a1 a5" order="1" />
  <bond atomRefs2="a1 a3" order="1" />
  <bond atomRefs2="a3 a6" order="1" />
  <bond atomRefs2="a6 a7" order="1" />
    <bond atomRefs2="a5 a9" order="1" />
    <bond atomRefs2="a5 a10" order="1" />
    <bond atomRefs2="a5 a11" order="1" />
    <bond atomRefs2="a2 a8" order="2" />
    <bond atomRefs2="a1 a2" order="1" />
</bondArray>
<propertyList>
  <property dictRef="me:ZPE">
    <scalar units="kcal/mol">-10.4</scalar>
  </property>
  <property dictRef="me:rotConsts">
    <array units="cm-1">0.131349695 0.111125411 0.065286949</array>
  </property>
  <property dictRef="me:symmetryNumber">
    <scalar>1</scalar>
  </property>
  <property dictRef="me:frequenciesScaleFactor">
    <scalar>1</scalar>
  </property>
  <property dictRef="me:vibFreqs">
    <array units="cm-1">84.0362 140.1260 179.6395 186.4707 241.3967 298.7336
363.9915 390.7807 498.1598 826.3831 867.8235 946.4621 1080.3370 1138.6187
1196.3859 1343.2065 1382.0938 1411.8039 1480.8700 1497.9828 1926.6867
3045.9431 3128.3977 3152.6257 3162.3120 3735.6955 </array>
  </property>
  <property dictRef="me:MW">
    <scalar units="amu">89</scalar>
  </property>
  <property dictRef="me:spinMultiplicity">
    <scalar>2</scalar>
  </property>
  <property dictRef="me:imFreqs">
    <scalar units="cm-1">374.7</scalar>
  </property>
</propertyList>
<me:DOSCMETHOD xsi:type="ClassicalRotors"/>
</molecule>
<molecule id="AA" description="acetaldehyde">
  <atomArray>
    <atom id="a1" elementType="O" />
    <atom id="a2" elementType="C" />
    <atom id="a3" elementType="H" />

```

```

    <atom id="a4" elementType="C" />
    <atom id="a5" elementType="H" />
    <atom id="a6" elementType="H" />
    <atom id="a7" elementType="H" />
  </atomArray>
  <bondArray>
    <bond atomRefs2="a1 a2" order="2" />
    <bond atomRefs2="a2 a3" order="1" />
    <bond atomRefs2="a2 a4" order="1" />
    <bond atomRefs2="a4 a5" order="1" />
    <bond atomRefs2="a4 a6" order="1" />
    <bond atomRefs2="a4 a7" order="1" />
  </bondArray>
  <propertyList>
    <property dictRef="me:ZPE">
      <scalar units="kcal/mol">-51.4</scalar>
    </property>
    <property dictRef="me:rotConsts">
      <array units="cm-1">1.88351209289 0.33339240642 0.29910086664</array>
    </property>
    <property dictRef="me:symmetryNumber">
      <scalar>1</scalar>
    </property>
    <property dictRef="me:frequenciesScaleFactor">
      <scalar>1</scalar>
    </property>
    <property dictRef="me:vibFreqs">
      <array units="cm-1">161.7390 500.1649 777.9218 893.4781 1133.4279
1133.9569 1386.6734 1436.2800 1470.5689 1480.9939 1788.1627 2942.3685
3046.0761 3124.4385 3173.3554 </array>
    </property>
    <property dictRef="me:MW">
      <scalar units="amu">44</scalar>
    </property>
    <property dictRef="me:spinMultiplicity">
      <scalar>1</scalar>
    </property>
  </propertyList>
  <me:DOSMethod xsi:type="ClassicalRotors"/>
</molecule>
<molecule id="HO2">
  <atomArray>
    <atom id="a1" elementType="O" />
    <atom id="a2" elementType="H" />
    <atom id="a3" elementType="O" />
  </atomArray>
  <bondArray>
    <bond atomRefs2="a1 a2" order="1" />
    <bond atomRefs2="a1 a3" order="1" />

```

```

</bondArray>
<propertyList>
  <property dictRef="me:ZPE">
    <scalar units="kcal/mol">0.0</scalar>
  </property>
  <property dictRef="me:rotConsts">
    <array units="cm-1">20.52618 1.113085 1.05583</array>
  </property>
  <property dictRef="me:symmetryNumber">
    <scalar>1</scalar>
  </property>
  <property dictRef="me:frequenciesScaleFactor">
    <scalar>1</scalar>
  </property>
  <property dictRef="me:vibFreqs">
    <array units="cm-1">3674 1434 1126</array>
  </property>
  <property dictRef="me:MW">
    <scalar units="amu">33</scalar>
  </property>
  <property dictRef="me:spinMultiplicity">
    <scalar>2</scalar>
  </property>
</propertyList>
<me:DOSCMMethod xsi:type="ClassicalRotors"/>
</molecule>
<molecule id="TS6" description="TS QR1 -> acrolein + HO2">
  <atomArray>
    <atom id="a1" elementType="O" />
    <atom id="a2" elementType="O" />
    <atom id="a3" elementType="H" />
    <atom id="a4" elementType="C" />
    <atom id="a5" elementType="C" />
    <atom id="a6" elementType="H" />
    <atom id="a7" elementType="C" />
    <atom id="a8" elementType="O" />
    <atom id="a9" elementType="H" />
    <atom id="a10" elementType="H" />
    <atom id="a11" elementType="H" />
  </atomArray>
  <bondArray>
    <bond atomRefs2="a1 a2" order="1" />
    <bond atomRefs2="a2 a3" order="1" />
    <bond atomRefs2="a1 a4" order="1" />
    <bond atomRefs2="a4 a6" order="1" />
    <bond atomRefs2="a4 a7" order="1" />
    <bond atomRefs2="a4 a5" order="1" />
    <bond atomRefs2="a7 a8" order="2" />
    <bond atomRefs2="a5 a9" order="1" />
  </bondArray>

```

```

        <bond atomRefs2="a5 a10" order="1" />
        <bond atomRefs2="a5 a11" order="1" />
    </bondArray>
    <propertyList>
      <property dictRef="me:ZPE">
        <scalar units="kcal/mol">5.4</scalar>
      </property>
      <property dictRef="me:rotConsts">
        <array units="cm-1">0.124845956 0.10580067 0.061647135 </array>
      </property>
      <property dictRef="me:symmetryNumber">
        <scalar>1</scalar>
      </property>
      <property dictRef="me:frequenciesScaleFactor">
        <scalar>1</scalar>
      </property>
      <property dictRef="me:vibFreqs">
        <array units="cm-1">66.0134 111.0556 166.4861 208.0358 215.7226 294.3885
417.8073 454.8312 587.6209 809.1091 853.0451 878.2032 1052.7450 1093.7971
1130.0228 1348.9879 1358.4240 1413.2528 1490.8083 1506.9533 2089.6717
3060.2337 3148.8575 3157.1418 3189.8719 3750.0007</array>
      </property>
      <property dictRef="me:MW">
        <scalar units="amu">89</scalar>
      </property>
      <property dictRef="me:spinMultiplicity">
        <scalar>2</scalar>
      </property>
      <property dictRef="me:imFreqs">
        <scalar units="cm-1">679.2</scalar>
      </property>
    </propertyList>
    <me:DOSCMETHOD xsi:type="ClassicalRotors"/>
  </molecule>
  <molecule id="TS5" description="TS PRa -> Acrolein + HO2">
    <atomArray>
      <atom id="a1" elementType="C" />
      <atom id="a2" elementType="C" />
      <atom id="a3" elementType="O" />
      <atom id="a4" elementType="C" />
      <atom id="a5" elementType="H" />
      <atom id="a6" elementType="H" />
      <atom id="a7" elementType="O" />
      <atom id="a8" elementType="O" />
      <atom id="a9" elementType="H" />
      <atom id="a10" elementType="H" />
      <atom id="a11" elementType="H" />
    </atomArray>
    <bondArray>

```

```

<bond atomRefs2="a1 a5" order="1" />
<bond atomRefs2="a1 a4" order="1" />
<bond atomRefs2="a1 a2" order="1" />
<bond atomRefs2="a4 a8" order="2" />
<bond atomRefs2="a4 a9" order="1" />
    <bond atomRefs2="a2 a10" order="1" />
    <bond atomRefs2="a2 a11" order="1" />
    <bond atomRefs2="a2 a6" order="1" />
    <bond atomRefs2="a3 a7" order="1" />
    <bond atomRefs2="a6 a7" order="1" />
</bondArray>
<propertyList>
  <property dictRef="me:ZPE">
    <scalar units="kcal/mol">5.8</scalar>
  </property>
  <property dictRef="me:rotConsts">
    <array units="cm-1">0.194135891 0.07945373 0.061507885 </array>
  </property>
  <property dictRef="me:symmetryNumber">
    <scalar>1</scalar>
  </property>
  <property dictRef="me:frequenciesScaleFactor">
    <scalar>1</scalar>
  </property>
  <property dictRef="me:vibFreqs">
    <array units="cm-1">101.1623 157.3840 198.2507 318.2747 336.2958 473.4515
563.2339 622.7663 652.7914 909.4821 967.1819 1009.6004 1038.2238 1169.4608
1249.9925 1282.0777 1298.4870 1387.5471 1448.0545 1557.2887 1588.3220
1760.2668 2955.4948 3126.4395 3212.6642 3228.5359</array>
  </property>
  <property dictRef="me:MW">
    <scalar units="amu">89</scalar>
  </property>
  <property dictRef="me:spinMultiplicity">
    <scalar>2</scalar>
  </property>
  <property dictRef="me:imFreqs">
    <scalar units="cm-1">1469.1</scalar>
  </property>
</propertyList>
<me:DOSCMETHOD xsi:type="ClassicalRotors"/>
</molecule>
<molecule id="MK" description="methylketene">
  <atomArray>
    <atom id="a1" elementType="C" />
    <atom id="a2" elementType="H" />
    <atom id="a3" elementType="C" />
    <atom id="a4" elementType="H" />
    <atom id="a5" elementType="H" />
  </atomArray>

```

```

    <atom id="a6" elementType="H" />
    <atom id="a7" elementType="C" />
    <atom id="a8" elementType="O" />
  </atomArray>
  <bondArray>
    <bond atomRefs2="a1 a2" order="1" />
    <bond atomRefs2="a1 a3" order="1" />
    <bond atomRefs2="a3 a4" order="1" />
    <bond atomRefs2="a3 a5" order="1" />
    <bond atomRefs2="a3 a6" order="1" />
    <bond atomRefs2="a1 a7" order="2" />
    <bond atomRefs2="a7 a8" order="2" />
  </bondArray>
  <propertyList>
    <property dictRef="me:ZPE">
      <scalar units="kcal/mol">-5.4</scalar>
    </property>
    <property dictRef="me:rotConsts">
      <array units="cm-1">1.27385261640 0.14765183986 0.13571183635</array>
    </property>
    <property dictRef="me:symmetryNumber">
      <scalar>1</scalar>
    </property>
    <property dictRef="me:frequenciesScaleFactor">
      <scalar>1</scalar>
    </property>
    <property dictRef="me:vibFreqs">
      <array units="cm-1">147.2285 210.9291 506.3963 516.6623 636.0791 899.6395
1058.8120 1086.0117 1146.0031 1403.4186 1426.0287 1491.2166 1518.9981
2183.5531 3047.8424 3122.7514 3142.6408 3223.7096</array>
    </property>
    <property dictRef="me:MW">
      <scalar units="amu">56</scalar>
    </property>
    <property dictRef="me:spinMultiplicity">
      <scalar>1</scalar>
    </property>
  </propertyList>
  <me:energyTransferModel xsi:type="me:ExponentialDown">
    <me:deltaEDown units="cm-1">130</me:deltaEDown>
  </me:energyTransferModel>
  <me:DOSCMETHOD xsi:type="ClassicalRotors"/>
</molecule>
  <molecule id="AC" description="acrolein">
  <atomArray>
    <atom id="a1" elementType="C" />
    <atom id="a2" elementType="C" />
    <atom id="a3" elementType="O" />
    <atom id="a4" elementType="H" />

```

```

    <atom id="a5" elementType="C" />
    <atom id="a6" elementType="H" />
    <atom id="a7" elementType="H" />
    <atom id="a8" elementType="H" />
  </atomArray>
  <bondArray>
    <bond atomRefs2="a1 a2" order="1" />
    <bond atomRefs2="a2 a3" order="2" />
    <bond atomRefs2="a2 a4" order="1" />
    <bond atomRefs2="a1 a5" order="2" />
    <bond atomRefs2="a1 a6" order="1" />
    <bond atomRefs2="a5 a7" order="1" />
    <bond atomRefs2="a5 a8" order="1" />
  </bondArray>
  <propertyList>
    <property dictRef="me:ZPE">
      <scalar units="kcal/mol">-5.8</scalar>
    </property>
    <property dictRef="me:rotConsts">
      <array units="cm-1">0.75150219423 0.20481030247 0.16094675404</array>
    </property>
    <property dictRef="me:symmetryNumber">
      <scalar>1</scalar>
    </property>
    <property dictRef="me:frequenciesScaleFactor">
      <scalar>1</scalar>
    </property>
    <property dictRef="me:vibFreqs">
      <array units="cm-1">146.8007 277.0260 548.9944 672.5681 930.6977 966.6829
1004.0936 1020.6778 1059.8673 1300.7811 1428.5506 1438.2732 1655.5894
1753.9522 2964.9658 3164.4652 3193.2212 3269.9215</array>
    </property>
    <property dictRef="me:MW">
      <scalar units="amu">56</scalar>
    </property>
    <property dictRef="me:spinMultiplicity">
      <scalar>1</scalar>
    </property>
  </propertyList>
  <me:energyTransferModel xsi:type="me:ExponentialDown">
    <me:deltaEDown units="cm-1">130</me:deltaEDown>
  </me:energyTransferModel>
  <me:DOSCMETHOD xsi:type="ClassicalRotors"/>
</molecule>
  <molecule id="CO">
  <atomArray>
    <atom id="a1" elementType="C" />
    <atom id="a2" elementType="O" />
  </atomArray>

```

```

<bondArray>
  <bond atomRefs2="a1 a2" order="2" />
</bondArray>
<propertyList>
  <property dictRef="me:ZPE">
    <scalar units="kcal/mol">0</scalar>
  </property>
  <property dictRef="me:rotConsts">
    <array units="cm-1">1.905061</array>
  </property>
  <property dictRef="me:symmetryNumber">
    <scalar>2</scalar>
  </property>
  <property dictRef="me:frequenciesScaleFactor">
    <scalar>1</scalar>
  </property>
  <property dictRef="me:vibFreqs">
    <array units="cm-1">2146</array>
  </property>
  <property dictRef="me:MW">
    <scalar units="amu">28</scalar>
  </property>
  <property dictRef="me:spinMultiplicity">
    <scalar>1</scalar>
  </property>
</propertyList>
<me:DOSCMMethod xsi:type="ClassicalRotors"/>
</molecule>
</moleculeList>
<reactionList>
<reaction id="R1">
  <reactant>
    <molecule ref="MVR" role="deficientReactant" />
  </reactant>
  <reactant>
    <molecule ref="O2" role="excessReactant" />
  </reactant>
  <product>
    <molecule ref="PRa" role="modelled" />
  </product>
  <me:MCRCMethod xsi:type="me:MesmerILT">
    <me:preExponential units="cm3molecule-1s-1">1.3e-12</me:preExponential>
    <me:activationEnergy units="kcal/mol">0.4</me:activationEnergy>
    <me:TInfinity>298.0</me:TInfinity>
    <me:nInfinity>-0.5</me:nInfinity>
  </me:MCRCMethod>
  <me:excessReactantConc>4.9E18</me:excessReactantConc>
</reaction>
  <reaction id="R2">

```

```

<reactant>
  <molecule ref="PRa" role="modelled" />
</reactant>
<product>
  <molecule ref="QR1" role="modelled" />
</product>
<me:transitionState>
  <molecule ref="TS1" role="transitionState" />
</me:transitionState>
<me:tunneling name="Eckart"/>
<me:MCRCMethod name="RRKM"/>
</reaction>
  <reaction id="R3">
<reactant>
  <molecule ref="PRa" role="modelled" />
</reactant>
<product>
  <molecule ref="AC" role="sink" />
</product>
  <product>
  <molecule ref="HO2" role="sink" />
</product>
<me:transitionState>
  <molecule ref="TS5" role="transitionState" />
</me:transitionState>
<me:MCRCMethod name="RRKM"/>
</reaction>
  <reaction id="R4">
<reactant>
  <molecule ref="QR1" role="modelled" />
</reactant>
<product>
  <molecule ref="AA" role="sink" />
</product>
  <product>
  <molecule ref="CO" role="sink" />
</product>
  <product>
  <molecule ref="OH" role="sink" />
</product>
<me:transitionState>
  <molecule ref="TS7" role="transitionState" />
</me:transitionState>
<me:MCRCMethod name="RRKM"/>
</reaction>
  <reaction id="R5">
<reactant>
  <molecule ref="QR1" role="modelled" />
</reactant>

```

```

<product>
  <molecule ref="MK" role="sink" />
</product>
  <product>
    <molecule ref="HO2" role="sink" />
  </product>
  <me:transitionState>
    <molecule ref="TS6" role="transitionState" />
  </me:transitionState>
  <me:MCRCMethod name="RRKM"/>
</reaction>
</reactionList>
<me:conditions>
  <me:bathGas>N2</me:bathGas>
  <me:PTs>
    <me:PTpair units="Torr" P="760" T="298." />
    <!--<me:PTpair units="Torr" P="201.60" T="298." />-->
    <!--<me:PTpair units="Torr" P="10.06" T="298." />-->
    <!--<me:PTpair units="Torr" P="15.01" T="298." />-->
  </me:PTs>
</me:conditions>
<me:modelParameters>
  <!--Specify grain size directly...-->
  <me:grainSize units="cm-1">100</me:grainSize>
  <!--...or by the total number of grains
    <me:numberOfGrains> 500 </me:numberOfGrains>-->
  <!--Specify increased energy range
    <me:maxTemperature>6000</me:maxTemperature>-->
  <me:energyAboveTheTopHill>25.0</me:energyAboveTheTopHill>
</me:modelParameters>
<me:control>
  <me:testDOS />
  <me:printSpeciesProfile />
  <!--<me:testMicroRates />-->
  <me:testRateConstant />
  <me:printGrainDOS />
  <!--<me:printCellDOS />-->
  <!--<me:printReactionOperatorColumnSums />-->
  <!--<me:printTunnellingCoefficients />-->
  <me:printGrainkfE />
  <!--<me:printGrainBoltzmann />-->
  <me:printGrainkbE />
  <me:eigenvalues>0</me:eigenvalues>
  <!--<me:hideInactive/>-->
  <me:diagramEnergyOffset ref="R1">0</me:diagramEnergyOffset>
</me:control>
</me:mesmer>

```

References

1. L. G. Dodson, L. Shen, J. D. Savee, N. C. Eddingsas, O. Welz, C. A. Taatjes, D. L. Osborn, S. P. Sander and M. Okumura, *J. Phys. Chem. A* **119**, 1279-1291 (2015).
2. F. Goulay, A. Derakhshan, E. Maher, A. J. Trevitt, J. D. Savee, A. M. Scheer, D. L. Osborn and C. A. Taatjes, *Phys. Chem. Chem. Phys.* **15**, 4049-4058 (2013).
3. F. N. Egolfopoulos, N. Hansen, Y. Ju, K. Kohse-Höinghaus, C. K. Law and F. Qi, *Prog. Energy Combust. Sci.* **43**, 36-67 (2014).
4. O. Welz, J. Zádor, J. D. Savee, M. Y. Ng, G. Meloni, R. X. Fernandez, L. Sheps, B. A. Simmons, T. S. Lee, D. L. Osborn and C. A. Taatjes, *Phys. Chem. Chem. Phys.* **14**, 3112-3127 (2012).
5. J. C. Traeger, R. G. McLoughlin and A. J. C. Nicholson, *J. Am. Chem. Soc.* **104**, 5318-5322 (1982).
6. J. L. Holmes, P. C. Burgers and Y. A. Mollah, *Org. Mass Spectrom.* **17**, 127-130 (1982).
7. M. Bobeldijk, W. J. Van der Zande and P. G. Kistemaker, *Chem. Phys.* **179**, 125-130 (1993).
8. J. C. Person and P. P. Nicole, *J. Chem. Phys.* **49**, 5421 (1968).
9. K. T. Kuwata and L. C. Valin, *Chem. Phys. Lett.* **451**, 186-191 (2008).
10. S. A. Carr, D. R. Glowacki, C.-H. Liang, M. T. Baeza-Romero, M. A. Blitz, M. J. Pilling and P. W. Seakins, *J. Phys. Chem A* **115**, 1069-1085 (2011).
11. J. D. Weidman, R. T. Allen, K. B. Moore III and H. F. Schaefer III, *J. Chem. Phys.* **148**, 184308 (2018).
12. M. M. Davis, J. D. Weidman, A. S. Abbott, G. E. Douberly, J. M. Turney and H. F. Schaefer III, *J. Chem. Phys.* **151**, 124302 (2019).

APPENDIX VI

FORMIC ACID CATALYZED ISOMERIZATION AND ADDUCT FORMATION OF AN ISOPRENE-DERIVED CRIEGEE INTERMEDIATE: EXPERIMENT AND THEORY SUPPORTING INFORMATION

The experimental research was performed with researchers Rebecca Caravan (*NASA Postdoctoral Program Fellow, NASA Jet Propulsion Laboratory, Combustion Research Facility, Sandia National Laboratories, Chemical Sciences and Engineering Division, Argonne National Laboratory*), Shubhrangshu Pandit (*Department of Chemistry, University of Pennsylvania, Department of Chemistry and Biochemistry, University of California San Diego*), Kristen Zuraski (*NASA Postdoctoral Program Fellow, NASA Jet Propulsion Laboratory*), Frank Winiberg (*NASA Jet Propulsion Laboratory, California Institute of Technology*), Kendrew Au (*Combustion Research Facility, Sandia National Laboratories*), Trisha Bhagde (*Department of Chemistry, University of Pennsylvania*), David Osborn (*Combustion Research Facility, Sandia National Laboratories*), Carl Percival (*NASA Jet Propulsion Laboratory, California Institute of Technology*), Craig Taatjes (*Combustion Research Facility, Sandia National Laboratories*), and Marsha Lester (*Department of Chemistry, University of Pennsylvania*). Synthetic work was performed by graduate student Nisalak Trongsiwat and Patrick J. Walsh (*Department of Chemistry, University of Pennsylvania*).

Section S1. MVK-oxide + H₂-formic acid

The identification of HPBD at m/z 87 in the D₂-formic acid experiments (discussed in the main text) is also supported by the time profiles of the m/z 86 data obtained in experiments using normal H₂-formic acid. With increasing formic acid concentration, an increase in signal appearing as a y-axis offset is observed at longer kinetic times in the time profiles of m/z 86 (Figure S1, *bottom*). The increase in absolute signal of m/z 86 at longer kinetic times (Figure S1, *top*) is indicative of increased production of an isomer of MVK-oxide that can be photoionized at 10.5 eV and is stable on the timescale and conditions of our experimental conditions (10 Torr, 298 K), such as HPBD from the acid catalyzed isomerization mechanism. The relative photoionization cross-sections of Criegee intermediates and their respective vinyl hydroperoxide isomers calculated by Huang *et al.*¹ indicates that the cross-sections of the latter are significantly larger than the former. The magnitude of the y-axis offset in the m/z 86 time profiles with respect to the $t = 0$ signal amplitude (Figure S1, *bottom*) is, therefore consistent with the small yield of HPBD determined from the D₂-formic acid experiments and calculated through high-level theoretical kinetics, as discussed in the main text.

Section S2: Theoretical reaction pathways

Overview

The present theoretical effort provides a detailed analysis of the kinetics for the reaction of MVK-oxide with formic acid (FA). It builds from the theoretical analysis presented in our prior study for the reaction of *syn-trans* MVK-oxide with FA,² with explorations of a variety of additional channels, and with an exploration of the kinetics for

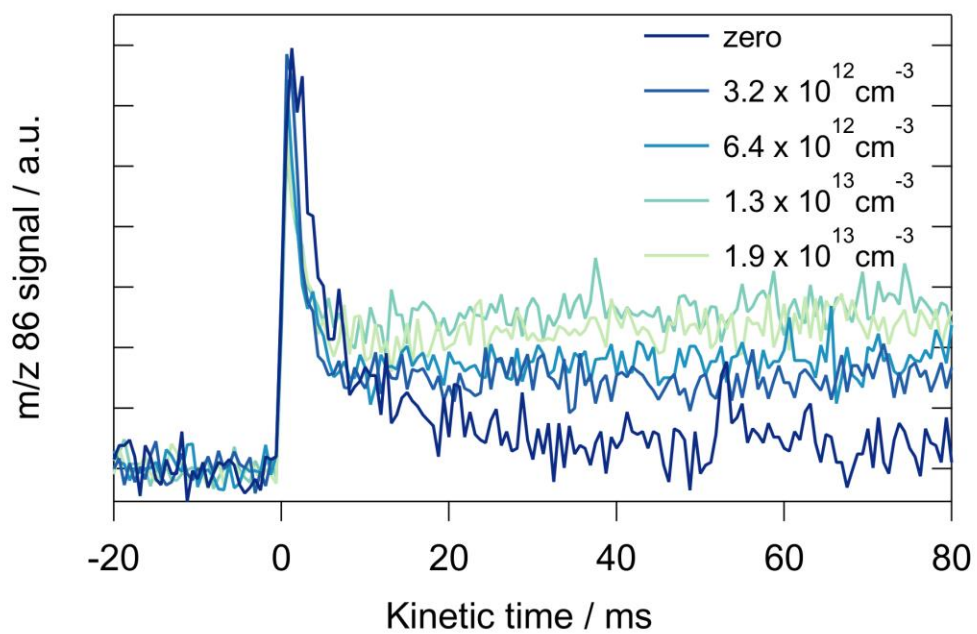
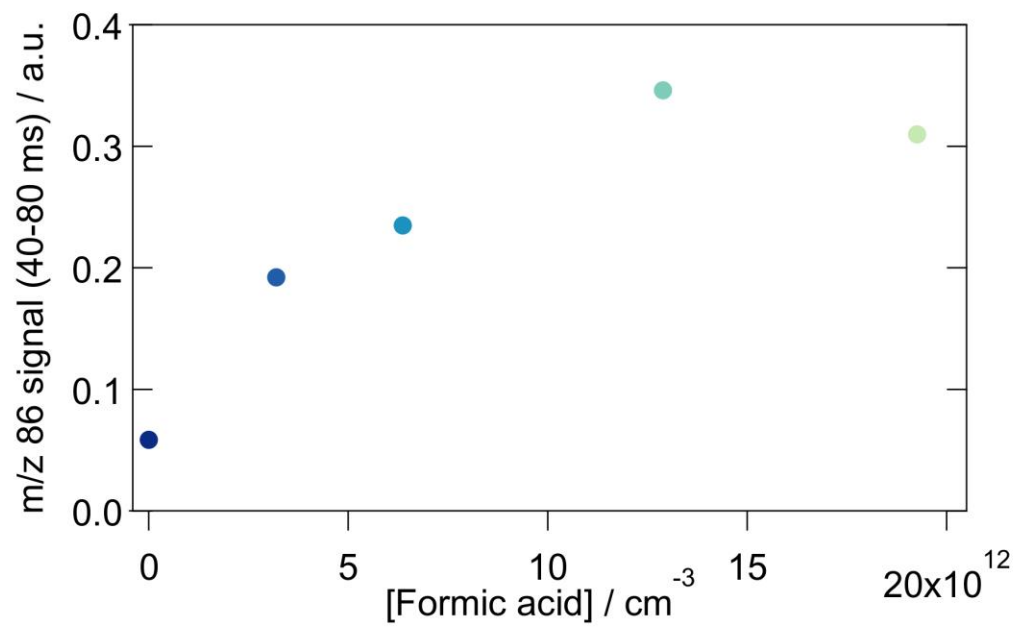


Figure S1. *Top* Summed absolute amplitudes of the m/z 86 signal (between 40-80 ms) in the MVK-oxide + H₂-formic acid reaction as a function of formic acid concentration, obtained using a photoionization energy of 10.5 eV. *Bottom* Time profiles of the m/z 86 signal, presented in the top figure, recorded at various formic acid concentrations. The data are each normalized for their experimental conditions (e.g. MVK-oxide precursor concentration, photolysis laser power and the photocurrent of the 10.5 eV photoionization radiation) using the maxima in the amplitudes of the respective I atom time traces as a reference.

all four conformers of MVK-oxide. The primary focus is on the inclusion of the chemical catalysis channel that is observed experimentally in the present study, and which was previously explored theoretically in the work of Kumar et al. at the CCSD(T)/aug-cc-pVTZ//M06-2X/cc-pVTZ level.³ The present analysis expands on that earlier theoretical work with more definitive ab initio electronic structure calculations, exploration of additional reaction channels, and, most significantly, through the implementation of a *priori* kinetic estimates. For completeness, we explore (i) analogues of the low-lying transition states explored by Vereecken and coworkers in their study of the reaction of CH₂OO with FA,⁴ (ii) spectator catalysis, (iii) *cis-trans* isomerization in reactant pre-reactive complexes (PRCs), (iv) new reaction channels for the *anti* conformers, and (v) isotope exchange in the product PRC. The *cis-trans* isomerizations in the PRCs dramatically modulate the product distributions for the *cis* reactants. The predicted isotope exchange rate for the reaction between hydroperoxyl butadiene (HPBD) and deuterated FA (D₂-formic acid) is used to delineate the possible role of isotopic exchange from HPBD (possibly formed as a secondary product in the photolytic generation of MVK-oxide) interfering with the isotopic observations of deuterated HPBD.

Stationary Point Energies

The stationary point energies for the various reaction channels in the reaction of all four conformers of MVK-oxide with FA were determined at the CCSD(T)-F12/cc-pVTZ-F12//B2PLYP-D3/cc-pVTZ level coupled with the following ad hoc correction. The CCSD(T) method is known to underestimate the stability of Criegee intermediates (CIs) due to significant multireference effects arising from resonances between zwitterionic and singlet diradical electronic configurations. Furthermore, these multireference effects persist to some extent for both the entrance channel van der Waals wells (where the CI

retains much of its chemical character) and the transition states connecting them chemically to product species [e.g., HPBD, HPBF (hydroperoxybut-3-en-2-yl formate) adduct, HPBD-2, and dioxole]. Calculations at the CCSDT(Q) level largely capture these multireference effects, but such CCSDT(Q) calculations are impractical for a system with 9 heavy atoms (5 C atoms and 4 O atoms). Our prior studies provide CCSDT(Q) corrections for both MVK-oxide isomerizations⁵ and the chemical reaction of CH₂OO with SO₂.² Here we use those values to crudely estimate these corrections for the present system. In particular, the MVK-oxide PRCs and the *cis-trans* transition states within these PRCs are estimated to be raised relative to the reactants by 0.4 kcal mol⁻¹, the transition states for the chemical conversions from the PRCs are estimated to be raised relative to reactants by 0.8 kcal mol⁻¹ and the products are estimated to be raised by 1.5 kcal mol⁻¹. We estimate the uncertainties in these corrections to be about 0.2 kcal mol⁻¹ for the first two values, and about 0.4 kcal mol⁻¹ for the last one.

The results of these calculations are reported in Table S1. Note that the present energies differ slightly from those reported in our earlier study of the *syn-trans* MVK-oxide + FA reaction.² This difference arises from the prior neglect of the above described ad hoc CCSDT(Q) correction due to our focus there on just the addition rate. Overall, we expect 2 σ uncertainties in our predicted energies of about 0.6 kcal mol⁻¹. Zero-point energy (ZPE) corrections evaluated for the stationary points corresponding to the reaction of deuterated FA with *syn-trans* and *syn-cis* MVK-oxide are also reported in Table S1. Note that for the radical-radical PRCs [e.g., OBD...OH, where OBD is oxybutadiene – CH₂CHC(O)CH₂] we evaluate the energy of the triplet state complex in order to avoid multireference issues for singlet radical-radical pre-reactive complexes. It is our experience that typically the energies of singlet and triplet PRCs agree to within a

Table S1. Stationary point energies (kcal mol⁻¹) for the reaction of *syn/anti-cis/trans* (*s/a-c/t*)MVK-oxide with formic acid (FA).^a Energies include ZPE corrections and are reported relative to reactants.^a

Stationary Point	ω B97XD 6-31+G*	B2PLYPD3 cc-pVTZ	CCSD(T)- F12 cc-pVTZ- F12	E0 ^b	Total ^c	Corr. Total ^d
<i>Reactants</i>						
<i>s-t</i> -MVK-oxide + FA	0	0	0	0	0	0
<i>s-c</i> -MVK-oxide + FA	1.3	2.3	1.9	-0.2	1.8	1.8
<i>a-t</i> -MVK-oxide+ FA	2.2	3.0	2.7	-0.1	2.6	2.6
<i>a-c</i> -MVK-oxide+ FA	1.8	2.8	2.8	0.0	2.8	2.8
<i>s-t</i> -MVK-oxide+ FA excited	5.1	4.5	4.2	-0.2	4.0	4.0
<i>van der Waals</i>						
Reactant Wells						
<i>s-t</i> -MVK-oxide...FA	-17.4	-17.0	-15.8	1.1 (1.1)	-14.7	-14.3
<i>s-c</i> -MVK-oxide...FA	-16.3	-15.1	-14.1	0.8 (0.8)	-13.2	-12.8
<i>a-t</i> -MVK-oxide...FA	-16.5	-15.9	-14.7	0.9	-13.8	-13.4
<i>a-c</i> -MVK-oxide...FA	-15.5	-14.8	-13.2	1.0	-12.1	-11.7
Product Wells						
<i>s-t</i> -HPBD...FA	-20.8	-24.5	-24.3	1.5	-22.7	-21.2
<i>s-c</i> -HPBD...FA	-22.2	-26.5	-26.1	1.7	-24.4	-22.9
<i>a-t</i> -HPBD...FA	-18.8	-22.3	-22.2	1.4	-20.8	-19.3
<i>a-c</i> -HPBD...FA	-17.6	-21.5	-21.6	1.4	-20.3	-18.8
<i>Transition States</i>						
Cis/Trans						
<i>s-t</i> -MVK-oxide = <i>s-c</i> -MVK-oxide	7.6	9.4	8.2	-0.6	7.5	7.9
<i>a-t</i> -MVK-oxide = <i>a-c</i> -MVK-oxide	11.1	13.0	11.6	-0.7	10.9	11.3
<i>s-t</i> -MVK-oxide...FA = <i>s-c</i> -MVK-oxide...FA	-11.9	-10.6	-10.2	0.4 (0.5)	-9.7	-9.3
<i>a-t</i> -MVK-oxide...FA = <i>a-c</i> -MVK-oxide...FA	-9.5	-8.4	-10.2	0.3	-9.9	-9.5
H Transfer (TS1)						
<i>s-t</i> -MVK-oxide = <i>s-t</i> -HPBD	21.9	18.9	19.7	-2.5	17.2	18.0
<i>s-c</i> -MVK-oxide = <i>s-c</i> -HPBD	23.0	20.2	21.0	-2.6	18.4	19.2
Acid Catalyzed – Spectator (TS _{spec})						

<i>s-t</i> -MVK-oxide...FA =	9.3	5.8	8.1	-1.4	6.7	7.5
<i>s-t</i> -HPBD...FA						
<i>s-c</i> -MVK-oxide...FA =	10.3	6.8	9.2	-1.5	7.7	8.5
<i>s-c</i> -HPBD...FA						
Acid Catalyzed – Chemically (TS2)						
<i>s-t</i> -MVK-oxide...FA =	-5.3	-6.7	-3.1	-1.8	-4.9	-4.1
<i>s-t</i> -HPBD...FA				(-1.4)		
<i>s-c</i> -MVK-oxide...FA =	-5.3	-6.2	-2.7	-1.9	-4.6	-3.8
<i>s-c</i> -HPBD...FA				(-1.4)		
<i>a-t</i> -MVK-oxide...FA =	-0.5	-0.8	1.9	-1.0	0.8	1.6
<i>a-t</i> -HPBD...FA						
<i>a-c</i> -MVK-oxide...FA =	2.5	2.0	4.7	-1.0	3.7	4.5
=						
<i>a-c</i> -HPBD...FA						
1,4 Insertion (TS3)						
<i>s-t</i> -MVK-oxide...FA =	-13.8	-14.5	-12.6	-0.9	-13.5	-12.7
<i>s-t</i> -HPBF Adduct				(-0.1)		
<i>s-c</i> -MVK-oxide...FA =	-13.2	-13.6	-11.9	-0.6	-12.6	-11.8
<i>s-c</i> -HPBF Adduct				(-0.0)		
<i>a-t</i> -MVK-oxide...FA =	-14.0	-14.7	-12.7	-1.0	-13.6	-12.8
<i>a-t</i> -HPBF Adduct						
<i>a-c</i> -MVK-oxide...FA =	-12.5	-13.2	-11.0	-0.8	-11.8	-11.0
<i>a-c</i> -HPBF Adduct						
1,2 Insertion (TS _{1,2-insertion})						
<i>s-t</i> -MVK-oxide...FA =	-2.3	-1.4	0.4	0.4	0.6	1.4
<i>s-t</i> -HPBF Adduct						
Cyclic Addition – SOZ Formation (TS _{SOZ})						
<i>s-t</i> -MVK-oxide...FA =	3.9	3.9	3.7	1.7	5.4	6.2
SOZ						
<i>s-t</i> -MVK-oxide...FA =	3.7	3.9	3.7	1.7	5.5	6.3
SOZ						
Geometry 2						
Acid Catalysis at C ₂ H ₃ (TS _{vinyl})						
<i>a-t</i> -MVK-oxide...FA =	6.2	4.3	8.3	-2.6	5.7	6.5
HPBD-2						
HPBD Product Acid Catalysis (TS _{H,exchange})						
<i>s-t</i> -HPBD...FA =	-1.8	-9.1	-7.4	-2.1	-9.5	-8.0
<i>s-t</i> -HPBD...FA						
<i>s-c</i> -HPBD...FA =	-3.4	-11.2	-9.4	-1.9	-11.3	-9.8
<i>s-c</i> -HPBD...FA						
<i>a-t</i> -HPBD...FA =	-0.7	-8.0	-6.2	-2.3	-8.5	-7.0
<i>a-t</i> -HPBD...FA						
<i>a-c</i> -HPBD...FA =	-0.9	-8.6	-6.9	-2.2	-9.1	-7.6
<i>a-c</i> -HPBD...FA						
Dioxole Formation; w and w/o Spectator Catalysis (TS _d , TS _{d,cat})						
<i>a-c</i> -MVK-oxide =	14.4	13.6	14.6	-0.3	14.4	15.2
Dioxole						
<i>a-c</i> -MVK-oxide...FA =	-0.0	-0.6	2.2	0.7	3.0	4.2

Dioxole...FA						
<i>a-c</i> -MVK-oxide...FA =	-0.3	-1.3	1.8	0.9	2.6	3.8
Dioxole...FA						
Geometry 2						
	Product OO Fission (HPBD)					
<i>s-t</i> -HPBD...FA =	-0.1	0.5	-5.9	-1.1	-7.0	-5.5
OBD...OH...FA; <i>syn-trans</i>						
	<hr/> <i>Products</i> <hr/>					
HPBF Adduct; optimized	-33.0	-30.8	-33.0	2.8	-30.3	-28.8
				(2.6)		
<i>s-t</i> -HPBF Adduct	-31.5	-29.2	-31.4	2.8	-28.6	-27.1
<i>s-c</i> -HPBF Adduct	-32.5	-30.3	-32.5	2.8	-29.6	-28.1
<i>a-t</i> -HPBF Adduct	-31.4	-29.2	-31.4	2.8	-28.6	-27.1
<i>a-c</i> -HPBF Adduct	-30.5	-28.4	-30.4	2.6	-27.9	-26.4
ABF+OH	13.7	17.7	16.6	-2.7	13.9	15.4
<i>s-t</i> -HPBD + FA	-8.2	-11.8	-13.1	-0.2	-13.2	-11.7
<i>s-c</i> -HPBD + FA	-9.8	-13.8	-13.8	0.0	-15.0	-13.5
<i>a-t</i> -HPBD + FA	-6.6	-10.0	-11.4	-0.3	-11.7	-10.2
<i>a-c</i> -HPBD + FA	-7.2	-10.9	-12.5	-0.2	-12.8	-11.3
SOZ	-29.6	-25.8	-30.4	3.7	-26.8	-25.3
SOZ; Geometry 2	-30.9	-24.4	-31.8	3.6	-28.2	-26.7
OBD + FA + OH	11.5	11.7	10.4	-5.2	5.8	7.3
³ OBD...FA...OH	-4.3	-5.2	-2.7	-1.8	-4.5	-3.0
OBD...FA + OH	-0.8	-2.1	-0.8	-3.7	-4.5	-3.0

^a All energies are relative to MVKOO;*syn,trans* + OCHOH. The first three columns are electronic energies, the next is the zero-point vibrational energy, and the last is a sum of the electronic and zero-point energies.

^b Zero-point energies from harmonic B2PLYP-D3/cc-pVTZ calculations. The numbers in parentheses are for the reaction with OCDOD.

^c Total corresponds to the sum of the CCSD(T)-F12b energy and E0.

^d The total energy corrected by crude estimates for higher level corrections from CCSDT(Q) calculations for related systems. These are estimated as 0.4 kcal/mol for reactant van der Waals complexes, 0.8 kcal/mol for entrance channel transition states, and 1.2 kcal/mol for all other species. These corrections are meant to account for known shortcomings in the CCSD(T) method for Criegee intermediates.

few tenths of a kcal mol⁻¹. When necessary, we have employed random sampling of initial torsional angles to obtain the lowest conformers.

Table S2 presents stationary point energies (kcal mol⁻¹) for the FA catalyzed isomerization of *syn-trans*-MVK-oxide evaluated by two different methods, and compared with earlier calculations by Kumar et al.³ We repeated the prior calculations of Kumar et al. since the differences between the present CCSD(T)-F12/CBS based calculations and the prior CCSD(T)/aug-cc-pVTZ based results are larger than would be expected for these levels of theory (ca. 2.0 kcal mol⁻¹). However, we found that the present CCSD(T)/aug-cc-pVTZ//M06-2x/aug-cc-pVTZ calculations show a roughly constant increase of 4 kcal mol⁻¹ compared to the prior report; the origin of this discrepancy is not known. The present CCSD(T)/aug-cc-pVTZ calculations are in much improved agreement with the CCSD(T)-F12/CBS based results.

The reaction coordinates for the interconversion between *syn-trans* and *syn-cis* configurations of MVK-oxide and of MVK-oxide...FA PRC are illustrated in Figure S2. The interaction between MVK-oxide and FA results in an isomerization transition state that lies far below the MVK-oxide + FA asymptote. As a result, the reaction of the *syn-trans* and *syn-cis* conformers effectively occurs through an equilibrated pair of *syn-trans* and *syn-cis* MVK-oxide...FA PRC conformers. Note, however, that this does not imply that the rates and products arising from the *syn-trans* and *syn-cis* conformers will be identical; the *syn-cis* reaction is initiated at the higher energy of the *syn-cis* conformer and this additional energy affects the product distributions (as shown below). The reaction coordinate diagram for the isomerization of *anti-trans* and *anti-cis* configurations (not shown) is similar and so the reaction of the *anti-trans* and *anti-cis* conformers also occurs as an equilibrated pair of *anti-trans* and *anti-cis* MVK-oxide...FA PRC

Table S2. Stationary point energies (kcal mol⁻¹) for the formic acid catalyzed isomerization of *syn-trans*-MVK-oxide. Energies include ZPE corrections and are reported relative to reactants.

Species	This work ^a	This work ^b	Kumar <i>et al.</i> ^c
	CCSD(T)-F12/CBS	CCSD(T)/aug-cc-pVTZ	CCSD(T)/aug-cc-pVTZ
MVK-oxide + FA	-14.3	-16.0	-20.5
TS2	-3.8	-6.5	-11.1
HPBD...FA	-21.5	-23.6	-27.0
HPBD + FA	-13.8	-12.9	-11.8

- a. CCSD(T)-F12/CBS(TZ-F12,QZ-F12)//B2PLYP-D3/cc-pVTZ with estimated CCSDT(Q) corrections.
b. CCSD(T)/aug-cc-pVTZ//M06-2X/aug-cc-pVTZ.
c. Ref. 3, CCSD(T)/aug-cc-pVTZ//M06-2X/aug-cc-pVTZ.

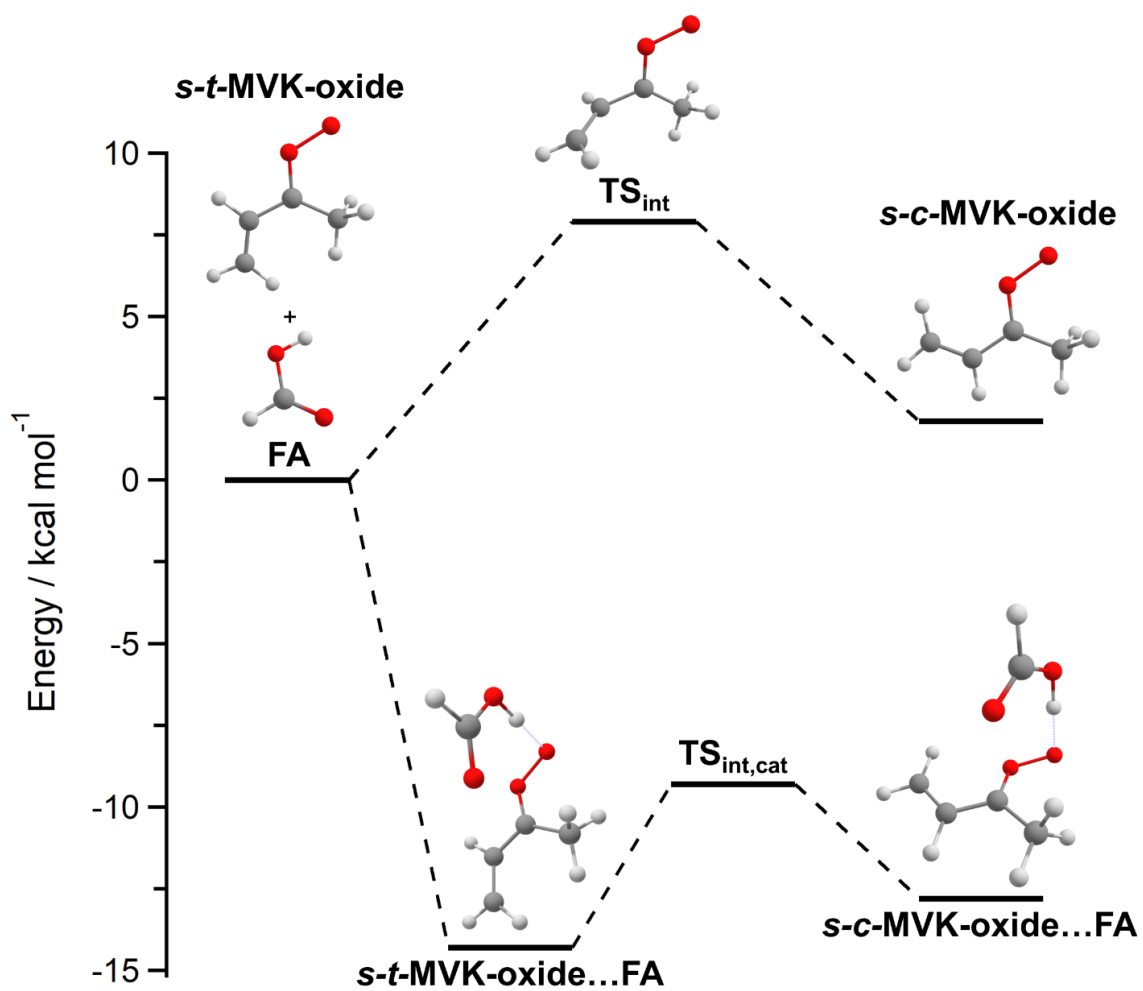


Figure S2. Reaction coordinate showing the barrier (TS_{int}) for interconversion between *syn-trans* and *syn-cis* configurations of MVK-oxide. A pre-reactive complex (PRC) formed between MVK-oxide and formic acid substantially lowers the barrier ($TS_{int,cat}$) and provides a route for rapid interconversion between *trans* (s-t) and *cis* (s-c) forms.

conformers. The barrier to transformation from *syn* to *anti* conformers is high enough (31 kcal mol⁻¹)⁵ that we do not expect the *syn* to *anti* transformation to be rapid even within the PRCs.

The reaction paths for the two reaction channels of primary interest here – the acid-catalyzed pathway through TS2 to form HPBD with release of FA and the adduct formation pathway through TS3 to form the HPBF adduct– are illustrated for the lowest energy *syn-trans* MVK-oxide conformer in the main text (Figure 4). From this diagram it is clear that both TS2 and TS3 saddle points are submerged below reactants, and so can provide effective channels for low-temperature kinetics. Although TS2 lies considerably higher in energy than TS3, simple inspection of the TS structures does not make it clear which channel is favored entropically. The two channels are predicted to proceed through the same PRC.

The process through TS2 directly leads to a complex (Int) between HPBD and FA, which is expected to dissociate directly and rapidly to HPBD and FA. Indeed, the master equation calculations find no indication of stabilization of the HPBD...FA complex for any conditions of relevance to atmospheric chemistry. Meanwhile, the dissociation of HPBD to OBD + OH (the lowest bond fission process) is predicted to be endoergic by 7.3 kcal mol⁻¹ relative to MVK-oxide + FA reactants. As discussed in Ref. 5, an alternative roaming induced formation of HB (hydroxybutadiene) has a maximum barrier at only 4.0 kcal mol⁻¹ relative to *syn-trans* reactants. This pathway might just be energetically accessible from thermally excited *syn-cis* reactants.

It is interesting to ponder further the possible products that might be formed from the HPBD...FA complex (Int). Notably, a termolecular complex between OBD, OH, and FA is predicted to lie 3.0 kcal mol⁻¹ below *syn-trans* reactants. From this complex, which would be formed via partial OO bond fission in HPBD...FA at an energy of -5.5 kcal mol⁻¹

¹, the loss of OH to form OBD...FA + OH has an asymptotic energy of 2.4 kcal mol⁻¹. Meanwhile, the maximum barrier for the roaming isomerization to HB...FA would likely also be weakly submerged. Lastly, the loss of FA to form OBD...OH + FA would have an energy of 2.4 kcal mol⁻¹. However, it seems unlikely that any of these processes would be competitive with the simple loss of FA from the HPBD...FA, which occurs at a much lower energy (-13.5 kcal mol⁻¹) and should also have the highest entropy.

The likely lowest energy bond fission for the HPBF adduct (OO fission as in the CH₂OO + FA case⁴) lies at 15 kcal mol⁻¹ relative to *syn-trans* MVK-oxide + FA. We expect that the lowest energy molecular eliminations involve CH₃OH and CH₂CHOH loss as analogues of the H₂O loss channel explored for the CH₂OO case.⁴ We have not explored these here as we do not expect them to be energetically accessible.

Figure S3 provides a corresponding illustration of these same two reaction paths (TS2 and TS3 analogues) for the reaction of the *anti-trans* MVK-oxide conformer with FA. The reaction path energies are remarkably similar to those for the *syn-trans* case, with the most significant difference being that TS2 for the acid catalysis pathway is not as deeply submerged (-1.0 vs -4.1 kcal mol⁻¹, where both are specified relative to their respective reactants). Thus, we expect the branching through this channel to be smaller than that for *syn-trans*.

For isolated *anti-cis* MVK-oxide, the dominant reaction pathway involves electrocyclic ring closure to yield dioxole. The reaction coordinate diagram provided in Figure S4 demonstrates that, even with the spectator catalytic lowering of the barrier, this process is endoergic (by 1.0 kcal mol⁻¹ relative to *anti-cis* MVK-oxide reactants) and not competitive with the HPBF adduct formation pathway. The acid catalyzed isomerization of *anti-cis*-MVK-oxide to HPBD is also more favorable than spectator catalysis yielding dioxole.

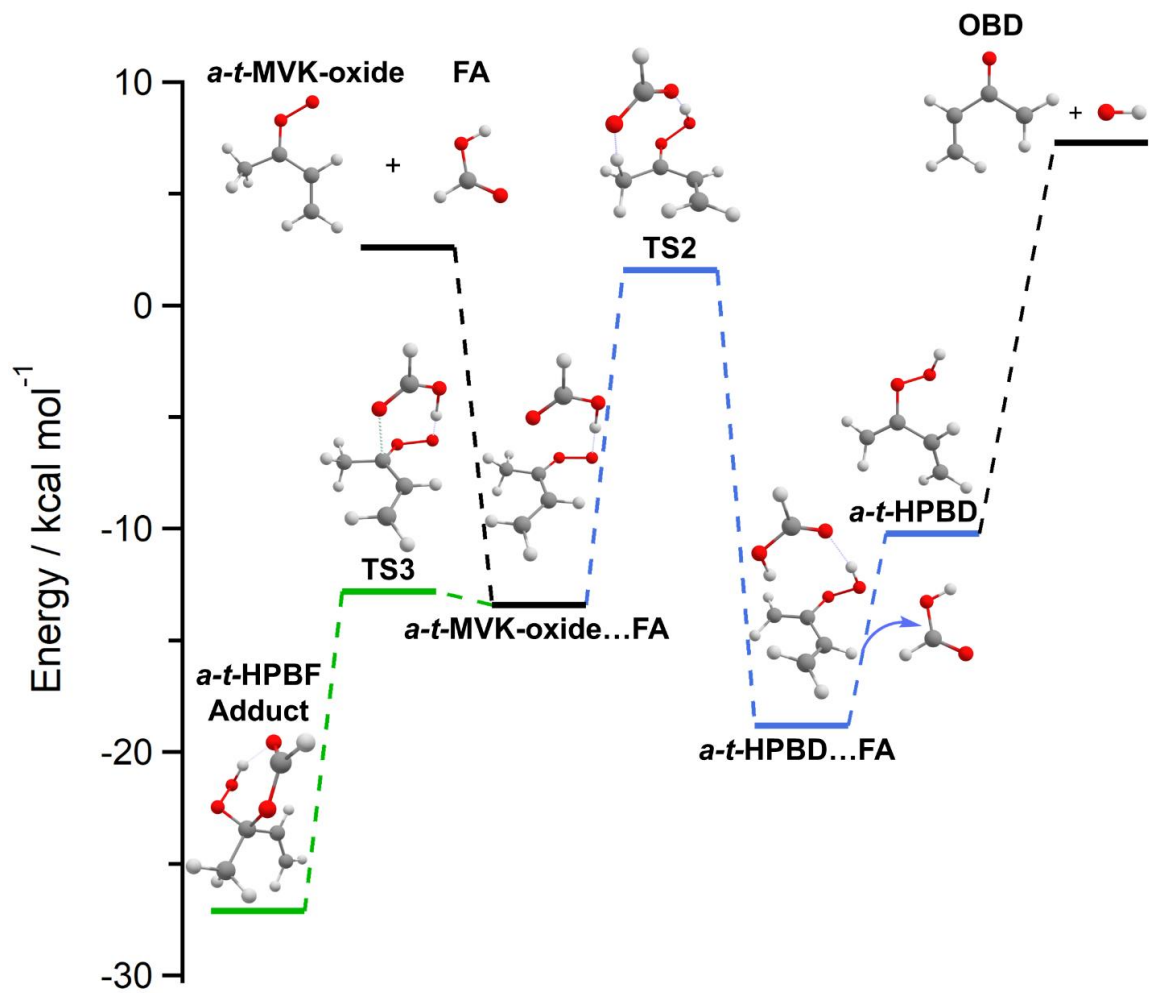


Figure S3. Reaction coordinates showing the formic acid catalyzed isomerization of *anti-trans*-MVK-oxide (blue) and the more favorable adduct formation pathway arising from the 1,4-insertion reaction of *anti-trans*-MVK-oxide with formic acid (green) at the CCSD(T)-F12/CBS(TZ-F12,QZ-F12)//B2PLYP-D3/cc-pVTZ level of theory with estimated CCSDT(Q) corrections (Table S1).

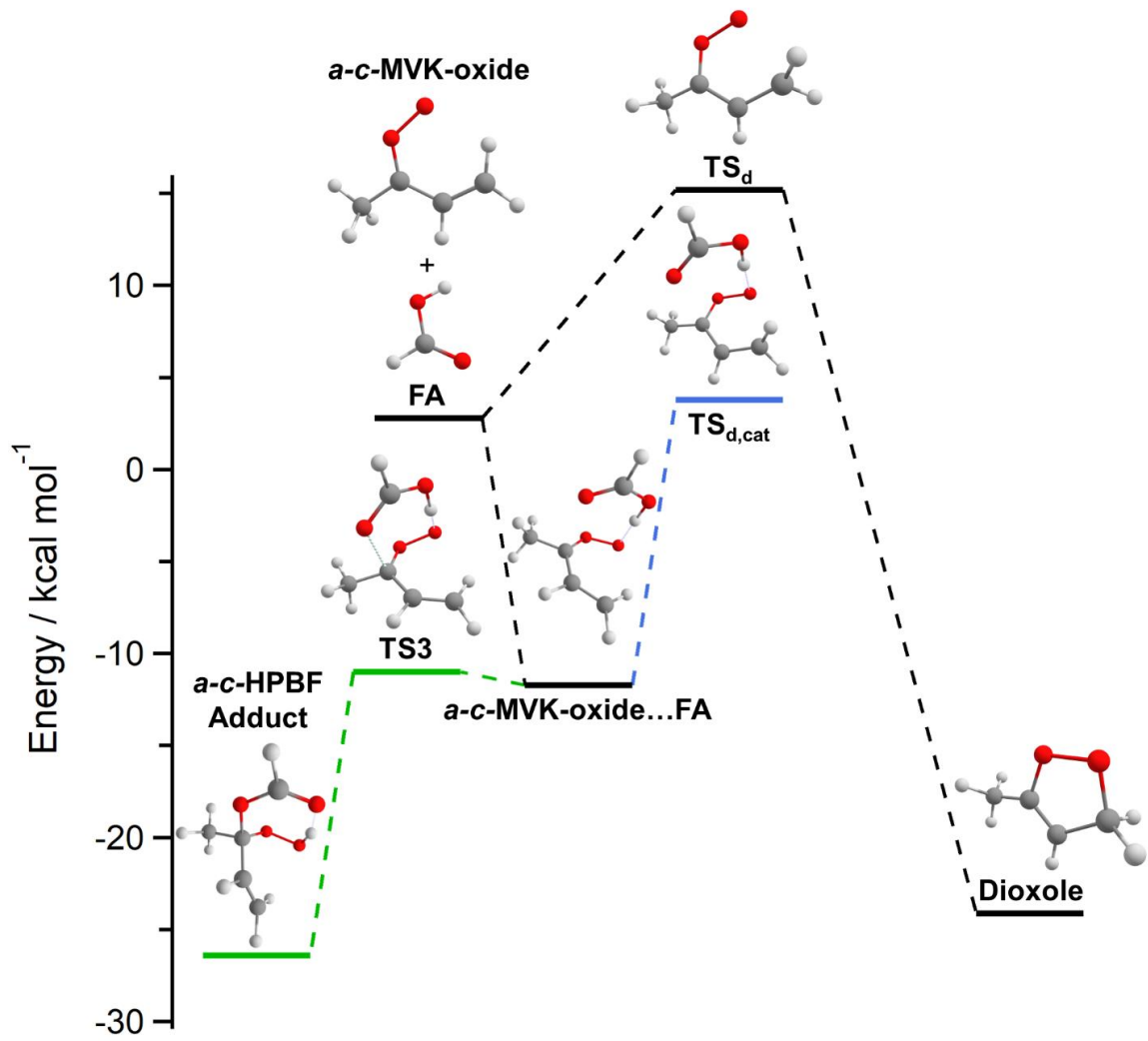


Figure S4. Reaction coordinate for electrocyclic ring closure of *anti-cis*-MVK-oxide to dioxole (black) compared to that for the formic acid spectator catalyzed pathway to dioxole (blue). Also shown is the energetically favorable adduct formation pathway (green) for the *anti-cis*-MVK-oxide + formic acid reaction. Energies are reported at the CCSD(T)-F12/CBS(TZ-F12,QZ-F12)//B2PLYP-D3/cc-pVTZ level of theory with estimated CCSDT(Q) corrections (Table S1).

For *anti-trans* MVK-oxide + FA, an alternative chemical catalysis pathway would involve an H transfer from the vinyl group to the FA. However, as illustrated in Figure S5, this catalytic pathway is not competitive with the catalytic pathway involving H transfer from the methyl group. Thus, the reaction of the *anti* conformers of MVK-oxide with FA should predominantly yield the HPBF adduct (Figure S4) with secondary production of an acid-catalyzed HPBD product as for the *syn* conformers (Figure S5).

Vereecken also found that a 1,2 insertion pathway⁴ (where the OH group of FA inserts across the COO moiety in the CI) is slightly submerged (i.e. at -2.4 kcal mol⁻¹). As illustrated in Figure S6, for *syn-trans* MVK-oxide the analogous 1,2 insertion pathway is predicted to be slightly endoergic (1.4 kcal mol⁻¹) and is thus not expected to play a significant role in the kinetics. Vereecken also explored a cyclo addition process to yield a primary ozonide, which was submerged by 1.7 kcal mol⁻¹. As illustrated in Figure S7, for *syn-trans* MVK-oxide the analogous secondary ozonide (SOZ) forming process is highly endoergic, with a predicted barrier of 6.2 kcal mol⁻¹. These increased barrier heights for MVK-oxide relative to CH₂OO are largely the result of the need to break the resonance between the vinyl π bond and the COO π bond prior to bond formation. The extra resonance stabilization in MVK-oxide also leads to decreased bond strengths for the complexes formed. Tables S3-S5 provide a comparison of the reaction pathway energies for the reaction of FA with CH₂OO and *syn-trans* MVK-oxide. For *syn-trans* MVK-oxide in isolation the primary unimolecular decomposition involves an H transfer from the methyl group to the OO group, as studied in detail in Ref. 5. As illustrated in Figure S8, spectator catalysis⁶ lowers the isomerization barrier from 18.0 to 7.9 kcal mol⁻¹. Although the barrier is significantly lowered, it is not expected to be an effective kinetic process because of the lower energy channels accessible to the MVK-oxide...FA PRC. The master equation calculations including all the channels validate this expectation.

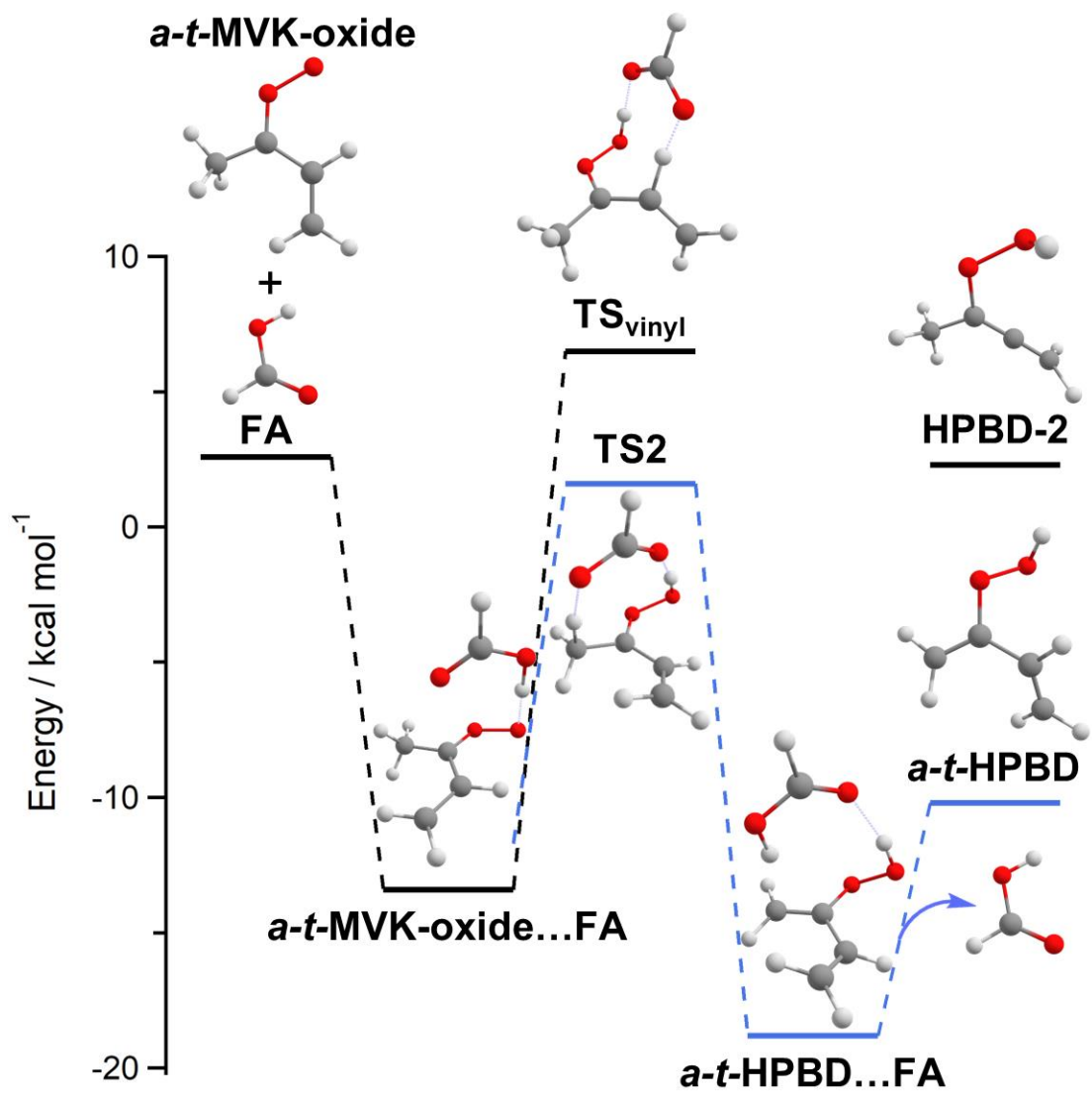


Figure S5. Reaction coordinates comparing different acid catalyzed reaction pathways for the *anti-trans*-MVK-oxide + formic acid reaction. TS2 (blue) and TS_{vinyl} illustrate the barriers for H-atom transfer from the methyl and vinyl group of MVK-oxide, respectively. Energies (Table S1) are determined at the CCSD(T)-F12/CBS(TZ-F12, QZ-F12)//B2PLYP-D3/cc-pVTZ level of theory (with estimated CCSDT(Q) corrections) and indicate that the methyl H-atom transfer pathway is more favorable.

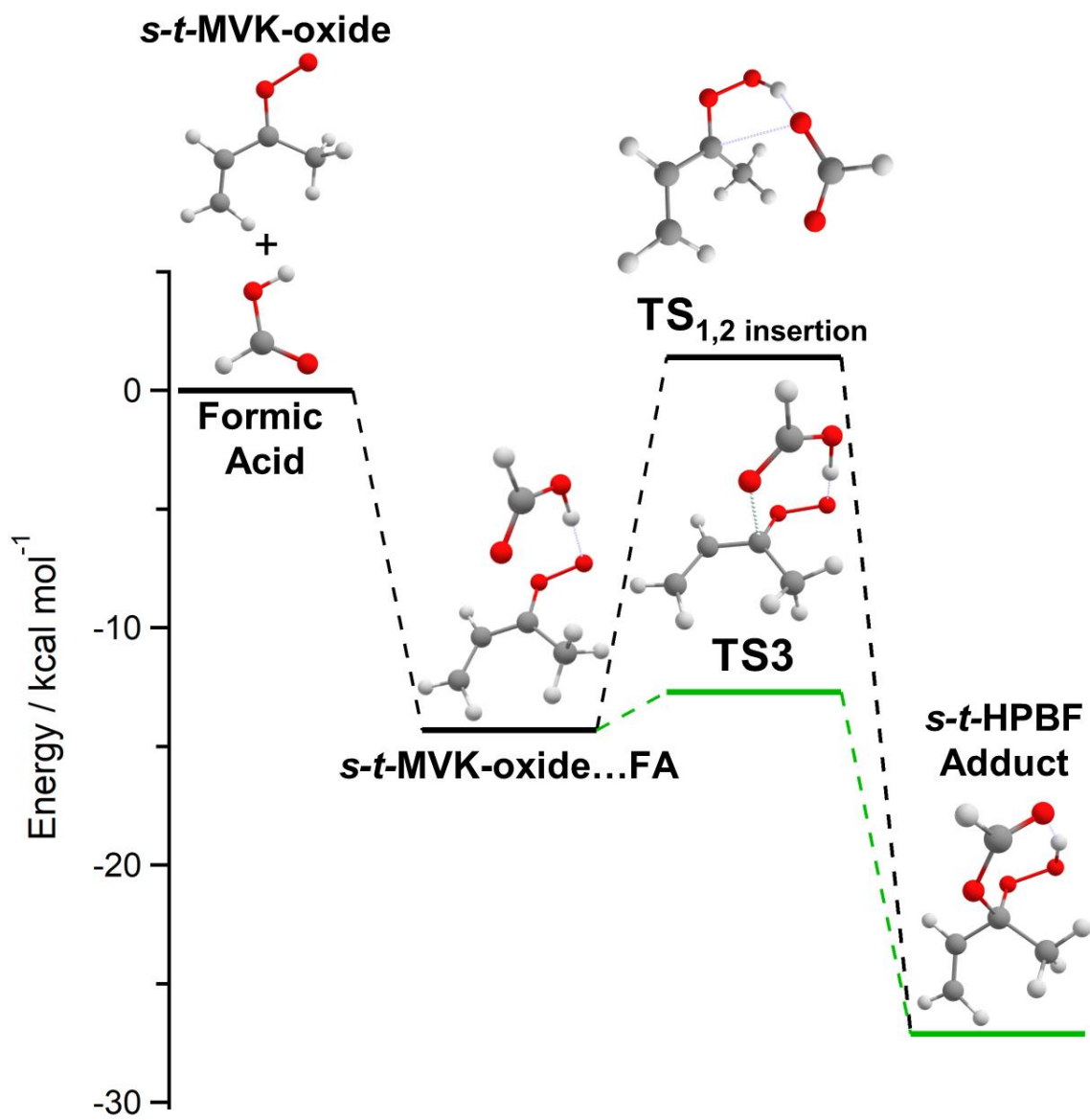


Figure S6. Reaction coordinates comparing adduct formation from the *syn*-MVK-oxide + formic acid reaction via the 1,2-insertion (TS_{1,2 insertion}, black) and 1,4-insertion (TS3, green) mechanisms. Energies are reported at the CCSD(T)-F12/CBS(TZ-F12,QZ-F12)//B2PLYP-D3/cc-pVTZ level of theory with estimated CCSDT(Q) corrections (Table S1).

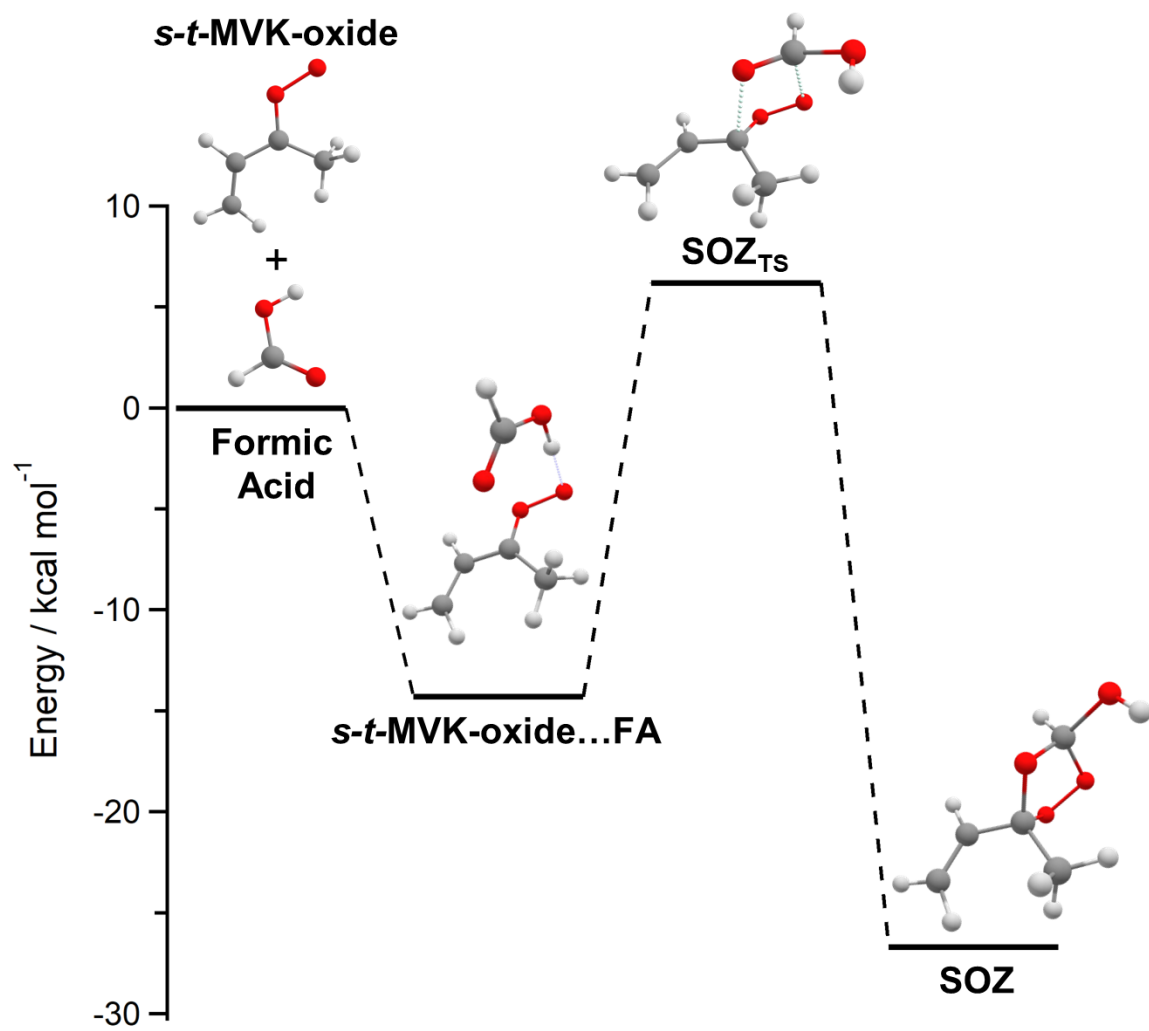


Figure S7. Reaction coordinate showing TS barrier (SOZ_{ts}) to secondary ozonide (SOZ) formation from the *syn*-MVK-oxide + formic acid reaction. Energies are reported at the CCSD(T)-F12/CBS(TZ-F12,QZ-F12)//B2PLYP-D3/cc-pVTZ level of theory with estimated CCSDT(Q) corrections (Table S1).

Table S3. Stationary point energies (kcal mol⁻¹) for adduct formation from the reactions of CH₂OO (Vereecken, Ref. 4) and *syn-trans*-MVK-oxide with formic acid via the 1,4-insertion mechanism. Energies include ZPE corrections and are reported relative to reactants.

Species	<i>syn-trans</i> -MVK-oxide ^a	CH ₂ OO ^b
PRC	-14.3	N/A ^c
TS3	-12.7	N/A ^c
HPBF Adduct	-27.1	-44.4

- CCSD(T)-F12/CBS(TZ-F12,QZ-F12)//B2PLYP-D3/cc-pVTZ with estimated CCSDT(Q) corrections.
- Ref. 4, CCSD(T)/aug-cc-pVTZ//M06-2X/aug-cc-pVTZ.
- There was no apparent saddle point for the 1,4-insertion mechanism with CH₂OO.

Table S4. Stationary point energies (kcal mol⁻¹) for adduct formation from the reactions of CH₂OO (Vereecken, Ref. 4) and *syn-trans*-MVK-oxide with formic acid via the 1,2-insertion mechanism. Energies include ZPE corrections and are reported relative to reactants.

Species	<i>syn-trans</i>-MVK-oxide^a	CH₂OO^b
PRC	-14.3	N/A
TS3	1.4	-2.4
Adduct	-27.1	-44.4

a. CCSD(T)-F12/CBS(TZ-F12,QZ-F12)//B2PLYP-D3/cc-pVTZ with estimated CCSDT(Q) corrections

b. Ref. 4, CCSD(T)/aug-cc-pVTZ//M06-2X/aug-cc-pVTZ

Table S5. Stationary point energies (kcal mol⁻¹) for SOZ formation from the reaction of CH₂OO (Vereecken, Ref. 4) and *syn-trans*-MVK-oxide with formic acid. Energies include ZPE corrections and are reported relative to reactants.

Species	<i>syn-trans</i> -MVK-oxide ^a	CH ₂ OO ^b
PRC	-14.3	-6.0
TS _{SOZ}	6.2	-1.7
SOZ	-25.3	-40.2

a. CCSD(T)-F12/CBS(TZ-F12,QZ-F12)//B2PLYP-D3/cc-pVTZ with estimated CCSDT(Q) corrections

b. Ref. 4, CCSD(T)/aug-cc-pVTZ//M06-2X/aug-cc-pVTZ

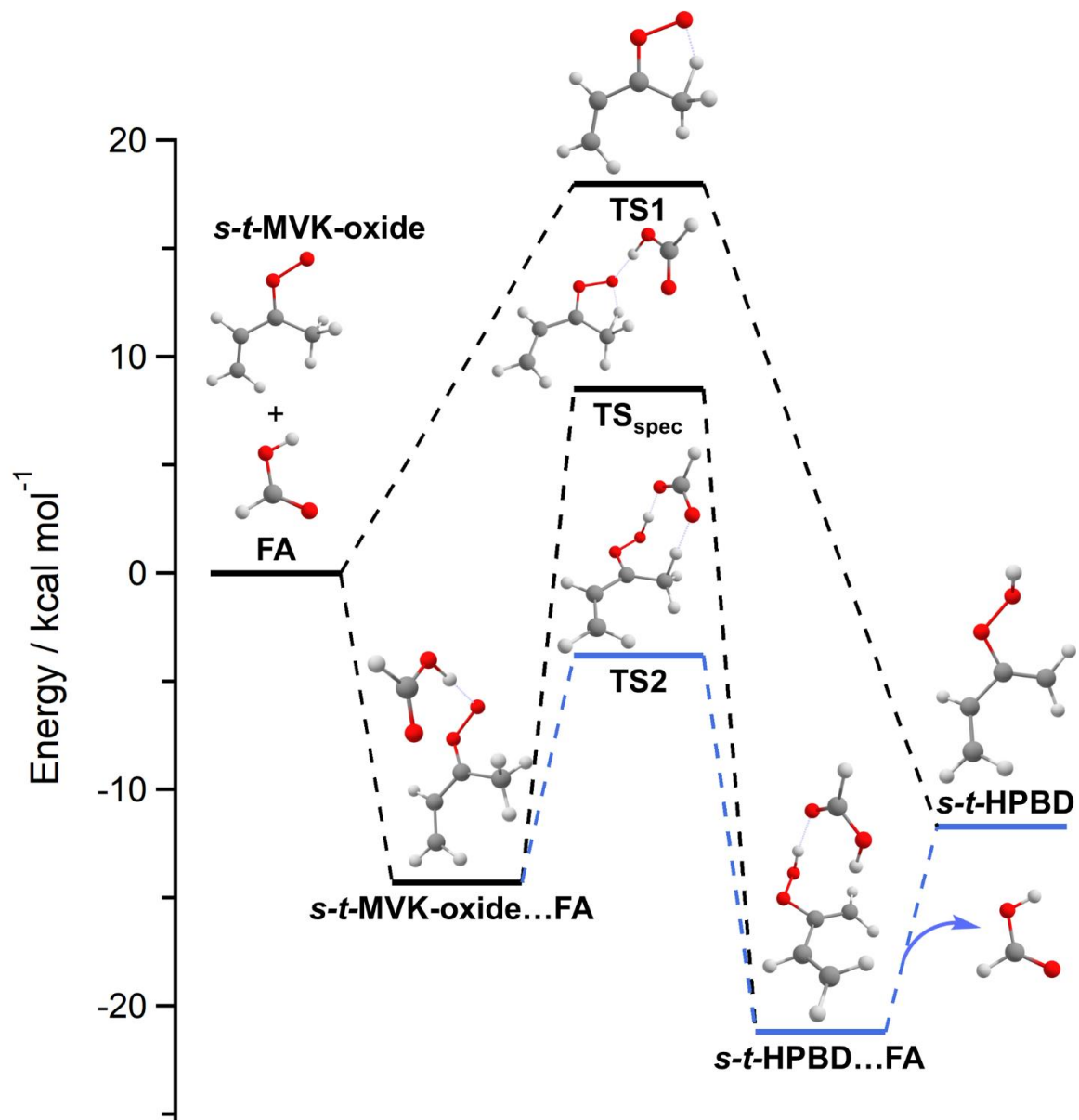


Figure S8. Reaction coordinates showing the chemical catalysis (TS2, blue), spectator catalysis (TS_{spec}), and uncatalyzed isomerization (TS1) pathways for the formation of HPBD from the *syn*-MVK-oxide + formic acid reaction. Energies are from calculations at the CCSD(T)-F12/CBS(TZ-F12,QZ-F12)//B2PLYP-D3/cc-pVTZ level of theory with estimated CCSDT(Q) corrections (see Table S1).

Although not illustrated here, the reaction pathways for *syn-cis* MVK-oxide reacting with FA closely mimic those for *syn-trans* MVK-oxide. The key kinetic difference is that the rapid equilibration of the *syn-trans* and *syn-cis* PRCs (Figure S2) allows for rapid dissociation of the PRC to *syn-trans* MVK-oxide + FA. Furthermore, the extra 1.8 kcal mol⁻¹ conformational energy of the *syn-cis* conformer maps into additional excess energy in the initially formed HPBF adduct. These two effects lower the net adduct formation rate for *syn-cis* relative to *syn-trans* as they both make it harder to stabilize the HPBF adduct. However, in the high-pressure limit, the two rates are predicted to be nearly identical. In the following temperature and pressure dependent kinetic analysis subsection, we explore the extent to which the reactions are occurring in the high-pressure limit via master equation calculations.

As illustrated in Figure S9, the reaction of FA with HPBD can yield H exchange at the hydroperoxyl group. The barriers for the deuterated FA reaction with *syn-cis*, *syn-trans*, *anti-cis*, and *anti-trans* HPBD are 4.2, 4.2, 4.2, and 4.7 kcal mol⁻¹, respectively, relative to the respective HPBD + FA asymptotes (Table S6). These barriers are low enough that it seems worth considering the possible ramifications of this process. Thus, we also performed ab initio TST based master equation calculations of the rate constants for this isotopic exchange process (with deuterated FA). There is unlikely to be any direct formation of HPBD from *anti*-MVK-oxide in the photolytic generation process due to the presence of the much lower energy dioxole channel. However, HPBD that might be formed from *syn* conformers in the photolytic preparation of MVK-oxide will likely equilibrate rapidly amongst all four *syn/anti cis/trans* conformers. Thus, these master equation analyses considered the kinetics for each of the four conformers and included the transition states for interconversion between them. There is little variation in the isotopic exchange reaction paths for the different HPBD conformers.

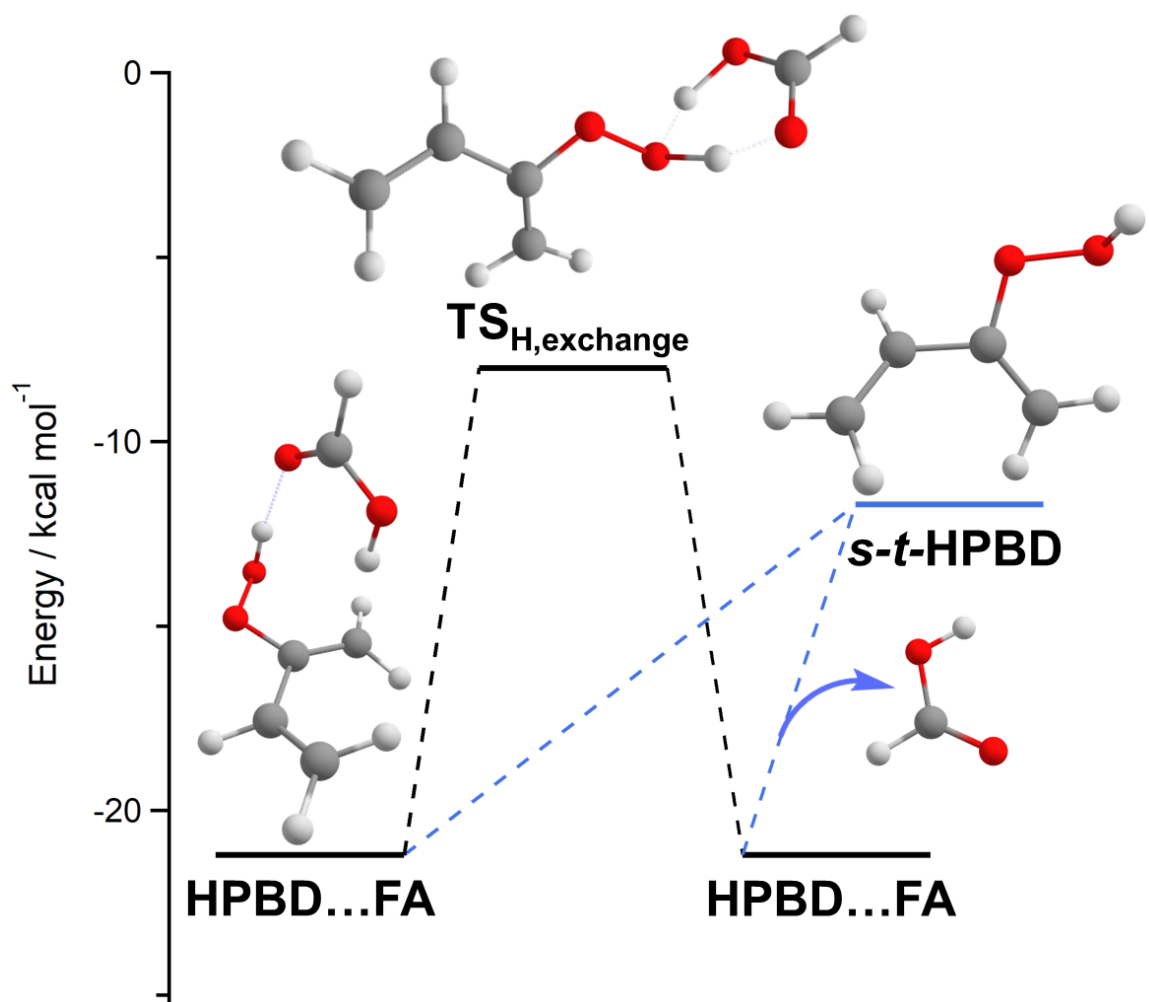


Figure S9. Reaction coordinate for H-atom exchange between the $-OOH$ and $-OH$ functional groups of HPBD and formic acid, respectively. Separation of HPBD and formic acid products is energetically favored compared to H-atom exchange.

Table S6. Stationary point energies (kcal mol⁻¹) for H-exchange in HPBD + FA for both OCHOH and OCDOD isotopes of FA.^a Energies include ZPE corrections and are reported relative to *syn-cis*-HPBD + FA.

Species	OCHOH	OCDOD
<i>syn-cis</i> -HPBD +FA	0.0	0.0
<i>syn-cis</i> -HPBD...FA	-9.4	-9.5
<i>syn-cis</i> -HPBD...FA =	3.7	4.2
(<i>syn-cis</i> -HPBD...FA) exchange		
(<i>syn-cis</i> -HPBD...FA) exchange	-9.4	-9.5
(<i>syn-cis</i> -HPBD + FA) exchange	0.0	0.1
<i>syn-trans</i> -HPBD + FA	1.8	1.8
<i>syn-trans</i> -HPBD...FA	-7.7	-7.8
<i>syn-trans</i> -HPBD...FA =	5.5	6.0
(<i>syn-trans</i> -HPBD...FA) exchange		
(<i>syn-trans</i> -HPBD...FA) exchange	-7.7	-7.8
(<i>syn-trans</i> -HPBD + FA) exchange	1.8	1.9
<i>anti-cis</i> -HPBD + FA	2.3	2.3
<i>anti-cis</i> -HPBD...FA	-5.2	-5.1
<i>anti-cis</i> -HPBD...FA =	6.0	6.5
(<i>anti-cis</i> -HPBD...FA) exchange		
(<i>anti-cis</i> -HPBD...FA) exchange	-5.2	-5.4
(<i>anti-cis</i> -HPBD + FA) exchange	2.3	2.4
<i>anti-trans</i> -HPBD + FA	3.3	3.3
<i>anti-trans</i> -HPBD...FA	-5.7	-5.8
<i>anti-trans</i> -HPBD...FA =	6.5	7.0
(<i>anti-trans</i> -HPBD...FA) exchange		
(<i>anti-trans</i> -HPBD...FA) exchange	-5.7	-5.8
(<i>anti-trans</i> -HPBD + FA) exchange	3.3	3.4
<i>syn-cis</i> -HPBD...FA =	-4.7 ^b	-4.7 ^b
<i>syn-trans</i> -HPBD...FA		
(<i>syn-cis</i> -HPBD...FA) exchange =	-4.7 ^b	-4.9 ^b
(<i>syn-trans</i> -HPBD...FA) exchange		
<i>anti-trans</i> -HPBD...FA =	-0.4 ^b	-0.4 ^b
<i>anti-cis</i> -HPBD...FA		
(<i>anti-trans</i> -HPBD...FA) exchange	-0.4 ^b	-0.5 ^b
=		
(<i>anti-cis</i> -HPBD...FA) exchange		
<i>syn-trans</i> -HPBD...FA =	-1.0 ^b	-1.1 ^b
<i>syn-cis</i> -HPBD...FA		
(<i>syn-trans</i> -HPBD...FA) exchange	-1.0 ^b	-1.1 ^b
=		

(anti-trans-HPBD...FA) exchange

- a. CCSD(T)-F12/CBS(TZ-F12,QZ-F12)//B2PLYP-D3/cc-pVTZ energies with B2PLYPD3/cc-pVTZ ZPE.
- b. B2PLYP-D3/cc-pVTZ energies and ZPE.

and included the transition states for interconversion between them. There is little variation in the isotopic exchange reaction paths for the different HPBD conformers.

Temperature and Pressure Dependent Kinetics

Predictions for the thermal rate constants for the reaction of MVK-oxide with FA are obtained from *ab initio* transition state theory-based master equation calculations. In this master equation model, we employ standard exponential down energy transfer probabilities with a temperature dependent expression for the average downwards energy transferred given by $\langle \Delta E_{\text{down}} \rangle = 400 (T/298)^{0.85} \text{ cm}^{-1}$ and Lennard-Jones collision rate appropriate for He. The increased value for ΔE_{down} employed here (400 vs 300 cm^{-1} in Ref. 2) is likely a better estimate for a molecule the size of the HPBF adduct with 9 heavy atoms.⁷ The majority of the calculations were performed for reaction with normal FA (H₂-formic acid). However, sample calculations were also performed to explore the effect of deuteration on the predicted branching.

The requisite partition functions were largely evaluated as discussed in Ref. 2. This mostly involves fixed transition state assumptions employing rigid-rotor harmonic oscillator approximations coupled with hindered rotor treatments of the torsional motions as appropriate. For the HPBF adduct, whose stabilization is central to understanding the temperature and pressure dependence of the kinetics, we include one dimensional hindered rotor representations for all 6 hindered rotor modes. For the other stationary points, the hindered rotor analyses are largely restricted to treatments of the methyl rotor. The vinyl rotor is treated in the harmonic oscillator limit in order to retain a distinction between *cis* and *trans* conformers.

For the entrance channel, which is the primary flux bottleneck for the overall reaction, we employ a VRC-TST analyses with a center-of-mass reaction coordinate to

predict the rate of forming the MVK-oxide...FA PRC. This ω B97XD/6-31+G* direct sampling based VRC-TST analyses was implemented here for all four (*syn-trans*, *syn-cis*, *anti-trans*, and *anti-cis*) conformers of MVK-oxide interacting with FA. A dynamical correction factor of 0.85, based on earlier related reference comparisons of trajectories and TST, is applied to these VRC-TST results. For the conversion from the PRC to the HPBF adduct as well as the other conversions, we now employ fixed transition states. The additional variational components of the treatments described in Ref. 2 for the PRC to HPBF adduct conversion yield only a 10% reduction in the *syn-trans* rate at the conditions of the present experiment. Variational effects are expected to be similar for the other channels. Thus, the present restriction to fixed TST analyses for these conversion steps was deemed appropriate. The interaction energies in the VRC-TST analyses were evaluated via direct sampling of ω B97XD/6-31+G* energies.

As illustrated in FigureS10 and S11, the estimated branching to HPBD + FA (i.e., the acid catalyzed isomerization products) is quite sensitive to both temperature and pressure and is quite a bit larger (~ a factor of four) for the *syn-cis* MVK-oxide reactant than that for the *syn-trans* reactant. TS2 provides the primary bottleneck for acid-catalyzed formation of HPBD and release of FA. In contrast, the rate for forming the HPBF adduct is primarily determined by the rate for forming the MVK-oxide...FA PRC coupled with the probability of stabilization of the HPBF adduct rather than redissociation back to reactants. Also, note that we see no indication of stabilization of the MVK-oxide...FA PRCs under the experimentally relevant ranges of temperature and pressure. Thus, the branching to HPBD + FA is essentially an indication of the competition between passage through TS2 and stabilization of the HPBF adduct.

MVKOxide + Formic Acid

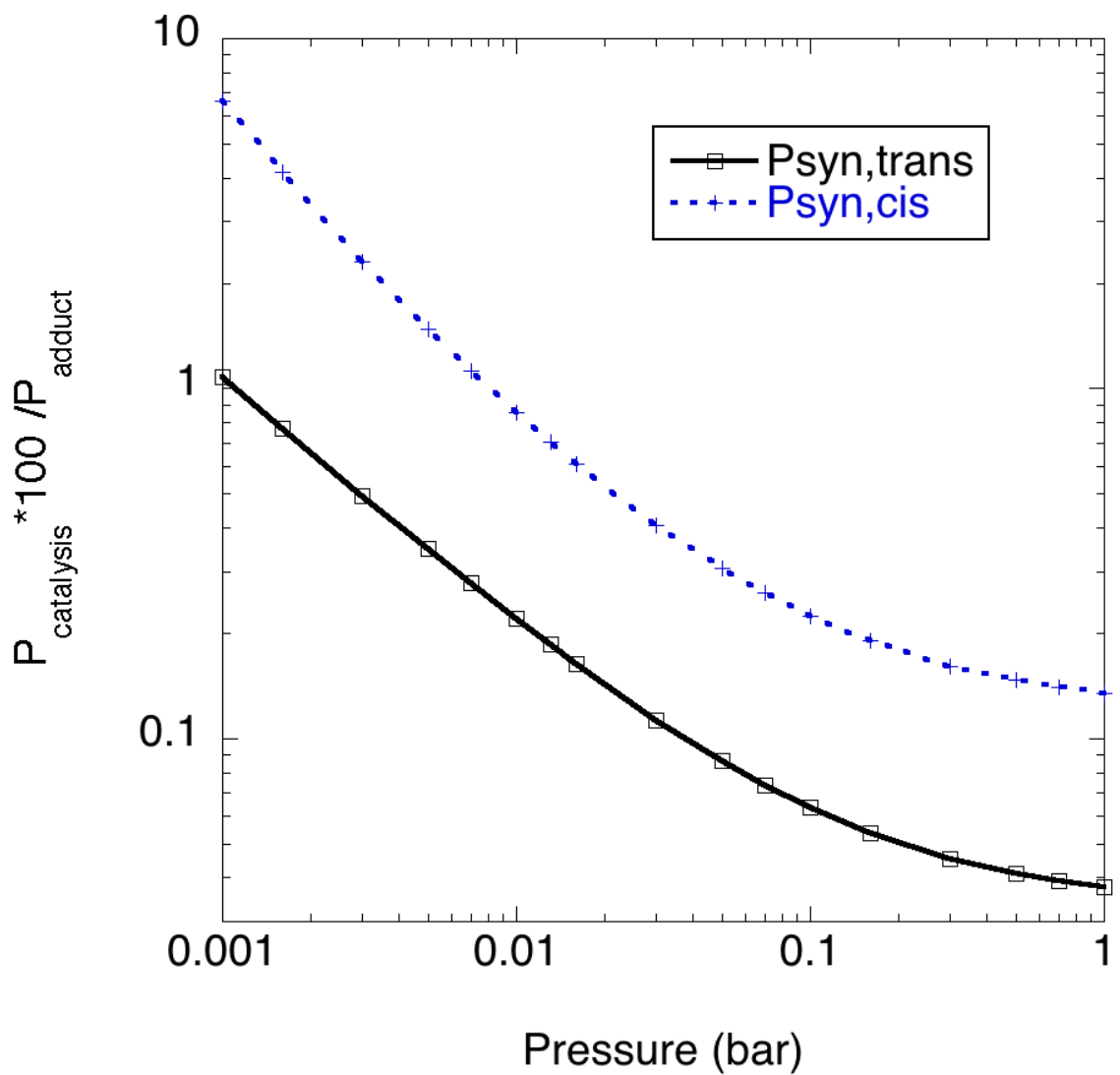


Figure S10. Plot of the pressure dependence for the predicted branching between the acid catalyzed reaction, yielding HPBD with regeneration of formic acid, and chemical adduct formation, yielding the HBPF adduct, in the reaction of *syn-trans* (black solid line) and *syn-cis* (blue dashed line) MVK-oxide with formic acid at 300 K.

MVKOxide + Formic Acid

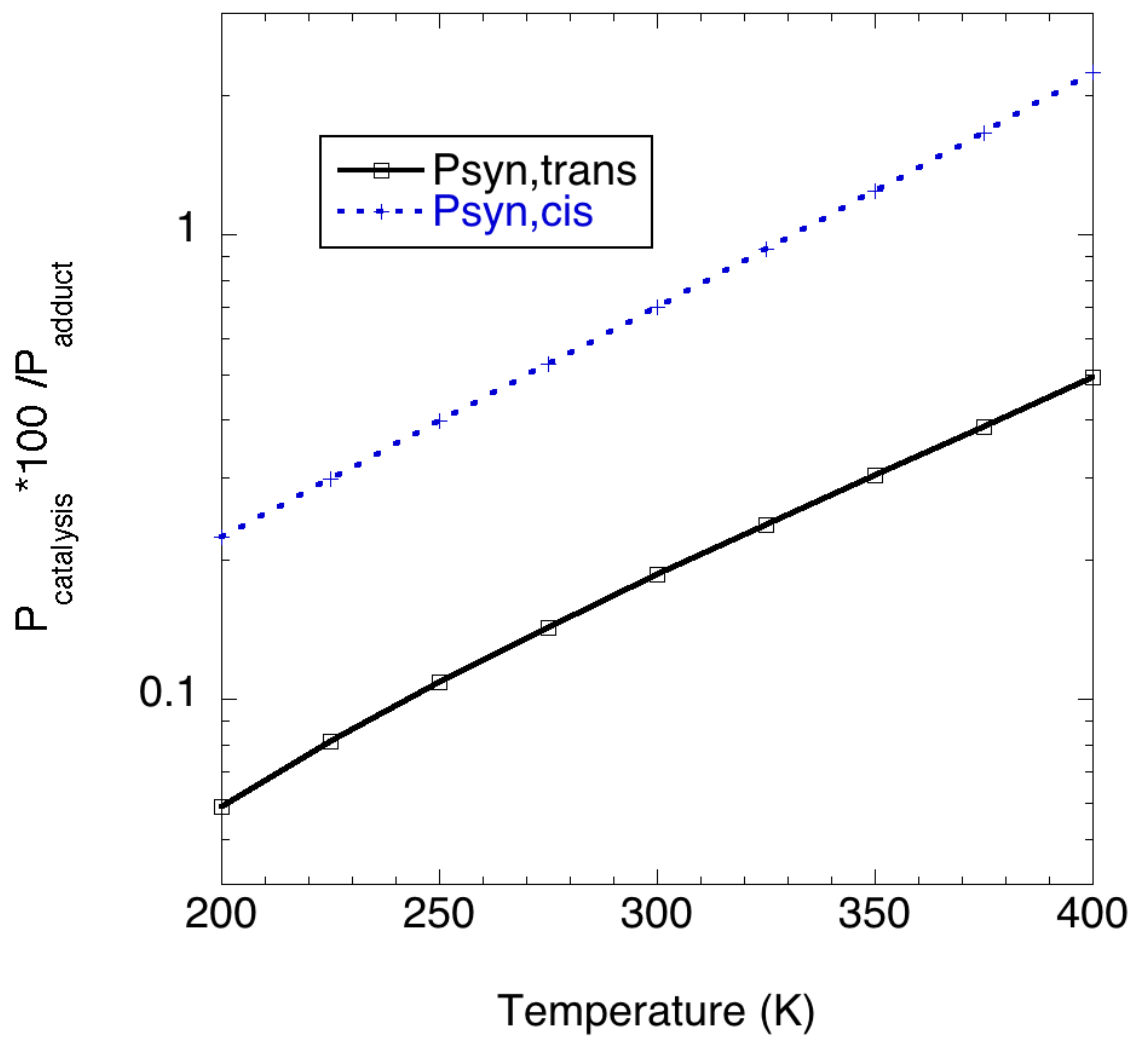


Figure S11. Plot of the temperature dependence of the predicted branching between acid catalyzed reaction, yielding HPBD with regeneration of formic acid, and chemical adduct formation, yielding the HBPF adduct, in the reaction of *syn-trans* (black solid line) and *syn-cis* (blue dashed line) MVK-oxide with formic acid at 1 bar.

Interestingly, the increase in the branching for the *syn-cis* reactant is partly due to a rapid equilibration of the *syn-trans*...FA and *syn-cis*...FA PRCs. This equilibration allows the *syn-cis* reactants to proceed through the *syn-trans* TS2 bottleneck, which is 5.9 kcal mol⁻¹ below the *syn-cis* reactant asymptote, rather than the *syn-cis* TS2 bottleneck, which is 5.6 kcal mol⁻¹ below the *syn-cis* reactant asymptote. In contrast, the *syn-trans* TS2 barrier is only 4.1 kcal mol⁻¹ below the *syn-trans* reactant asymptote. This additional excess energy allows the process through TS2 to more effectively compete with the other processes. Meanwhile, the same increased excess energy also makes it more difficult for the HPBF adduct to be stabilized.

The predicted branching for the acid catalyzed path to HPBD with release of FA is 2 orders of magnitude lower for the *anti-cis* and *anti-trans* MVK-oxide compared to *syn*-MVK-oxide with FA. This reduction is largely due to the increased energies of the TS2 saddle points (-1.0 and 1.7 kcal mol⁻¹) relative to their asymptotic reactant states. For the experimentally studied condition of room temperature and a pressure of 10 Torr of He, our reference calculations yield estimated acid catalyzed product branching fractions for the *syn-trans* and *syn-cis* MVK-oxide of 0.19% and 0.70%, respectively. With an estimated equilibrium concentration ratio of *syn-cis* to *syn-trans* of 0.92, the overall branching fraction for the acid catalyzed isomerization is then predicted to be 0.26%. This value is an order of magnitude below that observed experimentally, which ranges from 3-6% depending on the starting *syn/anti* ratio and assuming equivalent photoionization cross sections for the products detected. The latter assumption carries with it considerable uncertainty, with factor of three sorts of deviations in photoionization cross sections amongst related species fairly typical. For example, a recent theoretical study of the photoionization cross sections for ten C1–C4 CIs are about 5 Mb, while those for the corresponding vinyl hydroperoxides (VHPs) are about 20 Mb.¹ If the

photoionization cross section for the daughter ions derived from the HPBF adduct was four times that for HPBD, then the present experimental measure of the branching ratio would be 0.8-1.5%, which would be in much better agreement with the theoretical prediction.

We explored the sensitivity of the acid catalysis branching to the uncertainties in various components of the theoretical predictions. The sensitivities reported here are for the experimentally studied condition of room temperature and a pressure of 10 Torr of He. For the most part, these sensitivities are not particularly dependent on conditions for P, T values near these. For simplicity, we report the sensitivities for only the *syn-trans* MVK-oxide reactant; those for the *syn-cis* are similar when considered as multiplicative factor changes. The most significant observation is that lowering the acid catalysis barriers (i.e., TS2 for *syn-trans* and *syn-cis*) by 0.6 kcal mol⁻¹, which is a reasonable estimate of the uncertainty in this parameter, increases the acid catalysis branching by a factor of 2.1. Similarly, lowering $\langle\Delta E_{\text{down}}\rangle$ by a factor of two, which roughly mimics the uncertainty in the pressure dependence, increases the branching ratio by a factor of 1.9. There is also considerable uncertainty arising from the use of 1D hindered rotors for the torsional modes of HBPF. However, the experimentally observed rate constant from Ref. 2 ($3.0 \pm 0.1 \times 10^{-10} \text{ cm}^3 \text{ molecule}^{-1} \text{ s}^{-1}$) constrains the extent of the deviations that one can consider for the stabilization rate. For example, the aforementioned decrease in $\langle\Delta E_{\text{down}}\rangle$ by a factor of two also decreases the predicted total reactive rate constant for the *syn-trans* conformer by a factor of 0.75 and for the *syn-cis* conformer by a factor of 0.53. The present total reactive rate constant for the equilibrium mixture of *syn-trans* and *syn-cis* at T = 300 K is $3.1 \times 10^{-10} \text{ cm}^3 \text{ molecule}^{-1} \text{ s}^{-1}$, which is essentially identical to the experimental value. Thus, this variation would slightly worsen the agreement for the total

rate constant. In contrast, the lowering of TS2 has essentially no effect on the estimated total rate constant. Notably, raising the barrier for formation of the HPBF adduct by 0.6 kcal mol⁻¹ has no effect on the branching. An error in the *cis-trans* conformer splitting could also affect the estimated branching ratio. Indeed, shifting the *syn-cis* conformer of MVK-oxide up by 0.5 kcal mol⁻¹ increases the predicted catalysis branching ratio for the *syn-cis* reactant by about a factor of 1.6. However, this increased branching ratio is ameliorated by a decreased probability for thermal population of the *syn-cis* conformer.

In summary, the branching to the acid catalysis channel is largely determined by the competition between passage over TS2 and stabilization of the HPBF chemical adduct. Our best theoretical estimate is that this branching is 0.3 %. The above sensitivity analysis suggests that there may be about a factor of four uncertainty in the estimate, with the measured total rate constant providing a strong constraint on the uncertainty in the stabilization rate.

It is perhaps worth emphasizing that the predicted branching fraction is a fairly strong function of temperature (Figure S11). The incipient MVK-oxide suffers numerous collisions with the bath gas prior to reaction, which should cool it to somewhere near room temperature. However, if it was not completely thermalized the observed branching would be significantly greater. For example, at a temperature of 350 K the *syn-trans* and *syn-cis* branching ratios are factors of 1.6 and 1.8 larger. Furthermore, at 350 K, the equilibrium ratio of *syn-cis/syn-trans* is larger (0.12 vs. 0.08), which yields an effective branching fraction of 0.42. Indeed, with a barrier lowering of 0.6 and a decrease in $\langle \Delta E_{\text{down}} \rangle$ by a factor of two, the predicted branching at 350 K is 1.7, which is within the error bars of the experimental estimate.

The present analysis presumes that the HPBF adduct is a stable product channel. If it were to dissociate on the time scale of the reaction, perhaps via a low

barrier process during the initial reaction, then this also would yield an increased value for the predicted catalytic channel branching. However, it seems unlikely that such low energy dissociation channels exist. In addition to these predictions for the reaction of normal FA (H₂-formic acid) with MVK-oxide conformers, we have also predicted the rate constants for fully deuterated FA (D₂-formic acid). Over the experimentally relevant range of conditions, for the *syn-cis* case, the branching ratio is predicted to be a factor of 2-3 lower, while for the *syn-trans* case, it is predicted to be a factor 3 to 4 lower. This smaller predicted branching for the deuterated case arises in part from a 0.4 kcal mol⁻¹ increase in the TS2 zero-point correct barriers relative to separated reactants. While the TS3 ZPE corrected point is shifted by an even larger 0.8 kcal mol⁻¹, this barrier plays little role in the HBPF adduct formation rate. Instead, it is largely determined by the stabilization rate, which is significantly increased by the increased rovibrational state densities for the heavier D atoms in deuterated FA.

In summary, although the present prediction for the branching to the catalysis channel is an order of magnitude below the experimentally estimated branching, the uncertainty in this prediction and in its correlation to the experiment is at least a factor of 5 to 10.

Section S3: H/D Exchange

As discussed in main text (Sec. IV), we found evidence of H/D exchange following introduction of D₂-formic acid into the flow cell (Figure S12-S15, Scheme S1, Table S7). Single energy measurements at 11.5 eV (without 248 nm photolysis, 6.4×10^{12} cm⁻³ formic acid) revealed that the D₂-formic acid underwent significant H/D exchange to form D₁-formic acid, yielding a ratio of 1.8:1 of D₂-formic acid (m/z 48) to D₁-formic acid (m/z

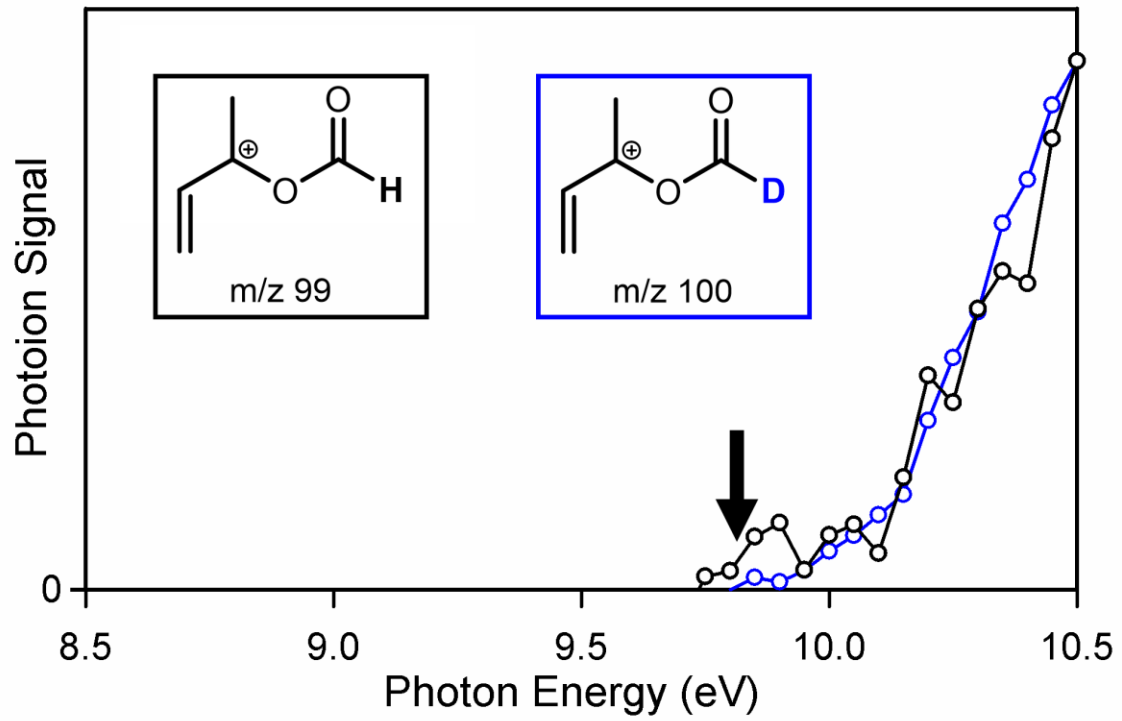


Figure S12. PIE curves of the -H/DO_2 daughter ions (m/z 99 and 100, respectively) from the photoionization of H/DPBF. The photoionization signal is integrated over the full kinetic time window (0-80 ms). The PIE curves are identical and the appearance energies agree well with the adiabatic ionization energy of 9.82 eV (black arrow) computed at the CCSD(T)-F12/CBS(TZ-F12,QZ-F12)//B2PLYP-D3/cc-pVTZ level of theory.²

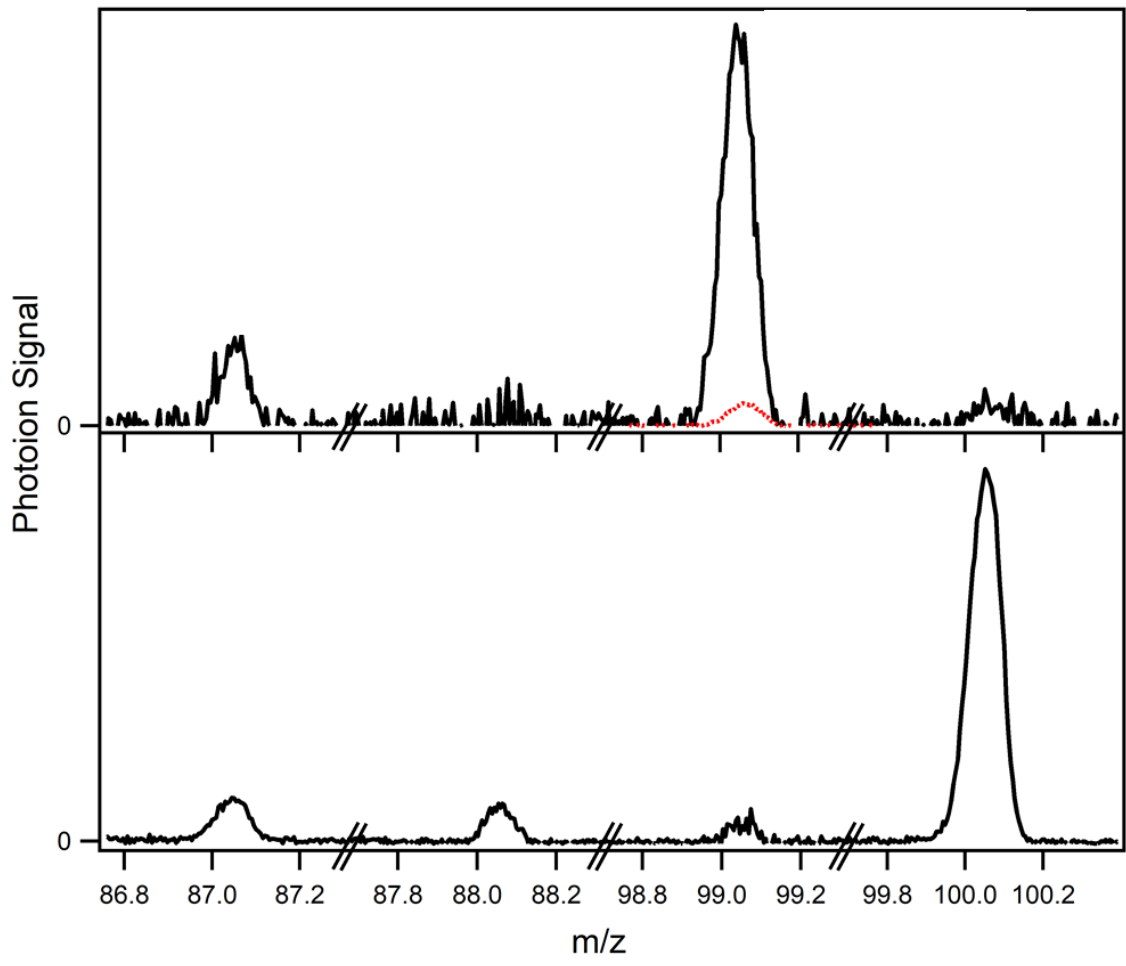


Figure S13. Comparison of relevant features in the mass spectrum obtained from the reaction of MVK-oxide with H₂-formic acid (top panel) and D₂/D₁-formic acid (bottom panel) using MPIMS (10.5 eV, 6.4 × 10¹² cm⁻³ formic acid). (Top panel) Data reproduced from Caravan et al., *Proc. Natl. Acad. Sci.*, 2020, **117**, 9733-9740 (Ref. 2). Mass channels m/z 87 and 99 appear upon introduction of formic acid and are attributed to –HCO₂ and –HO₂ daughter ions from the 1,4-insertion product, respectively.² The magnitude of the signal on the m/z 100 mass channel is consistent with the natural abundance of ¹³C associated with the m/z 99 signal (red dashed line). (Bottom panel) Partially deuterated analogs generated from the reaction of MVK-oxide with formic acid (D₂, D₁, and H₂-formic acid). The fractional contribution to each mass channel is shown in Table S7.

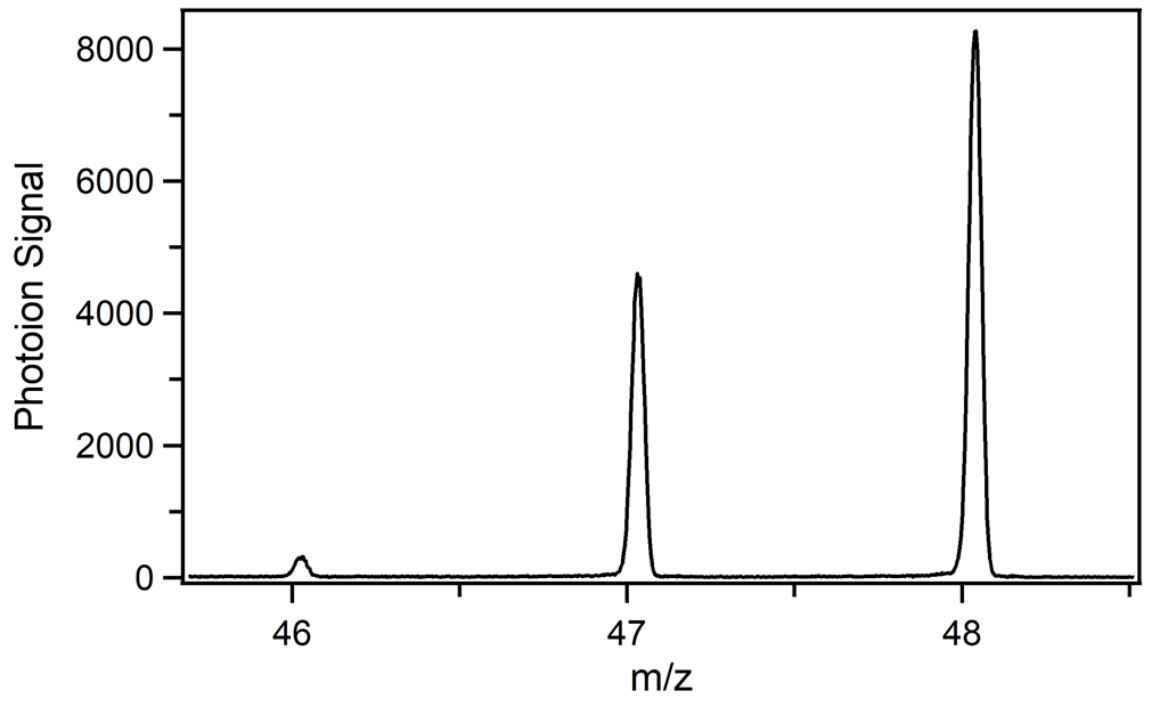


Figure S14. Photoionization signal of D₂-formic acid (m/z 48), D₁-formic acid (m/z47), and non-deuterated formic acid (m/z 46) obtained with a photoionization energy of 11.5 eV, $6.4 \times 10^{12} \text{ cm}^{-3}$ formic acid, and in the absence of 248 nm photolysis.

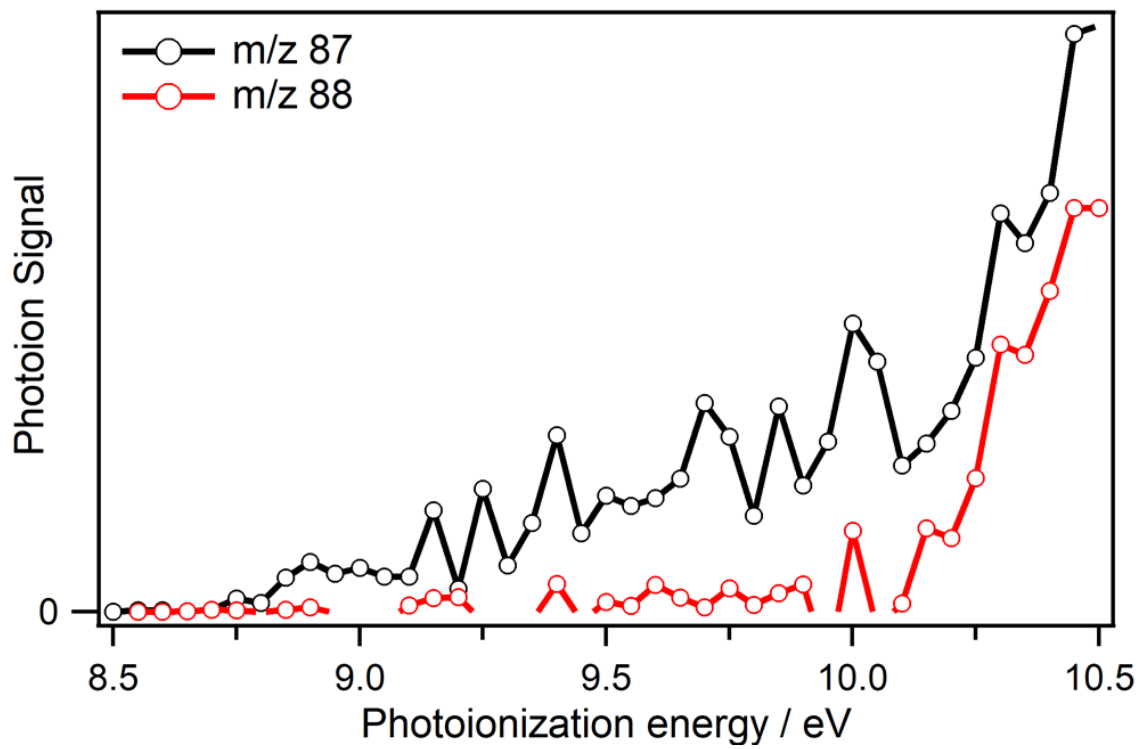
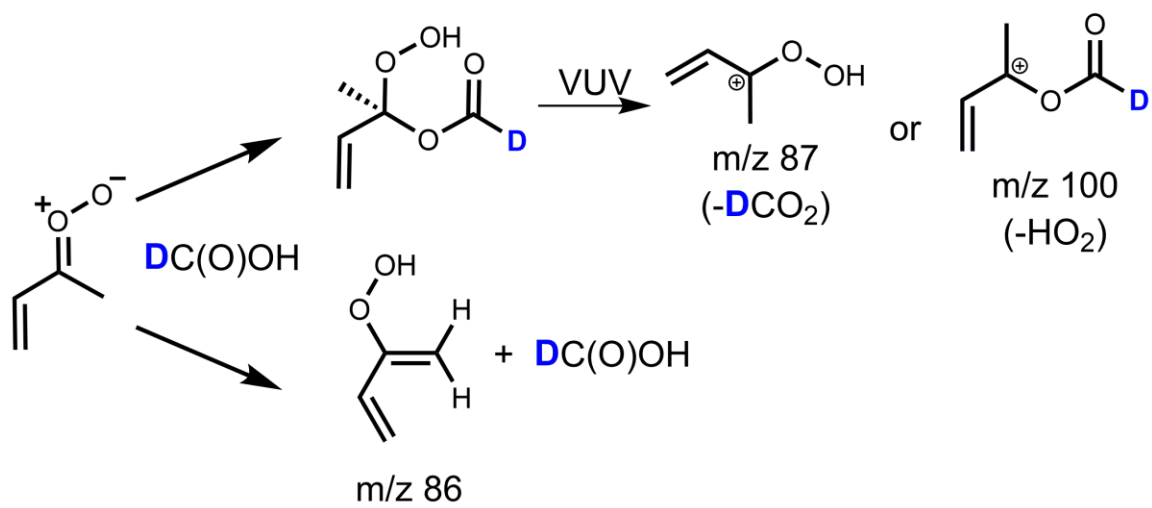


Figure S15. Photoionization efficiency curve of m/z 87 and 88 obtained by integration over the full kinetic time window (0-80 ms) in the reaction of MVK-oxide with D₂-formic acid ($6.4 \times 10^{12} \text{ cm}^{-3}$). The m/z 88 PIE curve matches the onset energy and shape of the higher energy component of m/z 87 and is scaled to represent the fraction of the daughter ion contributing to the m/z 87 signal at 10.5 eV (Table S7).

MVK-oxide + DC(O)OH



Scheme S1. Products for the reaction between *syn*-MVK-oxide and DC(O)OH (top) and HC(O)OD (bottom) and predicted m/z for the daughter ions formed from the respective adducts.

Table S7. Fractional contributions to the m/z 87, 88, 99, and 100 mass channels from the reaction of MVK-oxide with formic acid (D₂, D₁, and H₂-formic acid) using MPIMS (6.4 × 10¹² cm⁻³ formic acid). The isotope of formic acid that reacts with MVK-oxide to yield the corresponding species is given in parenthesis.

Species	Fractional Contribution (10.5 eV)	Fractional Contribution (8.5-9.8 eV)
m/z 87		
Adduct - DCO ₂ (D ₁ -formic acid)	0.00	0.69
DPBD (D ₂ -formic acid)	1.00	0.27
Adduct - HCO ₂ (H ₂ -formic acid)	0.00	0.04
m/z 88		
Adduct - DCO ₂ (D ₂ -formic acid)	0.00	0.97
C ¹³ Adduct - DCO ₂ (D ₁ -formic acid)	0.00	0.02
C ¹³ DPBD (D ₂ -formic acid)	1.00	0.01
C ¹³ Adduct - HCO ₂ (H ₂ -formic acid)	0.00	0.00
m/z 99		
Adduct - HO ₂ (H ₂ -formic acid)	0.00	1.00
m/z 100		
Adduct - DO ₂ (D ₂ -formic acid)	0.00	0.64
Adduct - HO ₂ (D ₁ -formic acid)	0.00	0.36
C ¹³ Adduct – HO ₂ (H ₂ -formic acid)	0.00	0.00

47) as shown in Figure S14. We find that H/D exchange occurs mostly at the OD group of D₂-formic acid, producing DC(O)OH, consistent with prior literature.⁸⁻¹⁴ Reaction will yield MVK-oxide + D₁-formic acid adducts, which will fragment upon photoionization to form m/z 87 (-DCO₂) and 100 (-HO₂) daughter ions (Scheme S1). The daughter ions (m/z 87) from photoionization of MVK-oxide + DC(O)OH adducts are similar to the daughter ions (m/z 88) from MVK-oxide + D₂-formic acid, the latter of which has a photoionization onset at ca. 10.3 eV (Figure S15).

A portion of the m/z 87 photoionization signal at 10.5 eV arises from daughter ions (-DCO₂) associated with the MVK-oxide + D₁-formic acid adduct. The magnitude of this signal is estimated from the m/z 88 daughter ions (-DCO₂) arising from the MVK-oxide + D₂-formic acid adduct by considering the 1.8:1 ratio of D₂- to D₁-formic acid. The remaining signal on m/z 87 at 10.5 eV is attributed to DPBD. DPBD arising from the D₂-formic acid-catalyzed reaction with MVK-oxide is clearly evident on m/z 86 at lower photoionization energies from 8.7 to 10.2 eV. In addition, MVK-oxide + D₁-formic acid will result in HPBD signal on m/z 86, which again is estimated by considering the 1.8:1 ratio of D₂- to D₁-formic acid.

We also considered whether formation of DPBD from isotopic exchange of HPBD with D₂-formic acid might occur, but concluded that this process is unlikely because HPBD formation from thermal unimolecular decay of *syn*-MVK-oxide is slow (33 s⁻¹, 298 K) compared to reaction with formic acid under the experimental conditions (ca. 1900 s⁻¹). Nevertheless, we considered the possibility that our photolytically generated *syn*-MVK-oxide might be sufficiently hot initially (prior to thermalization) to result in more rapid isomerization to HPBD. In this scenario, the initial reactant pool could contain some HPBD as well as MVK-oxide. For this reason, additional electronic structure calculations and master equation modeling were carried out to assess the isotopic

exchange rate of HPBD with D₂-formic acid to form DPBD. As shown in Figure S9, the barrier for isotopic exchange is significant (ca. 4.2 kcal mol⁻¹ relative to HPBD + FA for *syn-cis* HPBD) and the associated rate constants (1×10^{-16} , 2×10^{-17} , 1×10^{-16} , and 3×10^{-17} cm³ s⁻¹ for *syn-trans*, *syn-cis*, *anti-trans*, and *anti-cis* HPBD reacting with deuterated FA) indicate that isotopic exchange would be negligible on the timescale of the experiment (ca. $2\text{-}6 \times 10^{-4}$ s⁻¹).

Section S4. Stationary point geometries

Structure and Frequencies at the B2PLYPD3/cc-pVTZ level

Reactants

Formic Acid

Ground Conformer

1	8	0	-1.030691	-0.442769	0.000000
2	6	0	0.000000	0.421203	0.000000
3	1	0	-0.650948	-1.334313	0.000000
4	1	0	-0.381240	1.445918	0.000000
5	8	0	1.159715	0.112917	0.000000
Frequencies --	629.6563		686.8589		1062.1848
Frequencies --	1129.9053		1313.9525		1413.8309
Frequencies --	1813.0629		3087.3525		3744.3339

Excited Conformer

1	8	0	1.057366	-0.280350	0.000007
2	6	0	-0.132069	0.361181	-0.000016
3	1	0	1.768925	0.369415	-0.000024
4	1	0	-0.036282	1.457149	0.000043
5	8	0	-1.174895	-0.218856	0.000003
Frequencies --	529.8905		661.3040		1042.0529
Frequencies --	1118.2063		1283.0471		1428.5019
Frequencies --	1857.3853		2996.2484		3813.7007

MVK-oxide

syn-trans-MVK-oxide

1	6	0	-0.281002	-2.428825	0.000000
2	6	0	0.489860	-1.332579	0.000000
3	6	0	0.000000	0.017627	0.000000
4	6	0	-1.397431	0.477385	0.000000
5	8	0	0.934365	0.910720	0.000000
6	8	0	0.561182	2.203583	0.000000
7	1	0	-1.359012	-2.376515	0.000000
8	1	0	0.163693	-3.411629	0.000000

9	1	0	1.567972	-1.424436	0.000000
10	1	0	-2.098829	-0.348501	0.000000
11	1	0	-1.553379	1.122502	0.866535
12	1	0	-1.553379	1.122502	-0.866535
Frequencies --	119.9147		198.1647		256.1167
Frequencies --	283.2193		331.6966		459.4209
Frequencies --	496.8539		609.8350		682.4911
Frequencies --	814.7146		950.8478		998.3597
Frequencies --	1026.7698		1041.7510		1047.8678
Frequencies --	1076.4570		1292.3767		1337.6406
Frequencies --	1400.1620		1449.9665		1453.0141
Frequencies --	1472.8403		1504.9644		1662.0030
Frequencies --	3052.6351		3097.5438		3178.5451
Frequencies --	3186.9118		3194.4379		3270.2727

syn-cis-MVK-oxide

1	6	0	-2.181296	-0.839531	0.000000
2	6	0	-1.445765	0.279851	0.000000
3	6	0	0.000000	0.334288	0.000000
4	6	0	0.795556	1.572979	0.000000
5	8	0	0.625731	-0.789133	0.000000
6	8	0	1.976736	-0.749625	0.000000
7	1	0	-1.722960	-1.817168	0.000000
8	1	0	-3.258737	-0.787750	0.000000
9	1	0	-1.934488	1.244081	0.000000
10	1	0	0.161642	2.453346	0.000000
11	1	0	1.461921	1.566019	0.865256
12	1	0	1.461921	1.566019	-0.865256
Frequencies --	66.4658		206.2188		228.8220
Frequencies --	275.2111		327.6923		442.9534
Frequencies --	485.9721		623.2547		665.9256
Frequencies --	815.8805		971.1810		992.1262
Frequencies --	1024.2898		1041.0284		1044.4521
Frequencies --	1108.3087		1286.3487		1340.7090
Frequencies --	1397.3938		1418.9712		1451.4392
Frequencies --	1475.0005		1500.5024		1669.4449
Frequencies --	3044.5296		3088.3513		3171.9026
Frequencies --	3177.8055		3200.0465		3272.9201

anti-trans-MVK-oxide

1	6	0	-1.894146	-1.185090	0.000000
2	6	0	-0.571837	-0.965527	0.000000
3	6	0	0.000000	0.349961	0.000000
4	6	0	-0.769734	1.622704	0.000000
5	8	0	1.282506	0.506388	0.000000
6	8	0	2.101575	-0.560185	0.000000
7	1	0	-2.612894	-0.378124	0.000000
8	1	0	-2.286939	-2.190359	0.000000
9	1	0	0.144815	-1.772424	0.000000

10	1	0	-0.083752	2.464487	0.000000
11	1	0	-1.409789	1.687253	0.880050
12	1	0	-1.409789	1.687253	-0.880050
Frequencies --	113.8309		150.9705		244.3138
Frequencies --	280.5671		326.0586		377.0466
Frequencies --	479.0748		640.2948		718.3130
Frequencies --	798.5875		977.2758		985.0386
Frequencies --	1021.2924		1049.6643		1057.6112
Frequencies --	1065.0237		1281.3674		1373.2418
Frequencies --	1391.3621		1436.2627		1469.0936
Frequencies --	1486.0836		1512.5356		1657.6094
Frequencies --	3054.8184		3111.1078		3162.1730
Frequencies --	3170.5660		3228.1091		3261.6980

anti-cis-MVK-oxide

1	6	0	-1.352990	-1.521124	0.000000
2	6	0	-1.214381	-0.180848	0.000000
3	6	0	0.000000	0.576665	0.000000
4	6	0	-0.021963	2.069054	0.000000
5	8	0	1.191358	0.084982	0.000000
6	8	0	1.382201	-1.251687	0.000000
7	1	0	-0.494812	-2.166647	0.000000
8	1	0	-2.348757	-1.942692	0.000000
9	1	0	-2.104292	0.435798	0.000000
10	1	0	0.990778	2.459965	0.000000
11	1	0	-0.547687	2.442365	0.879064
12	1	0	-0.547687	2.442365	-0.879064
Frequencies --	116.7361		165.5085		285.0024
Frequencies --	305.2060		339.0183		368.0726
Frequencies --	411.2073		640.2272		717.5908
Frequencies --	823.6757		990.3387		1004.8285
Frequencies --	1029.1718		1053.3593		1054.9509
Frequencies --	1099.6379		1269.7395		1340.3444
Frequencies --	1418.9240		1438.3092		1463.9237
Frequencies --	1487.0283		1508.1717		1640.9833
Frequencies --	3054.6683		3110.9627		3165.1107
Frequencies --	3167.2660		3181.8932		3314.1293

van der Waals

Pre-reactive Complex (PRC)

syn-trans-MVK-oxide...FA

1	6	0	0.000000	0.000000	0.000000
2	8	0	0.000000	0.000000	1.275955
3	8	0	1.245775	0.000000	1.892005
4	8	0	0.606398	-2.800437	0.381749
5	6	0	1.017466	-3.231013	1.441733
6	8	0	1.418780	-2.525602	2.475900
7	1	0	1.096188	-4.304566	1.647652

8	1	0	1.354816	-1.531258	2.273211
9	6	0	1.271230	0.075133	-0.735745
10	6	0	-1.329184	-0.043379	-0.564140
11	6	0	-1.585380	-0.054876	-1.875686
12	1	0	1.115967	0.238392	-1.795234
13	1	0	1.804535	-0.859772	-0.570167
14	1	0	1.877193	0.865388	-0.294599
15	1	0	-2.132100	-0.086121	0.158207
16	1	0	-0.802662	-0.028630	-2.617617
17	1	0	-2.601700	-0.103459	-2.234886
Frequencies --	46.8365		56.9407		93.3520
Frequencies --	126.3653		148.3550		156.9454
Frequencies --	221.9254		247.4525		269.3290
Frequencies --	338.2014		358.9841		455.7681
Frequencies --	493.3374		597.9164		688.1404
Frequencies --	708.0896		808.8531		926.4019
Frequencies --	991.7365		1019.5153		1028.1072
Frequencies --	1041.7520		1047.0099		1071.0999
Frequencies --	1116.5869		1260.2678		1313.3572
Frequencies --	1342.3675		1392.1696		1408.1414
Frequencies --	1457.3675		1471.1291		1492.7186
Frequencies --	1502.5265		1519.0126		1678.8845
Frequencies --	1747.2199		2799.5379		3051.0151
Frequencies --	3073.7270		3135.1225		3183.0650
Frequencies --	3193.5201		3207.7761		3275.1933

syn-cis-MVK-oxide...FA

1	6	0	1.132193	0.487665	0.158859
2	8	0	0.487589	0.599430	-0.930436
3	8	0	-0.565686	1.519350	-0.926426
4	8	0	-1.133433	-1.064330	0.956327
5	6	0	-2.204612	-0.979901	0.386149
6	8	0	-2.542801	-0.097738	-0.526240
7	1	0	-3.031630	-1.669855	0.589658
8	1	0	-1.771294	0.547472	-0.701533
9	6	0	0.841254	1.378681	1.293104
10	6	0	2.172951	-0.525711	0.186349
11	6	0	2.254705	-1.523727	-0.697945
12	1	0	1.599302	1.287444	2.063809
13	1	0	-0.134383	1.101857	1.691311
14	1	0	0.749633	2.400404	0.926418
15	1	0	2.872152	-0.453729	1.006188
16	1	0	1.532375	-1.628481	-1.493344
17	1	0	3.039543	-2.260842	-0.627391
Frequencies --	35.9783		50.7715		78.9710
Frequencies --	116.7747		153.3154		153.8978
Frequencies --	211.7184		245.5213		248.6897
Frequencies --	328.7333		358.1968		438.8406
Frequencies --	491.6183		609.4323		663.3595

Frequencies --	711.2670	806.6051	918.5517
Frequencies --	1010.0395	1016.2609	1037.2922
Frequencies --	1038.6597	1049.7664	1105.8282
Frequencies --	1125.9262	1265.2711	1281.1358
Frequencies --	1343.0359	1390.0446	1408.5084
Frequencies --	1455.4723	1457.6423	1500.0159
Frequencies --	1503.4379	1526.5403	1682.5908
Frequencies --	1743.2214	2726.6027	3049.1261
Frequencies --	3066.8455	3130.2559	3177.4779
Frequencies --	3180.3431	3213.5756	3276.5370

anti-trans-MVK-oxide...FA

1	6	0	-1.022369	0.452648	0.256137
2	8	0	-0.201217	1.417145	0.383966
3	8	0	0.623181	1.716719	-0.712649
4	8	0	0.954579	-1.265658	0.680425
5	6	0	2.083787	-1.045449	0.277626
6	8	0	2.502603	0.019599	-0.357573
7	1	0	2.897372	-1.765381	0.420660
8	1	0	1.746193	0.709203	-0.490734
9	6	0	-1.757051	0.111386	1.500844
10	6	0	-1.245512	-0.177821	-1.022322
11	6	0	-2.106148	-1.188613	-1.175042
12	1	0	-1.486192	-0.902416	1.791548
13	1	0	-2.832570	0.157903	1.342765
14	1	0	-1.471195	0.794945	2.293514
15	1	0	-0.680581	0.233483	-1.842294
16	1	0	-2.651151	-1.614467	-0.345551
17	1	0	-2.271295	-1.628631	-2.146727

Frequencies --	38.2490	81.2065	90.2153
Frequencies --	114.6818	143.0581	172.2867
Frequencies --	236.4631	263.1843	267.8510
Frequencies --	334.8430	361.0513	397.7478
Frequencies --	478.6417	617.2783	714.8686
Frequencies --	728.4973	786.2993	905.4232
Frequencies --	1000.8521	1009.3523	1045.0559
Frequencies --	1052.4088	1056.9474	1073.2713
Frequencies --	1134.4290	1279.6998	1291.1061
Frequencies --	1367.3684	1407.5916	1428.1451
Frequencies --	1451.6054	1471.6484	1488.8877
Frequencies --	1541.3926	1546.9739	1676.2008
Frequencies --	1723.1635	2533.3470	3052.0352
Frequencies --	3072.3139	3142.5181	3175.9221
Frequencies --	3176.7554	3246.6418	3268.6392

anti-cis-MVK-oxide...FA

1	6	0	-1.204491	-0.289284	0.179447
2	8	0	-0.636027	-0.003481	1.281377
3	8	0	0.114207	1.173135	1.362642

4	8	0	1.132216	-1.243681	-0.736726
5	6	0	2.170139	-0.653559	-0.502650
6	8	0	2.330754	0.391270	0.275683
7	1	0	3.124247	-0.957045	-0.947481
8	1	0	1.453547	0.682670	0.711459
9	6	0	-1.864028	-1.622886	0.181619
10	6	0	-1.301847	0.547844	-0.990871
11	6	0	-0.919455	1.827305	-1.122501
12	1	0	-1.365943	-2.244171	-0.562172
13	1	0	-2.913278	-1.528862	-0.094753
14	1	0	-1.776075	-2.090435	1.156419
15	1	0	-1.783638	0.053676	-1.823398
16	1	0	-0.433607	2.350864	-0.319851
17	1	0	-1.116355	2.338842	-2.054295
Frequencies --	39.8470		85.7734		91.7024
Frequencies --	130.0329		140.2337		166.4205
Frequencies --	233.1651		254.0281		308.4005
Frequencies --	335.8177		350.7360		393.5006
Frequencies --	415.9963		627.4836		709.1692
Frequencies --	722.9086		807.4474		928.5132
Frequencies --	1024.9488		1028.6116		1030.0566
Frequencies --	1041.7744		1056.0029		1107.6739
Frequencies --	1111.9206		1266.5495		1269.9390
Frequencies --	1350.0981		1407.6782		1411.3172
Frequencies --	1463.0391		1472.7066		1486.6933
Frequencies --	1519.7626		1553.1145		1661.2570
Frequencies --	1734.9712		2704.5444		3054.8259
Frequencies --	3065.4124		3132.2939		3174.3881
Frequencies --	3178.4393		3195.5629		3310.1617

HPBD...FA Intermediate

syn-trans-HPBD...FA

1	6	0	-1.113347	0.483162	0.213380
2	6	0	-0.789321	0.219768	1.488724
3	6	0	-2.193604	-0.151394	-0.555793
4	6	0	-2.613372	-1.401824	-0.375908
5	8	0	-0.484608	1.381974	-0.596283
6	8	0	0.546691	2.099813	0.108319
7	1	0	0.646454	-1.043147	0.585778
8	1	0	-1.403495	-0.465438	2.048304
9	1	0	-0.011072	0.766084	1.991856
10	1	0	-2.634630	0.469306	-1.324331
11	1	0	-2.158531	-2.056579	0.353460
12	1	0	-3.425728	-1.802047	-0.962893
13	1	0	1.311624	1.519682	-0.092344
14	8	0	2.444316	0.160210	-0.423857
15	6	0	2.347215	-1.037303	-0.272221
16	8	0	1.334997	-1.682182	0.287448

17	1	0	3.118786	-1.740831	-0.593940
Frequencies --	46.5745		50.6495		76.8325
Frequencies --	101.0929		156.5767		166.8105
Frequencies --	191.9483		245.8305		252.7712
Frequencies --	358.4808		417.7017		516.8706
Frequencies --	590.4674		646.1497		674.9499
Frequencies --	751.6216		759.5421		797.7795
Frequencies --	861.0808		877.9018		930.4440
Frequencies --	970.8882		992.6994		1027.8803
Frequencies --	1076.1521		1089.2622		1200.4982
Frequencies --	1259.7690		1333.5512		1372.7183
Frequencies --	1420.5872		1430.2878		1471.8952
Frequencies --	1513.4595		1671.1401		1696.0523
Frequencies --	1769.4375		3094.2923		3169.3976
Frequencies --	3192.7316		3203.4099		3260.2551
Frequencies --	3303.4610		3391.3563		3517.8522

syn-cis-HPBD...FA

1	6	0	-1.106616	0.139014	0.525862
2	6	0	-0.549047	0.062319	1.747273
3	6	0	-2.115450	-0.806775	0.048019
4	6	0	-2.689988	-0.766416	-1.154468
5	8	0	-0.799963	1.062956	-0.423771
6	8	0	0.170524	2.012240	0.057824
7	1	0	0.983742	-0.980473	0.681893
8	1	0	-0.891338	-0.707007	2.420023
9	1	0	0.146686	0.802891	2.099755
10	1	0	-2.385068	-1.574248	0.760209
11	1	0	-2.436860	-0.006443	-1.877268
12	1	0	-3.432687	-1.498360	-1.432634
13	1	0	0.991865	1.571558	-0.248272
14	8	0	2.314600	0.447523	-0.697342
15	6	0	2.500861	-0.721527	-0.441810
16	8	0	1.744163	-1.492893	0.323271
17	1	0	3.350501	-1.286216	-0.832811
Frequencies --	39.4279		49.1022		87.3141
Frequencies --	117.3395		160.4916		169.4570
Frequencies --	190.3720		235.0266		253.7995
Frequencies --	367.4218		471.6775		489.3651
Frequencies --	583.9892		648.6302		675.2249
Frequencies --	753.7946		774.0511		796.6665
Frequencies --	854.5213		872.2213		933.9484
Frequencies --	971.2825		996.8084		1022.9112
Frequencies --	1073.6384		1076.7413		1199.9679
Frequencies --	1327.2299		1337.7576		1369.1387
Frequencies --	1415.2292		1429.8431		1466.5098
Frequencies --	1516.2999		1636.3173		1705.7378
Frequencies --	1769.6104		3095.2739		3178.1779
Frequencies --	3196.2712		3200.8333		3271.8125

Frequencies -- 3302.4741 3411.2610 3512.8846

anti-trans-HPBD...FA

1	6	0	1.464908	-1.575683	-1.295623
2	6	0	1.707972	-0.384726	-0.750680
3	6	0	1.180891	0.032789	0.552291
4	6	0	0.988640	-0.769230	1.613557
5	8	0	-2.015175	0.831474	-0.492652
6	6	0	-2.469138	-0.259613	-0.234985
7	8	0	-1.858108	-1.232043	0.427411
8	8	0	0.933520	1.365220	0.736973
9	8	0	0.520379	1.973970	-0.514909
10	1	0	0.811225	-2.294492	-0.821601
11	1	0	1.906944	-1.855507	-2.239649
12	1	0	2.310763	0.346386	-1.268938
13	1	0	-0.955730	-0.948436	0.697641
14	1	0	1.352037	-1.783129	1.596644
15	1	0	0.584150	-0.369503	2.531077
16	1	0	-3.473313	-0.573346	-0.530749
17	1	0	-0.420645	1.707839	-0.526373

Frequencies --	41.0731	47.3932	94.9233
Frequencies --	127.0441	132.0509	172.8078
Frequencies --	175.5243	231.9939	269.1057
Frequencies --	318.6582	429.3863	524.8193
Frequencies --	574.5071	641.0168	662.1786
Frequencies --	737.6015	761.6599	822.5788
Frequencies --	832.9682	869.8769	913.3878
Frequencies --	969.1926	996.9055	1023.4182
Frequencies --	1076.1336	1091.9785	1190.4044
Frequencies --	1273.1133	1338.1650	1359.5755
Frequencies --	1418.3968	1428.0048	1471.9323
Frequencies --	1488.4244	1656.6350	1689.1365
Frequencies --	1774.2204	3091.9155	3165.6439
Frequencies --	3182.6729	3211.9066	3257.3763
Frequencies --	3284.2094	3432.1712	3569.8252

anti-cis-HPBD...FA

1	6	0	-1.053097	0.579828	0.464112
2	6	0	-0.475277	1.686648	0.963243
3	6	0	-1.953259	0.597989	-0.686000
4	6	0	-2.731588	-0.411313	-1.076458
5	8	0	-0.862414	-0.576964	1.179410
6	8	0	-0.485639	-1.662524	0.278729
7	1	0	-0.710618	2.656716	0.553938
8	1	0	1.242860	1.080634	-0.242961
9	1	0	0.147198	1.626993	1.842870
10	1	0	-1.987892	1.542785	-1.212807
11	1	0	-2.712735	-1.365982	-0.576934
12	1	0	-3.401260	-0.291060	-1.914662

13	1	0	0.485432	-1.552191	0.293355
14	8	0	2.227211	-1.067926	0.051458
15	6	0	2.719688	-0.095524	-0.472455
16	8	0	2.141515	1.087403	-0.636608
17	1	0	3.732841	-0.083565	-0.881366
Frequencies --	31.6378		35.8582		86.1594
Frequencies --	119.3072		135.7814		155.3607
Frequencies --	183.2784		218.9154		256.9134
Frequencies --	324.1310		419.4058		486.3974
Frequencies --	608.7873		634.7813		663.6092
Frequencies --	745.8742		764.5178		797.2146
Frequencies --	832.9567		886.4097		907.7395
Frequencies --	976.2320		987.8707		1022.8438
Frequencies --	1067.6367		1074.6317		1186.9295
Frequencies --	1328.7805		1335.9665		1357.7756
Frequencies --	1408.3983		1426.2500		1470.1134
Frequencies --	1484.9619		1632.0100		1702.8002
Frequencies --	1773.9460		3094.7773		3174.9689
Frequencies --	3178.2508		3188.6921		3275.6266
Frequencies --	3280.1709		3484.7147		3573.1287

OBD...OH...FA

1	6	0	1.508587	0.555215	-0.066165
2	6	0	2.214454	1.810886	-0.034072
3	6	0	2.243686	-0.731428	-0.018802
4	6	0	3.562627	-0.864269	0.110448
5	8	0	0.274484	0.558028	-0.137362
6	8	0	-0.758179	-1.645734	-0.075226
7	1	0	3.288084	1.879116	0.016630
8	1	0	1.627344	2.714077	-0.068161
9	1	0	1.597672	-1.595251	-0.092381
10	1	0	4.230740	-0.019711	0.192434
11	1	0	4.017632	-1.843097	0.142282
12	1	0	-1.230944	-1.158684	-0.783184
13	8	0	-2.799890	0.040203	-1.065746
14	6	0	-3.087446	0.444051	0.039852
15	8	0	-2.528648	0.064064	1.180526
16	1	0	-3.869483	1.186686	0.221336
17	1	0	-1.814631	-0.582354	0.965942
Frequencies --	12.8365		37.7491		41.6075
Frequencies --	64.7754		83.9403		89.2718
Frequencies --	129.2158		191.7825		203.1544
Frequencies --	221.7980		312.3144		331.9120
Frequencies --	444.5577		491.8802		539.2342
Frequencies --	556.5038		680.2494		701.6017
Frequencies --	732.4066		808.4855		828.7349
Frequencies --	878.3105		989.1015		995.1214
Frequencies --	1062.7285		1072.9715		1075.1237
Frequencies --	1217.4119		1319.9187		1323.9939

Frequencies --	1398.0611	1459.9535	1462.9129
Frequencies --	1490.7518	1629.4834	1732.0362
Frequencies --	1771.4272	3078.4852	3172.4788
Frequencies --	3190.6529	3206.5243	3257.8809
Frequencies --	3307.0517	3387.8060	3580.6863

Dioxole...FA

1	6	0	-2.736056	-1.111334	-0.716698
2	6	0	-1.731340	-0.128679	-0.237518
3	6	0	-1.252097	0.998767	-0.747768
4	6	0	-0.300557	1.594592	0.239170
5	8	0	-1.208145	-0.447460	0.991977
6	8	0	-0.112336	0.523859	1.202890
7	1	0	-3.553392	-1.197970	-0.001902
8	1	0	-3.136870	-0.789957	-1.673244
9	1	0	-2.284019	-2.095474	-0.829874
10	1	0	-1.526889	1.436101	-1.689435
11	1	0	-0.707061	2.468355	0.755816
12	1	0	0.687091	1.808274	-0.165842
13	1	0	1.242126	-0.547486	0.780361
14	8	0	1.956835	-1.169320	0.507202
15	6	0	2.714270	-0.580174	-0.412334
16	8	0	2.563341	0.534591	-0.851439
17	1	0	3.516124	-1.254229	-0.730027

Frequencies --	27.0442	32.2631	86.4180
Frequencies --	124.7751	157.0360	165.9333
Frequencies --	194.0732	240.7651	254.0830
Frequencies --	329.7220	555.3170	622.2615
Frequencies --	680.6148	722.0972	746.4992
Frequencies --	828.9997	912.7445	916.6697
Frequencies --	954.9729	1016.8334	1034.6405
Frequencies --	1066.2811	1076.0187	1079.9911
Frequencies --	1201.6205	1210.1360	1216.8408
Frequencies --	1290.7510	1379.5502	1388.1202
Frequencies --	1425.7684	1440.5033	1485.8000
Frequencies --	1502.6756	1526.9130	1743.0102
Frequencies --	1783.6200	3022.8944	3064.8210
Frequencies --	3067.2565	3114.1484	3126.3679
Frequencies --	3163.3924	3285.0520	3400.6808

Saddle Points

MVK-oxide *cis/trans* interconversion

syn-trans-MVK-oxide = *syn-cis*-MVK-oxide

1	6	0	2.327858	-0.267919	0.425627
2	6	0	1.381300	-0.133215	-0.497496
3	6	0	-0.027092	0.153355	-0.167281
4	6	0	-0.602629	1.490867	0.045170

5	8	0	-0.796694	-0.864200	-0.093452
6	8	0	-2.103652	-0.635657	0.189406
7	1	0	2.105556	-0.189953	1.480296
8	1	0	3.351766	-0.466552	0.146356
9	1	0	1.626162	-0.217122	-1.550508
10	1	0	-1.070284	1.516480	1.033036
11	1	0	-1.432790	1.629417	-0.652467
12	1	0	0.145734	2.268058	-0.060451
Frequencies --			-155.8236	160.3454	206.9403
Frequencies --			272.9053	318.6863	393.4493
Frequencies --			519.1815	618.1650	677.8188
Frequencies --			801.6223	973.9469	989.5462
Frequencies --			996.7350	1008.2812	1048.2105
Frequencies --			1090.0645	1299.6607	1324.2466
Frequencies --			1397.9023	1440.7421	1448.6849
Frequencies --			1456.7181	1494.5998	1693.0250
Frequencies --			3035.8504	3076.2762	3155.4400
Frequencies --			3168.9422	3179.8447	3258.5054

anti-trans-MVK-oxide = *anti-cis*-MVK-oxide

1	6	0	2.007829	-0.418699	-0.342971
2	6	0	0.984974	-0.461235	0.502459
3	6	0	-0.412755	-0.301218	0.080860
4	6	0	-1.331026	-1.454707	-0.099639
5	8	0	-0.925829	0.850993	-0.119854
6	8	0	-0.181649	1.963910	0.046691
7	1	0	1.863784	-0.218324	-1.394427
8	1	0	3.019565	-0.567451	0.002037
9	1	0	1.146198	-0.648731	1.558247
10	1	0	-2.328717	-1.110049	-0.356799
11	1	0	-1.377214	-2.045749	0.816530
12	1	0	-0.957925	-2.113760	-0.884538
Frequencies --			-172.4811	152.1270	208.0108
Frequencies --			231.6809	294.2586	330.2831
Frequencies --			521.8294	599.3025	696.2792
Frequencies --			802.6304	974.6524	982.0157
Frequencies --			993.4085	1013.3162	1031.6387
Frequencies --			1096.0715	1286.3799	1328.8923
Frequencies --			1414.9866	1434.1413	1473.1757
Frequencies --			1478.4513	1514.3980	1695.7927
Frequencies --			3046.9529	3100.6707	3156.9139
Frequencies --			3158.0516	3173.6061	3263.0241

MVK-oxide pre-reactive complex (PRC) *cis/trans* interconversion

syn-trans-MVK-oxide...FA = *syn-cis*-MVK-oxide...FA

1	6	0	-1.119161	-0.567213	0.048738
2	8	0	-0.340125	-0.999219	-0.847648
3	8	0	0.732073	-1.787407	-0.402364
4	8	0	0.949819	1.349499	0.510030

5	6	0	2.092030	1.138745	0.139620
6	8	0	2.566442	0.018246	-0.343349
7	1	0	2.867219	1.911785	0.180266
8	1	0	1.842763	-0.707639	-0.374539
9	6	0	-0.955142	-0.962295	1.456667
10	6	0	-2.210670	0.296792	-0.440682
11	6	0	-2.144870	1.621913	-0.367033
12	1	0	-1.845801	-0.725090	2.027776
13	1	0	-0.101418	-0.409203	1.851236
14	1	0	-0.692656	-2.018225	1.500223
15	1	0	-3.074078	-0.211703	-0.852441
16	1	0	-1.271235	2.114572	0.033441
17	1	0	-2.963582	2.228894	-0.723171
Frequencies --			-133.9452	58.2378	92.9406
Frequencies --			109.2354	123.4468	148.0852
Frequencies --			204.5360	247.3918	273.2048
Frequencies --			294.6929	339.5556	413.9882
Frequencies --			528.7150	607.7970	665.6096
Frequencies --			715.9043	798.3492	900.5086
Frequencies --			981.4570	1002.2993	1020.6978
Frequencies --			1046.3892	1053.4022	1105.8825
Frequencies --			1137.3757	1278.5620	1288.8692
Frequencies --			1325.8681	1380.8629	1411.1151
Frequencies --			1454.6381	1461.8802	1488.9666
Frequencies --			1512.6641	1543.5190	1687.4723
Frequencies --			1730.9835	2655.8785	3055.7842
Frequencies --			3062.5950	3125.5221	3167.5236
Frequencies --			3177.5878	3183.7870	3271.3087

anti-trans-MVK-oxide...FA = *anti-cis*-MVK-oxide...FA

1	6	0	-0.961063	0.388212	-0.330351
2	8	0	-0.359437	-0.199773	-1.269270
3	8	0	0.168229	-1.474750	-0.977504
4	8	0	1.312296	1.067136	0.746164
5	6	0	2.320541	0.396185	0.579893
6	8	0	2.415939	-0.738572	-0.056045
7	1	0	3.289796	0.715424	0.978062
8	1	0	1.498492	-1.051269	-0.435681
9	6	0	-1.401006	1.773659	-0.614996
10	6	0	-1.293572	-0.273518	0.942193
11	6	0	-2.376881	-1.030025	1.069193
12	1	0	-0.962181	2.422862	0.141944
13	1	0	-2.485010	1.838818	-0.524306
14	1	0	-1.078866	2.088497	-1.602519
15	1	0	-0.631902	-0.054704	1.766592
16	1	0	-3.026324	-1.246007	0.233210
17	1	0	-2.628348	-1.473023	2.020349
Frequencies --			-146.5178	54.4412	85.9999
Frequencies --			120.8789	154.5564	176.7642

Frequencies --	213.1547	245.6434	253.3806
Frequencies --	287.0740	331.8027	375.1406
Frequencies --	525.0896	599.9257	688.7097
Frequencies --	730.7215	793.4260	892.4437
Frequencies --	974.4115	1001.4054	1013.3538
Frequencies --	1036.1963	1058.9710	1103.9822
Frequencies --	1158.3710	1273.7360	1294.9430
Frequencies --	1320.1855	1405.7011	1410.4784
Frequencies --	1455.9622	1472.5534	1478.7020
Frequencies --	1553.3314	1579.7157	1691.1137
Frequencies --	1708.9486	2400.4030	3056.2864
Frequencies --	3063.3660	3131.2883	3171.3402
Frequencies --	3174.3852	3220.6571	3263.7551

MVK-oxide 1,4 H-atom transfer (TS1)

syn-trans-MVK-oxide = *syn-trans*-HPBD

1	6	0	2.457115	0.070170	0.032784
2	6	0	1.316473	-0.618112	-0.055817
3	6	0	0.010731	-0.001078	0.060352
4	6	0	-0.383451	1.346869	-0.052273
5	8	0	-0.977463	-0.869354	0.073675
6	8	0	-2.202077	-0.190060	-0.031532
7	1	0	2.460619	1.133723	0.220400
8	1	0	3.411786	-0.420028	-0.080885
9	1	0	1.320065	-1.687395	-0.219937
10	1	0	-1.560158	0.884857	-0.502121
11	1	0	-0.952622	1.745026	0.784583
12	1	0	0.351428	2.032029	-0.449460
Frequencies --	-1629.7695	122.2150	243.4351		
Frequencies --	276.3347	470.4620	494.5344		
Frequencies --	546.3726	635.4669	737.6518		
Frequencies --	757.6567	904.9782	937.8313		
Frequencies --	962.2955	990.4016	1027.7607		
Frequencies --	1037.2315	1067.7425	1293.7400		
Frequencies --	1346.8057	1351.3202	1466.9007		
Frequencies --	1477.4722	1548.1219	1682.1434		
Frequencies --	1839.3159	3110.2935	3174.6357		
Frequencies --	3196.1290	3217.2816	3267.8889		

syn-cis-MVK-oxide = *syn-cis*-HPBD

1	6	0	2.297324	-0.481816	0.019876
2	6	0	1.411571	0.515143	-0.053642
3	6	0	-0.026106	0.342616	0.063494
4	6	0	-1.022147	1.338205	0.014306
5	8	0	-0.472178	-0.889564	0.025294
6	8	0	-1.877499	-0.876092	-0.057740
7	1	0	1.982914	-1.505554	0.158002
8	1	0	3.356161	-0.285350	-0.047200
9	1	0	1.739610	1.538093	-0.170472

10	1	0	-1.833037	0.412863	-0.487093
11	1	0	-1.712231	1.363363	0.854875
12	1	0	-0.699849	2.316944	-0.312739
Frequencies --			-1621.2741	81.9648	229.5546
Frequencies --			266.0867	476.5977	496.4703
Frequencies --			537.9626	646.5707	725.1641
Frequencies --			751.7414	903.9521	944.4949
Frequencies --			956.8335	989.7721	1025.4711
Frequencies --			1033.7173	1086.5539	1315.6873
Frequencies --			1347.7589	1368.0379	1436.4872
Frequencies --			1488.4045	1534.2193	1686.2915
Frequencies --			1843.8806	3107.0926	3177.1727
Frequencies --			3204.9130	3211.2610	3271.6925

MVK-oxide + HC(O)OH Spectator Catalysis (TS_{spec})

syn-trans-MVK-oxide...FA = *syn-trans*-HPBD...FA

1	6	0	-1.328526	-0.194698	0.112768
2	8	0	-0.658231	-1.292444	-0.201755
3	8	0	0.449685	-1.418902	0.681626
4	8	0	2.182037	1.458940	0.139373
5	6	0	2.899587	0.670069	-0.434077
6	8	0	2.691533	-0.629139	-0.568687
7	1	0	3.835239	0.961004	-0.923377
8	1	0	1.846107	-0.889006	-0.111422
9	6	0	-0.778502	0.591520	1.127904
10	6	0	-2.625720	-0.130048	-0.534413
11	6	0	-3.386817	0.965897	-0.505154
12	1	0	-1.453940	1.249714	1.652974
13	1	0	0.212579	1.006974	0.936098
14	1	0	-0.083482	-0.519388	1.484621
15	1	0	-2.944342	-1.022733	-1.055143
16	1	0	-3.056953	1.867085	-0.009732
17	1	0	-4.355519	0.982263	-0.980646
Frequencies --			-1619.5992	36.1864	41.4330
Frequencies --			86.0767	127.5592	134.9963
Frequencies --			203.5753	209.0236	251.3755
Frequencies --			312.8601	474.3481	495.0176
Frequencies --			586.0329	636.1406	685.9332
Frequencies --			750.5329	778.9893	910.2849
Frequencies --			933.6084	957.7666	1004.7380
Frequencies --			1008.0108	1027.0935	1039.9439
Frequencies --			1072.1405	1094.7722	1221.8891
Frequencies --			1281.0016	1312.4225	1353.3064
Frequencies --			1395.2671	1436.5805	1467.6309
Frequencies --			1471.5440	1566.7206	1684.0863
Frequencies --			1769.5521	1809.4227	3056.2536
Frequencies --			3058.8757	3175.4253	3199.9618
Frequencies --			3209.2346	3226.7428	3269.5534

syn-cis-MVK-oxide...FA = *syn-cis*-HPBD...FA

1	6	0	1.310000	-0.362991	0.185501
2	8	0	0.883397	0.875936	0.346937
3	8	0	-0.257914	0.855669	1.201332
4	8	0	-2.449001	-1.155439	-0.431711
5	6	0	-2.947866	-0.074322	-0.653856
6	8	0	-2.481681	1.101419	-0.269139
7	1	0	-3.876288	0.047718	-1.221901
8	1	0	-1.644493	0.982018	0.259086
9	6	0	0.531967	-1.363316	0.771960
10	6	0	2.626054	-0.500574	-0.417190
11	6	0	3.337675	0.522186	-0.897563
12	1	0	1.021494	-2.309697	0.948628
13	1	0	-0.503434	-1.444341	0.432118
14	1	0	0.035970	-0.400945	1.566146
15	1	0	2.990983	-1.514634	-0.489364
16	1	0	2.973949	1.537346	-0.843203
17	1	0	4.296433	0.355963	-1.363977
Frequencies --	-1614.8640		32.0659		42.9546
Frequencies --	79.6974		104.0764		138.5301
Frequencies --	194.3823		206.0776		247.0365
Frequencies --	312.6558		476.4856		502.0277
Frequencies --	578.6757		643.1789		687.4903
Frequencies --	738.4168		775.3117		907.2298
Frequencies --	936.2919		959.0045		1003.8376
Frequencies --	1015.3897		1026.4607		1037.6955
Frequencies --	1082.8387		1098.6969		1224.4337
Frequencies --	1296.4780		1327.2110		1366.0240
Frequencies --	1397.4520		1434.8454		1442.8708
Frequencies --	1483.5084		1551.3566		1687.7454
Frequencies --	1767.3053		1813.7509		3042.2522
Frequencies --	3056.9034		3178.4842		3183.5276
Frequencies --	3211.1108		3219.7403		3273.2819

MVK-oxide + HC(O)OH Chemical catalysis (TS2)

syn-trans-MVK-oxide...FA = *syn-trans*-HPBD...FA

1	6	0	-1.080704	0.377209	0.188540
2	6	0	-0.555295	-0.356308	1.279037
3	6	0	-2.239660	0.027415	-0.620712
4	6	0	-3.035280	-1.011786	-0.361340
5	8	0	-0.489331	1.425459	-0.300170
6	8	0	0.673982	1.830693	0.436289
7	1	0	0.371272	-0.947087	0.762110
8	1	0	-1.238463	-1.081474	1.698825
9	1	0	-0.051844	0.267701	2.007860
10	1	0	-2.418070	0.667711	-1.472752
11	1	0	-2.872813	-1.666940	0.480550
12	1	0	-3.873946	-1.232751	-1.003573

13	1	0	1.406116	1.164991	0.009601
14	8	0	2.356160	0.334044	-0.562840
15	6	0	2.384541	-0.914667	-0.403353
16	8	0	1.530251	-1.649541	0.156394
17	1	0	3.267642	-1.428570	-0.813027
Frequencies --	-534.8581		49.5601		61.5051
Frequencies --	93.0114		133.7931		197.7074
Frequencies --	255.7488		269.8051		376.9820
Frequencies --	419.6663		482.3724		487.0736
Frequencies --	549.5547		602.6145		715.7893
Frequencies --	762.5884		855.8855		889.6618
Frequencies --	937.3861		1015.0995		1028.4686
Frequencies --	1034.6164		1036.7626		1076.1186
Frequencies --	1094.2163		1172.0474		1317.9591
Frequencies --	1359.0010		1370.9333		1376.8074
Frequencies --	1413.0707		1443.5561		1474.8938
Frequencies --	1493.0554		1591.1083		1667.1251
Frequencies --	1687.4280		1773.2908		1995.0004
Frequencies --	2986.7198		3141.5776		3183.5139
Frequencies --	3210.4235		3229.1369		3275.6609

syn-cis-MVK-oxide...FA = *syn-cis*-HPBD...FA

1	6	0	-1.078834	-0.103432	0.481965
2	6	0	-0.270354	-0.805076	1.416639
3	6	0	-2.222285	-0.718156	-0.182706
4	6	0	-2.940371	-0.111522	-1.131420
5	8	0	-0.801093	1.088736	0.070501
6	8	0	0.339628	1.673008	0.721539
7	1	0	0.669001	-1.105688	0.740330
8	1	0	-0.740205	-1.702353	1.798546
9	1	0	0.180093	-0.165547	2.166731
10	1	0	-2.460005	-1.718666	0.144950
11	1	0	-2.703708	0.886861	-1.467265
12	1	0	-3.781495	-0.610554	-1.587586
13	1	0	1.145067	1.250511	0.106381
14	8	0	2.138429	0.772783	-0.669324
15	6	0	2.468582	-0.446855	-0.682376
16	8	0	1.895156	-1.414935	-0.129125
17	1	0	3.373860	-0.681050	-1.263425
Frequencies --	-489.0263		32.9454		58.7812
Frequencies --	102.2931		126.4769		198.1492
Frequencies --	234.9037		259.1731		368.9102
Frequencies --	418.9812		477.1252		484.1433
Frequencies --	553.6979		606.3183		694.0498
Frequencies --	756.6221		844.5250		908.9340
Frequencies --	938.7210		1021.9035		1030.1369
Frequencies --	1037.3734		1062.5528		1076.2332
Frequencies --	1103.6397		1221.9108		1319.3426
Frequencies --	1353.8798		1366.0180		1378.6005

Frequencies --	1413.3946	1442.8830	1462.8745
Frequencies --	1497.8126	1561.1631	1668.2735
Frequencies --	1684.2685	1829.9010	1883.8613
Frequencies --	2985.5777	3133.1881	3180.8731
Frequencies --	3218.7206	3223.8573	3277.1215

anti-trans-MVK-oxide...FA = *anti-trans*-HPBD...FA

1	6	0	-0.640244	1.802366	-1.339619
2	6	0	-1.220185	0.682845	-0.896293
3	6	0	-1.048998	0.233095	0.466616
4	6	0	-0.556621	1.048560	1.527261
5	8	0	1.326398	-1.152261	-0.575219
6	6	0	2.165620	-0.298990	-0.191075
7	8	0	1.987142	0.708599	0.544640
8	8	0	-1.212686	-1.017049	0.781594
9	8	0	-1.083955	-1.892479	-0.361489
10	1	0	0.020100	2.387982	-0.718116
11	1	0	-0.773879	2.119491	-2.362551
12	1	0	-1.792417	0.041082	-1.545933
13	1	0	0.586439	0.946324	1.179359
14	1	0	-0.853372	2.087734	1.490449
15	1	0	-0.630426	0.591112	2.506699
16	1	0	3.198293	-0.444917	-0.551409
17	1	0	-0.087352	-1.710544	-0.516051
Frequencies --	-429.6501	59.6039	82.6856		
Frequencies --	96.7238	121.6146	163.8226		
Frequencies --	238.5437	287.1099	329.8363		
Frequencies --	361.0465	430.5272	501.9798		
Frequencies --	541.4288	575.7868	705.0996		
Frequencies --	750.6971	806.7752	870.4764		
Frequencies --	918.4146	948.6564	1011.1905		
Frequencies --	1025.9536	1046.2794	1075.4536		
Frequencies --	1079.5032	1180.8126	1313.9823		
Frequencies --	1371.2961	1409.5689	1418.6823		
Frequencies --	1424.9234	1436.8928	1478.7021		
Frequencies --	1509.5474	1556.4926	1630.1030		
Frequencies --	1673.9240	1886.9935	2766.8441		
Frequencies --	2954.7679	3143.0130	3181.5497		
Frequencies --	3228.9677	3241.7875	3276.9028		

anti-cis-MVK-oxide...FA = *anti-cis*-HPBD...FA

1	6	0	0.598672	0.737540	-0.332058
2	6	0	-0.295281	1.822561	-0.578511
3	6	0	1.219267	0.577712	0.968460
4	6	0	2.384499	-0.035089	1.190521
5	8	0	0.766688	-0.055524	-1.353358
6	8	0	1.130270	-1.408256	-0.985489
7	1	0	-0.095475	2.709318	0.010972
8	1	0	-1.280780	1.300814	-0.145245

9	1	0	-0.491549	2.010575	-1.627718
10	1	0	0.713363	1.110848	1.759309
11	1	0	2.909323	-0.564347	0.412814
12	1	0	2.831226	-0.000616	2.172668
13	1	0	0.307239	-1.601387	-0.438804
14	8	0	-0.953972	-1.174206	0.473205
15	6	0	-2.143702	-0.751914	0.411857
16	8	0	-2.509145	0.442599	0.291535
17	1	0	-2.944811	-1.506958	0.487248
Frequencies --			-368.1729	52.5610	82.4123
Frequencies --			111.9447	127.8068	154.7988
Frequencies --			249.6457	267.9650	300.1926
Frequencies --			353.3522	396.9342	482.8032
Frequencies --			538.0406	616.3751	709.0883
Frequencies --			746.9811	809.5570	828.4949
Frequencies --			907.2965	917.4848	1015.4159
Frequencies --			1018.4944	1051.8117	1077.9866
Frequencies --			1098.8167	1164.9608	1340.3861
Frequencies --			1369.9285	1399.6753	1410.3061
Frequencies --			1411.4989	1427.5623	1472.4686
Frequencies --			1505.4355	1535.9277	1582.9696
Frequencies --			1681.3705	1873.6266	2952.2355
Frequencies --			3063.5428	3130.7084	3186.6097
Frequencies --			3215.0857	3219.0675	3288.4898

MVK-oxide + HC(O)OH 1,4-insertion (TS3)

syn-trans-MVK-oxide...FA = *syn-trans*-HPBF Adduct

1	6	0	0.735502	0.454862	0.005429
2	8	0	-0.012061	1.158611	-0.764566
3	8	0	-1.165269	1.718647	-0.142895
4	8	0	-0.488945	-1.447803	0.047960
5	6	0	-1.725710	-1.379711	-0.017457
6	8	0	-2.456497	-0.330435	-0.094877
7	1	0	-2.299636	-2.314001	-0.008477
8	1	0	-1.862852	0.675446	-0.120004
9	6	0	0.665065	0.556642	1.481842
10	6	0	1.860444	-0.120030	-0.717072
11	6	0	2.908772	-0.687222	-0.120910
12	1	0	1.082850	-0.330317	1.941562
13	1	0	1.249719	1.432001	1.776493
14	1	0	-0.355806	0.708391	1.801768
15	1	0	1.796939	-0.048340	-1.793121
16	1	0	2.983701	-0.776058	0.951796
17	1	0	3.722827	-1.086513	-0.705978
Frequencies --			-598.0338	58.5295	83.8810
Frequencies --			142.1704	169.6873	192.1403
Frequencies --			250.3268	271.1921	305.4575
Frequencies --			345.1720	376.8882	461.5846
Frequencies --			484.5414	575.6331	662.7502

Frequencies --	706.2328	774.5847	819.0039
Frequencies --	939.2021	995.0411	1000.5989
Frequencies --	1028.5869	1060.3462	1066.7508
Frequencies --	1078.1853	1271.7963	1318.4128
Frequencies --	1346.0554	1354.1718	1403.3264
Frequencies --	1417.4923	1456.9270	1475.3778
Frequencies --	1496.8015	1526.9577	1669.0611
Frequencies --	1691.6501	1744.9004	3039.1798
Frequencies --	3057.8435	3169.0449	3183.6576
Frequencies --	3213.6016	3225.2961	3273.7312

syn-cis-MVK-oxide...FA = *syn-trans*-HPBF Adduct

1	6	0	0.765938	0.251319	0.369668
2	8	0	0.401376	0.949070	-0.634030
3	8	0	-0.730201	1.788150	-0.400938
4	8	0	-0.765726	-1.435154	0.230274
5	6	0	-1.898953	-1.162037	-0.182719
6	8	0	-2.363178	-0.015020	-0.533569
7	1	0	-2.635756	-1.968065	-0.274764
8	1	0	-1.627624	0.845160	-0.478002
9	6	0	0.320028	0.552866	1.749948
10	6	0	1.906477	-0.630983	0.129397
11	6	0	2.738632	-0.487794	-0.901713
12	1	0	0.514166	-0.296839	2.394435
13	1	0	0.911469	1.407665	2.091403
14	1	0	-0.722029	0.838039	1.777438
15	1	0	2.049293	-1.404518	0.867968
16	1	0	2.600420	0.294747	-1.632516
17	1	0	3.579156	-1.152767	-1.027342
Frequencies --	-335.6255	52.6315	81.0603		
Frequencies --	135.1120	181.6510	183.0212		
Frequencies --	229.4599	266.1835	316.4766		
Frequencies --	346.8078	381.7988	435.7899		
Frequencies --	503.2674	604.7698	676.1709		
Frequencies --	750.3469	784.6604	892.3250		
Frequencies --	984.6236	1008.8152	1015.6960		
Frequencies --	1025.9930	1064.8159	1065.5608		
Frequencies --	1111.3095	1261.9815	1288.8785		
Frequencies --	1340.9716	1342.1872	1411.9670		
Frequencies --	1417.0960	1451.9362	1474.0738		
Frequencies --	1493.0829	1542.4368	1656.9518		
Frequencies --	1690.2947	1758.4095	3046.9518		
Frequencies --	3049.7852	3157.4781	3179.0293		
Frequencies --	3220.3575	3225.5885	3274.1898		

anti-trans-MVK-oxide...FA = *anti-trans*-HPBF Adduct

1	6	0	0.825182	0.427532	0.292669
2	6	0	1.630233	0.108083	1.501824
3	6	0	1.143999	-0.063969	-1.035023

4	6	0	2.126701	-0.940390	-1.251695
5	8	0	0.020819	1.410634	0.466041
6	8	0	-0.834550	1.703592	-0.639281
7	1	0	2.631771	0.523829	1.394623
8	1	0	1.699350	-0.968701	1.616014
9	1	0	1.152771	0.532449	2.378350
10	1	0	0.560690	0.356526	-1.836691
11	1	0	2.701869	-1.377157	-0.449135
12	1	0	2.370537	-1.252472	-2.255728
13	1	0	-1.633065	0.739262	-0.512437
14	8	0	-2.340300	-0.177030	-0.379581
15	6	0	-1.813030	-1.171180	0.232822
16	8	0	-0.653590	-1.274934	0.658286
17	1	0	-2.501468	-2.012293	0.377709
Frequencies --			-533.3679	48.5684	85.3667
Frequencies --			132.3468	173.0964	195.0681
Frequencies --			251.9218	273.6320	298.8173
Frequencies --			336.1784	352.4457	441.5295
Frequencies --			475.0791	601.3365	644.9041
Frequencies --			738.5756	774.3844	805.1464
Frequencies --			927.4014	1004.9935	1007.3295
Frequencies --			1046.1509	1062.5612	1066.6956
Frequencies --			1076.7233	1264.7986	1302.0853
Frequencies --			1351.9233	1362.2992	1403.0938
Frequencies --			1430.0085	1442.7723	1465.7720
Frequencies --			1493.2001	1542.5711	1673.9648
Frequencies --			1683.2205	1747.2926	3038.7694
Frequencies --			3075.3584	3157.2057	3178.5405
Frequencies --			3188.7304	3250.1203	3270.7228

anti-cis-MVK-oxide...FA = *anti-cis*-HPBF Adduct

1	6	0	0.972909	-0.331584	0.199133
2	6	0	1.683363	-1.637282	0.302893
3	6	0	1.149660	0.459347	-1.009931
4	6	0	1.065260	1.788171	-1.126332
5	8	0	0.516510	0.072723	1.323896
6	8	0	-0.248626	1.277296	1.303086
7	1	0	2.757821	-1.453059	0.344982
8	1	0	1.464274	-2.231934	-0.578185
9	1	0	1.369900	-2.168903	1.194666
10	1	0	1.454483	-0.137129	-1.857603
11	1	0	0.754268	2.408816	-0.304950
12	1	0	1.323470	2.251161	-2.067801
13	1	0	-1.269163	0.835194	0.692960
14	8	0	-2.182971	0.408244	0.125782
15	6	0	-1.963032	-0.665550	-0.537013
16	8	0	-0.890845	-1.272944	-0.673539
17	1	0	-2.856550	-1.065310	-1.030362
Frequencies --			-510.7037	54.2275	109.8598

Frequencies --	145.6613	177.3272	196.6995
Frequencies --	256.2488	298.1436	312.5872
Frequencies --	330.0583	356.7362	397.6463
Frequencies --	472.3527	618.9639	646.0874
Frequencies --	750.4431	782.8750	817.8670
Frequencies --	935.0425	1025.8260	1035.7259
Frequencies --	1039.1614	1062.1600	1065.5649
Frequencies --	1109.5076	1244.6272	1267.9168
Frequencies --	1351.0535	1352.6226	1404.8237
Frequencies --	1414.2389	1458.4383	1468.2622
Frequencies --	1491.2436	1558.0727	1670.3953
Frequencies --	1675.7153	1749.5880	3043.5184
Frequencies --	3066.4061	3150.4026	3179.3026
Frequencies --	3189.7453	3206.8386	3300.4674

MVK-oxide + HC(O)OH Chemical Catalysis (Vinyl H-atom)

anti-trans-MVK-oxide...FA = *trans*-HPBD-2

1	6	0	-1.319153	-0.276721	0.173401
2	6	0	-2.387923	-0.368121	1.204644
3	6	0	-0.759708	0.929188	-0.247433
4	6	0	-1.276074	1.962763	-0.905043
5	8	0	-0.836120	-1.436892	-0.150040
6	8	0	0.108672	-1.348954	-1.239277
7	1	0	-3.278063	0.130055	0.818655
8	1	0	-2.076706	0.172259	2.096377
9	1	0	-2.610187	-1.401338	1.452813
10	1	0	0.459623	1.027897	0.137577
11	1	0	-2.239337	1.922265	-1.398843
12	1	0	-0.702639	2.871098	-1.023748
13	1	0	0.982382	-1.172520	-0.706832
14	8	0	2.211878	-0.878693	0.060934
15	6	0	2.479167	0.268026	0.471258
16	8	0	1.709064	1.278337	0.528751
17	1	0	3.499114	0.449090	0.840103
Frequencies --	-896.7737	56.7959	74.2582		
Frequencies --	103.1404	121.3808	155.2350		
Frequencies --	208.2114	221.7051	249.0315		
Frequencies --	301.8563	383.9833	448.2472		
Frequencies --	494.7112	595.5098	638.7857		
Frequencies --	744.2849	766.0403	838.9508		
Frequencies --	926.7701	982.4224	1035.4183		
Frequencies --	1039.1149	1049.1226	1073.7053		
Frequencies --	1102.2736	1212.9510	1307.9068		
Frequencies --	1362.1666	1395.4673	1413.7908		
Frequencies --	1418.8840	1466.0078	1479.8649		
Frequencies --	1488.3922	1542.5313	1640.0440		
Frequencies --	1679.1691	1761.6799	2501.1101		
Frequencies --	3002.5854	3062.5602	3132.5949		
Frequencies --	3139.3827	3173.4830	3230.7535		

HPBD Product Acid Catalysis (TS_{H,exchange})*syn-trans*-HPBD...FA = *syn-trans*-HPBD...FA

1	6	0	-1.531737	0.270165	-0.142604
2	6	0	-1.792370	1.574484	-0.068199
3	6	0	-2.513318	-0.819516	-0.216003
4	6	0	-3.702038	-0.799923	0.383668
5	8	0	-0.275133	-0.296688	-0.186703
6	8	0	0.745086	0.731020	-0.211635
7	1	0	-2.819474	1.896627	-0.090742
8	1	0	-1.008943	2.308147	-0.010953
9	1	0	-2.211226	-1.681185	-0.797475
10	1	0	-4.007590	0.028866	1.005610
11	1	0	-4.396354	-1.617547	0.263482
12	1	0	1.485349	0.423226	0.724233
13	8	0	2.502918	-0.024331	1.209172
14	6	0	3.140356	-0.437784	0.194828
15	8	0	2.727388	-0.331458	-0.998447
16	1	0	4.105615	-0.914081	0.359495
17	1	0	1.645198	0.203053	-0.862887
Frequencies --	-1603.1048		1.4786		57.2097
Frequencies --	67.7031		99.9953		207.1727
Frequencies --	224.2705		287.8611		329.1158
Frequencies --	395.8273		470.6643		571.9532
Frequencies --	576.5467		643.6319		733.7901
Frequencies --	744.2329		850.2178		856.1461
Frequencies --	866.7927		922.2949		965.4762
Frequencies --	994.5418		1026.5167		1080.6693
Frequencies --	1088.8540		1197.5386		1292.2541
Frequencies --	1332.9295		1374.5493		1377.2372
Frequencies --	1388.5928		1426.6051		1469.2157
Frequencies --	1532.8067		1597.8087		1693.6358
Frequencies --	1706.5763		1712.4758		1933.7363
Frequencies --	3138.3969		3168.4695		3183.9081
Frequencies --	3209.9838		3260.2795		3309.7109

syn-cis-HPBD...FA = *syn-cis*-HPBD...FA

1	6	0	1.657435	0.503052	-0.000045
2	6	0	1.846634	1.824970	0.000007
3	6	0	2.743622	-0.472651	0.000191
4	6	0	2.597969	-1.798524	0.000151
5	8	0	0.435853	-0.127004	-0.000327
6	8	0	-0.634645	0.846972	-0.000517
7	1	0	2.857898	2.196212	0.000241
8	1	0	1.029099	2.522296	-0.000180
9	1	0	3.731329	-0.032559	0.000412
10	1	0	1.624726	-2.264208	-0.000068
11	1	0	3.461951	-2.445140	0.000338
12	1	0	-1.440069	0.374101	-0.806993

13	8	0	-2.467883	-0.184351	-1.119935
14	6	0	-2.982703	-0.477802	0.000313
15	8	0	-2.467573	-0.183501	1.120196
16	1	0	-3.928842	-1.016598	0.000650
17	1	0	-1.439846	0.374710	0.806548
Frequencies --	-1600.7447		-7.0920		55.2583
Frequencies --	57.8931		142.4909		208.3735
Frequencies --	224.1359		270.3055		338.6807
Frequencies --	451.1011		472.7713		534.9090
Frequencies --	572.8371		655.7153		727.1813
Frequencies --	764.1784		851.8203		855.2240
Frequencies --	858.5466		928.0467		951.1098
Frequencies --	1000.0804		1021.8736		1068.5207
Frequencies --	1080.8562		1231.4735		1325.4597
Frequencies --	1347.9790		1374.6261		1377.2054
Frequencies --	1389.6664		1422.5595		1468.5169
Frequencies --	1532.9088		1599.5590		1654.6886
Frequencies --	1711.8075		1720.6024		1931.6378
Frequencies --	3139.8580		3177.5529		3195.9745
Frequencies --	3207.6910		3269.0680		3310.4980

anti-trans-HPBD...FA = *anti-trans*-HPBD...FA

1	6	0	-1.515069	0.486711	-0.299936
2	6	0	-2.029065	1.707796	-0.135021
3	6	0	-2.225960	-0.789149	-0.201391
4	6	0	-3.234437	-1.012709	0.639356
5	8	0	-0.206074	0.429831	-0.734773
6	8	0	0.482173	-0.626068	0.025280
7	1	0	-3.090650	1.836126	-0.002841
8	1	0	-1.395566	2.578520	-0.190875
9	1	0	-1.877349	-1.573221	-0.859897
10	1	0	-3.556729	-0.259565	1.344276
11	1	0	-3.754054	-1.958656	0.647781
12	1	0	1.512763	-0.759346	-0.597901
13	8	0	2.726217	-0.622702	-0.778824
14	6	0	3.079296	0.068513	0.222242
15	8	0	2.294698	0.445861	1.143075
16	1	0	4.127362	0.356825	0.297668
17	1	0	1.209525	-0.003030	0.772228
Frequencies --	-1600.6277		17.9084		53.5243
Frequencies --	81.5663		115.3588		173.4415
Frequencies --	228.3193		284.8755		328.9778
Frequencies --	433.2394		457.3290		558.5721
Frequencies --	568.9826		625.4588		737.7972
Frequencies --	761.4659		824.3384		850.3551
Frequencies --	884.2050		902.6315		964.6721
Frequencies --	976.7683		1025.0063		1079.8868
Frequencies --	1091.4430		1180.0407		1284.4578
Frequencies --	1337.2008		1374.7083		1378.3778

Frequencies --	1386.8911	1421.8023	1469.4305
Frequencies --	1536.0214	1582.9452	1684.3362
Frequencies --	1691.4294	1716.4142	1946.5765
Frequencies --	3128.5364	3166.9029	3190.0080
Frequencies --	3193.4707	3258.4562	3288.4564

anti-cis-HPBD...FA = *anti-cis*-HPBD...FA

1	6	0	1.560820	0.628946	0.179133
2	6	0	1.713670	1.955560	0.222311
3	6	0	2.579042	-0.313708	-0.268411
4	6	0	2.490189	-1.639485	-0.163847
5	8	0	0.385456	0.125355	0.710986
6	8	0	-0.350010	-0.546421	-0.382983
7	1	0	2.654467	2.406915	-0.051689
8	1	0	0.909900	2.587630	0.564192
9	1	0	3.461878	0.139327	-0.700309
10	1	0	1.617206	-2.113164	0.256655
11	1	0	3.293810	-2.275114	-0.502762
12	1	0	-1.304479	-0.977166	0.204860
13	8	0	-2.503835	-0.982253	0.546174
14	6	0	-2.951162	0.063174	-0.010574
15	8	0	-2.262294	0.834170	-0.743976
16	1	0	-3.998964	0.317221	0.149651
17	1	0	-1.143705	0.300622	-0.713884
Frequencies --	-1590.0275	17.9402	51.3294		
Frequencies --	90.3258	147.7162	148.6563		
Frequencies --	213.4848	293.4471	327.9973		
Frequencies --	423.7610	464.5927	569.1739		
Frequencies --	575.0792	630.1288	742.8803		
Frequencies --	765.5214	833.6329	839.6901		
Frequencies --	877.8500	923.4904	960.7476		
Frequencies --	974.0755	1023.7322	1057.1576		
Frequencies --	1079.6612	1211.0372	1325.6118		
Frequencies --	1327.6159	1375.0725	1379.9716		
Frequencies --	1391.8436	1412.3241	1469.6310		
Frequencies --	1543.9967	1572.7716	1649.7743		
Frequencies --	1711.6395	1717.7210	1953.5116		
Frequencies --	3123.3689	3176.8209	3184.2182		
Frequencies --	3189.1887	3273.2006	3283.1271		

MVK-oxide + HC(O)OH SOZ Formation (TS_{soz})

syn-trans-MVK-oxide...FA = SOZ

1	6	0	-0.784362	0.304551	0.221130
2	8	0	-0.120481	1.397401	-0.018725
3	8	0	1.214481	1.291813	0.362159
4	6	0	1.693912	-0.220558	-0.699116
5	8	0	0.584511	-0.763544	-0.932682
6	8	0	2.607222	-0.815652	0.115525
7	1	0	2.198051	0.405698	-1.429815

8	1	0	2.143842	-1.530395	0.568941
9	6	0	-0.561550	-0.494008	1.459371
10	6	0	-2.037806	0.262804	-0.516733
11	6	0	-2.997793	-0.634292	-0.288979
12	1	0	-1.311294	-0.192946	2.194217
13	1	0	-0.677580	-1.553133	1.257517
14	1	0	0.427048	-0.290476	1.850267
15	1	0	-2.133094	0.998978	-1.301931
16	1	0	-2.906734	-1.389698	0.476822
17	1	0	-3.900503	-0.639156	-0.880263
Frequencies --			-360.3426	83.3302	91.9426
Frequencies --			161.9644	220.1409	252.0331
Frequencies --			264.5245	308.8371	348.3251
Frequencies --			396.4673	421.1496	491.0744
Frequencies --			505.9320	593.9885	613.0639
Frequencies --			654.8811	698.2384	805.6680
Frequencies --			958.7928	983.7118	993.1586
Frequencies --			1028.9134	1041.1489	1067.4147
Frequencies --			1075.2862	1122.0594	1297.7853
Frequencies --			1308.8522	1344.2672	1367.0865
Frequencies --			1398.6596	1439.6015	1464.3650
Frequencies --			1504.8121	1513.0169	1547.6288
Frequencies --			1688.1198	3057.3002	3133.0402
Frequencies --			3151.8502	3179.4857	3203.9918
Frequencies --			3210.3938	3269.2902	3794.3344

syn-trans-MVK-oxide...FA = SOZ Geometry 2

1	6	0	-0.795699	0.326159	-0.210104
2	8	0	0.088732	0.500830	-1.147136
3	8	0	1.230002	1.153056	-0.678518
4	6	0	1.733543	-0.199624	0.596996
5	8	0	0.617903	-0.651784	0.961780
6	8	0	2.590214	-0.987978	-0.096953
7	1	0	2.281353	0.549407	1.162984
8	1	0	2.069435	-1.737720	-0.412420
9	6	0	-1.056104	1.354912	0.833071
10	6	0	-1.789223	-0.667997	-0.590588
11	6	0	-2.905537	-0.896982	0.101906
12	1	0	-1.902289	1.962039	0.503956
13	1	0	-1.304353	0.882764	1.776844
14	1	0	-0.182002	1.980388	0.953257
15	1	0	-1.549561	-1.244465	-1.472910
16	1	0	-3.148234	-0.342677	0.995734
17	1	0	-3.601039	-1.661532	-0.208514
Frequencies --			-375.3655	62.6853	93.6043
Frequencies --			178.5469	202.4328	215.6575
Frequencies --			263.1857	287.4049	359.7552
Frequencies --			388.9185	435.7127	489.4479
Frequencies --			506.9477	593.3510	630.0092

Frequencies --	683.5802	706.8002	804.3914
Frequencies --	952.2295	981.8290	994.0522
Frequencies --	1029.0509	1043.9073	1072.0856
Frequencies --	1074.6048	1138.8653	1305.8611
Frequencies --	1310.8909	1339.1331	1357.1059
Frequencies --	1399.1749	1442.4413	1462.3623
Frequencies --	1501.6016	1504.1030	1548.0373
Frequencies --	1688.0862	3058.0552	3126.2501
Frequencies --	3158.9405	3179.9044	3206.0361
Frequencies --	3212.5352	3270.1096	3783.3239

HPBD...FA = OBD...OH...FA; *syn-trans*

1	6	0	1.719273	-0.210677	-0.176920
2	6	0	2.994206	-0.100560	0.358866
3	6	0	0.893136	0.946747	-0.567019
4	6	0	1.009504	2.153778	-0.022497
5	8	0	1.301979	-1.393095	-0.428190
6	8	0	-0.295986	-1.668250	0.439796
7	1	0	3.546495	0.824790	0.317136
8	1	0	3.479351	-0.993947	0.717468
9	1	0	0.131489	0.738166	-1.305989
10	1	0	1.732290	2.360878	0.754366
11	1	0	0.366833	2.966894	-0.324012
12	1	0	-0.787000	-1.716714	-0.397072
13	8	0	-2.453863	-0.232725	-0.991976
14	6	0	-2.676586	0.378354	0.030080
15	8	0	-1.972820	0.303808	1.150456
16	1	0	-3.507315	1.082626	0.140474
17	1	0	-1.233828	-0.346454	1.001881
Frequencies --	-564.9137	24.3927	52.1604		
Frequencies --	66.6408	82.8210	107.2179		
Frequencies --	150.2703	180.0324	205.6601		
Frequencies --	250.8057	279.3976	423.9241		
Frequencies --	497.8270	528.0804	559.3172		
Frequencies --	592.0097	699.6568	761.6631		
Frequencies --	837.1282	893.9019	921.6734		
Frequencies --	984.5515	998.2639	1039.8068		
Frequencies --	1048.8616	1070.9004	1080.4061		
Frequencies --	1221.3163	1273.3525	1332.1575		
Frequencies --	1391.6491	1396.0969	1465.5202		
Frequencies --	1477.2916	1530.9983	1735.3118		
Frequencies --	1768.8278	3063.9414	3167.4383		
Frequencies --	3185.2159	3199.8608	3206.8688		
Frequencies --	3257.2876	3297.8634	3725.9709		

***syn-trans*-MVK-oxide + FA 1,2-insertion (TS_{1,2-insertion})**

1	6	0	1.023375	0.095565	0.160477
2	8	0	1.460800	-0.953416	-0.453370
3	8	0	0.895966	-2.167886	0.058231

4	1	0	-0.076820	-1.916625	-0.168482
5	8	0	-1.170538	-0.989519	-0.650328
6	6	0	-2.175145	-0.266088	-0.330666
7	8	0	-2.166801	0.765638	0.355662
8	1	0	-3.141474	-0.613458	-0.739514
9	6	0	0.464545	0.088865	1.519176
10	6	0	1.294135	1.303548	-0.581909
11	6	0	0.639211	2.435838	-0.303241
12	1	0	1.034286	0.796825	2.120203
13	1	0	-0.574925	0.439397	1.441206
14	1	0	0.492967	-0.903919	1.947156
15	1	0	1.945154	1.212014	-1.438960
16	1	0	-0.091443	2.487184	0.489267
17	1	0	0.780111	3.313679	-0.915453
Frequencies --		-163.9269	55.7009	69.5916	
Frequencies --		97.8697	155.8109	213.5566	
Frequencies --		249.7706	275.2135	294.0929	
Frequencies --		338.3040	383.2531	402.5422	
Frequencies --		496.7181	579.3271	680.6326	
Frequencies --		744.7251	809.4464	913.6348	
Frequencies --		947.3907	987.9028	1006.4702	
Frequencies --		1036.0714	1055.0691	1074.4474	
Frequencies --		1087.8731	1312.4848	1346.3515	
Frequencies --		1357.7065	1403.7739	1411.4036	
Frequencies --		1433.7237	1474.9757	1492.6662	
Frequencies --		1521.2474	1566.6586	1653.9803	
Frequencies --		1676.0952	2678.3918	2916.1385	
Frequencies --		2933.3398	3099.7182	3183.4906	
Frequencies --		3207.7456	3215.8154	3281.6363	

MVK-oxide, Dioxole Formation (TS_d)

anti-cis-MVK-oxide = Dioxole

1	6	0	2.113823	0.224472	0.046960
2	6	0	0.631136	0.106616	0.056598
3	6	0	-0.289484	1.134011	0.002167
4	6	0	-1.658696	0.880700	0.034722
5	8	0	0.192038	-1.122782	-0.127554
6	8	0	-1.177527	-1.228705	0.016537
7	1	0	2.550605	-0.538418	-0.594098
8	1	0	2.411928	1.209438	-0.302360
9	1	0	2.509711	0.088426	1.053507
10	1	0	0.081305	2.079491	-0.370189
11	1	0	-2.293385	1.513012	-0.583405
12	1	0	-2.156925	0.385158	0.842006
Frequencies --		-471.2006	129.9630	232.4944	
Frequencies --		267.8180	345.0662	520.7306	
Frequencies --		585.7959	638.2258	724.1134	
Frequencies --		808.1880	912.1419	959.4270	
Frequencies --		1042.9633	1044.6798	1056.1667	

Frequencies --	1089.9579	1243.2361	1282.7912
Frequencies --	1383.9647	1424.2076	1486.9383
Frequencies --	1498.0863	1540.0503	1595.2316
Frequencies --	3061.7131	3105.9572	3125.9347
Frequencies --	3157.3046	3189.7207	3304.8678

MVK-oxide + HC(O)OH, Dioxole Formation from Spectator Catalysis (TS_{d,cat})

anti-cis-MVK-oxide...FA = Dioxole...FA

1	6	0	-2.135974	-1.600554	-0.223567
2	6	0	-1.469198	-0.276899	-0.123822
3	6	0	-1.453706	0.567260	0.964753
4	6	0	-0.773330	1.778993	0.901700
5	8	0	-0.633003	-0.040766	-1.110808
6	8	0	-0.013864	1.217329	-1.009389
7	1	0	-1.439848	-2.340204	-0.612410
8	1	0	-2.491825	-1.911032	0.754056
9	1	0	-2.989859	-1.540387	-0.898172
10	1	0	-1.663021	0.104698	1.918380
11	1	0	-0.227391	2.093541	1.788265
12	1	0	-1.020845	2.563652	0.214598
13	1	0	1.537967	0.644218	-0.731914
14	8	0	2.453091	0.287033	-0.540926
15	6	0	2.388458	-0.687593	0.352168
16	8	0	1.389434	-1.116902	0.883232
17	1	0	3.392056	-1.075286	0.562921

Frequencies --	-484.5859	31.3998	52.2362
Frequencies --	66.6163	91.4748	132.9860
Frequencies --	196.0533	220.2800	231.1508
Frequencies --	305.9134	351.5718	530.0819
Frequencies --	575.3184	637.7306	694.9380
Frequencies --	709.6615	814.9991	918.8497
Frequencies --	938.8683	1010.9507	1041.3059
Frequencies --	1056.5512	1071.4225	1092.0081
Frequencies --	1098.7011	1229.3687	1246.2301
Frequencies --	1287.7024	1387.9984	1403.2139
Frequencies --	1422.2810	1460.6611	1486.2892
Frequencies --	1492.4166	1544.4523	1603.4700
Frequencies --	1770.9274	3038.8323	3066.8795
Frequencies --	3110.9434	3119.6086	3134.7853
Frequencies --	3169.0056	3206.7122	3289.1762

anti-cis-MVK-oxide...FA = Dioxole...FA Geometry 2

1	6	0	1.854177	1.733388	0.123705
2	6	0	1.279971	0.368525	0.055331
3	6	0	1.456472	-0.568950	-0.939456
4	6	0	0.778288	-1.783990	-0.889753
5	8	0	0.729141	-0.031977	1.185450
6	8	0	0.071347	-1.262297	1.039032
7	1	0	2.191299	1.959422	1.132859

8	1	0	2.679473	1.834122	-0.575483
9	1	0	1.073987	2.442739	-0.150423
10	1	0	2.342483	-0.457100	-1.548247
11	1	0	1.318999	-2.676034	-1.199281
12	1	0	-0.289381	-1.872243	-0.946020
13	1	0	-1.415546	-0.758775	0.597259
14	8	0	-2.337867	-0.505932	0.285841
15	6	0	-2.309546	0.650421	-0.356836
16	8	0	-1.330040	1.324608	-0.584591
17	1	0	-3.318132	0.936287	-0.674475
Frequencies --		-482.6382	48.1541	74.5436	
Frequencies --		92.7216	134.4808	151.6611	
Frequencies --		206.5350	236.7073	243.7265	
Frequencies --		335.4986	347.2842	533.4764	
Frequencies --		581.8828	638.0656	703.9008	
Frequencies --		716.5556	809.6137	922.2277	
Frequencies --		944.2503	1018.4753	1038.8088	
Frequencies --		1050.5333	1068.3592	1091.3569	
Frequencies --		1113.1034	1229.8195	1237.7700	
Frequencies --		1287.1369	1384.3028	1404.2313	
Frequencies --		1415.1753	1477.1696	1485.3205	
Frequencies --		1498.8356	1550.7078	1607.1082	
Frequencies --		1763.6291	2993.5918	3063.4820	
Frequencies --		3068.3399	3112.9995	3139.0380	
Frequencies --		3163.1134	3201.8645	3277.1725	

Products

HPBF Adduct

Optimal Geometry

1	6	0	-0.883500	1.834737	1.149530
2	6	0	-1.034160	0.529419	0.971859
3	1	0	-1.227925	2.310005	2.055163
4	1	0	-0.413804	2.462367	0.407125
5	6	0	-0.655954	-0.226175	-0.267616
6	1	0	-1.504382	-0.086180	1.724944
7	6	0	-1.836046	-0.471726	-1.191482
8	8	0	0.260416	0.584631	-1.104752
9	8	0	-0.134272	-1.492675	-0.000581
10	1	0	-2.188107	0.474285	-1.591477
11	1	0	-1.526585	-1.121755	-2.006710
12	1	0	-2.634634	-0.952142	-0.633379
13	6	0	1.553524	0.719314	-0.833830
14	8	0	0.585099	-1.524915	1.255073
15	8	0	2.195498	0.210024	0.055430
16	1	0	1.998607	1.390186	-1.573964
17	1	0	1.379722	-1.006701	1.006175
Frequencies --		76.0580	98.5864	202.2503	
Frequencies --		212.1732	245.6072	272.8544	

Frequencies --	294.5828	305.7747	332.8314
Frequencies --	358.7746	474.4106	526.5001
Frequencies --	574.6054	651.3611	692.4755
Frequencies --	702.5520	816.2610	842.2525
Frequencies --	933.1789	971.4580	989.3940
Frequencies --	1026.7452	1051.0041	1054.5359
Frequencies --	1135.5926	1177.0500	1242.5607
Frequencies --	1267.6093	1327.8929	1415.3733
Frequencies --	1422.0245	1461.0687	1496.5053
Frequencies --	1499.6251	1507.1182	1708.6714
Frequencies --	1757.4064	3077.6396	3079.7797
Frequencies --	3160.8343	3172.7541	3174.8347
Frequencies --	3210.0886	3263.1153	3498.3543

syn-trans-HPBF Adduct

1	6	0	0.457237	0.046294	0.005130
2	8	0	-0.075554	1.015498	-0.847125
3	8	0	-1.059222	1.851939	-0.197027
4	8	0	-0.293821	-1.250478	-0.114982
5	6	0	-1.613958	-1.322395	-0.043737
6	8	0	-2.413821	-0.419832	0.077857
7	1	0	-1.917747	-2.370481	-0.116553
8	1	0	-1.801330	1.213890	-0.130503
9	6	0	0.496098	0.423415	1.466002
10	6	0	1.772322	-0.298626	-0.634737
11	6	0	2.945464	-0.315131	-0.017306
12	1	0	0.994455	-0.363908	2.023926
13	1	0	1.034795	1.359260	1.585088
14	1	0	-0.507512	0.555272	1.852386
15	1	0	1.695699	-0.524314	-1.689723
16	1	0	3.051351	-0.090139	1.033042
17	1	0	3.846645	-0.557931	-0.559563
Frequencies --	73.2685	75.1436	188.1957		
Frequencies --	237.5739	256.0780	260.8648		
Frequencies --	273.0045	302.7491	358.1477		
Frequencies --	404.2583	435.7289	498.3230		
Frequencies --	570.0881	632.0803	676.6209		
Frequencies --	726.4038	813.9231	837.0692		
Frequencies --	927.2139	971.4672	978.0580		
Frequencies --	1029.4082	1035.4653	1053.2503		
Frequencies --	1102.2452	1194.6455	1245.1457		
Frequencies --	1317.3552	1340.0749	1418.6744		
Frequencies --	1425.7382	1464.0844	1503.3446		
Frequencies --	1504.8200	1508.4557	1715.3735		
Frequencies --	1742.3090	3079.1638	3091.7916		
Frequencies --	3170.2909	3176.0730	3188.2658		
Frequencies --	3197.1056	3262.7404	3498.1199		

syn-cis-HPBF Adduct

1	6	0	0.432215	-0.145618	0.222804
2	8	0	0.282486	0.928543	-0.646123
3	8	0	-0.616192	1.936191	-0.128090
4	8	0	-0.492551	-1.270172	-0.139827
5	6	0	-1.787431	-1.075427	-0.334991
6	8	0	-2.405668	-0.033666	-0.298601
7	1	0	-2.264329	-2.035409	-0.551756
8	1	0	-1.469893	1.469880	-0.250398
9	6	0	0.222927	0.170168	1.690624
10	6	0	1.782477	-0.748174	-0.050487
11	6	0	2.800194	-0.078783	-0.575293
12	1	0	0.489315	-0.706360	2.275938
13	1	0	0.870494	0.997342	1.967264
14	1	0	-0.805895	0.444888	1.895966
15	1	0	1.877531	-1.784329	0.242571
16	1	0	2.700058	0.953190	-0.873416
17	1	0	3.755828	-0.559354	-0.720982
Frequencies --	73.4005		110.1686		174.4288
Frequencies --	228.9413		254.5921		270.9765
Frequencies --	291.4448		294.5732		352.5409
Frequencies --	383.9210		473.1621		504.2500
Frequencies --	563.3891		653.0899		687.3126
Frequencies --	723.9887		807.4825		833.5515
Frequencies --	930.2589		980.2527		990.3255
Frequencies --	1031.0189		1052.6068		1062.1014
Frequencies --	1102.6922		1204.1195		1252.5150
Frequencies --	1280.7503		1329.9955		1419.0919
Frequencies --	1421.6878		1456.2658		1496.4532
Frequencies --	1500.6437		1502.5567		1707.2892
Frequencies --	1745.0153		3079.6122		3084.1918
Frequencies --	3163.3912		3176.6113		3180.0032
Frequencies --	3202.6234		3271.2006		3509.9004

anti-trans-HPBF Adduct

1	6	0	0.478038	-0.197619	0.338885
2	6	0	1.474202	-0.948701	1.193335
3	6	0	0.990416	0.370788	-0.951236
4	6	0	2.257079	0.313244	-1.342234
5	8	0	-0.100731	0.733612	1.201497
6	8	0	-0.654464	1.875760	0.507737
7	1	0	2.291019	-0.288781	1.468341
8	1	0	1.854392	-1.812727	0.657381
9	1	0	0.972227	-1.283022	2.097192
10	1	0	0.248828	0.840354	-1.577807
11	1	0	3.032076	-0.138917	-0.742348
12	1	0	2.556104	0.733849	-2.290482
13	1	0	-1.450259	1.461522	0.112903
14	8	0	-2.252965	0.072138	-0.627810
15	6	0	-1.723768	-1.008117	-0.478493

16	8	0	-0.508013	-1.274192	-0.028153
17	1	0	-2.230804	-1.948393	-0.712893
Frequencies --	67.2305		78.6126		190.4383
Frequencies --	230.7580		261.1112		271.1780
Frequencies --	295.9908		316.7984		332.7954
Frequencies --	386.2570		431.9330		497.3510
Frequencies --	555.9419		640.5126		674.8534
Frequencies --	747.3335		796.6004		827.2875
Frequencies --	929.1544		981.2899		987.2412
Frequencies --	1030.0845		1039.4254		1053.3609
Frequencies --	1098.2499		1196.5287		1249.4094
Frequencies --	1319.5076		1347.4390		1417.2472
Frequencies --	1423.6114		1465.4914		1500.4579
Frequencies --	1503.5173		1509.4884		1708.8719
Frequencies --	1742.8042		3078.8912		3086.7923
Frequencies --	3167.6353		3176.1550		3178.7332
Frequencies --	3226.9347		3262.8343		3513.2659

anti-cis-HPBF Adduct

1	6	0	0.442256	0.538765	-0.117107
2	6	0	1.238904	1.769289	-0.517064
3	6	0	1.028468	-0.153815	1.079460
4	6	0	1.865296	-1.181875	1.034309
5	8	0	0.316607	-0.189194	-1.293323
6	8	0	-0.021159	-1.585110	-1.103847
7	1	0	2.245016	1.464290	-0.787545
8	1	0	1.280360	2.465937	0.315370
9	1	0	0.758387	2.250474	-1.365607
10	1	0	0.777690	0.314395	2.021856
11	1	0	2.120935	-1.666049	0.105950
12	1	0	2.299573	-1.569839	1.943632
13	1	0	-0.895132	-1.503203	-0.664768
14	8	0	-2.122731	-0.762499	0.291004
15	6	0	-1.957663	0.418659	0.502294
16	8	0	-0.865209	1.141113	0.312152
17	1	0	-2.750456	1.063374	0.891870
Frequencies --	54.9770		93.2607		192.8808
Frequencies --	219.1618		241.6570		261.2429
Frequencies --	293.4247		303.6928		333.2523
Frequencies --	345.9031		457.1580		495.2571
Frequencies --	557.1344		649.6134		680.8966
Frequencies --	720.5570		795.0306		828.8901
Frequencies --	928.0345		982.6728		993.0687
Frequencies --	1026.6763		1054.9804		1063.3948
Frequencies --	1100.0391		1183.3306		1244.3178
Frequencies --	1292.9461		1334.9574		1413.7217
Frequencies --	1418.8021		1461.7654		1496.2762
Frequencies --	1498.5126		1528.3769		1706.7824
Frequencies --	1749.0678		3078.7048		3080.2442

Frequencies --	3162.2933	3174.6873	3176.8041
Frequencies --	3192.5660	3276.2360	3478.1191

HPBD

syn-trans-HPBD

1	6	0	-2.464345	-0.116911	0.238336
2	6	0	-1.300331	-0.569685	-0.223392
3	6	0	-0.023440	0.144293	-0.096181
4	6	0	0.153909	1.464923	-0.121176
5	8	0	0.974393	-0.800835	0.028511
6	8	0	2.277865	-0.181514	0.024577
7	1	0	2.519831	-0.297426	0.953085
8	1	0	-2.533913	0.816122	0.778558
9	1	0	-3.375915	-0.673859	0.083750
10	1	0	-1.248384	-1.528655	-0.722786
11	1	0	-0.703042	2.098371	-0.274497
12	1	0	1.128601	1.908518	-0.028332
Frequencies --	91.1217	140.1924	169.7015		
Frequencies --	243.2428	349.8817	408.7866		
Frequencies --	502.1832	589.5903	736.3323		
Frequencies --	745.8301	849.6965	868.4701		
Frequencies --	922.0106	964.0224	976.9689		
Frequencies --	1028.0828	1089.9308	1240.0390		
Frequencies --	1331.5374	1387.2291	1427.9310		
Frequencies --	1469.2457	1693.9399	1701.3359		
Frequencies --	3168.0011	3184.9250	3209.6562		
Frequencies --	3259.4138	3308.4327	3771.5467		

syn-cis-HPBD

1	6	0	-2.190756	-0.692912	-0.003071
2	6	0	-1.445754	0.413306	0.020214
3	6	0	0.013806	0.455029	-0.002236
4	6	0	0.721715	1.588008	-0.003222
5	8	0	0.539944	-0.815903	-0.022748
6	8	0	1.979630	-0.777544	-0.088691
7	1	0	2.195300	-1.033111	0.818326
8	1	0	-1.747752	-1.675824	-0.043861
9	1	0	-3.267941	-0.629017	0.014193
10	1	0	-1.915634	1.386564	0.056377
11	1	0	0.189628	2.524463	0.015143
12	1	0	1.795734	1.593910	-0.038780
Frequencies --	99.0342	162.6828	176.4313		
Frequencies --	230.8765	363.0424	454.0321		
Frequencies --	488.9352	579.9838	730.7037		
Frequencies --	765.9635	852.2737	856.3530		
Frequencies --	927.7028	954.1402	983.4222		
Frequencies --	1022.9381	1069.6216	1323.0288		
Frequencies --	1327.5623	1390.0403	1423.6910		
Frequencies --	1468.7354	1652.4983	1716.5707		

Frequencies --	3177.2189	3195.4080	3207.3442
Frequencies --	3269.2861	3308.8785	3767.8216

anti-trans-HPBD

1	6	0	2.069742	-0.797939	-0.201142
2	6	0	0.879834	-0.636682	0.374692
3	6	0	-0.000569	0.507687	0.128656
4	6	0	0.381169	1.765231	-0.109365
5	8	0	-1.353529	0.296846	0.281053
6	8	0	-1.705151	-0.935857	-0.435125
7	1	0	-2.223304	-1.369313	0.254952
8	1	0	2.434117	-0.099974	-0.941304
9	1	0	2.701239	-1.637326	0.047202
10	1	0	0.509155	-1.377298	1.071012
11	1	0	1.420127	2.040287	-0.035189
12	1	0	-0.352948	2.525925	-0.321141
Frequencies --	113.0745	121.3547	200.1393		
Frequencies --	249.5238	303.3254	430.7176		
Frequencies --	516.4303	557.4750	739.1487		
Frequencies --	753.9756	828.3306	876.4466		
Frequencies --	900.0855	962.3258	975.0875		
Frequencies --	1020.7666	1090.5332	1245.4733		
Frequencies --	1333.1117	1379.4282	1420.9404		
Frequencies --	1468.9497	1683.9993	1691.8021		
Frequencies --	3166.6610	3186.0957	3190.9837		
Frequencies --	3258.0684	3289.4386	3786.3994		

anti-cis-HPBD

1	6	0	2.006728	-0.206092	0.130891
2	6	0	0.923509	-0.922618	-0.169353
3	6	0	-0.450908	-0.491134	0.058825
4	6	0	-1.523980	-1.275577	-0.081242
5	8	0	-0.667196	0.774334	0.577688
6	8	0	-0.175382	1.761679	-0.392059
7	1	0	-1.017223	2.018838	-0.790669
8	1	0	1.927156	0.783354	0.553037
9	1	0	2.995465	-0.600597	-0.047377
10	1	0	1.027080	-1.910009	-0.600254
11	1	0	-1.411493	-2.313506	-0.353075
12	1	0	-2.512460	-0.893666	0.118584
Frequencies --	115.5187	151.2819	207.7804		
Frequencies --	233.2235	317.4068	424.1100		
Frequencies --	487.0421	610.5668	738.5384		
Frequencies --	765.7953	838.3784	864.7669		
Frequencies --	913.2348	962.9370	971.9975		
Frequencies --	1024.6076	1062.1145	1312.5338		
Frequencies --	1326.5261	1362.7279	1412.5634		
Frequencies --	1469.7362	1649.4072	1711.9771		
Frequencies --	3174.9533	3182.5028	3187.7437		

Frequencies -- 3272.1195 3279.5509 3769.7587

HPBD-2

cis-HPBD-2

1	6	0	2.317255	-0.082131	-0.008589
2	6	0	1.034673	0.155715	0.013236
3	6	0	-0.237919	0.453645	0.003115
4	6	0	-0.818488	1.832443	-0.002134
5	8	0	-1.267177	-0.475261	0.018225
6	8	0	-0.746161	-1.811628	-0.116279
7	1	0	2.892995	-0.185416	0.903526
8	1	0	2.857427	-0.191956	-0.941420
9	1	0	-0.020776	2.568205	0.012381
10	1	0	-1.426278	1.979665	-0.894237
11	1	0	-1.455743	1.981111	0.869162
12	1	0	-0.514049	-2.014530	0.801259

Frequencies --	123.2222	147.2663	159.6806
Frequencies --	181.9859	234.3641	289.3167
Frequencies --	436.0598	472.8574	643.6710
Frequencies --	650.5356	775.7473	923.3288
Frequencies --	930.8642	1007.2837	1039.6457
Frequencies --	1073.8875	1198.1988	1337.1285
Frequencies --	1398.8254	1417.6773	1486.2407
Frequencies --	1492.7342	1523.0317	2064.9205
Frequencies --	3058.6458	3119.5494	3122.8748
Frequencies --	3165.8351	3193.5637	3743.3575

trans-HPBD-2

1	6	0	2.520720	-0.452916	-0.134163
2	6	0	1.280534	-0.073369	-0.011105
3	6	0	0.030621	0.291993	0.127942
4	6	0	-0.518009	1.665903	-0.079347
5	8	0	-0.848147	-0.667322	0.619027
6	8	0	-1.947144	-0.805672	-0.349262
7	1	0	3.202389	-0.446108	0.706916
8	1	0	2.914244	-0.784465	-1.086628
9	1	0	0.266176	2.344762	-0.402154
10	1	0	-1.303059	1.644464	-0.832389
11	1	0	-0.953598	2.034525	0.849242
12	1	0	-1.647028	-1.598896	-0.813060

Frequencies --	81.9338	167.1076	178.1649
Frequencies --	237.5646	255.7472	321.4638
Frequencies --	421.5491	523.2995	588.0691
Frequencies --	667.1507	784.2386	839.3043
Frequencies --	913.4833	994.7043	1028.8299
Frequencies --	1073.8319	1193.2906	1308.4319
Frequencies --	1346.2114	1415.4147	1482.7656
Frequencies --	1487.5845	1514.2043	2052.0952
Frequencies --	3061.3715	3128.6071	3136.2007

Frequencies -- 3157.8898 3210.5376 3765.1591

SOZ

1	6	0	0.605263	0.119462	0.017252
2	8	0	0.045851	-0.112114	1.323349
3	8	0	-1.358215	0.169470	1.094850
4	6	0	-1.588881	-0.553473	-0.111683
5	8	0	-0.410389	-0.370511	-0.866370
6	8	0	-2.698050	-0.058363	-0.729262
7	1	0	-1.762655	-1.608381	0.091917
8	1	0	-2.508660	0.851960	-0.987028
9	6	0	0.836912	1.594589	-0.227548
10	6	0	1.804261	-0.773946	-0.074132
11	6	0	3.050189	-0.370618	-0.289551
12	1	0	1.612216	1.974167	0.433045
13	1	0	1.126337	1.762698	-1.262014
14	1	0	-0.084833	2.132415	-0.024024
15	1	0	1.573543	-1.823569	0.047834
16	1	0	3.305308	0.670396	-0.418315
17	1	0	3.858708	-1.083618	-0.347974

Frequencies --	67.8607	73.2070	205.2698
Frequencies --	247.6267	277.8925	305.3963
Frequencies --	322.7793	392.1122	414.9188
Frequencies --	474.5515	487.6597	572.6376
Frequencies --	656.9024	679.2307	724.7180
Frequencies --	818.0148	901.2113	920.3294
Frequencies --	941.6198	983.1285	990.4383
Frequencies --	1018.8756	1029.1674	1046.6565
Frequencies --	1144.5795	1177.9216	1211.4823
Frequencies --	1298.5922	1331.6679	1342.3299
Frequencies --	1345.8385	1416.4678	1454.8866
Frequencies --	1463.6620	1502.1686	1511.7156
Frequencies --	1710.9530	3076.4739	3112.6541
Frequencies --	3157.3922	3160.9413	3175.0021
Frequencies --	3196.3289	3261.8504	3797.2718

Geometry 2

1	6	0	0.583489	0.195188	-0.044411
2	8	0	-0.153576	0.277939	1.181437
3	8	0	-1.407243	0.864245	0.707581
4	6	0	-1.675214	0.053805	-0.422636
5	8	0	-0.414305	-0.211552	-0.990523
6	8	0	-2.369317	-1.097403	-0.135870
7	1	0	-2.294460	0.646443	-1.089925
8	1	0	-1.830842	-1.626561	0.463977
9	6	0	1.163029	1.535949	-0.438873
10	6	0	1.556535	-0.929945	0.141014
11	6	0	2.876527	-0.825241	0.055522
12	1	0	1.907361	1.857085	0.285356

13	1	0	1.618195	1.469085	-1.423784
14	1	0	0.363402	2.270026	-0.467536
15	1	0	1.089967	-1.882977	0.351124
16	1	0	3.367273	0.111544	-0.160607
17	1	0	3.508436	-1.689028	0.196713
Frequencies --	69.4712		74.8706		184.3687
Frequencies --	256.1995		291.1910		298.8414
Frequencies --	306.9989		359.2658		425.2914
Frequencies --	485.8813		539.9597		575.0712
Frequencies --	663.7208		674.9655		800.0369
Frequencies --	817.4105		867.3488		901.4383
Frequencies --	939.2299		966.2538		984.4719
Frequencies --	1002.5508		1024.2063		1046.1675
Frequencies --	1124.0878		1146.8876		1203.9039
Frequencies --	1294.6568		1312.1961		1321.7208
Frequencies --	1335.5380		1417.7963		1446.8489
Frequencies --	1462.5576		1502.5040		1510.9146
Frequencies --	1711.3281		3078.9022		3147.4541
Frequencies --	3158.3426		3167.3113		3175.5891
Frequencies --	3193.3870		3263.3750		3805.5868

Dioxole

1	6	0	-2.167553	0.060489	-0.004807
2	6	0	-0.683232	0.125915	-0.003925
3	6	0	0.170081	1.143757	-0.033828
4	6	0	1.554460	0.584898	0.051521
5	8	0	-0.085539	-1.098560	0.054088
6	8	0	1.362919	-0.838086	-0.081663
7	1	0	-2.525051	-0.449745	0.888636
8	1	0	-2.582146	1.063800	-0.028217
9	1	0	-2.524516	-0.494143	-0.871307
10	1	0	-0.084916	2.186780	-0.064608
11	1	0	2.044633	0.802223	1.007160
12	1	0	2.210411	0.893894	-0.764831
Frequencies --	91.1365		158.0101		224.3964
Frequencies --	328.3782		558.4446		624.7729
Frequencies --	710.0235		755.0948		830.1219
Frequencies --	928.9588		970.0706		1025.9198
Frequencies --	1037.0761		1058.7527		1078.5195
Frequencies --	1184.0051		1220.5280		1299.6887
Frequencies --	1371.3908		1425.1484		1486.1439
Frequencies --	1503.4467		1539.6591		1739.4168
Frequencies --	2995.1827		3056.1346		3064.3626
Frequencies --	3125.3228		3161.7358		3281.3841

OBD...FA + OH

1	6	0	-2.229908	2.605921	0.000000
2	6	0	-2.340609	1.278466	0.000000
3	6	0	-1.144980	0.401021	0.000000

4	6	0	-1.353939	-1.017300	0.000000
5	8	0	-0.000000	0.884653	0.000000
6	1	0	-1.252242	3.066174	0.000000
7	1	0	-3.098903	3.246071	0.000000
8	1	0	-3.309606	0.798664	0.000000
9	1	0	-2.354062	-1.422347	0.000000
10	1	0	-0.496548	-1.674922	0.000000
11	8	0	2.462717	-0.194105	0.000000
12	6	0	2.539514	-1.514397	0.000000
13	1	0	1.515209	0.101318	0.000000
14	1	0	3.586529	-1.835444	0.000000
15	8	0	1.610927	-2.290771	0.000000

Frequencies --	36.9248	49.9848	104.7519
Frequencies --	113.3620	131.9970	178.3828
Frequencies --	204.9212	314.8904	402.4129
Frequencies --	448.2982	485.4281	619.8588
Frequencies --	690.6406	727.3866	820.7788
Frequencies --	872.4641	953.1017	1014.5611
Frequencies --	1016.4360	1026.9626	1083.9120
Frequencies --	1100.0746	1224.3791	1272.9143
Frequencies --	1344.1951	1400.9060	1444.6482
Frequencies --	1455.3042	1499.7777	1615.3304
Frequencies --	1682.0530	1774.7684	3059.8447
Frequencies --	3156.9986	3170.9939	3196.7681
Frequencies --	3268.3070	3271.3896	3288.7752

References

1. C. Huang, B. Yang and F. Zhang, *J. Chem. Phys.* **150**, 164305 (2019).
2. R. L. Caravan, M. F. Vansco, K. Au, M. A. H. Khan, Y.-L. Li, F. A. F. Winiberg, K. Zuraski, Y.-H. Lin, W. Chao, N. Trongsiriwat, P. J. Walsh, D. L. Osborn, C. J. Percival, J. J.-M. Lin, D. E. Shallcross, L. Sheps, S. J. Klippenstein, C. A. Taatjes and M. I. Lester, *Proc. Natl. Acad. Sci.* **117**, 9733-9740 (2020).
3. M. Kumar, D. H. Busch, B. Subramaniam and W. H. Thompson, *Phys. Chem. Chem. Phys.* **16** (42), 22968-22973 (2014).
4. L. Vereecken, *Phys. Chem. Chem. Phys.* **19**, 28630-28640 (2017).
5. V. P. Barber, S. Pandit, A. M. Green, N. Trongsiriwat, P. J. Walsh, S. J. Klippenstein and M. I. Lester, *J. Am. Chem. Soc.* **140**, 10866-10880 (2018).
6. T. A. Burd, X. Shan and D. C. Clary, *Phys. Chem. Chem. Phys.* **20**, 25224-25234 (2018).
7. A. W. Jasper, *International Journal of Chemical Kinetics* **52**, 387-402 (2020).
8. J. K. Klassen and G. M. Nathanson, **273**, 333-335 (1996).
9. S. Miura, M. E. Tuckerman and M. L. Klein, *J. Chem. Phys.* **109**, 5290-5299 (1998).
10. D. Luckhaus, *Phys. Chem. Chem. Phys.* **12**, 8357-8361 (2010).
11. Y.-S. Wang, K.-L. Shen and S. D. Chao, *ChJPh* **55**, 719-728 (2017).
12. T. Järvinen, J. Lundell and P. Dopieralski, *Theor. Chem. Acc.* **137**, 1-8 (2018).
13. S. Gómez, Y. Oueis, A. Restrepo and A. Wasserman, *Int. J. Quantum. Chem.* **119**, 1-9 (2019).
14. N. J. Leonard, *J. Am. Chem. Soc.* **79**, 6210-6214 (1957).